Christian U. Grosse
Masayasu Ohtsu
Editors

Acoustic Emission Testing

Basics for Research – Applications in Civil Engineering

Springer

Acoustic Emission Testing

Christian U. Grosse · Masayasu Ohtsu (Eds.)

Acoustic Emission Testing

Springer

Christian U. Grosse
Department of Non-destructive Testing
and Monitoring Techniques
Material Testing Institute MPA
University of Stuttgart
Pfaffenwaldring 4
70550 Stuttgart
Germany
christian.grosse@mpa.uni-stuttgart.de

Masayasu Ohtsu
Graduate School of Science & Technology
Kumamoto University
2-39-1 Kurokami
Kumamoto 860-8555
Japan
ohtsu@gpo.kumamoto-u.ac.jp

ISBN 978-3-540-69895-1 e-ISBN 978-3-540-69972-9

DOI 10.1007/978-3-540-69972-9

Library of Congress Control Number: 2008930125

Typesetting: camera ready by the editors
Production: le-tex publishing services oHG, Leipzig, Germany
Cover design: eStudioCalamar S.L., F. Steinen-Broo, Girona, Spain

Printed on acid-free paper

9 8 7 6 5 4 3 2 1

springer.com

Preface

This book addresses one of the most interesting techniques used for the non-destructive evaluation of materials: The acoustic emission technique (AET). Compared to other non-destructive testing (NDT) methods, AET can monitor changes in materials behavior over a long time and without moving one of its components i.e. sensors. This makes the technique quite unique along with the ability to detect crack propagations occurring not only on the surface but also deep inside a material. Consequently, AET is an important addition to NDT methods surveying actively a structure by scanning for geometric defects as well as to visual inspection methods observing a materials surface.

There are many reports on successful AE applications in engineering at a broad variety of materials, material compositions and structures. Applications to many different materials are addressed in this book, but the success of these applications does not necessarily mean that the AET is easy to be applied. Depending on the degree of heterogeneity of the material and the complexity of the structure under test there could exist a variety of problems that need to be solved. The status of applications ranges from scientific/experimental to industrial/routine. A monitoring experiment or application should therefore take the experience into account that is compiled in this book. Although the setup necessary to conduct AE measurements appear to be very easy on the forehand, many issues need to be solved to obtain reliable results and to interpret them in the right way.

The introduction will give some ideas about techniques and the frame of applications addressed in this book. It will also draw boundaries to related techniques. Chap. 2 summarizes the historical backgrounds of AET and some names of the researchers being responsible for significant discoveries and improvements. Since the choice of sensors and instruments influences the quality of the recorded data, Chap. 3 is dedicated to these issues.

Due to the complexity of the material or structure and vice versa, the degree of accuracy or detailing of information should vary in different classes of AE applications. Where the number of AE phenomena in a certain time period exceeds the amount of data where full signal waveforms can be recorded or analyzed, the online extraction of data – called parameters – out of these waveforms shall still give valuable information. The parametric AE analysis techniques to be performed are described in Chap. 4. Chap. 5 summarizes basics of signal-based analysis techniques.

One of the most important features of AET is the ability to localize the source of an AE event. Following the evolution of source locations, the technique can lead to a better insight into the materials behavior under load resulting in the four-dimensional image of defect developments. Chap. 6 describes in detail most of the existing techniques and algorithms for the source localization. However, an AE signal contains much more information about the fracture process and source parameters. Therefore, the two following Chaps. 7 and 8 are dedicated to describe the mathematical and physical principles of AET. Additionally, this closed the first part of this book dealing more with the background and basic principles.

The second part is mostly addressed to the practical engineer giving after some general remarks (Chap. 9) numerous examples of AET to applications including AE in concrete (Chap. 10), rock (Chap. 11) and wood (Chap. 12). These are followed by chapters dealing with superstructures (Chap. 13) and substructures (Chap. 14). Since the use of cables limits sometimes the number of successful AE applications, Chap. 15 describes AE methods based on wireless sensor networks. Wireless techniques demand a new class of data processing procedures that are called array techniques as summarized.

Finally for applications, it is essential to be aware of the limitations and accuracy of AET as well as the necessary skills of the operators handling the equipment and analyzing the data. Chap. 16 will give an introduction to these issues.

The editors hope that the subdivision of this book into the first part dealing more with basic principles and the second with a selection of applications is useful to the reader. In some chapters, redundancies of similar problems addressed by different authors are allowed with purpose. This should demonstrate the benefits of diverse approaches to problems. The described techniques have by far not reached their full potential and the developments in the field of microelectronics and sensing techniques will certainly lead to further improvements of these methods in the next years.

The editors would like to acknowledge first of all the contributions by their colleagues acting as authors of the individual chapters. They certainly represent some of the most active and respected scientists in their field. The editors are also grateful for the help of Mrs. Anne Lehan, Mrs. Ingeborg Bathelt and Mrs. Lioba Elli-Meier that were hard working on the preparation and formatting of the manuscripts. This book would certainly not have been possible without their help. Finally are all readers encouraged to suggest corrections and additions to the editors that will be included in a future edition.

April 2008

Christian U. Grosse and Masayasu Ohtsu
(Editors)

Authors

Jürgen Eisenblätter
Gesellschaft für Materialprüfung und Geophysik mbH,
Dieselstr. 6a, 61239 Ober Mörlen, Germany
Phone: +49 6002 7971
Email: gmugmbh@t-online.de

Christian U. Grosse
Department of Non-destructive Testing and Monitoring Techniques
Material Testing Institute MPA, University of Stuttgart
Pfaffenwaldring 4, 70550 Stuttgart; Germany
Phone: + 49 (711) 685 66786
Email: christian.grosse@mpa.uni-stuttgart.de
http://www.iwb.uni-stuttgart.de/grosse/

Stefan Köppel
Benzinger und Partner, formerly ETH Zürich
Bellerivestr. 217, 8008 Zürich, Switzerland
Phone: +41 797725016
Email: s.koeppel@bp-ing.ch

Jochen H. Kurz
Fraunhofer Institute Nondestructive Testing (IZfP), University Building 37,
66123 Saarbrücken, Germany
Phone: +49 (681) 9302 3880
Email: jochen.kurz@izfp.fraunhofer.de

Eric N. Landis
Department of Civil and Environmental Engineering
University of Maine, 5711 Boardman Hall
Orono, Maine 04469, USA
Phone: +1 207 581 2170
landis@maine.edu

Lindsay M. Linzer
PO Box 91230 Auckland Park 2006 Johannesburg,
CSIR: NRE- Mining, SouthAfrica
Phone: +27 (11) 358 0261
Email: lindsay.linzer@gmail.com

Gerd Manthei
University of Applied Science Giessen Friedberg,
Wiesenstr. 14, 35390 Gießen, Germany
Phone: +49 (641) 309 2129
Email: gerd.manthei@mmew.fh-giessen.de

Masayasu Ohtsu
Graduate School of Science & Technology
Kumamoto University
2-39-1 Kurokami, Kumamoto 860-8555, Japan
phone +81 (96) 342 3542
Email: mohtsu@ethz.ch

Barbara Schechinger
Formerly ETH Zürich
Titlisstrasse 7
5022 Rombach, Switzerland
phone: +41 (62) 827 38 91
email: b.schechinger@gmx.net

Mitsuhiro Shigeishi
Associate Professor
Department of Civil & Environmental Engineering Kumamoto University
2-39-1 Kurokami, Kumamoto 860-8555, Japan
Email: shigeishi@civil.kumamoto-u.ac.jp

Tomoki Shiotani
Department of Urban Management, Kyoto University,
C-Cluster C1-2 Katsura Campus
Phone: +81 (75) 383 3261
Email: shiotani@toshi.kuciv.kyoto-u.ac.jp

Thomas Vogel
ETH Zürich, Institute für Baustatik und Konstruktionen, HIL E 33.3,
Wolfgang-Pauli-Str. 15, 8093 Zürich, Switzerland
Phone: +41 (44) 633 3134
Email: vogel@ibk.bang.ethz.ch

Table of Contents

Preface V
Authors VII

Part A Basics

1. Introduction....3
Christian U. Grosse

2. History and Fundamentals....11
Masayasu Ohtsu

3. Sensors and Instruments....19
Masayasu Ohtsu

4. Parametric AE Analysis....41
Tomoki Shiotani

5. Signal-Based AE Analysis....53
Christian U. Grosse, Lindsay M. Linzer

6. Source Localization....101
Jochen H. Kurz, Stefan Köppel, Lindsay Linzer, Barbara Schechinger, Christian U. Grosse

7. Source Mechanisms....149
Masayasu Ohtsu

8. Moment Tensor Analysis....175
Masayasu Ohtsu

Part B Applications

9. General Remarks on Applications 203
Masayasu Ohtsu

10. AE in Concrete 211
Masayasu Ohtsu

11. Acoustic Emission in Study of Rock Stability 239
Gerd Manthei, Jürgen Eisenblätter

12. AE in Wood 311
Eric N. Landis

13. Superstructures 323
Mitsuhiro Shigeishi

14. Substructures 341
Tomoki Shiotani

15. Wireless AE techniques 367
Christian U. Grosse

16. Opportunities, Limitations, Accuracy and Skill 383
Thomas Vogel, Barbara Schechinger

Synonyms and often used Abbreviations 397
Index 399

Part A
Basics

1 Introduction

Christian U. Grosse

1.1 AET in the Context of Other Techniques

AET is considered quite unique among the non-destructive testing methods, what starts with the question of whether this method should be classified as completely non-destructive or not, since fracture of the material is necessary for testing. In contrast to other NDT methods, however, AET is usually applied during loading, while most others are applied before or after loading of a structure. Following these arguments, and according to the way in which the signals are recorded, AET is correctly described as non-destructive. The statement is certainly true if a material is tested under a working load without any additional load. On the other hand, AE is often used to detect a failure at a very early stage, long before a structure completely fails.

A more dominant attribute to distinguish the different NDT techniques is addressing the way the technique is applied and sort of information that can be obtained. The ultrasound method, for example, is able to detect the geometric shape of a defect in a specimen using an artificially generated source signal and a receiver, whereas the AET detects the elastic waves radiated by a growing fracture. Therefore, the acoustic emission (AE) method should be considered to be a "passive" non-destructive technique, because it usually identifies defects only while they develop during the test. AE is often used to detect a failure at a very early stage of damage long before a structure completely fails. **Fig. 1.1** illustrates the idea behind the terms “active” and “passive” in NDT. In essence, the source emitting the waves is generally applied to the material in active methods (**Fig. 1.1**, top) using for example scanning techniques, whereas, in the passive methods, the sources are within the material (**Fig. 1.1**, bottom); they quasi “produce” the test signal. These characteristic features of the AE method result in advantages as well as disadvantages that will be addressed in the next sec-

tion. However, the nature of the signals usually being recorded should be described first in more detail.

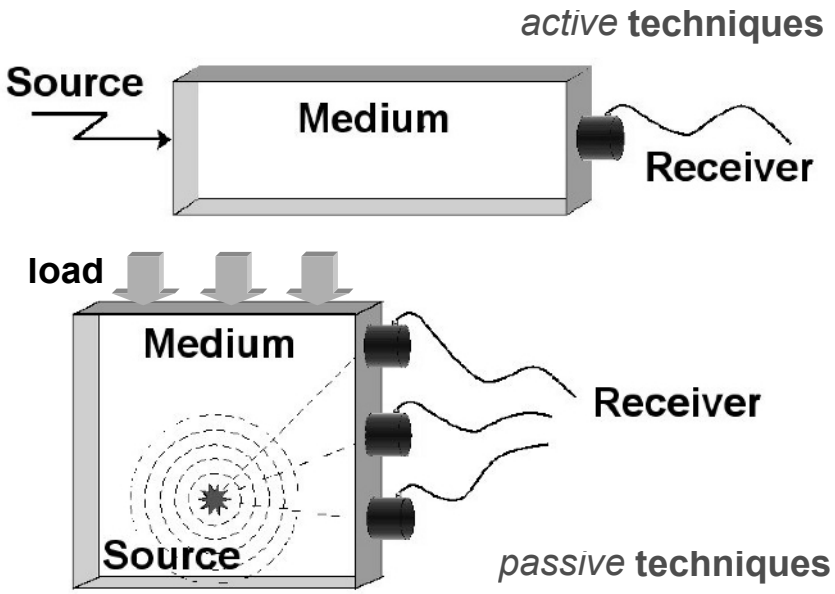

Fig. 1.1. Comparison of NDE principles using active or passive techniques.

The sources of acoustic emissions can have widely varying characteristics due to significant differences in the source signals. These differences get more pronounced using non-resonant transducers and after separating signals from noise, which can arise from artificial or natural sources with origins inside or outside the tested object. Continuous emissions, produced for instance during metal cutting or by friction in rotating bearings (Miller and McIntire 1987), show very different signal characteristics when compared to burst signals caused by the spontaneous release of energy during cracking (**Fig. 1.2**). Monitoring of continuous acoustic emissions can be used to control the operation of machines, although it is often difficult to localize the source of the emission. Most techniques used in the AET are better suited for burst signals and therefore will generally be addressed in the following chapters.

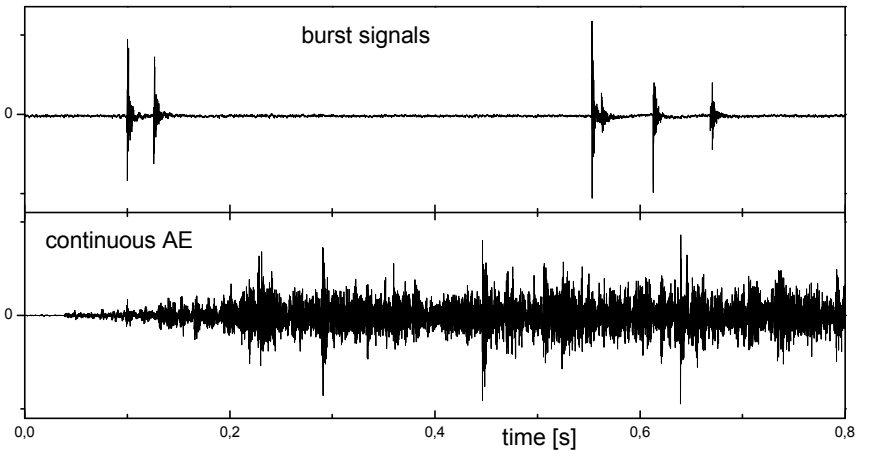

Fig. 1.2. Example of burst signals compared to a continuous emission of acoustic waves.

1.2 Advantages and Disadvantages of AET

An advantage of AE techniques, compared to other non-destructive testing techniques, is that damage processes in materials being tested can be observed during the entire load history, without any disturbance to the specimen. Ultrasonic analysis techniques, for instance, have to be applied in conjunction with scanning techniques to detect a defect. They usually require stopping the loading of a structure. In contrast, AE studies require under favorable conditions only a few sensors being able to monitor the AE activity of a structure, provided there are sufficiently strong signals to cross a threshold called trigger level. The sensors can be fixed to the surface of the specimen for the duration of the test and do not have to be moved for scanning the whole structure point by point. Access to both sides of an object, which is necessary for all through-transmission methods, is not required in AET.

The stress field in the specimen being tested is related to the applied force. When a material is stressed, the deformations are controlled by what is known as the constitutive behavior of the material. For example, some materials respond to stress linear elastically, and others behave elasto-plastically. The linear elastic stress-strain relationship is called Hooke's Law. AE however, are more strongly dependent on the irreversible (non-elastic) deformations in a material. Therefore, this method is only capable of detecting the formation of new cracks and the progression of existing

cracks or friction processes. These phenomena are often related to internal mechanical or thermal loads or pressures applied from outside the specimen. AE tests can be conducted under normal, service conditions or during a slight enhancement of the load. Therefore, it is extremely useful in testing structures under real load conditions to record a possible failure process.

A disadvantage of the AET method is that a particular test is not perfectly reproducible due to the nature of the signal source, e.g. the sudden and sometimes random formation of a crack. Although specimens of the same shape and same material properties should cause similar AE activities under load, this is not always the case. Materials with scattered inhomogeneities of a particular dimension, such as concrete, will not give similar AE results if the wavelength of the signals is of a similar size as the heterogeneities. This is one of the reasons why it is useful to compare the results of acoustic emission tests with other testing methods, for example using a visual inspection of the surface or ultrasound methods, X-Ray or RADAR.

Another point addresses the energy released by an acoustic emission. Signals – in particular those used as precursors of failure – are usually several magnitudes smaller compared to signals used in ultrasonic techniques. This requires much more sensitive sensors as well as reliable amplifiers and pre-amplifiers. Problems related to this are the influence of ambient noise, the attenuation of signals and the probably resulting low signal-to-noise ratio. It requires sophisticated data processing techniques to detect acoustic emissions, to localize them and to apply other advanced techniques or inversions.

A reliable analysis of acoustic emission signals and the interpretation of the data in material testing are usually only possible in cases where the signals have been localized successfully. Signal localization is the basis of all analysis techniques used in AE, and the various methods will be described in detail in Chap. 6. Before the localization topic is dealt with, however, a short characterization of the way acoustic emissions are recorded will be given. Knowing how signals are recorded is essential in understanding the AET in general, and also provides insights into interpreting the results.

1.3 Acoustic Emission in Context to Seismology

An earthquake is a sudden movement of the Earth's crust that generates elastic disturbances, known as seismic waves. These waves propagate spherically outwards from the source, as a result of transient stress imbal-

ances in the rock, and vibrate the ground. These vibrations can cause damage at the earth's surface, which can be correlated to the magnitude of the earthquake and the local geological conditions.

Several large magnitude earthquakes, that destroyed huge areas and caused many deaths, are well remembered in human history. The San Francisco earthquake in 1906, for example, (**Fig. 1.3**) radiated waves that were recorded as far away as Germany. The waves are physical waves and can be recorded by instruments called seismometers, which record ground motion. The recordings of ground motion as a function of time are called seismograms. An example of seismograms of the San Francisco earthquake, recorded by a seismometer in Germany, some 9100 miles (ca. 14600 km) from the earthquake source is shown in **Fig. 1.4**.

Fig. 1.3. Earthquake damage in San Francisco after the 1906 earthquake.

Acoustic emissions (AE) can be considered to be a form of microseismicity generated during the failure process as materials are loaded. AE is defined as the spontaneous release of localized strain energy in stressed material. This energy release can be due to, for example, microcracking in the material and can be recorded by transducers (sensors) on the material's surface. This is the reason why AET are so similar compared to seismological techniques – they basically address the same concept but at a different scale. Far-field seismology investigates earthquakes in a distance of thousands of kilometers, near-field seismology in distances of several hundred kilometers. Acoustic emission techniques are usually applied for source-receiver distances of up to several tenth meters, but specimen can also be much smaller down to even millimeters. However, applications in the

range in between the given distances (i.e. 10 to 100 meters) are sometimes called micro-seismology and sometimes large-scale acoustic emission analysis. It is simple to see the similarities of these techniques based on signal interpretations looking at the earthquake recording in **Fig. 1.4** and comparing it to acoustic emission recordings in the following chapters of this book. The basic difference concerns the scale of the time axis.

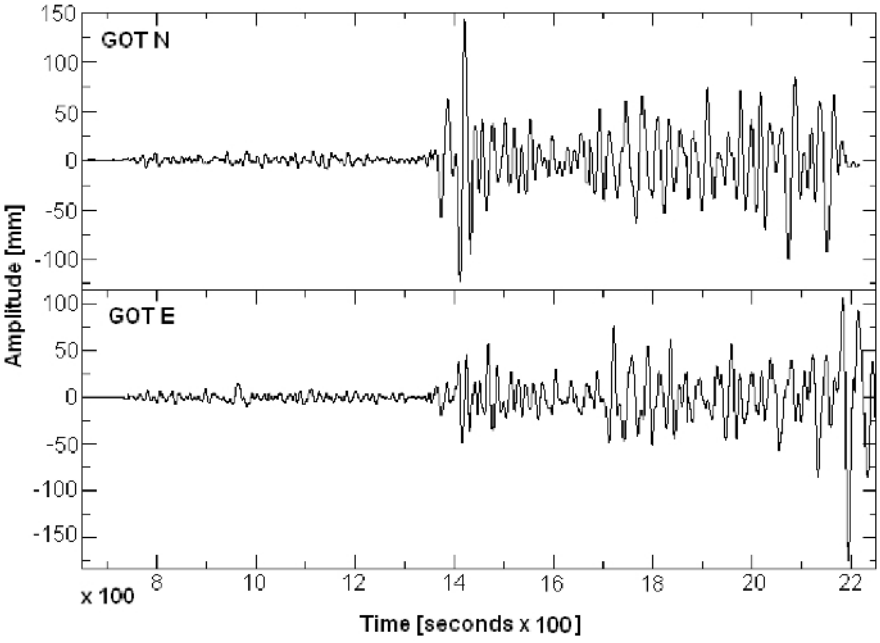

Fig. 1.4. Seismograms of the 1906 San Francisco earthquake recorded in Göttingen, Germany, some 9100 miles away from the earthquake source; (top) NS components, (bottom) EW component (from Wald et al. 1993).

Seismological data are usually analyzed on the basis of their full waveform or of a significant part of this (in **Fig. 1.4** are only the first 22 seconds shown). In acoustic emission this was not always the case and is probably still not the case for many applications. Historically speaking, former recording techniques based on very basic electronic components were simply not able to handle the large amount of high frequency data. This led to the workaround to extract parameters out of the waveforms that were afterwards not recorded what means they were not converted from analog to digital data. The parameter-based approach will be described in detail later. Some successful parameter-based AET applications used to study for example cementitious materials can be found in the literature (McCabe,

Koerner et al. 1976; Notter 1982; Feineis 1982; Reinhardt and Hordijk 1989; Kapphahn 1990; Sklarczyk, Gries et al. 1990). Some authors began in the late 1980's and in the early 1990's with the theoretical development of quantitative techniques based on waveform analysis (Scruby 1985; Sachse and Kim 1987; Ono 1993). A point motivating these developments was the interconnection between AE and seismology. Seismological techniques were adapted for example for civil engineering by some authors (Ohtsu 1982, 1994; Ouyang et al. 1991; Ohtsu et al. 1991; Maji and Sahu 1994; Maji 1995). Ono and Ohtsu have been probably some of the first scientists transferring earthquake data processing techniques to AE data processing. The basic for these advances are developments in microelectronics and in computer-based analysis techniques. AE is usually dealing with high signal rates and events at relatively high frequencies (from 20 kHz up to several megahertz). Recording and analysis devices need powerful techniques to handle these data. It is remarkable that even sophisticated techniques such as the three dimensional localization of events, the moment tensor inversion or wavelet techniques are nowadays routinely applied in the AE environment and it is expected that other methods will stimulate further developments.

New developments raise new problems. However, the demands on the equipment are still very high. This is particularly true concerning the sensor technology. Resonant transducers are increasingly replaced by sensors with broader frequency characteristics. Issues of flat response, sensitivity and calibration have to be addressed more carefully in the future. Other sensor techniques that are currently discussed in the field of AE applications (e.g. in structural health monitoring) use network techniques, wireless communication and Micro-Electro-Mechanical Systems (MEMS). These promising ideas ensure that the acoustic emission technology will be a field of interesting future developments and applications.

References

Feineis N (1982) Anwendung der Schallemissionsanalyse (SEA) als zerstörungsfreies Prüfverfahren für Beton. Thesis, Universität Darmstadt, p 59

Kapphahn G, Quade J, Steffens K (1993) SEA-Prüfung bei der in-Situ - Traglastermittlung von Stahl- und Spannbetonkonstruktionen. Vorträge und Plakatberichte 37 (1), Garmisch-Partenkirchen, DGZfP, pp 506-513

Maji AK, Sahu R. (1994) Acoustic emissions from reinforced concrete. Exper. Mech. 51:379-388

McCabe WM, Koerner RM, Lord AE (1976) Acoustic emission behavior of concrete laboratory specimens. ACI J. 73:367-371

Miller RK, McIntire P (eds) (1987) Acoustic emission testing. Nondestructive testing handbook, Vol. 5. American Society for Nondestructive Testing. 2. Edition, p 603

Notter R (1982) Schallemissionsanalyse für Beton im dehnungsgesteuerten Zugversuch. Thesis, ETH Zürich, Switzerland, p 215

Ohtsu M (1994) New trends in non-destructive and in-place testing of concrete structures. Aguado A, Gettu R, Shah, SP (eds) Proc. Concrete Technology: New Trends, Industrial Applications. London, E&FN Spon

Ohtsu M (1982) Theoretical treatment of acoustic emission and source mechanisms in concrete. Mem. Fac. Eng. 27:1-21

Ohtsu M, Shigeishi M, Iwase H, Koyanagi W (1991) Determination of crack location, type and orientation in concrete structures by acoustic emission. Mag. Conc. Res. 155:127-134

Ono K (1993) Trends of recent acoustic emission literature. J. of Ac. Emission 12:177-198

Ouyang C, Landis, EN, Shah, SP (1991) Damage assessment in concrete using quantitative acoustic emission. J. Eng. Mech. 117:2681-2697

Reinhardt HW, Hordijk DA (1989) Cracking and Damage. Mazars J, Bazant ZP (eds.) Elsevier, London, pp 3-14

Sachse W, Kim KY (1987) Quantitative acoustic emission and failure mechanics of composite materials. Ultrasonics 25:195-203

Sklarczyk C, Gries H, Waschkies E (1990) Testing during concrete construction. Reinhardt HW (ed.), Chapman and Hall, London, pp 297-208

2 History and Fundamentals

Masayasu Ohtsu

2.1 Introduction

It is realized that AE technology began to be investigated in the middle of the 20th Century. Two historical articles have been already published (Drouillard 1979) and (Drouillard 1987). Drouillard also reported a comprehensive summary on AE history (1996). Referring to these publications, founders and historical topics on AE are briefly stated. Since AE history is closely associated with development of measuring devices, fundamentals of the measurement are additionally stated.

2.2 Discovery of AE

We can often listen to noises of fracture or breaking sounds in materials. In the large scale, sensible and audible phenomena associated with generation of elastic waves are known as earthquakes and rock-bursts in mines. In metallurgy, the first AE phenomenon was considered to be an audible tin-cry, which is produced by twinning of pure tin during plastic deformation. Martensite transformation in steel is also accompanied by audible noises. Other AE phenomenon is creaking of timber prior to break. Related to this phenomenon, the oldest and the first report on a scientifically planned AE experiment was found (Drouillard 1990), which was delivered by F. Kishinoue on November 21, 1933 at a meeting of the Earthquake Research Institute in the University of Tokyo (Imperial University of Tokyo). The article was published in 1934 as shown in **Fig. 2.1**, which was translated into English by K. Ono and published in the Journal of Acoustic Emission (Kishinoue 1990). The process of shock occurrence in a wood specimen under flexural stress was studied. The apparatus for the experiment is shown in **Fig. 2.2**. It consisted of a phonograph pick-up using a steel

needle inserted into the tension side of a wooden beam under bending stress. The electrical current was recorded with an oscillograph. As bending proceeded, cracking sounds were heard, while the oscillograms recorded many inaudible vibrations.

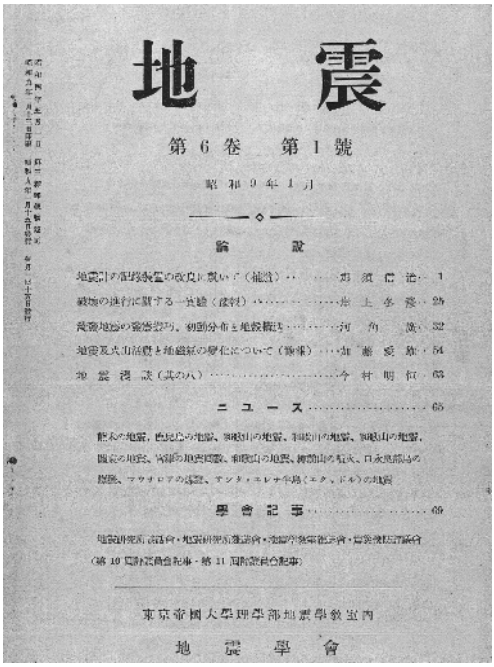
地　震

第 6 卷　第 1 號

昭和 9 年 1 月

論　說

地震計の記録装置の改良に就いて（補遺）……　和　田　雄　治　1

破壊の進行に關する一實驗（豫報）……　寺　田　寅　彦　25

震源地點の震度分布。初動分布と地殻構造……　河　角　廣　32

地震及火山活動と地殻變化について（豫報）……　坪　井　忠　二　64

地震雜錄（其の八）……　今　村　明　恒　68

ニ　ュ　ー　ス……　65

鹿本の地震、色尼古の地震、羽根田の地震、羽根田の地震、羽根田の地震、
臨海の地震、宮崎の地震調査、羽根田の地震、御前山の噴火、日永星附近の
震動、マヤロアの噴火、マンタ・エレナ半島（エクヽドル）の地震

學會記事……　69

地震研究所、高層台・地震研究所遠望台・地震学教室地震台・震災豫防評議会
（第 10 回評議會記事・第 11 回評議員會記事）

東京帝國大學理學部地震學教室內

地　震　學　會

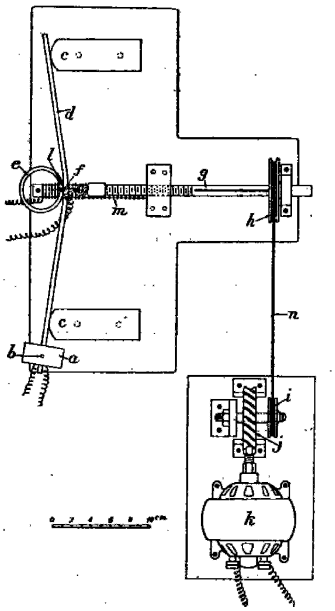

第　4　圖

Fig. 2.1. Top page of "Jisin" report in 1933.

Fig. 2.2. Experimental apparatus by Kishinoue.

In Germany, early AE experiments were performed by F. Förster in **Fig. 2.3** (Förster & Scheil 1936). Measuring extremely small voltage changes due to resistance variations, AE phenomena caused by martensite transformations could be detected in a wire-shaped nickel-steel specimen. This was because they had built an electro-dynamic transmitter/receiver system to transform mechanical vibrations into electrical voltages.

In the geological field, micro-seismic activity, which was identical to AE phenomenon, had been studied. L. Obert in **Fig. 2.4** reported the discovery of micro-seismic emissions in rock (Obert 1977). In 1938, he was conducting seismic velocity tests in the lead-zinc mines of northern Oklahoma. Throughout the test, spurious signals kept triggering the interval time between two geophones. After eliminating possible equipment defects, eventually he discovered that the triggering was caused by self-generated sig-

nals in the rock. Then, he clarified that micro-seismic activity could be detected in controlled experiments of rocks (Obert & Duvall 1945).

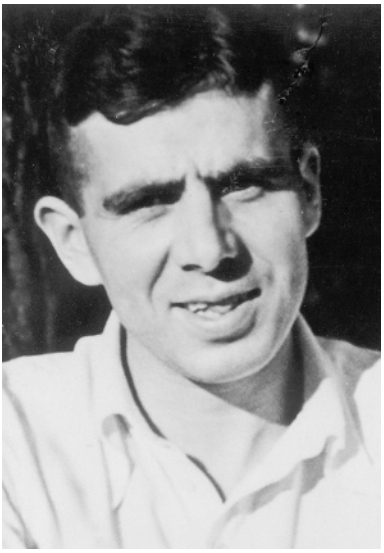

Fig. 2.3. Photo of Friedrich Förster.

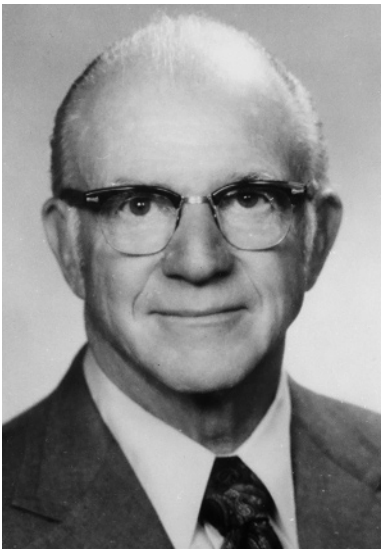

Fig. 2.4. Photo of Leonard A. Obert.

2.3 Founders and Terminology

It has been often quoted that AE history started in 1950 with publication of Kaiser's dissertation (Kaiser 1950). J. Kaiser in **Fig. 2.5** tested tensile specimens of metallic materials, recording AE signals. He discovered a famous irreversibility, which is now called the Kaiser effect. B.H. Schofield in **Fig. 2.6** found Kaiser's article in USA and reexamined it. He published his pioneering work as entitled "Acoustic Emission" (Schofielde 1961). This is the first use of the terminology of AE in history.

2.4 AE in Concrete Engineering

Tracing back to 1960's, three papers were well known in concrete technology. Interestingly it was reported that Ruesch had known J. Kaiser in the institute. So, he studied the noise emitted during application of compressive load in concrete [1959]. This has been known as one of the first stu-

dies on the Kaiser effect in engineering materials. He found that the Kaiser effect was observed up to around 75% load level of failure load, and reported that generating behavior of AE signals was closely related with the volumetric change and the absorption on ultrasonic waves.

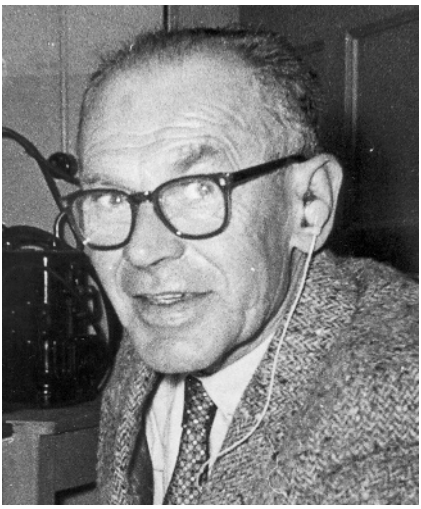

Fig. 2.5. Photo of Joseh Kaiser.

Fig. 2.6. Photo of Bradford H. Schofield.

Under compressive load in concrete, the relation among the decrease in ultrasonic velocity, active AE generation above 75% of the failure load, and the increase in Poisson's ratio was summarized by L'Hermite [1960]. His experimental results are given in **Fig. 2.7**. Following AE activities observed, both Poisson's ratio and axial strain start to increase, while the wave velocity in concrete decreases. Robinson further compared AE behaviors with X-Ray observation [1965].

These historical findings in concrete led to one misleading episode, which attracted a kind of attention in Japan. Based on high AE activity over 75% of the failure load, the concept of "genuine strength of concrete" was proposed by H. Yokomichi of Hokkaido University [1964]. He attempted to describe that the stress level at the onset of AE activity at 75% of the failure load was closely related with the characteristic strengths of concrete, such as the fatigue strength and the strength of creep failure. Unfortunately, one journalist misinterpreted his concept, and erroneously reported in a newspaper that accidental failure of concrete structures might occur due to a bad design based on the "non-genuine" strength. Temporari-

ly, this article brought about extensive and widespread debates on the genuine strength of the concrete in Japan.

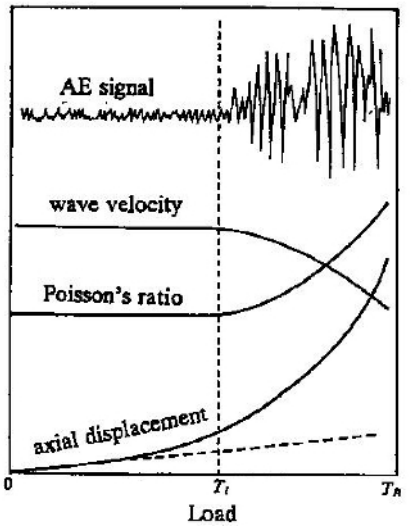

Fig. 2.7. Experimental results by L'Hermite.

2.5 Development of AE Techniques

Following Schofield's study, A. T. Green and H. L. Dunegan were known to develope standard procedures and devices (Drouillard 1996). In relation to the micro-seismic activity, H. R. Hardy, Jr. organized and held the series of five Conferences on Acoustic Emission/Microseismic Activity in Geologic Structures and Materials [1974, 1978, 1981, 1985 and 1991]. These obviously contributed to the development of AE techniques in geological fields.

In the USA, the Acoustic Emission Working Group (AEWG) was conceived in 1967 by J. C. Spanner. Since then, the meeting has kept held and the 49th meeting was held in 2006. The Japanese Committee on AE was founded in 1969. Since 1980 the committee has been organized as an *ad hoc* technical committee in the Japanese Society for Nondestructive Inspection (JSNDI). The International Acoustic Emission Symposia (IAES) were inaugurated in 1972 and has been biennially held in Japan. In 2006, the 18th IAES was held. In Europe, research activity on AE led to the Eu-

ropean Working Group on AE (EWGAE). The first meeting was held in 1972, and in 2006, the 27th meeting was held.

Professor K. Ono at University of California, Los Angeles has been editing the Journal of AE, based on the exponentially increasing number of papers. The first issue was published in 1982. Since then, the journal has kept providing the state of the art on AE researches. In addition, the Nondestructive Testing Handbook, Vol. 5: Acoustic Emission Testing [1987] introduced methods along with sections of the physical properties of AE testing, signal recording and applications.

2.6 Fundamentals of AE Measurement

F. Kishinoue already made comments on the problems with background or environmental noises. Care was needed during the experiment. This was because detection of AE signals was affected by vibrations from a string wind, passers-by and a truck passing on a nearby street. Many of these problems have been eliminated with development of instrumentation systems. In updated equipments, the frequency range of the measurement is normally set above that of audio and environmental noises, which are substantially minimized by grounding the equipments. Owing to advances of measuring systems, the use of a band-pass filter effectively eliminates background noises and allow meaningful tests under usual laboratory environments.

Physically, failure takes place due to the release of stored strain energy, nucleating cracks and generating elastic waves. Elastic waves due to crack nucleation are detected as AE waves, which propagate inside concrete and are detected by an AE sensor on the surface. Although recent AE devices are fully digitized, detection systems are basically of analog type.

A typical AE detection system commercially available is illustrates in **Fig. 2.8**. AE waves are detected by AE sensor, which converts dynamic motions at the surface of a material into electrical signals. Because AE signals are weak, they are normally amplified by two amplifiers of a preamplifier and a main amplifier. The signal-to-noise ratio of equipments shall be low, and the amplifiers often provide more than 1000 times gain. Lately, it is set to normally 100 times or so. As discussed above, the band-pass filter is successfully employed to eliminate the noises. In engineering materials, the band width from several kHz to several 100 kHz or 1 MHz is recommended in the measurement.

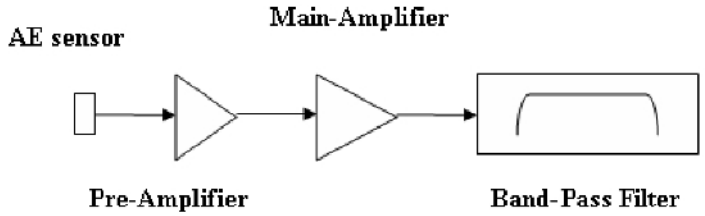

Fig. 2.8. AE detection system.

2.7 Concluding Remarks

Fracture sounds (sonic waves in air) must be original AE phenomena. These are acoustic and audible. In the definition nowadays, AE waves are not sonic waves, but elastic waves in a solid. The frequency range of the waves could cover the inaudible range over the audible range (acoustic or lower than 20 kHz). The sonic waves higher than the audible range are defined as ultrasonic waves. Rigorously speaking, AE waves are neither ultrasonic nor acoustic.

Based on the historical development, AE technique is now in the practical stage. Rationally in the case of cracking sources, AE waves are elastic waves due to dislocation motions (discontinuity of displacements as cracking) in a solid. As a result, they consist of P-wave (longitudinal wave or volumetric), S-wave (transverse wave or shear), and such other interfacial waves as surface waves (Rayleigh wave and Love wave), reflected waves, diffracted waves and guided waves (Lamb wave and other plate waves). The latter portion of AE waveform, in addition, often is associated with resonance vibration of AE sensor, which turns wave motions into electrical signals. Consequently, it is noted that AE waveforms and waveform parameters are not completely associated with generating mechanisms, but mostly responsible for the effects of travel paths, media and detection systems.

References

Drouillard TF (1979) Acoustic emission: A bibliography with abstracts. ed. Laner FJ, New York: Plenum Publ., 806 p

Drouillard TF (1987) Introduction to acoustic emission technology. Nondestructive Testing Handbook, eds. Miller RK and McIntire P, ASNT, Vol. 5:1-10

Drouillard TF (1990) Anecdotal history of acoustic emission from wood. Journal of AE 9(3): 155-176

Drouillard TF (1996) A history of acoustic emission. Journal of AE 14(1): 1-34

Förster F, Scheil E (1936) Akustische Untersuchung der Bildung von Martensitnadeln (Acoustic Study of the Formation of Martensile Needels). Zeitschrift für Metallkunde 28(9): 245-247

Kaiser J (1950) A study of acoustic phenomena in tensile tests. Dr.-Ing. dissertation, Technical University of Munich

Kishinoue F (1990) An experiment on the progression of fracture (A preliminary report). Jisin 6:24-31(1934) translated and published by Ono K, Journal of AE 9(3): 177-180

L'Hermite RG (1960) Volume change of concrete. Proc. 4th Int. Symp. Chemistry of Cement, V-3, NBS Monograph 43: 659-694

Nondestructive Testing Handbook, Vol. 5: Acoustic Emission Testing (1987) Miller RK & McIntire P (eds.), American Soc. for Nondestructive Testing

Obert L and Duvall W (1945) The microseismic method of predicting rock failure in underground mining, Part II: Laboratory Experiments. Report of Investigations 3803, U. S. Bureau of Mines, Washington D. C.

Obert L (1977) The microseismic method: Discovery and early history. Proc. 1st Conference on AE/MS. In: Hardy Jr., Leighton F.W. (Eds) Geologic Structures and Materials. Trans Tech Publication, Clausthal, Germany

Proc. 1st(1974). 2nd(1978). 3rd(1981). 4th(1985). and 5th (1991) Conferences on AE/MS in Geologic Structures and Materials, Trans Tech Publication, Clausthal, Germany

Robinson GS (1965) Methods of detecting the formation and propagation of microcracks in concrete. Proc. Int. Conf. On the Structure of Concrete and Its Behavior under Load. Cement and Concrete Association, pp 131-145

Ruesch H. (1959) Physical problems in the testing of concrete. Zement Kalk-Gips 12(1): 1-9

Schofield BH (1961) Acoustic emission under applied stress. Report ARL-150, Lessels and Associates, Boston

Yokomichi H, Ikeda I and Matsuoka K (1964) Elastic wave propagation due to cracking of concrete. Cement Concrete Japan 212: 2-6

3 Sensor and Instrument

Masayasu Ohtsu

3.1 Introduction

Fracture in a material takes place with the release of stored strain energy, which is consumed by nucleating new external surfaces (cracks) and emitting elastic waves, which are defined as AE waves. The elastic waves propagate inside a material and are detected by an AE sensor. Except for contactless sensors, AE sensors are directly attached on the surface as shown in **Fig. 3.1**.

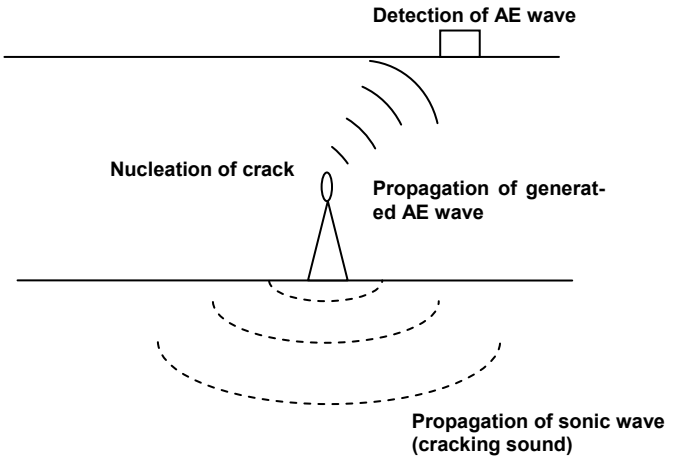

Fig. 3.1. Detection of AE wave.

A contact type of the sensor is normally employed in AE measurement, and is commercially available. In the most cases, a piezoelectric element in a protective housing (Beattie 1983) as illustrated in **Fig. 3.2** is applied to detection. Thus the sensors are exclusively based on the piezoelectric ef-

fect out of lead zirconate titanate (PZT).

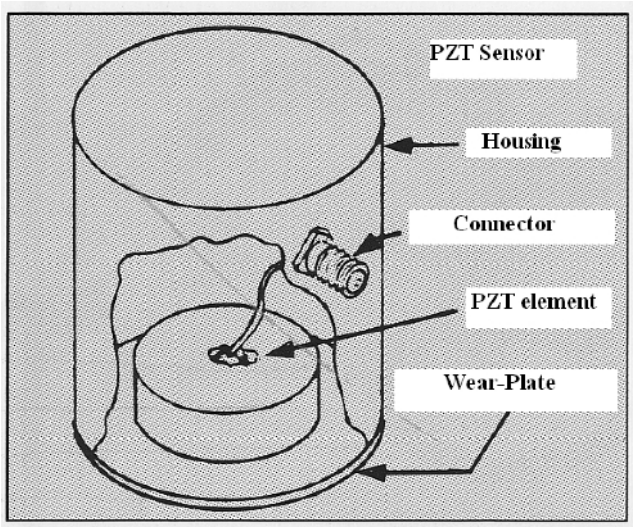

Fig. 3.2. AE sensor of the piezoelectric element.

For a specialized purpose of sensor calibration, a capacitive sensor (transducer) is developed (Breckenridge 1982). Compared with other types of AE sensors, it is well known that piezoelectric sensors provide the best combination of low cost, high sensitivity, ease of handling and selective frequency responses. Although PZT sensors are not normally suited for broad-band detection in basic studies of AE waveform analysis, they are practically useful for most AE experiments and applications.

3.2 Sensor and System Response

AE signals are detected, as dynamic motions at the surface of a material are converted into electric signals. Then the electrical signals are amplified and filtered. Mathematically, the system response is formulated by a linear system in **Fig. 3.3**. Here, input function $f(t)$ of surface motions is transformed into function $g(t)$ of electric signals by transfer function $L[\ ]$ of AE sensor. This system is mathematically represented,

$$g(t) = L\left[f(t) \right] \; g(t) = L\left[f(t) \right]. \tag{3.1}$$

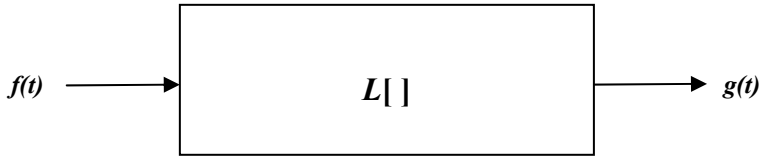

Fig. 3.3. A linear system.

Here, the convolution integral is defined as an integration of two functions *f(t)* and *w(t),*

$$s(t) = \int f(t-\tau) w(\tau) \, d\tau = f(t) * w(t). \tag{3.2}$$

The symbol * represents the convolution. Then Dirac's delta function $\delta(t)$ plays an important role. From the definition, it is expressed,

$$f(t) * \delta(t). \; f(t) * \delta(t). \tag{3.3}$$

In the case of the linear system, Eq. 3.1 becomes,

$$g(t) = L\left[f(t) * \delta(t) \right] = f(t) * L\left[\delta(t) \right].$$
$$g(t) = L\left[f(t) * \delta(t) \right] = f(t) * L\left[\delta(t) \right].$$

Setting $L[\delta(t)]$ as *w(t),* we have,

$$g(t) = f(t) * w(t). \; g(t) = f(t) * w(t). \tag{3.4}$$

This implies that the sensor response *g(t)* is obtained from the convolution of the input *f(t)* with the impulse response of the system *w(t),* because the function $L[\delta(t)]$ is the response of the system due to the input of the delta function. Introducing the Fourier transform,

$$G(f) = \int g(t)\exp(-j2\pi ft)\,dt = \iint f(t-\tau)\,w(\tau)\,d\tau\exp(-j2\pi ft)\,dt,$$
$$G(f) = \int g(t)\exp(-j2\pi ft)\,dt = \iint f(t-\tau)\,w(\tau)\,d\tau\exp(-j2\pi ft)\,dt,$$

and setting $t-\tau = s$

$$\begin{aligned} G(f) &= \int f(s)\exp(-j2\pi fs)\,ds\int w(\tau)\exp(-j2pf\tau)\,d\tau \\ &= F(t)W(t) \\ G(f) &= \int f(s)\exp(-j2\pi fs)\,ds\int w(\tau)\exp(-j2pf\tau)\,d\tau \\ &= F(t)W(t) \end{aligned} \tag{3.5}$$

Here *G(f), F(f)* and *W(f)* are Fourier transforms of *g(t), f(t)* and *w(t),* respectively. *w(t)* and *W(f)* are named the transfer function and the function of frequency response. A calibration of AE sensor is equivalent to determination of function *W(f)*. On the other hand, it implies that frequency contents of AE waves are usually smeared by function *W(f)* of AE sensor. Thus, the absolute calibration means quantitative estimation of function *w(t)* or *W(f)*.

The signals measured using AE sensor are of small magnitude compared to other methods. As a result, AE signals obtained by the sensors are very weak and have to be so amplified as to be detected and recorded. All of these influences can be assigned by different transfer functions. Consequently, AE signal *a(t)* recorded in the system illustrated in **Fig. 2.8** are mathematically represented as,

$$\begin{aligned} a(t) &= w_f(t) * w_a(t) * w(t) * f(t), \\ a(t) &= w_f(t) * w_a(t) * w(t) * f(t), \end{aligned} \tag{3.6}$$

where $w_f(t)$ and $w_a(t)$ are transfer functions of the filter and the amplifiers. For characterizing AE sources theoretically, it is so important to know the weights of these functions as to eliminate their influences. In usual cases, the frequency responses of both the filter $w_f(f)$ and the amplifier $w_a(f)$ are known to be fairly flat or almost constant in the frequency domain. As a

result, it is found that the frequency response or the transfer function *W(f)* or *w(t)* of AE sensor significantly affects the frequency contents of AE signals.

3.3 Response of PZT Sensor

In the case of piezoelectric or PZT sensors, the sensors are usually operated in resonance, i. e. the signals are recorded in a small frequency range due to the frequency characteristics of the sensor to enhance the detection of AE signals. Very damped sensors are operated outside their resonance frequencies allowing a broadband detection, although they are usually less sensitive to wave motions.

So far various analyses of PZT sensors have been performed. These can be classified into two groups. One employed equivalent electric circuit (Mason 1958) and the other applied solutions of the field equations (Auld 1973). These are based on one-dimensional analysis, and thus results can not be readily extended to three-dimensional (3-D) analysis. This is because the PZT element used in an AE sensor is neither an infinite bar nor an infinite plate.

A few solutions exist for 3-D PZT bodies. Most well-known solutions for finite PZT plates were obtained from approximated two-dimensional (2-D) equations of extended Mindlin's solutions (Herrmann 1974). But, these solutions are not directly applicable to the analysis of AE sensors commercially available. In order to clarify the frequency response of AE sensor (function *W(f)* in eq. 3.5) and to optimize the design of PZT elements, resonance characteristics of PZT element were analyzed by using the finite element method (FEM) (Ohtsu & Ono 1983).

Electro-mechanical vibrations of PZT bodies can be solved in a similar manner to the corresponding mechanical vibration problem, but with additional variables. The constitutive laws of PZT materials are represented, as follow (Holland & EerNisse 1969) and (Kawabata 1973),

$$\{\varepsilon\} = [C]\{\sigma\} + [d]^T \{E\}, \tag{3.7}$$

$$\{D\} = [d]\{\sigma\} + [p] \{E\}. \tag{3.8}$$

Here {ε}are the elastic strains, {σ}are the stresses, {E} are the electric potentials and {D} are the electric displacements. [C] represents the adiabatic elastic compliance tensor at constant electric filed, [d] is the adiabatic piezoelectric tensor and [p] is the adiabatic electric permittivity at constant stress. From these constitutive equations, it is readily known that the piezoelectric element generates electric signals due to mechanical motions and vice versa.

As analytical results, three PZT-5A elements were analyzed by the FEM, of which material properties were known. These are a cylindrical element of 9.53 mm diameter and 12.19 mm height, a disk-shaped element of 9.53 mm diameter and 1.45 mm height, and a truncated conical element of 6 mm base-diameter, 1 mm truncated end-diameter and 2.5 mm height.

Nominal resonance frequencies are calculated from Eqs. 3.7 and 3.8 as a cylindrical bar and a disk-shaped solid. So, resonances of shear, radial and compression modes are calculated without taking into account the boundary conditions. These are denoted in **Table 3.1**.

In the FEM analysis, axi-symmetric models were analyzed. In order to investigate the coupling effect between the sensor and the medium, two cases of stress-free boundary (free vibration) and fixed boundary at the contact surface were analyzed to determine resonance frequencies and modes.

Table 3.1. Resonance frequencies of PZT elements

Shape	Free vibration (kHz)			Fixed boundary (kHz)		
	Nominal	FEM analysis	Experiment	Nominal	FEM analysis	Experiment
Cylindrical element	71 (shear)	109	133	71 (shear)	61	42
	160 (comp.)	196		160 (comp.)	167	152
	201 (radial)	207	210	201 (radial)	191	204
		217	251		245	
		298	312		316	
Disk-shaped element			42			
		116	91		382	291
			146			516
	201 (radial)	206	166		766	720
		322	231		1219	
		541	536	1343 (comp.)	1476	
	597 (shear)	581			2245	
Conical element		80	66		404	404
		262	278			500
		414	494			570
		567	713		803	766

774	878
	1099
	1874

In **Table 3.1**, resonance frequencies obtained are denoted as compatible to nominal resonances as possible. In the cases of the cylindrical and disk-shaped elements, the resonance frequencies are obtained as in reasonable agreement with nominal resonances of the shear and the radial for free vibration, while the nominal resonance of the compression seems to be analyzed for fixed boundary.

Resonance vibration modes of the conical element for the case of free vibration and of fixed boundary are shown in **Fig. 3.4**. To show the vibration modes clearly, scales of displacements are highly exaggerated. In all the cases, simple modes of the vibration envisaged in the nominal modes are not observed. When the bottom boundary is constrained in motions, the resonance frequencies are shifted to the higher range. In addition, the vibration modes change from a bending mode to a mixture of shear and compression. Thus, the resonance frequencies appear as different modes from the nominal modes, because a PZT element vibrates three-dimensionally. As illustrated in **Fig. 3.2**, a PZT element is fixed in a housing case. So, the case of fixed boundary might be of possible resonance mode in the sensor.

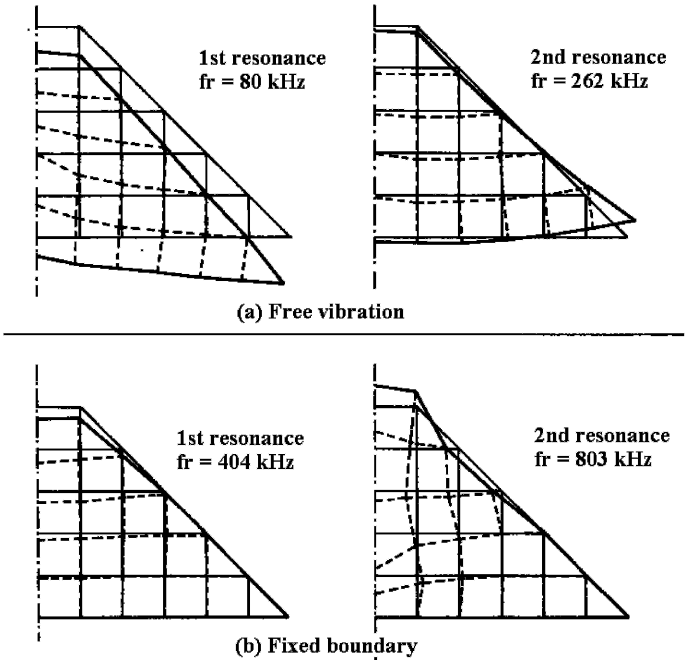

Fig. 3.4. Resonance vibration modes of the conical element.

In order to evaluate the resonance frequencies analyzed, experiments were conducted by employing a block diagram in **Fig. 3.5**. For free vibration, a PZT-5A element was placed on a steel block of dimensions 570 mm x 130 mm x 180 mm without bonding to the block. Sweeping sinusoidal input from DC to 2 MHz was supplied by a function generator to a broad-band sensor (FC500 model, AET), which was coupled to the same surface of the block as a transmitter in the figure. The input voltage was kept constant during a sweeping time of about 50 sec., but it was adjusted to obtain enough output voltage for recording. The output voltage of the PZT-5A element was amplified as 80 dB in total and filtered with the band-pass from 30 kHz to 2 MHz.

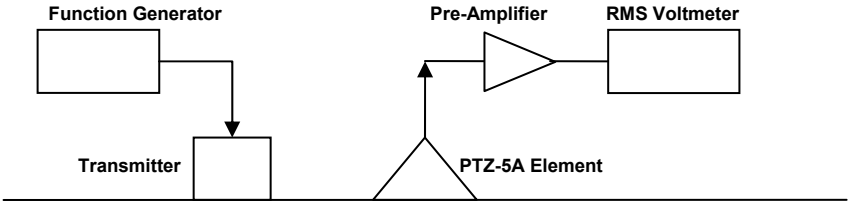

Fig. 3.5. Experimental set-up for frequency responses of PZT elements.

The root-mean-square (RMS) voltage output was recorded. In the case of fixed boundary, the PZT-5A element was bonded with wax. Results of the conical element are shown in **Fig. 3.6**. In the case of free vibration, more than ten peak frequencies are found from 66 kHz to 2 MHz. The main effect of the steel block is to confine the peak frequencies to the 400 to 600 kHz range. A strong peak is observed at around 500 kHz both in the free vibration and after bonding to the steel block.

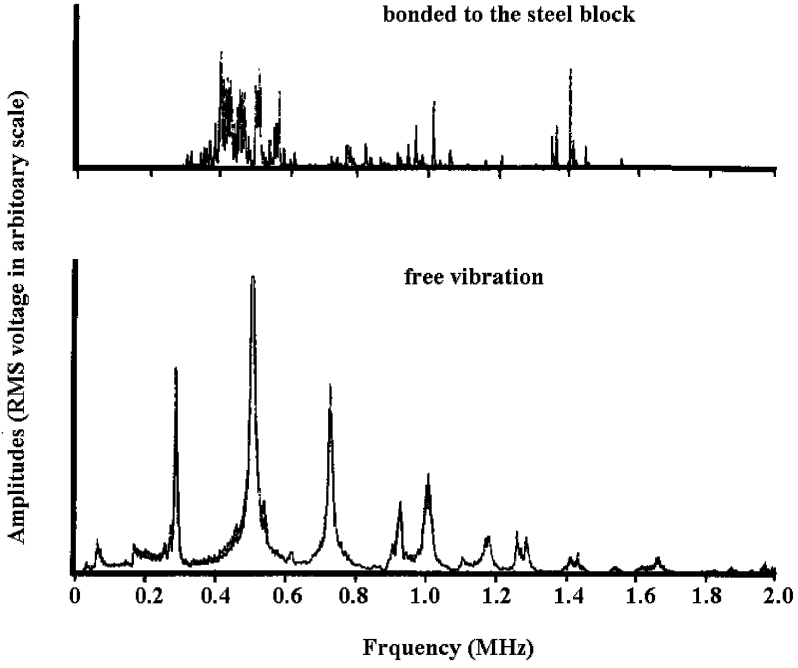

Fig. 3.6. Frequency responses of the conical element.

All the major peak or resonance frequencies obtained are also listed and compared with the nominal resonances and the resonances by the FEM analysis in **Table 3.1**. Generally speaking, the peak frequencies determined by three different methods are in reasonable agreement. In the case of the nominal resonance frequencies, no boundary conditions are assigned. The values of resonances are listed as possible corresponding values. In the cylindrical element, the effect of fixed boundary is minor, because the small area at the bottom is only constraint. It is noted that the resonance frequency lower than the compression mode is obtained in the case of fixed boundary, which is close to the resonance of the shear mode. In the disk-shaped element, lower resonance frequencies than that of the radial mode is obtained in both the FEM analysis and the experiment in the case of free vibration. These disapper in the case of fixed boundary, where the resonance frequency corresponds to the compression mode obtained in the FEM analysis. In the conical element, higher resonance frequencies are obtained in the case of fixed boundary. According to **Fig. 3.6**, the responses of these resonance frequencies are fairly weak.

A NIST (National Institute for Standards and Technology, USA) conical transducer developed (Proctor 1982) has been known as a reference sensor of flat response. Because the sensor consists of a conical element of 1.5 mm truncated-end in diameter bonded to a brass cylinder as illustrated in **Fig. 3.7**. Comparing with the frequency spectrum in the bonded case in **Fig. 3.6**, it should have fairly weak peak frequencies in the low frequency range from 100 kHz to 1 MHz and could be of low sensitivity.

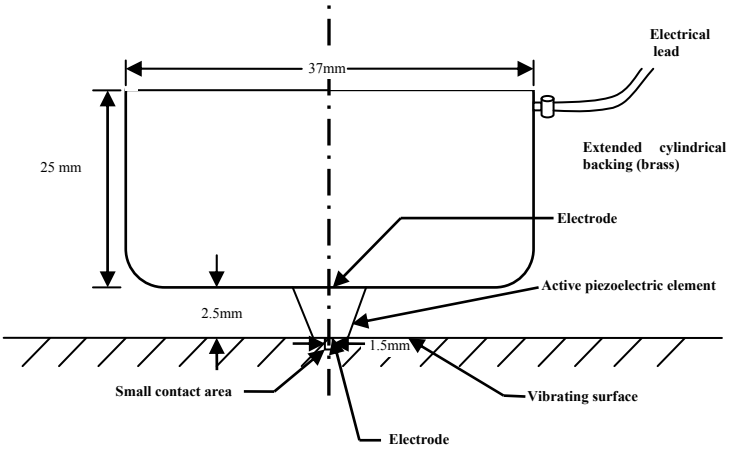

Fig. 3.7. Sketch of NIST conical transducer.

3.4 Calibration and Detection

A typical AE sensor of PZT element transforms elastic motions of 1 pm displacement into electrical signals of 1 μV voltage. As an example, frequency responses of AE sensors commercially available are given in **Fig. 3.8**.

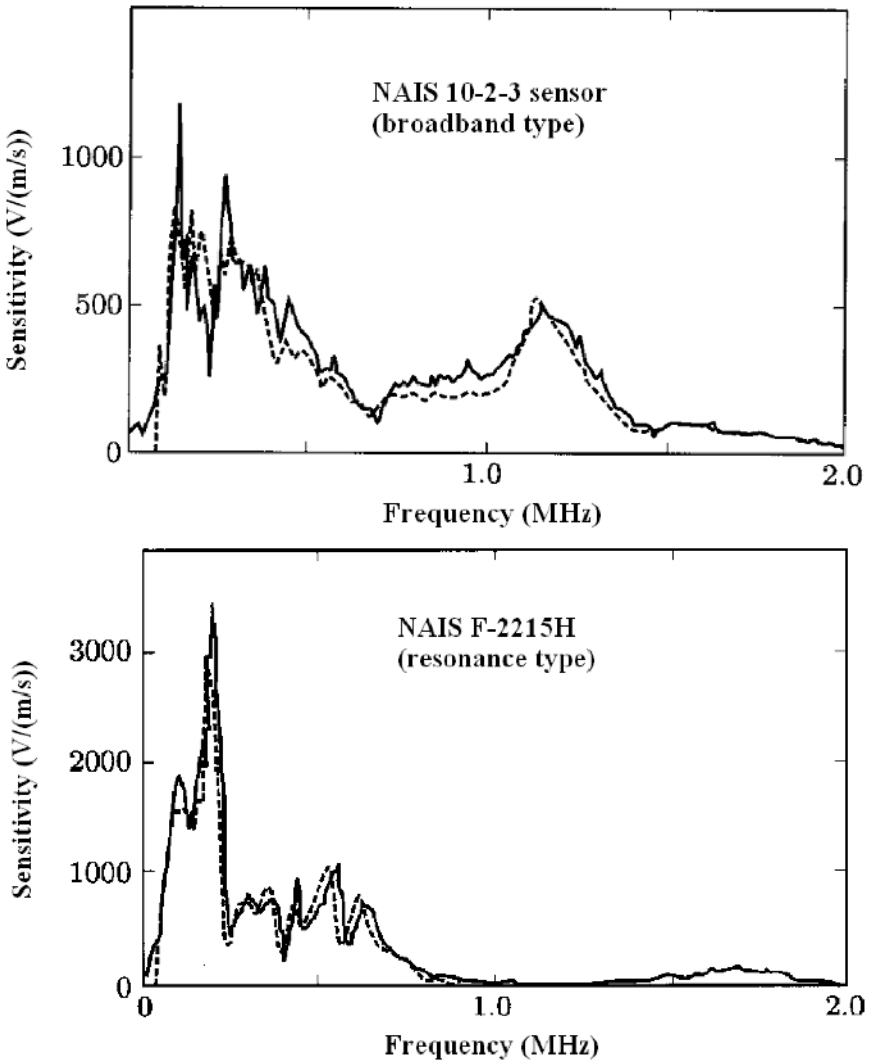

Fig. 3.8. Calibration curves of frequency responses of commercial AE sensors.

The top figure shows the response of a broadband sensor and the bottom is that of a resonance type. Although both sensors respond irregularly, the sensitivity of the broadband type is lower than that of the resonance type. This fact is so general that selection of AE sensors should be based on either the sensitivity (resonance type) or the flat response in frequency (broadband type). In any case where AE waves are detected by AE sensor, frequency contents are smeared by the transfer function *W(f)* of the sensor as discussed in Eq. 3.6.

When the sensor cannot directly be attached to the structure, waveguides as illustrated in **Fig. 3.9** are employed. It is noted that the use of waveguides introduces further complexity to frequency contents of AE waves.

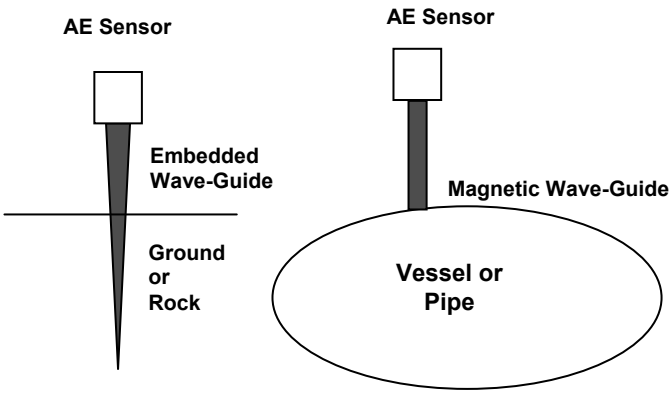

Fig. 3.9. Examples of AE wave-guides.

The responses in **Fig. 3.8** are calibrated results by two methods of the sensor calibration. One is a calibration method by NIST, as illustrated in **Fig. 3.10** (Breckenridge 1982). A large steel block of 90 cm diameter and 43 cm deep was employed. As a step-function impulse, a glass capillary source was employed, and elastic waves were detected by a capacitive transducer and by a sensor under test. The calibration curve was obtained as a ratio of the response of the sensor to that of the capacitive transducer. The capacitive transducer (sensor) could record a Lamb's solution due to surface pulse as discussed in Chapter 7. It is reasonably assumed that the capacitive transducer detect the vertical displacement at the surface due to a step-function force. The other is known as a reciprocity method, which Hatano and Watanabe (Hatano & Watanabe 1997) suggested to use, and confirmed an agreement with the NIST methods. As seen in **Fig. 3.8**, it is demonstrated that both method can provide similar calibration curves.

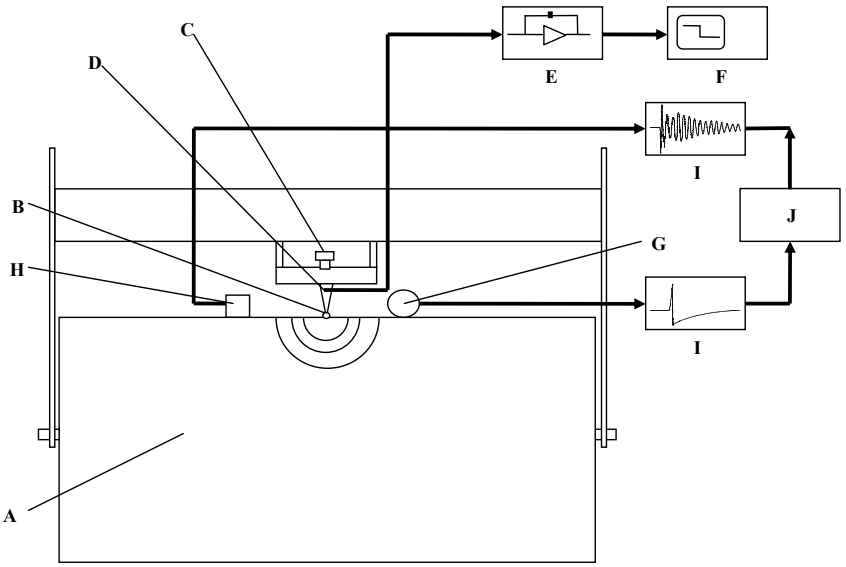

Schematic diagram of a apparatus:
A. Steel transfer block; B. Capillary source;
C. Loading screw; D. PZT disc; E. Charge amplifier;
F. Storage oscilloscope; G. Standard transducer;
H. Transducer under test; I. Transient recorders;
J. Computer

Fig. 3.10. Experimental set-up for the absolute calibration of AE sensor by NIST.

In the absolute calibration proposed by NIST, the capacitive transducer was employed. This is because the transducer could detect displacements motions without unnecessary distortion. Recently, a laser vibrometer is also available as a displacement-meter, although its sensitivity is as low as the capacitive transducer. In the NIST procedure, a standard source was generated by a capillary break and later by a pencil-lead break (Hsu & Breckenridge 1981) as a step-function. They compared detected displacement motions with Lamb's solution of the surface pulse (Pekeris 1955). A numerical program to compute Lamb's solutions was published before (Ohtsu & Ono 1984). By employing this program, surface motions due to steel-ball drop were numerically computed. The laser vibrometer is usually applied to detect velocity motions. So, velocity motions of numerical re-

sults were compared with those detected by the laser vibrometer. Results are shown in **Fig. 3.11**. According to Sansalone & Streett [1997], contact time *Tc* of steel-ball drop is given by

$$Tc = 0.0043D, \tag{3.9}$$

where *D* is the radius of the steel ball. The time function *S(t)* of steel-ball drop is assumed as,

$$S(t) = \cos^4\left(\frac{\pi}{2Tc}t - \frac{\pi}{2}\right). \; S(t) = \cos^4\left(\frac{\pi}{2Tc}t - \frac{\pi}{2}\right). \tag{3.10}$$

In this case, the upper-bound frequency *fc* is given by,

$$fc = 1.25 / Tc \;\; fc = 1.25 / Tc \tag{3.11}$$

In **Fig. 3.11**, velocity motion detected by the laser vibrometer is shown at the middle and that of Lamb's solution is shown at the bottom. Remarkable agreement is confirmed except the latter reflections in the detected wave. Because a concrete block was employed in the experiment, these reflected motions are observed. At the top, frequency spectrum of the detected wave is shown as a solid curve and is compared with that of Lamb's solution denoted by a broken curve. Reasonable agreement is again confirmed. This result suggests an application of the laser vibrometer for the absolute calibration instead of the capacitive transducer.

As shown in **Fig. 3.8**, sensitivity of AE sensor is often expressed in voltage output per vertical velocity (1V/(m/s)). In another way, the face-to-face technique has been conventionally applied to estimate the sensitivity based on voltage output per unit pressure input (1V/mbar). The broadband sensor is employed as a reference. Some examples are given in **Fig. 3.12**.

For the PZT sensors, contactless measurement is an exception in AE measurement. Coupling between sensors and a member is important due to the low amplitudes of AE signals. Besides the different means of coupling, various methods exist for fixing the sensors to the structure. Adhesives or gluey coupling materials and couplant like wax or grease are often used due to their low impedance. If the structure has a metallic surface, magnetic or immersion techniques are widely used. Different methods using a spring or rapid cement can be used. In general, the coupling should reduce the loss of signal energy and should have a low acoustic impedance compared to the material to be tested.

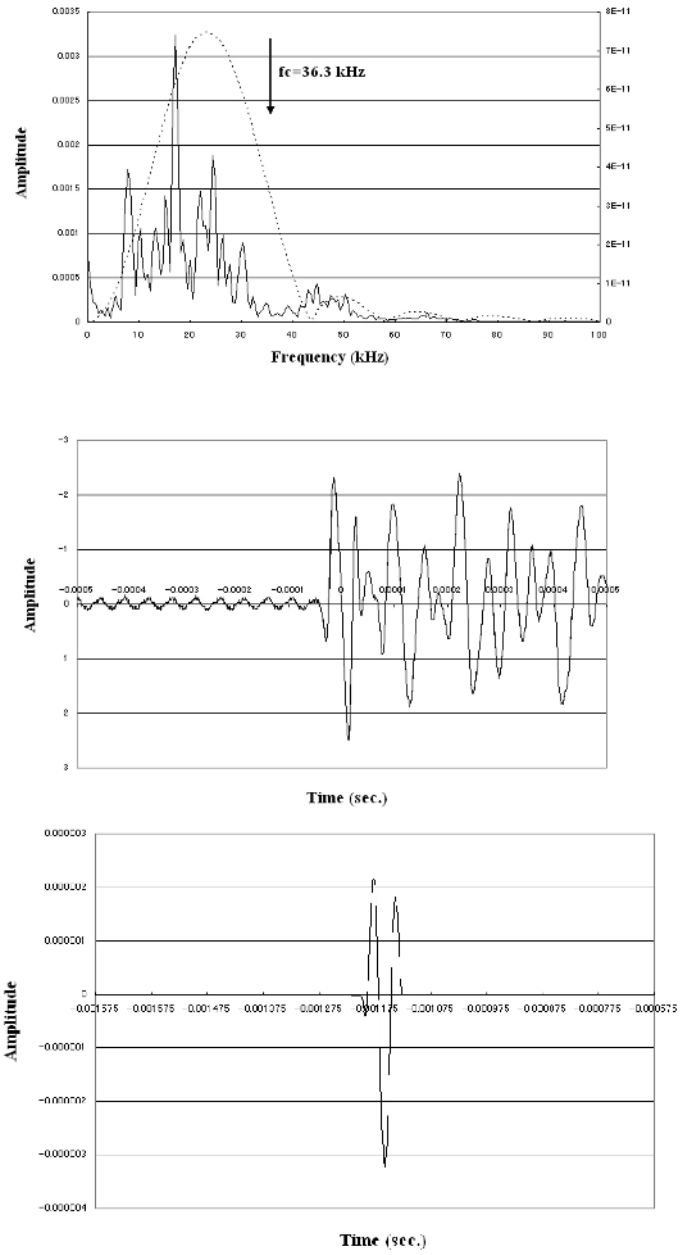

Fig. 3.11. Lamb's solutions of velocity motions detected (middle) and calculated (bottom), and their frequency spectra (top).

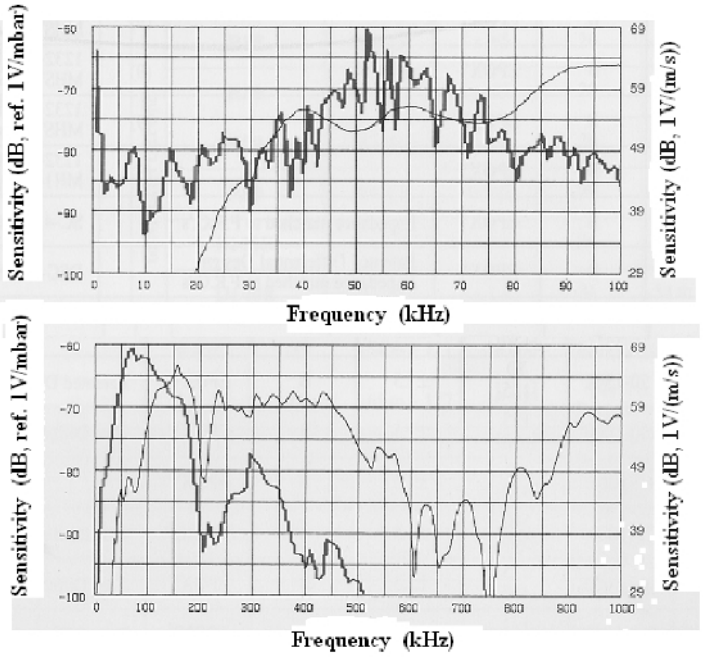

Fig. 3.12. Calibration curves of AE sensors.

An essential requirement in mounting a sensor is sufficient acoustic-coupling between the sensor's surface and the structure surface. The sensor's surface shall be smooth and clean, allowing for maximum couplant adhesion. Application of a couplant layer should be thin, so it can fill gaps caused by surface roughness and eliminate air gaps to ensure good acoustic transmission. Commonly used couplants are vacuum greases, water-soluble glycols, solvent-soluble resins, and proprietary ultrasonic couplants.

In addition to coupling, the sensor must always be stationary. One way to achieve this is to use glue, which can also serve as a couplant. Before using a glue, the ease and technique of removal should be taken into care, since not all sensors can withstand a large removal force between the housing and the mounting face (wear plate). To prevent attenuation it is recommended to avoid air bubbles and thick glue layers. Another way to help a sensor stationary is to use a holding devices such as tapes, elastic bands, springs, magnetic hold-downs, and other special fixtures. It is important that any mechanical mount does not make electrical contact between the sensor case and the structure. Accordingly, grounding the case is often ne-

cessary.

3.5 Other Types of Sensors

Besides PZT sensors, new types of sensors are under development. As discussed before, the laser system has been applied for AE detection. It is a contactless measurement but less sensitive than the PZT sensors. Consequently, it has been applied to AE phenomena of large amplitudes. An example is illustrated in **Fig. 3.13** (Nishinoiri & Enoki 2004). PZT sensors have a limitation in application at elevated temperature, because PZT has Curie point. The laser system is applied to AE measurement in ceramics under firing. This is because cracking under firing of structural ceramics causes a serious problem for fabrication. Cracks are generated in heating, sintering or cooling, so that AE monitoring was applied to optimize firing conditions.

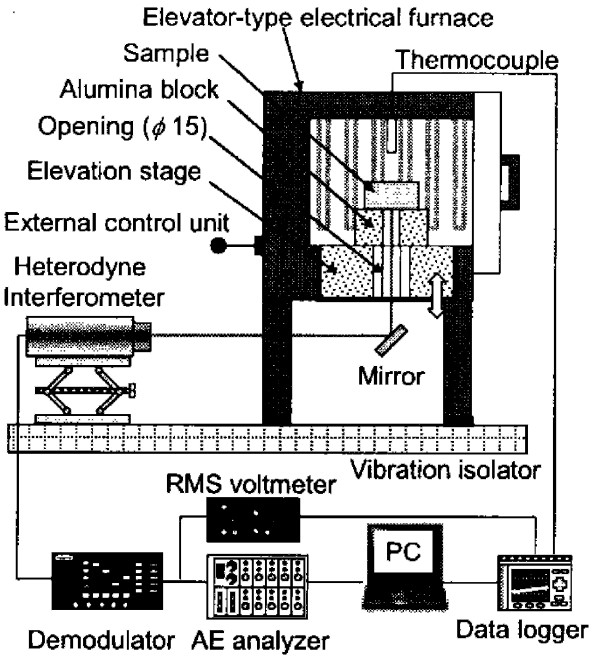

Fig. 3.13. Laser AE system at high temperature.

An optical fiber sensor is a new and an attractive AE sensor as alternative to the PZT sensor. It can offer a number of advantages such as the long-term monitoring, the condition free from electro-magnetic noises, and the use of corrosive and elevated environments. One example applied to a pipe structure is illustrated in **Fig. 3.14** (Cho, Arai et al. 2004). According to their results, the sensitivity depends on the number of fiber winding, and is still 10 times lower than a conventional PZT sensor.

It is noted that physical quantity of measured AE signals is not confirmed yet. It is expected that radial displacement motions could be associated with AE signals detected.

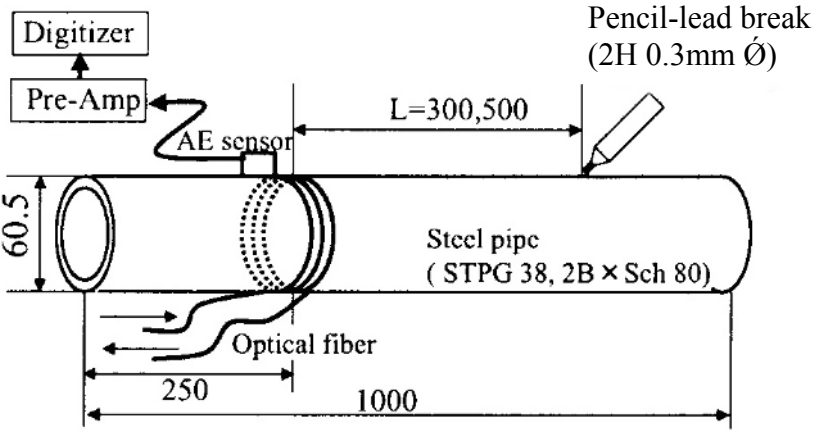

Fig. 3.14. Fiber-optic AE sensor for a pipe structure.

3.6 Instrument

AE sensors transform surface motions into electric signals. Thus, the amplifiers are usually employed to magnify AE signals. Because cables from the sensor to the amplifier are subjected to electro-magnetic noise, specially coated cables of short length shall be used. Preamplifiers with sate-of-the-art transistors should be used to minimize the amount of electronic noise. Amplifiers with a flat response in the frequency range are best use.

AE signals are normally amplified both by a pre-amplifier and by a main-amplifier, and are filtered. The gain of the amplifier is given in dB (decibels), which means the ratio between input voltage V_i and output voltage V_o as,

$$dB = 20\log_{10}\left(V_0/V_i\right).\ dB = 20\log_{10}\left(V_0/V_i\right). \tag{3. 12}$$

In concrete and rocks, the signals are usually amplified 60 dB to 100 dB in total to be detected.

A filter of variable band-width between 1 kHz and 2 MHz is generally employed. The choice of the frequency range depends on noise level and attenuation property of concrete. As given in **Fig. 3.15**, it is noted that the use of the band-pass filter drastically changes AE signals as the time records.

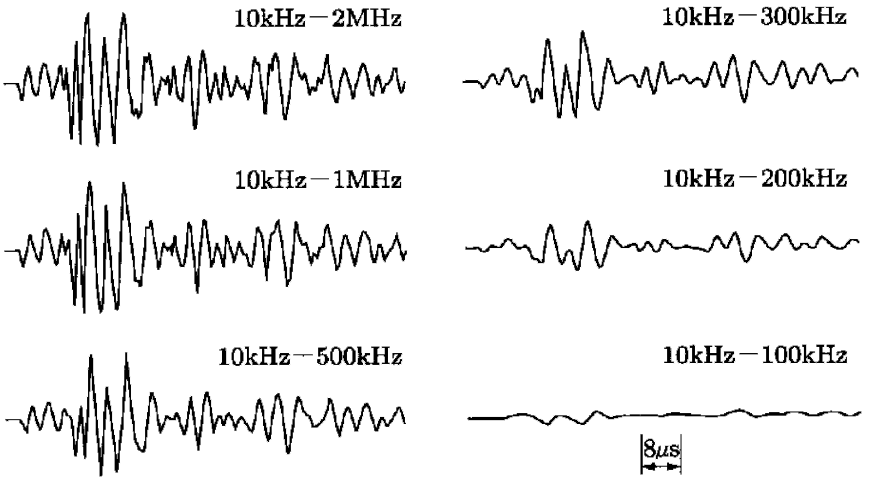

Fig. 3.15. Effect of the band-pass filter on AE waveforms.

The attenuation of elastic waves is quantitatively represented by Q value. When the wave with energy level E is attenuated by ΔE over one-wavelength propagation, Q is defined as,

$$Q = 2\pi E/\Delta E\ \ Q = 2\pi E/\Delta E \tag{3.13}$$

In the case of a pure elastic material, $\Delta E = 0$ and Q = infinite. The larger Q is, the lower the attenuation is. Q is larger than 1000 for typical metals, while Q is reported as lower than 100 in concrete [Ohtsu 1987]. When AE waves propagate for distance D, the amplitude $U(f)$ of frequency components f attenuates from U_0 to,

$$U(f) = U_0 \exp(-\pi fD/vQ). U(f) = U_0 \exp(-\pi fD/vQ). \quad (3.14)$$

Substituting frequency f = 1 MHz, distance D = 1 m, velocity of P-wave v = 4000 m/s, and Q = 100, the attenuation $U(f)/U_0$ becomes –68 dB/m. Thus, the higher frequency components are, the more quickly they attenuate.

3.7 Data Acquisition and Wave Parameters

Main concern for data acquisition results from the A/D(analog to digital) conversion and the triggering. Fast A/D units have to be used to ensure that a large number of events are recorded. Usually, the A/D converter is equipped for each channel of the recording unit. Anti-aliasing filters are required so that the signals can be properly transformed to the frequency domain. A sketch of AE instrument is shown in **Fig. 3.16**. Signal data are mostly digitized by employing a personal computer system.

A monitoring system can analyze such parameters as count, hit, event, rise time, duration, peak amplitude, energy, RMS (root mean square) voltage, frequency spectrum, and arrival-time difference as discussed in Chapter 4. Normally AE signals are processed after the amplitude becomes larger than the threshold level.

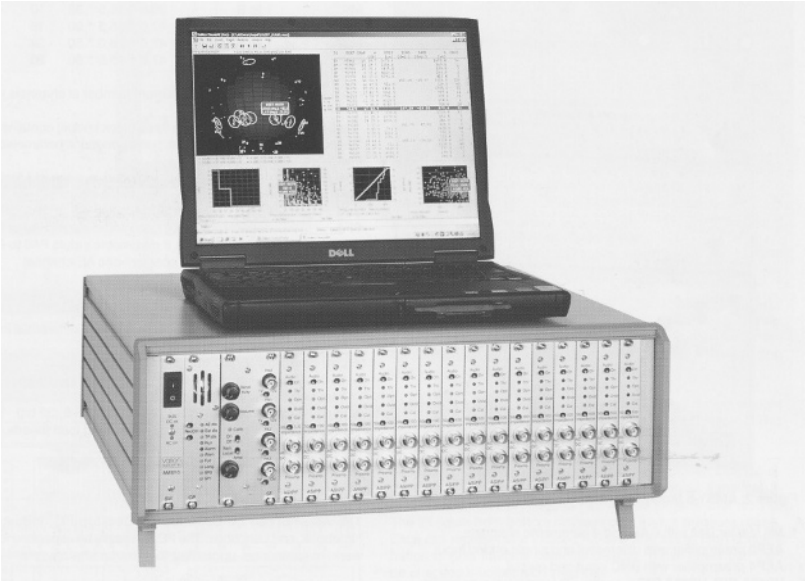

Fig. 3.16 AE instrument.

3.8 Concluding Remarks

Sensors and AE equipments are already commercially available. In this concern, important aspects are to select proper devices and systems. Depending upon materials and structures, selection of sensors, decision of frequency range, techniques to eliminate noises and conditions for system setting may change. Some of standardized procedures and requirements for systems are stated in chapters dealing with applications.

References

Auld BA (1973) Acoustic fields and waves in solids. John Wiley & Sons, New York

Beatttie AG (1983) Acoustic emission, principles and Instrumentation. J. Acoustic Emission 2(1/2): 95-128

Breckenridge FR (1982) Acoustic emission transducer calibration by means of the seismic surface pulse. J. Acoustic Emission 1(2): 87-94

Cho H, Arai Y, Takemoto M (2004) Development of stabilized and high sensitive optical fiber acoustic emission system and its application. Progress in AE XII:43-48, JSNDI

Hatano H, Watanabe T (1997) Reciprocity calibration of acoustic emission transducers in Rayleigh wave and longitudinal wave sound field. J. Acoust Soc. Am. 101(3): 1450-1455

Herrmann G (1974) R.D. Mindlin and applied mechanics. Pergamon Press, New York

Holland R, EerNisse EP (1969) Design of resonance piezoelectric devices. Research Monograph 56, MIT Press, Cambridge

Hsu N.N., Breckenridge F.R (1981) Characterization and calibration of acoustic emission sensors. Materials Evaluation 39: 60-68

Kawabata A (1973) Ultrasonic piezoelectric sensors and their application. J. Soc. Materials Science Japan 22(232): 96-101

Mason WP (1958) Physical acoustic and properties of solids. D van Nodtrand Company, Princeton

Nishinoiri S, Enoki M (2004) Development of in-situ monitoring system for sintering of ceramics using laser AE technique. Progress in AE XII:69-76, JSNDI

Ohtsu M, Ono K (1983) Resonance analysis of piezoelectric transducer Elements. J. Acoustic Emission 2(4): 247-260

Ohtsu M, Ono K (1984) A generalized theory of acoustic emission and Green's functions in a half space. J. Acoustic Emission 3(1): 124-133

Ohtsu M (1987) Acoustic emission characteristics in concrete and diagnostic applications. J. Acoiustic Emission 6(2): 99-108

Perkeris CL (1955) The seismic surface pulse. Proc. Natl. Acad. Sci. 41: 469-480

Proctor TM (1982) Some details on the NBS conical transducer. J. Acoustic Emission 1(3): 173-178

Sansalone MJ, Streett WB (1997) Impact-Echo. NY Burier Press, Ithaca

4 Parameter Analysis

Tomoki Shiotani

4.1 Introduction

Final goal of monitoring AE phenomena is to provide beneficial information to prevent fatal fracture, by correlating detected AE signals with growing fracture process or deterioration. AE activity is observed transiently or unexpectedly, and the signals generally contain higher frequency components over the audible range as well as a variety of durations. A signal triggering is conventionally made by setting threshold. In the case of trigger-monitoring, only the signals, of which amplitudes exceed the threshold levels, are recognized as AE signals. In the early age of AE measurement, the performance of transient waveform-recorders was so poor in the early age of AE monitoring as that parametric features of the waveforms were normally employed for evaluating AE characteristics. These are hit, amplitude, counts, duration and so forth.

Currently, as rapid progress of computer technology, AE waveforms can be recorded readily as well as the parametric features. Thus, such waveform-based features as peak frequency and frequency centroid are additionally determined in real time from the fast Fourier transform (FFT) of recorded waveforms. AE parametric features are thus extracted and provide good information to correlate the failure behavior of materials.

4.2 Identification of AE Signal

Different from detected waves in ultrasonic or vibration tests, AE signals emerge rapidly and randomly. As a result, the discrimination of AE signals from running waves is the first step for analyzing AE activity. To this end, the voltage threshold of AE wave, which is equivalent to a voltage level on an electronic comparator, is set. Then, the signals which exceed the vol-

tage threshold are identified as AE signals. Termination of the AE signal or the duration is determined as the period when the signal does not exceed the voltage threshold. Conventionally, the duration is defined by users and set as a constant time (e.g. hit-lockout time or dead time). It is noted that the above-mentioned protocol for identifying AE signals has been developed for extracting parametric AE features in analog.

In the case of digital recording, the condition is slightly different due to the capacity of data storage. Normally the start time to record the waveform is the same as the parametric feature extraction by means of the voltage threshold. The length or duration of a waveform to be recorded is determined independently by users. In practice, users shall determine the both of sampling rate and total number of samples in addition to the voltage threshold. For example, the waveform length of 1024 microseconds is set up as 1 MHz sampling rate in 1024 samples. The duration of recorded waveforms is identical to that of parametric feature.

4.3 AE Signal Parameters

4.3.1 Conventional/Classical Parameters

The electrical signal identified as an AE signal is generated by fracture phenomena. Therefore characteristics of AE parameters have been studied to infer fracture or physical phenomena. In what follows, signal parameters most widely used are explained from definitions (ISO 12716 2001).

1. Hit: a signal that exceeds the threshold and causes a system channel to accumulate data. It is frequently used to show the AE activity with counted number for a period (rate) or accumulated numbers. In **Fig. 4.1**, one waveform correspond one "hit".
2. Count/ring-down count/emission count: the number of times within the duration, where one signal (waveform) exceeds a present threshold. In **Fig. 4.1**, nine counts are observed. "Count" is also employed to quantify the AE activity as well as "hit". It is noted that "counts" depend strongly on the employed threshold and the operating frequency. Sometimes, counts between the triggering time over the threshold and the peak amplitude is referred to as "Counts to Peak", which is equal to four in **Fig. 4.1**.
3. Amplitude: a peak voltage of the signal waveform is usually assigned. Amplitudes are expressed on a decibel scale instead of linear scale

where 1μV at the sensor is defined as 0 dB AE. The amplitude is closely related to the magnitude of source event. As mentioned the AE signals are detected on the basis of the voltage threshold, the amplitude is also important parameter to determine the system's detectability. Generally the detected amplitude shall be understood as the value does not represent the emission-source but the sensor response after losing the energy due to propagation. The magnitude of amplitude in each signal has been often analyzed in relation with frequency distribution.

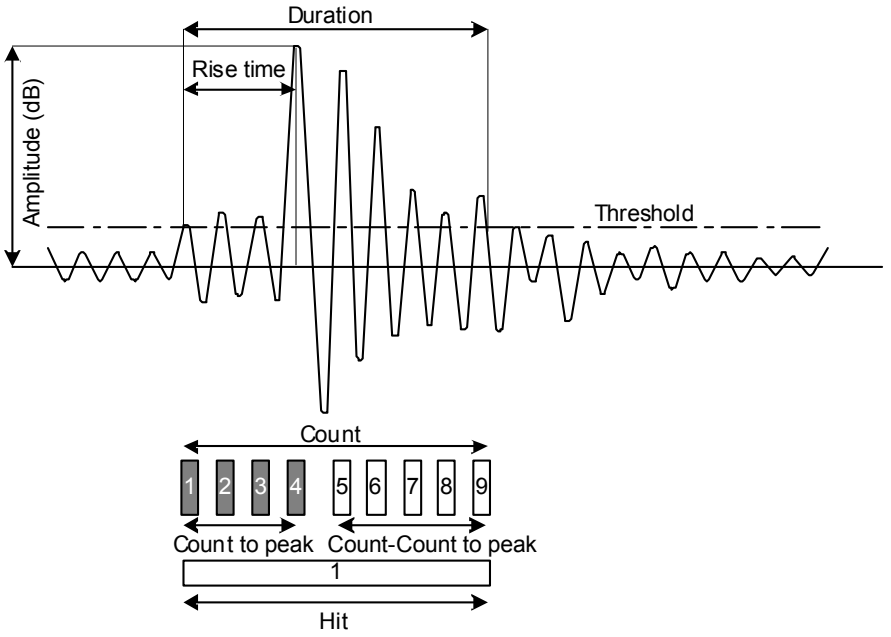

Fig. 4.1. Conventional AE signal features.

4. Duration: a time interval between the triggered time of one AE signal (waveform) and the time of disappearance is assigned. The duration is expressed generally on microseconds, which depends on source magnitude and noise filtering.
5. Rise time: a time interval between the triggering time of AE signal and the time of the peak amplitude is assigned. The rise time is closely related to the source-time function, and applied to classify the type of fracture or eliminate noise signals.

6. Energy: definitions of energies are different in AE system suppliers, but it is generally defined as a measured area under the rectified signal envelope. The energy is preferred to interpret the magnitude of source event over counts because it is sensitive to the amplitude as well as the duration, and less dependent on the voltage threshold and operating frequencies.

4.3.2 Other Parameters

1. Average frequency: a calculated feature obtained from "Count" divided by "Duration", which determines an average frequency over one AE hit. The average frequency is used customarily when signal waveforms are practically difficult to be recorded.
2. Initial frequency: a calculated feature derived from "Count to Peak" divided by "Rise time".
3. Reverberation frequency: a calculated feature derived from "Count-Count to Peak" divided by "Duration-Rise time".
4. RA value: a calculated feature derived from "Rise time" divided by "Amplitude", showing the reciprocal of gradient in AE signal waveforms, which is reported in ms/V. the RA values have been used to classify the type of cracks.

4.3.3 Frequency Parameters

Recent AE systems are so powerful that AE signal waveforms, which characterize AE source mechanisms, can be recorded sufficiently in real time. Presently such frequency-domain features as shown in **Fig. 4.2** play an important role in AE data interpretation. Attention should be paid, because the resolution of frequency parameters depends on the sampling rate and the waveform length employed.

1. Frequency centroid: a calculated frequency feature reported in kilohertz, which results from a sum of magnitude times frequency divided by a sum of magnitude, as equivalent to the first moment of inertia.
2. Peak frequency: a frequency feature reported in kilohertz, which is defined as the point in the power spectrum at which the peak magnitude is observed.

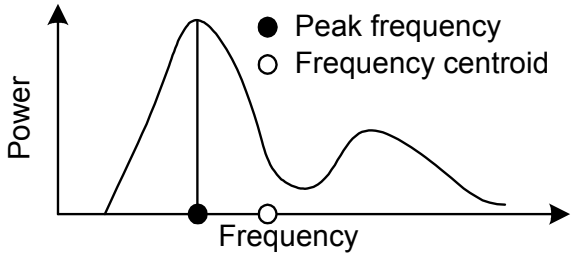

Fig. 4.2. Configuration of peak frequency and frequency centroid.

4.4 Parametric Analysis

In order to interpret acquired AE data, correlation-based, time-based or external parameter-based AE parametric features are customarily used with their occurrence rate or accumulated trend. In addition, statistical values of the parameter and some combinations among AE parameters as well as external parameters have been studied intensively for relating to the scale of fracture or the degree of damage in the materials/structures. Some examples applied to AE research are given.

4.4.1 Kaiser Effect

The Kaiser effect (Kaiser 1953) has been applied as to know the initial stress condition of rock materials (Yoshikawa and Mogi 1989). Based on the Kaiser effect, T. Fowler proposed the Felicity ratio (Fowler 1986), which can show the damage quantitatively in tank structures. The Felicity ratio was established because of the following fact. The Kaiser effect can only hold in the stable condition of the materials (i.e., intact condition). As to progress the internal instability, the Kaiser effect is gradually breaking down. As a result, AE activity starts to be observed even under lower stress than that of the maximum stress experienced.

The Felicity ratio is defined as,

$$Felicity\ ratio = \frac{P_{AE}}{P_{1st}} \tag{4.1}$$

where P_{AE} is a stress at which AE activity starts to generate, and P_{1st} is the maximum stress. The Felicity ratio becomes equal to or larger than one in an intact or stable state, while in a damaged condition it reveals smaller than one.

Recently, the same idea as the Felicity ratio has been applied for the damage assessment of concrete structures (NDIS2421 2000). In this reference the ratio was referred to as the load ratio (ratio of load at the onset of AE activity to previous load). Fundamentally the load ratio is obtained from Eq. 4.1. Differed from the Felicity ratio, the load ratio is obtained from any kinds of AE parameters at the onset of AE activity P_{AE}.

The load ratio is sometimes difficult to be applied for in-situ monitoring, because the maximum stress experienced is not readily estimated. Instead, the RTRI ratio has been proposed (Luo et al. 2002).

The RTRI ratio is defined as in the following procedure: the onset of AE activity is estimated from any measured parameters of stress/load, strain/deformation and so forth, and then the ratio is obtained as the ratio of the parameter's value corresponding to the onset of the AE activity to the maximum value (or peak value) during the whole inspection period instead of the maximum stress of which the structure has experienced.

To correlate the cracking behavior with AE parameters, two typical crack modes of mode I and mode II are to be considered. It is well known in concrete structures that the fracture mode of cracking is changing from the tensile type of fracture (mode I) to the shear type of fracture (mode II) with the progress of fracture. Crack opening is a principal motion when the mode-I cracks are nucleated, while fretting or sliding on an existing crack is a major motion to generate the mode-II cracks. In general, AE activity accompanied with crack growth or crack formation is referred to as 'primary AE activity,' while the case without crack growth is referred to as 'secondary AE activity.' In the stable stage of fracture growth, AE activity accompanied with the mode-I cracks is normally observed. As a result, few AE events are expected during the unloading process. As approaching the final failure, AE activity during the unloading process could be generated as the mod-II cracks. Thus, AE activity during unloading has a potential to show the damage degree.

Accordingly, paying an attention to AE activity during the unloading processes, the calm ratio is defined as the ratio of the number of cumulative AE activity during unloading to that of the complete loading cycle. Based on these two parameters, one criterion to evaluate the damage is proposed and schematically shown in **Fig. 4.3**. Applying this criterion, the deterioration process and the current conditions of the civil structures can be estimated under repeated or active traffic loads (Ohtsu, Uchida et al. 2002; Luo, Haya et al. 2004).

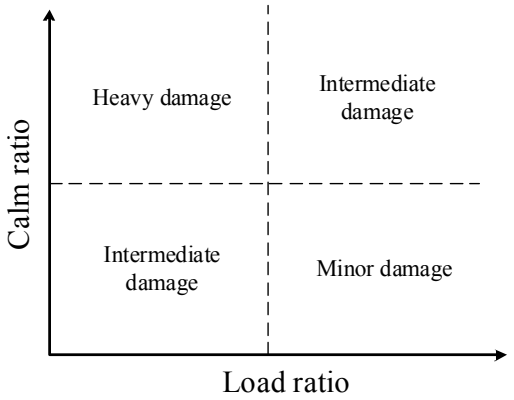

Fig. 4.3. Damage quantification with a combination of Calm and Load ratio.

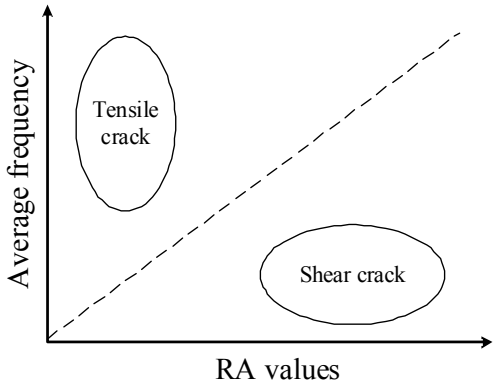

Fig. 4.4. Crack type classification with a combination of average frequency and RA values.

4.4.2 Crack Classification

In concrete materials, the classification of crack types is proposed, using the combination of the average frequency and the RA values. This classification technique has been standardized (JCMS 2003) and is shown in **Fig. 4.4**.

In the case of rock materials, the reciprocal of the RA values, namely the gradient of signal waveforms, is elsewhere referred to as “grade” (Shiotani, Ikeda et al. 2001).

4.4.3 Amplitude Distribution

Because AE peak amplitude is associated with the magnitude of fracture, the *b*-value that is defined as a slope of the amplitude distribution is known as an effective index related to the states of fracture (Mogi 1962; Scholz 1968). The larger *b*-value shows the state of materials where microscopic fractures occur more predominantly than macroscopic fractures. In the other case, the smaller *b*-value indicates prevailing the occurrence of macro-fractures. Since the *b*-value was originally defined in seismology, there existed a problem to be applied to AE signals in engineering materials. One application to assessing damage in reinforced concrete beam was reported (Colombo, Main et al. 2003). Instead of the seismic *b*-value, an improved *b*-value (*Ib*-value) has been proposed (Shiotani, Fujii et al. 1994), which is suitable for AE applications to concrete and rock.

In the improved *b*-value analysis, the number of peak amplitudes to be calculated should be first set. Roughly classified, two methods for determining the calculation number have been employed: a) accumulated numbers from the beginning data; and b) numbers per unit time. In the former case, the number determining the *b*-value is increasing with elapsed time. In the latter case, because the AE activity increases exponentially with approaching final failure, it is apparent that the number determining the *b*-value is increasing with elapsing time. It sometimes results in non-quantitative evaluation. Accordingly, it is important to determine the *b*-value as to apply the constant number of data to calculation. To improve the calculation of the *b*-value, the number of AE data is formulated by,

$$\int_0^{\infty} n(a)da = \beta \tag{4.2}$$

where $n(a)$ is a number of AE at da and β is a number of AE data. 50 to 100 of β values are thought to be an appropriate number by the results of the correlation coefficient when the data is fitted to the Gutenburg- Richter’s equation (Shiotani, Li et al. 2001).

The value of AE peak amplitude is varied with such monitoring conditions as methods of sensor setup, propagation media, and occurrence locations. Thus, the AE amplitude distribution is also dependent on these conditions. In order to obtain the *b*-value qualitatively, a method to determine the amplitude range as independent of the range of amplitude is necessary.

In the improved *b*-value analysis, the range of AE amplitude is determined based on such statistical values as the mean μ and standard deviation σ, where the upper amplitude w_2 and lower w_1 are formulated as $\mu+\alpha_1\sigma$ and $\mu-\alpha_2\sigma$, respectively. Setting accumulated numbers of amplitude over w_1 and w_2, as N (w_1) and N (w_2), which is obtained by,

$$N(w_1) = N(\mu - \alpha_2\sigma) = \int_{\mu-\alpha_2\sigma}^{\infty} n(a)da \tag{4.3}$$

$$N(w_2) = N(\mu + \alpha_1\sigma) = \int_{\mu+\alpha_1\sigma}^{\infty} n(a)da \tag{4.4}$$

where, the range of amplitude would be $(\alpha_1+\alpha_2)\sigma$, then the *Ib*-value is given by

$$Ib = \frac{\log_{10} N(w_1) - \log_{10} N(w_2)}{(\alpha_1 + \alpha_2)\sigma} \tag{4.5}$$

where, α_1 and α_2 are constants. It is noted that since I*b*-value is calculated on the basis of decibel unit. When comparing with seismic *b*-value, the *Ib*-value shall be multiplied by 20. The *Ib*-value has successfully been applied to evaluate developing process of fracture in such fields as soil (Shiotani & Ohtsu 1999), rock (Shiotani, Ohtsu et al. 1998; Shiotani, Kumagai et al. 2004), and concrete (Shiotani, Li et al., 2001; Shiotani, Bisschop et al., 2003; Shiotani, Nakanishi et al. 2006).

4.5 Concluding Remarks

AE parameter analysis, of which parametric features are mostly derived by analog processing, are discussed. After explaining definitions and properties of AE parameters, signal processing to evaluate the fracture processes in concrete and rock is discussed. Results obtained by applying these parameters are delivered in the following chapters, associated with applications.

References

Colombo S, Main IG, Forde MC (2003) Assessing damage of reinforced concrete beam using "b-value" analysis of acoustic emission signals. J Materials in Civil Eng., ASCE /May/June:280-288

Fowler TJ (1986) Experience with acoustic emission monitoring of chemical Process industry vessels. Progress in AE III, pp 150-162

Kaiser VJ (1953) Knowledge and research on noise measurements during the tensile stressing of metals. Archiv für das Eisenhüttenwesen, 24:43-44

ISO 12716 (2001) Nondestructive testing-acoustic emission inspection: Vocabulary. ISO

JCMS-III B5706 (2003) Monitoring method for active cracks in concrete by acoustic emission. Federation of Construction Materials Industries, Japan

Luo X, Haya H, Inaba T, Shiotani T, Nakanishi Y (2002) Experimental study on evaluation of breakage in foundations using train-induced acoustic emission. Proc. Structural Engineering World Congress 2002:T9-1-e-3

Luo X, Haya H, Inaba T, Shiotani T, Nakanishi Y (2004) Damage evaluation of railway structures by using train-induced AE. Construction and Building Materials, 18(3): 215-223

Mogi K (1962) Magnitude frequency relation for elastic shocks accompanying fractures of various materials and some related problems in earthquakes. Bull. Earthq. Res. Inst., 40: 831-853

NDIS 2421 (2000) Recommended practice for in situ monitoring of concrete structures by acoustic emission. JSNDI, Tokyo

Ohtsu M, Uchida M, Okamoto T, Yuyama S (2002) Damage assessment of reinforced concrete beams qualified by acoustic emission. ACI Structural Journal, 99-S42:411-417

Scholz H (1968) The frequency-magnitude relation of microfracturing in rock and its relation to earthquakes. Bull. Seismo. So. America, 58(1):399-415

Shiotani T, Fujii K, Aoki T, Amou K (1994) Evaluation of progressive failure using AE sources and improved *b*-value on slope model tests. Progress in AE VII, pp 529-534

Shiotani T, Ohtsu M, Monma K (1998) Rock failure evaluation by AE improved *b*-value. JSNDI & ASNT, Proc. 2nd Japan-US Sym. on Advances in NDT, pp 421-426

Shiotani T, Ohtsu M (1999) Prediction of slope failure based on AE activity. ASTM Acoustic Emission: Standards and Technology Update, ASTM STP 1353: 156-172

Shiotani T, Li Z, Yuyama S, Ohtsu M (2001) Application of the AE improved *b*-value to quantitative evaluation of fracture process in concrete materials. Journal of AE 19: 118-133

Shiotani T, Ikeda K, Ohtsu M (2001) Detection and evaluation of AE waves due to rock deformation. Construction and Building Materials 15(5-6):235-246

Shiotani T, Bisschop J, van Mier JGM (2003) Temporal and spatial development of drying shrinkage cracking in cement-based materials. Engineering Fracture Mechanics:1509-1525

Shiotani T, Kumagai K, Matsumoto K, Kobayashi K, Chikahisa H (2004) Evaluation of excavation-induced microcracks during construction of an underground power plant using acoustic emission. Contribution of Rock Mechanics to the New Century, Millpress, Rotterdam: 573-578

Shiotani T, Nakanishi Y, Iwaki K, Luo X, Haya H (2006) Evaluation of reinforcement in damaged railway concrete piers by means of acoustic emission, Journal of AE 23: 260-271

Yoshikawa S, Mogi K (1989) Experimental studies on the effect of stress history on acoustic emission activity – A possibility for estimation of rock stress. Journal of AE 8(4): 113-123

5 Signal-Based AE Analysis

Christian U. Grosse, Lindsay M. Linzer

5.1 Differences Between Parameter- and Signal-based AET

Approaches in recording and analyzing AE signals can be divided into two main groups: parameter-based (classical) and signal-based (quantitative) AE techniques. Both approaches are currently applied, with success for different applications, and it is useful to understand their differences, which should here be summarized in addition to the more detailed description of parameter-based techniques in Chap. 4. The reason that two approaches exist is related to the rapid developments in microelectronics over the last few decades. Previously, it was not possible to record and store a large number of waveforms (signals) over a sufficiently short period of time. Even though significant technical advances have been made in recent years, it is still not possible to use signal-based techniques to monitor large structures and buildings. In addition, the relatively high financial costs and the time required to apply modern signal-based techniques, are a reason why parameter-based techniques are still popular. Before the differences are described in detail, it should be emphasized that the discrepancies between the two approaches are becoming smaller. Some of the devices used for the classical AE technique are now able to store the waveforms of the detected AE signals, even though this is not the primary function of these devices. For applications using signal-based analysis techniques, equipment based on transient recorders is typically used. It is easy to apply custom software tools to extract AE parameters for statistical analyses of the data obtained with these instruments. The best instruments are those that can be adapted to different applications, and can record waveforms if a signal-based approach is being taken, or record large event numbers if a parameter-based approach is being taken requiring the statistical analysis of many events.

If AE events are recorded with one or more sensors, such that a set of parameters are extracted from the signal and later stored but the signal itself is not stored, the procedure is usually referred to as a parameter-based (or classical) AE technique. The idea is that the signals are completely described by the set of parameters, and storing this relatively small amount of parameter data consumes less time and storage space, than if entire waveforms are stored. Some typical AE parameters extracted by conventional AE equipment are the maximum peak-to-peak amplitude, the arrival time (defined as the first crossing of a given amplitude threshold), the rise time (defined as the duration between the arrival time and the time where the maximum amplitude is recorded) and the duration (defined by the last crossing of a given amplitude threshold) (ASTM E610 1982; CEN 1330-9 1999). A typical signal measured (but not stored) in AE analysis using the classical approach is given in **Fig. 5.1**.

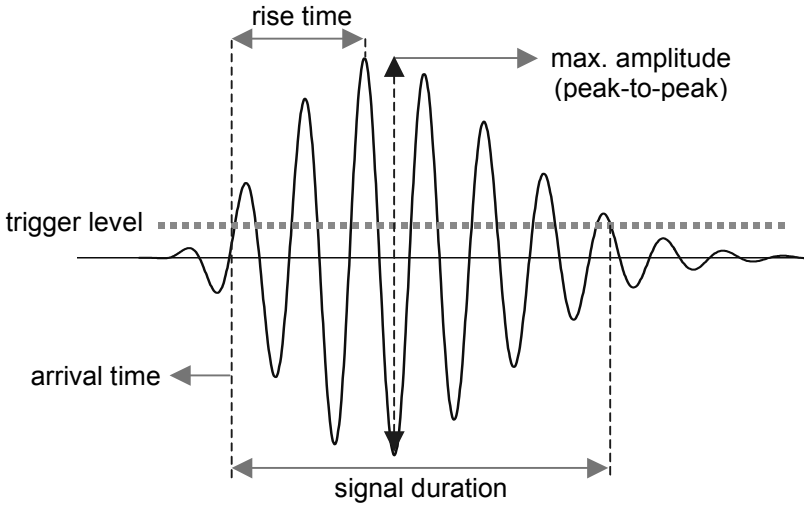

Fig. 5.1. Example of typical 'AE parameters' according to international and national standards (ASTM E610 1982; Berger 1977; DGZFP SE-3 1991).

Using the so-called quantitative AE technique, as many signals as possible are recorded and stored, along with their waveforms, which have been converted from analogue-to-digital (A/D) signals. A more comprehensive (and time-consuming) analysis of the data is possible using this approach, but usually only in a post-processing environment and not in real-time. The term 'quantitative', as it is used in AET, was first introduced by several authors (Scruby 1985; Sachse and Kim 1987) in the 1980's to compare this technique of waveform analysis with the classical techniques. Further

to this, the two different approaches are more related to the way the information is stored, although the terms ‘parameter-based’ or ‘signal-based’ AET are used with preference in this text.

When discussing the pros and cons of these two approaches it is important to keep the specific application in mind. This is true for the simple counting of the number of AE occurrences in a material under load by a single sensor, as well as for arrays of many sensors, used for localizing and analysing data in the time and frequency domain.

5.1.1 Pros and Cons of Using Parameter-based AE Techniques

The main advantages of the classical AE techniques are the high recording and data storing speeds that facilitate fast visualization of the data. This makes the technique very economical. In contrast, when an entire signal waveform recorded by several sensors is stored (signal-based approaches), the recording system shuts down for a short period (called the delay or dead time) while the information is being stored. This can result in a loss of information. Storing only some parameters reduces this delay time significantly.

Conversely, reducing a complicated signal to only a few parameters can be a significant limitation, and sometimes be downright misleading. In practical applications it can be difficult to discriminate an AE signal from noise (e.g. caused by electronic pulses) after the signal has been reduced to a few parameters. This is especially true when resonant sensors (Chap. 5.3.2) are used because such sensors result in the signal differences being further hidden. The extraction of simple parameters characterizing the signal can also be difficult when broadband sensors are used. An added complexity is that in many experiments the parameters of AE signals are strongly related to the material and the geometry of the structure. Different wave modes related to compressional, shear or surface waves, as well as reflections contribute to the shape of the signal enhancing its complexity. It is very instructive to imagine how parameters could be extracted, as described in **Fig. 5.1**, from highly complex signals such as the ones shown in **Fig. 5.9**.

The latest measurement devices are able to extract AE parameters while automatically localizing the signals. In these cases, it is usually not possible to control the algorithms used for this procedure, or to influence the accuracy of localization. Several hundreds, or even thousands, of events can be parameterized and localized by these black-box devices per minute. However, even for situations where a large number of AE signals have to be handled and the “classical” approach of AE testing is the chosen me-

thod, it is highly recommended that some AE signal waveforms, selected at random, are recorded and inspected to assess whether the monitoring system is working properly and to check the noise conditions.

5.1.2 Pros and Cons of Using Signal-based AE Techniques

If a signal-based approach is used, the waveforms recorded by the sensors (preferably broadband sensors) need to be analyzed. A suite of analysis procedures exists to evaluate fracture parameters. The first step in the analysis is usually the 3D localization of the rupture. More advanced analyses may then be applied, for instance, source mechanism calculations.

One of the biggest advantages of signal-based AET is the capability of signal-to-noise discrimination based on waveforms, because the waveforms are still available after the measurement and not deleted like it is done usually in parameter-based applications. Additionally, it is possible to apply different signal analysis methods using post-processing software. This software might include classification algorithms or different filtering techniques to enhance the signal-to-noise ratio and thus help to extract information about the material properties.

The reliability of the data interpretation can be improved significantly if signal-based methods are used. The drawback of signal-based approaches is that usually a smaller number of events can be recorded. Although the time for immediate parameter extraction is saved, a large number of signals have to be stored digitally. This is best illustrated by an example. If 100 acoustic emission signals are recorded by eight sensors, and A/D converted with 12 Bit resolution at a sampling frequency of 1 MHz with 1000 samples each (1 ms), the digital data size will be 1.56 megabytes. During an AE test of brittle materials this amount of data can be occur easily in minutes or even seconds, causing problems even for modern computer-based equipment. To reduce the amount of data not related to the material failure, sophisticated trigger algorithms (reference band, slew rate, etc.) have to be applied. On one hand his may appear to add an artificial interference. However, one has to recognize that parameter-based methods usually use an arbitrarily set threshold level to trigger the parameter extraction process and this can cause even more artifacts. On the other hand, not all the AE signals can be recorded anyway because of dissipation and geometrical spreading effects that absorb many of the weak signals before they reach the surface of the structure.

The question of which of the parameter or signal-based AE techniques are more useful does not have a definite answer. The attributes of the different methods are summarized in **Table 5.1**. As stated, the differences be-

tween the methods are vanishing as technology improves. However, current trends definitely favor the signal-based techniques rather than others. The decision of which technique should be applied is primarily a matter of data storage capacity and electronic components and is limited also by the financial constraints of a project.

Table 5.1. Comparison of the two AE techniques

	Parameter-based AET	Signal-based AET
Failure detection	Large scale	Small scale
Localization:		
• 1D (zonal)	requires many sensors	requires many sensors
• 2D (planar)	minimum 3 sensors	minimum 3 sensors
• 3D	minimum 4 sensors	minimum 4 sensors
Fast real-time data analysis	requires PC with memory	–
Statistical analysis	requires PC with memory	requires PC with memory
Analysis of:		
• amplitudes	Only statistical analysis	resolution > 12 Bit
• frequencies	–	requires broadband sensors
• waveforms	–	sampling frequency > 1MHz
Fracture analysis:		Min. 6 sensors in the farfield
• Fault-plane orientation	–	Distributed sensors
• Fault-plane size	–	Moment tensor inversion
• Fault-plane energy	–	Moment tensor inversion
• Fracture mode (I, II, III, mixed)	–	Moment tensor inversion

The signal-based methods will be the focus of the following sections. However, this is a relatively young field of research, and as a result, there remains a lack of algorithms and software to be used in an environment where very large number of AE signals must be processed automatically.

5.1.3 Illustration of the Capabilities of Parameter-based AE Techniques

Before the potential of signal-based techniques is demonstrated, two examples of statistical analyses of AE data are given.

The Kaiser effect, which was first investigated by Wilhelm Kaiser in 1950, describes the phenomenon where a material under load emits acoustic waves only after a primary load level is exceeded. During reloading, these materials behave elastically before the previous maximum load level is reached. If the Kaiser effect is permanent for these materials, little or no AE will be recorded before the previous maximum stress level is achieved.

The effect is illustrated in **Fig. 5.2** in an experiment where a concrete cube, subject to compression, was tested under a cyclic load. The figure shows the AE rate versus time, and the applied load versus time.

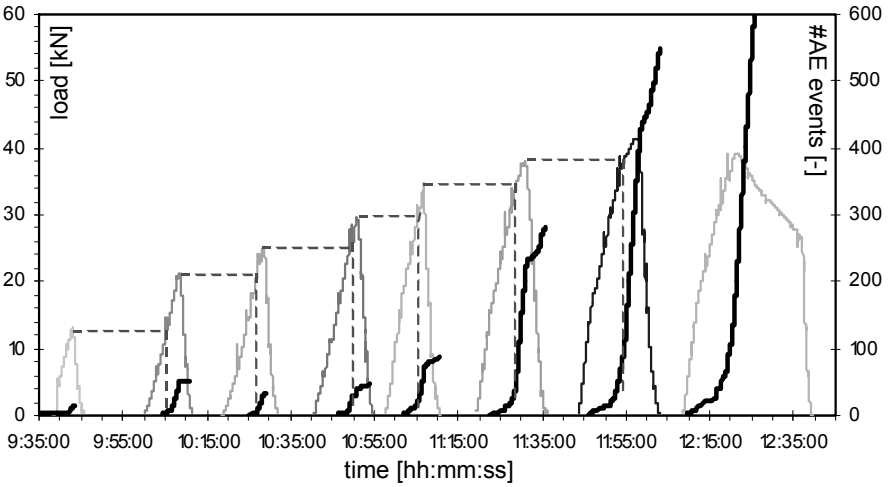

Fig. 5.2. Example of the Kaiser effect occurred in a cyclically loaded concrete specimen. Thick black lines represents the AE activity, thin lines the load and the dashed lines indicate the Kaiser effect.

In a second example, eight sensors have been coupled to the surface of a concrete cube (100 mm side length) having a centrally placed reinforcement bar of 16 mm diameter with limited bond (**Fig. 5.3**). The bond length was limited to 40 mm (5 ribs) to minimize the number of sources producing acoustic emissions due to local damage. During a pull-out test, the bar was pulled downwards, while acoustic emissions were recorded at all eight sensors. The results of the force and slip measurements for tests with different load histories (monotonically increasing displacements, cyclic loads and long term loads) are summarized in Balázs et al. [1996b].

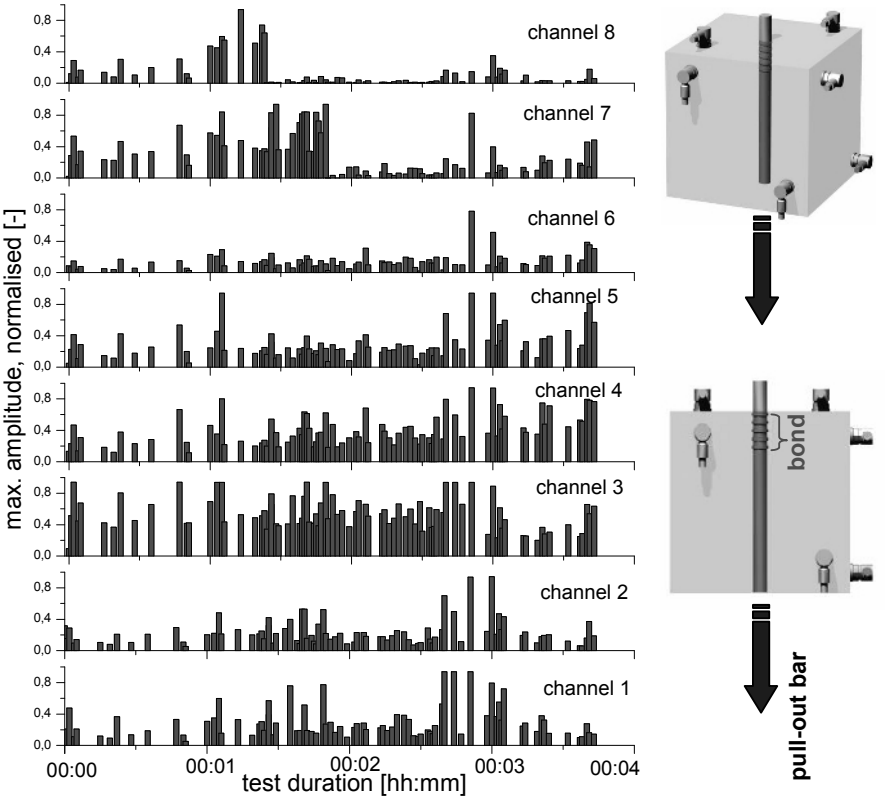

Fig. 5.3. Statistical interpretation of AE activity measured with eight sensors on a cube.

The results also show the automatically extracted peak amplitudes of the burst signals versus time in the form of histograms that represent a statistical evaluation of acoustic emissions. Unfortunately, this procedure does not consider the relative location of the sensors and the sources, which can lead to false interpretations of the data. For example, in **Fig. 5.3** the peak amplitudes of the first AE events, which are related to fractures in the upper region of the specimen, are higher for channel number 7 and 8, while channels 1 to 6 suggest later events to be the ones with higher amplitudes. The reason for this is that sensors 7 and 8 are located closer to the cracks in the upper region that is more active at the beginning of load, while the other sensors represent the evolving cracks at later stages. This shows clearly that the histogram graph of acoustic emission data is sometimes more dependent on the location of the sensors, than on the failure of the material. In this case, the interpretation of the results is difficult, somewhat

limited and can even be misleading. These effects lead to the development of signal-based AE techniques.

5.2 The Influence of Sensing Techniques to Signal-based AET

Signal-based AE techniques depend on the characteristics of all parts of the equipment used to record and analyze acoustic emissions and probably most of all on the type of sensor used. Therefore and in addition to Chap. 3 some general remarks about sensors will be given in this section.

5.2.1 The Concept of Transfer Functions

The signals measured using AET (which are related to relative moments of very small cracks) are of low magnitude compared to other active methods, i.e. methods that induce a source signal in a specimen. Usually, the signals radiated as acoustic emissions are very weak, and must be amplified if they are to be recorded. AE signals are subject to many different influences caused by variations in the material along the raypath (heterogeneities, anisotropy) and the recording system (coupling, sensor characteristic, etc.). To reduce the influence of artifacts to the signals, the methods used in system theory can be applied. This process is also known as *linear filter theory*, where the output is treated as a sequence of linear filters and each filter accounts for some aspect of the source or propagation or sensor

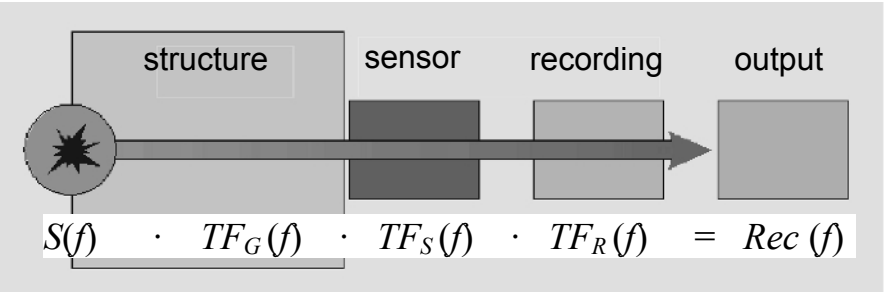

Fig. 5.4. Concept for the use of transfer functions in non-destructive testing.

To apply system theory, all of the known influences are assigned a different transfer function. In AE applications it is important to know or guess the weight of these functions as a precondition to eliminate their influence if possible. The different influences can be depicted conceptually as shown

in **Fig. 5.4**, which is valid also for other methods, such as ultrasound. Mathematically this is represented in the frequency domain by

$$\mathrm{Rec}(f) = S(f) \cdot TF_G(f) \cdot TF_S(f) \cdot TF_R(f) \tag{5.1}$$

where *Rec* represents the recorded signal, *S* is the source function, TF_G represents the Green's functions of material, TF_S describes the transfer function of the sensor and the coupling, and, TF_R is the transfer function of the recording system.

In signal-based AET the source function *S* is of great interest, because it represents the failure. Using non-AE methods the Green's functions of the material are first calculated using waves emitted by a known source function *S*. While the intention of non-destructive testing methods is the investigation of material parameters or material failure and not the characterization of the measuring system, one has to reduce the effects related to sensors, coupling or the recording system with care. Several problems related to undesired effects still need to be addressed in more detail. Many journal papers and conference proceeding articles deal with these issues.

5.2.2 Sensors used for AE Measurements

The type of sensors used in AET almost exclusively are sensors that exploit the piezoelectric effect of lead zirconate titanate (PZT). While piezoelectric sensors and their design are described in numerous books and papers (e.g. Krautkrämer and Krautkrämer 1986; Kino 1987; Hykes et al. 1992), some characteristics play an influential role in AE measurements and need to be highlighted. These features are important for the sensitive recording of acoustic emissions (sensitivity) and the broadband analysis of the signals with reference to fracture mechanics (frequency).

To enhance the detection radius of piezoelectric sensors to AE signals, they are usually operated in resonance, i.e. the signals are recorded within a small frequency range due to the frequency characteristics of the transducer. The disadvantage is that an analysis of the frequencies present in the signal is of no value, because these frequencies are always the same. Very well damped sensors, such as those used for vibration analysis, are operated outside of their resonant frequency allowing broadband analyses to be performed, but are usually less sensitive to acoustic emission signals. Progress in the development of the theory of AE has led to the need for high sensitivity, wideband displacement sensors that have a flat frequency response (i.e. the sensor gives the same response over a wide frequency range).

There are many papers dealing with a solution of this problem. For many years a NIST (National Institute for Standards and Technology) conical transducer developed by Proctor [1982, 1986] out of a Standard Reference Material (SRM) and mass-backed (600 gr.) was used as a reference for AE measurements. Several new approaches have explored other transducer materials out of polyvinylidene fluoride (PVDF) or copolymers (Hamstad 1994; Hamstad and Fortunko 1005; Bar-Cohen et al. 1996; Hamstad 1997) as well as embedded sensors (Glaser et al. 1998).

However, most sensors used currently in AE applications for concrete are manufactured in a more traditional way, showing either a resonant behavior or several particular resonances. These sensors, which are called multi-resonance transducers, have a higher sensitivity than sensors with a backward mass used outside of their resonance frequency. Such sensors should not, however, be considered as (true) broadband and it is essential to know their frequency response function. Otherwise, signal characteristics from the source are not distinguishable from artifacts introduced by incorrect knowledge of the frequency response. A calibration of the sensors' frequency response, as well as understanding of the direction sensitivity, is important for many applications of AET.

5.2.3 Calibration

In the literature (e.g. Hsu and Breckenridge 1981; Wood and Harris 1982; Miller and McIntire 1987) different methods of calibrating sensors and determining their transfer functions are described. Measurements used in sensor calibration should include the frequency, as well as the phase response function. To demonstrate the basic principles, only the frequency is considered in the following.

Most calibration methods described in the literature are based on the 'face-to-face' method, in which two sensors of the same kind are coupled using one as a transmitter and the other as a receiver. Another method of calibration is to use a defined sharp pulse (e.g. by breaking a glass capillary rod) while the sensor is coupled to a large block made of a homogeneous material (steel or aluminum) or to a steel rod.

Hatano and Moro [1976] suggested the use of a reciprocity method, where sensors are coupled onto a steel plate. This approach uses Rayleigh waves. Other methods described in the literature suggest using a laser-vibrometer to measure the displacement of the free surface of the sensor, or a network analyzer (Weiler and Grosse 1995; Grosse 1996).

The sensor calibration process encounters several problems due to aperture effects (diameter of the sensor element is of the order of the wave-

length), the mass of the sensor (which affects the measurement of the displacement) or the measurement technique itself (recording of vertical motions instead of a three-dimensional vector). Because of these factors, calibration is always not absolute, but is subject to some simplifications.

In the following, the results of the face-to-face method are compared to measurements of the displacement of the free oscillating surface of the sensor. In **Fig. 5.5**, a typical frequency transfer function of a resonant transducer is compared to a multi-resonant (so-called broadband) sensor (bottom). Both functions are measured using the face-to-face method. For comparison, the same multi-resonant sensor was additionally calibrated using a laser vibrometer, sweeping through a frequency range of 0-500 kHz (Lyamshev et al. 1995). For the face-to-face measurements, a delta pulse was used containing all relevant frequencies in a selected range.

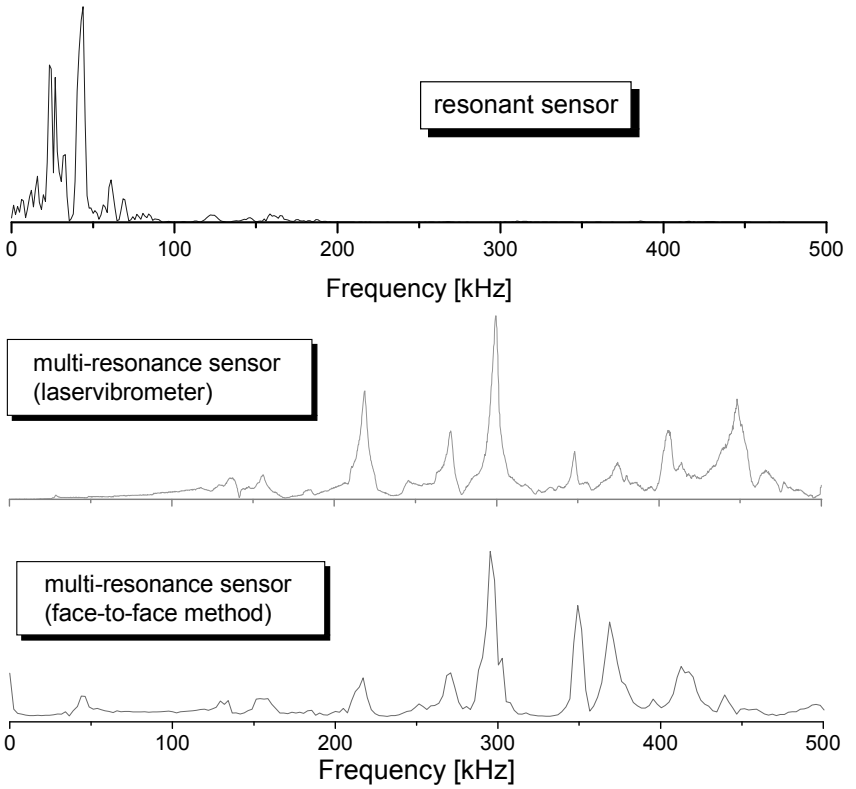

Fig. 5.5. (top) Example of frequency response functions of a resonant and a so-called broadband transducer. The frequency response function was measured using a laser-vibrometer (middle) and a face-to-face method (bottom). Amplitudes are on a linear scale.

There are significant differences between resonant and broadband transducers. The resonant sensor for which the response is shown in the top part of **Fig. 5.5** is sensitive in a small range around 40 kHz; and the multi-resonance sensor shown below is sensitive to a broader range between 50 and 450 kHz with resonances at 50, 130, 160, 215, 270, 300, 350, 370, 420 and 450 kHz. The graphs in the middle and bottom of **Fig. 5.5** are very similar, and appear to be independent of the particular calibration techniques, with regard to the position of the natural frequencies.

The calibration sheets of frequency transfer functions provided by the sensor manufactures are often displayed on a logarithmic scale. Resonances are more difficult to detect in this format and, therefore, it is advised to ask for calibration sheets on both linear and logarithmic scales. The record of the frequency responses should be available in electronic, as well as in paper form, to allow for the application of deconvolution techniques.

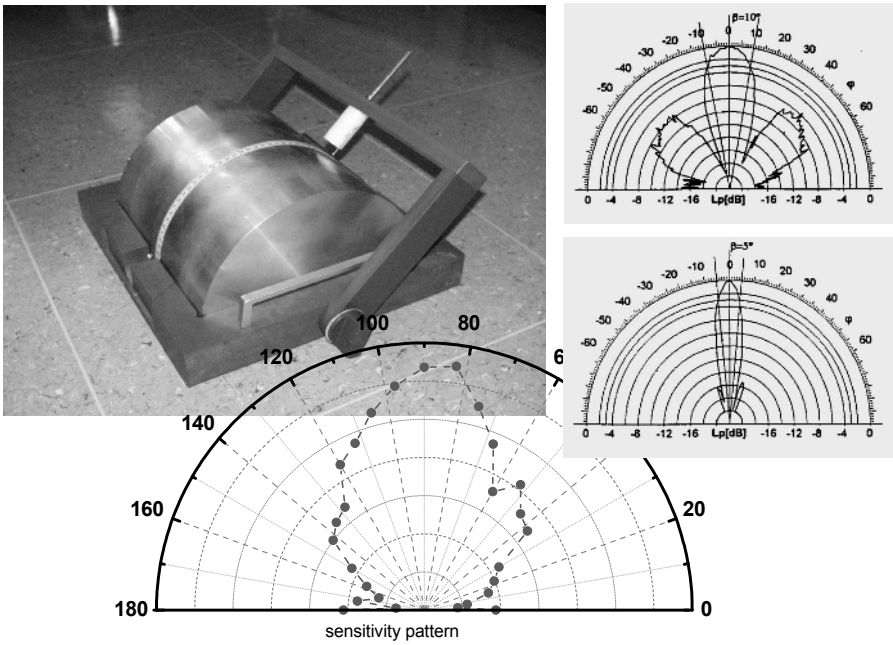

Fig. 5.6. Examples showing measurements of the sensitivity of sensors to incident angle.

There are many other influences caused by sensor characteristics that affect an AE signal. One example is that the sensitivity depends on the incident angle of the signal with respect to the sensor orientation. The described measurement techniques for frequency response assume that the

signal has an angle of incidence perpendicular to the contact plane of the sensor. This assumption is not always valid in AET. Analyses based on amplitude calculations are not reliable if the angle dependence of the sensor is not taken into account (refer to **Fig. 5.3** where this effect is misleading). This directivity effect varies from sensor to sensor, and can be measured using a cylindrical aluminum probe, as demonstrated in **Fig. 5.6**. The piezo-electric sensors measured can show a maximum response at 90° incidence of the signal and some peaks at other incidence angles. Besides this, the aperture size of the sensors can have an effect on the high frequency sensitivity. Unfortunately, the directional sensitivity pattern is usually not delivered with sensors commercially available for acoustic emission experiments.

5.2.4 Coupling

Contactless measurements are an exception in the field of AET. Coupling between sensors and a specimen is very important because the amplitudes of AE signals are so small, and poor coupling can result in signal loss. In addition to the different ways of coupling, various methods exist for fixing the sensors to the structure. Adhesives or gluey coupling materials, and substances like wax or grease, are often used due to their low impedance. Impedance, which is defined in AET as the loss of signal energy as waves travel from the surface of the structure to the sensor, is the most important factor in the selection of a coupling technique. If the structure has a metallic surface, magnetic or immersion techniques are widely used. Different methods using a spring mechanism or rapid cement can be used for other surfaces. In general, the coupling should reduce the loss of signal energy and have low acoustic impedance compared to the material being tested. In all cases, the total volume of air bubbles between the sensor and the structure has to be minimized.

5.3 The Influence of Amplifiers and Data Acquisition Techniques to Signal-based AET

This section is concluded with some remarks regarding existing acquisition systems for acoustic emissions. Commercially available AE devices differ from transient recorders. Some are also able to record AE events but have to be treated as black-box devices – this chapter deals mainly with devices based on transient recorders (TR) or plug-in TR-boards.

Piezoelectric sensors transform displacement into a voltage and amplifiers are usually used to magnify the AE signals. Because cables from the sensor to the (primary) amplifier are subject to electromagnetic noise, specially coated cables of short length should be used. Preamplifiers with state-of-the-art transistors should be used to minimize the amount of electronic noise. Amplifiers with a flat response in the frequency range of interest are best. If available, transducers with integrated preamplifiers for an appropriate frequency band are often desirable. Another issue is the astonishing dynamic range of AE signals. The broad dynamic range requires gain-ranging amplifiers (storing the signal in analogue into a buffer for best amplification adjustment prior to digitization), but they are not yet available in commercial AE equipment.

With regard to the data acquisition system (DAS), there are two main problems concerning the A/D conversion and the triggering. Fast A/D units have to be used to ensure that a large number of events are recorded – usually there are A/D converters for each channel of the recording unit. Anti-aliasing (low pass) filters are required so that the signal can be properly transformed to the frequency domain by means of Shannon's Theorem (Rikitake et al. 1987).

If possible, applying different triggering conditions can reduce the amount of noise that is recorded. Simple threshold triggers are usually not adequate for many purposes in AET. More sophisticated techniques such as slew-rate, slope or reference band triggers are more appropriate. In modern computer based systems, the time used to convert a signal from analogue to digital, and to store it to a hard disk, is in the range of microseconds depending on the signal length. There are still many areas, however, where AE equipment can be improved. It is important to keep being informed about the recent developments in AE recording technology.

5.4 Localization Techniques

Quantitative methods in AET rely on localization techniques to determine the coordinates of the emission source, to image cracks in the material. The method used to localize AE events depends on the geometry of the object being tested, and whether the resolution is required in one, two or three dimensions. Although a detailed description of these methods is the focus of Chap. 6, basic concepts – in particular using full waveforms – are described in this chapter for completion and to understand signal-based procedures.

5.4.1 Zonal and Planar Location Methods

The simplest way to locate the source of AE is the so-called zone location method. The exact source coordinates are not determined, but the defect is located within a radius of the sensor's sensitivity range (or in the case of a plate-like structure, within a zone).

The zone location method is frequently used to monitor large structures such as buildings, pipes, vessels, etc. Sensors are distributed over a wide area on the surface of the structure and/or concentrated at the most critical locations. To enhance the detection radius, resonant transducers, which are more sensitive than broadband sensors, are the first choice. **Fig. 5.7** shows an example of a sensor configuration used to monitor leaks in pipes. The leak or failure must be within the detection range of the sensor, to allow the AE to be detected. If AE is recorded by a particular sensor, the technician should inspect the vicinity next to this sensor for leaks or cracks.

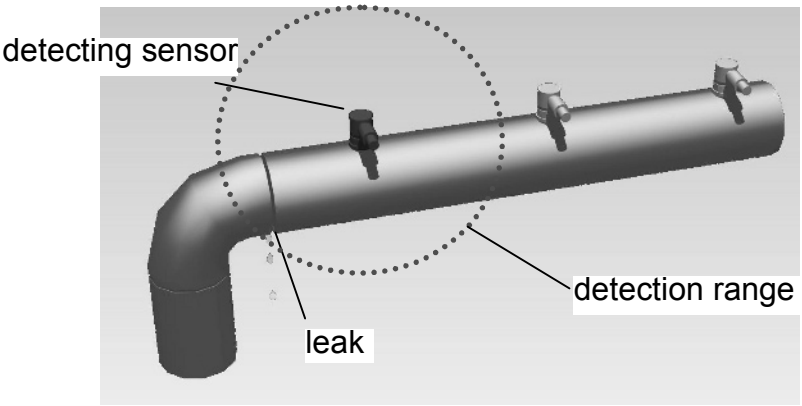

Fig. 5.7. Example of the zonal monitoring of leakages in a pipe using AET.

The planar localization technique is applied to two-dimensional structures, where the thickness is small compared to the length extent of the object and source coordinates are only required in two directions. Simple planar localization of cracks in a plate is shown in **Fig. 5.8**. While only three unknowns (the two source coordinates and the time of origin) have to be determined (see Chapter 6), recordings from only three sensors are sufficient (**Fig. 5.8**). Since compressional waves are used, the equations applied to calculate the source locations are similar to those of 3D localization techniques (see Chapter 6).

In the case where the waves have wavelengths shorter than the thickness of the structure, plate or Lamb waves have to be used and their group velocities considered. The 2D method to locate AE sources is usually applied when the accuracy of zonal technique is inadequate for the application. Applications of the 2D method in civil engineering are generally for monitoring large structures, like bridges (Kapphahn et al. 1993).

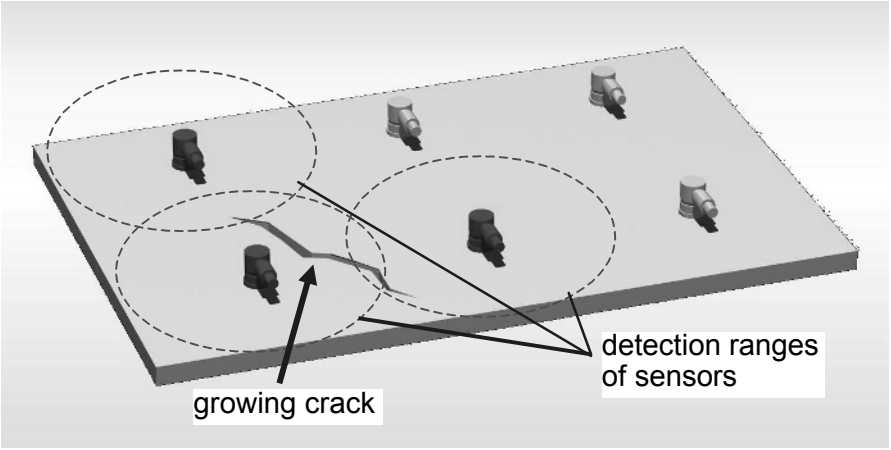

Fig. 5.8. Configuration illustrating the principle of planar localization.

5.4.2 Basics of 3D Localization

Several authors have applied 3D localization methods to AE in civil engineering (Berthelot and Robert 1987; Labusz et al. 1988; Grosse 1996; Köppel and Grosse 2000). The technique is similar to those applied in seismology, where earthquake hypocentres are determined using the arrival times of earthquake waves recorded at multiple seismometers. A commonly used method (the so-called 'Geiger' method) is based on the ideas of the German seismologist Ludwig Geiger [1910] and uses the arrival times of the first and second arrivals, the compressional (or P) and shear (or S) waves. The compressional waves travel at a higher velocity than the shear waves, so arrive at the sensors first, followed by the shear waves. This concept is well illustrated by the seismogram in **Fig. 5.14**, where the arrival time of the P-wave (t_P) is less than that of the S-wave (t_S).

These algorithms can be adapted to the requirements in material testing and enable the study of different specimen geometries by considering the number of transducers and their position around the object. For the deter-

mination of the AE hypocenter (source) using the arrival times, the problem is exactly determined when four arrival times are used to calculate the four unknowns: three coordinates and the source time of an event. When more than four arrival times are available, the problem is over-determined and the calculation is performed using an iteration algorithm, where the coordinates are estimated by minimizing the errors of the unknown parameters (Salamon and Wiebols 1975; Buland 1976). The more recordings, the more over-determined the system, and the more reliable the evaluation will be.

In seismology it is very common to use both P- and S-waves, because of the clear arrival times of shear waves (**Fig. 5.9**). However, in AET of small structures, the P-waves are followed closely by S-waves, resulting in the onset time (or first arrival, t_S) of the S-wave being hidden in the coda[1] of the P-wave. Compare the waveform in **Fig. 5.13** (recorded in the mining environment) to those of **Fig. 5.10** (AE data), where only the P-wave onset times are indicated. Onset time detection methods are described in detail in Chapter 6.

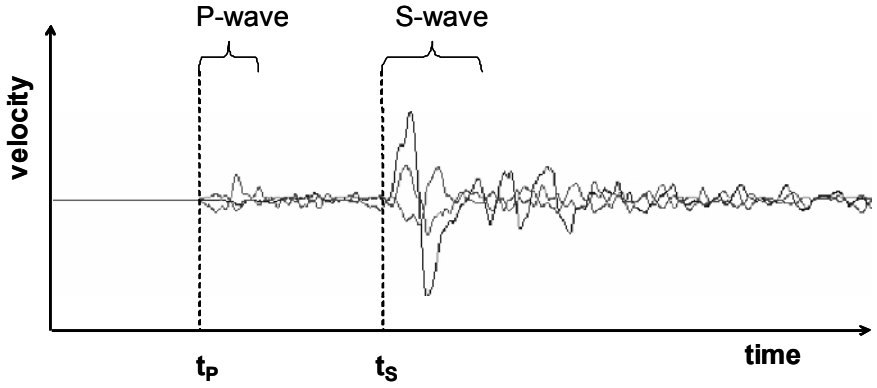

Fig. 5.9. Seismograms recorded by a triaxial sensor in the underground mining environment showing very clear P and S-wave arrivals.

Software to perform AE source localization should be able to calculate the standard deviations of the hypocenter and the source time, the weight of a single station, the number of iterations to be used and the residual of each channel with respect to the determined best arrival time (e.g. Oncescu and

[1] Coda is defined as the vibrations following the arrival of a certain wave mode. The vibrations are mainly caused by geometric effects (reflections from boundaries) or due to sensor characteristics (free oscillations of a piezo element vibrating in resonance).

Grosse 1998; Grosse 2000). The equations used generally assume that the material is homogeneous and isotropic, and that the AE source resembles a point source. If this is not the case (e.g. for an anisotropic material like wood) the computational approach has to be modified – this is covered in detail in Chap. 6.

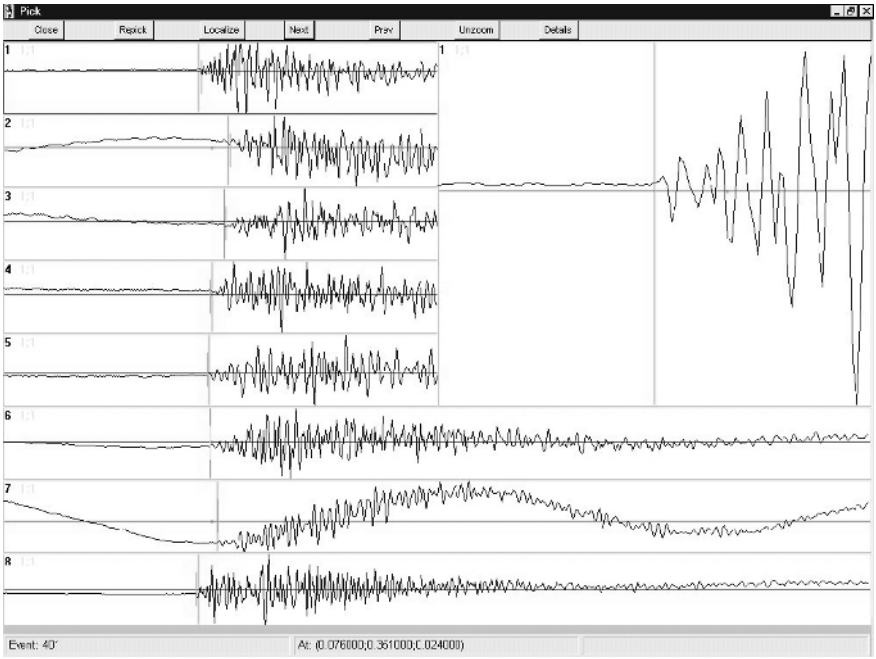

Fig. 5.10. Example of the onset time extraction for the 3D localization of AE.

Visual representation of data

The graphical representation of AE data that has been localized in 3D is a very important aspect of acoustic emission analysis. There are several ways to visually represent the data. A common approach is to draw projections of the x/y, y/z or x/z planes. The representation in a 3D coordinate system, as shown in **Fig. 5.15**, can lead to useful insights when the graphical data is animated – such features are implemented in most modern AE data analysis software. Representing 4D data (three coordinates of the sources and the time of occurrence of all events) using print media, however, is difficult.

Fig. 5.11 shows an example of the AE localizations during a pull-out test of a steel reinforcement bar, in a concrete cube having a side length of

200 mm. The bond between steel and concrete is limited to a length of 40 mm, in the middle of the cube. The large spheres indicate the position of the 3D AE localization in the cube, while the small points at the bottom are projections on the x/y plane. As expected, most of the AE sources are located near the ribbed portion of the bar, which is the area of largest load amplitude in the cube, resulting in local crushing at the concrete bar interface due to compression by the steel ribs. The energy of each acoustic emission event emitted is represented by the radius of the spheres (Grosse 2000).

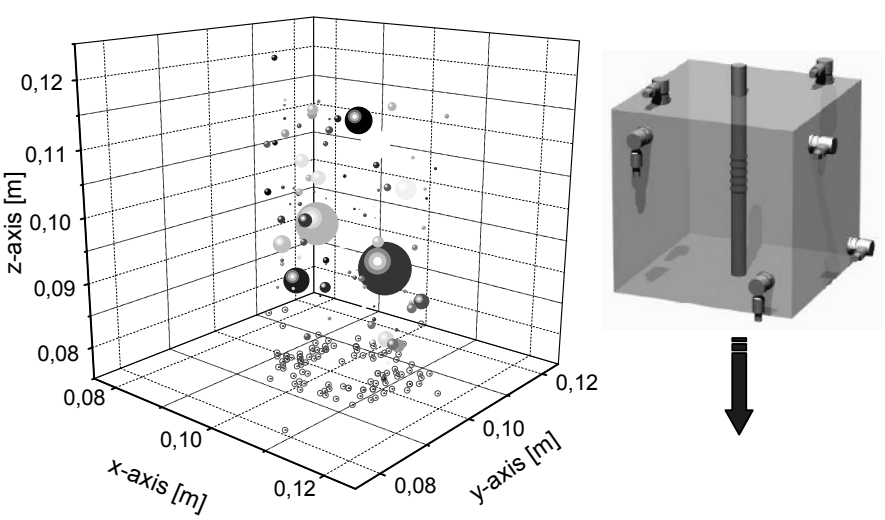

Fig. 5.11. Example of the 3D visualization of AE data (zoomed to 50 mm³) along with the energy emitted by each acoustic emission as represented by the radius of the sphere. The dots on the bottom are the projections of the spheres to the x/y plane.

Upon analyzing the x/y projection in conjunction with a visualization of the standard deviation of the calculated source coordinates (**Fig. 5.12**), further interesting details can be observed. We would expect that no sources would exist within the steel bar. The events localized inside the dashed line, which represents the perimeter of the bar, must surely originate directly from the surface of the bar. An inspection of the error bars reveals that many of these sources have error limits extending outside the bar, indicating that they probably originated from the surface of the bar.

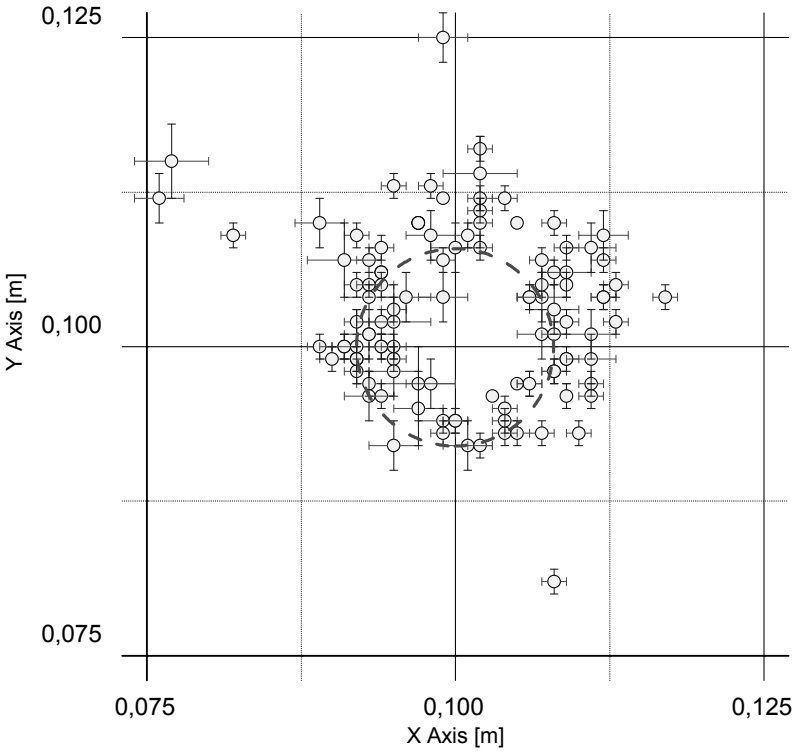

Fig. 5.12. Example of the standard errors for a localization in the x/y plane (projection of the data shown in **Fig. 5.15**). The length of the error bars depend on the standard deviation of the localization. The dashed ring in the middle of the graph marks the perimeter of the bar.

A record of the chronology of the AE events can be shown by simply numbering the source points. Additionally, the influence of heterogeneities (voids, reinforcement) can be evaluated (Grosse et al. 1995) via the analysis of the arrival time residuals at sensors in the shadow zone, which is the zone where the reinforcement bar is in between source and receiver.

Accuracy

The accuracy of AE localization is limited by several factors, such as the signal-to-noise ratio and the sampling interval of the digital acquisition system equipment. If the sampling frequency is set to 1 MHz for each channel, for example, the accuracy of the arrival times is limited to 2 µsec or less. In concrete, the error for localization using currently available equipment is usually between 1 mm and 1 m, depending on the size of the

tested structure and the distance of the sources to the sensors. Providing error information about location calculations is essential to interpret the results. Without this information, there is no way to assess the reliability of localization.

Picking signal onset times

Another factor affecting the accuracy of AE calculations is the onset time determination. During a routine test usually hundreds, or even thousands, of events are recorded, and automatic picking algorithms to extract the arrival times at each sensor are essential. Using a simple threshold algorithm is not sufficient in many cases. Under good signal-to-noise conditions, the accuracy of automatic algorithms should be in the range of several data samples.

In applications where a detailed analysis of failure is required, the need for high localization precision is combined with a high AE event rate, and more advanced onset picking algorithms should be used. The main trends are outlined in Chapter 6. The reader is also referred to publications written by Landis et al. [1992]; Zang et al. [1998]; Grosse and Reinhardt [1999] and Grosse [2000].

5.5 Signal-based Acoustic Emission Techniques

Up to this point in the chapter, the analysis techniques presented only use a fraction of the information present in the AE signals to interpret a local failure – there is scope for much richer interpretations. Quantitative acoustic emission techniques include the recording and evaluation of the entire waveform based on the 3D localization of the AE sources. Using the entire AE waveform it is possible to gain insight into the failure mechanism and fracture mechanics, and noise discrimination can reliably be carried out. In addition, the elimination of artifacts due to sensor characteristics is more consistent. The possibilities for applying signal processing is almost unlimited. Some of these techniques will be discussed in the following section.

5.5.1 Frequency and Correlation Techniques

Frequency analysis and frequency-based correlation techniques are widely discussed in the AE community. After the introduction of the Fast Fourier Transform (FFT) in the 1960's, frequency analysis techniques became easy to apply and numerous applications for AET have been suggested.

These include simple filtering techniques to eliminate noise, to more sophisticated approaches that correlate the frequency content of a signal to the source parameters to classify the events in terms of fracture mechanics.

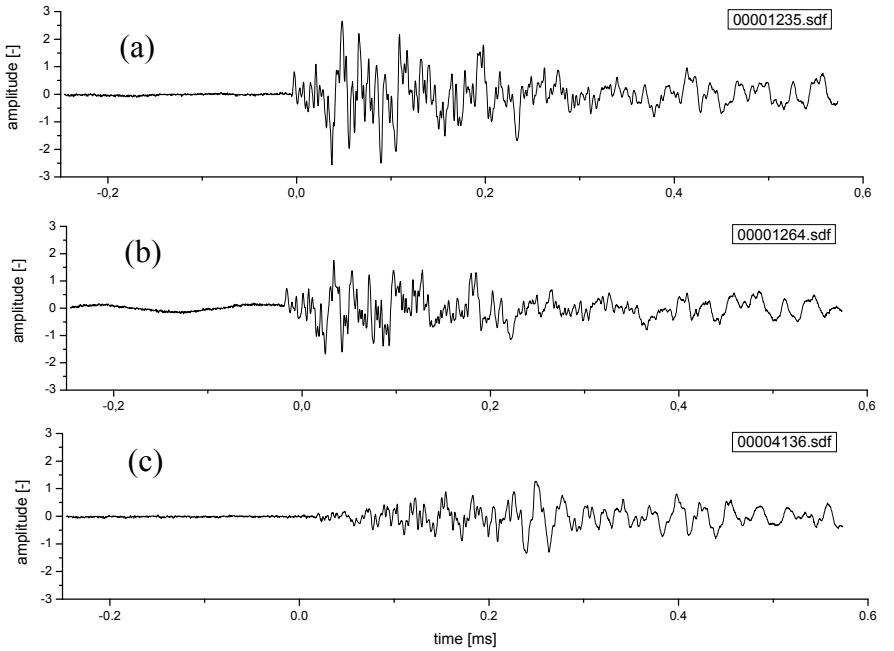

Fig. 5.13. Three different AE signals including a pair (1+2) of events with similar waveforms.

To give an example, the similarity of two different acoustic emission signals can be assessed by determining their coherence functions. Such an assessment is useful because similar signals, having similar frequency content, can indicate that their source mechanisms are also similar (assuming that the influence of the medium and transducer characteristics is small). The similarity of two signals can be quantified using a mathematical tool called *magnitude squared coherence* (MSC) (Carter and Ferrie 1979). Applying a Discrete Fourier Transform (DFT) the signals are converted from the time to the frequency domain. Consider two transient signals x and y (e.g. signal *a* and *b* in **Fig. 5.13**). The auto spectral density G_{xx} and G_{yy} and the cross spectral density G_{xy} of the signals must first be calculated. Then, the coherence spectrum C_{xy} is defined by the squared cross spectrum divided by the product of the two autospectra:

$$C_{xy}(\nu) = \frac{\left|\Gamma_{xy}(\nu)\right|^2}{\Gamma_{xx}(\nu) \cdot \Gamma_{yy}(\nu)} \tag{5.4}$$

where ν indicates frequency. A complete derivation of the formulas can be found in Balázs et al. (1993). The mean coherence $\hat{C}_{xy}$ of the coherence functions is calculated for all channels of two signals.

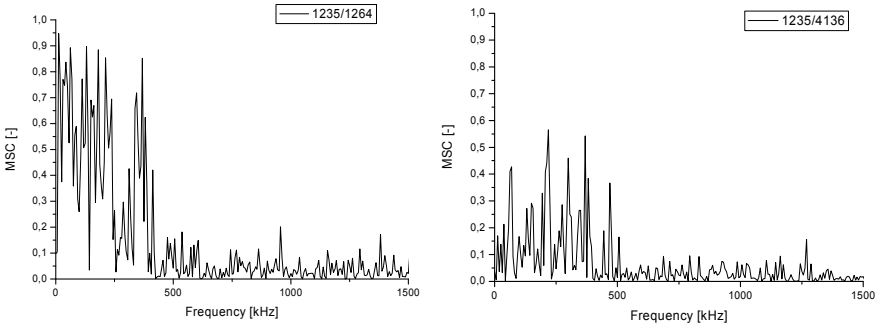

Fig. 5.14. MSC of a signal pair with high (left) and low similarity (right).

An example of the mean coherence for two data pairs is given in **Fig. 5.14**. This figure was generated using two events with high similarity (**Fig. 5.13** a+b) and two others with less similarity (**Fig. 5.13** a+c). In the frequency range below the noise level of this experiment (400 kHz), a high coherence is found for the first signal pair. A perfect coherence is only obtained by two identical signals and would result in a coherence value of 1 over the whole frequency range. For comparison, the coherence function of two less similar events (**Fig. 5.14**, right) is shown. It is possible to find a value that represents the overall coherence of the signals using the mean coherence function

$$\hat{C}_{xy}^{(\nu_{\min}/\nu_{\max})} = \frac{1}{\nu_{\max} - \nu_{\min}} \cdot \int_{\nu_{\min}}^{\nu_{\max}} C_{xy}(\nu)\, d\nu \tag{5.5}$$

Grosse [1996] suggested deriving a coherence sum $\hat{C}_{xy}$ that can be calculated as the area underneath the curves using numeric integration in the range from from $\nu_{\min}$ to $\nu_{\max}$. Here the upper frequency is chosen being the upper corner frequency where still signal is dominating compared to noise.

The lower frequency limit can usually set to zero, if there is no signal offset in the data.

Selecting a frequency band of 0 to 400 kHz a coherence sum of 0.533 and 0.151, respectively, is calculated using Eq. 5.5. **Fig. 5.15** gives an example for a data analysis using the software *Signal similarity analysis MSC* (SiSimA-MSC, University of Stuttgart). In the case of a perfect coherence the MSC sum value would be equal to 1.

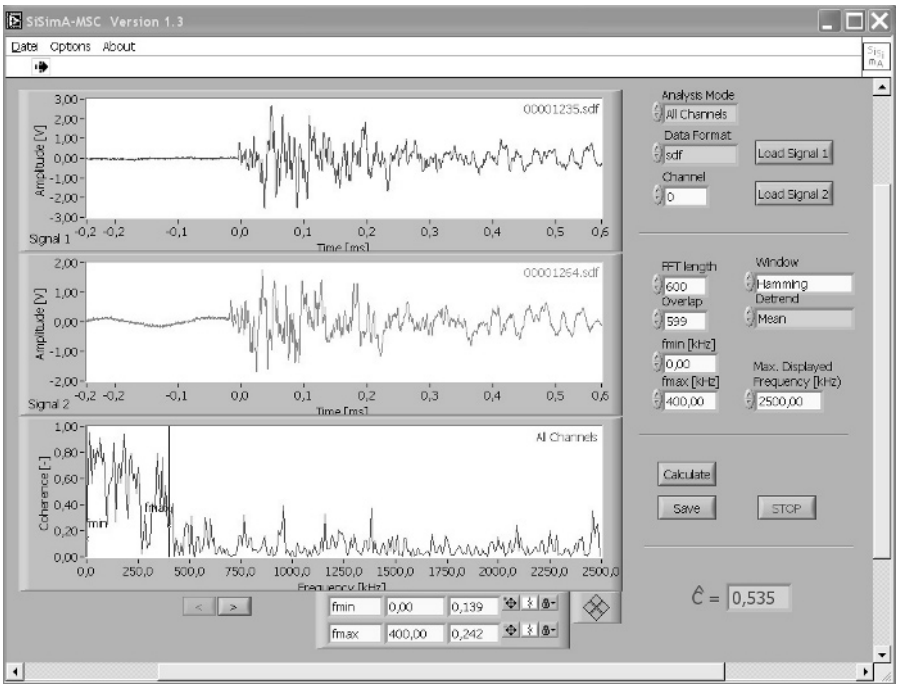

Fig. 5.15. MSC of a signal pair with high (left) and low similarity (right).

By transforming the signals to the frequency domain and calculating their coherence functions, it is therefore possible to find a quantitative relationship between the waveforms of signals with similar source mechanisms. This method is intended allow for rapid, systematic classification of the AE signals to recognize similarities and differences in signal pattern.

There are other signal classification approaches available that can be used to detect different fracture mechanisms using various measures of signal similarity. They are often referred to as 'feature extraction algorithms'. Some are based on wavelet analysis techniques (Hamstad 2001; Vallen 2001; Pazdera and Smutny 2001). All feature extraction algorithms face the problem that AE are usually only directly influenced by the frac-

ture process, in an undisturbed way, for a short part of the signal – the very first part. Generally speaking, the signal is dominated after a few oscillations by side reflections or other influences related to the material (anisotropy, heterogeneity, etc.), the propagation path or the sensor characteristics (sensor resonance, coupling, etc.) than by the source (Köppel 2002). In the example above, events from the same source region with similar failure mechanisms would result, for example, in a very low coherence sum if they were recorded with different types of sensors. Furthermore, recording these signals with sensors of the same type at different locations influenced by different coupling or signal transmission conditions would also result in a low coherence sum. Without a good knowledge of all these influences, the signal classification algorithms are of little value, especially if the material is complex in structure and geometry.

5.6 Inversion Techniques

Fracture types are of interest in fracture mechanics in understanding and classifying the way a material fails. Different terms are used to describe the cracking behavior. In the following section the terms ‘opening crack’ and ‘mode I’ are synonymous, as well as ‘mode II’ and ‘mode III’ for shear cracks, with forces parallel to the crack (in-plane shear) or forces perpendicular to the crack (out-of-plane shear). In seismology, shear dislocations are described by a double couple (DC) source because the DC force representation allows simplification of some mathematics – this is explained later in more detail (see chapter 5.6.3).

Inversion methods are used to determine the fracture type and orientation of a rupture (fault), as well as the seismic moment, which describes the rupture area that is related to the released energy from the waveforms of the recorded AE events. As illustrated in **Fig. 5.16**, the failure of a brittle specimen is accompanied by a sudden release of energy in the form of acoustic waves. Using an inversion algorithm, in combination with three-dimensional localization, a fault plane solution can be determined that enables the analysis of the fracture process in the material. Another more comprehensive method of fracture analysis is the application of moment tensor inversion methods. In this section, some examples of simple inversion techniques are given along with the basics of moment tensor inversion.

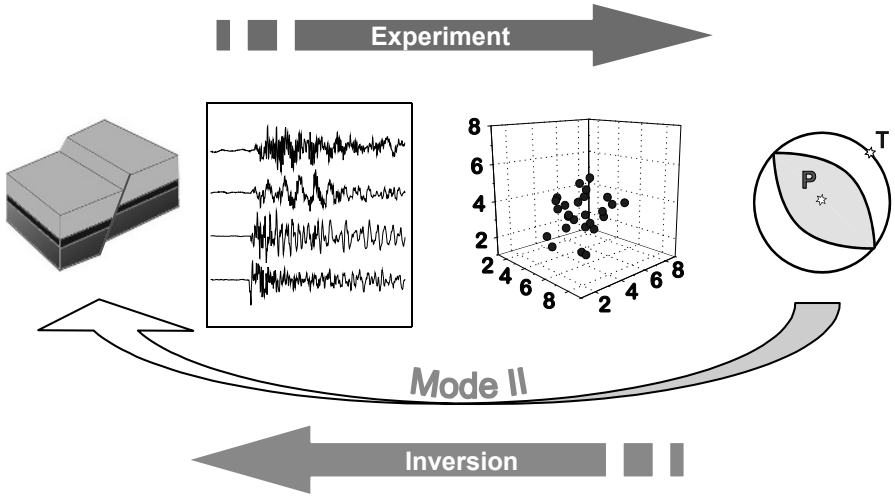

Fig. 5.16. Principle of inversion techniques in AE analysis.

5.6.1 Fault Plane Solution – First Motion Technique

There are several ways to determine the crack type and orientation of AE sources. One way is to use the polarities of initial P-wave pulses – this is known as the first motion technique. The distribution of the two senses of the wave polarity around the focus is determined by the radiation pattern of the source. Using the distribution of the polarities, it is possible to estimate the orientation of the nodal planes (where no displacement takes place) and thus the mechanism of the source. However, it is important to bear in mind that, due to the symmetry of the radiation pattern, two orthogonal planes can be fitted. These planes are often referred to as the 'fault plane' and the 'auxiliary plane'.

Positive polarities would be measured at all sensors, in the case of an opening crack (mode I). In the case of a shear fracture, the polarity of the P-wave onset changes from positive (upward deflection of waveform) to negative (downward deflection) according to the position of the sensor relative to the source and the shear planes (**Fig. 5.17**). These two examples assume that the sensors have been calibrated properly, so that a positive deflection of the signal indicates movement away from the source (i.e. compression).

If the radiation pattern of the source is to be analyzed, it is important that the pattern is sampled adequately over the focal sphere. This implies that many transducers are used, providing good coverage of the focal

sphere, i.e. a good distribution of sensors over all angles with respect to the fault plane. A minimum of 23 sensors is required to uniquely characterize the mechanism (Lockner 1993). For a smaller set of sensors, moment tensor inversion is more suitable (see next section) to estimate the failure mechanisms.

Unfortunately, it is not possible to quantify the deviation from a pure shear dislocation and to determine isotropic components of the source with this first motion technique.

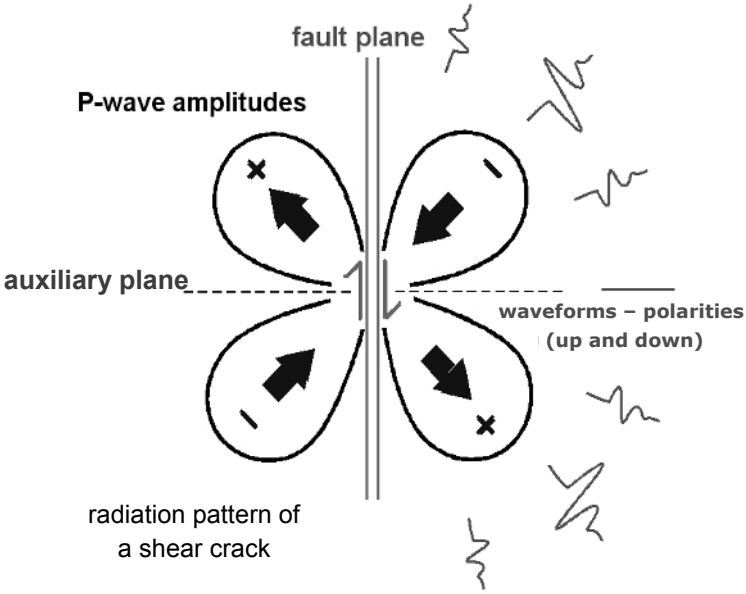

Fig. 5.17. Radiation pattern of a vertically oriented shear crack showing variation of polarities and amplitudes with angle from the source.

5.6.2 Basics of Moment Tensor Inversion

The seismic moment tensor consists of a set of point sources that describe the source mechanism and allow the slip planes (nodal planes) to be determined. The moment tensor is a useful concept because it can be used to completely describe the radiation pattern and the strength of the source.

The moment tensor **M** is defined by a combination of force couples and dipoles as:

$$\mathbf{M} = \begin{bmatrix} M_{xx} & M_{xy} & M_{xz} \\ M_{yx} & M_{yy} & M_{yz} \\ M_{zx} & M_{zy} & M_{zz} \end{bmatrix} \tag{5.6}$$

where each element of the matrix represents the force couples or dipoles as shown in **Fig. 5.22**.

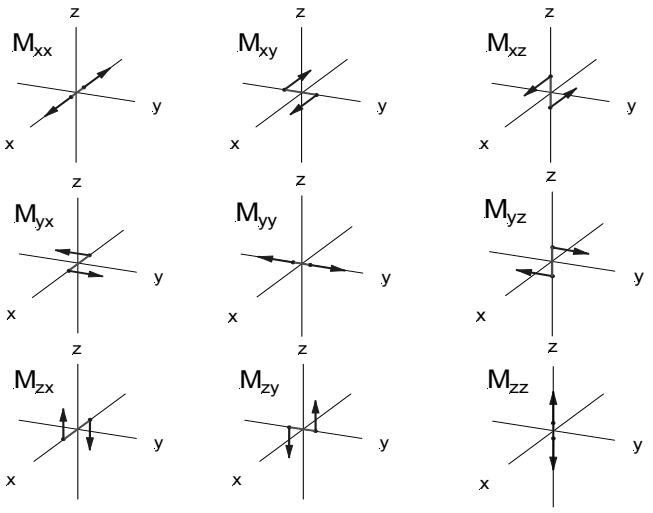

Fig. 5.18. Representation of the nine components of the moment tensor.

The first subscript of the force couple represents the direction of the two forces and the second subscript gives the direction of the arm of the couple. For example, the element M_{xy} is a force couple comprising two forces acting in the $+x$ and $-x$ direction on an arm parallel to the y-axis (**Fig. 5.18**, top row, middle position). The magnitude of M_{xy} is called the 'moment' of the force couple. Another example, element M_{xx} is a vector dipole consisting of two forces acting in the $+x$ and $-x$ directions, where the arm is parallel to the x-axis (**Fig. 5.18**, top, left) and hence has no moment.

In the case of a purely explosive source, the source mechanism can be described by summing the diagonal components of the moment tensor (**Fig. 5.19**).

The source mechanism of an idealized shearing source can be described by summing the off-diagonal components, $-(M_{xy}+ M_{yx})$ of the moment tensor (**Fig. 5.18**).

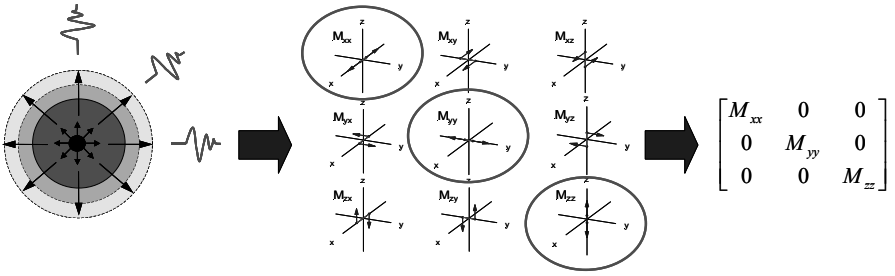

Fig. 5.19. (left) Idealized radiation pattern and force diagram of explosive source (middle); forces summed to describe source; (right) moment tensor of explosion.

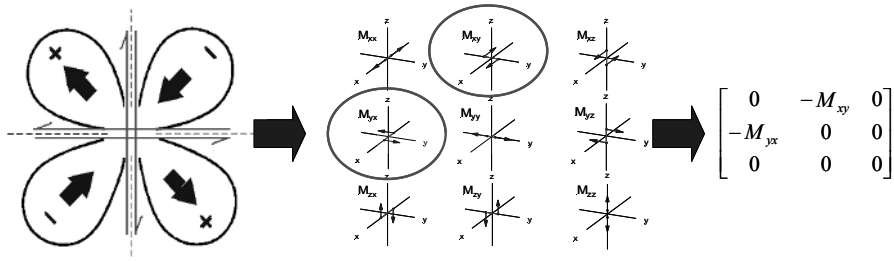

Fig. 5.20. (left) Radiation pattern and force diagram of idealised vertical shear source (middle); forces summed to describe source; (right) moment tensor of shearing source.

The term ‘inversion’ describes the mathematical process where measurements of displacement, and an assumed Earth or material model (the Green’s function) are used to determine the moment tensor of the source. This computation is possible because a linear relationship, first noted by Gilbert [1973], exists between the ground displacement and the Green’s function (**Fig. 5.21**).

Typical input data for a moment tensor inversion consist of the network geometry (coordinates of the sensors); knowledge of sensor polarity (i.e. whether an upwards deflection at the sensor indicates a compression or dilatation); sensor orientation; source coordinates; P and/or S-wave displacement amplitudes recorded at each sensor (time-domain inversion) or P and/or S-wave spectral amplitudes (frequency-domain inversion); and the polarities of the wave phases.

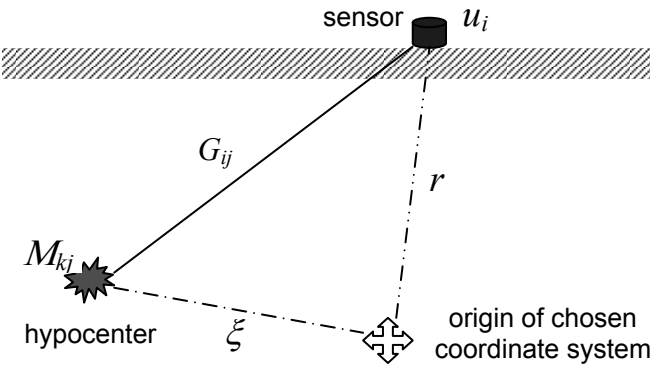

Fig. 5.21. Relation between the moment tensor and Green's functions.

Additional information that can be used are quality factors for each of the measurements (describing, for example, the quality of the spectral fits), which can be used to weight the equations; and, the corner frequency for the P and S-wave, for each sensor. The corner frequencies are particularly useful because their variation in space with respect to the rupture plane can be used to resolve the ambiguity of the fault plane solution. The propagation of the rupture front toward (or away from) an observer can cause an apparent corner frequency shift similar to a Doppler effect. In **Fig. 5.22**, the constant rupturing process begins at a single point and moves at a constant speed towards an end point. The wavefield measured by geophones oriented 'ahead' of the moving source experiences a Doppler shift towards the higher frequencies. In a similar way, the wavefield measured by geophones 'behind' the rupture will show a shift towards the lower frequencies. This model assumes that the waves are measured in the far-field and that the small scale rupturing process is of much shorter duration than the total rupturing process. As a result, the corner frequencies can vary in a systematic fashion according to the angle between the propagation direction and the recording station.

The relationship between the observed frequencies f and angle θ between the slip vector and station is given by Brawn [1989] as follows:

$$T - \frac{V \cdot T \cos(\theta)}{\beta} = \frac{1}{f}, \tag{5.7}$$

where β is the shear wave speed, V is the rupture velocity and T is the total duration of the rupture process. In an attempt to observe the Doppler

shift, a linear-linear plot of $\cos(\theta)$ versus $\frac{1}{f_c}$ where f_c is the corner frequency can be plotted for each station-slip vector pair, for both possible slip vectors.

The Doppler shift is used in the deep-level gold mining environment to discriminate between the fault plane and auxiliary plane of the nodal plane solution (Brawn 1989; Goldbach et al. 2006). In **Fig. 5.23**, graphs of $1/f_c$ are plotted versus the cosine of the angle θ between the slip vectors of the two fault plane solutions and each recording site, where f_c is the corner frequency of the S-wave measured from the velocity spectra. It can be seen that plane 1 (shown in red) is the 'real' fault plane, and that the rupture direction is in the opposite direction as the slip vector.

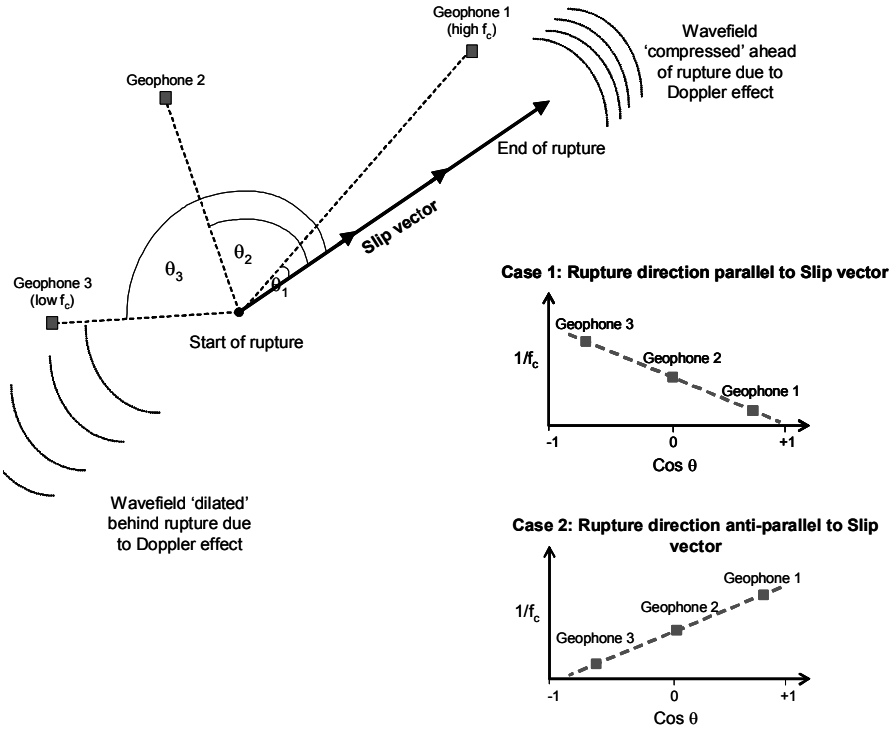

Fig. 5.22. Cartoon illustrating a 1-dimensional rupture model. The propagating source results in a Doppler shift in frequencies for geophones positioned 'ahead' and behind' the propagating source (Goldbach et al. 2006).

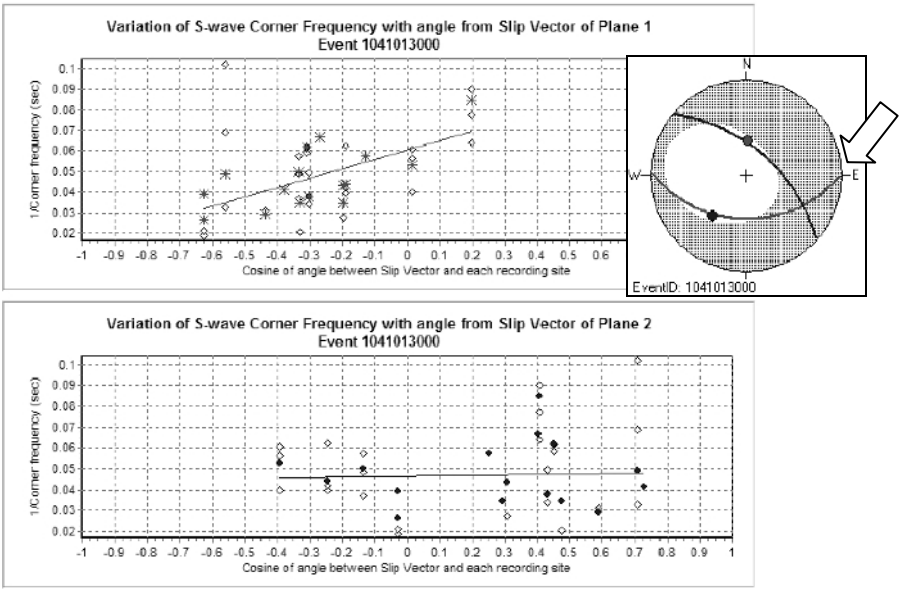

Fig. 5.23. Example showing the Doppler shift in corner frequencies (plane 1, red) for an event recorded in a deep level gold mine allowing the ambiguity of the fault plane solution to be resolved.

Moment tensor inversion (MTI) can provide quantitative information regarding the failure modes causing the AE. A moment tensor analysis using all the AE waveform data during the loading of a specimen can give insight into the complete failure history.

Before the fundamental equations used in MTI are discussed, the variety of MTI approaches and their applications are described.

Classification of moment tensor inversion methods

Numbers of moment tensor inversion (MTI) techniques have been proposed in the literature. The methods applied differ greatly according to the available data and the purpose of the study. For the purposes of this textbook, it is useful to distinguish between the 'absolute' and 'relative' methods. These broad classes of inversion procedure are based on methods used to estimate the Green's functions, which describe the wave propagation between the source and receiver.

In the absolute methods, the Green's functions are evaluated theoretically, or determined empirically from observations and a known source. The most straightforward approach is to use a homogeneous isotropic material model (Ohtsu 1991). However, this is often not adequate for many of the

materials used in civil engineering. More suitable are approaches based on finite-difference methods (Fukunaga and Kishi 1986; Enoki and Kishi 1988; Napier et al. 2005; Hildyard et al. 2005), which can take into account the heterogeneity of the materials. Methods based on a combination of the above mentioned techniques (Landis 1993; Landis and Shah 1995) are often not sufficient due the attenuation of the material.

The absolute methods are often used in global seismology, but are difficult to apply in environments where there are possible lateral inhomogeneities, such as the underground mining environment and in materials often used in civil engineering. In these cases, it is not always possible to calculate the Green's functions with adequate accuracy, resulting in systematic errors being introduced into the moment tensor solution.

For the absolute methods to be properly applied, the influence of material parameters has to be well known. This is usually not the case for fractures in concrete, where aggregates, reinforcement and air-filled pores are common. In addition, the sensor characteristics must be well known (this is not a problem in geophysics where seismometers with a flat response over the signal frequency range are usually used). Poor coupling of transducers also limits the application of these simple inversion techniques.

In contrast to the absolute methods, the relative inversion methods do not require the calculation of theoretical Green's functions for each event. Relative methods are based on the concept of a common ray-path between a cluster of seismic sources and any receiver, and assume that all the events in the cluster experience the same wave propagation effects to each receiver (**Fig. 5.23**).

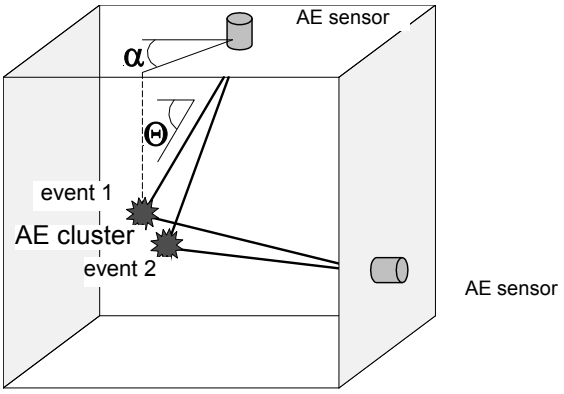

Fig. 5.24. Cluster of AE events with approximately the same path to the sensors. a indicates the azimuth and Q the incidence angle (Grosse et al. 1997).

These methods are applicable to clusters of events where the distance between the hypocenters (AE focuses) of all the AE events is small compared to the travel path to the sensors.

In the relative methods, the Green's function of a well-known reference event(s) can be used to calculate the Green's function of the medium for other nearby events (e.g. Patton 1980; Strelitz 1980; Oncescu 1986). This method also has its limitations, when only a few reference events are available or when their fracture mechanisms are not well known.

In the relative method proposed by Dahm [1996] (known as the relative method without a reference mechanism) the path effects described by the Green's functions are eliminated analytically – thereby completely avoiding the explicit use of the Green's functions. However, this method is applicable to clusters of events having different radiation patterns only and, because there is no absolute reference, any of the six components of the moment tensors can be incorrect by an unknown scaling factor. This syndrome can be reduced, but not eliminated, through reference to scalar moment estimates. Furthermore, when the mechanisms are similar the method is extremely sensitive to noise. This is a serious disadvantage in cases where clusters of recorded events might have very similar mechanisms. This problem is accentuated when the method is applied to very small events having similar mechanisms and with signals just above the noise level (Andersen 2001).

A problem common to the absolute and relative MTI methods is their sensitivity to noise/errors in the observations and their dependency on accurate Green's functions to describe the wave propagation. Factors such as the focusing and defocusing of the ray-paths due to the presence of lateral inhomogeneities in complex materials, the degradation of the velocity model due to fracturing, the presence of voids on the seismic ray-paths, low signal-to-noise ratios all have adverse effects on the accuracy of the MTI. For example, the deviations in the ray-paths due to the presence of an inhomogeneity between a cluster of seismic sources and a particular sensor can result in consistently high or low amplitudes being recorded at that sensor (for all the events in a cluster). This would result in systematic errors being introduced into the moment tensor elements. To compensate for such errors, hybrid MTI methods have been developed by Andersen [2001]. These methods apply to clusters of events, are iterative, and are a combination of the absolute and relative MTI methods. The hybrid methods are essentially weighting schemes that aim to increase the accuracy of the computed moment tensor by reducing the effect of noisy data on the system of equations and correct for site effects. These methods can also be used to enhance signals recorded near a nodal plane in the radiation pattern or to decrease the influence of a low quality observation.

Various weighting schemes, that apply to individual events, have been proposed in the literature (Udias & Baumann 1969; Šílený et al. 1992). The new aspect of the hybrid methods is that the correction or weight applied to a particular observation is based on the residuals (for a particular geophone site, channel and phase) calculated using all of the events in the cluster – this constitutes the relative component of the hybrid methods.

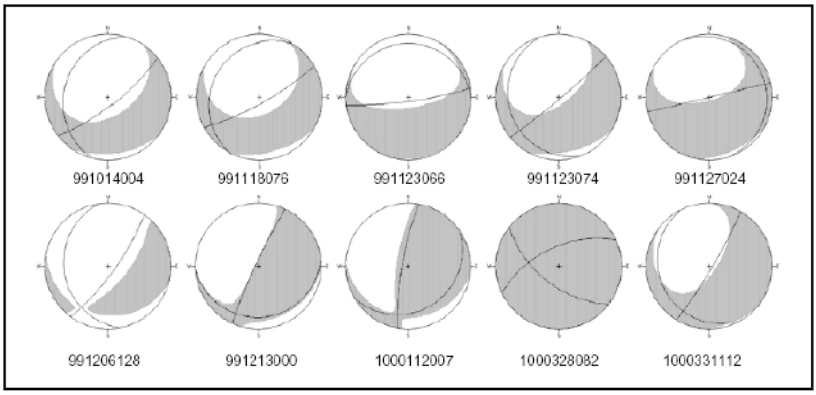

Fig. 5.25. Radiation patterns and nodal plane solutions, calculated using absolute MTI methods, for a data set of highly similar events, recorded in a deep level gold mine (Linzer 2005).

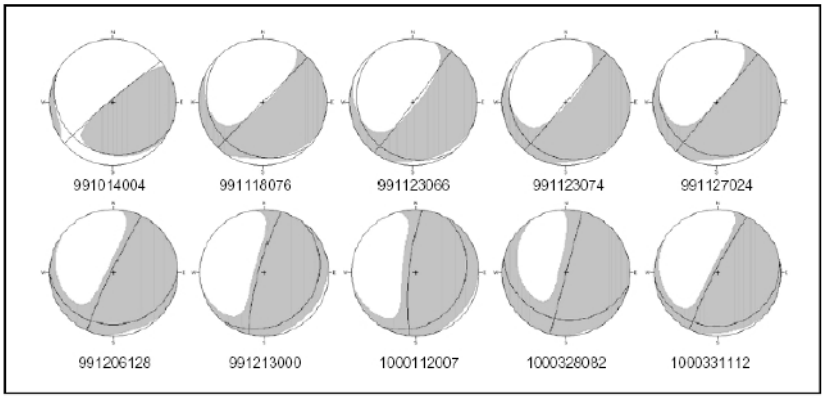

Fig. 5.26. Radiation patterns and nodal plane solutions of a data set of similar events calculated using hybrid MTI methods (Linzer 2005).

Fig. 5.25 shows the radiation patterns and nodal plane solutions, calculated using absolute MTI methods, for data recorded in a deep level gold mine. These 10 events had highly similar waveforms, and were therefore expected to have similar solutions. As is evident from **Fig. 5.25**, there is a

fair amount of scatter in the patterns. The situation is much improved in **Fig. 5.26** after applying the hybrid MTI method to the data.

Summary of MTI method

The goal of all MTI methods is to use observed values of ground displacement to infer properties of the source, as characterized by the moment tensor. By using the representation theorem for seismic sources (Aki & Richards 1980) and assuming a point source, the displacement field u_k recorded at a receiver k is given by:

$$u_k(x,t) = G_{ki,j}(x, t; \xi, t') * M_{ij}(\xi, t') \tag{5.8}$$

where $G_{ki}(x,t;\xi,t')$ are the elastodynamic Green's functions containing the propagation effects between the source (ξ,t') and receiver. The comma between the indices in Eq. 5.8 describes the partial derivatives at the source with respect to the coordinates after the comma, i.e. $G_{ki,j} = \frac{\partial G_{ki}}{\partial \xi_j}$.

The $M_{ij}(\xi,t)$ terms are the nine time-dependent components of the moment tensor. This equation can be simplified dramatically by assuming that the source time function is an impulse and that all of the moment tensor components have the same time-dependency (synchronous source approximation). In addition, since the equivalent body forces conserve angular momentum, $M_{ij} = M_{ji}$, only six of the components are required. Applying these assumptions, Eq. 5.8 reduces to the following linear relationship:

$$u_k = G_{ki,j} M_{ij} \tag{5.9}$$

which can be written using matrix notation as:

$$\mathbf{u} = \mathbf{G}\,\mathbf{m} \tag{5.10}$$

where **u** is a vector of dimension n of sampled values of the integrated ground displacement or spectral plateaus depending on whether a time or a frequency-domain approach is being taken; **G** is a $n \times 6$ matrix of Green's functions in the coordinate system of the receivers; and, **m** is a vector consisting of the moment tensor components M_{11}, M_{22}, M_{33}, M_{12}, M_{13} and M_{23}. In most cases $n >> 6$ and the system of equations is, in principle, overdetermined. To solve for the components of the moment tensor **m**, Eq. 5.10 is written as an inverse problem such that:

$$\mathbf{m} = \mathbf{G}^{-1}\mathbf{u} \tag{5.11}$$

where $\mathbf{G}^{-1}$ is the generalized inverse of $\mathbf{G}$. The system of linear equations can then be solved using standard least-squares techniques.

Interpretation of the moment tensor

Once the moment tensor has been computed, a number of source parameters can be calculated to aid interpretation. The most basic of the source parameters is the scalar seismic moment M_o which is a measure of the irreversible inelastic deformation in the area of the rupture and is the root-mean-squared average of the moment tensor elements:

$$M_o = \sqrt{\tfrac{1}{2}\sum_{i,j=1}^{3} M_{ij}^2} \tag{5.12}$$

The scalar moment can be related to attributes of the source:

$$M_o = \mu A \overline{D} \tag{5.13}$$

where μ is the rigidity (described by the Young or shear modulus of the medium), A is the surface area of the rupture, and $\overline{D}$ is the average final static displacement after the rupture. The rigidity modulus μ has a relatively simple physical meaning and measures the resistance of the elastic body to shearing deformation.

Slightly more complicated analyses involve decomposing the moment tensor into its isotropic and deviatoric components, which represent the volume change and shearing contributions to the source mechanism. To do this, the moment tensor is first diagonalized and the deviatoric component is calculated by subtracting the one third of the trace from each of the eigenvalues:

$$\mathbf{M}_{dev} = \begin{bmatrix} e_1 - \frac{1}{3}tr(M) & 0 & 0 \\ 0 & e_2 - \frac{1}{3}tr(M) & 0 \\ 0 & 0 & e_3 - \frac{1}{3}tr(M) \end{bmatrix} \tag{5.14}$$

where *tr(M)* is the trace of the moment tensor, and is equal to the sum of the eigenvalues: $tr(M) = e_1 + e_2 + e_3$. The trace is a measure of the volume change at the source and the sign of *tr(M)* gives the direction of motion relative to the source with positive outwards. For example, *tr(M)* that is negative indicates an implosion.

The deviatoric component can be further decomposed into a variety of eigenvalue combinations that represent simple arrangements of equivalent body forces, adapted from fracture mechanics, like that of an opening crack (mode I) or of shear cracks (mode II or III) (**Fig. 5.27**).

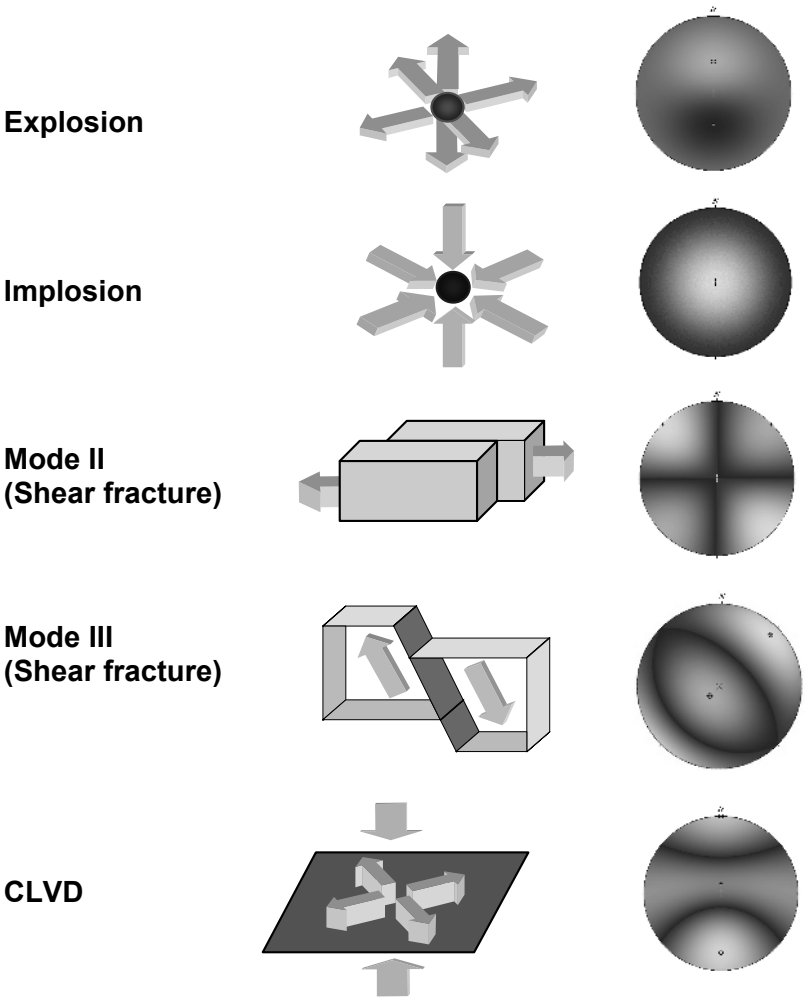

Fig. 5.27. Physical models along with a sketch of fault plane movements and the associated radiation pattern (P-waves).

The coseismic volume change at the source can be calculated from

$$\Delta V = \frac{tr(M)}{(3\lambda + 2\mu)} \tag{5.15}$$

where λ and μ are Lamé's elastic moduli (McGarr 1992). The constant λ is not simply related to experimentally observed quantities and its value is usually calculated from those of μ and one of the other experimentally determined coefficients. For quartzitic strata, $3\lambda + 2\mu = 1.63 \times 10^5$ MPa (McGarr 1992).

The deviatoric moment tensor can also be expressed as a sum of double-couples, M_1 and M_2:

$$\mathbf{M}_{dev} = \begin{bmatrix} M_1 & 0 & 0 \\ 0 & 0 & 0 \\ 0 & 0 & -M_1 \end{bmatrix} + \begin{bmatrix} 0 & 0 & 0 \\ 0 & M_2 & 0 \\ 0 & 0 & -M_2 \end{bmatrix} \tag{5.16}$$

Each of the double-couple terms has scalar seismic moment defined by Eq. 5.13. Therefore, the total shear deformation can be computed using:

$$M_o = \mu A \bar{D} = M_1 + M_2 \tag{5.17}$$

Perhaps one of the most useful parameters that can be computed from the deviatoric moment tensor is the fault plane solution. This consists of the orientations of the two planes (usually expressed as strike, dip and rake, **Fig. 5.28**) that can be fitted to the deviatoric moment tensor along which zero displacement takes place (i.e. the nodal planes). The moment tensor components for a double-couple of arbitrary orientation are given by Aki & Richards (1980) as

$$M_{ij} = M_0 \left(s_i n_j + s_j n_i \right) \tag{5.18}$$

where **s** is a unit slip vector lying in a fault plane and **n** is a unit vector normal to the plane. Since the moment tensor **M** is symmetric, $M_{ij} = M_{ji}$, the vectors **s** and **n** can be interchanged, which means that the vector normal could be the slip vector to the other plane, and vice versa. These two nodal planes are called the fault plane and auxiliary plane, and together are called the fault plane solution. The fault plane solution indicates the type of faulting that is taking place in the source area (**Fig. 5.29**) and also gives an indication of the stress regime of the area, for example, normal faulting indicates that the maximum principle stress direction is vertical.

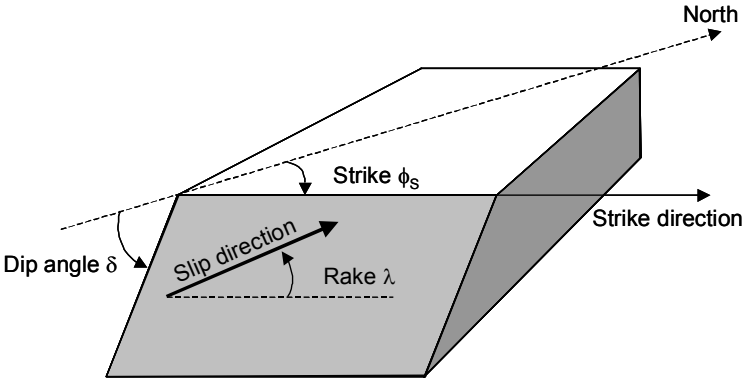

Fig. 5.28. Definition of fault orientation parameters: strike, dip and rake (Andersen 2001).

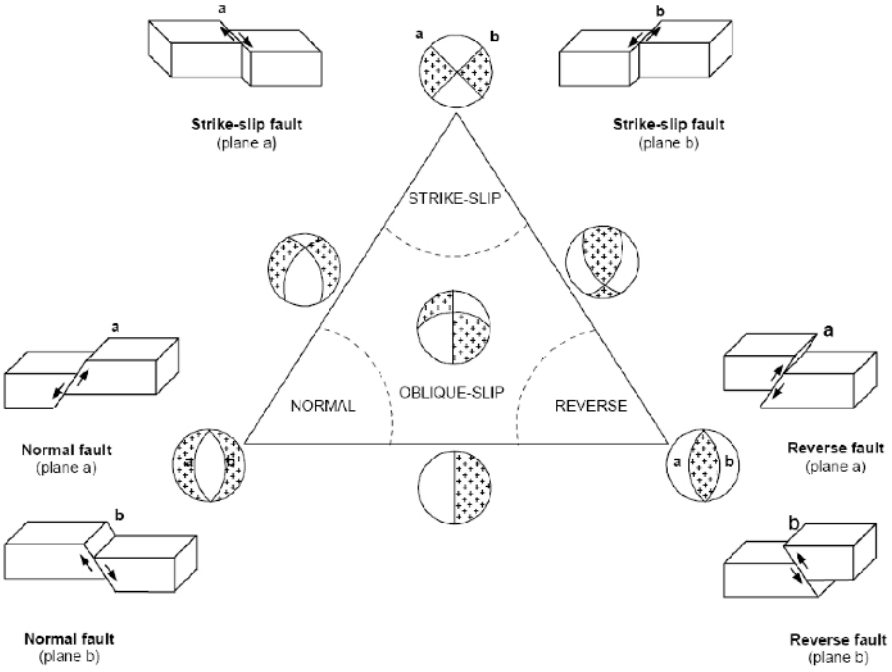

Fig. 5.29. Triangle diagram for displaying the focal mechanism projections for common fault types. The three vertices correspond to pure strike-slip (top), reverse (right) and normal fault (left) mechanisms. Planes *a* and *b* represent either the fault plane or auxiliary plane. Shaded regions (++) indicate compressional P-wave motions (Andersen 2001).

A plethora of decompositions is possible, but many are physically implausible. It is important to have an idea of the likely failure modes, and apply the relevant decomposition. Reports are available illustrating different ways to decompose the moment tensor (e.g. Jost & Hermann [1989]).

Another parameter that can be calculated is the deviation, ε, of the seismic source from that of a pure double-couple:

$$\varepsilon = \left| \frac{e_3^*}{e_1^*} \right| \tag{5.19}$$

where e_1^* and e_3^* are the maximum and minimum deviatoric eigenvalues and $\left|e_1^*\right| \geq \left|e_2^*\right| \geq \left|e_3^*\right|$. $\varepsilon = 0$ for a pure double-couple source, and $\varepsilon = 0.5$ for a pure compensated linear vector dipole (CLVD) [Dziewonski et al. 1981]. The percentage of double-couple contributions, $\%DC$, to the deviatoric moment tensor can be calculated from ε using:

$$\%\mathrm{DC} = 100 \cdot (1 - 2\varepsilon) \tag{5.20}$$

[Jost & Hermann 1989]. The percentage of CLVD contributions, $\%CLVD$, to the deviatoric moment tensor can be calculated from ε using:

$$\%CLVD = 200\ \varepsilon \tag{5.21}$$

The sum of % *DC* and % *CLVD* should be 100.

Another measure of the nature of the moment tensor is the R-ratio introduced by Feigner & Young [1992]. Ratio R is essentially the ratio of volumetric to shear components and is defined as:

$$R = \frac{tr(M)}{\left|tr(M)\right| + \sum_{k=1}^{3} \left|e_k^*\right|} \cdot 100 \tag{5.22}$$

where e_k^* are the deviatoric eigenvalues. If R>30, the event is considered to be dominantly tensile; if $-30 \leq R \leq 30$, the event is a dominantly shear event; if $R < -30$ the event is dominantly implosive. An event could show implosive components if there is collapse towards a void, for example, closure of an underground excavation.

References

Aki K, Richards PG (1980) Quantitative seismology. Freeman, San Francisco

Andersen LM (2001) A relative moment tensor inversion technique applied to seismicity induced by mining. PhD thesis, University of the Witwatersrand, Johannesburg, p 230

ASTM (1982) E610 - Standard Definitions of Terms Relating to Acoustic Emission. ASTM, pp 579-581

Backus GE, Mulcahy M (1976) Moment tensor and other phenomenological descriptions of seismic sources. J. R. astr. Soc. 46:341-361

Balázs GL, Grosse CU, Koch R, Reinhardt HW (1993) Acoustic emission monitoring on steel-concrete interaction. Otto Graf Journal 4:56-90

Balázs GL, Grosse CU, Koch R (1996a) Acoustic emission technique for detection of internal cracking in concrete. Bratislava, 2. RILEM Int. Conf. on the Diagn. of Concrete Structures

Balázs GL, Grosse CU, Koch R, Reinhardt HW (1996b) Damage accumulation on deformed steel bar to concrete interaction detected by acoustic emission technique. Mag. of Concrete Research 48:311-320

Bar-Cohen Y, Xue T, Lih SS (1996) Polymer piezoelectric transducers for ultrasonic NDE. NDTnet 1(9):7

Barker JS, Langston CA (1982) Moment tensor inversion of complex earthquakes. Geophys. J. R. Astr. Soc. 46:341–371

Ben-Menahem A, Singh SJ (1981) Seismic waves and sources. Springer, New York

Berger H (ed) (1977) Nondestructive testing standards - a review. Gaithersburg, ASTM, Philadelphia

Berthelot JM, Robert JL (1987) Modeling concrete damage by acoustic emission. J. of Ac. Emission 6:43-60

Brawn DR (1989) A maximum entropy approach to underconstraint and inconsistency in the seismic source inverse problem; Finding and interpreting seismic source moments, Ph.D. Thesis, University of the Witwatersrand, Johannesburg

Buland R (1976) The mechanics of locating earthquakes. Bull. Seis. Soc. Am. 66:173-187

Calvalho FCS, Shah KR, Labuz J (1998) Source model of acoustic emission using displacement discontinuities. Int. J. Rock. Mech. Min. Sci. Geomech. Abstr., 35:514–515

Carter GC, Ferrie JF (1979) A coherence spectral estimation program. Weinstein CJ (Programs for digital signal processing), IEEE Press, 2.3-1-2.3-18

CEN (2000) European Standard EN 1330-9 – Nondestructive Testing - Terminology - Part 9: Terms used in Acoustic Emission Analysis. Comité Européan de Normalisation CEN. (1330-9) release 2000-3, pp 1-23

Dahm T (1993) Relativmethoden zur Bestimmung der Abstrahlcharakteristik von seismischen Quellen. Thesis, University of Karlsruhe, Germany, p 122

Dahm T (1996) Relative moment tensor inversion based on ray theory: theory and synthetic tests. Geophys. J. Int. 124:245-257

DGZfP. Merkblatt SE-3(1991) Richtlinie zur Charakterisierung des Schallemissionsprüfgerätes im Labor. Deutsche Gesellschaft für Zerstörungsfreie Prüfung. Recommendation SE-3

Drouillard TF (1979) Acoustic emission - a bibliography with abstracts. Plenum Publishing Corporation p 787

Drouillard TF (1988) Introduction to acoustic emission. Materials Evaluation 46:174-179

Drouillard TF (1996) A history of acoustic emission. J. Acoustic Emission 14 (1):1-34

Efron B, Tibshirani R (1986) Bootstrap methods for standard errors, confidence intervals and other measures of statistical accuracy. Statistical Science 1:54-77

Enoki M, Kishi T (1988) Theory and analysis of deformation moment tensor due to microcracking. Int. J. Frac. 38:295-310

Feignier B, Young RP (1992) Moment tensor inversion of induced microseismic events: Evidence of nonshear failures in the $-4 < M < -2$ moment magnitude range, Geophys. Res. Lett. 19:1503–1506

Förster F, Scheil E (1936) Akustische Untersuchungen der Bildung von Martensitnadeln. Zeitschrift für Metallkunde 28:245-247

Fukunaga Y, Kishi T (1986) Progress in Acoustic Emission III. Yamaguchi, K. et al. (eds), Jap. Soc. of Non-Destr. Insp., Tokyo, pp 722-731

Geiger L (1910) Herdbestimmung bei Erdbeben aus den Ankunftszeiten. Nachrichten von der Königlichen Gesellschaft der Wissenschaften zu Göttingen 4:331-349

Glaser SD, Weiss GG, Johnson LR (1998) Body waves recorded inside an elastic half-space by an embedded, wideband velocity sensor. L. Ac. Soc. Am. 104 (3), Pt. 1:1404-1412

Goldbach OD, Rangasamy T, Linzer LM, Spottiswoode SM, Kataka MO, du Pisani P (2006) SIMRAC 04-03-03: Lead-lag design criteria and seismicity patterns. SIMRAC Final Project Report, Department of Minerals and Energy, South Africa. Under review

Grosse CU, Reinhardt HW, Balázs GL (1995) Acoustic emission data from pull-out tests of reinforced concrete analysed with respect to passive US-tomography. Jones JP (ed) 21,. Laguna Beach, Plenum Press, New York, pp 635-647

Grosse CU (1996) Quantitative zerstörungsfreie Prüfung von Baustoffen mittels Schallemissionsanalyse und Ultraschall. Thesis, University of Stuttgart, Germany, p 168

Grosse CU, Weiler B, Reinhardt HW (1997) Relative moment tensor inversion applied to concrete fracture tests. J. of Acoustic Emission, 14(3-4):64-87

Grosse CU, Reinhardt HW, Dahm T (1997) Localization and classification of fracture types in concrete with quantitative acoustic emission measurement techniques. NDT&E International 30:223-230

Grosse CU, Reinhardt HW (1999) Schallemissionsquellen automatisch lokalisieren. Materialprüfung 41:342-346

Grosse CU (2000) WinPecker - Programm zur vollautomatischen dreidimensionalen Lokalisierung von Schallemissionsquellen. DGZfP Report 72:191-204

Grosse CU, Ruck HJ, Bahr G (2001) Analyse von Schallemissionssignalen unter Verwendung der Wavelettransformation, 13. Colloquium AE DGZfP Report 78, pp 41-50

Hamstad MA (1994) An examination of piezoelectric polymers as wideband acoustic emission displacement sensors. Progress in AE VII, Jap. Soc. for NDI, pp 79-86

Hamstad MA (1997) Improved signal-to-noise wideband acoustic/ultrasonic contact displacement sensors for wood and polymers. Wood and fibre science 29 (3):239-248

Hamstad MA (2001) An illustrated overview of the use and value of a wavelet transformation to acoustic emission technology. NIST, Boulder, report

Hamstad MA, Fortunko CM (1995) Development of practical wideband high-fidelity acoustic emission sensors. Proc. of SPIE Conf. on NDE of Aging Infrastructure 2456, pp 281-288

Hatano H, Mori E (1976) Acoustic-emission transducer and its absolute calibration. J. Acoust. Soc. Am. 59(2):344-349

Hildyard MW, Milev A, Linzer LM, Roberts MKC, Jager AJ, Spottiswoode SM (2005) PLATMINE 3.7: Assess the hazard posed by dynamic failure of pillars in the back areas of platinum mines. PLATMINE final project report. Under review

Hsu NN, Breckenridge FR (1981) Characterization and calibration of acoustic emission sensors. Materials Evaluation 39:60-68

Hykes DL, Hedrick WR, Starchman DE (1992) Ultrasound Physics and Instrumentation. Mosby-Year Book, 2. ed.

Jost ML, Hermann R (1989) A students guide to and review of moment tensors. Seism. Res. Letters 60:37-57

Kaiser J (1950) Untersuchungen über das Auftreten von Geräuschen beim Zugversuch. Thesis, University of Munich, Germany, pp 1-38

Kapphahn G (1990) Messtechnische Grundlagen der Schallemissionsanalyse als Prüfverfahren an nichtmetallischen Baustoffen. Thesis, TH Leipzig, Germany

Kino GS (1987) Acoustic waves: Devices, Imaging, and analog signal processing. Prentice Hall

Köppel S, Vogel T (2000) Localization and identification of cracking mechanisms in reinforced concrete using acoustic emission analysis. Proc. 4. Int. Conf. on Bridge Management, Surrey pp 88-95

Köppel S, Grosse CU (2000) Advanced acoustic emission techniques for failure analysis in concrete. Proc. of 15. World Conf. on NDT, Rome, on CD-ROM

Köppel S (2002) Schallemissionsanalyse zur Untersuchung von Stahlbetontragwerken. Thesis ETH No. 14490, Swiss Federal Institute of Technology (ETH) Zürich, Switzerland, p 172

Krautkrämer J, Krautkrämer H (1986) Werkstoffprüfung mit Ultraschall. Springer, Berlin

Labusz JF, Chang HS, Dowding CH, Shah SP (1988) Parametric study of AE location using only four sensors. Rock mechanics and rock engineering 21:139-148

Landis EN, Ouyang C, Shah SP (1992) Automated Determination of First P-Wave Arrival and Acoustic Emission Source Location. J. of Acoustic Em. 10(1-2):97-103

Landis EN (1993) A quantitative acoustic emission investigation of microfractures in cement based materials. Thesis, Northwestern University, Evanston, USA, p 185

Landis EN, Shah SP (1995) Frequency-Dependent Stress Wave Attenuation in Cement-Based Materials. Journal of Engineering Mechanics 121(6):737-743

Lawson CH, Hanson RJ (1974) Solving Least Squares Problems, Prentice-Hall, Engelwood Cliffs, New Jersey

Linzer LM (2005) Manuel Rocha Medal Recipient: A relative moment tensor inversion technique applied to seismicity induced by mining. Journal of Rock Mechanics and Rock Engineering 38, No. 2:81–104

Lockner AD, Byerlee JD, Kuksenko V, Ponomarev A, Sidrin A (1993) Quasi-static fault growth and shear fracture energy in granite. Nature 350:39–42

Lyamshev ML, Stanullo J, Busse G (1995) Thermoacoustic vibrometry. Materialprüfung 37:1-2

McCabe WM, Koerner RM, Lord AE (1976) Acoustic emission behavior of concrete laboratory specimens. ACI J. 73:367-371

McGarr A (1992) Moment tensors of ten Witwatersrand mine tremors. Pageoph. 139:781–800

Miller RK, McIntire P (eds) (1987) Acoustic emission testing. Nondestructive testing handbook, vol.5. American Society for Nondestructive Testing. 2. edition, p 603

Napier JAL, Spottiswoode SM, Sellers E, Hildyard MW, Linzer LM (2005) SIMRAC 02-03-01: New criteria for rock mass stability and control using integration of seismicity and numerical modeling. SIMRAC Final Project Report, Department of Minerals and Energy, South Africa. Under review. Downloadable from www.simrac.co.za

Ohtsu M (1991) Simplified Moment Tensor Analysis and Unified Decomposition of Acoustic Emission Source: Application to in-Situ Hydrofracturing Test. JGR 96:6211-6221

Ohtsu M, Shigeishi M, Iwase H, Koyanagi W (1991) Determination of crack location, type and orientation in concrete structures by acoustic emission. Mag. Conc. Res. 155:127-134

Oncescu L, Grosse CU (1998) HYPOAE - A program for the localization of hypocenters of acoustic emissions. Computer Program, Rev.2.1

Oncescu MC (1986) Relative seismic moment tensor determination for Vrancea intermediate depth earthquakes. Pure Appl. Geophys. 124:931–940

Patton H (1980) Reference point equalisation method for determining the source and path of surface waves. JGR 85:821-848

Pazdera L, Smutny J (2001) Using non-traditional tool – discrete wavelet transformation to analysis of acoustic emission signal. Acoustic Emission AE2001,

Int. Conf. on Internet, March - September 2001, Brno, Czech republic, <http://cmspro.fme.vutbr.cz/uk/odbory/vav/konf.htm>

Proctor TM (1982) Some Details on the NBS Conical Transducer. J. of Acoustic Em. 1(3):173-178

Proctor TM (1986) More Recent Improvements on the NBS Conical Transducer. J. of Acoustic Em. 5(4):134-142

Reinhardt HW, Hordijk DA (1989) Cracking and Damage. Mazars J, Bazant ZP (eds), Elsevier, London, pp 3-14

Rikitake T, Sato R, Hagiwara Y (1987) Applied mathematics for earth scientists, Mathematical approaches to geophysics. Kluwer Academic Pub., Dordrecht

Ruzzante JE, Serrano EP (2000) Estimation of differences in event arrival times through wavelet transform techniques. (on CD-ROM) Proc. 15th World Conference on NDT, Rome

Sachse W, Kim KY (1987) Quantitative acoustic emission and failure mechanics of composite materials. Ultrasonics 25:195-203

Salamon MDG, Wiebols GA (1974) Digital location of seismic events by an underground network of seismometers using the arrival times of compressional waves. Rock Mech. 6:141-166

Sellers EJ, Kataka MO, Linzer, LM (2003) Source parameters of acoustic emission events and scaling with mining-induced seismicity. J. Geophys. Res., 108, B9:2418–2430

Šílený J, Panza GF, Campus P (1992) Waveform inversion for point source moment retrieval with variable hypocentral depth and structural model. Geophys. J. Int. 109:259–274

Scruby CB (1985) Quantitative acoustic emission techniques. Nondestr. Test. 8:141-210

Shah KR, Labuz JF (1995) Damage mechanism in stressed rock from acoustic emission. J. Geophys. Res., 100:15527–15339

Sklarczyk C, Gries H, Waschkies E (1990) Testing during concrete construction. Reinhardt HW (ed), Chapman and Hall, London, pp 297-208

Strelitz RA (1980) The fate of the downgoing slab: A study of the moment tensors from body waves of complex deep-focus earthquakes, Phys. Earth. Planet. Int. 21:83–96

Udias A, Baumann D (1969) A computer program for focal mechanism determination combining P and S wave data. Bull. Seism. Soc. Am. 59:503–519

Vallen H, Forker J (2001) Optimierung der Analyse von Daten der Schallemissionsprüfung eines vorgeschädigten Objekts während dem Bersttest. 13. Kolloquium Schallemission, DGZfP Berichtsband 78:11-21

Wald DJ, Kanamori H, Helmberger DV, Heaton TH (1993) Source Study of the 1906 San Francisco Earthquake. Bull. Seism. Soc. Am. 83:981-1019

Weiler B, Grosse CU (1995) Calibration of Ultrasonic transducers - a comparative study of different methods. Otto Graf Journal 6:153-167

Wood BRA, Harris RW (1982) An evaluation of the breaking pencil lead calibration technique. Jap. Soc. NDI. Progress in acoustic emission VI, Tokyo, pp 423-439.

Yoon DJ, Weiss WJ, Shah SP (2000) Assessing damage in corroded reinforced concrete using acoustic emission. J. Eng. Mech. 126(3):273-283

Zang A, Wagner FC, Stanchits S, Dresen G, Andresen R, Haidekker MA (1998) Source Analysis of Acoustic Emissions in Granite Cores under Symmetric and Asymmetric Compressive Load. Geophys. J. Int. 135:1113-1130

Zhao J, Ma Y, Gao H, Yang J (2000) Denoising Method of AE Signal by Using Wavelet Transform. (on CD-ROM), Proc. of 15th World Conf. on NDT, Rome

6 Source Localization

Jochen H. Kurz, Stefan Köppel, Lindsay M. Linzer, Barbara Schechinger and Christian U. Grosse

6.1 Introduction

Quantitative methods in acoustic emission analysis require localization techniques to extract the source coordinates of the acoustic emission events as accurately as possible. There are many different ways to localize AEs in practice that can be used to obtain the required resolution in one, two, or three dimensions. The most appropriate technique depends on the objective of the experiment, the required solution and on the geometric shape.

The methods of acoustic emission localization which will be presented in the following section were developed in the framework of earthquake seismology. The principal of earthquake source localization can be applied directly to acoustic emission source localization with minor modifications. A detailed description of earthquake localization methods can be found in, for example, Bormann [2002], Aki and Richards [1980] or Shearer [1999]. These are also the main references for this chapter. Acoustic emission localization is applied to all kinds of construction materials and even in medical and electrotechnical sciences. Examples of acoustic emission localization can be found in Grosse [1996], Zang et al. [1998], Ohtsu [1998], Köppel and Grosse [2000], Moriya et al. [2002], Finck et al. [2003], Sellers et al. [2003], Finck [2005], Schechinger [2005] and Kurz [2005].

Source location determination is an inverse problem. Due to the arrival time differences of the elastic wave emitted by the fracture and recorded at each sensor, the source location can be calculated. The acoustic emission source location is defined by the origin time (start of the rupture) and the source position in Cartesian coordinates (x_0, y_0, z_0). The computed location corresponds to the point in space and time where the fracture initiated. Therefore, a point source is assumed. The first arrival time of the elastic

wave at each sensor is the onset time of the compressional wave (P-wave). If the onset of the shear wave (S-wave) is detectable this information can be used either in combination with or instead of the P-wave onset. However, the S-wave is often difficult to identify in acoustic emission analysis. If the distance between source and receiver is only a few wavelengths, the onset of the S-wave is hidden in the coda of the P-wave. In addition, due to the very short source-receiver separation, near field effects can be detected, i.e. P-wave and S-wave are not yet completely separated (Finck and Manthei 2004). Since the particle motion of a S-wave is normal to the propagation direction, and that of a P-wave is parallel to the propagation direction, a P-wave sensor is not designed to detect S-waves (see also Chap. 3, Sensor and Instrument). The onset times, the coordinates of each corresponding sensor and the velocities of the compressional and shear wave (if the shear wave can be detected) are needed for any kind of localization (1-dimensional, 2-dimensional and 3-dimensional). Provided a homogeneous and isotropic material can be assumed, the direct ray path between source and receiver can be used for calculation of the source location. However, if a layered or even a heterogeneous and anisotropic material is considered, the effects of the material on wave propagation and the raypath must be taken into consideration for an accurate localization. Most of the methods discussed in this chapter assume a homogeneous and isotropic material, an assumption that is generally valid for acoustic emission analysis of construction materials. However, some examples considering non-homogeneous and non-isotropic materials will be also shown, for example, acoustic emission analysis of wood.

The following section starts with the description of automatic onset detection methods, which are extremely useful when dealing with large data sets, but are the most error-prone of the localization algorithms.

There are also general differences in the type of localization procedure. Different localization techniques will be discussed after the automatic onset detection description, beginning with methods that provide only a rough estimate of the source coordinates, and building up to more complex methods that derive these coordinates with best possible accuracy.

6.2 Principal of Localization Procedures

6.2.1 Automatic Onset Detection

The determination of the onset time of a transient signal is an important task in many fields of science. Seismology and acoustic emission studies are related fields which use the phenomenon of stored elastic energy being released as elastic waves due to sudden fracturing in a rigid body (Spies et al. 2004). A strong relation exists between localization techniques in both seismology and acoustic emission analysis because both fields place similar importance on determining accurate onset times.

Accurate onset time determination can be carried out visually by an operator or automatically by a picking algorithm and depends on the onset definition itself. Leonard [2000] describes the true onset time of a seismic phase as the moment in time when the first energy of a particular phase arrives at a sensor. However, this definition is applicable to elastic waves in nearly all media. The onset time is usually picked as the point where the difference from the noise occurs first, although an experienced analyst will often extrapolate slightly back into the noise (Leonard 2000). These are also the requirements to a reliable automatic picker.

With some modifications, the algorithms used in seismology can be applied to acoustic emissions. Since the number of recorded acoustic emissions can be up to several thousands during one test, it is clear that automatic onset determination is a necessity.

In this context, it is refered to the convention suggested by Allen [1982], pickers are algorithms used to estimate the onset time of a phase and detectors are algorithms used to detect a phase (phase means e.g. longitudinal or transversal wave).

In seismology, a variety of automatic onset time picking approaches is applied. Two general procedures can be distinguished. On the one hand a global strategy can be used, where the whole signal is scanned for the onset. On the other hand is an iterative strategy where a particular region is preselected, from which the onset is determined exactly (Kurz et al. 2005). The main trends will be summarized in the following.

The simplest form of onset picking is to use an amplitude threshold picker. However, a pure threshold approach is not applicable to signals with small amplitudes and/or signals with a high noise levels (Trnkoczy 2002). A widespread approach which uses a dynamic threshold, is the so called STA/LTA (STA Short Term Average, LTA Long Term Average) picker by Baer and Kradolfer [1987]. The approach is not applied to the

raw signal directly, but a characteristic function based on the signal's envelope is defined. Here, the STA measures the instantaneous amplitude of the signal and the LTA contains information about the current average seismic noise amplitude. The difference between STA and LTA function is further defined by multiplying the characteristic function with frequency dependent parameters. Earle and Shearer [1994] chose a similar approach using a different envelope function. Due to that fact that signal and noise of acoustic emissions in concrete are often to be found in the same frequency range (20 kHz up to 300 kHz), the STA/LTA picker did not produce results having sufficient accuracy.

Joswig [1990] combined the STA/LTA trigger with a sonogram analysis of the seismic signal. This approach has been tested by Kurz [2006] on acoustic emissions and was found to be acceptable for acoustic emissions.

Dai and MacBeth [1995] used an artificial neural network for automatic picking of local earthquake data. The network is trained on noise and P-wave segments. This method is also not applied to the raw signal directly, but to the modulus of a windowed segment of the signal. The output of the network consists of two values, which are parameters of a function that accentuates the difference between the actual output and ideal noise. The disadvantage of this approach is that it is time intensive.

Modelling the signal as an autoregressive process is another approach for onset time determination. A detailed description of theory and application for seismic signals can be found in Sleeman and van Eck [1999], Leonard [2000] and Zhang et al. [2003]. Akaike [1974], as well as Kitagawa and Akaike [1974], showed that a time series could be divided into locally stationary segments, each of which could be modeled as an autoregressive process (Akaike Information Criterion, abbreviated as AIC). To solve the seismological localization problem, a seismic signal including the onset and a first estimate of the onset time is needed. The intervals before and after the onset time are assumed to be two different stationary time series. For a fixed order autoregressive process, the point at which the AIC is minimized determines the seperation point of the two time series (noise and signal) and therefore the onset point (Sleeman and van Eck 1999).

In the domain of acoustic emissions, Kurz et al. [2005] applied the principle of the autoregressive AIC picker in an automatic onset detection procedure. The results of the autoregressive AIC picker were then compared to manual picks and to an auto picker based on the Hinkley criterion, developed for acoustic emissions by Grosse and Reinhardt [1999]. Details about these approaches and the results can be found in Kurz et al. [2005]. In the following, only a short summary will be given.

The problem concerning acoustic emissions in concrete is that signal and noise are often in the same frequency range. Furthermore, the signal to

noise ratio is affected by the degree of damage of the tested specimen and therefore, by the failure process itself. Due to this dependency, the signal to noise ratio of acoustic emissions is generally not constant during an experiment. Therefore, a reliable automatic picker which can handle data of varying quality is needed.

An autoregressive AIC picker gives picks (where the term 'picks' refers to the determined onset times) of higher quality when the AIC is only applied to a part of the signal which contains the onset (Zhang et al. 2003). Therefore, the onset is defined coarsely by using the complex wavelet transform or the Hilbert transform. Both transforms lead to an envelope of the signal (**Fig. 6.1**).

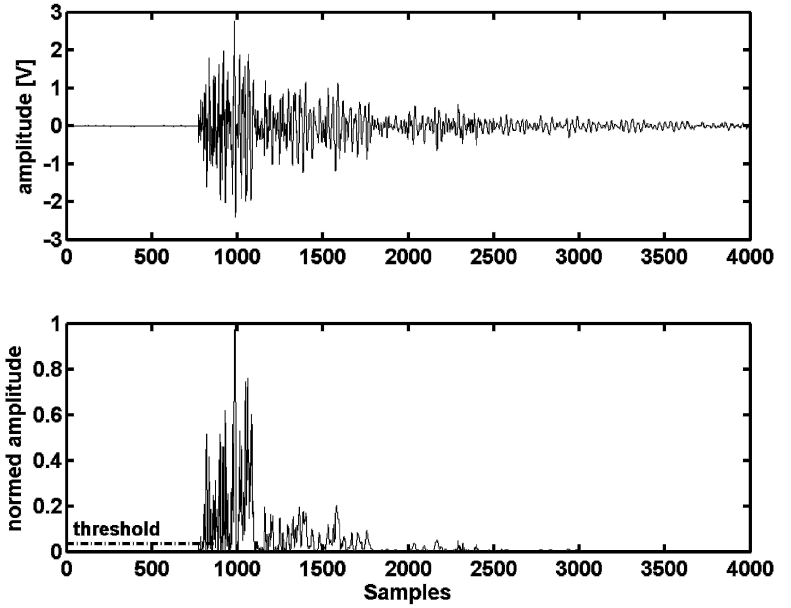

Fig. 6.1. Acoustic emission signal (top) and corresponding squared and normed amplitude (bottom) calculated with the Hilbert transform. An example threshold is drawn on the envelope.

The envelope is then used for a coarse definition of the onset by a simple threshold. Each envelope is squared and normed, so that a constant threshold value can be applied to all signals (**Fig. 6.1**). A window of several hundred samples, e.g. 400 before and 150 after this point, is then cut off the signal. Within this signal the onset is determined exactly using the AIC.

The advantage using an envelope calculated by the wavelet transform is that even for noisy signals the prearrangement of the onset by a threshold works consistently. The envelope is calculated only for one scale while most of the noise of the signals is found in different scales.

However, if two or more signals of different amplitude and frequency superpose each other, i.e. if acoustic emissions occur in such a fast succession that more than one signal is recorded within the normal blocklength, the envelope calculated by the Hilbert transform should be used. In such a case, the wavelet transform can identify the wrong signal because of the automatic scaling.

The exact onset is determined by calculating the AIC function directly from the signal according to Maeda [1985]:

$$AIC(t_w) = t_w * \log\left(\mathrm{var}\left(R_w\left(t_{w,1}\right)\right)\right) + \left(T_w - t_w - 1\right) * \log\left(\mathrm{var}\left(R_w\left(1 + t_w, T_w\right)\right)\right)\right) \tag{6.1}$$

The index w from the time series R_w indicates that not the whole time series is taken, but only the chosen window containing the onset (described above). T_w is the last sample of the curtate time series, t_w ranges through all samples of R_w and *var* denotes the variance function. The term $R_w\ (t_w,\ 1)$ means that the variance function is only calculated from the current value of t_w while $R_w\ (1 + t_w,\ T_w)$ indicates that all samples ranging from $1 + t_w$ to T_w are taken. The sample variance *var* or $\sigma^2_{N\text{-}1}$ is defined as (Kreyszig 1993):

$$\sigma^2_{N-1} = \frac{1}{1-N}\sum_{i=1}^{N}\left(R_i - \Gamma\right)^2 \tag{6.2}$$

N denotes the length of the signal, R_i is sample i of the time series R and Γ is the mean value of the whole time series R.

The global minimum of the AIC function defines the onset point of the signal (**Fig. 6.2**).

A comparison of the AIC-picker to the Hinkley picker shows that the AIC-picker produces significantly better results (**Fig. 6.3**). The value of the deviation (in percentage) between the localization using manual picks and the localization using the AIC-picker greater than 5 mm is 11%. The Hinkley-picker produces a deviation of up to 68% compared to the manual picks. The number of well localized events using the Hinkley-picker can be sufficient to visualize the general shape of the fracture process. How-

ever, this might not be valuable for all cases and a higher rate of correct picks is recommended.

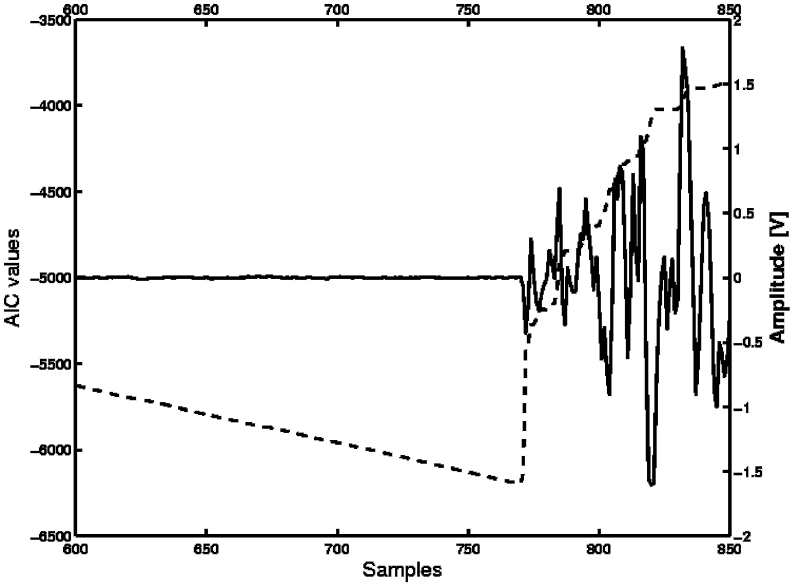

Fig. 6.2. The AIC is used for onset determination only for the selected part of the signal containing the onset, which is displayed by the solid line. The minimum of the AIC function, which is represented by the dashed line, denotes the onset time of the signal.

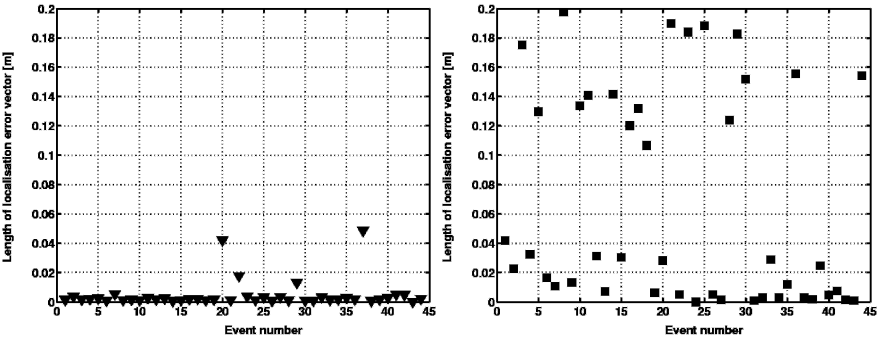

Fig. 6.3. Length of the mislocation vectors for (left) the comparison of the AIC-picker vs. manual picks and (right) the comparison of the Hinkley-picker vs. manual picks.

Taking into consideration that manual onset determination is also subject to various errors, it was shown that the AIC-picker produces sufficiently reliable results for acoustic emission localization. Therefore, the AIC-

picker, or at least an iterative strategy, is generally recommended for automatic onset determination of acoustic emissions.

6.2.2 Zone and 1-Dimensional Localization

The easiest way to locate the source of acoustic emissions is the so-called *zone location method*, where the exact source coordinates are not determined. Here, localization means detecting a signal and the radius (or in plate structures, the zone) of the sensor sensitivity range defines the localization accuracy. However, this is also the most imprecise localization method. The principal of zone localization is simple. For a particular sensor distribution, the sensor that records the arrival of the elastic wave first is the sensor closest to the source. An example for such a case is shown in **Fig. 6.4**.

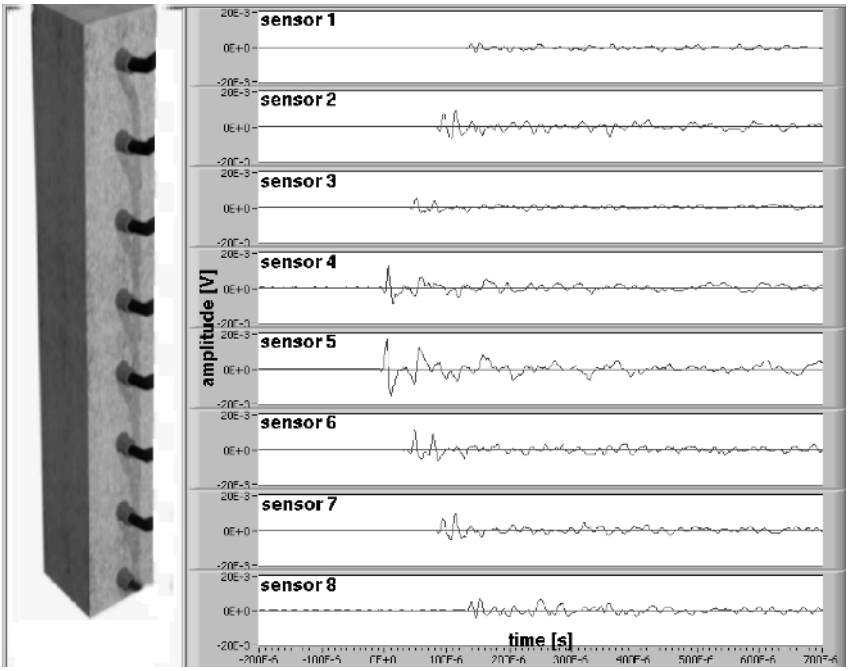

Fig. 6.4. Sketch of the concrete beam with eight sensors (left) and recorded acoustic emission signal from a pencil lead break (right). The source was between sensor 4 and sensor 5. The amplitude of the signals shows that the source was closer to sensor 5.

The left side of **Fig. 6.4** shows a concrete beam (height 1 m) with 8 sensors. The signal emitted from breaking a lead at the surface of the beam and recorded by each sensor is shown on the right side of **Fig. 6.4**. Sensor 4 and 5 (numeration top down) are the first and second sensors to record the event. This is also the region of the lead break.

This localization method only requires the coordinates of the sensors. However, an exact determination of the source location is not possible. The geometry of the structure being tested can influence the 1-dimensional (1-D) localization accuracy. For example, the expansion of a wire-like structure is very high in one direction compared to the expansion in the two other directions, allowing more detailed 1-D localization. In this case, the source can be determined as a 1-D point between two sensors (**Fig. 6.2**) (Reinhardt and Grosse 1999). However, the speed of sound of the structure being tested is needed.

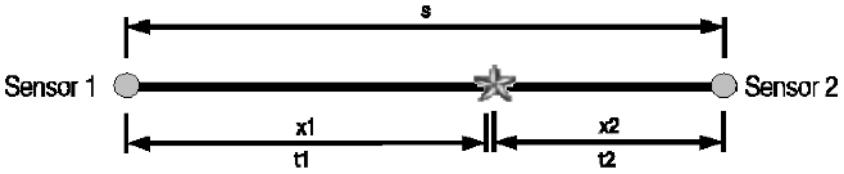

Fig. 6.5. Principle of a 1-dimensional localization on a wire like structure. The source location is marked by a grey star.

The distance s between the two sensors is known, as well as the onset time at each sensor and the sound velocity v of the material. We wish to determine the source time t_0 and the 1-D source location x_0. The distances x_1 and x_2 from the source to the sensors can be expressed as:

$$v*\left(t_1 - t_0\right) = x_2 \tag{6.3}$$

$$v*\left(t_2 - t_0\right) = x_1 \tag{6.4}$$

Knowing x_1 or x_2 the 1-D source localization can be calculated by:

$$s = x_1 + x_2 \tag{6.5}$$

Inserting Eq. 6.5 into Eq. 6.3 or 6.4 gives a linear system of two unknowns (t_0 and x_1 or x_2) that has to be solved. This gives the source time and the source location relative to the two sensors can now be calculated using Eq. 6.5.

6.2.3 2-Dimensional Localization

The next enhancement in localization accuracy would be to perform a 2-dimensional (2-D) localization to determine the coordinates x_0 and y_0 of the source. Since no information about the depth of the source is provided, this technique is sometimes referred to as a *planar localization*. The *planar localization technique* is applied to 2-D structures, where the thickness is small compared to the extent of the object, and the source coordinates are only required in two directions. The equations for 2-D and 3-D localization techniques that use compressional waves are similar, and will be handled in the next paragraph. In case of waves having wavelengths longer than the thickness of the structure, plate or Lamb waves have to be used and their group velocities considered. The 2-D method to determine acoustic emission sources is usually applied when the accuracy of *zone* technique is insufficient. Applications in civil engineering are reported by authors dealing with the monitoring of large structures like bridges (Kapphahn et al. 1993).

In seismology a 2-D source location with no information about the depth of the event is called epicenter. At least 3 sensors are needed for a 2-D localization. Assuming constant velocity and three measured arrival times t_1, t_2 and t_3 of the compressional wave, at three different sensors, the epicenter can be calculated by the hyperbola method (Bath 1979; Pujol 2004). The epicenter must be located on a curve for which the arrival time difference between two sensors e.g. $t_2 - t_1$ is constant (**Fig. 6.6**). Such a curve is a hyperbola with the corresponding sensor coordinates of sensor 1 and sensor 2 as foci.

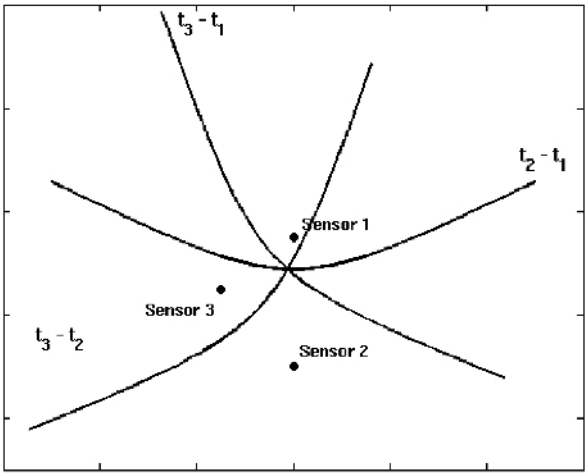

Fig. 6.6. 2-dimensional localization using the hyperbola method. t_1, t_2 and t_3 are the arrival times of the compressional wave at the corresponding sensors.

Due to the fact that generally one arrival time is greater than the other e.g. $t_2 > t_1$ the epicenter location is limited to one branch of the hyperbola. The hyperbolas of the other station pairs (t_1, t_3 and t_2, t_3) are calculated in a similar way. The epicenter is the intersection point of the 3 hyperbolas (**Fig. 6.5**). Due to measurement errors the three hyperbolas may not intersect at one point. For such a case, using more than 3 sensors should improve the localization accuracy and statistical methods must be applied. For example, Joswig [2004] uses a jackknife test to improve the results of the hyperbola method in an overdetermined case.

Besides the hyperbola method, a circle method for 2-D manual localization that uses only the arrival times of the compressional wave can be applied (Bath 1979). Another circle method that requires the arrival times of both the compressional and the shear waves (Havskov et al. 2002) can also be used.

6.3 High Order Localization Algorithms

6.3.1 Principal of Computational Localization Techniques

Several authors have worked on high order localization algorithms (Berthelot and Robert 1987; Labusz et al. 1988; Grosse 1996; Köppel 2000). The principal is similar to the determination of earthquake hypocenters in seismology and uses the arrival of earthquake waves recorded at multiple seismometers. These algorithms can be adapted to the requirements in material testing, enabling the study of different specimen geometries, as well as taking into account the number of transducers and their position around the object. The 3-D localization problem is exactly determined when four travel times are available to calculate the three coordinates and the source time of an event. For a 2-D localization problem to be exactly determined, only three travel times are needed.

The use of more sensors than unknown location parameters results in the system of equations being over-determined, and statistical methods such as the methods of least-squares can be used. Such approaches no longer fall into the category of manual localization methods and are generally solved using a computer. Usually these methods improve the localization accuracy.

Generally localization methods are applied as described in the following. The arrival time is measured at each sensor and is used as the reference value for a calculated arrival time. The calculated arrival time is

computed from a trial or a 'guessed' location and a user-defined velocity model. The location guess is corrected using the residuals (or difference) between the measured and calculated arrival time. The calculated arrival time t_i^c can be written as:

$$t_i^c = t\left(x_i, y_i, z_i, x_0, y_0, z_0\right) + t_0 \tag{6.6}$$

The calculated arrival time is composed of the travel time *t,* which is a function of the location of the sensors (x_i, y_i, z_i) and the hypocenter (x_0, y_0, z_0), and the source time t_0. Since this equation consists of four unknowns, at least four arrival times are needed to determine the hypocenter and the origin time; three arrival times are necessary if only the epicenter and the arrival time are to be calculated. If n arrival times from n sensors are measured the system is over-determined because there are more knowns than unknowns. The over-determined system has to be solved in a way that the residuals r_i between calculated and measured arrival time, at each sensor, are minimized.

$$r_i = t_i^0 - t_i^c \overset{!}{=} Min \tag{6.7}$$

Several methods to solve this nonlinear problem will be discussed in the next section.

6.3.2 Grid Search

In a grid search, the test specimen is discretized or divided into a particular grid, and the travel times from any point in the grid to each sensor are calculated. Since the number of grid points depends on the available computer memory, the grid can be made as fine as what is computationally possible. Comparison of the hypocentral location and the origin time can be used to determine the point of best agreement between the observed and calculated travel times. Several methods can be used to measure the point of best agreement. Each of the methods has case specific advantages and disadvantages and the user should decide from case to case which approach should be taken.

A common approach is the method of least squares (L_2 norm) which leads to root mean squared residuals (where the residual is the difference between the observed and calculated travel times). However, the use of least squares procedures requires the assumption that the distribution of the residuals is of Gaussian nature (Mendecki 1997). This is generally not true.

Furthermore, the mean square approach is sensitive to residual outliers (outliers are data points that lie 'far' from the mean or median). Another possibility is to use the variance of the residuals. Since the variance is approximately equal to the mean squared residuals, the problem with the non-Gaussian residual distribution persists and the use of the L_1 norm is preferable. The L_1 norm minimizes the absolute values of the residuals and is less sensitive to outliers. For further approaches concerning the measurement of the best agreement between observed and calculated traveltime, refer to Ružek and Kvasnička [2001].

The point having the lowest misfit (L_1 or L_2 norm) is usually the best hypocenter with the corresponding source time. Due to the possibility of there being multiple similar minima, the misfit uncertainties of the solutions should be estimated. One simple possibility is to investigate how the misfit value increases when moving away from the minimum. A criterion for a good solution is a rapidly growing misfit value (Hasvskov et al. 2002).

Dill-Langer et al. [2002] applied a 2-dimensional grid search localization procedure for wood.

Wood is an anisotropic material and therefore the velocity is a function of the angle of wave propagation and fiber direction (**Fig. 6.7**). By reducing the full 3D problem to a 2D approximation, the complexity of the localization problem in an anisotropic medium can be reduced. As many wooden building components can be approximated as two-dimensional structures the 2D localization concept may deliver valuable results in many cases.

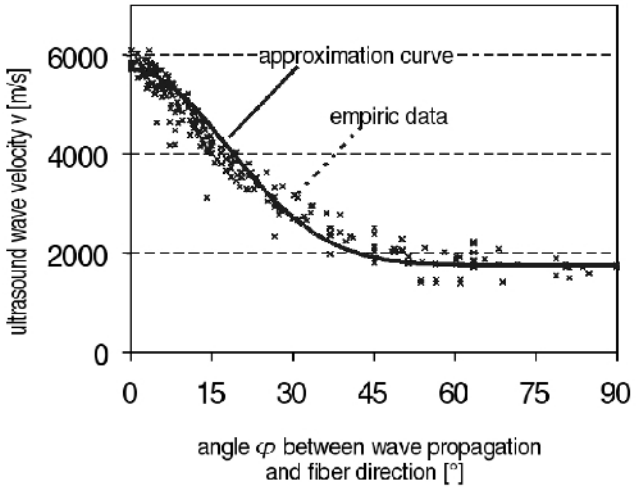

Fig. 6.7. Empirically determined ultrasound wave velocity as a function of angle φ between propagation and fibre direction.

In order to lay the foundations for a verifiable localization of AE sources, the ultrasound velocity of the compressional wave, which depends on the angle between the wave propagation direction and the fiber direction, has been measured (**Fig. 6.7**).

The investigated material was European spruce lumber (picea abies). The geometry and dimensions of the shoulder-shaped specimens were the following: the width b_T (perpendicular to grain, defined as x-direction) and the length l_T (parallel to grain and load direction; defined as y-direction) of the actual test section with reduced cross-sectional width were b_T = 120 mm and l_T = 500 mm. The width b of the clamping sections was 165 mm and the total length l of the specimen was 2400 mm. Since the thickness of the planed specimen was d = 25 mm which was the distinctly smallest dimension, the structure could be approximated by a 2-D structure. The test sections of specimen contained zones with pronounced accumulations of knots. The zone of highest knot density was located approximately at mid-length (**Fig. 6.8**).

If the experimental results are roughly summarized, it was found that more than 90% of the calculated source coordinates were located within about ± 8 mm from the true pulse source with respect to x-direction and ± 22 mm with respect to y-direction (parallel to grain).

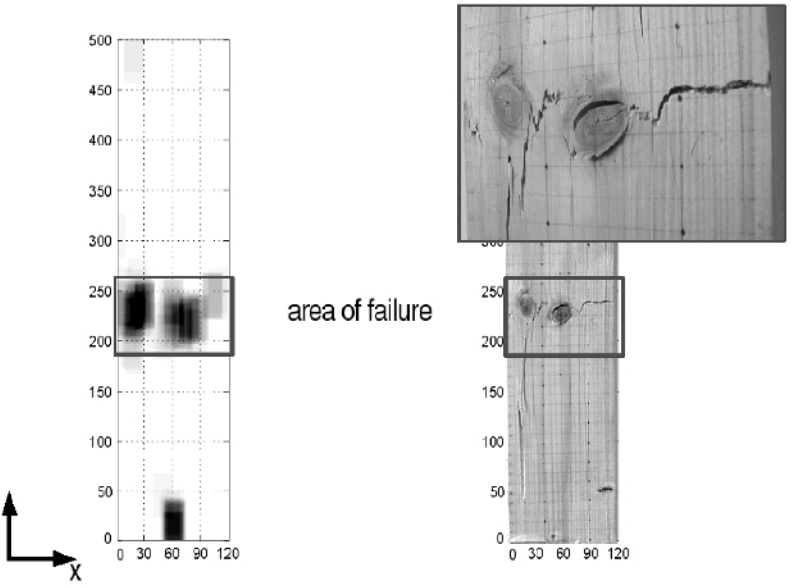

Fig. 6.8. Comparative representations of AE sources and defects for specimen. Results of 2-D localization of acoustic emission sources (left) and locations of natural and artificial defects (knots) and line of ultimate failure (right).

Fig. 6.8 gives a graphical overview of the 2-D results of the located acoustic emission sources compared to the location of natural defects (knots). For the test specimen, the majority of located AE sources were quite well correlated with the location of the two main knots near mid-length of the specimen. As anticipated, the vast majority of AE sources were located around the two relatively large knots, where local fiber deviations occurred. The fracture line was complex with both tension and shear modes and was located predominantly slightly above the centers of the located AE clusters.

The results of the reported tests prove the feasibility of 2-D acoustic emission source localization in wooden board-like structurally sized specimens, despite the pronounced anisotropy of wave velocities in the plane parallel and perpendicular to the fiber direction and despite some material inhomogenities.

6.3.3 Array Localization

A further approach for 2-D localization of acoustic emissions is array localization. The term *array localization* implies that an array (or group) of sensors is used to determine the origin of acoustic emissions outside this array. In such a configuration have the events usually a large epicentral distance compared to the aperture (extension) of the array – the distance between the center of the array and the epicenter is usually more than 2-3 times the array aperture.

This setup has several advantages and disadvantages. It allows usually for a rough localization only determining for example the direction and the incidence angle of the approaching elastic wave (**Fig. 6.9**). As an acoustic emission method applied to civil engineering structures it is a relatively new technique (Grosse et al. 2006). The adoption of the techniques aims to applications of wireless sensor nodes to monitor large structures; the sensors of the array can be distributed around one or two nodes and monitor a relatively large area of the structure. More details regarding the application of such techniques are included in Chap. 15. However, the principle of array technology was first applied in electrical engineering (e.g. for antenna arrays) and is also used in seismology (e.g. for monitoring purposes in the frame of the nuclear test ban treaty). Due to the similarity between acoustic emission analysis and seismology, and that in both cases elastic waves are investigated, the references of this subsection are mainly of seismologic origin. Schweitzer et al. [2002], Rost and Thomas [2002] and Capon [1969] provide an overview in theory and applications of array seismology and are used as main references for this topic.

In a sensor array numerous sensors are placed at discrete points in a well-defined configuration (Rost and Thomas 2002) as shown in **Fig. 6.9** (right). The idea of installing arrays of sensors is to improve the signal-to-noise ratio. The superior signal detection capability of arrays is obtained by applying *beam forming* techniques, which suppress the noise while preserving the signal, thus enhancing the signal-to-noise ratio (Schweitzer et al. 2002). Furthermore, arrays allow the station-to-event azimuth, called the back-azimuth, to be calculated.

The array methods presented here assume that a plane wave arrives at the array. The wave must have traveled a certain distance depending on the wavelength for this assumption to be valid. The direction of a propagating elastic wave can be described by the vertical incidence angle *i* (**Fig. 6.9**, left) and the back azimuth Θ (**Fig. 6.9**, right) which is measured relative to the reference sensor (S4 in **Fig. 6.9**, right) of the array.

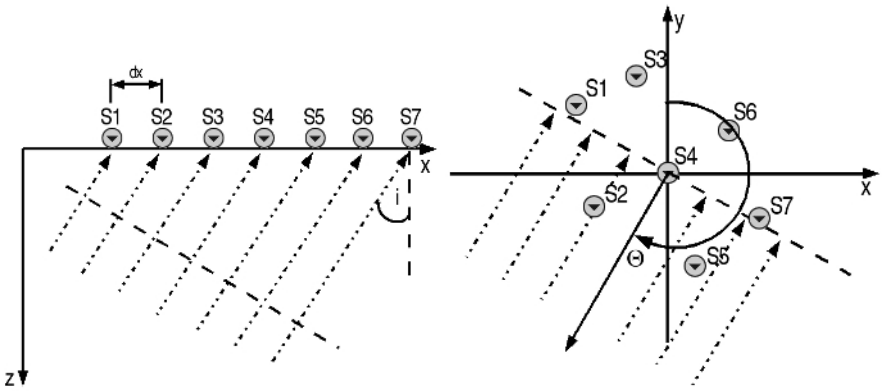

Fig. 6.9. *Left*: cross section of the incident wave front (dashed line) crossing an array of 7 sensors (S1 to S7) at an incidence angle *i*. *Right*: horizontal plane of an incident plane wave front (dashed line) arriving with a back-azimuth Θ relative to the reference sensor S4 at an array of 7 sensors (S1 to S7).

In practice, the incidence angle *i* is not used, but an apparent velocity, which will be derived in the following. The wavefronts arriving at, for example, two sensors at time *t* and time *t*+*dt* are separated by distance *ds* along the raypath (**Fig. 6.10**). The distances *dx* and *ds* are related to the incidence angle through (Shearer 1999):

$$ds = dx \ \sin i \tag{6.8}$$

Assuming uniform velocity in the material $v_0 = ds/dt$, Eq. 6.8 can be rewritten as:

$$v_0 \; dt = dx \; \sin i \tag{6.9}$$

Eq. 6.9 can be rearranged as:

$$\frac{dt}{dx} = \frac{\sin i}{v_0} = s \tag{6.10}$$

The slowness s is the inverse apparent velocity of the wavefront crossing the array and defined as $v_{app} = dx/dt$. The apparent velocity is a constant for a specific ray travelling through a material. If the slowness vector $\boldsymbol{s} = (s_x, s_y, s_z)$ is used rather than the absolute value of the slowness s, the components of the slowness can be expressed as functions of the back-azimuth and the incidence angle (Rost and Thomas 2002):

$$s = \left(\frac{\sin \Theta}{v_{app}}, \frac{\cos \Theta}{v_{app}}, \frac{1}{v_{app} \tan i} \right) \tag{6.11}$$

Sensor arrays, as presented here, are used for the separation of coherent signals and noise. The basic method used to separate the coherent and incoherent parts of a signal is known as 'array beam forming'. Array beam forming enables the determination of the back-azimuth of the incident wave. One sensor is chosen as a reference sensor and all parameters are taken relative to this sensor (**Fig. 6.9**).

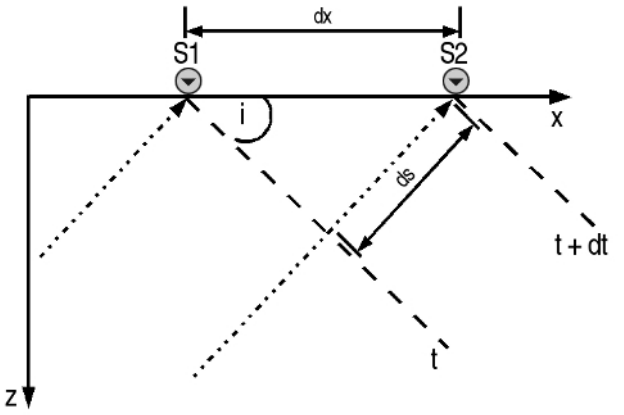

Fig. 6.10. Plane wave front incident on a surface with two sensors (S1 and S2). The angle i is the incidence angle defined in Fig. 6.9 (left).

For most applications all sensors are in the same horizontal plane. In such a case, the vertical component of the slowness vector s_z is zero. The special case where all the sensors of the array are not in one plane is considered in Schweizer et al. [2002].

The beam forming method uses the differential travel times of the plane wavefront for each source-receiver combination and depend on the particular slowness and back-azimuth to individual array stations. Therefore, the main goal of the array beam forming method is to find the best delay times for shifting the individual signals. If the single-sensor recordings are appropriately shifted in time, for a certain back-azimuth and slowness, all signals with the matching back-azimuth and slowness will sum constructively (Rost and Thomas 2002). The delay times τ_j are the sensor position vector $\boldsymbol{r}_j$ (relative to the reference sensor) multiplied by the slowness vector $\boldsymbol{s}$:

$$\tau_j = r_j * s \tag{6.12}$$

The complete geometrical derivation of Eq. 6.12 for the sensors of an array can also be found in Schweitzer et al. [2002].

An array beam *B(t)* can be calculated using the following formula:

$$B(t) = \frac{1}{M} \sum_{j=1}^{M} R_j \left(t + \tau_j \right), \tag{6.13}$$

where $R_j(\boldsymbol{r}_j, t)$ is the digital sample of the signal from sensor j at time t. **Fig. 6.11** shows an example of beam forming. The top trace shows an array beam that results from applying the beam forming method to the other eight channels. This example shows how the signal-to-noise ratio can increase during beam forming. The signal-to-noise ratio of the array increases with the square root of the number of sensors of the array, and is significantly lower than the signal-to-noise ratio of a single sensor (Rost and Thomas 2002).

When acoustic emissions are located with a sensor array, the back-azimuths of the propagating elastic waves are determined. The true beam can only be calculated for the correct back-azimuth. However, the back-azimuth is the parameter we want to determine. Eq. 6.12 shows that any delay time for each sensor can be calculated by multiplying the coordinates of each sensor with a slowness vector. Since the slowness is a function of back-azimuth and incidence angle (Eq. 6.11) it is possible to calculate the true beam by beam forming calculations on a grid of different slowness values. More specifically, a grid of s_x and s_y values is defined and for every

combination of the horizontal slowness values, the energy of the beam (integrating over the squared amplitudes) is calculated. The maximum energy indicates the true beam since only the coherent signals of a phase (e. g. compressional wave) interfer constructively. Searching for the true beam can be performed in the time domain, where the method is called 'beam packing' (**Fig. 6.12**, left) and in the frequency domain, where it is referred to as 'frequency wavenumber analysis' (**Fig. 6.12**, right).

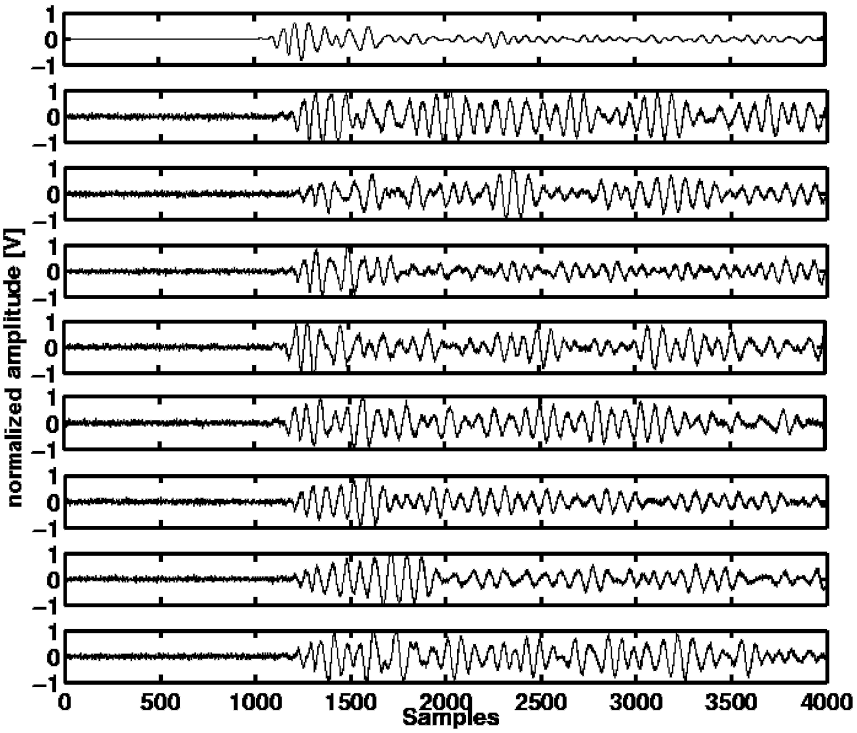

Fig. 6.11. Beam forming example, where the top trace is the beam of an artificial acoustic emission source. Note the increase of signal-to-noise ratio when the top trace is compared with the traces below.

Beam packing is directly applied to the signal in the time domain. Since a time shift in the time domain is equivalent to a phase shift in the frequency domain, beam packing is equivalent to frequency wavenumber (*f-k*) analysis. The *f-k* analysis has the advantage that it is faster than the corresponding procedure in the time domain, and is more accurate.

The total energy of a record at an array is defined as:

$$E = \int_{-\infty}^{\infty} B(t)^2 dt = \int_{-\infty}^{\infty} \left[\frac{1}{M} \sum_{j=1}^{M} R_j \left(t + \tau_j \right) \right]^2 dt \tag{6.14}$$

Using Parseval's theorem, Eq. 6.12 can be written in the frequency domain:

$$E\left(\omega, \mathrm{k} - \mathrm{k}_0\right) = \int_{-\infty}^{\infty} \left| B(\omega) \right|^2 \left| \frac{1}{M} \sum_{j=1}^{M} e^{i\omega r_j k} \right|^2 d\omega \tag{6.15}$$

$\boldsymbol{B(\omega)}$ is the Fourier transform of $B(t)$. The wavenumber vector $\boldsymbol{k}$ is defined as $\boldsymbol{k} = \omega \cdot \boldsymbol{s}$. The back-azimuth is calculated from an *f-k* diagram or a beam packing diagram in the following way. It is assumed that the incident wave travels through an imaginary half sphere beneath the array to a particular point. The half sphere is projected to the surface in the corresponding diagram. Therefore, the slowness and wavenumber are measured in polar coordinates and the back-azimuth can be calculated by:

$$\Theta = \tan^{-1}\left(\frac{k_x}{k_y} \right) = \tan^{-1}\left(\frac{s_x}{s_y} \right) \tag{6.16}$$

A detailed description of *f-k* analysis can be found in, for example, Capon [1969], Smart and Flinn [1971] or Aki and Richards [1980].

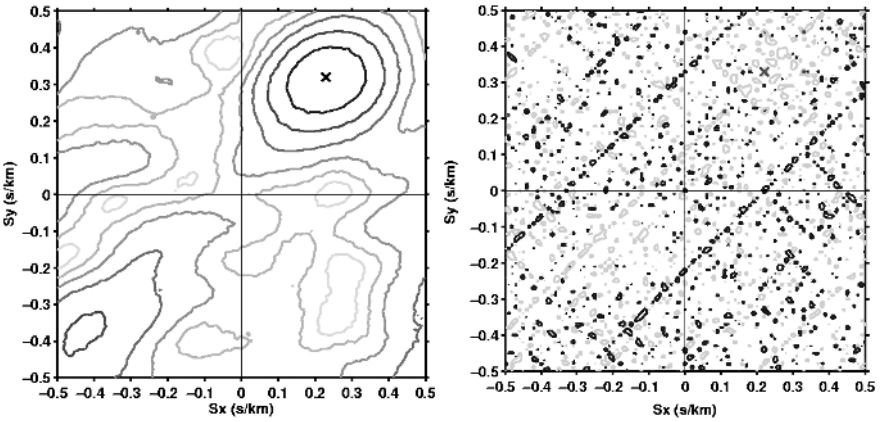

Fig. 6.12. Calculation of the back-azimuth of the same incoming wave using the beampacking method (left) and f-k analysis (right). The cross indicates the calculated maximum energy at particular slowness values s_x and s_y. The back-azimuth is the angle between the centre of the coordinate plane and the point of maximum energy.

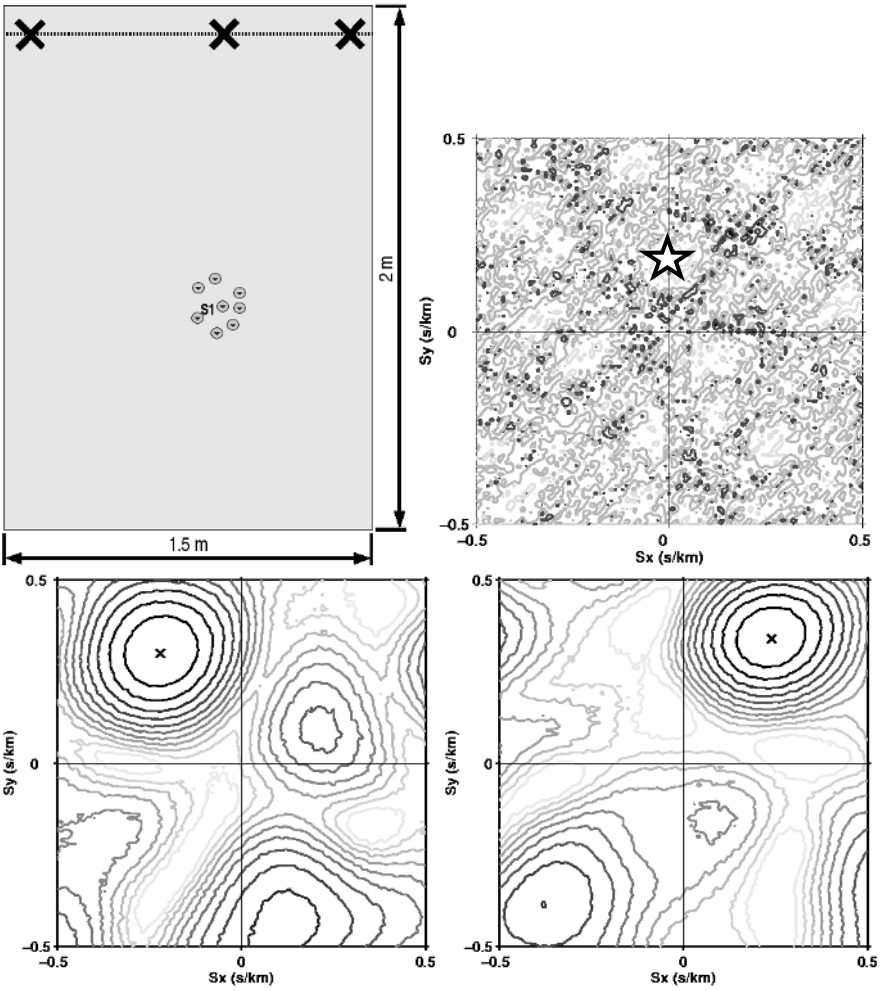

Fig. 6.13. *Top left*: sketch of a typical array experiment. A sensor array, with reference sensor S_1, is placed on a concrete plate (2 m *x* 1.5 m *x* 0.3 m). Artificial sources (pencil lead breaks or small impacts) are generated at one side of the concrete plate. The source points are marked by black crosses. *Top right*: f-k analysis of the data from the source point perpendicular to sensor S_1. The maximum energy is marked by a cross. *Bottom left and bottom right*: results of the beampacking analysis of the data from the left source point (left) and from the right source point (right). The maximum energy is again marked by a cross.

Fig. 6.13 shows a sketch illustrating the principle and results of a typical array experiment. Three different source points of artificial sources were chosen, which are marked by black crosses in **Fig. 6.13**, top left. The *f-k* analysis of the data from the source perpendicular to sensor S_1 shows that

the back-azimuth is zero degrees (star in **Fig. 6.13**, top right). The measured back-azimuth agrees exactly with the true value. This is not the case for the two source points near the edges of the concrete plate. Due to reflections from the side-walls, the back-azimuth determined from the data of the source on left side differs by an amount of 4.9 degrees from the true value and the one of the right side differs by 3.7 degrees from the true value. For comparison, a beam-packing analysis was also applied (**Fig. 6.13**, bottom). In addition, the array geometry can also have an influence on the results because the quality of the results can depend on the direction to the source. If more than one array is used, a 2D localization of the source of the incident wave can be applied, by calculating the point of intersection of the two back-azimuth lines.

6.3.4 Iterative Localization

The standard technique for 3-D localization is to linearize the problem. The equations used to calculate a 3-D location (hypocenter or source of an acoustic emission) are based on the assumptions that the material is homogeneous and isotropic and that the AE source resembles a point source. If this is not the case, the following approach has to be modified.

Three dimensional localization requires the onset times from at least 4 sensors. The most common approach is to use an iterative localization algorithm, which requires the linearization of the problem. To do this, a 'first guess' or trial hypocenter (x_0, y_0, z_0, t_0) is required. This first guess hypocenter must lie relatively close to the true hypocenter, which is not known. The travel time residuals r_i of the first guess hypocenter are then a linear function of the correction in hypocentral distance (Havskov et al. 2002).

For smaller specimens, the middle of the specimen is an adequate choice for the first guess hypocenter. For larger specimens, the sensor which recorded the event first can be chosen.

In the case of acoustic emission analysis of concrete, the material can be assumed to be homogeneous and isotropic. The travel times for 3-D localization can then be calculated using (see also Eq. 6.6):

$$t_i = \frac{\sqrt{\left(x - x_i\right)^2 + \left(y - y_i\right)^2 + \left(z - z_i\right)^2}}{v} + t_0 \tag{6.17}$$

The coordinates (x, y, z) represent the point at which the travel time to each sensor (x_i, y_i, z_i) is calculated, i.e. the first guess of the hypocenter. The

body wave velocity of the material is denoted by v and t_0 is the first guess origin time, which is taken as the centre point of the specimen.

Due to the first guess hypocenter being a trial solution, the calculated travel times differ from the measured ones. A correction (Δx, Δy, Δz, Δt) of the first guess hypocenter is needed to minimize the travel time residuals (see also Eq. 6.7). If the necessary corrections are relatively small, the travel time function (Eq. 6.17) can be linearized. Therefore, Eq. 6.17 can be approximated by a Taylor series, from which only the first term is used. Eq. 6.7 can be rewritten as:

$$r_i = \left(\frac{\partial t}{\partial x_i} * \Delta x\right) + \left(\frac{\partial t}{\partial y_i} * \Delta y\right) + \left(\frac{\partial t}{\partial z_i} * \Delta z\right) + \Delta t \tag{6.18}$$

In matrix form this is:

$$r = G * \Delta x \tag{6.19}$$

$\boldsymbol{G}$ is the matrix of partial derivatives and $\Delta\boldsymbol{x}$ is the correction vector. Due to the source time correction term, the last column of this matrix is always 1. The partial derivatives of one component of Eq. 6.17 is:

$$\frac{\partial t_i}{\partial x} = \frac{\left(x - x_i\right)}{v} * \frac{1}{\sqrt{\left(x - x_i\right)^2 + \left(y - y_i\right)^2 + \left(z - z_i\right)^2}} \tag{6.20}$$

To calculate the correction vector, Eq. 6.19 is solved via matrix inversion, e.g. by calculating the Moore-Penrose generalized matrix inverse:

$$\Delta x = \left(\mathbf{G}^T\mathbf{G}\right)^{-1}\mathbf{G}^T\mathbf{r} \tag{6.21}$$

If more than four sensors are used, this procedure is repeated and the correction vector is minimized iteratively. Convergence criteria can be set for terminating the iteration when a particular desired accuracy has been reached, or if the procedure is diverging.

This localization algorithm also provides the possibility to correct the body wave velocity iteratively. To do this, velocities are calculated from the travel time of all events (e. g. recorded during a certain period of the experiment) and the distance calculated between sensor and hypocenter. The linear extrapolation of all these calculated velocities gives a new average velocity for the localization. This procedure can be performed iteratively, in combination with the localization.

The solution can be further stabilized by introducing a weight matrix $\boldsymbol{W}$ to Eq. 6.19 (Thurber and Engdahl 2000). The data can be weighted according to the quality, the distance etc. The diagonal elements of the weight matrix are equal to the square root of the weight value, which is normally between 0 and 1:

$$\mathbf{Wr} = \mathbf{WG} \cdot \Delta x \tag{6.22}$$

6.3.5 Localization Errors

An error analysis is necessary for assessing the accuracy and reliability of any localization result. There are different sources of errors that are not clearly separated. Uncertainties in the determination of the arrival times generally depend on data quality, and how impulsive onsets are. In the presence of noise, low amplitude onsets are easily overlooked. Estimated onset times then are too late or even according to wrong phases. Moreover, the widely used assumption of a homogeneous behavior of the wave propagation may not be correct for a tested structure.

For the iterative linearized localization method that was presented above localization errors are described by the symmetric covariance matrix **C**. For the least squares inversion method, **C** can be easily calculated from matrix **G** as (Flinn 1965)

$$\mathbf{C} = \sigma_d \left(\mathbf{G}^T \mathbf{G} \right)^{-1}, \tag{6.23}$$

where σ_d is the data variance of the arrival times. The diagonal elements of C give the variances of the source coordinates in the direction of each coordinate axis. Only spatial errors are of interest, which can be visualized by a 3-D-error ellipsoid (**Fig. 6.14**). Its shape is defined by the eigenvectors and eigenvalues of **C,** which give its orientation as well as its dimensions. For the 68%-error ellipsoid, the square of the semiaxis is given by scaling the eigenvalues by 3.53 (Press et al. 1992).

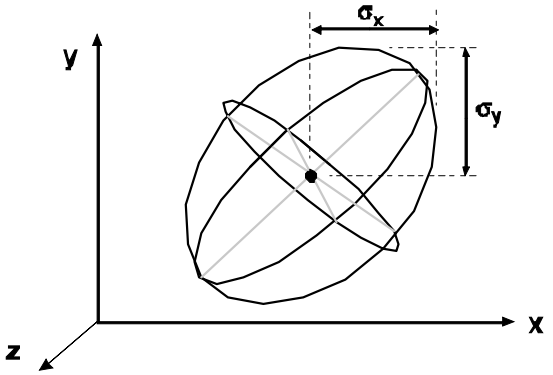

Fig. 6.14. 3-D-error ellipsoid for visualization of the spatial localization errors. Errors σ_x, σ_y and σ_z can be found as the projections of the ellipsoid in the direction of x, y and z, respectively.

It is an important fact that for a homogeneous material the shape of the error ellipsoid is determined by geometrical relationships between source location and sensor distribution only, as summarized in the matrix **G** of the partial derivatives (Eq. 6.16 and 6.17). The data uncertainty σ_d is assumed to obey Gaussian statistics and acts as a scaling factor for **C**.

In the case that AE are expected to occur in certain regions of the test object, it generally can be calculated whether a given sensor arrangement is suitable for an accurate localization of these AE sources or where additional sensors should be placed. Localization accuracy is highest for events that have a good azimuthal coverage by the sensors. This can be illustrated by the following theoretical example where four sensors, arranged in a square are used to localize AE-sources in two dimensions. The arrangement is over determined allowing for error analysis. Assuming an AE source with a known location and time of origin, the arrival times at the four sensors can be calculated with the given wave velocity ν. Inserting these arrival times into Eq. 6.16 yields three independent equations which can each be plotted as a hyperbola. They intersect in one point, the AE-source location as depicted in **Fig. 6.15**, left. Top left shows a source within and bottom left a source outside the sensor array. In real applications the arrival times contain an uncertainty and the hyperbola will not intersect in one point but rather an area. In the present example this is simulated by adding random errors between +5μs and –5μs to the calculated arrival times. **Fig. 6.15** right demonstrates the effect of the sensor arrangement on the localization result. In the diagram below, where the AE-source is outside the sensor array, the hyperbolas intersect in a much larger area then in the case, where the AE-source is within the sensor array.

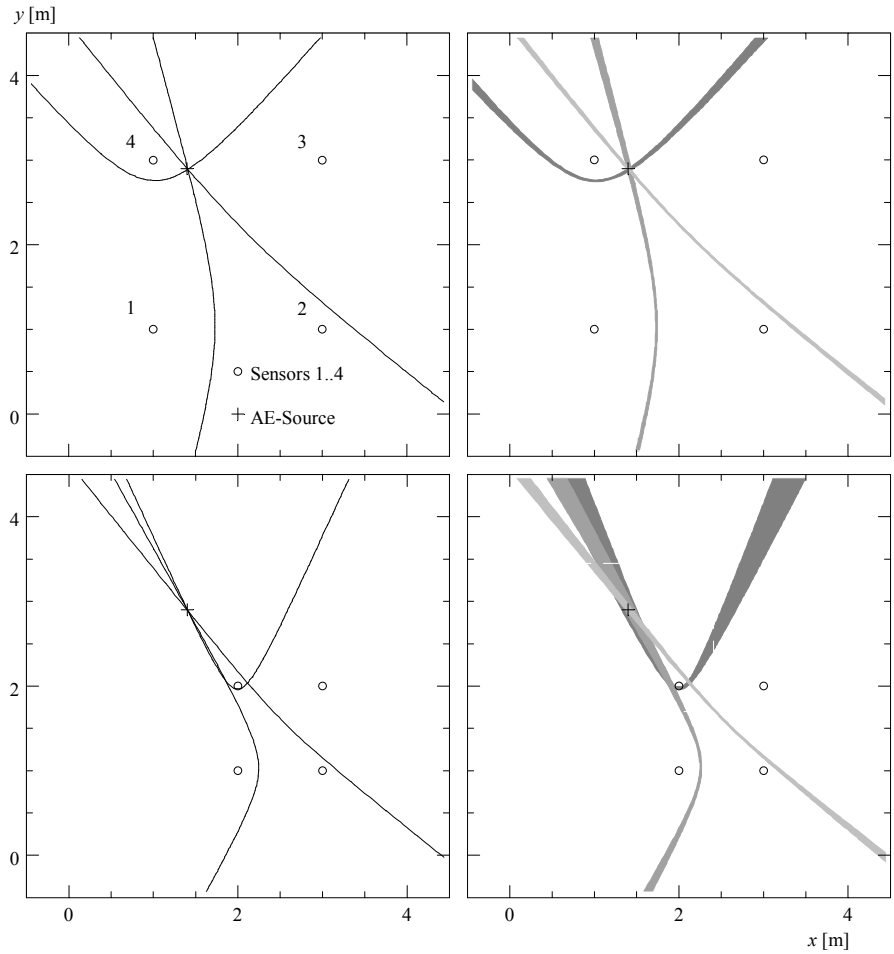

Fig. 6.15. Theoretical example to demonstrate the effect of the sensor arrangement on the localization accuracy. *Top*: AE-source within sensor array; *bottom*: AE-source outside. *Left*: accurate arrival times; *right*: arrival times with an error of +/- 5 µs. $\nu = 4500$ m/s.

In principal, the variances of the arrival time data are unknown unless they are estimated for each signal in a visual inspection of the waveforms. However, it is possible to estimate σ_d^2 from the remaining discrepancies between observed travel times t_i^0 and calculated travel times t_i^c after source localization, divided by the degree of freedom of the problem with four unknown source parameters. For n observations it is

$$\sigma_d^2 = \frac{1}{n-4}\sum_i \left(t_i^0 - t_i^c\right)^2. \tag{6.24}$$

Thus it is possible to visualize the localization results and to interpret them according to their location uncertainties by defining a maximal spatial error as the length of the major axis of the error ellipsoid.

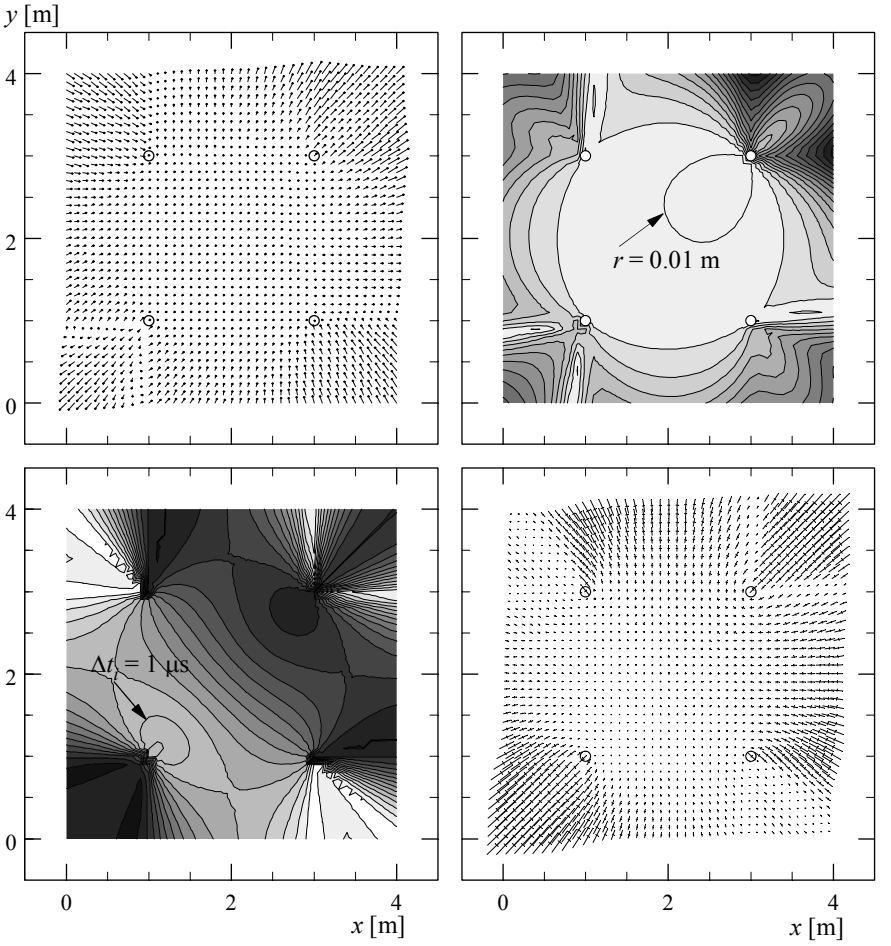

Fig. 6.16. Localization errors resulting from an erroneous arrival time (same arrangement as **Fig. 6.15**, arrival time at sensor 1 altered by 5 μs) calculated and depicted for an array of 40 by 40 points. *Top left*: actual localization errors as vector; *Top right*: actual localization errors as density function (equidistance: 0.01 m); *Bottom left*: mean arrival time residuals as density function (equidistance: 0.25 μs); *Bottom right*: major axis of the error ellipsoid.

Using the same theoretical example as mentioned above, **Fig. 6.16** illustrates the effect of a systematically erroneous arrival time on the source localization. For an array of 40 by 40 AE-sources the theoretical arrival times at the four sensors were calculated. To introduce an error, 5 μs were added to the arrival times of Sensor 1. The iterative localization algorithm then yields AE-source locations that minimize the travel time residuals and thus distribute the error in arrival times over all sensors. **Fig. 6.16** top depicts the difference between the actual and the calculated AE-source location, on the left side as error vectors and on the right side as a density function of the error value. **Fig. 6.16** bottom left shows a density function of the minimized travel time residuals (mean value over all sensors) and bottom right the major axis of the error ellipsoid. In most cases the size and orientation of calculated location uncertainties (bottom right) corresponds well to the actual error vector (top left).

Whether the calculated value of σ corresponds to the usually unknown actual localization error, depends on the source of error. While inaccurate localization results due to erroneous arrival time determinations or sensor locations are well recognized by high values of σ, a false assumption of the wave velocity v leads to low σ but nonetheless wrong localization results. In practical application the value of σ proves to be the best indicator to distinguish reliable from erroneous localization results.

6.4 Application and Practical Considerations of the Iterative Localization Method

AE-source localization is being used in a wide range of field applications as well as in research. In field applications it is typically part of a monitoring process of civil engineering structures allowing for example to detect and localize wire breaks in cable stay bridges (1-dimensional localization), in prestressed decks or in bridge girders (2- or 3-dimensional localization). In research applications source localization is often required as a prerequisite for quantitative AE analysis with the aim of observing fracture processes within the specimen.

The requirements for the testing equipment i.e. sensors and acquisition unit are relatively low, compared to more sophisticated analysis methods. At the same time the interpretation of the results is – at least at first sight – unambiguous and requires little understanding. AE source locations can easily be depicted for example in a plan view of the observed structure. Commercially available analysis software or entire testing units allowing

for the on line localization of AE sources are usually based on the iterative localization method described in Chap. 6.3.4.

6.4.1 Reliability and Accuracy

In practical applications AE-source localization is often applied to large amounts of data. In order to interpret the results it is crucial to recognize erroneous source locations and concentrate on the reliable portion. As mentioned above, this distinction can be achieved based on the variance σ of the location result.

The AE-Source locations depicted in **Fig. 6.17** were collected during pull out tests on concrete cubes of 200 x 200 x 200 mm with a rebar Ø 14 mm embedded centrically and bonded only over the length of Ø 3 mm (Köppel and Vogel 2000; Köppel 2002). During pull out AE-Signals were recorded on eight sensors mounted on the concrete surface. The diagram in **Fig. 6.17** left displays 3639 AE events recorded on all eight channels and localized with the iterative localization method described in Chap. 6.3.4. While failure was observed in the bond region of the rebar only, AE-Events were localized throughout the specimen i.e. also in places where the occurrence of cracks is highly unlikely. The brightness of the dots marking the AE location indicates their accuracy. Localization results with a high variance σ i.e. a low accuracy are marked in light gray and localization results with a low variance σ in black.

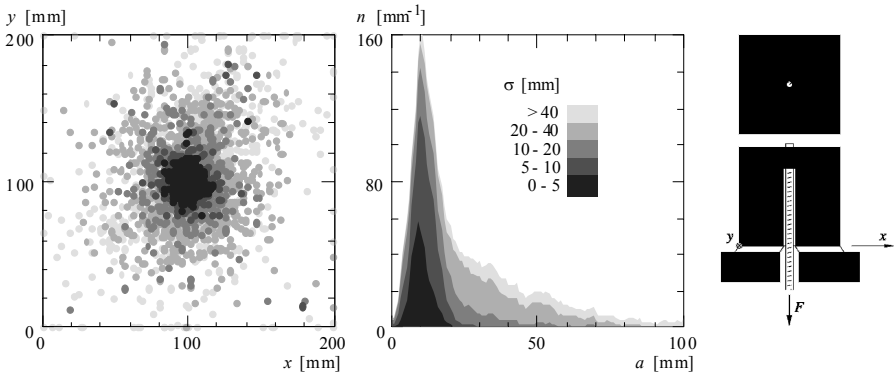

Fig. 6.17. AE-Source locations of 3639 AE-Events obtained during a pull out test. The variance σ (= $1/3(\sigma_x + \sigma_y + \sigma_z)$) of the location results is indicated via gray tone. Plausible AE sources in the bond region correspond to AE-Source locations with low σ.

In **Fig. 6.17** it can be observed, that the localization results with a low σ tend to be located around the boundary between rebar and concrete where AE-Sources are expected in this test. If a high number of AE locations are available, displaying only those with low σ increases the reliability of the result and thus facilitates the interpretation.

If regions of high AE activity rather then the exact location of single events are of interest, visualizing the localization results as density functions instead of data points facilitates the interpretation. Assuming erroneous localization results to be distributed uniformly while correct locations are concentrated in actual fracture regions, this procedure increases also the accuracy of the result. In **Fig. 6.18** the AE locations of three pull out tests are displayed as density functions. AE are located in the bond region and clearly concentrated at the ribs of the rebar.

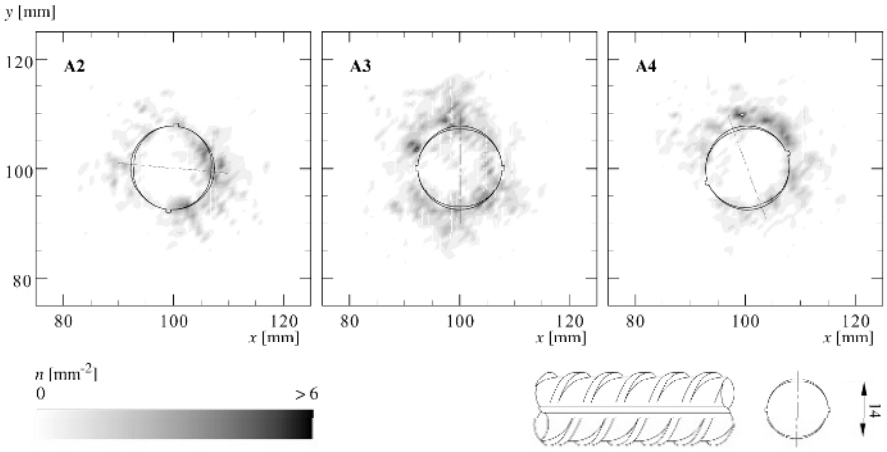

Fig. 6.18. Localization results of three pull out tests displayed as density functions. Regions of high AE-activity correspond with the ribs of the rebar.

6.4.2 Limitations

Like all high order localization methods the iterative localization method works with arrival times of certain wave types like P-waves, S-waves, surface waves or Lamb waves. A complex test specimen with irregular boundaries and an inhomogeneous structure causes reflections or scattered waves, which interfere in the signal and thus have no obvious onsets. The first onset usually is the clearest one and is therefore in most cases used for the localization. It corresponds to the compressional P-wave, which has the highest propagation velocity, but may not be detectable in a noisy envi-

ronment or over long distances in concrete due to its relatively high attenuation.

It results, that AE-sources can only be reliably located over a limited distance and as long as the assumption of a homogenous media is valid for the considered wavelength. While inhomogenities due to the reinforcement or tendons have a limited impact on the localization result, cracks restrict the area, where localization is possible. AE-sources beyond existing cracks cannot be located. The following two examples of large scale laboratory experiments demonstrate this effect.

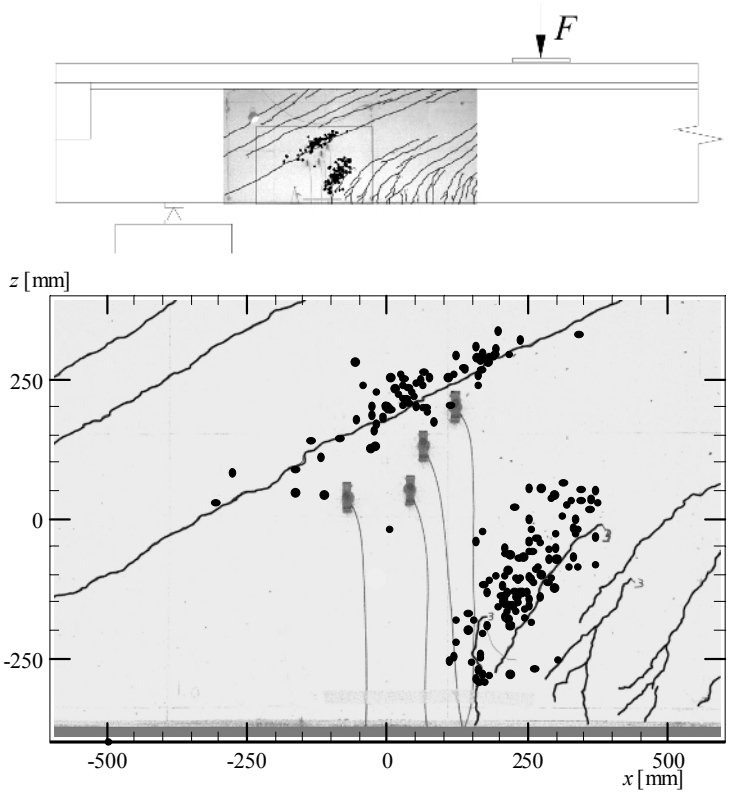

Fig. 6.19. AE-sources registered and located during the three point bending of a 21 m long prestressed bridge girder. Depicted are only localization results with $\sigma < 15$ mm.

The AE-localization results displayed in **Fig. 6.19** were recorded during the loading of a 21 m long prestressed bridge girder (Köppel and Vogel 2000; Zwicky and Vogel 2000). It was removed from the bridge and subjected to a three-point-bending test in an outdoor facility of the ETH

Zürich. To provoke a shear failure, the load was applied close to the abutment. AE were recorded by eight sensors located in close vicinity on both sides of the girder in the shear field.

All AE-sources registered by eight sensors and located with a satisfying accuracy i.e. with a variance σ below 15 mm can be attributed to the two cracks adjacent to the sensor array. AE-sources originating from beyond those cracks could not be properly localized.

As another example for the application of the iterative localization method, location results of AE during the loading of a reinforced concrete beam are presented in the following (Schechinger 2005). An overview of the test setup can be seen in **Fig. 6.20** (top). The specimen had a cross section of 440 x 440 mm and a total length of 4.50 m. The beam was assembled with four steel reinforcement bars of 22 mm diameter and an ungrouted steel duct of 93/99 mm diameter in its axis (**Fig. 6.20**, bottom left side). The experiment was carried out as a symmetric four-point-bending test, as shown in **Fig. 6.20** (bottom right side). The maximum bending stress occurred between the two loading points on a length of 0.96 m. In that region eight AE sensors were mounted onto the concrete surface to record the AE signals from the expected bending cracks. AE events were located if arrival times of at least six sensors were available.

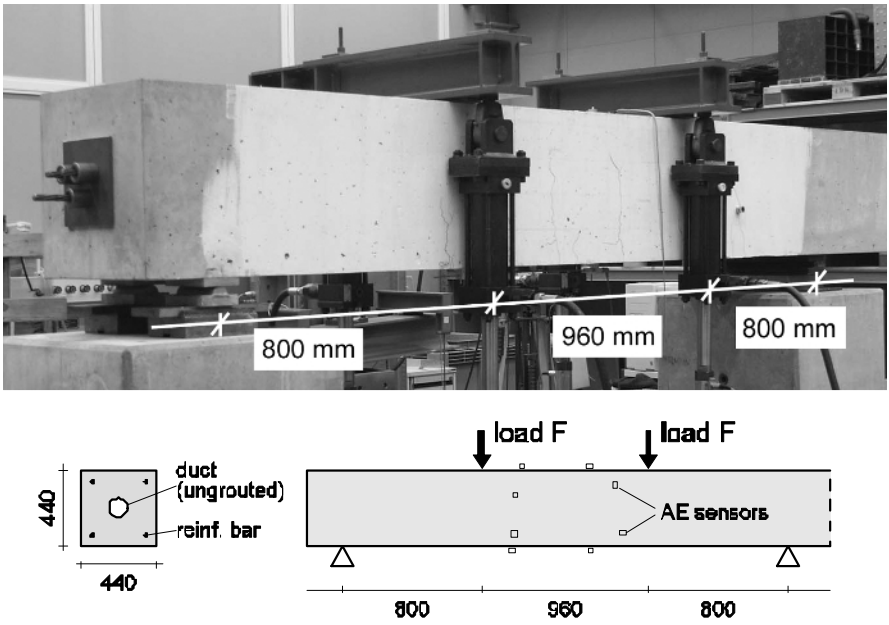

Fig. 6.20. Overview of the four-point-bending experiment (top), cross section of the reinforced concrete test beam (bottom left side) and side view of the experimental setup (bottom right side). Measure units given in [mm].

Fig. 6.21 shows the located AE events that occurred from the initial loading up to that time the cracking load was reached. First hair line cracks were visible on the bottom side where the bending causes tension of the concrete. Only those results are displayed which satisfy the chosen criterion for good localizations. Located AE coincide with the topography of two evolving cracks. Results from a later loading step, where sudden crack growing occurred, are shown in **Fig. 6.22**. Numerous AE events were detected and located around one opening crack. Further active cracks, however, do not express in the location results at all. Waves will not propagate directly when there are open cracks in the volume and therefore the source localization method will fail.

In the example given above it becomes apparent that only a subset of all AE could be detected and even be located with an acceptable accuracy. Results then represent the ongoing deterioration processes only at a fraction. Localization capability decreases with increasing damage of the test specimen, especially when cracking of the material occurs in some regions and elastic waves are scattered and reflected.

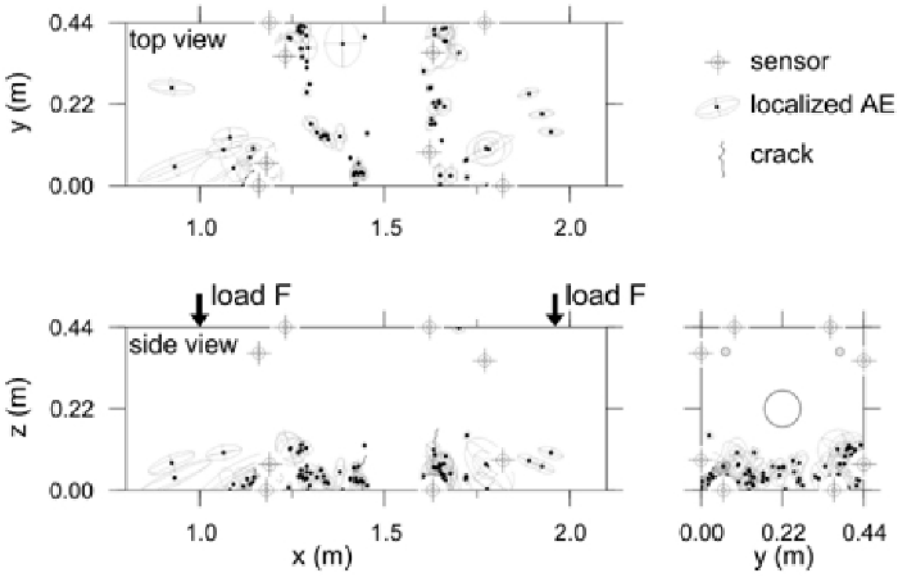

Fig. 6.21. Localization results during initial crack formation. Top view (top), side view (bottom, with cracks seen from the front side), and cross section (bottom right) of the loaded part of the test beam.

Fig. 6.22. Localization results during crack growing. Top view (top), side view (bottom, with cracks seen from the front side), and cross section (bottom right) of the loaded part of the test beam.

6.4.3 Measures to Ensure High Localization Accuracy

The localization accuracy is influenced by various factors. In the following table some measures to ensure high localization accuracy are listed and discussed.

Tab. 6.1. Factors influencing the accuracy of AE results.

Measure		Effect
Data acquisition	Use of an adequate number of sensors	Using more sensors than necessary, the localization algorithm is over determined and the variance σ can be calculated as a value for the accuracy of the result. In general the localization accuracy increases with the amount of sensors applied. Due to the limited reach of AE sensors, high numbers of sensors are needed to cover real life structures. If only a certain amount of sensors is available, concentration on confined areas is recommended.
	Appropriate sensor arrangement	Uniform azimuthal coverage of the AE-source ensures that errors in arrival time determination do not lead to high uncertainties in the AE localization. As the AE-source localization in practical applications is generally not known in advance, the sensor arrangement cannot be adjusted to it. Limitations to the optimal sensor arrangement are posed by the specimen geometry.
	Reduction of noise	The reduction of noise improves the signal-to-noise ratio and therefore also the accuracy of the arrival time determination.
Propagation model	Determination of the wave speed ν in advance	Determining the wave speed ν in advance can be done without much effort. Applying the iterative localization method with a wrong ν leads to systematic mislocalizations that might not be recognized by high values of σ.
	Considering inhomogeneous material properties	By neglecting sensors beyond known inhomogenities such as cracks the accuracy of the localization result can be improved. This method requires an iterative procedure and the use of a higher amount of sensors.
	Use of further wave modes (other than P-waves)	The use of surface waves, which are not as much attenuated as P-waves, for the localization of AE-sources increases the reach of the sensors. Using P- and S-waves the accuracy can be improved. The onsets of surface- and S-waves are generally difficult to recognize in the wave form.
Arrival time determination	Appropriate choice of the threshold value	If the arrival time is determined by the first threshold crossing, the choice of the threshold value is crucial to the quality of the result. For AE-signals with a large variability in amplitude this method is not appropriate.
	Use of sophisticated methods for arrival time determination	The use of sophisticated methods for example the AIC-Picker (see chapter 6.2.1) for the arrival time determination leads to higher localization accuracies.
	Manual arrival time determination	For AE signals with poor signal quality a manual determination is necessary to obtain reasonable localization results. For AE signals with good signal quality the localization accuracy can be increased significantly. The time needed for manual arrival time determination increases exponentially and can only be justified if few AE-events have to be localized accurately for further analysis.

6.5 Further Methods

The methods described in this section were so far only partly applied to acoustic emissions. Since they are related to the approaches described in the preceding sections, they should be highly applicable to the acoustic emission localization problem. Numerous applications of these slightly more advanced methods, which consider clusters of sources rather than individual sources, exist in seismology.

6.5.1 Relative Localization Methods

If lateral velocity variations are present within the test specimen, and lead to uncertainties in the measured travel times at distant stations, the application of a relative localization procedure could improve the localization accuracy. This procedure can be only applied to a local region, i.e. the inter-event distances must be small compared to the event-receiver distance. The events within this region are relocated relative to one particularly well-located event, called master event. It is assumed that these velocity variations have nearly the same effect on all events from the local region (Shearer 1999). Eq. 6.7 can be rewritten as:

$$r_i^{rel} = t_i^0 - t_i^{master} \tag{6.25}$$

The master event is used as the first guess location and Eq. 6.19 can be easily rewritten as:

$$r^{rel} = G \cdot \Delta x \tag{6.26}$$

The correction vector $\Delta \boldsymbol{x}$ must still be relatively small so that the linearization of the problem is valid. Since the principle of the relative localization procedure does not differ from the iterative one, the relative localization of acoustic emissions should also be possible. Further information about relative localization methods can be found in Deichmann and Garcia-Fernandez [1992], Mendecki [1997] or Shearer [1999].

6.5.2 Joint Hypocenter Determination

The relative localization method and joint hypocenter determination are both efficient ways to account for lateral velocity variations. However, in contrast to the relative localization method, the joint hypocenter determination method locates a group of events simultaneously and a common set of sensor corrections is gained. The following short overview of the method is referenced to the detailed outline of Pujol [2000].

The only difference between the single-event localization described in Chap. 6.3.4 and the joint hypocenter determination is that a correction term $\Delta \boldsymbol{s}$ for each sensor is added.

The system of $i = 1, \ldots, n$ sensors and $j = 1, \ldots, m$ events has to be solved simultaneously. Therefore, Eq. 6.19 can be rewritten as:

$$r_j = G_j \cdot \Delta x_j + \Delta s \tag{6.27}$$

The system of linear equations for joint hypocentre determination (Eq. 6.25) can be very large if many sensors and a large number of events are used. However, Pujol [2000] describes several methods in detail for an efficient solution of this problem.

Certain restrictions have also to be considered before a joint hypocenter determination can be applied. If the events are clustered very tightly the solution will be affected by intrinsic numerical errors (Pujol 2000). The joint hypocenter determination is used when unmodeled velocity variations are to be considered by determining station corrections. However, if the joint hypocenter should improve single event localization, the velocity variations need to be restricted to the portions of the raypath close to the sensor. Therefore, for improved results to be obtained, each station correction has to approximately represent the same traveltime anomaly.

6.5.3 Advanced Nonlinear Methods

Besides the iterative localization method, which is based on a linearization of the problem, and still most frequently used of the methods, several nonlinear approaches exist for 3-D localization. Three methods will be summarized in the following. The referenced papers contain further information about nonlinear source localization methods.

A novel approach to the nonlinear localization problem is the differential evolution algorithm by Ružek and Kvasnička [2001]. The differential evolution algorithm is structured like a genetic algorithm and works efficiently and reliably. It is a robust global optimizer which does not use the

linearized form of the problem, but minimizes Eq. 6.5 using a nonlinear approach.

As described in Chap. 6.5.1 a number of relocation methods have been proposed in recent years. These methods apply to clusters of events and aim to reduce the hypocentral scatter of an event *cloud*. A popular method known as the *double-difference* method and developed by Waldhauser and Ellsworth [2000], considers both the P- and S-wave differential travel times, derived from cross-spectral methods, with travel time differences calculated for pairs of events. The method simultaneously determines inter-event distances between clusters of correlated events while determining the relative locations of other clusters and uncorrelated events. The *double-difference* earthquake localization algorithm allows the simultaneous relocalization of large numbers of events over large distances without the need of station corrections (see also joint hypocenter determination)

The residual between the observed and calculated travel times between the two events, i and j recorded at site k, is defined by Waldhauser and Ellsworth [2000] as the *double-difference* and can be expressed as:

$$r_{ijk} = \left(t_{ik} - t_{jk}\right)^{obs} - \left(t_{ik} - t_{jk}\right)^{th} \tag{6.28}$$

Waldhauser and Ellsworth [2000] use a two-step iterative solution procedure, where *a priori* weights describing data quality are first applied to the arrival times. Once a stable solution is obtained, the data are reweighted by multiplying the *a priori* quality weights with values that depend on the misfit of the data from the previous iteration and on the offset between events (to downweight event pairs with large inter-event differences).

The double-difference method has been further developed by Spottiswoode and Linzer [2005]. This method is referred to as the *hybrid* method because it is a combination of the double difference method and absolute (single event) methods, and is similar to the approach taken by Andersen (now Linzer) [2001] for moment tensor inversions. The *hybrid* method has evolved from the approach used by Spottiswoode and Milev [1998], who only considered groups of similar events.

One important enhancement is that events with additional constraints on their locations, such as e.g. the explosions produced when developing a tunnel underground, are used to constrain the *hybrid* localizations. Another enhancement is that the median of the distribution of residuals is used to weight the data. Experience gained by Andersen [2001] suggests that use of median corrections is both more stable and more accurate even while the localization of individual events is based on weighted least-squares minimization. Additionally, the data recorded from closer sensors is given

a greater weight, when absolute locations are computed using classical methods, to reduce errors caused by velocity errors from long ray paths.

For events *i* and *j* recorded at site *k*, Spottiswoode and Linzer [2005] define the residual as:

$$\begin{aligned}\left(r_{ijk}\right)^2 &= w^{ABS}\left[t_{ik}^{obs} - t_{ik}^{th}\right]^2 \\ &+ w^{2D}\left[\left(t_{ik}^{obs} - t_{ik}^{th}\right) - median\left(t_{ik}^{obs} - t_{jk}^{th}\right)\right]^2 \\ &+ \sum_2 w^{LINE}\left[d_i / v_k\right]^2\end{aligned} \tag{6.29}$$

where d_i is the distance of event i from either of two planes through a known line of events (in an underground mining context, such a line could be the line of explosions produced when mining a tunnel), and v_k is the velocity assumed for the wave phase along the ray path. Eq. 6.29 uses a reference *line* of events because this information was available. This formulation could be extended to include reference *points*, rather than lines. Although Eq. 6.29 may appear complicated, it is of a similar form to Eq. 6.28 if the travel times are regrouped as:

$$r_{ijk} = \left(t_{ik}^{obs} - t_{jk}^{th}\right) - \left(t_{jk}^{obs} - t_{jk}^{th}\right) \tag{6.30}$$

The first term in Eq. 6.29 is the absolute location component; the second term has the form of the double difference described by Eq. 6.28, and the last term represents the distance from two planes (oriented vertically and horizontally) that describe the reference line of events. The procedure is iterative and the weighting factors (w^{ABS}, w^{2D}, w^{LINE}) control the influence of each term on the system of equations and are recalculated for each iteration. The arrival-time differences between all pairs of events are used to obtain hybrid locations by minimizing the weighted sum of squares of all arrival-time differences. Minimization is done using the standard Gauss-Newton method (Press et al. 1990).

The hybrid localization procedure is being used successfully on data recorded in deep level mines in South Africa. A number of case studies are presented in Cichowicz et al. [2005].

Another alternative to standard iterative linearized localization methods is the probabilistic inversion approach of Tarantola and Valette [1982]. In recent years, software packages have become available that combine efficient, nonlinear, global search algorithms (e.g. *NonLinLoc*, Lomax et al. 2000). This method gained in importance for the precise localization of

earthquake hypocenters (Husen et al. 2003) and can be adapted to the needs of acoustic emission localization with little modifications (Schechinger 2005). Results are more accurate and reliable compared to that of linearized localization methods and show more stability when linearized methods fail for events recorded outside of a sensor network. The nonlinear localization method can be easily applied with high-contrast 3-D-varying velocity models, because localization algorithms need no calculation of partial derivatives.

Whereas standard linearized localization methods give a single point solution and uncertainty estimates (Schechinger and Vogel 2005), the result of the nonlinear method is a probability density function (PDF) over the unknown source coordinates. The optimal location is taken as the maximum likelihood point of the PDF. The PDF explicitly accounts for a priori known data errors, which are assumed to be Gaussian.

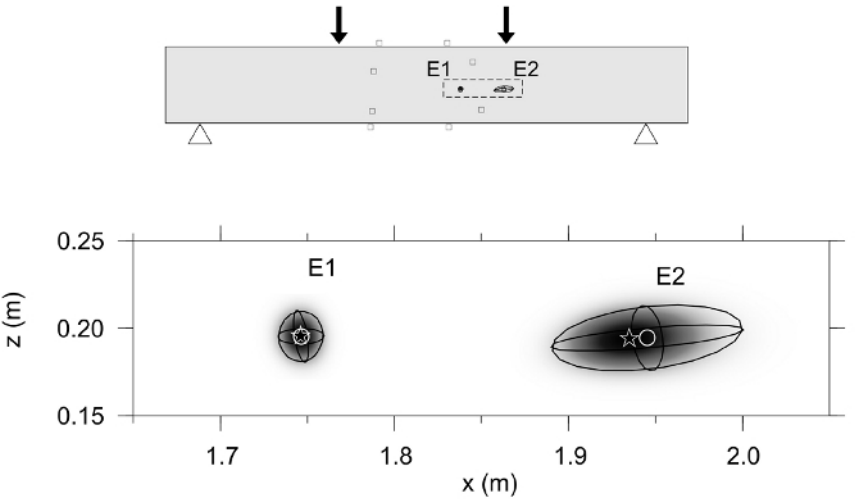

Fig. 6.23. Nonlinear localization results compared to linearized localization results. The 68%-error ellipsoid estimated by the standard linearized localization method is plotted. See also Fig. 6.20 for the experimental setup.

The model of the test specimen is parameterized by a 3-D grid. For all grid nodes, travel times of the first arrivals to each sensor position have to be available. In *NonLinLoc*, a finite-difference scheme is used to calculate the travel times for the given velocity model (Podvin and Lecomte 1991), but in principle, any method can be used. Different approaches are used for estimating the PDF. A systematic grid search algorithm over nested grids can be very time consuming but gives an exhaustive coverage of the search region. The faster stochastic Metropolis-Gibbs sampling approach or the

Oct-Tree Importance sampling algorithms are more practical for routine analysis (Lomax et al. 2000).

Two AE events *E1* and *E2* are shown in

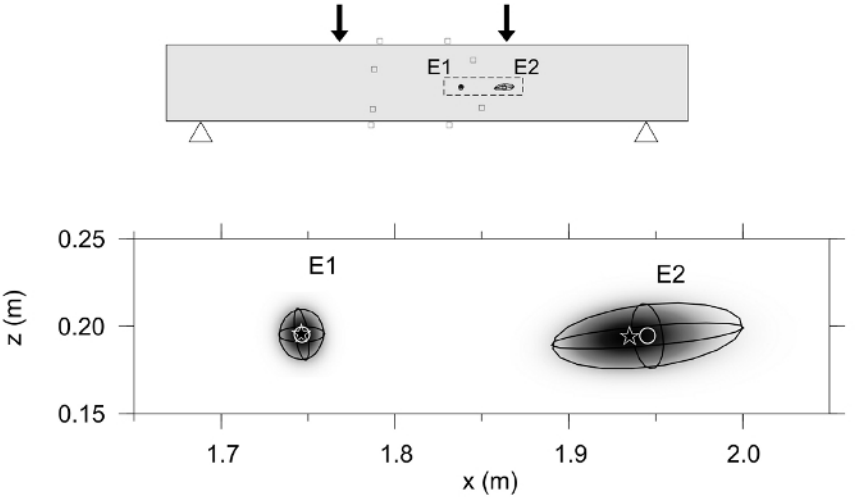

Fig. 6.23. They were recorded in a loading test of a reinforced concrete beam described in Chap. 6.4.2.

The results of the nonlinear localization (confidence volumes and maximum likelihood source coordinates, indicated by gray scales and white stars) are compared to the point source solution (white circles). The 68% error ellipsoid estimated by the standard linearized localization method is plotted. In both cases, a constant propagation velocity was assumed. For the well observed event *E1* no differences between both solutions are evident. The event *E2* occurred at the edge of the sensor network and therefore has a greater localization error. There are slight deviations between the error ellipsoid and the shape of the PDF, because the nonlinear relationship between source coordinates and travel times is taken into account. For this reason, the PDF can have a more irregular shape in the case of a 3-D velocity model.

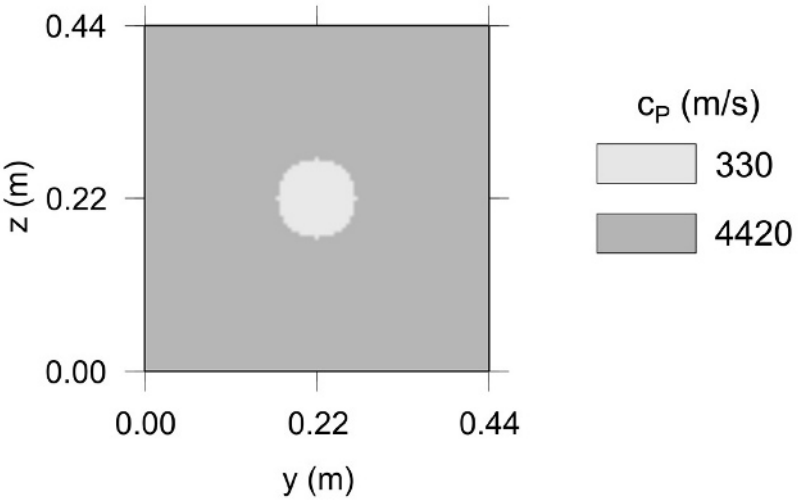

Fig. 6.24. Cross section of the 3-D velocity model with an air-filled void representing the ungrouted duct in the length axis of a concrete beam.

The nonlinear localization was tested using a 3D velocity model on some events close to an ungrouted duct in the length axis of the concrete beam. **Fig. 6.24** shows the cross section of the model with an air-filled cylindrical void, along its length axis, that disturbs the direct wave propagation and hence the travel times.
The AE locations obtained with the linearized method for a homogeneous model of plain concrete differ from the results of the nonlinear localization with the 3-D model (**Fig. 6.25**). Ongoing work is investigating in detail how acoustic emission localization results are improved by the nonlinear approach. Possibilities for applications would be structures with large scale inhomogeneities like hollow-cores.

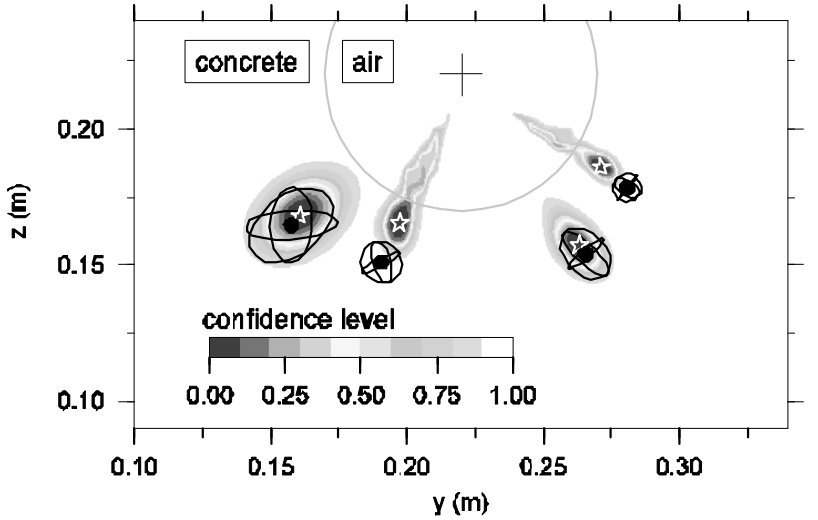

Fig. 6.25. Nonlinear localization results considering the air-filled duct (confidence levels in gray scales and maximum likelihood solution as stars) compared to linearized results for a plain concrete model (black circles as point source with error ellipsoid).

References

Akaike H (1974) Markovian representation of stochastic processes and its application to the analysis of of autoregressive moving average processes. Annals of the Institute of Statistical Mathematics 26: 363 – 387

Aki K, Richards P (1980) Quantitative Seismology Theory and Methods. Vol. 2 Freeman WH and Company, New York

Allen R (1982) Automatic phase pickers: their present use and future prospects. Bulletin of the Seismological Society of America 72: 225 – 242

Andersen LM (2001) A relative moment tensor inversion technique applied to seismicity induced by mining. PhD Thesis, University of the Witwatersrand, Johannesburg

Andersen LM, Spottiswoode SM (2001) A hybrid relative moment tensor methodology. 5th Int. Symposium on Rockbursts and Seismicity in Mines, South African Institute of Mining and Metallurgy, pp 371-378

Baer M, Kradolfer U (1987) An automatic phase picker for local and teleseismic events. Bulletin of the Seismological Society of America 77: 1437-1445

Bath M (1979) Introduction to Seismology. 2nd Edition, Birkhäuser Verlag, Basel

Berthelot JM, Robert J (1987). Modelling concrete damage by acoustic emission. Journal of Acoustic Emission 6: 43-66

Bormann P (ed) (2002) New Manual of Seismological Observatory Practice. Vol.1 & 2 GeoForschungsZentrum Potsdam

Capon J (1969) High-Resolution Frequency-Wavenumber Spectrum Analysis. Proceedings of the IEEE 57(8): 1408-1418

Cichowicz A, Spottiswoode SM, Linzer LM, Drent D, Heyns PS, Handley MF (2005) Improved Seismic Locations and Location Techniques. (SIMRAC Report SIM020304), Department of Minerals and Energy, South Africa, www.simrac.co.za.

Dai H, MacBeth C (1995) Automatic picking of seismic arrivals in local earthquake data using an artificial neural network. Geophysical Journal International 120: 758-774

Deichmann N, Garcia-Fernandez M (1992) Rupture geometry from high-precision relative hypocenter locations of microearthquake clusters. Geophysical Journal International 110: 501-517

Dill-Langer G, Ringger T, Höfflin L, Aicher S (2002) Location of Acoustic Emission Sources in Timber Loaded Parallel to Grain. In: 13th International Symposium on Nondestructive Testing of Wood. August 19-21, Berkeley, California

Earle P, Shearer P (1994) Characterization of global seismograms using an automatic picking algorithm. Bulletin of the Seismological Society of America 84 (2): 366-377

Finck F (2005) Untersuchung von Bruchprozessen in Beton mit Hilfe der Schallemissionsanalyse. Ph.D. thesis, University of Stuttgart

Finck F, Manthei G (2004) On near-field effects in signal based acoustic emission analysis. Otto Graf Journal 15: 121-134

Finck F, Yamanouchi M, Reinhardt HW, Grosse C (2003) Evaluation of mode-I failure of concrete in a splitting test using acoustic emission technique. International Journal of Fracture 124: 139-152

Flinn E (1965) Confidence regions and error determinations for seismic event location. Reviews of Geophysics 3(1): 157-185

Grosse CU (2000) WinPecker Version 1.2: Instruction Manual, University of Stuttgart

Grosse CU, Reinhardt HW (1999) Entwicklung eines Algorithmus zur automatischen Lokalisierung von Schallemissionen. Die Materialprüfung 41: 342-347

Grosse CU (1996) Quantitative zerstörungsfreie Prüfung von Baustoffen mittels Schallemissionsanalyse und Ultraschall. Ph.D. thesis, University of Stuttgart

Grosse CU, Glaser SD, Krüger M (2006) Condition monitoring of concrete structures using wireless sensor networks and MEMS. In: Tomizuka M, Yun CB, Giurgiutiu V (eds) Proc. SPIE Vol. 6174, Smart Structures and Materials 2006: Sensors and Smart Structures Technologies for Civil, Mechanical, and Aerospace Systems, pp 407-418

Havskov J, Bormann P, Schweitzer J (2002) Chapter IS 11.1: Earthquake location. In: Bormann P (ed), New Manual of Seismological Observatory Practice. Vol. 2. GeoForschungsZentrum Potsdam, p 28

Husen S, Kissling E, Deichmann N, Wiemer S, Giardini D, Baer M (2003) Probabilistic earthquake location in complex three-dimensional velocity models:

Application to Switzerland. Journal of Geophysical Research, 108(B2), 2077: doi:10.1029/2002JB001778

Joswig M (2004) Nanoseismic Monitoring – Part I: Theory and First Applications. Geophysical Journal International, submitted

Joswig M (1990) Pattern recognition for earthquake detection. Bulletin of the Seismological Society of America 80:170-186

Kapphahn G, Quade J, Steffens K (1993) SEA-Prüfung bei der insitu-Traglastermittlung von Stahl- und Spannbetonkonstruktionen. In: Jubiläungstagung 60 Jahre DGZfP, 17.–19. Mai 1993 in Garmisch-Partenkirchen, DGZfP Berlin

Kitagawa G, Akaike H (1978) A procedure for the modelling of non-stationary time series. Annals of the Institute of Statistical Mathematics 30 (Part B): 351-363

Köppel S (2002) Schallemissionsanalyse zur Untersuchung von Stahlbetontragwerken, ETH Zürich, IBK Bericht 272, Zürich, p 174

Köppel S, Vogel T (2000) Schallemissionsmessungen bei Versuchen an Stahlbeton. ETH Zürich, IBK Bericht 259, p 164

Köppel S, Grosse C (2000) Advanced Acoustic Emission Techniques for Failure Analysis in Concrete. In: WCNDT Proceedings 2000. Italian Society for Non-Destructive Testing and Monitoring Diagnostics

Kreyszig E (1993) Advanced Engineering Mathematics. 7th Edition, John Wiley & Sons Inc.

Kurz JH (2006) Verifikation von Bruchprozessen bei gleichzeitiger Automatisierung der Schallemissionsanalyse an Stahl- und Stahlfaserbeton. Ph.D. thesis, University of Stuttgart

Kurz JH, Grosse CU, Reinhardt HW (2005) Strategies for reliable automatic onset time picking of acoustic emissions and of ultrasound signals in concrete. Ultrasonics 43(7): 538-546

Labusz J, Chang H, Dowding C, Shah S (1988) Parametric study of AE location using only four sensors. Rock mechanics and rock engineering 21: 139-148

Leonard M (2000) Comparison of manual and automatic onset time picking. Bulletin of the Seismological Society of America 90(6): 1384-1390

Lomax A, Virieux J, Volant P, Berge-Thierry C (2000) Probabilistic earthquake location in 3D and layered models. In: Thurber C, Rabinowitz N (eds), Advances in Seismic Event Location. Kluwer Academic Publishers, pp 101-134

Maeda N (1985) A method for reading and checking phase times in auto-processing system of seismic wave data. Zisin (=Jishin) 38: 365-379

Mendecki A (ed) (1997) Seismic Monitoring in Mines. 1st Edition. Chapman & Hall, London

Moriya H, Manthei G, Mochizuki S, Asanuma H, Niitsuma H, Jones R, Eisenblätter J (2002) Collapsing method for delineation of structures inside AE cloud associated with compression test of salt rock specimen. In: 16th Int. Acoustic Emission Symposium, November 12-15 2002, Tokushima, Japan

Ohtsu M (1998) Basics of acoustic emission and apllications to concrete engineering. Materials Science Research International 4(3): 131-140

Podvin P, Lecomte I (1991) Finite difference computation of traveltimes in very contrasted velocity models: a massively parallel approach and its associated tools. Geophysical Journal International 105: 271-284

Press W, Teukolsky S, Vetterling W, Flannery B (1992) Numerical recipes in C. Cambridge University Press, New York, chap. 15.6, pp 689-699

Press WH, Flannery BP, Teukolsky SA, Vetterling WT (1990) Numerical recipes: The Art of Scientific Computing, Cambridge University Press, New York

Pujol J (2000) Joint event location – the jhd technique and application to data from local seismic networks. In: Thurber C, Rabinowitz N (eds), Advances in Seismic Event Location. Kluwer Academic Publishers, pp 163-204

Pujol J (2004) Earthquake location tutorial: graphical approach and approximate epicentral location techniques. Seismological Res. Letters 75(1): 63-74

Reinhardt HW, Grosse CU (1999) Zerstörungsfreie Prüfung von Aramidbewehrung. In: Teutsch M (ed), Festschrift zum 60. Geburtstag von Univ.-Prof. Dr.-Ing. Horst Falkner. Vol. 142. Institut für Baustoffe, Massivbau und Brandsschutz, pp 233-240

Rost S, Thomas C (2002) Array Seismology: Methods and Applications. Reviews of Geophysics 40(3), 1008: doi:10.1029/2000RG000100.

Ružek B, Kvasnička M (2001) Differential Evaluation Algorithm in the Earthquake Hypocenter Location. Pure and Applied Geophysics 158: 667-693

Schechinger B, Vogel T (2006) Acoustic emission for monitoring a reinforced concrete beam subject to four-point-bending. Construction and Building Materials, 21(3): 483-490

Schechinger B (2005) Schallemissionsanalyse zur Überwachung der Schädigung von Stahlbeton. Ph.D. thesis, Eidgenössische Technische Hochschule Zürich

Sellers E, Kataka M, Linzer L (2003) Source parameters of acoustic emission events and scaling with mining-induced seismicity. Journal of Geophysical Research 108 (B9): doi: 10.1029/2001JB000670

Sleeman R, van Eck T (1999) Robust automatic P-phase picking: an on-line implementation in the analysis of broadband seismogram recordings. Physics of the Earth and Planetary Interiors 113: 265-275

Spies T, Hesser I, Eisenblätter J (2004) Seismology on a small scale: acoustic emission measurements in rock mechanics. In: Schweitzer J (ed), Symposium in Memoriam of Prof. Gerhard Müller, Vol. I/2004, Mitteilungen Sonderband, Deutsche Geophysikalische Gesellschaft: 72-76

Spottiswoode SM, Linzer LM (2005) A hybrid location methodology. Journal of the South African Institute of Mining and Metallurgy 105: 417-425

Spottiswoode SM, Milev A (1998) The use of waveform similarity to define planes of mining-induced seismic events. Tectonophysics 289: 51-60

Schweitzer J, Fyen J, Mykkeltveit S, Kvaerna T (2002) Chapter 9: Seismic Arrays. In: Bormann P (ed), New Manual of Seismological Observatory Practice. Vol. 1. GeoForschungsZentrum Potsdam, p 51

Shearer P (1999) Introduction to Seismology. Cambridge University Press

Smart E, Flin E (1971) Fast Frequency-Wavenumber Analysis and Fisher Signal Detection in Real-Time Infrasonic Array Data Processing. Geophysical Journal of the Royal Astronomical Society 26: 279-284

Tarantola A, Valette B (1982) Inverse problems = Quest for information. Journal of Geophysics 50: 159-170

Thurber C, Engdahl E (2000) Advances in global seismic event location. In: Thurber C, Rabinowitz N (eds), Advances in Seismic Event Location. Kluwer Academic Publishers, pp 3-22

Trnkoczy A (2002) Understanding and paramter settings of STA/LTA trigger algorithm. In: Bormann P (ed), IASPEI New Manual of Seismological Observatory Practice, Vol. 2, GeoForschungsZentrum Potsdam, Ch. IS 8.1, pp 1-19

Waldhauser F, Ellsworth W (2000) A Double-Difference Earthquake Location Algorithm: Method and Application to the Northern Hayward Fault, California. Bulletin of the Seismological Society of America 90(6): 1353-1368

Zang A, Wagner C, Stanchits S, Dresen G, Andresen R, Haidekker M (1998) Source analysis of acoustic emissions in Aue granite cores under symmetric and asymmetric compressive loads. Geophysical Journal International 135: 1113-1130

Zhang H, Thurber C, Rowe C (2003) Automatic P-wave arrival detection and picking with multiscale wavelet analysis for single-component recordings. Bulletin of the Seismological Society of America 93(5): 1904-1912

Zwicky D, Vogel T (2000) Bruchversuche an ausgebauten Brückenträgern aus Spannbeton; ETH Zürich, IBK Bericht 258, Zürich, pp 167

7 Source Mechanisms of AE

Masayasu Ohtsu

7.1 Introduction

Elastic waves due to microcrack nucleation in a homogeneous medium are theoretically discussed here. Although many materials are not homogeneous but heterogeneous, the material properties in elastodynamics are fundamentally dependent on the characteristic dimensions of materials. For example, it is reasonable to refer to concrete and rock as homogeneous in AE measurement. This is because the dynamic heterogeneity is closely dependent on the relation between the wavelengths and the characteristic dimensions of heterogeneous materials. In the case that the wavelengths are even longer than the sizes of heterogeneous inclusions, the effect of heterogeneity is inconsequent. For AE waves in concrete, the velocity of elastic waves, is over 1000 m/s. Thus, the use of frequency range up to some 100 kHz corresponds to the case where the wavelength is longer than several centimeters. It results in the fact that concrete consisting of only normal aggregate (of around 10 mm diameter) or rock of minerals is reasonably referred to as homogeneous.

It is noted that the wavelengths detected should be physically present in the propagating medium. This is not the case of AE waves in steel plates, because the thickness of the plate is occasionally shorter than the wavelengths. The use of 1 MHz frequency range corresponds to detecting AE waves of around 5 millimeter wavelengths. In the case that wavelengths of propagating waves are longer than the thickness, diffracted and dispersive waves are generated. The amplitudes of these waves are mostly larger than those of P- and S-waves, and thus are dominant in the AE detection of plate samples. The dispersive waves are defined as waves of which velocities are dependent on frequency components (wavelengths). One example

is Lamb wave observed in a plate. This is one key factor for the flaw location in the plate-like members.

7.2 Integral Representation

Governing equations of elastodynamics can be solved both analytically and numerically. One of analytical solutions is an integral representation (Eringen 1975), which is mathematically essential for formulating AE waves. To derive equations, Gauss's integral theorem is necessary,

$$\int_v f_{,j}(x)dV = \int_v f(x)\, n_j dS, \tag{7.1}$$

where V is the domain of function $f(\boldsymbol{x})$, surrounded by the boundary surface S. Vector $\boldsymbol{n}$ is the outward-normal vector to the surface S. Then, one pair of elastic fields are considered in domain V. One is the displacement field $u_i(\boldsymbol{y},t)$, and the other is displacement field $v_i(\boldsymbol{y},t)$. In an isotropic and linear-elastic body, the reciprocal representation is derived as,

$$\begin{aligned}&\int_v \left\{ \frac{E}{2(1+\nu)(1-2\nu)} u_{i,jj}(\mathrm{y},t) + \frac{E}{2(1+\nu)} u_{i,jj}(\mathrm{y},t) - \rho\partial^2 u_i(\mathrm{y},t)/\partial t^2 \right\} * v_i(\mathrm{y},t)\, dV \\ &-\int_v u_i(\mathrm{y},t) * \left\{ \frac{E}{2(1+\nu)(1-2\nu)} v_{j,ij}(\mathrm{y},t) + \frac{E}{2(1+\nu)} v_{j,ij}(\mathrm{y},t) - \rho\partial^2 v_i(\mathrm{y},t)/\partial t^2 \right\} dV.\end{aligned} \tag{7.2}$$

Here E is the modulus of elasticity and ν is Poissons' ratio. The symbol $*$ means the convolution integral. Functions inside integration are modified as,

$$\begin{aligned}&\left\{E/\left[2(1+\nu)(1-2\nu)\right]u_{j,ij} + E/\left[2(1+\nu)\right]u_{i,jj} - \rho\partial^2 u_i/\partial t^2\right\} * v_i \\ &= \left\{v_i * \left[E/\left[2(1+\nu)(1-2\nu)\right]u_{j,i} + E/\left[2(1+\nu)\right]u_{i,j}\right]\right\}_{,j} \\ &-v_i * \rho\partial^2 u_i/\partial t^2 \\ &-v_{i,j} * \left\{E/\left[2(1+\nu)(1-2\nu)\right]u_{j,i} + E/\left[2(1+\nu)\right]u_{i,j}\right\}\end{aligned} \tag{7.3}$$

Substituting Eq. 7.3 into Eq. 7.2 and taking into account Gauss's theorem in Eq. 7. 1,

$$
\begin{aligned}
&\int_v \left\{ v_i * \left[E/\left[2(1+v)(1-2v)\right] u_{j,i} + E/\left[2(1+v)\right] u_{i,j} \right] \right\}_{,j} dV \\
&-\int_v v_i * \rho \partial^2 u_i / \partial t^2 dV \\
&-\int_v v_{i,j} * \left\{ E/\left[2(1+v)(1-2v)\right] u_{j,i} + E/\left[2(1+v)\right] u_{i,j} \right\} dV \\
&-\int_v \left\{ u_i * \left[E/\left[2(1+v)(1-2v)\right] v_{j,i} + E/\left[2(1+v)\right] v_{i,j} \right] \right\}_{,j} dV \\
&+\int_v u_i * \rho \partial^2 v_i / \partial t^2 dV \\
&+\int_v u_{i,j} * \left\{ E/\left[2(1+v)(1-2v)\right] v_{j,i} + E/\left[2(1+v)\right] v_{i,j} \right\} dV \\
&= \int_s v_i * \left\{ \left[E/\left[2(1+v)(1-2v)\right] u_{j,i} + E/\left[2(1+v)\right] u_{i,j} \right] n_j \right\} dS \\
&-\int_s u_i * \left\{ \left[E/\left\{2(1+v)(1-2v)\right\} v_{j,i} + E/\left[2(1+v)\right] v_{i,j} \right] n_j dS \right\}
\end{aligned}
\tag{7.4}
$$

Here an associated relation of the convolution integral,

$$v_i * \partial^2 u_i / \partial t^2 = u_i * \partial^2 v_i / \partial t^2$$

is applied. Assuming that displacement $u_i(\mathbf{y},t)$ is satisfied with the governing equation of elastodynamics, the first integration in Eq. 7.4 is equal to zero. Taking into account stress field $\sigma_{ij}(\mathbf{y},t)$ in the displacement field $u_i(\mathbf{y},t)$, Eq. 7.4 is summarized as,

$$
\begin{aligned}
&-\int_v u_i(\mathbf{y},t) * \left\{ E/\left[2(1+v)(1-2v)\right] v_{j,ij}(\mathbf{y},t) + E/\left[2(1+v)\right] v_{i,jj}(\mathbf{y},t) \right. \\
&\left. -\rho \partial^2 v_i(\mathbf{y},t) / \partial t^2 \right\} \\
&= \int_s \left[v_i(\mathbf{y},t) * \sigma_{ij}(\mathbf{y},t) n_j \right. \\
&\left. -u_i(\mathbf{y},t) * \left\{ E/\left[2(1+v)(1-2v)\right] v_{j,i}(\mathbf{y},t) + E/\left[2(1+v)\right] v_{i,j}(\mathbf{y},t) \right\} n_j \right] dS
\end{aligned}
\tag{7.5}
$$

7.3 Green's Functions

In Eq. 7.5, function $v_i(\mathbf{y},t)$ is replaced by Green's function $G_{ki}(\mathbf{x},\mathbf{y},t)$ which is the solution of the following differential equation and known as the singular solution in the boundary element method,

$$\begin{aligned} &E/\left[2(1+\nu)(1-2\nu)\right]G_{kj,ij}(\mathbf{x},\mathbf{y},t) \\ &+E/\left[2(1+\nu)\right]G_{ki,jj}(\mathbf{x},\mathbf{y},t)-\rho\partial^2 G_{ki}(\mathbf{x},\mathbf{y},t)/\partial t^2 \\ &=\delta_{ki}\delta(\mathbf{x}-\mathbf{y})\delta(t). \end{aligned} \tag{7.6}$$

where $\delta(\mathbf{x}\text{-}\mathbf{y})$ is the delta function in the space. Physically, Green's function $G_{ki}(\mathbf{x},\mathbf{y},t)$ corresponds to a solution of displacement at $\mathbf{x}$ in the x_k direction at time t due to an impulse at $\mathbf{y}$ in the x_i direction at time t = 0. In the definition, no boundary conditions are taken into account. Consequently, the solution of Eq. 7.6 is called Green's function in an infinite space, and can be solved analytically. As a matter of course, Green's functions in a half-space (Ohtsu 1984) and an infinite plate (Pao 1981) are also available, taking into the boundary conditions. In these cases, however, solutions are obtained numerically, because numerical integration along the ray paths is requisite (Eringen 1975). In the case of a finite body, Green's functions could be obtained only by numerical methods by the Finite Difference Method (FDM) (Enoki 1986) and by the Finite Element Method (FEM) (Hamstad 1999). Because elastic waves propagate, the problem in elastodynamics must be solved in the whole domain. Practically, however, only solutions at the sensor locations are necessary and sufficient for AE measurement. This is one reason why the numerical methods are not attractive in AE research.

Along with Green's functions, traction is introduced as defined,

$$t_i=\sigma_{ij}n_j. \tag{7.7}$$

Thus, the traction associated with Green's function is defined,

$$\begin{aligned} T_{ki}(\mathbf{x},\mathbf{y},t)&=\left\{E/\left[2(1+\nu)(1-2\nu)\right]G_{kj,i}(\mathbf{x},\mathbf{y},t)\right. \\ &\quad\left.+E/\left[2(1+\nu)\right]G_{ki,j}(\mathbf{x},\mathbf{y},t)\right\}n_j \\ &=G_{kp,q}(\mathbf{x},\mathbf{y},t)C_{pqij}n_j \end{aligned} \tag{7.8}$$

where C_{pqij} are the elastic tensor and defined as,

$$C_{pqij} = E/\left[(1+\nu)(1-2\nu)\right]\delta_{pq}\delta_{ij} + E/\left[2(1+\nu)\right]\delta_{pi}\delta_{qj} + E/\left[2(1+\nu)\right]\delta_{pj}\delta_{iq}.$$

Functions T_{ik} is also called Green's functions of the second kind. Substituting Eqs. 7.6, 7.7, and 7.8 into 7.5,

$$\begin{aligned} &-\int_v u_i(\mathbf{y},t) * \left\{-\delta_{ki}\delta(\mathbf{x}-\mathbf{y})\delta(t)\right\} dV = u_k(\mathbf{x},t) \\ &= \int_s \left[G_{ki}(\mathbf{x},\mathbf{y},t) * \sigma(\mathbf{y},t) n_j - u_i(\mathbf{y},t) * T_{ki}(\mathbf{x},\mathbf{y},t) \right] dS. \end{aligned} \tag{7.9}$$

Eventually, we have the integral representation of the solution in the elastodynamic field,

$$u_k(\mathbf{x},t) = \int_s \left[G_{ki}(\mathbf{x},\mathbf{y},t) * t_i(\mathbf{y},t) - T_{ki}(\mathbf{x},\mathbf{y},t) * u_i(\mathbf{y},t) \right] dS \tag{7.10}$$

7.4 AE Waves Due to a Point Force

In 1970's, it was first demonstrated that AE waves are elastic waves and could be synthesized theoretically. The famous paper by Breckenridge dealt with Lamb's problem (Beckenridge 1981). Later, the generalized theory of acoustic emission (AE) was established on the basis of elastodynamics (Ohtsu 1984). Historically, theoretical treatment started with AE waves due to an applied force. In those days, because an experiment could be done easily, many people attempted to detected AE waves due to an applied force and applied the results to source characterization (Pao 1978). Most papers were far from successful for source characterization, because the generalized theory was not understood enough. In particular, the difference between AE waves due to an applied force and those of cracking was not clearly realized. Even now, misunderstanding can be sometimes found in the literature. The main concept of the generalized theory results from the separation of AE waves due to an applied force and due to cracking.

Elastodynamic solutions of wave motions ***u(x,t)*** are mathematically represented by Eq. 7.10. The theory of the famous pencil-lead test is readily derived, by setting an applied force ***f(y,t)*** at point $\boldsymbol{y_0}$ on the boundary surface,

$$t_j(\boldsymbol{y},t) = f_j(t)\delta(\boldsymbol{y} - \boldsymbol{y_0}) \text{ and } u_j(\boldsymbol{y},t) = 0 \quad \text{on } S.$$

Substituting into Eq. 7.10,

$$\begin{aligned} u_i(\mathbf{x},t) &= \int G_{ij}(\mathbf{x},\mathbf{y},t) * f(t)\delta(\mathbf{y}-\mathbf{y_0})e_j \\ &= G_{ij}(\mathbf{x},\mathbf{y_0},t) * f_j(t) \end{aligned} \tag{7.11}$$

This is the governing equation in the case that dynamic force ***f(t)*** is applied at point $\boldsymbol{y_0}$ on the specimen. Taking into account the case that force $f_j(t)$ is the step function $h(t)e_j$,

$$\begin{aligned} u_i(\mathbf{x},t) &= G_{ij}(\mathbf{x},\mathbf{y},t) * h(t)e_j \\ &= G_{ij}(\mathbf{x},\mathbf{y_0},t) * \int \delta(t)dt\ e_j \\ &= \int G_{ij}(\mathbf{x},\mathbf{y_0},t) * \delta(t)\,dt\ e_j \\ &= \int G_{ij}(\mathbf{x},\mathbf{y_0},t)e_j dt \\ &= G_{ij}^{\ H}(\mathbf{x},\mathbf{y_0},t)e_j \end{aligned} \tag{7.12}$$

Here G_{ij}^{H} is Green's function due to the step-function force and,

$$dG_{ij}^{\ H}(\mathbf{x},\mathbf{y_0},t)/dt = G_{ij}(\mathbf{x},\mathbf{y},t) \tag{7.13}$$

From Eqs. 7.11 and 7.13, the physical meaning of Green's function is readily obtained. $G_{ij}(\boldsymbol{x},\boldsymbol{y},t)$ is an elastodynamic solution of the displacement in the x_i direction at point $\boldsymbol{x}$ and at time t due to a delta-function force in the x_j direction at point $\boldsymbol{y}$ and at time t = 0. Since Green's functions are dependent on not only material properties but also on configuration of the medium, they have to be computed numerically except for an infinite space where analytical solutions are known.

In elastodynamics as well as in seismology, the problem where a force is applied in a half space is called Lamb's problem. This is because the problem was first solved by Lamb [1904]. Then, Pekeris published famous results of Lamb's solutions due to a surface pulse (Pekeris 1955) and a buried pulse (Pekeris 1955).

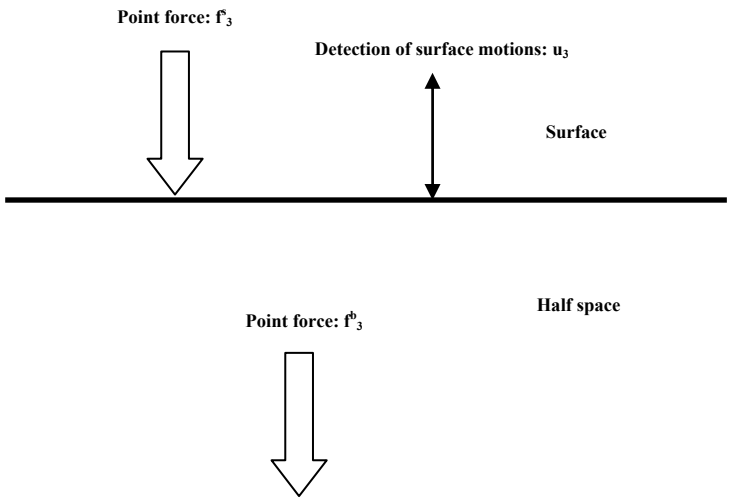

Fig. 7.1. Surface pulse $f^s_3(t)$ and buried pulse $f^b_3(t)$ in a half space.

A generalized solution suitable for numerical computation was comprehensively reported by Johnson [1974]. The computational code is already available in the literature (Ohtsu 1984). Accordingly, Green's functions in a half space are normally called Lamb's solutions. In most cases, the solutions due to step-function are presented as formulated in Eq. 7.13.

In the case that the force is applied in the x_3-direction and the displacement u_3 in the x_3-direction is observed, Eq, 7.12 becomes,

$$u_3(\boldsymbol{x},t) = G_{33}(\boldsymbol{x},\boldsymbol{y}_0,t) * f_3(t)$$

The configuration of the detection is illustrated in **Fig. 7.1**, showing two cases. One is the case of buried pulse (force) $f^b_3(t)$, and the other is that of surface pulse, $f^s_3(t)$. As published by Pekeris (Pekeris 1955), these two forces result in the completely different displacement fields at point $\boldsymbol{x}$. In **Fig. 7.2**, examples of Lamb's solutions due to a buried step-function force, where $f^b_3(t) = h_3(t)$, are given. The depth of the source, D, is 6 cm and the horizontal distance, R, is varied as 3 cm, 6 cm and 9 cm. Here P-wave velocity v_p is assumed as 4000 m/s and Poisson's ratio is 0.2. These material properties actually represent those of concrete. Near the epicenter, only P-wave and S-wave are observed as shown in **Fig. 7.2** (a).

With the increase in the horizontal distance, at 45° incident angle (D = 6 cm and R = 6 cm), SP-wave is observed right before arriving S-wave. Further the increase of the distance (R = 9 cm) leads to negative amplitude of SP-wave.

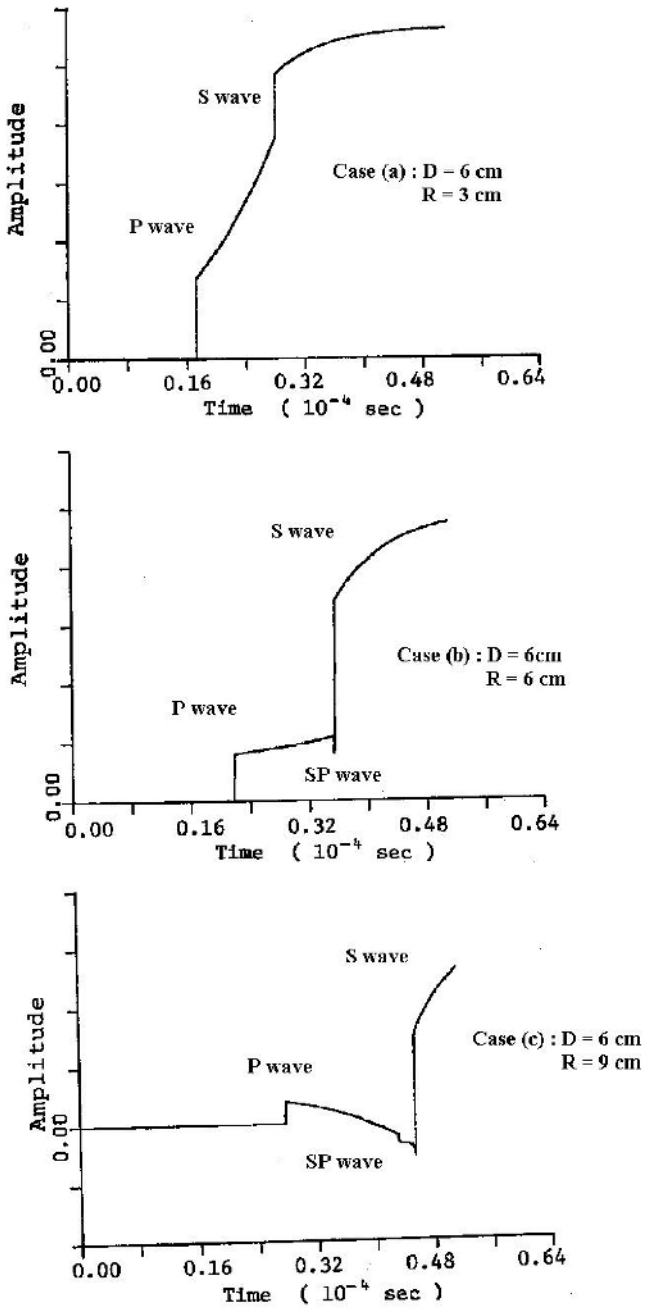

Fig. 7.2. Lamb's solutions due to a buried step-function pulse.

Mathematically, the limiting case that *R/D* is infinite leads to Lamb's solution due to the surface pulse. An example of Lamb's solution due to the surface pulse is shown in **Fig. 7.3**. To clarify the effect of Poisson's ratio, two cases that $\nu = 0.25$ and 0.3 are given. Corresponding to steel, the velocity of P-wave v_p is 6400 m/s. This is the case that $R = 10$ cm. As the limiting case, the amplitude of Rayleigh wave is theoretically infinite. Thus, the peak of the amplitudes indicates the arrival of Rayleigh wave. Right before the arrival of Rayleigh wave, S-wave is observed. Although the arrival of P-wave is numerically identified, the arrival is hard to be observed as magnified. Comparing **Fig. 7.2** with **Fig. 7.3**, it is obviously found that Green's functions are really configuration-dependent.

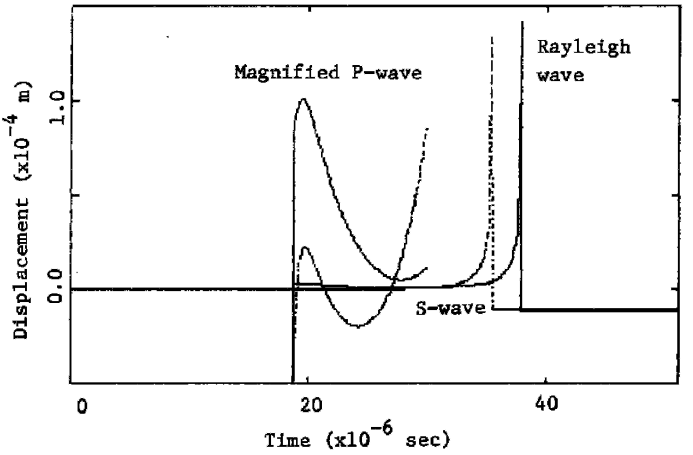

Fig. 7.3. Lamb's solutions due to a surface step-function pulse. A solid curve shows the case $\nu = 0.3$ and a broken shows the case $\nu = 0.25$.

As discussed in Chapter 3, Breckenridge et al. [1981] developed a capacitance-type sensor of very flat response, by which they detected AE waves due to a break of glass capillary shown in **Fig. 7.4**. Later, the capillary break was replaced by the pencil-lead break by Hsu [1978]. As compared **Fig. 7.3** with **Fig. 7.4,** first time, they showed that AE wave detected by the flat-type sensor due to the step-function force is actually identical to Lamb's solution due to the surface pulse. It was also demonstrated that Lamb's solution due to a buried pulse could be obtained by applying the force at the bottom of the block in Fig. 3.10. Thus, it is clarified by them that the displacement observed by the flat-type sensor due to capillary break or pencil-lead break is identical to $G^H_{33}(\boldsymbol{x},\boldsymbol{y}_0,t)$. This implies that Green's function of the specimen can be empirically obtained by just applying the pencil-lead break and recording the displacements.

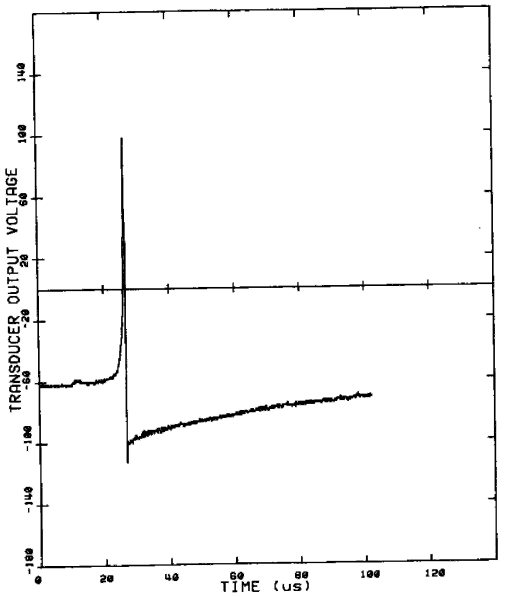

Fig. 7.4. A waveform detected by a capacitive transducer by NIST.

By employing a concrete block as shown in **Fig. 7.5**, AE waves due to surface pulse is detected at the point E. In **Fig. 7.6** (a), AE wave detected by AE sensor of resonance frequency 1 MHz is shown, where the force was applied by the same-type sensor driving an electric pulse at the distance R = 6 cm. In this case, the source-time function f(t) was reasonably assumed (Ohtsu 1982),

$$f(t) = \sin^4(\pi t/Tr), \quad 0 < t < Tr \tag{7.14}$$

Here Tr was set to be equal to 10 μs. The corresponding Lamb's solution $G^H_{33}(\boldsymbol{x},\boldsymbol{y}_0,t)$ due to a surface pulse was calculated, which was similar to those in **Fig. 7.3**. Material properties of concrete were obtained in the experiment as P-wave v_p = 4000 m/s and Poisson's ratio ν = 0.2. Then, AE wave was synthesized by,

$$u_3(\boldsymbol{x},t) = G_{33}{}^H(\boldsymbol{x},\boldsymbol{0},t) * df(t)/dt. \tag{7.15}$$

A result is shown in **Fig. 7.6** (b). Except for the resonance vibration of the sensor in the latter portion, remarkable agreement between **Fig. 7.6** (a) and **Fig. 7.6** (b) is observed.

The simulation of AE waves due to a point force was also conducted by FEM due to pencil-lead breaks on a thick plate (Hamstad 1996). Remarkable agreement was also reported between experimental data and computed. Thus, Eq. 7.15 is applicable to theoretically compute AE waves due to a point force provided that Green's functions are obtained.

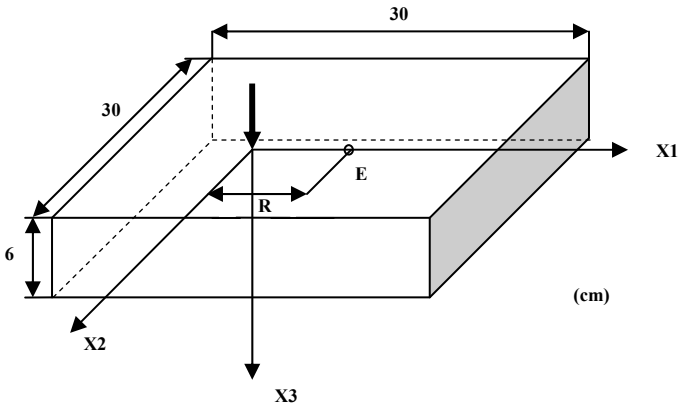

Fig. 7.5. Sketch of concrete block.

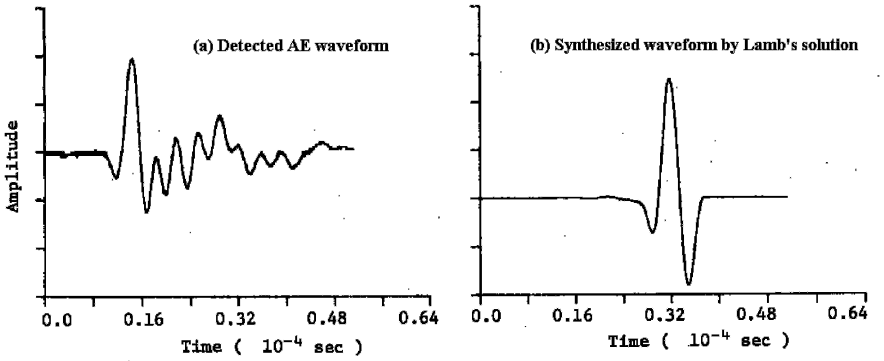

Fig. 7.6. (a) Detected AE wave due to a surface pulse, and **(b)** synthesized wave.

7.5 Theoretical AE Waveforms

According to the generalized theory of AE (Ohtsu 1984), it is already demonstrated that AE waves are elastic waves due to dynamic motions inside a solid. Theoretical treatment of AE in concrete can be performed as elastic waves due to microcracking in a homogeneous medium (Ohtsu 1982). As stated in the previous section, AE waves due to a point force are readily synthesized as elastic waves successfully in concrete. This is because elastodynamic properties of material constituents are physically dependent on the relation between the wavelengths and the characteristic dimensions of heterogeneity. Consequently, most AE waves due to cracking are also analyzed as elastic waves in a homogeneous material.

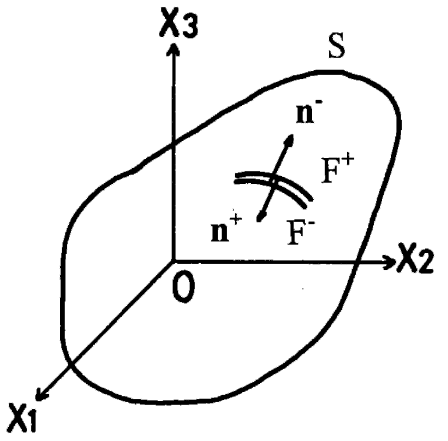

Fig. 7.7. Virtual crack surfaces F^+ and F^-.

In order to model a crack as an AE source, virtual two surfaces F^+ and F^- are considered as shown in **Fig. 7.7**. Before a crack is nucleated, these two surfaces make a common motion together. Due to cracking, the discontinuity of displacement $\boldsymbol{u(y,t)}$ is nucleated between the two surfaces and denoted by using superscripts + and - on surfaces F^+ and F^-, respectively,

$$b_i(\boldsymbol{y},t) = u_i^+(\boldsymbol{y},t) - u_i^-(\boldsymbol{y},t). \tag{7.16}$$

Vector $\boldsymbol{b(y,t)}$ is called the dislocation by Eshelby [1973] and is identical to the Burgers vector in the dislocation theory of crystalline motion. From Eq. 7.10, it leads to the following equation, assuming the equilibrium of traction ($\boldsymbol{t} = 0$) between the crack surfaces,

$$u_k(\mathbf{x},t) = \int_{F+}\left[-T_{ki}^{+}(\mathbf{x},\mathbf{y},t) * u_i^{+}(\mathbf{y},t)\right] dF^{+} \int_{F-}\left[-T_{ki}(\mathbf{x},\mathbf{y},t) * u_i^{-}(\mathbf{y},t)\right] dF^{-}. \tag{7.17}$$

Here T_{ik}^{+} and T_{ik}^{-} are Green's functions of the second kind which contain the normal vectors $\boldsymbol{n}^{+}$ and $\boldsymbol{n}^{-}$ to the crack surfaces F^{+} and F^{-}, respectively. Assuming $\boldsymbol{n} = \boldsymbol{n}^{-} = -\boldsymbol{n}^{+}$, and $F = F^{+} + F^{-}$, it is obtained from Eq. 7.17 as,

$$\begin{aligned} u_k(\mathbf{x},t) &= -\int_F^{+}\left[T_{ki}(\mathbf{x},\mathbf{y},t) * \left[-u_i^{+}(\mathbf{y},t)\right]\right] dF^{+} \\ &\int_F^{-}\left[-T_{ki}(\mathbf{x},\mathbf{y},t) * \left[u_i^{-}(\mathbf{y},t)\right]\right] dF^{-} \\ &= \int_F T_{ki}(\mathbf{x},\mathbf{y},t) * \left[u_i^{+}(\mathbf{y},t) - u_i^{-}(\mathbf{y},t)\right] dF \\ &= \int_F T_{ki}(\mathbf{x},\mathbf{y},t) * b(\mathbf{y},t)\, dF \\ &= \int_F G_{kpq}(\mathbf{x},\mathbf{y},t)\, C_{pqij} n_j * b_i(\mathbf{y},t)\; dF \\ &= G_{kpq}(\mathbf{x},y,t) * S(t) C_{pqij} n_j l_i \int_F b(y)\, dF \\ &= G_{kpq}(\mathbf{x},\mathbf{y},t) * S(t) C_{pqij} n_j l_i \Delta V, \end{aligned} \tag{7.18}$$

where crack vector $\boldsymbol{b(y,t)} = b(\boldsymbol{y},t)\boldsymbol{l}\, S(\boldsymbol{t})$ introducing the unit direction vector $\boldsymbol{l}$ and $S(t)$ of the source-time function. ΔV is the crack volume. Thus, it is easily realized the amplitude of AE waves, $\boldsymbol{u(x,t)}$, is directly associated with the crack volume.

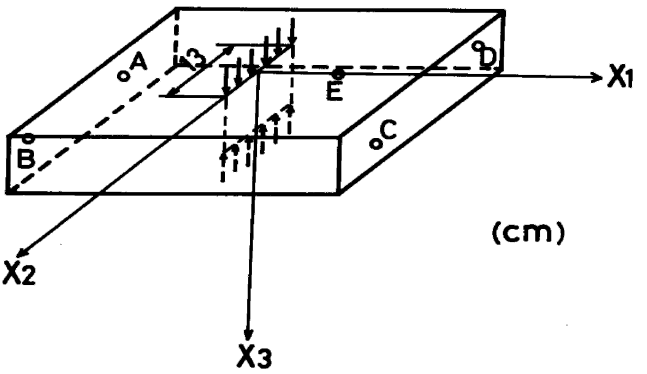

Fig. 7.8. Sketch of a split test in a concrete block.

Equation 7.18 is the integral representation of AE wave due to cracking and can be readily applied to the simulation analysis. By employing the concrete specimen in **Fig. 7.8**, AE waves due to cracking are detected. As shown, a split test was conducted, and a detected wave is shown in **Fig. 7.9** (a).

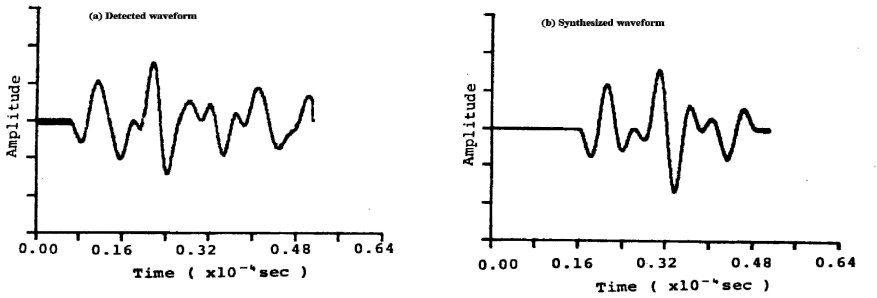

Fig. 7.9. (a) Detected AE waveform and **(b)** synthesized waveform due to a tensile crack.

This waveform is simulated by Eq. 7.18, taking into account the location, the crack-opening motion in the x_1-direction and the integrated source-time function of Eq. 7.14. *Tr* is varied to match the waveform with **Fig. 7.9** (a). A result with $Tr = 14$ μs computed in a half space is given in **Fig. 7.9** (b). Because the spatial derivatives $G_{kp,q}$ in Eq. 7.18 is computed in a half-space (Ohtsu 1984), only the first portion of the waveform is synthesized. Still, remarkable agreement is observed.

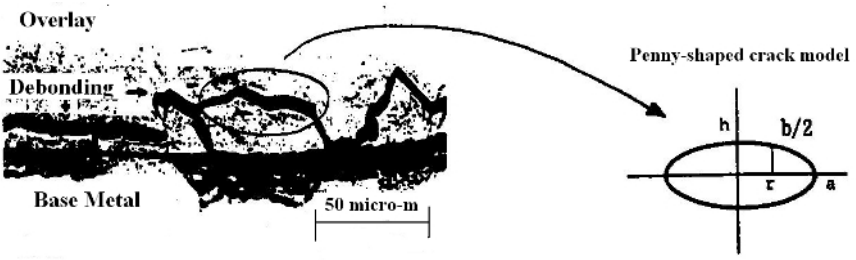

Fig. 7.10. Micrograph of debonding.

Based on the micrograph observation in **Fig. 7.10**, AE wave due to debonding of stainless steel from base metal is simulated. As illustrated in the figure, a penny-shaped tensile crack of 10 μm diameter and 1 μm crack opening is assumed from the observation. Results of detected AE wave

and synthesized with Tr = 2 μs are given in **Fig. 7.11**. AE wave detected is in remarkable agreement with the synthesized in the first portion prior to the reflected waves, including the amplitude. This implies that some attempts to determine the crack area or the magnitude of shear slip (Enoki 1986; Dai 2000) might be marginally successful, because they took into account only a disk-shaped crack. The crack volume estimated as a penny-shaped crack was more than 30% different from that of the disk-shaped (Ohtsu 1987).

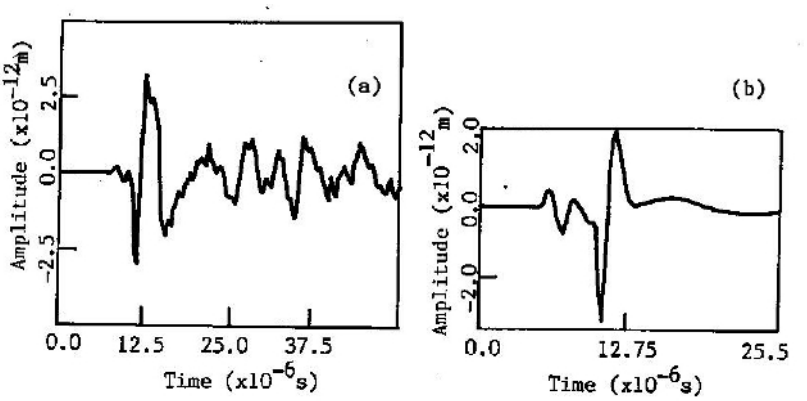

Fig. 7.11. (a) Detected AE waveform and **(b)** synthesized waveform due to a penny-shaped tensile crack of debonding.

7.6 Deconvolution Analysis

Equations 7.15 and 7.18 are represented by the convolution integral with the functions *f(t)* and *S(t)*. Thus, inversely solving them, the function can be computed. The procedure is named the deconvolution analysis (Wadley 1981). Conventionally the source characterization of AE implies this procedure. Because the convolution integral in the time domain can be replaced by the multiplication in the frequency domain, the deconvolution is mathematically conducted in the frequency domain. Thus, the Fourier transform of the detected wave, *U(f)*, is represented as the Fourier transform of the source time function, *S(f)*, times that of Green's function, *G(f)*, as,

$$U(f) = G(f)S(f) \tag{7.19}$$

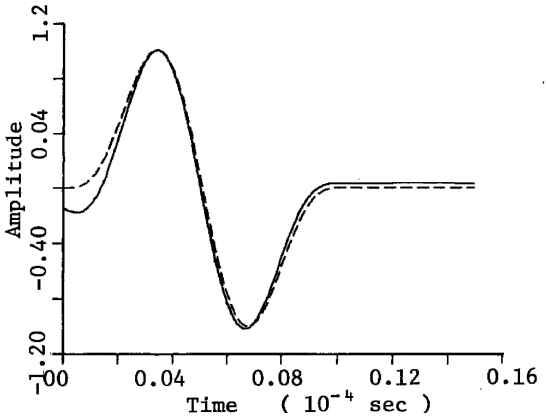

Fig. 7.12. Source-time functions *df(t)/dt* by deconvolution analysis of Lamb's problem due to a surface pulse. The solid curve is analyzed and the broken is assumed in the synthesized waveform.

The Fourier transform of the detected wave in **Fig. 7.6** (a) is substituted into the left-hand of Eq. 7.19, and then the function *S(f)* is solved as *U(f)/G(f)*, taking into account Lamb's solution *G(f)*. Solution *S(t)* after the inverse Fourier transform of *S(f)* is shown in **Fig. 7.12**. In the figure, the solid curve is the function, $S(t) = df(t)/dt$, and the broken curve represents the function assumed in Eq. 7.14. Remarkable agreement is observed between the computed and the assumed.

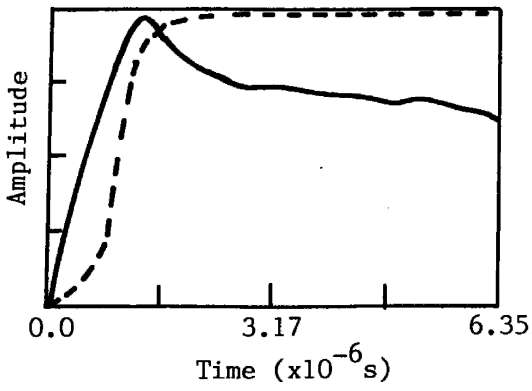

Fig. 7.13. Source-time function *S(t)* by deconvolution (solid) and assumed in the synthesized (broken).

Based on Eq. 7.18, AE waveform detected in **Fig. 7.11** (a) is also deconvoluted. Results are given in **Fig. 7.13**. Compared with the assumed function *S(t)* denoted by the broken curve, the resulted function by deconvolution is

indicated by the solid curve. It is observed that the source function of actual crack motion is fairly complicated. Thus, crack kinetics can be recovered by the deconvolution analysis.

7.7 Moment Tensor

The generalized theory of AE (Ohtsu 1984) presents that AE waves due to cracking are represented by,

$$u_k(\mathbf{x},t) = G_{kp,q}(\mathbf{x},\mathbf{y},t) * S(t)\, C_{pqij}\, n_j l_i \Delta V. \tag{7.20}$$

In comparison with Eq. 7. 11, it is found that AE waves are formulated not with Green's functions G_{ij} but with the spatial derivatives of Green's functions $G_{kp,q}$. This is a reason why empirical Green's functions recorded due to a pencil-lead break has nothing to do with AE waves due to cracking. Even though Green's functions are obtained experimentally, it is impossible to apply them because the spatial derivatives can not be computed numerically from detected waveforms in time domain. As reported, the empirical Green's functions are only useful for sensor calibration (Beckenridge 1975).

In micromechanics (Muta 1982), tensor $n_j l_i \Delta V$ in Eq. 7.20 is defined as the eigenstrain, which is explicitly equivalent to the damage tensor in damage mechanics (Kachanov 1980). In seismology, the following tensor product is defined as a moment tensor,

$$C_{pqkl} l_k n_l \Delta V = M_{pq.} \tag{7.21}$$

Thus, the moment tensor, M_{pq}, is defined by the product of the elastic constants C_{pqkl} [N/m^2] and the crack volume ΔV[m^3], which leads to the moment of physical unit [Nm]. This is a reason why the tensor M_{pq} is named the moment tensor. In the case of an isotropic material,

$$C_{pqkl} = \lambda \delta_{pq} \delta_{kl} + \mu \delta_{pk} \delta_{ql} + \mu \delta_{pl} \delta_{qk}$$

From Eq. 7.21, it is obtained,

$$M_{pq} = \begin{pmatrix} \lambda l_k n_k + 2\mu l_1 n_1 & \mu(l_1 n_2 + l_2 n_1) & \mu(l_1 n_3 + l_3 n_1) \\ \mu(l_1 n_1 + l_2 n_1) & \lambda l_k n_k + 2\mu l_2 n_2 & \mu(l_2 n_3 + l_3 n_2) \\ \mu(l_1 n_3 + l_3 n_1) & \mu(l_2 n_3 + l_3 n_2) & \lambda l_k n_k + 2\mu l_3 n_3 \end{pmatrix} \Delta V \tag{7.22}$$

where λ and μ are Lame constants. Mathematically, the moment tensor is comparable to a stress as a symmetric second-rank tensor, because components in Eq. 7.22 are readily obtained from the product of the eigenstrain and elastic constants. In a similar manner to the stress in elasticity, all components of the moment tensor are illustrated as shown in **Fig. 7.14**. Diagonal components represent normal components on an infinitesimal cubic element, while off-diagonal components are shown as tangential components.

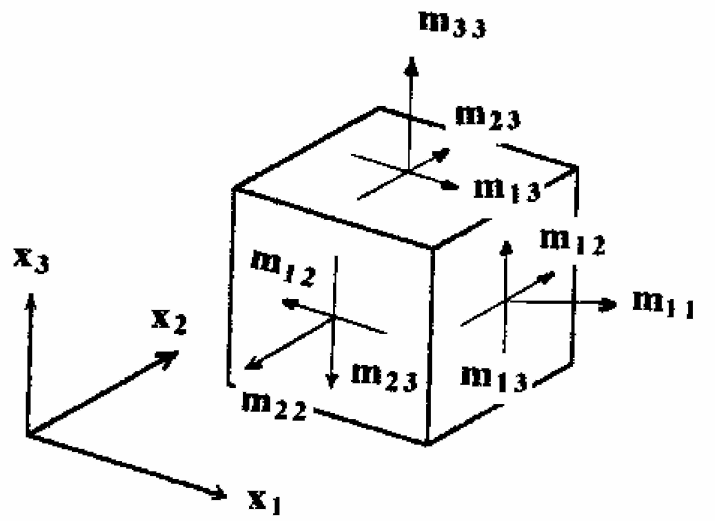

Fig. 7.14. Moment tensor components.

Originally, the seismic moment was defined as a scalar as given by the product $\mu b \Delta F$ of fault displacement b and the area of fault ΔF. Setting $\boldsymbol{l}$ = (1, 0, 0), $\boldsymbol{n}$ = (0, 1, 0) ($\boldsymbol{l}$ is perpendicular to $\boldsymbol{n}$) and $\Delta V = b\Delta F$ in Eq. 7.22, the moment tensor becomes,

$$M_{pq} = \begin{pmatrix} 0 & \mu b \Delta F & 0 \\ \mu b \Delta F & 0 & 0 \\ 0 & 0 & 0 \end{pmatrix}$$

This implies that the seismic moment is equivalent to off-diagonal component of the tensor, which corresponds to a shear component in the stress

tensor. The case mentioned above is derived, later, as a shear crack motion on a crack plane. Thus the moment tensor is quite comparable to the stress tensor.
The moment tensor physically represents kinematics of AE source. From Eq. 7.20, AE waves due to crack nucleation is represented,

$$u_k(\mathbf{x},t) = G_{kp,q}(\mathbf{x},\mathbf{y},t) M_{pq} * S(t). \tag{7.23}$$

Eventually AE source is represented by the moment tensor M_{pq} and the source-time function $S(t)$. This implies that crack kinetics is represented by $S(t)$, which is solved by the deconvolution analysis (Wadley 1981). In contrast, crack kinematics are represented by the moment tensor. In order to characterize crack kinematics, as a conclusion, the determination of the moment tensor is inevitable.

7.8 Spatial Derivative of Green's Functions

In the case that AE waves are formulated by Eq. 7.23, the moment tensor components are just the coefficient represent of the spatial derivatives of Green's function. Therefore, physical property of the moment tensor is derived inherently from Green's functions. Consider the spatial derivative of Green's function, $G_{il,1}$. From the definition, the differential expression is given as,

$$G_{il,1}(\mathbf{x},\mathbf{y_1},t) = \lim_{\Delta y_1 \to 0} \left[G_{il}(\mathbf{x},\mathbf{y_1}+\Delta y_1,t) - G_{il}(\mathbf{x},\mathbf{y_1},t) \right] / \Delta y_1. \tag{7.24}$$

Green's function $G_{i1}(\boldsymbol{x}, \boldsymbol{y_1}, t)$ represents the displacement in the x_i direction at location $\boldsymbol{x}$ due to the force at $\boldsymbol{y_1}$ in the x_1 direction. Therefore, the driving forces at $\boldsymbol{y_1}$ and $\boldsymbol{y_1}+\Delta y_1$ are graphically shown in **Fig. 7.15** as the corresponding moment tensor component m_{11}. As illustrated, $-G_{i1}(\boldsymbol{x}, \boldsymbol{y_1}, t)$ represents the displacement at $\boldsymbol{x}$ in the x_i direction due to the unit force at $\boldsymbol{y_1}$ in the $-x_1$ direction, and $G_{i1}(\boldsymbol{x}, \boldsymbol{y_1}, t)$ represents the displacement at the same location and direction due to the force in the x_1 direction apart Δy_2. From Eq. 7.24, it is found that as the limit case $G_{i1,1}$ corresponds to the displacement due to two forces at the same location with the opposite directions. The forces are normally called the dipole forces (Ben-Menahem 1981). As compared with the moment tensor components in **Fig. 7.14**, the dipole forces are actually identical to normal components. Thus, the dipole

forces are not a special model as a seismic source but are the components of the moment tensor which represents source kinematics.

The case of $G_{il,2}(\boldsymbol{x}, \boldsymbol{y}_2, t)$ for m_{12} is also illustrated in **Fig. 7.15**. Since it is expressed as,

$$G_{il,2}\left(\mathbf{x},\mathbf{y}_2,t\right)=\lim_{\Delta y_2\to 0}\left[G_{il}\left(\mathbf{x},\mathbf{y}_2+\Delta y_2,t\right)-G_{il}\left(\mathbf{x},\mathbf{y}_2,t\right)\right]\Big/\Delta y_2. \qquad (7.25)$$

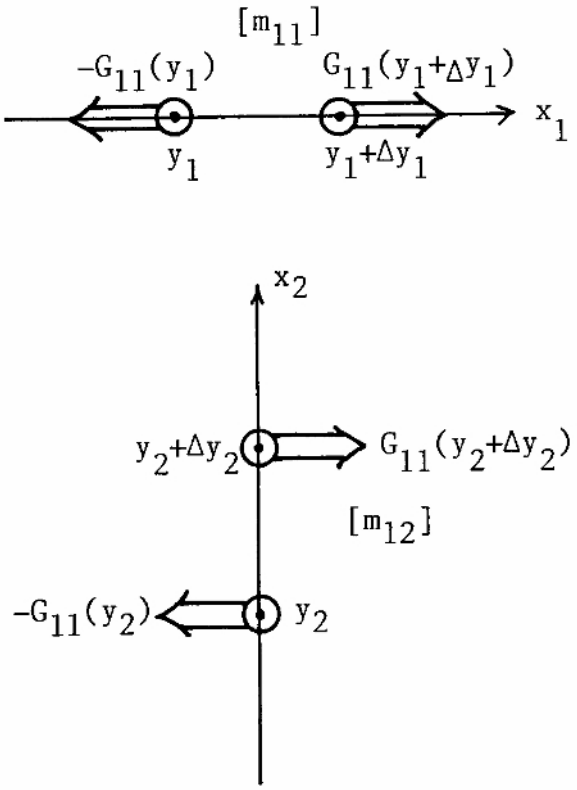

Fig. 7.15. Driving forces for the spatial derivatives of Green's function $G_{il,1}$ and $G_{il,2}$.

The spatial derivative represents the displacement in the x_i direction at $\boldsymbol{x}$ due to the force in $-x_1$ direction at $\boldsymbol{y}_2$ and the force in x_1 direction at $\boldsymbol{y}_2$. These two forces are not located on a line, but coupled as called the couple forces (Ben-Menahem 1981). Again, compared with the components in **Fig. 7.14**, the couple forces correspond to tangential components of the

moment tensor. As the same as the stress tensor, these components correspond to the off-diagonal components in Eq. 7.22 and are equivalent to shear components in the stress tensor. The couple forces are normally referred to as double couples, as rational as the shear (off-diagonal) components in the stress tensor. Although the dipole forces and the double-couple forces are often cited in the literature (Hamstad 1999), eventually the equivalent force models are not necessary to describe AE sources.

7.9 Dislocation Model

Relations between the dislocation models in **Fig. 7.7** and the moment tensor components in **Fig. 7.14** are straightforward. As virtual crack surfaces, surfaces F^+ and F^- on the x-y plane normal to the z-axis is considered, which is shown in **Fig. 7.16**. This is the case of a tensile crack, where the surface F^+ moves upward and parallel to normal vector $\boldsymbol{n}$. As a result, the crack opens. In this case, normal vector $\boldsymbol{n}$ = (0, 0, 1) and motion vector $\boldsymbol{l}$ = (0, 0, 1). The moment tensor in Eq. 7.22 becomes,

$$M_{pq} = \begin{pmatrix} \lambda & 0 & 0 \\ 0 & \lambda & 0 \\ 0 & 0 & \lambda + 2\mu \end{pmatrix} \Delta V \tag{7.26}$$

The corresponding moment tensor is represented in **Fig. 7.16** (b). This result is often modeled as three dipole-forces as illustrated in **Fig. 7.16** (c). Correctly speaking, however, the result should be plotted as given in **Fig. 7.16** (b) as three diagonal (normal) components of the tensor. The dislocation model for the tensile crack leads to the moment tensor in Eq. 7.26. This implies that the combination of three dipoles is necessary and sufficient to model the tensile crack. Consequently, a simulation analysis for only one dipole (Hamstad 1999) might be misleading.

In the case of a shear crack shown in **Fig. 7.17** (a), crack surface F^+ slides in the y-direction. In the case, crack normal $\boldsymbol{n}$ = (0, 0, 1) and motion vector $\boldsymbol{l}$ = (1, 0, 0). Equation 7.22 becomes,

$$M_{pq} = \begin{pmatrix} 0 & 0 & \mu \\ 0 & 0 & 0 \\ \mu & 0 & 0 \end{pmatrix} \Delta V \tag{7.27}$$

The corresponding moment tensor and a double-couple model are given in **Fig. 7.17** (b) and **Fig. 7.17** (c), respectively. Again, one couple force is irrational, because the equilibrium of forces is violated. From Eq. 7.27, it is readily found that the double-couples forces (off-diagonal components) just correspond to shear stresses in the stress tensor.

An application of the moment tensor analysis to AE waves was previously reported on cracking mechanisms of glass due to indentation (Kim 1984), where only diagonal components of the tensor were assumed. From Eq. 7.22, it is realized that the presence of all components is not actually associated with the type of the crack, but closely related with the coordinate system. Although the crack orientations are often assumed as parallel to the coordinate system (Saito 1998 and Takemoto 2000), they are generally inclined to the coordinate system mostly because of the configuration of the specimen. As a result, the presence of all the components is consequent whether the type of the crack is of the tensile or of the shear.

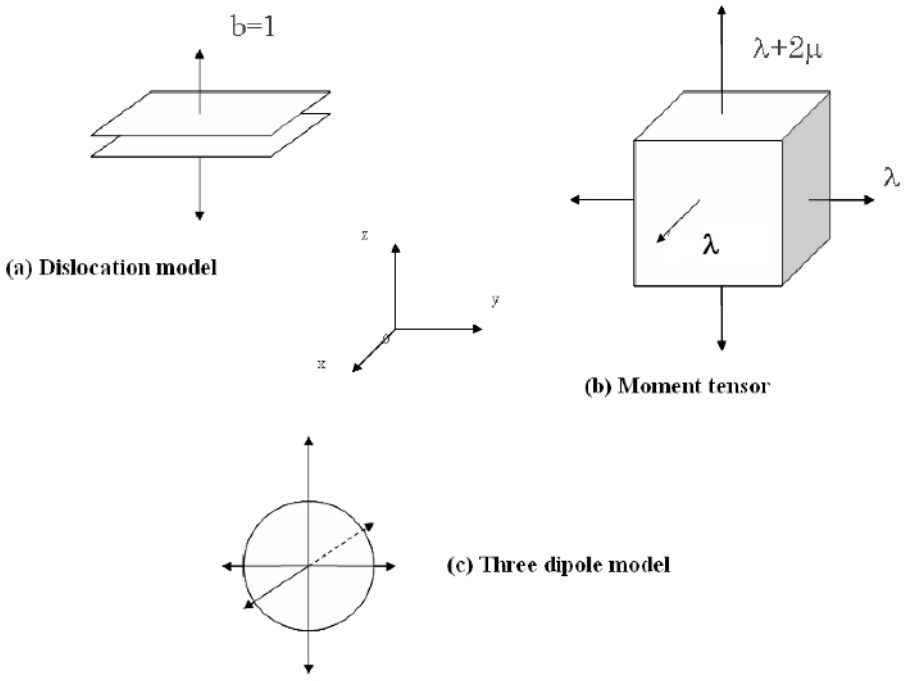

Fig. 7.16. (a) Dislocation model for a tensile crack, **(b)** the corresponding moment tensor and **(c)** three dipole model.

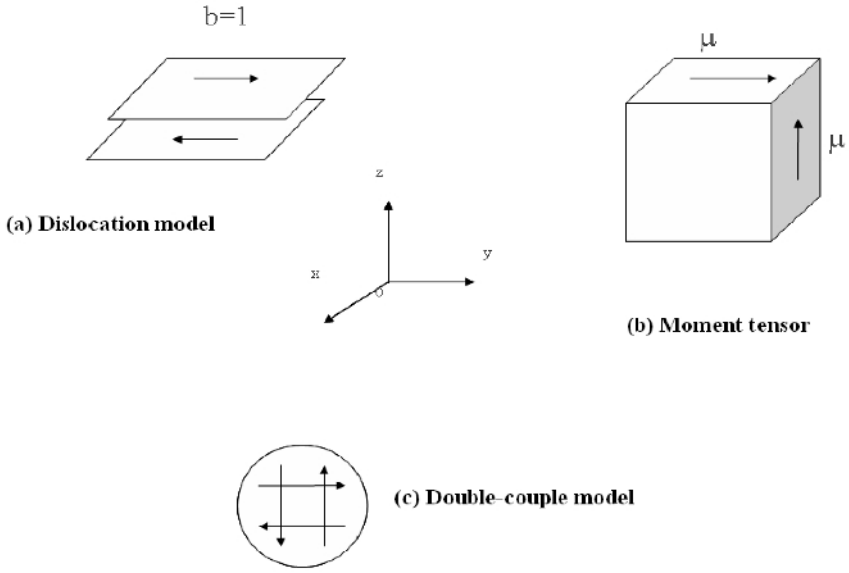

Fig. 7.17. (a) Dislocation model for a shear crack, **(b)** the corresponding moment tensor and **(c)** double-couple model.

7.10 Radiation Pattern

A product of the spatial derivatives of Green's functions and the moment tensor leads readily to the concept of the radiation pattern (Aki 1980). By taking into account only P-wave motion of the far field (*1/R* term) of Green's function in an infinite space of an isotropically elastic body, the displacement $U_i(\mathbf{x},t)$ of P-wave motion is obtained from Eq. 7. 23 as,

$$U_i(\mathbf{x},t) = -1/\left(4\pi\rho v_p^3\right) r_i r_p r_q / R \; dS(t)/dt \; M_{pq}. \tag{7.28}$$

Here is the density of the material and v_p is P-wave velocity. R is the distance between the source y and the observation point x, of which direction cosine is $r = (r1, r2, r3)$. To obtain the radiation pattern, normalized radial displacements *Rd(x)* at a constant distance are calculated from,

$$R_d(\mathbf{x}) = U_i(\mathbf{x}) r_i R / [C\Delta V] = r_p r_q M_{pq} / \Delta V. \tag{7.29}$$

Here $C = -1/(4\pi\rho v_p^3)$.

In two cases of a tensile crack, where $\boldsymbol{n} = (1, 0, 0)$ and $\boldsymbol{l} = (1, 0, 0)$, and a shear crack, where where $\boldsymbol{n} = (0, 0, 1)$ and $\boldsymbol{l} = (1, 0, 0)$, the radiation patterns are considered in the *x1-x3* plane as setting that $\boldsymbol{r} = (\cos\alpha, 0, \sin\alpha)$. In the case of the tensile crack , it is obtained from Eqs. 7.26 and 7 29 as,

$$R_d(x) = \begin{pmatrix} \cos\alpha & \sin\alpha \end{pmatrix} \begin{pmatrix} \lambda & 0 \\ 0 & \lambda + 2\mu \end{pmatrix} \begin{pmatrix} \cos\alpha \\ \sin\alpha \end{pmatrix} = \lambda + 2\mu \sin^2\alpha \tag{7.30}$$

In **Fig. 7.18** (a), $R_d(x)$ is plotted in the x_1-x_3 plane, as the case where crack orientation is inclined θ. This is the radiation pattern of the tensile crack for P-wave.

In the case of the shear crack, it is obtained from Eqs. 7.27 and 7.29,

$$R_d(x) = \begin{pmatrix} \cos\alpha & \sin\alpha \end{pmatrix} \begin{pmatrix} 0 & \mu \\ \mu & 0 \end{pmatrix} \begin{pmatrix} \cos\alpha \\ \sin\alpha \end{pmatrix} = 2\mu \sin\alpha \cos\alpha \tag{7.31}$$

The radiation pattern $R_d(x)$ for the shear crack, which is inclined θ, is plotted in (b). The solid curves indicate the positive displacements, while the broken curves denote the negative displacements. Thus, positive (push) and negative (pull) displacements are observed in four quadrants orderly as famous in seismology, where the fault model is sometimes referred to as the pull-push model.

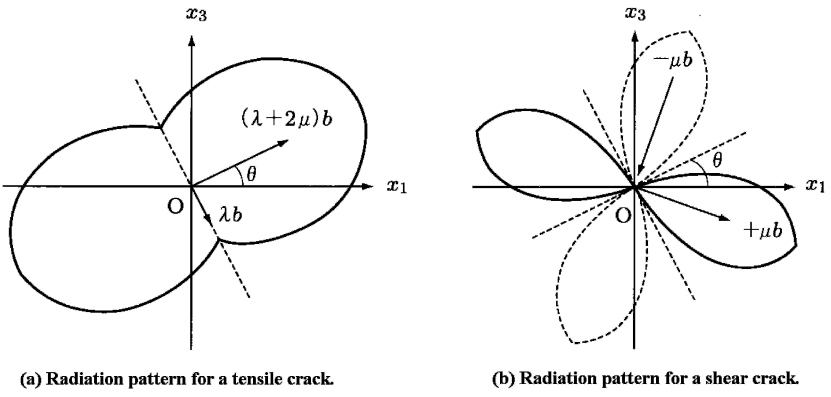

(a) Radiation pattern for a tensile crack. (b) Radiation pattern for a shear crack.

Fig. 7.18. Radiation patterns of (a) tensile crack and (b) shear crack.

It is possible to derive the radiation patterns of S-waves similarly. But, it is actually meaningless in AE research, because S-waves are mostly smeared by P-wave trails and other waves. To identify the portion or the amplitudes of S-wave from AE waveforms is practically impossible.

To close this chapter, it is noted that the radiation pattern and the equivalent force models of the dipole and the double-couple are not essential to study the source characterization of AE waves. The important result is the fact that kinetics of AE source is recovered by the deconvolution analysis, while kinematics can be represented by the moment tensor. The equivalent force models and the radiation patterns just show us the principal components of the moment tensor.

References

Aki K, Richards PG (1980) Quantitative seismology theory and methods. Vol. I, Freeman WH and Company, San Francisco

Ben-Menahem A, Singh SJ (1981) Seismic Waves and Sources. Springer-Verlag, New York

Breckenridge FR, Tschiegg CE, Greenspan M (1975) Acoustic Emission: Some Applications of Lamb's Problem. J Acoust Soc Am 57:626-631

Breckenridge R, Greenspan M (1981) Surface-Wave Displacement: Absolute Measurements using a Capacitance Transducer. J Acoust Soc Am 69:1177-1185

Dai ST, Labuz JF, Carvalho F (2000) Softening Response of Rock Observed in Plane-Strain Compression. Trends in Rock Mechanics, Geo SP-102:152-163

Enoki M, Kishi T, Kohara S (1986) Determination of Micro-cracking Moment Tensor of Quasi-cleavage Facet by AE Source Characterization. Progress in Acoustic Emission III:763-770

Eringen AC, Suhubi ES (1975) Elasodynamics. Vol. II Linear Theory, Academic Press, New York

Eshelby JD (1973) Dislocation Theory for Geophysical Applications. Phil Trans R Soc, London, A274:331-338

Hamstad MA, Gary J, O'Gallagher A (1996) Far-Field AE Waves by Three-Dimensional Finite Element Modeling of Pencil-Lead Breaks on a Thick Plate. Journal of AE, 14(2):103-114

Hamstad MA, O'Gallagher A, Gary J (1999) Modeling of Buried Monopole and Dipole Source of Acoustic Emission with a Finite Element Technique. Journal of AE, 17(3-4):97-110

Hsu NN, Hardy SC (1978) Experiments in Acoustic Emission Waveform Analysis for Characterization of AE Sources, Sensors and Structures. Elastic Waves and Nondestructive Testing of Materials, AMD-Vol. 29:85-106

Johnson LR (1974) Green's Function for Lamb's Problem. Geopys JR astr Soc, 37:99-131

Kachanov M (1980) Continuum Model of Medium with Cracks. J Engineering Mechanics, ASCE, 106(EM5):1039-1051
Kim KY, Sachse W (1984) Characterization of AE signals from identations cracks in glass. Progress in Acoustic Emission II:163-172
Lamb H (1904) On the Propagation of Tremors over the Surface of an Elastic Solid. Pilos Trans Roy Soc, A203:1-42
Muta T (1982) Micromechanics of Defects in Solids. Martinus Nijhoff Publishers, Den Hage
Ohtsu M (1982) Source Mechanism and Waveform Analysis of Acoustic Emission in Concrete. Journal of AE 2(1):103-112
Ohtsu M, Ono K (1984) A Generalized Theory of Acoustic Emission and Green's Functions in a Half Space. Journal of AE 3(1):124-133
Ohtsu M, Yuyama S, Imanaka T (1987) Theoretical Treatment of Acoustic Emission Sources in Microfracturing due to Disbonding. J Acoust Soc Am, 82(2):506-512
Pao YH (1978) Theory of Acoustic Emission. Elastic Waves and Nondestructive Testing of Materials. AMD-Vol. 29:107-128
Pao YH, Ceranoglu AN (1981) Propagation of Elastic Pulse and Acoustic Emission in a Plate. J Appl Mech 48:125-147
Pekeris CL (1955) The Seismic Buried Pulse. Proc Nat acad Sci 41:469-480
Pekeris CL (1955) The Seismic Buried Pulse. Proc Nat acad Sci 41:629-639
Saito N, Takemoto M, Suzuki H, Ono K (1998) Advanced AE Signal Classification for Studying the Progression of Fracture Modes in Loaded UD-GFRP. Progress in Acoustic Emission IX:V-1 - V-10
Takemoto M (2000) Acoustic Properties of Composite Materials and Fracture Behavior by the Waveform Simulation of AE Signals. J Japanes Soc for NDI 49(9):592-600
Wadley HNG, Scruby CB (1981) Acoustic Emission Source Characterization. Advances in Acoustic Emission. Dunhart Publishers, Knoxville, 125-153

8 Moment Tensor Analysis

Masayasu Ohtsu

8.1 Introduction

In seismology, linear inversion techniques were proposed to determine the moment tensor component in both time and frequency domains (Stump & Johnson 1977) and (Kanamori & Given 1981). Although all components of the moment tensor must be determined, the moment tensor inversion with constraints has been normally applied to obtaining stable solutions in seismology (Dziewonski & Woodhouse 1981). This is partly because a fault motion of an earthquake is primarily associated with shear motion, corresponding to off-diagonal components in the moment tensor. One application of the moment tensor inversion with constraints is found in rock mechanics (Dai, Labuz et al. 2000).

In contrast, both tensile motion of diagonal components and shear motion of off-diagonal are definitely present in crack motions as an AE source. Consequently, general treatment on the moment tensor components of diagonal and off-diagonal components is discussed. Elsewhere, another procedure named the relative moment tensor inversion is proposed (Dahm 1996).

8.2 Theoretical Background

As discussed in Chapter 7, AE wave due to cracking is theoretically represented by the moment tensor M_{pq} as,

$$u_k(\mathrm{x},t) = G_{ip,q}(\mathrm{x},\mathrm{y},t)M_{pq} * S(t)\,. \tag{8.1}$$

The components of the moment tensor consist of crack motion (dislocation vector), the normal vector to the crack surface and crack the volume. Thus,

crack motion is kinematically modeled by the components of the moment tensor as illustrated in **Fig. 8.1**.

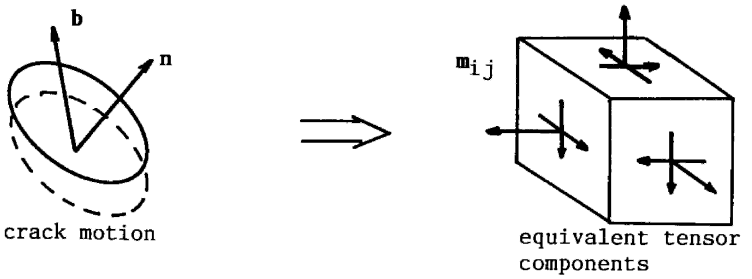

Fig. 8.1 Crack motion and equivalent tensor components.

To inversely solve Eq. 8.1 and to determine all components of the moment tensor, the spatial derivatives of Green's functions are inevitably required. Accordingly, numerical solutions are obtained by the Finite Difference Method (FDM) (Enoki, Kishi et al. 1986) and by the Finite Element Method (FEM) (Hamstad, O'Gallagher et al. 1999). These solutions, however, need a vector processor for computation and are not readily applicable to processing a large amount of AE waves. Consequently, based on the far-filed term of P wave, a simplified procedure was developed (Ohtsu, Okamoto et al. 1998), which is suitable for a PC-based processor as robust in computation. The procedure is now implemented as SiGMA (Simplified Green's functions for Moment tensor Analysis) code.

8.3 Far-Field Approximation

Taking into account only P-wave motion of the far field (1/R term) of Green's function in an infinite space, the displacement U_i (**x**,t) of P-wave motion is obtained from Eq. 8.1.

$$U_i(\mathbf{x},t) = \frac{1}{4\pi\rho v_p^3}\frac{r_i}{R} r_p r_q M_{pq} \frac{dS(t)}{dt} \tag{8.2}$$

Here ρ is the density of the material and v_p is the velocity of P wave. R is the distance between the source ***y*** and the observation point ***x***, of which direction cosine is $\boldsymbol{r} = (r_1, r_2, r_3)$. In the case that we are interested in motions

of AE waves at the observation point, the first approximation could be an elastic wave in a half space.

In the case that Eq. 8.2 is applied to the moment tensor analysis, the discrepancy between the half-space solution and the infinite-space solution should be studied. Accordingly, Lamb's solutions for a buried pulse are compared with Green's functions in an infinite space.

As stated in Chapter 7, a code for computing Lamb's solution due to a buried pulse was already published (Ohtsu & Ono 1984). An infinite-space solution is presented in the literature (Aki & Richards 1980). Thus a solution UN_{ij} in an infinite space due to a step-function force H(t) is obtained as,

$$\begin{aligned} UN_{ij}(\mathbf{x},\mathbf{y},t) = {} & \left(3r_i r_j - \delta_{ij}\right)/\left(4\pi\mu R\right)\left[\left\{\left(v_s t/R\right)^2 - \left(v_s/v_p\right)^2\right\}\right. \\ & \left. H\left(t - R/v_p\right)/2 - \left\{\left(v_s t/R\right)^2 - 1\right\} H\left(t - R/v_s\right)/2\right] \\ & + r_i r_j/\left(4\pi\mu R\right)\left\{\left(v_s/v_p\right)^2 H\left(t - R/v_p\right) - H\left(t - R/v_s\right)\right\} \\ & + \delta_{ij} H\left(t - R/v_s\right)/\left(\pi^2 \mu R\right). \end{aligned} \tag{8.3}$$

Taking only the far-field term out of Eq. 8.3,

$$\begin{aligned} UF_{ij}(x,y,t) = {} & r_i r_j/\left(4\pi\mu R\right)\left\{\left(v_s/v_p\right)^2 H\left(t - R/v_p\right) - H\left(t - R/v_s\right)\right\} \\ & + \delta_{ij} H\left(t - R/v_s\right)\left(\pi^2 \mu R\right). \end{aligned} \tag{8.4}$$

Here μ is the Lame constant and equivalent to the shear modulus. v_s is the velocity of S wave.

In the x_1-x_2-x_3 coordinate system in **Fig. 8.2**, it assumed that step-function force f is applied in the x_3-direction at the depth 6 cm, and elastic waves in the x_3-direction are detected at three locations A, B, and C on the stress-free surface. The velocity of P-wave is 4000 m/s and Poisson's ratio is 0.2. Thus, to investigate the discrepancy between the far-field approximation and the solutions in a half space, Lamb's solution G_{33}, infinite-space solution UN_{33}, and the far-field solution UF_{33} are computed.

Computed Green's functions at location A are given in **Fig. 8.3**. Lamb's solution due to a step-function force shows clear arrivals of P-wave and S-wave as similar to **Fig. 7.2** (a). The amplitudes of the infinite-space solu-

tion are a half of Lamb's solution, while the far-field approximation is rather different from Lamb's solution except for the amplitude of P-wave.

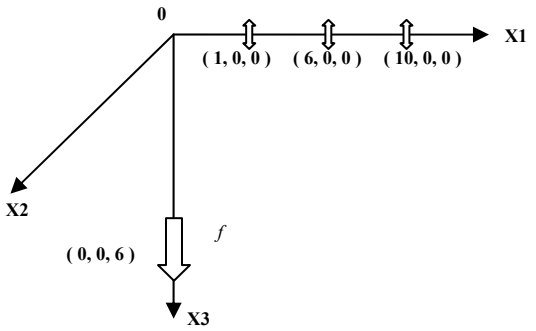

Fig. 8.2. Wave motions at locations A, B, and C on the stress-free surface due to a buried force ***f***.

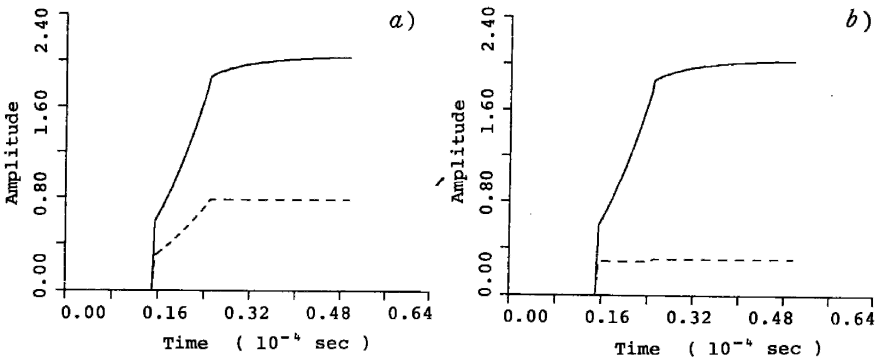

Fig. 8.3. Displacement motions detected at location A in a half space (solid curves in a) and b), compared with solutions in an infinite space (broken curve in a) and of the far-filed (broken curve in b).

In the case that elastic waves are observed at a stress-free surface in a half space, reflected waves are generated and also detected as well as incident waves. In the case that incident S-wave is reflected as P-wave, a relationship between reflected angle θ of P-wave and incident angle θ' is derived from Snell's law as,

$$\frac{\sin\theta}{v_p} = \frac{\sin\theta'}{v_s} \tag{8.5}$$

In the critical case of incident S-wave, reflected P-wave propagates along the surface ($\theta = \pi/2$), which is called SP-wave and arrives at the observation point after P-wave arrival and before S-wave arrival as well as in **Fig. 7.2** (b). The critical angle $\theta' = \theta c$ is obtained from $\sin^{-1}(v_s/v_p)$.

Green's functions at locations B and C are given in **Fig. 8.4** and **Fig. 8.5**. Because the incident angles are over the critical angle ($\theta c = 37.76^o$), SP-wave is generated at both locations. As a result, the differences from the infinite-space solution and the far-field solution are emphasized after P-wave arrival.

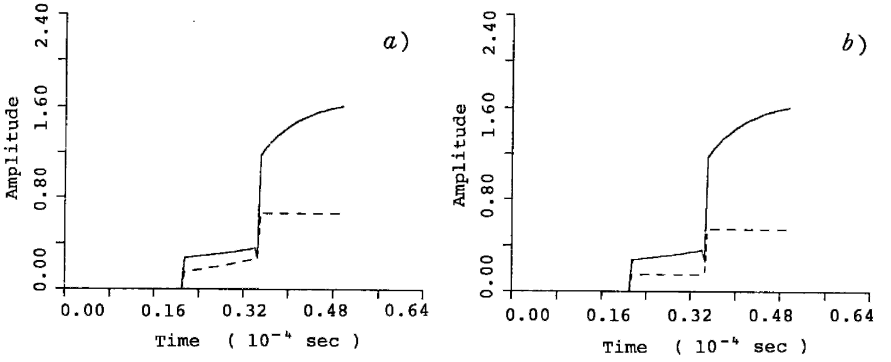

Fig. 8.4. Displacement motions detected at location B in a half space (solid curves in a) and b), compared with solutions in an infinite space (broken curve in a) and of the far-filed (broken curve in b).

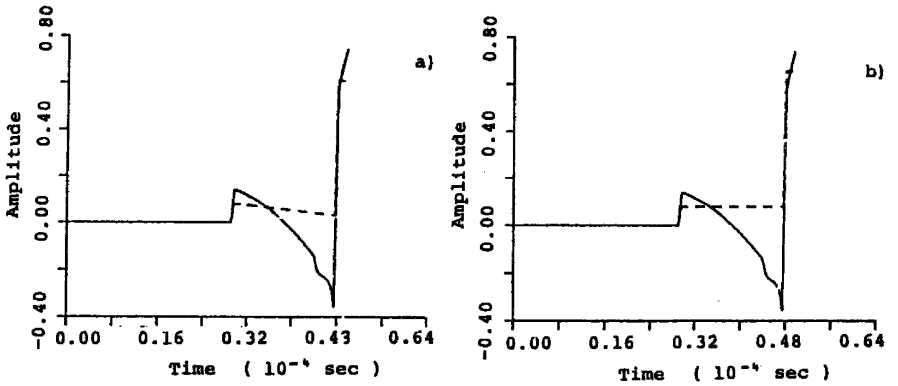

Fig. 8.5. Displacement motions detected at location C in a half space (solid curves in a) and b), compared with solutions in an infinite space (broken curve in a) and of the far-filed (broken curve in b).

In all the cases, it is observed that the amplitude of the first motion (P-wave) in a half space is almost as twice as the amplitudes of both the infinite-space solution and the far-filed solution. The ratio of the amplitude in a half space to that of the infinite space is equivalent to the reflection coefficient $Re(\mathbf{t},\mathbf{r})$,

$$R_e(t,r) = \frac{2k^2 a\left(k^2 - 2\left[1-a^2\right]\right)}{\left(k^2 - 2\left[1-a^2\right]\right)^2 + 4a\left[1-a^2\right]\sqrt{k^2-1+a^2}} \tag{8.6}$$

Here **t** is the orientation vector of sensor sensitivity and $k = v_p/v_s$ and a is the scalar product of vector **r** and vector **t**. In the case that P-wave is incident vertically to the surface (a=1), $Re(\mathbf{t},\mathbf{r})$ =2.

Consequently, it is found that the first motions of AE waves detected at the observation point can be approximated with the good accuracy as the product of the far-field solution and the reflection coefficient.

8.4 Sensor Calibration

Considering the effect of reflection at the surface, the amplitude of the first motion $A_o(\mathbf{x},t)$ in the far-field due to an applied force $\boldsymbol{f}(t)$ is derived from Eq. 8.4 and represented as,

$$A_0 = Cs\,\mathrm{Re}\left(\mathbf{t},\mathbf{r}\right)\frac{f\left(t\right)}{R} \tag{8.7}$$

where Cs is the magnitude of the sensor response including material constants. In the case that the sensors are absolutely calibrated, the coefficients Cs are known. In a general case, relative coefficients are readily obtained by a pencil-lead break test.

After the sensors are attached onto a specimen, a test is conducted as illustrated in **Fig. 8.6**. AE waves are recorded due to a pencil-lead break and then relative coefficients Cs are obtained from,

$$Cs = A_0 R \big/ \mathrm{Re}\left(\mathbf{t},\mathbf{r}\right) \tag{8.8}$$

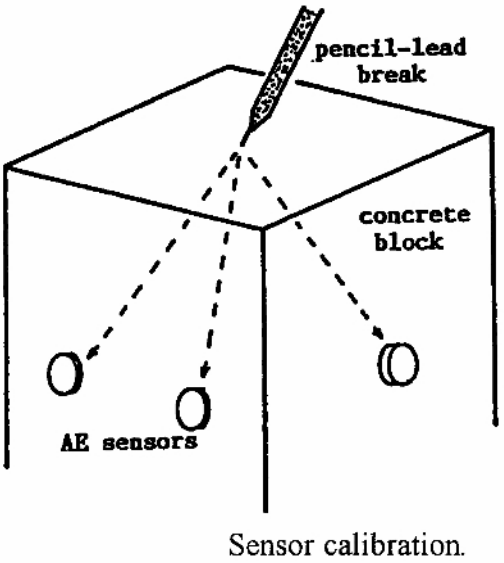

Fig. 8.6. Experiment for relative sensor calibration.

Thus, the relative calibration coefficient *Cs* of equivalent sensitivity is obtained for each sensor. In a few cases, absolutely calibrated sensors are available. In this respect, the moment tensor analysis to determine the relative tensor components is preferable in practical applications.

8.5 SiGMA Procedure

Based on Eqs. 8.2 and 8.6, the amplitude of the first motion is simply represented as,

$$A(\mathbf{x}) = Cs \frac{\mathrm{Re}(\mathbf{t},\mathbf{r})}{R} r_p r_q M_{pq} \tag{8.9}$$

This leads to a series of algebraic equations on unknown moment-tensor components M_{pq}. The procedure to solve Eq. 8.9 is named SiGMA (Simplified Green's function for Moment tensor Analysis) (Ohtsu 1991) and (Ohtsu 2000). It is shown as,

$$A(\mathbf{x}) = Cs \frac{\mathrm{Re}(t,r)}{R} \begin{pmatrix} r_1 & r_2 & r_3 \end{pmatrix} \begin{pmatrix} m_{11} & m_{12} & m_{13} \\ m_{12} & m_{22} & m_{23} \\ m_{13} & m_{23} & m_{33} \end{pmatrix} \begin{pmatrix} r_1 \\ r_2 \\ r_3 \end{pmatrix} \tag{8.10}$$

Since the moment tensor is a symmetric tensor of the 2nd rank, the number of independent components is six as m_{11}, m_{12}, m_{13}, m_{22}, m_{23}, and m_{33}. These components can be determined from the observation of the first motions at more than six sensor locations. To solve Eq. 8.10, the coefficient *Cs*, the reflection coefficient *Re*(**t**,**r**), the distance R, and its direction cosine vector **r** are necessary. The determination of *Cs* and *Re*(**t,r**) is discussed in the previous sections. Other values can be obtained from the source (flaw) location analysis. Thus, the location analysis is essential to perform the moment tensor analysis.

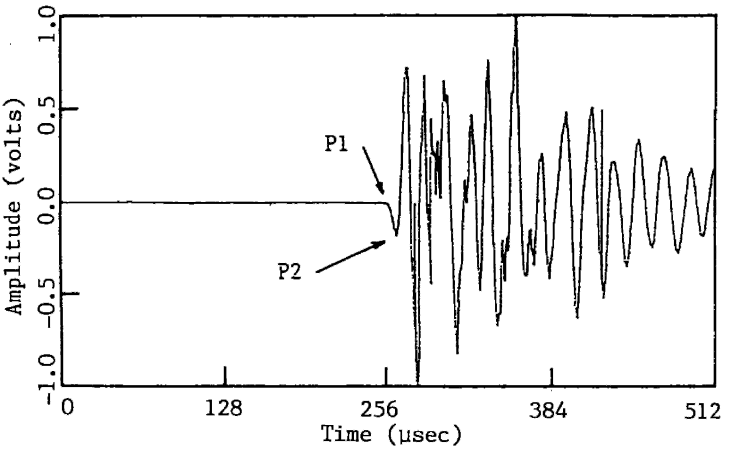

Fig. 8.7. Recorded AE waveform.

In the SiGMA analysis, two parameters of the arrival time (P1) and the amplitude of the first motion (P2) are visually determined from AE waveform as shown in **Fig. 8.7**. In this respect, a computer-aided procedure was elsewhere developed for automated determination of the first P-wave arrival (Landis, Ouyang et al. 1992).

In the location procedure, the crack location **y** is determined from the arrival time differences t_i between the observation $\mathbf{x_i}$ and $\mathbf{x_{i+1}}$, solving equations,

$$R_i - R_{i+1} = |x_i - y| - |x_{i+1} - y| = v_p t_i \tag{8.11}$$

Then, the distance R and its direction vector **r** are determined. The amplitudes of the first motions P2 in **Fig. 8.7** at more than 6 channels are substituted into Eq. 8.10, and thus the components of the moment tensor are determined from a series of algebraic equations. Since the SiGMA code requires only relative values of the moment tensor components, the relative calibration coefficient *Cs* of AE sensors is sufficient. The code is already implemented in the AE device.

8.6 Unified Decomposition of Eigenvalue

In the SiGMA code, classification of a crack is performed by the eigenvalue analysis of the moment tensor (Ohtsu 1991). From Eq. 7.27, a moment tensor for pure shear motion is obtained as,

$$M_{pq} = \begin{pmatrix} 0 & 0 & \mu\Delta V \\ 0 & 0 & 0 \\ \mu\Delta V & 0 & 0 \end{pmatrix} \tag{8.12}$$

From the eigenvalue analysis, three eigenvalues are obtained as $\mu\Delta V$, 0, and $-\mu\Delta V$. Setting the ratio of the maximum shear contribution as X, three eigenvalues for the shear crack are represented as X, 0, –X. In the case of a pure tensile crack, the moment tensor is represented from Eq. 7.26,

$$M_{pq} = \begin{pmatrix} \lambda\Delta V & 0 & 0 \\ 0 & \lambda\Delta V & 0 \\ 0 & 0 & (\lambda + 2\mu)\Delta V \end{pmatrix} \tag{8.13}$$

Because this is the case where the direction of crack motion is parallel to the coordinate axis, the matrix is already diagonalized, and diagonal components are identical to three eigenvalues: $\lambda\Delta V, \lambda\Delta V, (\lambda + 2\mu)\Delta V$. In the case of the shear crack, the components of the tensor are deviatoric, as the sum of all components is equal to zero (non-volumetric). Accordingly, the components in Eq. 8.13 can be decomposed into the deviatoric (non-volumetric) components and the isotropic components as,

$$\begin{pmatrix} \lambda\Delta V \\ \lambda\Delta V \\ (\lambda + 2\mu)\Delta V \end{pmatrix} = \begin{pmatrix} -\frac{2\mu\Delta V}{3} \\ -\frac{2\mu\Delta V}{3} \\ \frac{4\mu\Delta V}{3} \end{pmatrix} + \begin{pmatrix} \left(\lambda + \frac{2\mu}{3}\right)\Delta V \\ \left(\lambda + \frac{2\mu}{3}\right)\Delta V \\ \left(\lambda + \frac{2\mu}{3}\right)\Delta V \end{pmatrix} \tag{8.14}$$

Setting the ratio of the maximum deviatoric tensile component as Y and the isotropic tensile as Z, three eigenvalues are denoted as –Y/2 + Z, –Y/2 + Z and Y + Z. Then, it is assumed that the principal axes of the shear crack are identical to those of the tensile crack. As a result, the eigenvalues of the moment tensor for a general case are represented by the combination of the shear crack and the tensile crack. The following decomposition is obtained as the relative ratios X, Y and Z,

$$
\begin{aligned}
&1.0 = X + Y + Z,\\
&\text{the intermediate eigenvalue/the maximum eigenvalue} = 0 - Y/2 + Z,\\
&\text{the minimum eigenvalue/the maximum eigenvalue} = -X - Y/2 + Z.
\end{aligned}
\tag{8.15}
$$

These are schematically shown in **Fig. 8.8**. It should be pointed out that the ratio X becomes larger than 1.0 in the case that both the ratios Y and Z are negative (Suaris & van Mier 1995). The case happens only if the scalar product $l_k n_k$ is negative, because the eigenvalues are determined from relative tensor components. Recorrecting the value of the scalar product, the three ratios are determined as well-posed.

Another decomposition of the moment tensor is proposed elsewhere (Shah & Labuz 1995), introducing the term of the volume change. As can be seen in **Fig. 8.8**, however, the ratio Z clearly represents the volume change. Addition of other terms is unnecessary.

The ratios X, Y, and Z are mathematically determined in an isotropic solid. Setting the angle, c, between crack vector **l** and normal vector to the crack surface **n,** these are obtained as,

$$
\begin{aligned}
X &= \left[(1-2\nu)-(1-2\nu)\cos c\right] \Big/ \left[(1-2\nu)+\cos c\right],\\
Y &= 4(1-2\nu)\cos c \Big/ \left[3(1-2\nu)+3\cos c\right],\\
Z &= 2(1+\nu)\cos c \Big/ \left[3(1-2\nu)+3\cos c\right],
\end{aligned}
\tag{8.16}
$$

where $\cos c = l_k n_k$. The ratio X represents the contribution of shear motion. The raio Y is the contribution of deviatoric component of tensile motion, and the ratio Z is that of isotropic component. Hereinafter, the ratio X is called the shear ratio. Elsewhere, the classification of cracks was conducted on the basis of the angle c between two vectors **l** and **n** (Enoki, Kishi et al. 1986). Consequently, a relation between 1 – cos c and the shear ratio X is plotted as the case Poisson's ratio $\nu = 0.2$ in **Fig. 8.9**.

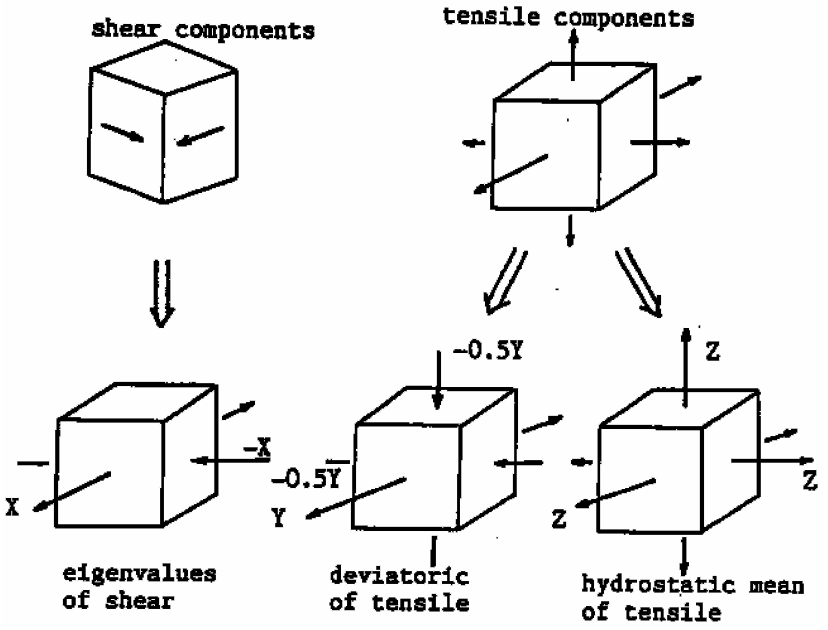

Fig. 8.8. Unified decomposition of eigenvalues of the moment tensor.

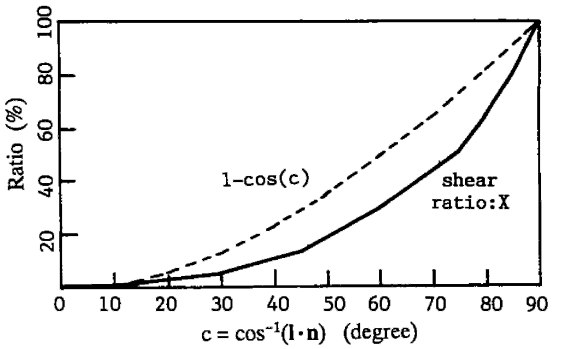

Fig. 8.9. Relation between shear ratios X and crack angles.

In the literature (Ouyang, Landis et al. 1992), cracks were classified as a tensile crack in the case $0^o<c<15^o$, which corresponds almost to a pure tensile crack as the shear ratio less than 5%. In contrast, shear cracks were classified with the condition $75^o<c<90^o$, in which the shear ratio X is just over 50%. Thus, the criterion on the crack classification based on the angle c is not reasonable, because the relationship between the angle c and the shear ratio X is nonlinear. In the SiGMA code, AE sources of which the

shear ratios are less than 40% are classified into tensile cracks. The sources of X > 60% are classified into shear cracks. In between 40% and 60%, cracks are referred to as mixed mode.

8.7 Crack Orientation

From the eigenvalue analysis of the moment tensor, three eigenvectors **e1**, **e2**, **e3** are also obtained. These are presented by the two vectors **l** and **n**,

$$\begin{aligned} e1 &= 1 + n \\ e2 &= 1 \times n \\ e3 &= 1 - n \end{aligned} \tag{8.17}$$

Here x denotes the vector product, and the vectors **l** and **n** are interchangeable. In the case of the tensile crack, the vector **l** is parallel to the vector **n**. Thus, the vector $\mathbf{e_1}$ could give the direction of crack opening, while the sum of $\mathbf{e_1}$+$\mathbf{e_3}$ and the subtraction $\mathbf{e_1}$-$\mathbf{e_3}$ derive the two vectors **l** and **n**. In the first version of SiGMA (Ohtsu 1991), the orientations of tensile cracks are determined from the vector $\mathbf{e_1}$, and those of shear cracks are presented by two vectors **l** and **n**, which are usually perpendicular.

One result which was analyzed in a hydro-fracturing test is shown in **Fig. 8.10**. Eight AE events are analyzed and plotted in the elevation view. AE events are plotted at their locations from the location analysis. Then, cracks are classified based on the shear ratio. Tensile crack are indicated by arrow symbols, of which directions are determined from the direction **e1**. Shear cracks are represented by cross symbols, of which two directions correspond to the two vectors **l** and **n**. Only the event No. 14 was classified into the mixed-mode cracking, and both orientations of the tensile and the shear are indicated. Results are so successful that AE events are located along the dip plane presumed from the dip angle. Remarkably, the directions of crack opening of the tensile cracks are vertical to, and the orientations of the shear cracks seem parallel to the dip plane.

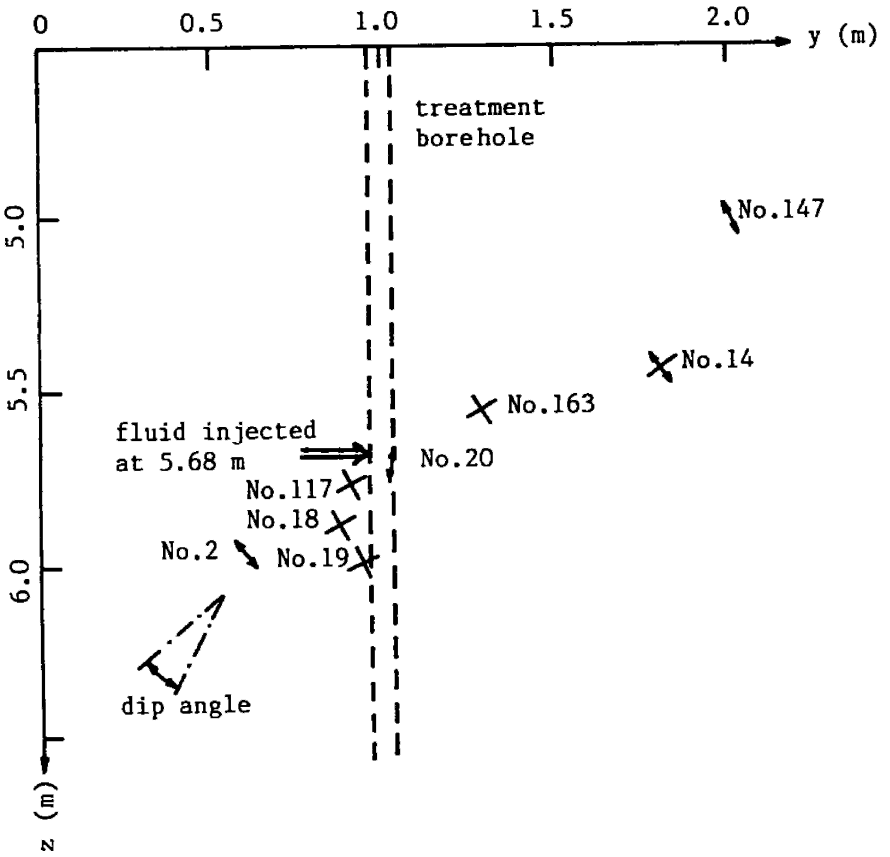

Fig. 8.10. Results of SiGMA analysis in a hydro-fracturing test.

According to the result in **Fig. 8.10**, a crack of which angle is over 60° could be classified as the tensile crack, because the shear ratio is less than 40%. Consequently, in one version of SiGMA (Ohtsu 2000), two vectors are always obtained and plotted. For the tensile crack, arrow symbol is employed. Results in a bending test of a reinforced concrete beam are given in **Fig. 8.11** (Ohtsu 1995).

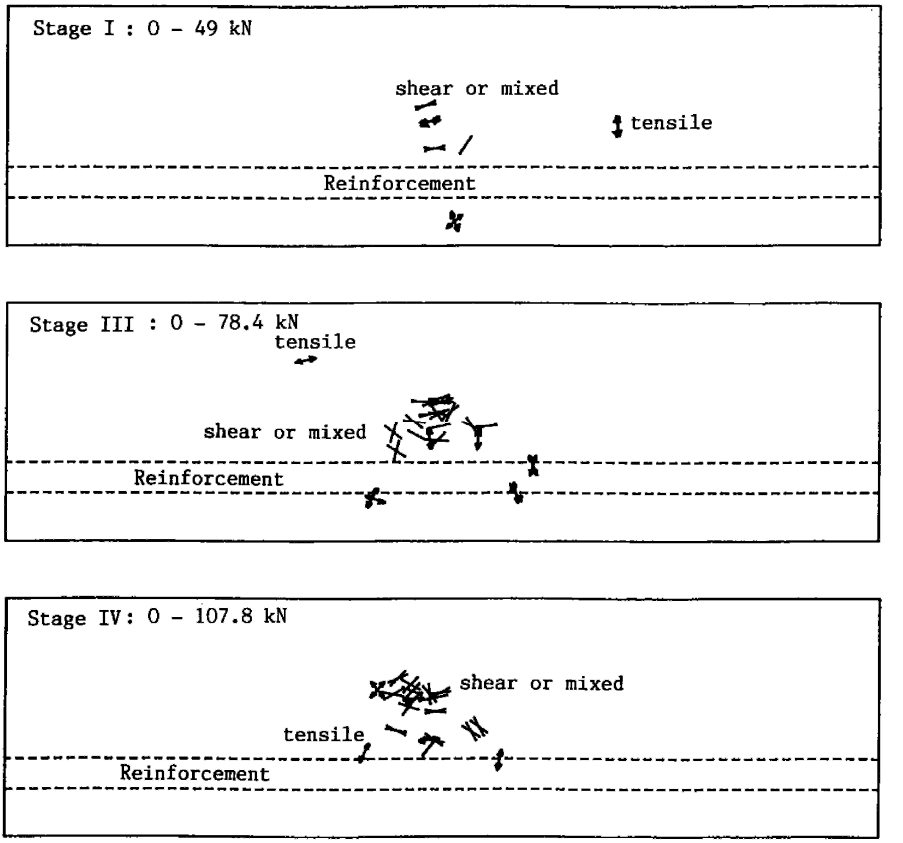

Fig. 8.11. Results of SiGMA analysis in a reinforced concrete beam under bending.

8.8 Two-Dimensional Treatment

A similar treatment can be applied to two-dimensional (2-D) problems. Deformations of the plate are classified into two motions. As illustrated in **Fig. 8.12**, one is in-plane motion where a crack surface is generated as the normal vector to the crack plane is vertical to the x_3-axis and AE waves are detected at the edge of the plate. The other is out-of-plane motion where the crack surface is created parallel to the x_1-x_2 plane.

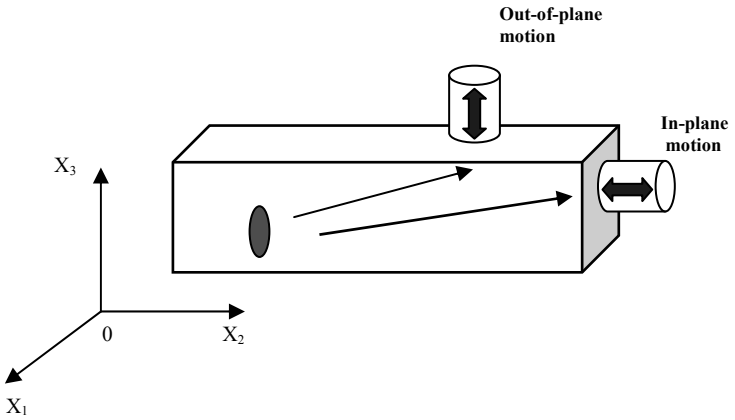

Fig. 8.12. AE detection in a plate specimen.

In the case of in-plane motions, the x_3-components in **Fig. 8.12** of both the vector **l** and **n** are equal to zero. Then, the moment tensor in an isotropic solid becomes,

$$M_{pq} = \begin{pmatrix} \lambda l_k n_k + 2\mu l_1 n_1 & \mu\left(l_1 n_2 + l_2 n_1\right) & 0 \\ \mu\left(l_1 n_2 + l_2 n_1\right) & \lambda l_k n_k + 2\mu l_2 n2 & 0 \\ 0 & 0 & \lambda l_k n_k \end{pmatrix} \Delta V \tag{8.18}$$

In the case that AE sensors are attached at the edge of the plate, the components of the tensor in Eq. 8.18 are readily defined except m_{33} component, because no motion in the x_3-direction is detected. The m_{33} component is actually determined from (Shigeishi & Ohtsu 1999),

$$\begin{aligned} m_{33} &= \lambda\lambda_k n_k \\ &= \lambda\left(m_{11} + m_{22}\right)/\left(2\lambda + 2\mu\right) = v\left(m_{11} + m_{22}\right). \end{aligned} \tag{8.19}$$

In the case of in-plane observation in **Fig. 8.13**, the component of the moment tensor: m_{11}, m_{12}, m_{22} are easily determined, solving the following equation,

$$A(x) = Cs\frac{R_e(t,r)}{R}\begin{pmatrix} r_1 & r_2 \end{pmatrix}\begin{pmatrix} m_{11} & m_{12} \\ m_{12} & m_{22} \end{pmatrix}\begin{pmatrix} r_1 \\ r_2 \end{pmatrix}$$

Since the m_{33} component is obtained from Eq. 8.19, the unified decomposition of the eigenvalues and the orientation analysis by the eigenvectors are readily performed in the same manner as those of the 3-D problems.

In the case of the out-of-plane observation, in contrast, only the case that a tensile crack is generated parallel to the x_1-x_2 plane in **Fig. 8.12** can be treated. Even though the shear motion exists, no information can be recovered.

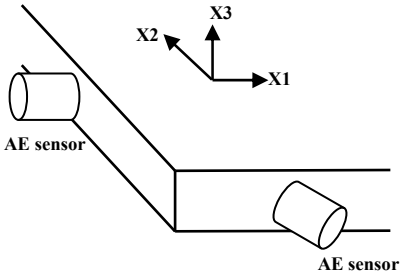

Fig. 8.13. AE detection (in-plane) at the edge of the plate.

To locate AE sources, 5-channel system is at least necessary for three-dimensional (3-D) analysis. Since 6-channnel system is the minimum requirement, 6-channel system is required for SiGMA. In contrast, 4-channel system is available for the 2-D analysis. One application is given in **Fig. 8.14** (Shigeishi and Ohtsu 1999). Uniaxial stress is applied vertical to the plate specimen made of concrete, which contains a through-thickness slit. 4-channel system was employed for the measurement. Results show the case that slit angle to the loading axis is equal to 45^o.

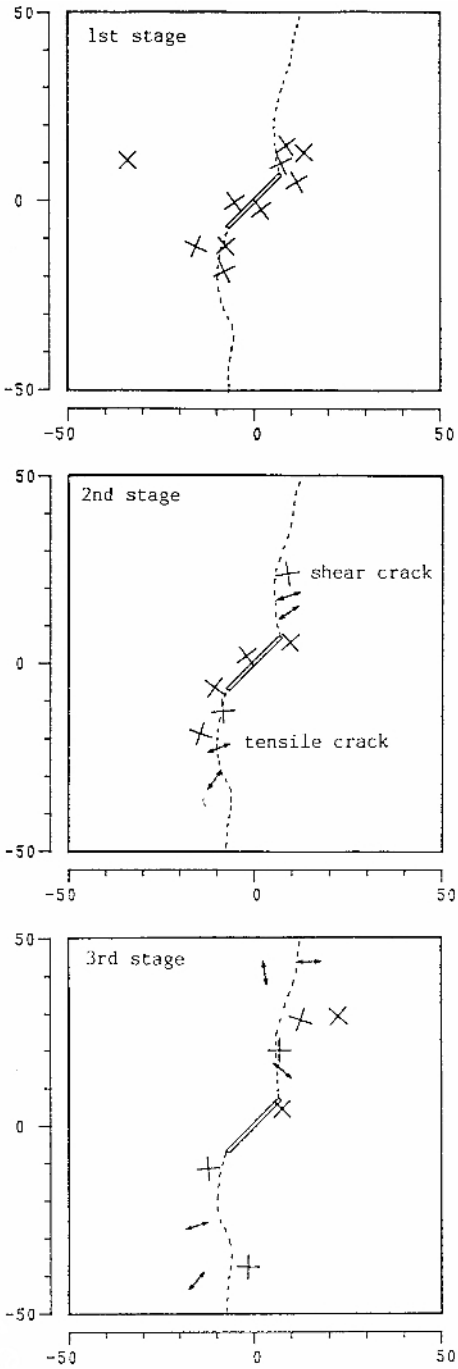

Fig. 8.14. Results of an in-plane problem.

8.9 Damage Mechanics

From the representation of the moment tensor, it is found that the trace components of the moment tensor is obtained as,

$$M_{kk} = (3\lambda + 2\mu) l_k n_k \Delta V. \tag{8.20}$$

A damage parameter in damage mechanics (Kachanov 1980) is defined,

$$D = \int n_i \left(b_i n_j \right) n_j \, dS = \Delta V l_k n_k = M_{kk} / (3\lambda + 2\mu) \tag{8.21}$$

From Eq. 8.21, the crack volume is further obtained,

$$\Delta V = M_{kk} / \left[(3\lambda + 2\mu) l_k n_k \right]. \tag{8.22}$$

where M_{kk} represents the trace components of the moment tensor, λ and μ are Lame constants.

These results imply that the damage evolution and the accumulation of relative crack volume are also estimated from the moment tensor analysis. One example is given in **Fig. 8.15**. From moment tensors determined in bending tests of concrete specimens with a notch (Ohtsu and Ohtsuka 1998), the damage parameter and the accumulation of crack volume are estimated. In the case of the center-notched specimen (type CC), the damage suddenly increases, while the damage evolution is gradual in the off-center notched specimen (type OC).

8.10 Error Estimation

Estimation of errors in the moment tensor analysis is fairly difficult (Ouyang, Landis et al. 1992). In the analysis of **Fig. 8.10** (Ohtsu 1991), the conditioning numbers were applied. Then, error estimation was conducted, assuming the errors. As a result, it is found that the error estimation has been a really complicated task, because the errors are dependent on a spatial relation between the source location and the observation points. Consequently, a post analysis is proposed (Ohtsu 2000), where AE waves to be detected at the observation points are synthesized from the source location and the moment tensor theoretically. For the simulation analysis of theoretical AE waves, the technique discussed in Chapter 7 is available.

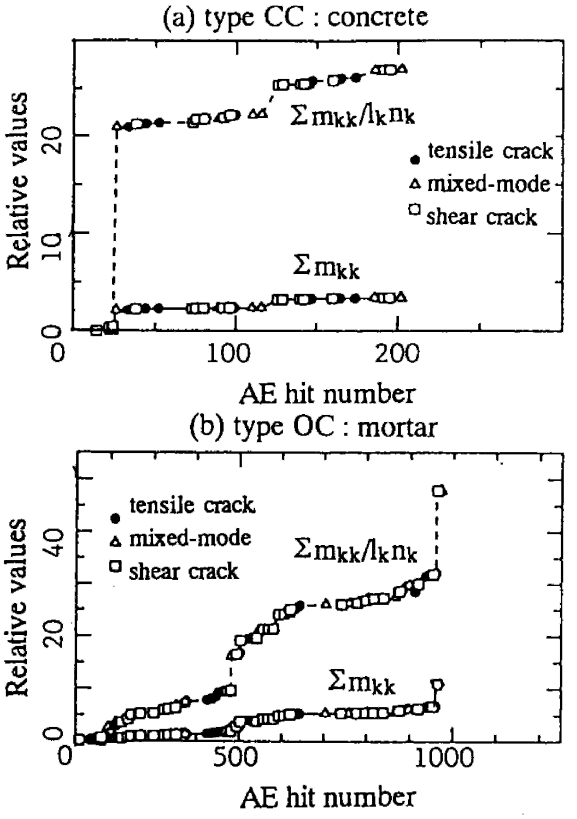

Fig. 8.15. Damage evolution analyzed from the moment tensor analysis.

By using the same size of a PMMA plate as in **Fig. 8.14**, the leakage test was conducted (Ohno, Suzuki et al. 2006) 102 AE events with detectable first arrivals were analyzed by the two-dimensional SiGMA analysis. Results are classified by the shear ratio X (%) and listed in **Table 8.1**. It is clearly found that almost 60% events have the shear ratios over 60%. This implies that dominant source motions at the slit-like defect due to leakage are of in-plane shear-type. It was, however, realized that AE sources were distributed widely on the specimen, not concentrated around the slit. These might result from the fact that only large AE events were identified as the burst-type and readable for the analysis. In addition, determination of both the amplitude of the first motion and the arrival time was actually not an easy task. This implies that some errors are unwillingly contained in results of the SiGMA analysis.

Consequently, the post analysis was performed. AE waveforms at sensor locations were synthesized in an infinite space, taking into the source location and the moment tensor components. The reflection coefficient was taken into consideration to simulate the waveforms. The SiGMA procedure was applied to synthetic waveform set as the post analysis. Results are also given in **Table 8.1**. Because one event was located out of the specimen, results of 101 events are shown. Except this event, location errors between the SiGMA analysis and the post analysis were within 1 mm. But, the shear ratio changed drastically as found in **Table 8.1**. Following the post analysis, events of the shear ratio less than 10% different from those of the SiGMA analysis were selected as reliable solutions. 46 events were selected and are listed in **Table 8.2**.

Table 8.1. Results of SiGMA-2D analysis

Shear ratio (%)	0 – 40 (%) Tensile	40 – 60 (%) Mixed-mode	60 – 100 (%) Shear
SiGMA analysis	20	20	62
Post analysis	12	10	79

Table 8.2. Reliable solution after the post analysis

Shear ratio (%)	0 – 40 (%) Tensile	40 – 60 (%) Mixed-mode	60 – 100 (%) Shear
No. of events	10	3	33

Kinematics of these 46 events are plotted in **Fig. 8.16**. Here, shear and mixed-mode cracks are indicated with the cross symbol, and tensile cracks are denoted by the arrow symbol. In the all cracks, directions of crack normal and crack motion are illustrated. It is found that AE sources of tensile types are mostly concentrated inside the pipe, where the water pressure was applied. The opening directions of tensile cracks are almost vertical to the slit surface, suggesting that water flows due to leakage open the slit.

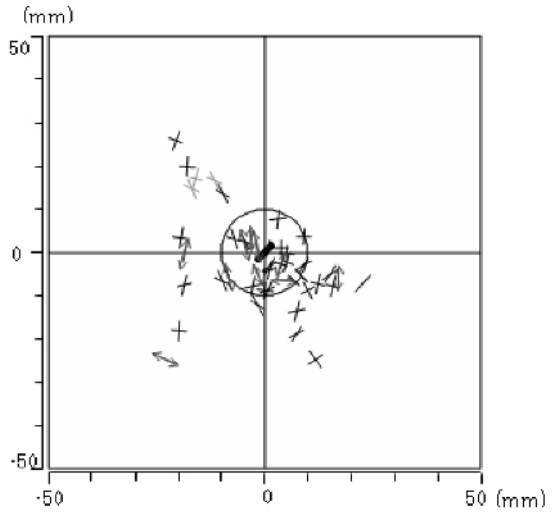

Fig. 8.16. Results of the post analysis.

8.11 Visualization by VRML

Visualization procedure is developed by using VRML (Virtual Reality Modeling Language). By applying the SiGMA code, AE events are displayed at their locations with symbols. In the results of **Fig. 8.10**, **Fig. 8.11**, **Fig. 8.14, Fig. 8.16**, a tensile crack is denoted by arrow symbol, of which direction is identical to that of crack opening. A shear crack is denoted by cross symbol, of which two directions correspond to two vectors **l** and **n**. Although classification of cracks was readily made, crack orientation was not easily recognized. This was because two-dimensional projection was adopted for illustration but analyzed results are inherently suitable for three-dimensional visualization. In this respect, VRML is introduced. Crack modes of tensile, mixed-mode and shear are given in **Fig. 8.17**. Here, an arrow vector indicate a crack motion vector, and a circular plate corresponds to a crack surface, which is perpendicular to a crack normal vector.

Experiments were conducted by using the same reinforcement concrete beams as shown in **Fig. 8.11**. As shown in **Fig. 8.18** (a), at the first stage, a few tensile cracks (**Fig. 8.17** (a)) and mixed-mode cracks (**Fig. 8.17** (c)) are mostly observed near reinforcement at the central region. Then, delamination between concrete and reinforcement occurred. Activity of cracking increased as the increase in mixed-mode cracks. Bending cracks were

visually observed. The tips of cracks extended upward, penetrating into the compressive zone of the upper half. Thus, at the intermediate stage in **Fig. 8.18** (b), AE cluster expands upward, increasing the number of shear cracks (**Fig. 8.17** (b)). The cracks then stopped due to compression, and the beam reached final failure of diagonal-shear failure or concrete crashing at the upper half. Approaching the final stage in **Fig. 8.18** (c) and (d), cluster of AE sources further expands and nucleation of cracks is really mixed up of tensile, mixed-mode, and shear cracks. Cracks distribute widely, probably corresponding to nucleation of diagonal shear cracks between the loading point and the support. Locations and orientations of the source can be visually identified. This is a merit by means of VRML.

(a) tensile crack **(b)** shear crack **(c)** mixed-mode

Fig. 8.17. 3-D display models for tensile, shear, and mixed-mode cracks.

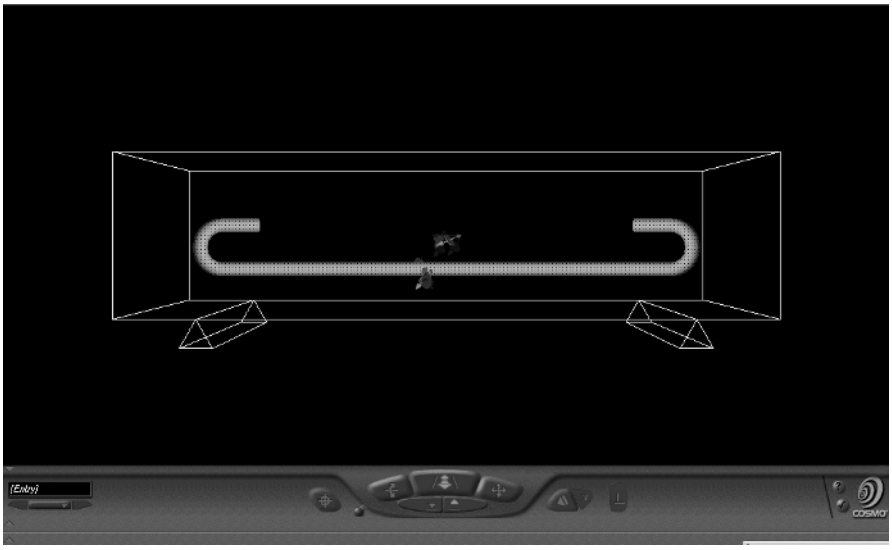

Fig. 8.18 (a). Results of SiGMA analysis visualized by VRML - 1st stage

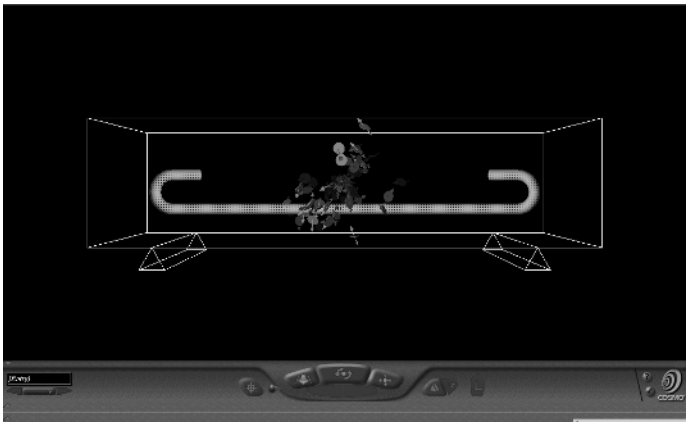

Fig. 8.19 (b). Results of SiGMA analysis - intermediate stage

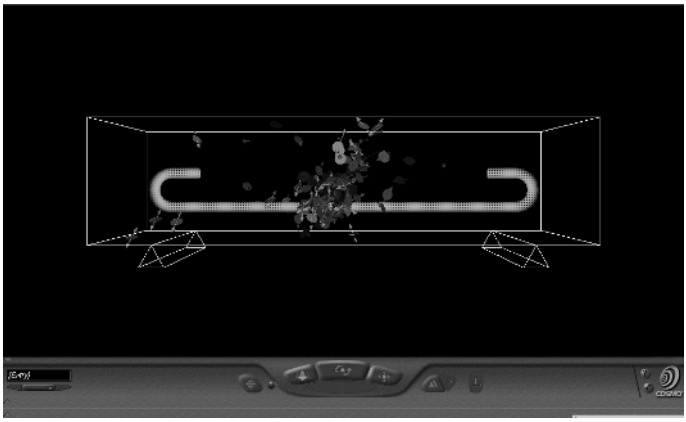

Fig. 8.20 (c). Results of SiGMA analysis - final stage

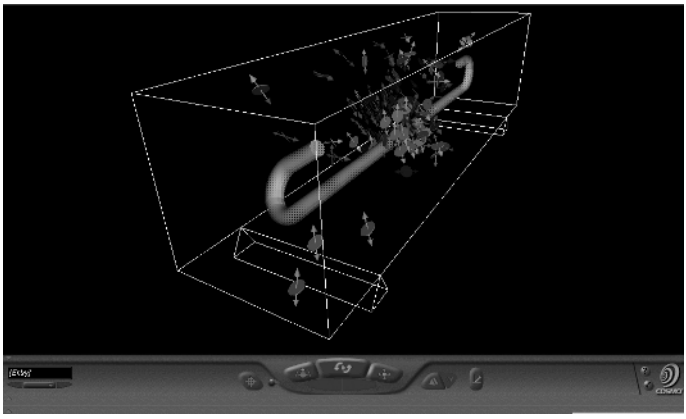

Fig. 8.21 (d). Results of SiGMA analysis - Visualization from an inclined angle

8.12 Concluding Remarks

Nucleation of cracks can be kinematically analyzed by the moment analysis. Applying the SiGMA (Simplified Green's functions for Moment tensor Analysis) code, crack kinematics on locations, types and orientations are determined three-dimensionally. Basic treatment and theoretical background are discussed, including the two-dimensional case.

For the two-dimensional soltution, in-plane motions of AE waves are treated. As a practical application, AE waves due to water leakage from a slit are detected and analyzed. The reliable solutions are selected by the post analysis. Because visualization of results is desirable, three-dimensional visualization procedure is developed by using VRML (Virtual Reality Modeling Language).

References

Aki K, Richards PG (1980) Quantitative seismology: Theory and methods. Vol. I, WH Freeman and Company, San Francisco

Dahm T (1996) Relative moment tensor inversion based on ray theory: Theory and Synthetic Tests. Geophys. J Int., 124:245-257

Dai ST, Labuz JF, Carvalho F (2000) Softening response of rock observed in plane-strain compression. Trends in Rock Mechanics, Geo SP-102, ASCE, pp 152-163

Dziewonski AM, Woodhouse JH (1981) An experiment in systematic study of global seismicity: Centroid-moment tensor solutions for 201 moderate and large earthquakes of 1981. J Geophys. Res. 88(B4):3247-3271

Enoki M, Kishi T, Kohara S (1986) Determination of micro-crackingmoment tensor of quasi-cleavage facet by AE source characterization. Progress in Acoustic Emission III, JSNDI, pp 763-770

Hamstad MA, O'Gallagher A, Gary J (1999) Modeling of buried monopole and dipole source of acoustic emission with a finite element technique. Journal of AE 17(3-4):97-110

Kachanov M (1980) Continuum model of medium with cracks. J Engineering Mechanics, ASCE, 106(EM5):1039-1051

Kanamori H, Given JW (1981) Use of long-period surface waves for fast determination of earthquake source parameters. Phys. Earth Planet Inter. 27:8-31

Landis E, Ouyang C, Shah SP (1992) Automated determination of first P-wave arrival on acoustic emission source location. Journal of AE 10(1/2):s97-s103

Ohno K, Suzuki T, Shimozono S, Ohtsu M (2006) Moment tensors of in-plane AE waves analyzed by SiGMA-2D. Progress in AE XIII, JSNDI, pp 239-246

Ohtsu M (1982) Source mechanism and waveform analysis of acoustic emission in concrete. Journal of AE, 2(1):103-112

Ohtsu M, Ono K (1984) A generalized theory of acoustic emission and Green's functions in a half space. Journal of AE, 3(1):124-133

Ohtsu M (1991) Simplified moment tensor analysis and unified decomposition of AE source: Application to in situ hydrofracturing test, J Geophys. Res., 96(B4):6211-6221

Ohtsu M (1995) Acoustic emission theory for moment tensor analysis. Res. Nondestr. Eval. 6:169-184

Ohtsu M, Okamoto T, Yuyama S (1998) Moment tensor analysis of acoustic emission for cracking mechanisms in concrete. ACI Structural Journal 95(2):87-95

Ohtsu M, Ohtsuka M (1998) Damage evolution by AE in the fracture process zone of concrete. J Materials, Conc. Struct. Pavement, JSCE, 599/V-40:177-184

Ohtsu M (2000) Moment tensor analysis of AE and SiGMA code. Acoustic Emission-Beyond the Millennium. Elsevier, pp 19-34

Ouyang C, Landis E, Shah SP (1992) Damage assessment in concrete using acoustic emission. Nondestructive Testing of Concrete Elements and Structures, ASCE, pp 13-24

Saito N, Takemoto M, Suzuki H, Ono K (1998) Advanced AE signal classification for studying the progression of fracture modes in loaded UD-GFRP. Progress in Acoustic Emission IX, JSNDI, V1, pp 1-10

Shah KR, Labuz JF (1995) Damage mechanisms in stressed rock from acoustic emission. J. Geophys. Res. 100(B8):15527-15539

Shigeishi M, Ohtsu M (1999) Identification of AE sources by using SiGMA-2D moment tensor analysis. Acoustic Emission: Standard and Technology Updated, ASTM STP 1353, pp 175-188

Stump BW, Johnson LR (1977) The determination of source properties by the linear inversion of sesimograms. Bull. Seismo. Soc. Am. 67(6):1489-1502

Suaris W, van Mier JGM (1995) Acoustic emission source characterization in concrete under biaxial loading. Materials and Structures 28:444-449

Part B
Applications

9 General Remarks on Applications

Masayasu Ohtsu

9.1 Introduction

AE techniques have been applied to a variety of structures and infrastructures in the field of civil engineering. Some of successful applications to concrete, rock, wood, superstructures of buildings and bridges, and substructures including railway structures are described in the following chapters. When the techniques are going to be applied to existing structures or local members, inspection procedure shall be based on the codes and standards. A few have been established on concrete structures only in Japan (NDIS 2421 2000) and (JCMS-III 2003). This is because concrete structures are known to be no longer maintenance-free. In the world, these are AE standards so far available as in the field of civil engineering except some codes and manuals only standardized in the governmental institutes and departments. In other kinds of structures, in-situ inspection techniques of AE measurement or monitoring are under development for maintenance. Accordingly general remarks on applications in engineering are discussed.

Due to damage evolution and deteriorations in the structures, AE events are observed, nucleating microcracks under in-service conditions. An inspection method for active cracks or defects is a target for AE applications in engineering.

9.2 Basics of Measurement

AE sensors shall be sensitive enough to detect AE signals generated in the target structure, taking acoustic coupling into consideration. Sensitivity calibration of AE sensors shall be performed by employing the standard source or an equivalent piezoelectric sensor. AE sensor also shall be robust

enough against temperature changes, moisture conditions and mechanical vibrations in the environments. Concerning coupling, several kinds of couplants are available. So far there exist no regulated techniques as long-term inspection or durability of couplants are not confirmed yet. This is because AE techniques are still immature for field applications.

In the devises for the measurement, a usual system is schematically illustrated in **Fig. 2.8.** In principle, amplifiers shall be set up as close as possible to AE sensors. The internal noise of the amplifier shall be inherently low and less than 20 μV as the peak voltage converted as input voltage. The amplifier shall be robust enough against the environmental conditions and be protected properly. The frequency range, which are usually controlled by filters, shall be determined prior to the measurement, taking into account the performance of AE sensors and the amplifiers.

Several AE parameters are available to be obtained from the measuring system. These are generally effective to identify deterioration mechanisms and useful to discriminate environmental noises. A measuring system records such parameters as count, hit, event, maximum amplitude, energy, rise time, duration, energy-moment, RMS (root mean square) voltage, frequency spectrum, and arrival-time difference. Some of them are illustrated in **Fig. 9.1**.

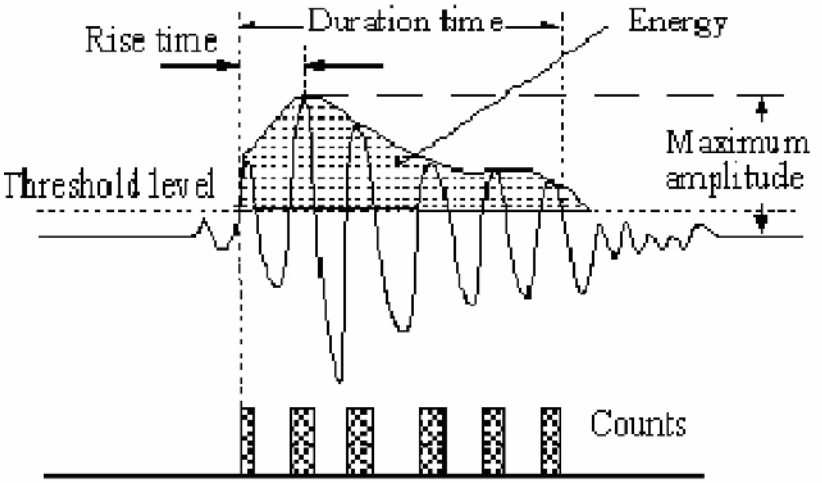

Fig. 9.1. AE parameters.

9.3 Elimination of Noise

Elimination of the noises is one of the most concerned aspects in the applications. Usually, it is achieved by simply setting the threshold level over the noise level, or by a band-pass filtering and a post-analysis of the data. In any cases, the averaged amplitude of the noise should be managed to be lower than 10 ΔV as input.

9.3.1 Environmental Noise

In advance to AE measurement, the noise level shall be estimated on site. Then, counteract against external noises, such as wind, rain, sunshine and so forth shall be conducted to decrease the noise level as low as possible.

9.3.2 Separation of Noise

In the case that the noises have similar frequency contents and amplitudes to AE signals, or sources of the noises are unknown, characteristics of the noises shall be estimated prior to the measurement. Then, separation of AE signals from the noises shall be made. In this respect, the use of filters is useful after determining the proper frequency range.

9.3.3 Post Analysis

According to JCMS-III [2003], such AE parameters as *RA* value and the average frequency *Fa* are defined to classify cracks as stated in Chapter 4. From these two parameters, traffic noises could be practically discriminated. In a buried water-pipeline, AE monitoring was conducted (Suzuki and Ohtsu 2004). Because the pipeline was located below road, traffic noises were often detected due to heavy vehicles. Consequently, AE monitoring was conducted when cars and trucks were passing. Results are summarized in **Fig. 9.2**.

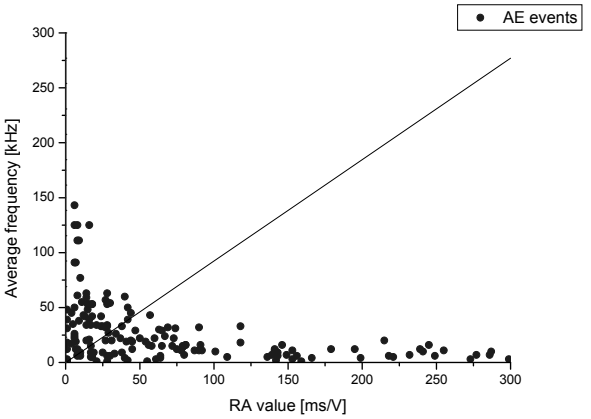

Fig. 9.2. AE events detected under traffic passing.

AE events due to traffic noises are observed in the region where the average frequencies are low. In another test, the measuring system was turned off in each case of traffic passing, and then AE data detected were analyzed. Results are given in **Fig. 9.3**.

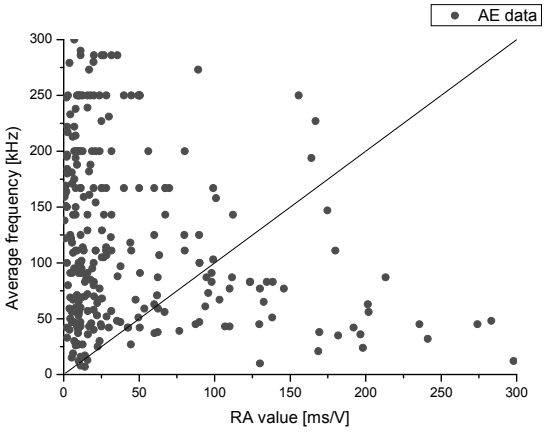

Fig. 9.3. AE data prevented from traffic noises.

The zone of plotted data in **Fig. 9.2** is fairly different from that of **Fig. 9.3**. In the latter case, the plotted data are distributed in the area where the average frequencies are high and RA values are low. It suggests that noises could be successfully eliminated by a post-analysis of AE parameters, even the case where filtering is not easily implemented. In addition, a spatial filter is available to eliminate the noises. This is a technique based on locat-

ing AE sources. In the case that the sources are located far from the zones surrounded by sensors, they are referred to as the noises. One example is given in Chapter 14.

9.4 Setup of AE System and Measurement

In order to set up the system and to carry out AE measurement, several requirements are found. For example, extensive research on AE in concrete has suggested the following requirements to properly set up AE system.

- A measurement system consists, as given in Fig. 2.8, of AE sensor, amplifier, and filter. Total amplification by the pre-amplifier and the main amplifier is usually set from 60 dB to 90 dB. To decrease the noises, a band-pass filter between several kHz and 1 MHz is mostly desirable. The noises should be lower than 20 μV as input voltage after detected by AE sensors.
- Elimination of the noises is achieved by simply setting the threshold level over the noise level, or by a band-pass filtering and a post-analysis of the data. In any cases, the averaged amplitude of the noise should be managed to be lower than 10 μV as input.
- Sensor array is determined from the attenuation properties of AE waves, setting the distance where attenuation during travel is less than 30 dB. In most cases, the distance between the sensor and an AE source is shorter than 1 m. In relation to the attenuation property, the frequency range from 20 kHz to 100 kHz is recommended for in situ monitoring of concrete structures. These are based on a relationship between measurable distance and detectable frequency as illustrated in **Fig. 9.4**.

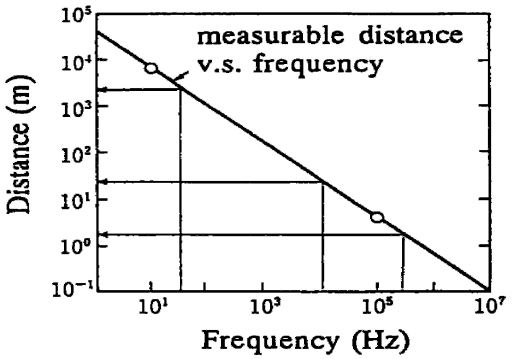

Fig. 9.4. Relation between measurable distance and frequency.

AE sensors are attached at proper locations to cover the target area. The period of the measurement shall be prescribed, depending on the following conditions:

a) Propagation property of AE signals in the target structure
b) Stress distribution in the structure under inspection

Sensitivity of AE channels shall be conducted routinely by employing the standard source. Variation within the channels shall be less than 3%. Based on the spatial area to be covered, AE sensors of proper frequency characteristics shall be selected.

In advance of the test, attenuation properties of the target structure shall be estimated, by employing the standard source or the equivalent. Then, a sensor array shall be determined so as to keep the equivalent sensitivities in all the sensors. Information can be given by the relationship in **Fig. 9.4**.

AE signals shall be detected properly for the period of the measurement. Concerning AE parameters detected, their trend, distribution, correlation, and locations are monitored and measured. In principle, AE tests are conducted under loads which must not cause any damages on functions of the structure during detection and location of active cracks.

The tests shall be carried out routinely or temporally under the following loads:

a) Service load lower than the serviceable limit
b) Incremental load lower than the serviceable limit
c) Variable and repeated load during service

Relations among AE parameters, at least AE hits, time, and loads shall be analyzed.

9.5 Concluding Remarks

Applied fields and structures of AE measurement are still under developing and expansion. This is because set-up conditions of AE measuring systems and target of analyses are different in each case and each site. As a result, it is stated that AE techniques in practical fields are still immature. But, the applicability is already confirmed and successful applications have been extensively reported. These are discussed in the following chapters.

References

JCMS-III B5706 (2003) Monitoring method for active cracks in concrete by acoustic emission. Federation of Construction Materials Industries, Japan

NDIS 2421 (2000) Recommended practice for in-situ monitoring of concrete structures by acoustic emission. JSNDI, Tokyo

Suzuki T, Ohtsu M (2005) Practical application of water-leaked pipeline by AE parameter analysis. In: Proc. 3rd US-Japan Sym. on Advancing Applications and Capabilities in NDEASTM, Hawaii, pp 202-208

10 Concrete

Masayasu Ohtsu

10.1 Introduction

AE techniques have been extensively studied in concrete engineering for approximately five decades (Ruesch 1959). They are applied to practical applications (Ohtsu 1987) and are standardized in the code (NDIS2421 2000). This is because the increase in aging structures and disastrous damages due to recent earthquakes urgently demand for maintenance and retrofit of reinforced concrete structures in service. It results in the need for the development of advanced and effective inspection techniques. Thus, AE techniques draw a great attention to diagnostic applications in concrete.

Modern AE research in concrete was started in the 1970's. Wells studied AE waveforms, finding the relationship between strain measurement and AE events (Wells 1970). Studies on fundamentals of AE activity and the effects of mixture proportion were conducted (McCabe et al. 1976; Nielsen and Griffith 1977; Mlakar, Walker et al. 1984). A frequency analysis and a source location analysis were also reported (Fetis 1976; Niwa, Kobayashi et al. 1978; Reymond, Raharinaivo et al. 1983; Berthelot and Robert 1987; Weiler, Xu et al. 1997). In due course, applications to reinforced concrete structures were investigated (Niwa, Kobayashi et al. 1977; Kobayashi, Hawkins et al. 1980). These studies have resulted in practical applications to monitor micro-cracks in concrete structures and going to be made practical as diagnostic applications (Ohtsu 1988).

In this chapter, fundamentals and successful applications in concrete from fresh stage to hardened stage are stated.

10.2 Concrete of Early Age

Nondestructive tests for fresh concrete at early ages have been summarized in the Rilem state of the art report (Reinhardt & Grosse 2005). AE applications to concrete of early ages are included in the report. Based on the article, noteworthy examples of the applications are briefly stated.

10.2.1 Under Mixing

Roller-compacted concrete is developed and extensively applied to construct concrete dams in Japan. In order to control the consistency of fresh concrete, the VC test is carried out. The test is illustrated in **Fig. 10.1**. Fresh concrete after mixed is placed in the mold on the vibratory table, which vibrates vertically with 1mm stroke and 10 gal acceleration. The surcharge weight is 20 kg. During the vibration, time is measured by second, which is named "VC value", until breeding water is observed at the surface of the mold.

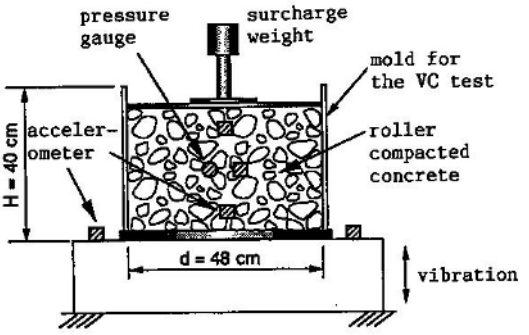

Fig. 10.1. Apparatus of VC test.

Although the consistency is defined by the VC value, this measurement is neither practical nor easy to estimate concrete properties of all mixes. In this respect, AE measurement was applied to estimate quickly the consistency of fresh concrete during mixing, where AE sensor was attached directly to the outer surface of a concrete mixer.

Results of AE energy observed during mixing are given in **Fig. 10.2** (Ohtsu, Murakami et al. 1995). For all mixes, AE energy increases bilinearly. It is clearly observed that the transition points are reasonably related with the VC values. With the increase in the VC value, concrete becomes so sticky due to low water content that fretting aggregate with the

mixer wall ceases earlier. As a result, the transition points of AE energy move lower. This implies that the consistency of concrete is successfully estimated by just observing AE energy under mixing.

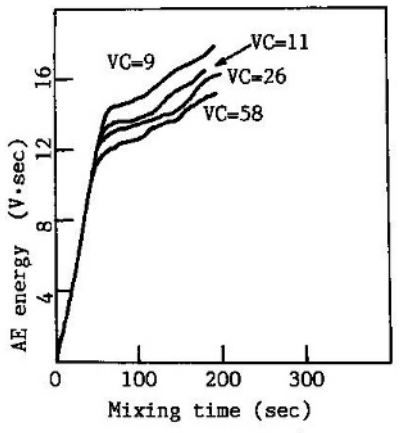

Fig. 10.2. AE total energy during mixing.

10.2.2 Dynamic Compaction

AE activities during dynamic compaction were measured to simply estimate the degree of compaction (Kunisue, Yokoyama et al. 2002). AE sensor was attached to the outer surface of mold. Results of three types of concrete are given in **Fig. 10.3**. In the ordinary concrete cases (W/C = 45% and 60%), both AE count rate and energy shift from the active state to the steady state at around 100 seconds elapsed.

In the case of non-slump concrete, the stable state is later reached than ordinary concretes after 400 seconds. Thus, it is demonstrated that fully-compacted state could be estimated by observing AE activity during dynamic compaction.

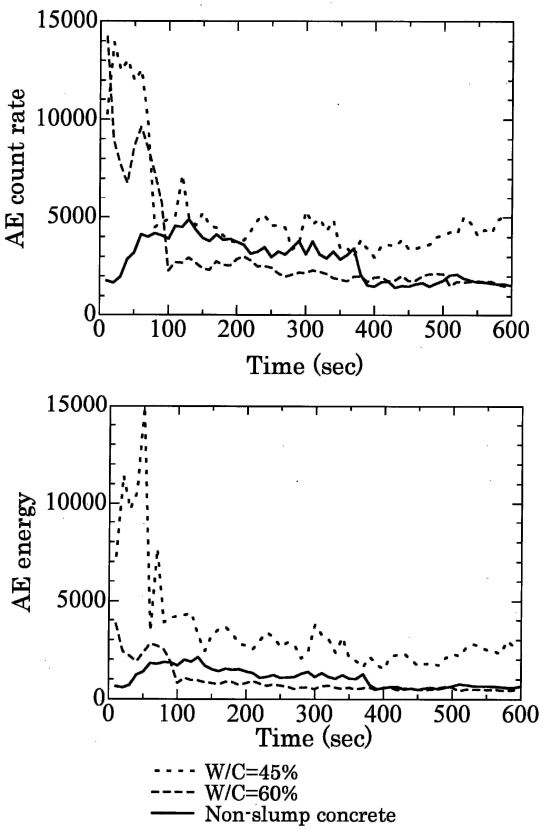

Fig. 10.3. AE total energy during mixing.

10.2.3 Drying Shrinkage

Micro-cracking due to drying shrinkage was studied in two types of cementitious materials i. e., plain cement paste and cement-based composite with 6-mm glass spheres as model aggregate (Shiotani, Bisschop et al. 2002). In the cement-based composite, 35% volume percentage of 6-mm glass sphere with smooth surface was mixed as aggregate. A cylindrical specimen shown in **Fig. 10.5** was tested. After 14-day moisture cure, all sides except the top surface were sealed to induce one-dimensional drying. Six AE sensors of 500 kHz resonance (from #1 to #6 in the figure) were mounted with wax onto the drying surface. The specimens were dried in an environmental cabin ventilated with air of 25% RH and temperature of 31^{o}C for 16 hours.

In comparison with the cement paste, approximately 3.5 times more AE events were recorded in the composite after 16 hour drying. In the both, a rapid increase of AE events was observed in the first stage of drying. In the plain cement paste, no further AE events were recorded after approximately one-hour drying. In contrast, AE events were continuously recorded and stepwise increase of AE energy was found in the composite.

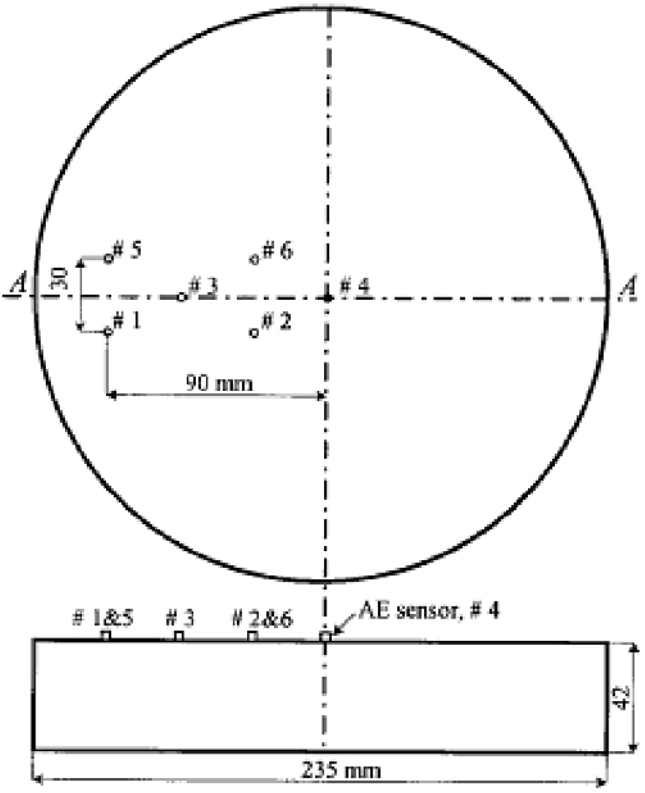

Fig. 10.4. A specimen for a drying shrinkage test.

These AE events were located one-dimensionally as shown in **Fig. 10.5**. AE locations derived from the two-dimensional analysis are projected along the center-line A-A in **Fig. 10.4**. In the cement paste, AE events disperse along the A-A axis in the first hour of drying. In the composite, in contrast, more AE events are recorded from the start of drying and kept to be generated throughout the drying experiment.

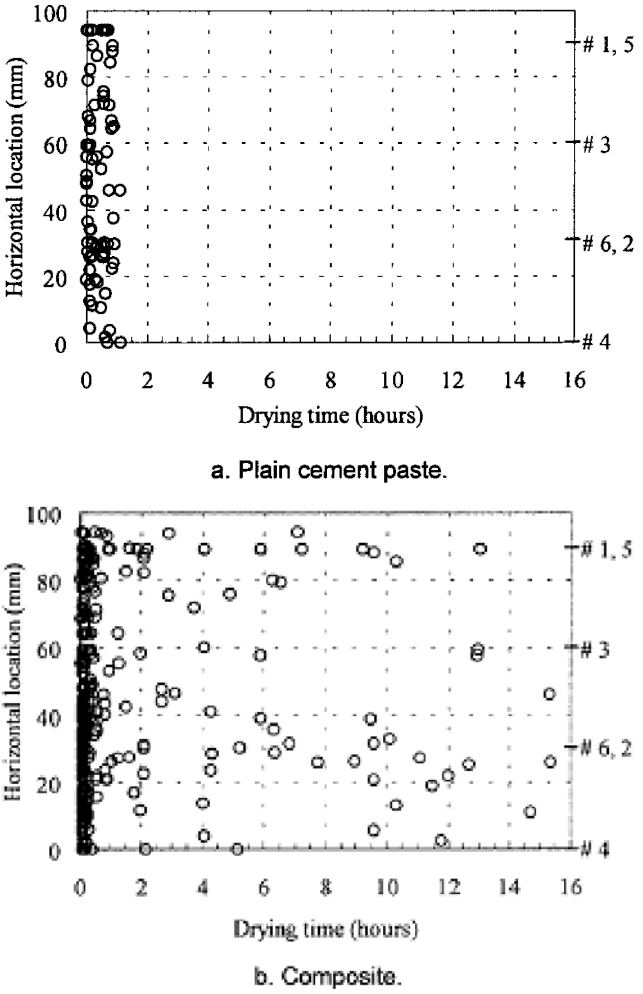

Fig. 10.5. A specimen for a drying shrinkage test.

It is known that micro-cracking in the plain cement paste is due to self-restraining, while cracking in the composite results from both self-restraint and aggregate-restraint stresses. Results of AE activities are in remarkable agreement with these micro-cracking process. In the cement paste, only early-age activity is observed due to self-restraint, while AE events keep to be generated continuously due to aggregate-restraint following self-restraint stress.

10.3 Hardened Concrete

10.3.1 Evaluation of Fatigue

Distributions of AE parameters are often analyzed in relation to the occurrence of AE counts, hits, and events. In hardened concrete, AE events are normally detected by micro-cracking. For example, it is known that the basic creep strain is proportional to the total number of AE hits, which are associated with micro-cracking created in concrete (Rossi, Godart et al. 1994).

Concerning the variation of AE parameter during the deterioration process, it is found that the amplitude distribution is useful. In **Fig. 10.6**, amplitude distributions observed in reinforced concrete beams under bending are shown. These beams were deteriorated by cyclic loading of prescribed level. After particular loading cycles, the beam was statically loaded up to the service-load limit, and AE counts were measured.

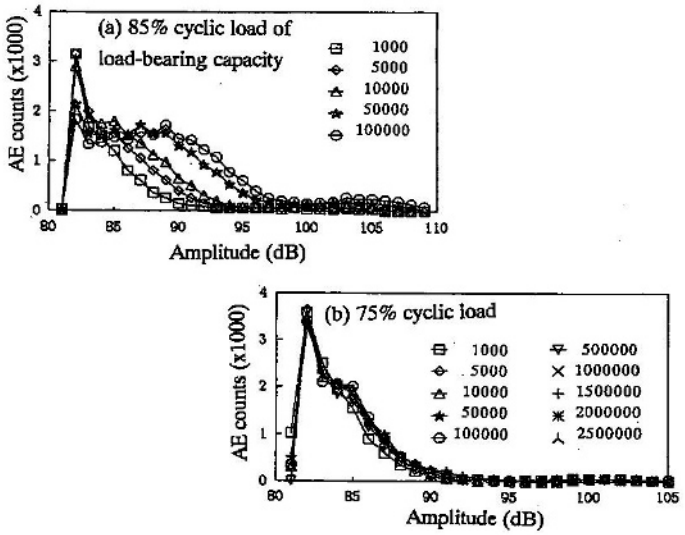

Fig. 10.6. AE amplitude distributions in reinforced concrete beams under cyclic loading.

In **Fig. 10.6** (a), the beam was repeatedly loaded at 85% static load-bearing capacity until final failure. After several cycles of loading, amplitude distributions of AE signals were measured under monotonous loading. With the increase in loading cycles, amplitude distributions shift to the

different distribution where AE signals of the larger amplitudes are dominant. In contrast, there exist no change of the amplitude distributions in the beam (**Fig. 10.6** (b)) which was repeatedly loaded at only 75% until 2,500,000 cycles. The beam was not broken in the test. This implies that amplitude distribution can be applied to routine inspection, investigating the variation of the distribution. The distribution is also quantitatively estimated from the gradient of the slope, which is called the b value.

10.3.2 Location of Micro-Cracks

From the arrival time differences, AE sources are located one-dimensionally in **Fig. 10.7** (Heam & Shield 1997), two-dimensionally, and three-dimensionally in **Fig. 10.8** (Ohtsu 1995). Thus, identification of crack locations and classification of failure mode are readily performed.

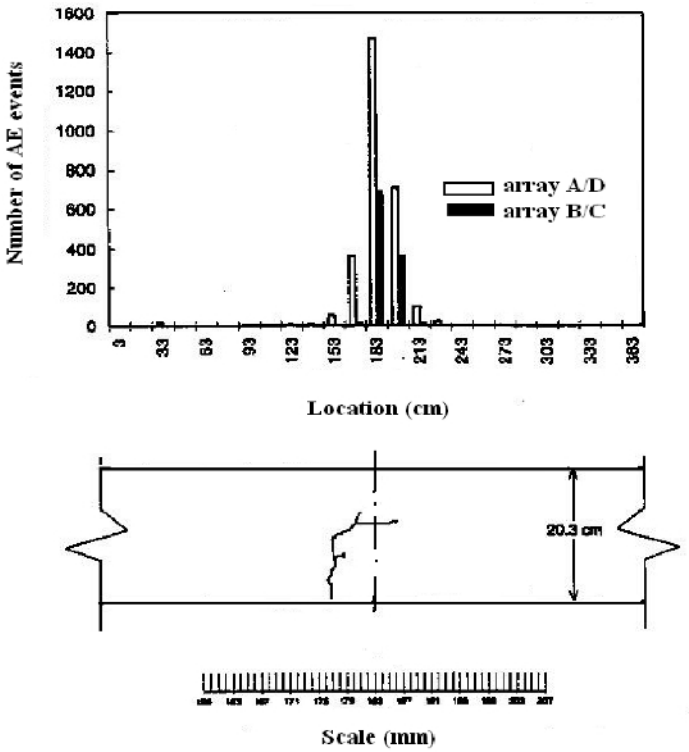

Fig. 10.7 Located AE sources in the one-dimensional location analysis.

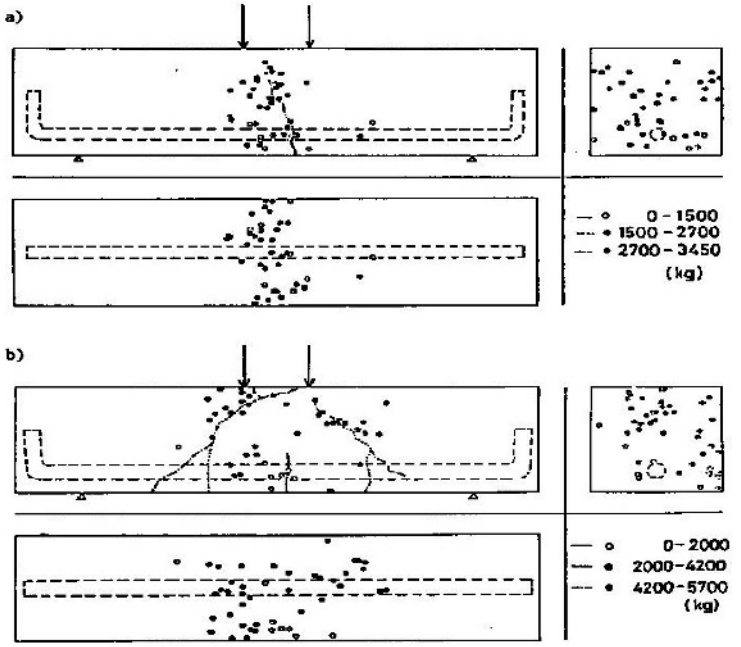

Fig. 10.8. Located AE sources in reinforced concrete beams of **(a)** bending-mode failure and **(b)** shear-mode failure.

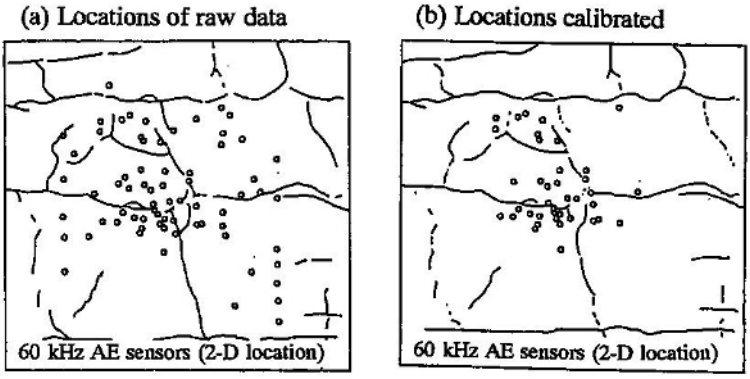

Fig. 10.9. Two-dimensional AE locations in a retaining wall.

Concerning the reinforced concrete, two types of failure modes are known. One is referred to as bending-mode failure. In the beginning of loading, tensile cracks are nucleated at the bottom of the moment span (a portion between loading points in the case of two-point loading) due to bending

moment. When the beam is under-reinforced, steel reinforcement yields and tensile cracks propagate further upward to final collapse. This is the case shown in **Fig. 10.8** (a). The other is called shear-mode failure. In the case that the beam is over-reinforced, final failure results from the sudden generation of diagonal cracks in the shear span (a portion between the support and the loading point). Clusters of AE sources are intensely observed around the diagonal shear cracks in **Fig. 10.8** (b).

By applying AE location procedure, a relation between the location of AE cluster and existing defects was studied in a retaining wall (Matsuyama, Fujiwara et al. 1997). According to the two-dimensional locations of the raw data, wide scattering of AE locations is observed as shown in **Fig. 10.9** (a). Eliminating the noises and compensating the effect of the existing surface cracks, AE locations are calibrated as given in **Fig. 10.9** (b). All signals are mainly observed along the existing cracks. This implies that AE events are mostly nucleated due to fretting of the existing cracks. Accordingly, the wall was repaired, just sealing the surface cracks.

10.4 Damage Assessment of Reinforced Concrete

In relation to two types of failure modes in the reinforced concrete beam, results AE observation in these types of failure mode are shown in **Fig. 10.10**. In the case of a under-reinforced beam (left figure), sliding between reinforcement and concrete was observed due to yielding of the reinforcement. As a result, AE count rate increases exponentially. In contrast, the reinforcement withstood in an over-reinforced specimen (right figure), and thus AE events are observed at constant rate until the final failure. Right before the final stage, diagonal cracks as shown in **Fig. 10.8** (b) were suddenly observed without any precursors. These results demonstrate a potential for the prediction of failure mode of reinforced concrete beams by AE observation. It is confirmed that AE events are sensitive to local instability of the structure.

As stated in Chapter 4, the recommended practice for in situ monitoring of concrete structures by AE is currently established (NDIS-2421 2000). In order to assess the damage levels of reinforced concrete beams, one criterion to qualify the damage levels is proposed on the basis of two ratios associated with the Kaiser effect. A feasibility of this practice is experimentally examined by testing reinforced concrete beams, which have been damaged under incremental cyclic loading.

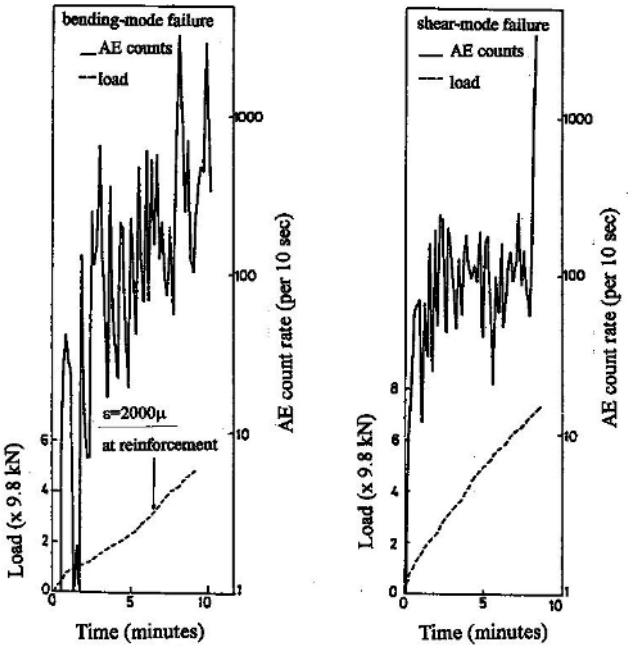

Fig. 10.10. AE activities and failure modes in reinforced concrete beams.

In principle, the concrete structures undamaged are statically stable with high redundancy. AE activity is very low in a stable structure, because the Kaiser effect is closely associated with structural stability. Such ratios as the load ratio and the calm ratio are defined to estimate the Kaiser effect.

The load ratio could become larger than 1.0 in a very sound structure. Due to damage accumulation, the ratio decreases lower than 1.0, generating AE events even at lower loading levels than before. AE activity during unloading is another indication of structural integrity. In the case that the structure is statically stable, AE activity is seldom observed in the unloading process. In the recommendation, the damage assessment is proposed to classify the damage levels as given in Fig. 4.3.

For damage qualification, two reinforced concrete beams of 3.2 m length were tested. Compressive strength and Young's modulus of concrete after 28-day moisture-curing were 31.1 MPa and 27.7 GPa, respectively. These beams were made without lateral reinforcement. To generate the bending-mode failure and the shear-mode in the same kind of specimens, the lateral reinforcement against diagonal shear cracks was not arranged and loading spans of the two were varied as 0.65 m and 1 m with 2.84 loading-span. AE sensor of 150 kHz resonance frequency (R15, PAC) was selected. Frequency range was set from 10 kHz to 1 MHz, and the to-

tal amplification was 80 dB gain. For event-counting, a threshold level was set up at 50 dB. The measuring system was a conventional multichannel AE system. After cracks were nucleated, clip gauges were attached to the specimen and the crack-mouth opening displacement (CMOD) were recorded.

The change of AE activities under cyclic loading is studied to qualify the damages. At each loading stage, two of the load ratio and the calm ratio were determined. Results are shown in **Fig. 10.11** (Ohtsu, Uchida et al. 2002). Based on the maximum CMOD observed in the beams, classification limits are set as 0.9 for the load ratio and 0.05 for the calm ratio. This is because the serviceability limit of the CMOD is less than 0.1 mm in the standard specification, and the Kaiser effect was not observed in the case of the CMOD over 0.1 – 0.2 mm.

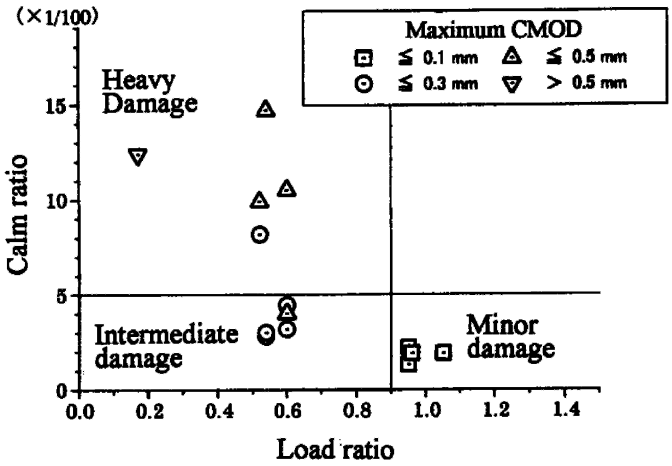

Fig. 10.11. Classification of AE data by the load and calm ratios.

Into three zones of the minor damage, the intermediate, and the heavy, data plotted are reasonably classified in good agreement with the maximum CMODs. This implies that the damage levels of RC beams can be qualified by the criterion based on the load ratio and the calm ratio, monitoring AE activity under cyclic loading or in the mobile-load test (Colombo, Forde et al. 2005). It is noted that the limits classified for qualification should be determined in advance, based on preliminary tests for practical applications.

10.5 Corrosion Monitoring in Reinforced Concrete

AE monitoring was conducted in reinforced concrete beams subjected to corrosion of reinforcing steel (Yoon, Weiss et al. 2000). A diagram of cumulative AE events as a function of test time under cyclic flexural loading is shown in **Fig. 10.12**. It is observed that total AE event counts decrease with the increase in the degree of corrosion. This might give information on the level of deterioration of RC structures due to corrosion. Further, AE activity was continuously monitored in a field, where RC beams were exposed under salt attack for three years. One result was given in **Fig. 10.13** (Ohtsu, Tomoda et al. 2003). Mostly observed AE events were generated due to rainfall. After three year exposure, at channel 6 in one beam, AE activity following raindrops was observed. Then, visual investigation was conducted and surface cracks were found. This implies that continuous AE monitoring is available for detecting corrosion cracking in existing structures (Li et al. 1998).

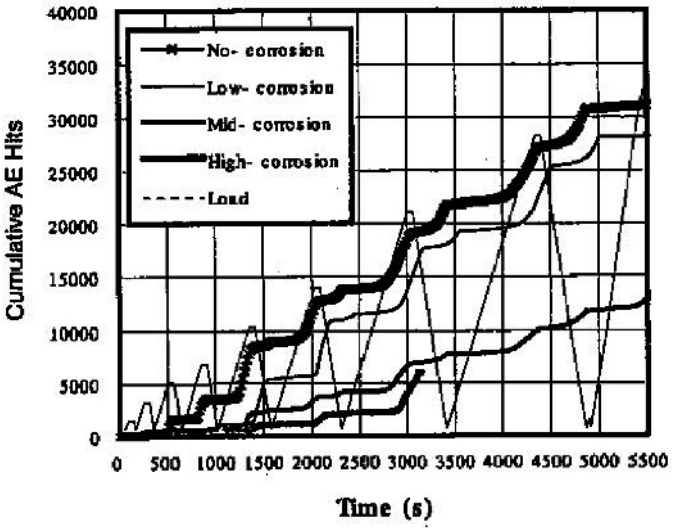

Fig. 10.12. Total number of AE hits in RC beams with corroded reinforcing bars under bending.

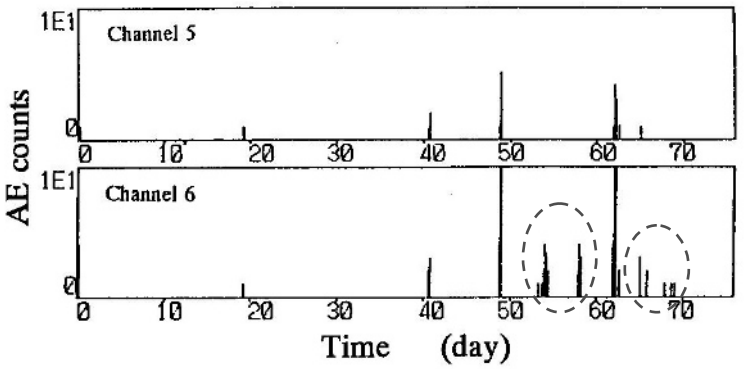

Fig. 10.13. AE observation under salt attack onshore.

In a laboratory test, a relation between AE activity and half-cell potentials was studied. Results in the accelerated corrosion test (Tomoda & Ohtsu 2005) is given in **Fig. 10.14**. Two highly active stages of AE activity (hits) are observed. At the first stage, the half-cell potentials start to decrease, where an abrupt increase in AE hits is observed at around three days. The potentials reach lower than –350 mV (C.S.E) after the second stage. The presence of these two stages is in remarkable agreement with the deterioration process due to salt attack, which is prescribed in the standard specification (JSCE 2001) as shown in **Fig. 10.15**.

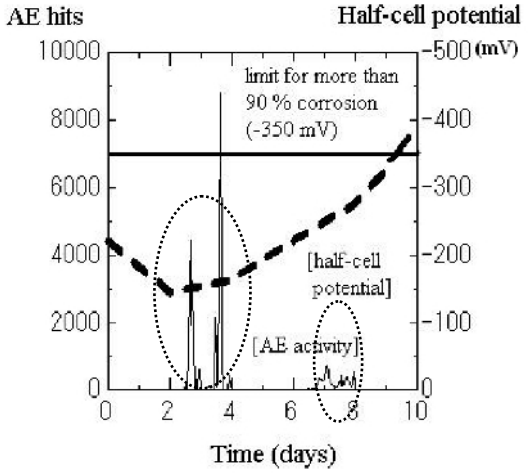

Fig. 10.14. AE activities and the half-cell potentials in the accelerated corrosion test.

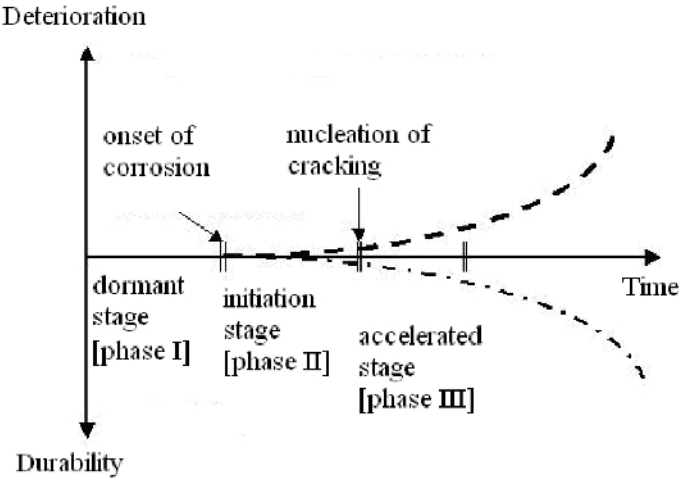

Fig. 10.15. Deterioration process of reinforced concrete due to corrosion.

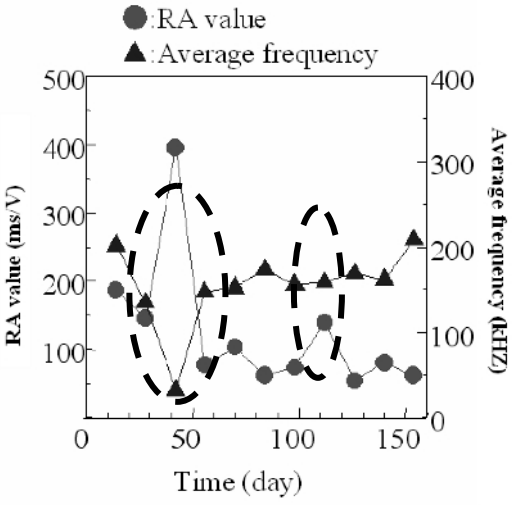

Fig. 10.16. Variations of AE parameters.

In order to clarify characteristics of AE sources (microcracks), AE parameter analysis was performed. Variations of RA values and the average frequencies in the cyclic wet-dry test are given in **Fig. 10.16**. Two stages are reasonably identified from the figure. At the first stage of around 40 days elapsed, RA value is high and the average frequency is low. According to

Fig. 4.4, this implies that shear cracks are actively generated. It is considered that the first stage corresponds to the onset of corrosion. At the second stage, RA value is not so high as the first stage and the average frequency is high. It is suggested that the tensile cracks occur. This implies that tensile cracks are nucleated in concrete due to corrosion products in reinforcement.

The condition of rebar at the 1st AE activity, a rebar skin in the left figure was examined by the scanning electron micrograph (SEM). Distributions of ferrous ions at the initial as received and at 42 days elapsed are compared in **Fig. 10.17**. At the initial stage, homogeneous distribution of ferrous ions is observed, while they disappear after 42 days. This implies the onset of corrosion occurs in rebars at the 1st period of high AE activities. Although no corrosion was observed visually, rebar was actually corroded as realized from SEM observation. Two periods of the corrosion process AE activities are to be identified from two periods of high AE activities. The first corresponds to the onset of corrosion in rebar, and the second could be generated due to concrete cracking. Thus, it is reasonably realized that two key periods in the corrosion process can be identified by AE monitoring. At the onset of corrosion in rebar, small AE events of shear cracks are observed actively. At the nucleation of cracking in concrete, tensile cracks are generated as fairly large.

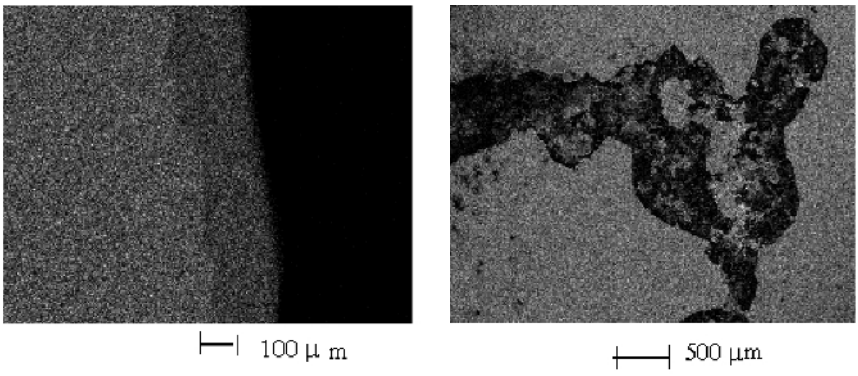

(a) Initial stage **(b)** After 1st stage

Fig. 10.17. Distributions of ferrous ions on rebar surface.

10.6 Quantitative Damage Evaluation of Concrete

Relations between any AE parameters and other physical parameters are quantitatively analyzed and then applied to the diagnosis of concrete structures. The change of AE activity could be related with the rate of the deterioration process. The rate process analysis was introduced to evaluate quantitatively the change of the activity (Ohtsu & Watanabe 2001). When concrete contains a number of critical micro-cracks, active AE occurrence is expected under loading due to crack propagation from existing defects or micro-cracks. In contrast, AE activity in sound concrete is known to be stable and low up to final failure.

To formulate these trends of AE activity under loading, probability function of AE occurrence from stress level V (%) to V+dV (%) is represented as a hyperbolic function in the rate process theory. Eventually, a relationship between the number of total AE events N and stress level V(%) is obtained as,

$$N = CV^a \exp(bV). \tag{10.1}$$

Here the probability function f(V) is formulated as a/V + b. a and b are empirical coefficients and C is the integration constant. As shown in **Fig. 10.18**, high activity under low stress is represented as the case that the coefficient a is positive, while the activity is low in the case a<0. From previous research, the coefficient a is known to be sensitive to the damage degree, and is named the rate.

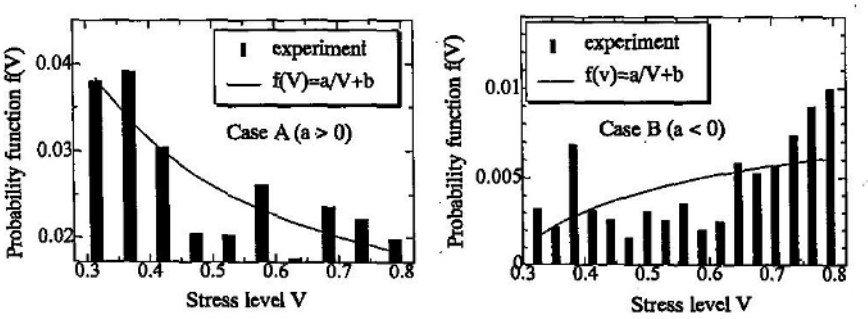

Fig. 10.18. Relations between probability functions and stress levels.

In a nuclear power plant, as one example, core samples were taken from outlet structure for cooling water which is shown in **Fig. 10.19**. For sampling, three sites were chosen, at the gate (Site A), 20 m inland (Site B),

and 30 m inland from the gate (Site C). Then, a uniaxial compression test of the sample was conducted. Three samples at each site were tested. The compressive strength and the rate a were determined as the averaged value of the three.

In order to quantify microscopic damage, distribution of pore radii was also measured by the mercury intrusion method from concrete fragments at the three sites. After determining the pore distribution, the volume of pore radii over 0.5 μm was determined. This is because microvoids over 0.5 μm are dominantly responsible for deterioration of concrete.

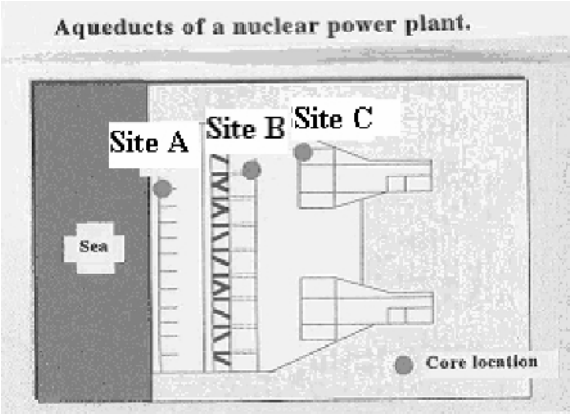

Fig. 10.19. Outlet of cooling water in a nuclear power plant.

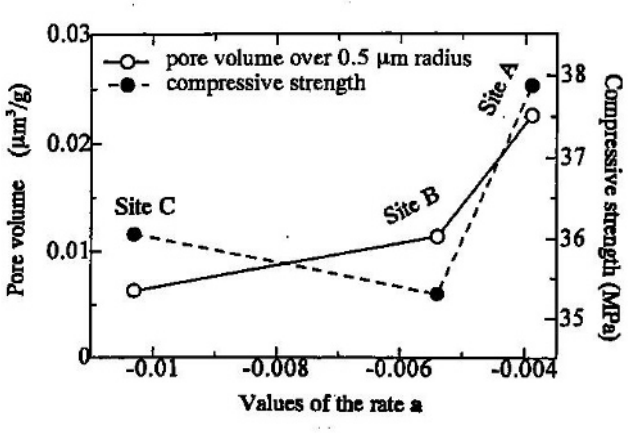

Fig. 10.20. Relations among pore volume, compressive strength and the rate a.

Results of the pore-volumes over 0.5 μm radius, the rate a, and the compressive strength are summarized in **Fig. 10.20**. From Site A to Site C, the pore volume over 0.5 μm radius decreases with the increase in the distance from the sea. This implies that the heaviest damage was introduced in concrete at the gate (Site A), where concrete was repeatedly deteriorated by seawater. Apart from the seaside, the damage of concrete decreases. In accordance with the increase of the pore volume over 0.5 μm radius, the rates a increase from Site C to Site A. Thus, the increase in the pore volume over 0.5 μm radius corresponds remarkably to the increase in the rate a. It suggests that with the increase in the rate a, the volume of the micro-voids responsible for damage increases. Consequently, the rate process analysis of AE occurrence could give information on the deterioration degree of concrete.

Concrete samples core-drilled from an existing bridge were tested. A sketch of piers and anchor of the bridge is given in **Fig. 10.21**. According to the continuum damage mechanics, the state of damage is represented by the scalar damage parameter Ω. In this case, Young's modulus E of a damaged material is expressed as (Loland 1989),

$$E = E*\left(1-\Omega\right), \tag{10.2}$$

where Young's modulus E* is that of an intact material. In the theory, a relation of stress versus strain is obtained as shown in **Fig. 10.22** (a), while damage evolution Ωc - Ωo during the uniaxial compression test is shown in **Fig. 10.22** (b). According to the results mentioned above, the damage evolution could be closely associated with AE activity during the test. It was found that the correlation of the rate a with the evolution Ωc - Ωo was the highest of all.

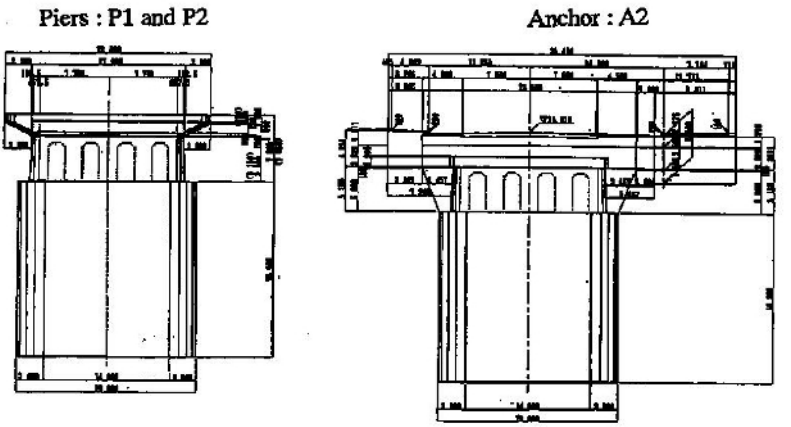

Fig. 10.21. Sketch of reinforced concrete pier and anchor.

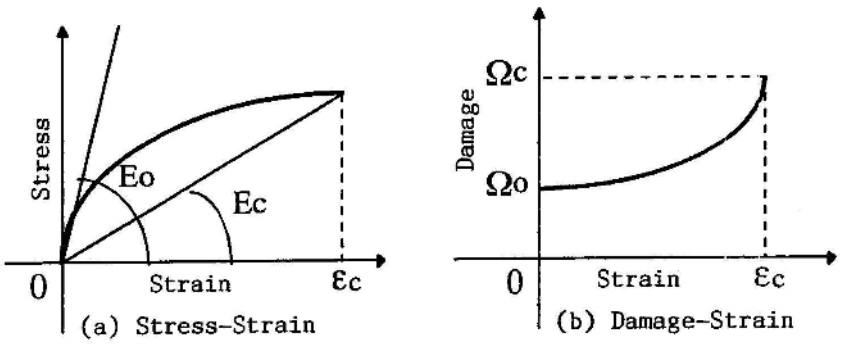

Fig. 10.22. (a) Stress-strain relation and **(b)** the corresponding damage-evolution process.

It is concluded that the damage evolution Ωc - Ωo could be simply estimated from the variation of the rate a. From Eq. 10.2, the increase in the damage corresponds to the decrease in Young's modulus (Eo-Ec) as,

$$E_0 - E_c = E*\left(1-\Omega_0\right) - E*\left(1-\Omega_c\right) \\ E*\left(\Omega_c - \Omega_0\right). \tag{10.3}$$

Thus, a linear correlation between $\log_e$(Eo - Ec) and the rate *a* value is represented as,

$$Log_e\left(E_0 - E_c\right) = Log_e\left[E*\left(\Omega_c - \Omega_0\right)\right] = Da + Y. \tag{10.4}$$

The relations are plotted in **Fig. 10.23**. Then, it is assumed that $E_0 = E^*$ when a = 0. This allows us to estimate Young's modulus of intact concrete E* from,

$$E* = E_c + \exp\left(Y\right). \tag{10.5}$$

From each structure in **Fig. 10.21**, three samples were core-drilled and tested. Results of estimated Eo/E* are summarized in **Fig. 10.24**. All results are plotted as the histogram, and the averaged values are indicated by open circles. It is estimated that the concrete of anchor A is not deteriorated, but the concrete of piers B and C are slightly deteriorated as Eo/E* > 1.0. The trend of these results is found to be in good agreement with analytical estimation on fatigue damage of the bridge piers. Thus, an applicability of the procedure is demonstrated. In this case, the damage of concrete at the current (initial) state can be estimated from AE rate process analysis without knowing the original state at construction.

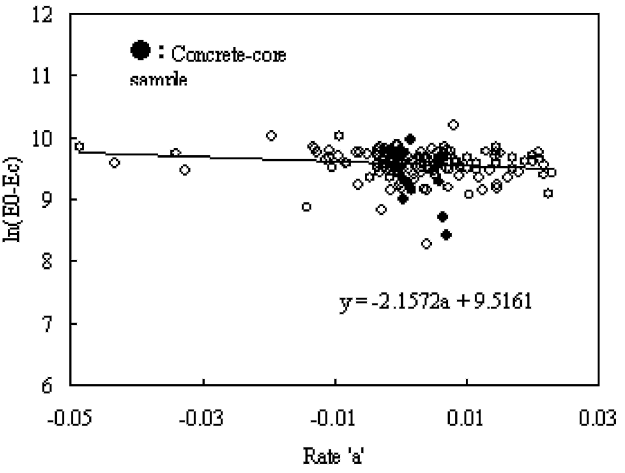

Fig. 10.23. Relations between variation of Young's modulus Eo-Ec and the rate a.

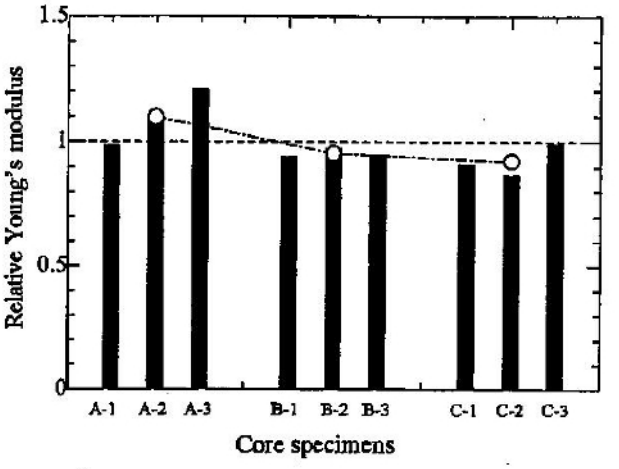

Fig. 10.24. Relative Young's moduli estimated in core samples.

10.7 Application to Fracture Mechanics

It is well known in concrete engineering that the fracture process zone is created ahead of a notch (crack) in concrete, without revealing the notch sensitivity. Nucleation of micro-cracks in the fracture process zone is clarified as shown in **Fig. 10.25** (Nomura, Mihashi et al. 1991). The fracture process zone was ideally introduced in order to explain the tension-softening behavior. Then, as shown in the figure, the presence of the zone is physically confirmed.

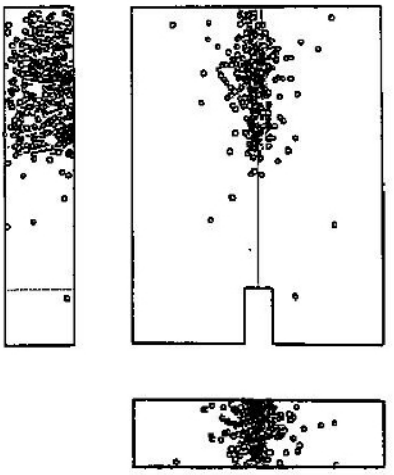

Fig. 10.25. AE locations in the fracture process zone.

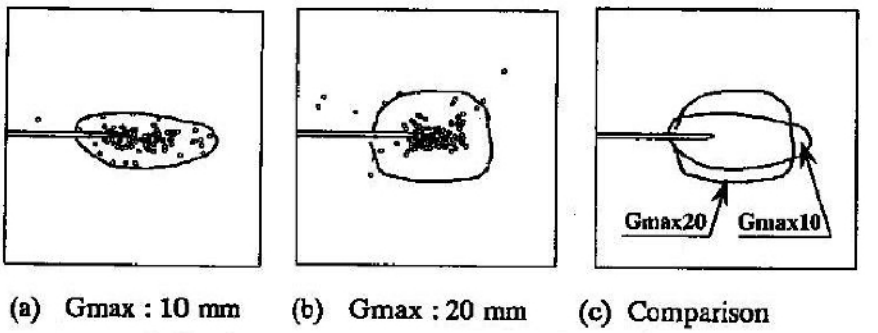

Fig. 10.26. Relations between AE cluster and aggregate size.

Further, a relation between the area of the zone and the size of aggregate was studied as given in **Fig. 10.26** (Ohtsuka, Date et al. 1998). With the increase in the size of aggregate, the fracture process zone grows broadly.

By applying the moment tensor analysis, kinematics of cracks can be analyzed (Ouyang, Landis et al. 1992). In the expansion test, which simulates crack propagation due to corrosion of reinforcing steel-bar, the moment tensor analysis was performed to identify cracking mechanisms. Here, crack modes of micro-cracks are classified into a tensile crack, shear crack and the mix-mode as illustrated in **Fig. 10.27**.

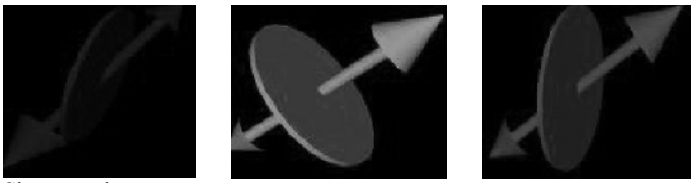

Fig. 10.27. Crack models.

Results of the moment tensor analysis is shown in **Fig. 10.28** (Uddin, Numata et al. 2004). Three-dimensional visualization is developed by using VRML (Virtual Reality Modeling Language). Observed cracks are also shown in the figure. Microscopically, all the types of crack were observed as AE sources. This implies that micro-cracks are accumulated and macroscopically the cracks are nucleated. In the photo, the crack which propagated from the hole to the bottom corresponds to the surface crack. Around this crack, tensile cracks of AE sources are mostly observed, which are almost oriented as vertical to the surface crack plane. During the test, the surface crack was observed first, and then two diagonal cracks propagated. Around these cracks, AE sources are really mixed up of tensile, mixed-mode and shear cracks. It is noted that the final cracks of the surface crack and the diagonal cracks consist of one crack surface, but actually lots of micro-cracks are nucleated around them. This is a typical cracking mechanism in concrete. Mechanisms of corrosion cracking in concrete are of crack-opening failure, but the cracks follow zigzag paths, thus explaining nearly equal contributions of mixed-mode and shear cracks. As a result, fracture mechanics of crack patterns nucleated are successfully visualized.

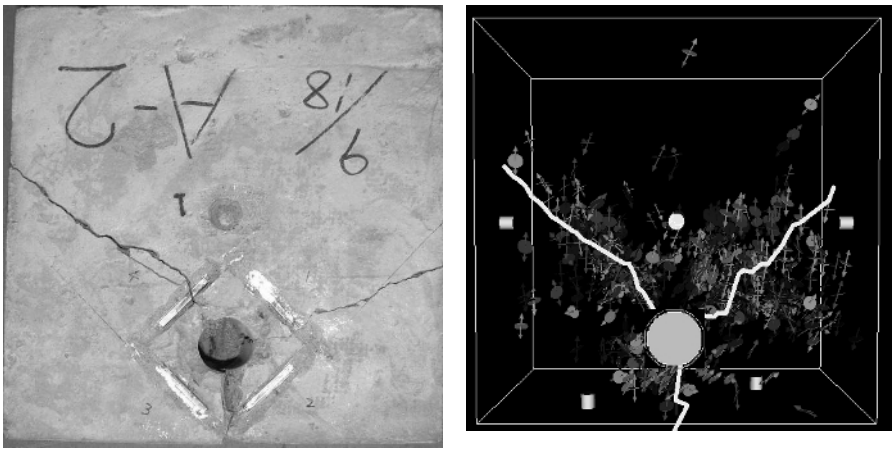

Fig. 10.28 Observed cracks (left) and visualized results of SiGMA analysis (right).

10.8 Concluding Remarks

AE techniques have been applied to concrete engineering for more than five decades. A variety of practical applications are achieved and further going to be standardized. Based on these research activities, RILEM technical committee: TC 212-ACD (Acoustic Emission and Related NDE Techniques for Crack Detection and Damage Evaluation in Concrete) has been established from 2004 to 2009. Recommendation practices are under preparation. Thus, the world-wide standards are to be established in concrete engineering.

References

Berthelot JM, Robert JL (1987) Modeling concrete damage by acoustic emission. Journal of AE, 6(1):43-60

Colombo S, Forde MC, Main IG, Shigeishi M (2005) Predicting the ultimate bending capacity of concrete beams from the "relaxation ratio" analysis of AR signals. Construction and Building Materials 19:746-754

Fertis DG (1976) Concrete material response by acoustic spectral analysis. J Structrual Division, ASCE 102(ST2):387-400

Heam SW, Shield CK (1997) Acoustic emission monitoring as a nondestructive testing technique in reinforced concrete. ACI Materials Journal 94(6):510-519

JCMS-III B5706 (2003) Monitoring method for active cracks in concrete by acoustic emission. Federation of Construction Materials Industries, Japan
JSCE (2001) Standard specifications for concrete and concrete structures on maintenance. JSCE, Tokyo
Kobayashi AS, Hawkins NM, Chan YA, Lin IJ (1980) A feasibility study of detecting reinforcing-bar debonding by acoustic emission technique. Experimental Mechanics 20(9):301-308
Kunisue F, Yokoyama Y, Nogami K, Ohtsu M (2002) Quantitative evaluation of dynamic compaction process in fresh concrete. Proc. 1st fib Congress, Session 15-43
Li ZG, Li F, Zdunek A, Landis E, Shah SP (1998) Application of acoustic emission Technique to Detection of Reinforcing Steel Corrosion in concrete. ACI Materials Journal 95(1):68-76
Loland KE (1989) Continuous damage model for load-response estimation of concrete. Cement and Concrete Research 10:395-402
Matsuyama K, Fujiwara T, Ishibashi A, Fukuchi S (1997) AE measurement of reinforced concrete retaining wall. JSNDI, Proc. 9th AE Conf:131-136 (in Japanese)
McCabe W, Koerner M, Loard Jr. A (1976) Acoustic emission behavior of concrete laboratory specimens. ACI Journal 13(3):367-371
Mlakar PF, Walker R E, Sullivan B R, Chiarito V P (1984) AE behavior of concrete. In Situ/NDT Testing of Concrete. CANMET/ACI SP-82:619-637
NDIS 2421 (2000) Recommended practice for in-situ monitoring of concrete structures by acoustic emission. JSNDI, Tokyo
Nielsen J, Griffith DF (1977) Acoustic emission of plain concrete. J Testing and Evaluation 5(6):476-483
Niwa Y, Kobayashi S, Ohtsu M (1977) Studies of AE in concrete structures. Proc. JSCE 261:101-112
Niwa Y, Kobayashi S, Ohtsu M (1978) Studies of source location by AE. Proc. JSCE 276:135-147
Nomura N, Mihashi H, Niiseki S (1991) Influence of coarse aggregate size on fracture energy and tension softening of concrete. Concrete Research and Technology JCI 2(1):57-66
Ohtsu M (1987) Acoustic emission characteristics in concrete and diagnostic applications. Journal of AE 6(2):99-108
Ohtsu M (1988) Diagnostics of cracks in concrete based on acoustic emission. Nondestructive Testing, ACI SP-112:63-82
Ohtsu M, Murakami Y, Yuyama S (1995) AE generating behavior under Ccncrete Ppacement and application to process control. ASNT, Proc. AECM-5:332-339
Ohtsu M (1995) The history and development of acoustic emission in concrete engineering. Concrete Library of JSCE 25:121-134
Ohtsu M, Watanabe H (2001) Quantitative damage estimation of concrete by AE. Construction and Building Materials 15(5-6):217-224
Ohtsu M, Uchida M, Okamoto T, Yuyama S (2002) Damage assessment of reinforced concrete beams qualified by AE. ACI Structural Journal 99(4):411-417

Ohtsu M, Tomoda Y, Sakata Y, Murata M, Matsushita H (2003) In situ monitoring and diagnosis of RC members in an exposure test against salt attack. Proc. 10th Int. Conf. Structural Faults & Repair

Ohtsuka K, Date H, Kurita T (1998) Fracture process zone in concrete tension specimens by X-ray and AE techniques. Fracture Mechanics of Concrete Structures. Proc. FRAMCOS-3, AEDIFICATIO Publishers l. I:3-16

Ouyang C, Landis E, Shah SP (1992) Damage assessment in concrete using acoustic emission. ASCE, Nondestructive Testing of Concrete Elements and Structures:13-24

Reymond MC, Raharinaivo A, Brachet M (1983) Characterization of concrete damages by acoustic emission analysis. Journal of AE 2(3):159-168

Reinhardt HW, Grosse CU (2005) Final report of Rilem TC-185ATC: Advanced testing of cement-based materials during setting and hardening. RILEM Publications S. A. R. L., Bagneux, France

Rossi P, Godart N, Robert L, Gervais JP, Bruhat D (1994) Investigation of the basic creep of concrete by acoustic emission. Materials and Structures 27:510-514

Rusch H (1959) Physical problems in the testing of concrete. Zement Kalk Gips 12(1):1-9

Shiotani T, Bisschop J, van Mier JG (2002) Drying shrinkage microcrack measurements in cementitious composites using AE and FLM. SEM Annual Conference on Experimental and Applied Mechanics, Milwaukee

Tomoda Y, Ohtsu M (2005) Monitoring salt damage in reinforced concrete by AE. Proc. 3rd US-Japan Sym. on Advancing Applications and Capabilities in NDE, Maui, pp 236-241

Uddin FAKM, Numata K, Shimazaki J, Shigeishi M, Ohtsu M (2004) Mechanisms of crack propagation due to corrosion of reinforcement in concrete by AE-SiGMA and BEM. Construction and Building Materials 18:181-185

Weiler B, Xu SL, Mayer U (1997) Acoustic emission analysis applied to concrete under different loading conditions. Otto-Graf Journal 8:255-272

Wells D (1970) An acoustic apparatus to record emissions from concrete under strain. Nuclear Engineering and Design 12:80-88

Yoon DJ, Weiss W, Shah SP (2000) Assessing damage in corroded reinforced concrete using acoustic emission. J Engineering Mechanics, ASCE 26(3):189-194

11 Acoustic Emission in Study of Rock Stability

Gerd Manthei, Jürgen Eisenblätter

11.1 Introduction

This chapter will review applications of acoustic emission (AE) in two fields, mine monitoring and testing of rock specimens in the laboratory that means in much differing scales of some hundred metres down to several centimeters. Nevertheless, the principal mechanism does not depend on the scale: The rapid release of elastic energy by processes of crack growth or deformation within the rock generates transient pulses of elastic wave energy as AE events. In an even larger scale, the same is true for earthquakes. Therefore, most of the theory of earthquakes can be transferred to AE sources.

The sources of tectonic earthquakes can be studied very closely in some cases where their results become visible on faults at the earth's surface (see **Fig. 11.1**). Exact geodetic mapping on faults allows the slow movement of one side against the other to be followed. Due to this movement, high stresses can build up at the fault slowly over a long time until the friction at one point is exceeded. When this occurs, one side of the fault suddenly slips with respect to the other side by a displacement vector up to some metres at very large earthquakes and part of the stored elastic energy is set free as earthquake tremors. Those observations lead Reid [1910] to his so-called shear stress hypothesis as schematically shown in **Fig. 11.2**. This mechanism is nowadays called a double-couple mechanism.

AE events as well as tectonic earthquakes always occur when slip suddenly takes place over a certain area (the so-called focal area) and thereby stored energy is set free. The primary events are characterized by

- the displacement or dislocation vector,
- the slip area,
- the slip velocity, and
- the stress drop.

It should be mentioned, that elastic energy is only radiated by events whose propagation velocity is in the order of the shear velocity (which is scale-independent). Slow processes like creep events do not emit energy to an extent which is worth mentioning. Such events are aseismic. It should be further noted, that in acoustic emission other than double-couple mechanisms like tensile mechanisms play a more prominent role than in earthquake theory.

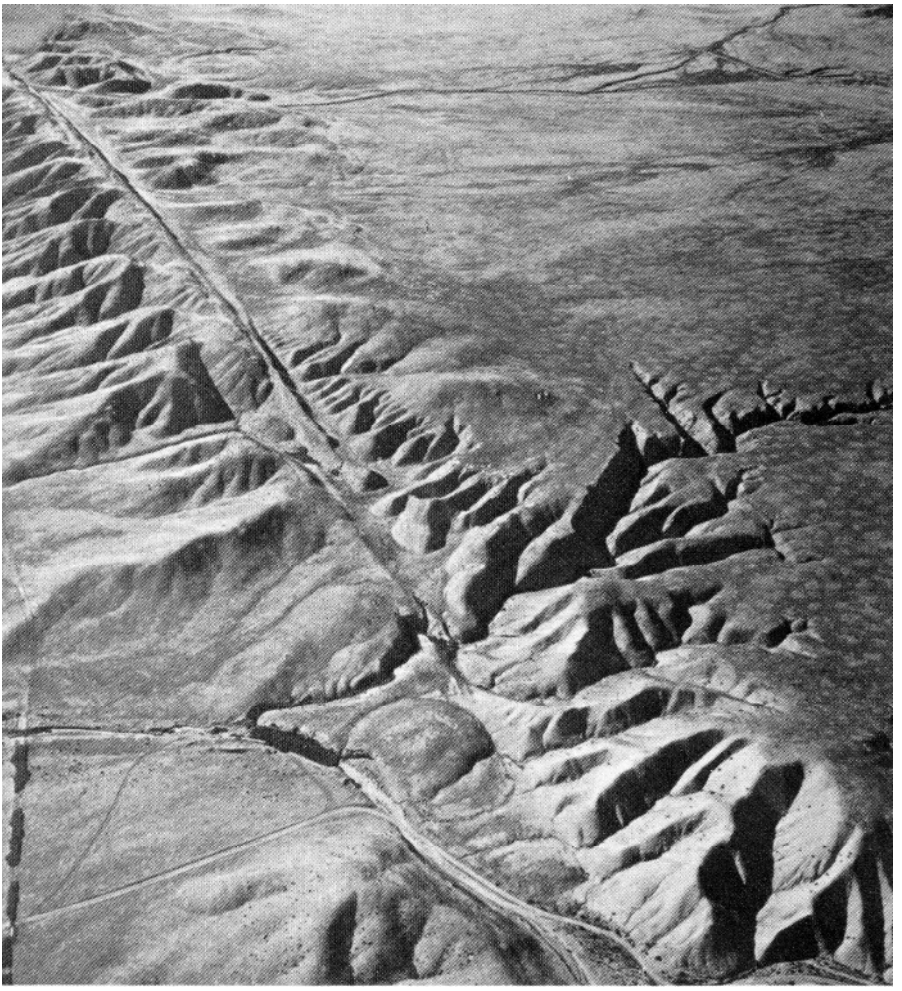

Fig. 11.1. Relief of a part of the San Andreas Fault in California seen in top view (Strobach 1983).

Table 11.1 shows a comparison of some parameters of small and large seismic events. The size of the source determines the duration of the primary pulse (the slip velocity is independent of the source size) and thus the upper limit of frequency spectra which corresponds to the reciprocal of pulse duration. On the other side with increasing frequency, i.e. with smaller source dimensions, the mean attenuation of elastic waves increases and, therefore, the distance between sensors has to be reduced to smaller values.

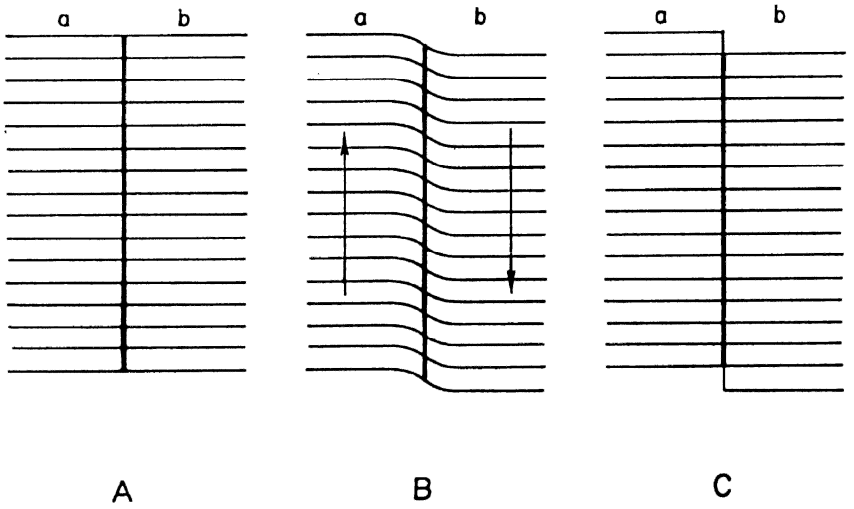

Fig. 11.2. Principal mechanism of a tectonic earthquake after Reid. (A: original state, B: after a long time strains build up at the fault, C: after earthquake).

Table 11.1. Comparison of seismic signal parameters for large events (e.g. earthquakes) and small events (e.g. microcracks in rock)

Parameter	Large events	Small events
Pulse duration	long	short
Frequency range	low	high
Seismic energy	high	low
Frequency of occurrence	rare events	frequent events
Covered area	large	small

The frequency range of AE phenomena in the broadest sense extends from the infrasonic range (less than 16 Hz) far into the ultrasonic range (higher

than 16 kHz). The largest and therefore longest events as well, namely earthquakes, are found at the lowest end of the frequency scale (**Fig. 11.3**). The focus length and displacement of an earthquake can amount to more than several hundred kilometres and up to several metres, respectively. The frequencies used in seismology extend to some Hertz.

On the other side, the highest ultrasonic frequencies may be generated by AE events in the microscopic region, for instance by dislocation movement. In this case the source area may extend to some micrometres and the displacement (Burgers vector) is to be measured in nanometres.

The range of microseismic (MS) measurement as used for mine monitoring lies between the frequency ranges of seismology and typical AE measurements as used for instance in materials testing.

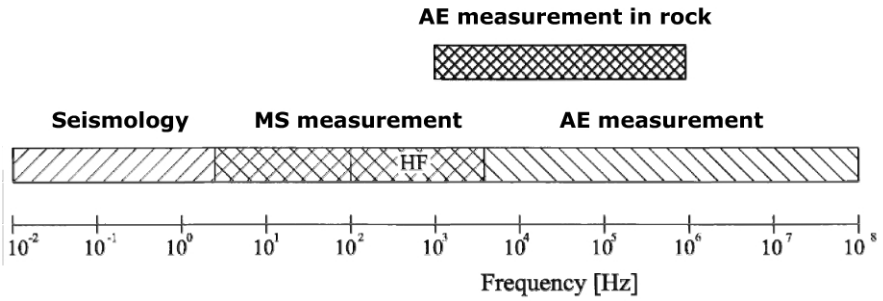

Fig. 11.3. Frequency range of AE measurement as compared with seismology and MS measurement (HF: high frequency; Manthei et al. 2000).

The following sections of this chapter present some examples of applications of AE/MS measurement in rock structures of different extension. Sections 11.2 to 11.4 deal with monitoring of parts of mines with typical dimensions of 100 to 250 m. After a list of various applications found in the literature (in Subsection 11.2.1) and the historical background of AE/MS measurement (in Subsection 11.2.2), examples on monitoring in granite and rock salt are given in Section 11.3 and 11.4, respectively.

Section 11.5 deals with AE measurement during hydraulic fracturing tests which are used for in-situ stress measurement in rock. The typical linear dimension of the covered region in this case is up to 10 m.

Section 11.6 reports on AE measurements in laboratory studies on rock specimens whose typical dimensions are in the centimetre or decimetre range. After an extensive overview about AE measurements on rock specimens (Subsection 11.6.1), fundamental relationships found from simple AE event counting will be presented in Subsection 11.6.2. Subsection

11.6.3 will demonstrate the application of a systematic search for clusters and advanced source location methods in rock specimens. Subsection 11.6.4 describes new methods of source characterization by automatic procedures. Subsection 11.6.5 of this chapter will discuss the dependence of AE activity on dilatancy in rock.

11.2 AE Monitoring in Mines Fundamentals

11.2.1 Characteristics of MS and AE Measurements

Many examples of application of AE/MS measurement as found in the literature are given in **Table 11.2**. This table shows the monitored area, the linear dimension of the covered area, the type of sensors used, the rate of events, the upper limit of the frequency region of the sensors and the Richter magnitude range, if available.

These applications can be roughly classified in low- and high-frequency MS measurements and AE measurements (see also **Fig. 11.3**). The low-frequency MS measurements range between 5 Hz and some hundred Hertz; they are used for surveillance of whole mining regions like the Ruhr coal district in Germany or the Upper Silesian coal fields in Poland and Czech Republic. In this case seismometers are utilized. Measurements in the higher-frequency range from 100 Hz up to 500 Hz, so-called high-frequency MS measurements, are applied for monitoring whole mines or mine segments up to linear dimensions of one kilometre. High-frequency MS monitoring is also used in geothermal areas during stimulation and circulation tests where information about the size of the reservoir, location of fractures, and whether the reservoir volume is expanding during circulation is from upmost importance to control reservoir generation. For these measurements geophones are in use.

Above these frequencies the range of AE measurement in rock begins with applications in mines as well as in laboratory studies. In the frequency region of about 1 kHz up to 100 kHz accelerometers or typical piezoelectric AE sensors are used in mines. The typical distances between sensors may amount up to 50 m; the covered areas may have linear dimensions of up to 200 m.

11.2.2 Historical Background

In rock, acoustic emission is generated by crack formation under high stress. This phenomenon provides the basis for a method which is able to detect zones of microcracking or macrocracking or highly stressed zones in rock without any knowledge of the mechanical properties or the state of stress. The "microseismic method" was discovered by Obert [1938] from the U.S. Bureau of Mines, Denver/Colorado, rather by chance. An experiment was being conducted in a lead-zinc mine in order to determine whether the seismic velocity in mine pillars was dependent on stress. These measurements were often disturbed by signals which obviously were generated by the pillar itself.

Table 11.2. Characteristics of low-frequency and high-frequency MS measurements and AE measurements

Authors	Monitored area	Typical distances	Seismic network	Rate of located events	Corner frequency	Magnitude
MS measurements (lower frequency)						
Cete [1977]	Ruhr District, Germany	50 km	3 seismometers	not available	200 Hz	not available
Ahorner and Sobisch [1988]	Potash basin, Germany	50 km	4 arrays of 4 seismometers each	not available	50 Hz	2 to 2.6
McGarr and Bicknell [1990]	Witwatersrand Basin, South Africa	200 km	7 seismometers	not available	100 Hz	0 to 3
Talebi et al. [1997]	Sudbury Basin, Canada	50 km	6 one-component seismometers	28 in one year	40 Hz	1.5 to 3
Mutke and Stec [1997]	Upper Silesian coal basin, Poland	10 km	10 seismometers	50,000 in 22 years	100 Hz	up to 4.5

Authors	Monitored area	Typical distances	Seismic network	Rate of located events	Corner frequency	Magnitude
MS measurements (higher frequency)						
Hente et al. [1989]	Salt mine Asse, Germany	1 km	7 geophones	209 in two years	300 Hz	–2.3 to 1.7
Will [1980]	Coal mine in the Ruhr district, Germany	100 m	17 three-component geophones	1,000 in four months	400 Hz	not available
Albrigth and Pearson [1982]	Fenton Hill hot dry rock site, USA	400 m	Hydraulic fracturing tool, 12 geophones	1,979 in one hydraulic fracturing test	100 Hz	–6 to–2
Trifu et al. [1997]	Strathcona mine Sudbury, Canada	200 m	49 uniaxial and 5 triaxial accelerometers	1,503 in two months	10 kHz	0.5
Scott et al. [1997]	Sunshine mine, Kellogg, USA	1 km	triaxial geophones	31 in three months	500 Hz	0.5 to 2.5
Phillips et al. [2002]	Austin Chalk, USA	600 m	3 geophones (1 three-component geophone)	1,250 during two stimulations	100 Hz	–4 to –2
Phillips et al. [2002]	Frio formation, USA	200 m	25 three-component geophones	2,900 during stimulation	100 Hz	–4 to –2
Phillips et al. [2002]	Cotton Valley, USA	60 m	two 48-level three-component geophones	290 during one stimulation	100 Hz	–4 to –2
Phillips et al. [2002]	Clinton County, USA	60 m	3 geophones	1,200 locations, one stimulation	100 Hz	–4 to –2
Phillips et al. [2002]	Fenton Hill, USA	1000 m	3 geophones	11,000 during one stimulation	100 Hz	–4 to –2
Phillips et al. [2002]	Soultz, France	2000 m	3 four-component geophones, one hydrophone	16,000 during one stimulation	100 Hz	–4 to–2

Authors	Monitored area	Typical distances	Seismic network	Rate of located events	Corner frequency	Magnitude
AE measurements in rock						
Martin and Young [1993]	Underground research laboratory, Canada	50 m	16 triaxial accelerometers	3,500 in 10 months	20 kHz	–4 to 1–2
Yaramanci [1992]	Salt mine Asse, Germany	300 m	7 triaxial accelerometers	3,407 in 14.5 months	10 kHz	–5.6 to –3.3
Ohtsu [1991]	Underground tunnel, Japan	10 m	17 accelerometers, 17 AE sensors	200 during four hydraulic fracturing tests	100 kHz	not available
Niitsuma et al. [1993]	Kamaishi mine, Japan	30 m	triaxial piezoelectric accelerometers	234 during four hydraulic fracturing tests	10 kHz	not available
Eisenblätter et al. [1998]	Salt mine Asse, Germany	100 m	29 AE sensors	250,000 in 11 months	100 kHz	not available
Manthei et al. [1998]	Salt mine Bernburg, Germany	10 m	8 AE sensors	1,500 during eleven hydraulic fracturing tests	250 kHz	not available
Young and Collins [2001]	Underground research laboratory, Canada	10 m	16 accelerometers, 16 AE sensors	15,350 in 5 months	250 kHz	–6.6 to –5
Manthei et al. [2003]	Salt mine Bernburg	5 m	hydraulic fracturing tool, 8 AE sensors	15,000 during four hydraulic fracturing tests	1.25 MHz	not available
Spies et al. [2004]	Southern part of salt mine Morsleben, Germany	100 m	24 AE sensors	50,000 in one month	100 kHz	–8.6 to –2.2
Spies et al. [2005]	Central part of salt mine Morsleben, Germany	200 m	48 AE sensors	100,000 in one month	100 kHz	–8.6 to –2.2

During the late 1930s and early 1940s, Obert and Duvall showed in the laboratory as well as in the field that the rate of such events clearly increased as the structure became more highly loaded. Their original monitoring facilities consisted of a geophone (with a Rochelle salt cantilever beam element in a metal cylinder), a battery operated amplifier and a paper recorder. A set of headphones provided also an audible means of monitoring AE

activity. In field measurements the geophones were located underground in boreholes. This monitoring system was sensitive to acoustic signals in the region of 1000 Hz. Obert and Duvall carried out an extensive study of AE in nine mines including two deep mines in Canada. Using multi-channel recording systems they were able, by comparison of amplitudes and coincidences, to roughly locate zones of higher acoustic activity.

Considerable application of AE measurement in underground mines started in the 1950s and 1960s in Canada, Europe, and South Africa. All applications of AE associated with geologic materials were initiated in order to study the stability of underground structures like mines or parts of mines. The main goal of all these investigations was the prediction of rock bursts and roof falls as well as the indication of areas of higher stress. During the above-mentioned period more sophisticated techniques for monitoring AE activity, in particular techniques for accurate source location were developed. Considerable is the work of Cook [1963], who developed a monitoring system which was capable of recording signals of up to 8 geophones on magnetic tape for a continuous period of about one day. Cook located the events by re-recording the signals on a multichannel oscilloscope to determine a series of travel time differences of the P- and S-wave onsets. Astonishing is in particular the good source location accuracy, which he attained without any digital signal recording system and without any computers. By the way, rock burst prediction like earthquake prediction has remained an unsolved problem up to now.

By the late 1960s a number of important AE studies were done. These studies were associated with mining, civil engineering, petroleum and natural gas engineering, and other geomechanics areas. Many studies have been conducted in North American coal mines and European coal mines in Poland, Czechoslovakia, Germany, and Russia. These coal mines were relatively deep (up to 1000 m) and therefore the stress conditions were very high and in many cases rock bursts occurred. Successful applications in hard rock mines were done by the U.S. Bureau of Mines in Idaho. These studies were carried out by Blake and Leighton [1970] and by Blake [1972]. They utilized commercially available piezoelectric accelerometers as sensors in the frequency range of 20 Hz up to 10 kHz. The sensors were located in boreholes and the signals were transmitted by cable to an underground monitoring system. The data were used to calculate the source location and relative amplitudes. Other studies in hard rock were done in South Africa and to a limited extent in Europe (Sweden, East Germany, and Poland). The majority of research has been in South Africa (Salmon and Wiebols 1974). Further details about geotechnical field applications of AE/MS techniques until the late 1980s are given in a review article by Hardy [1989], about both the laboratory and field developments, and in the

proceedings of the six Penn State AE/MS Conferences. The First International Symposium on Rockburst and Seismicity in Mines (RaSiM) was held in South Africa 1982. Six years later in 1988 followed the Second International Symposium in the United States. The Third to Sixth International Symposia took place in Canada 1993, in Poland 1997, in South Africa 2001, and in Australia 2005, respectively.

Nowadays, the application of AE on rock is an inherent part of each AE conference, in particular the Japanese International Acoustic Emission Symposia (IAES), the European Conferences on Acoustic Emission Testing (EWGAE), and various national colloquia on acoustic emission.

11.3 AE monitoring in Granite

The first example on AE monitoring in mines refers to crack formation in granite caused by stress redistribution around a newly excavated tunnel. A research program has been undertaken by the Atomic Energy of Canada Limited to develop the technology needed for the safe and permanent disposal of nuclear waste. The main objectives were to investigate the response of a rock mass to excavation and to study the long term stability of underground openings.

Therefore, in the Underground Research Laboratory (URL) located in Pinawa, Manitoba, a "Mine-by" experiment at 420 m depth in the Canadian shield granite has been carried out. In the experiment a 46 m long test tunnel has been excavated in 1 m or 0.5 m increments (**Fig. 11.4**) using drilling and mechanical breaking of the rock stub. The in-situ stresses at the test site have been measured using overcoring and hydraulic fracturing methods. The test tunnel was in direction of the intermediate principal stress σ_2 in order to maximize the stress concentration around the test tunnel (for direction of principal stresses see insert in **Fig. 11.4**, right-hand side). One topic of the experiment was to study the rock behaviour during excavation utilizing AE measurement. In addition to mechanical instrumentation, around the test tunnel a network of 16 triaxial accelerometers was installed as MS array (MS1 to MS16). The AE network was located in boreholes (filled circles) in such a way as to give a focal sphere coverage of the tunnel.

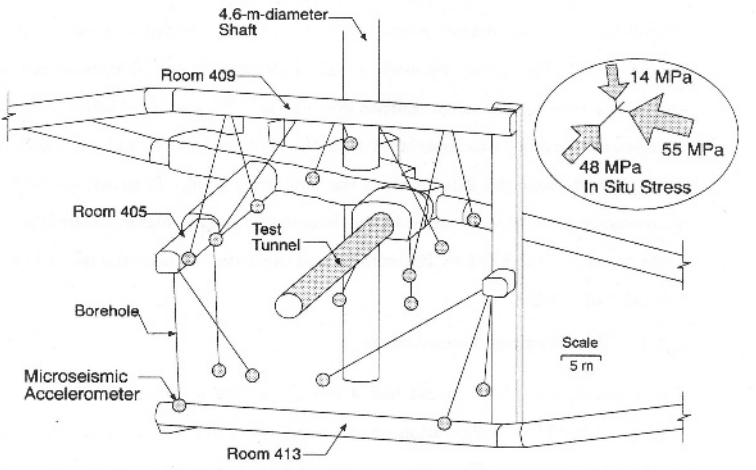

Fig. 11.4. Site of the Mine-by test tunnel with the locations of the AE sensors (filled circles) and the orientation of the principal stresses (Young and Martin 1993).

During excavation of the "Mine-by" tunnel between October 1991 and July 1992, 25,000 events were recorded, of which some 3500 sources were located. **Fig. 11.5** shows only a part of those, namely 359 events, together with the contour of the tunnel in cross-section (upper figure at right-hand side) and in longitudinal view (lower figure) and a photograph of the tunnel after finishing excavation (Young and Martin 1993). The arrows in the upper figure indicate the direction of the maximum principal stress.

The figure shows that most events occur in the roof and floor of the tunnel. In these areas the maximum tangential stresses occur. The zones of maximal AE event density correspond with breakout notches which formed in the roof and in the floor of the tunnel after excavation began and which deepened by spalling during ongoing excavation (see photograph at the left-hand side of **Fig. 11.5**). The notch formed orthogonal to the direction of maximum principal stress σ_1. The spalling planes were parallel to σ_1 and σ_2 and normal to the direction of the smallest principal stress σ_3. Post-test analysis using the moment tensor method which was applied to 37 strong events located at the roof, pointed out that most of the events show a significant non-shear component (Cai et al. 1998).

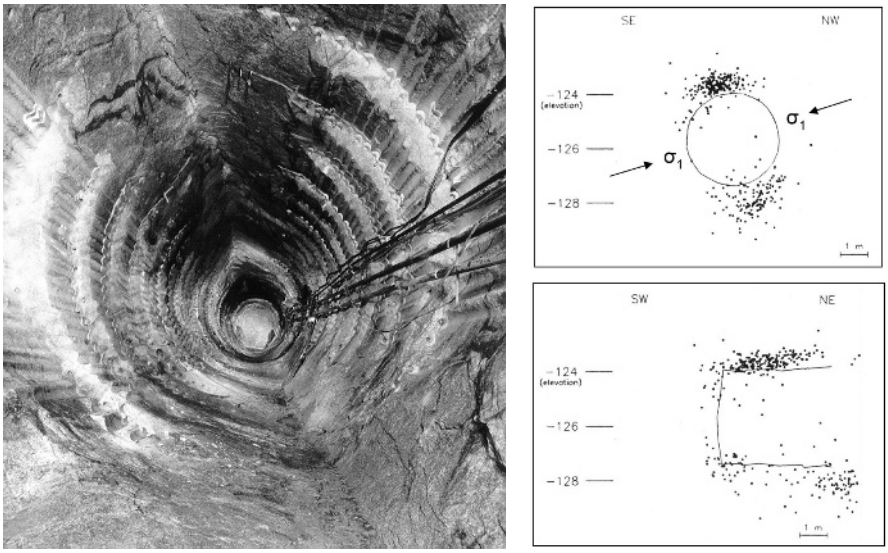

Fig. 11.5. Photograph of the excavated Mine-by tunnel with breakout notches in the roof and floor (left-hand side) and the location of the 359 AE events in two projections (right-hand side; Young and Martin 1993).

Some years after the Mine-by experiment, in June 1997 a sealing experiment was conducted to observe the integrity of different sealing technologies subjected to high hydraulic pressures. Two bulkheads had been constructed and keyed into the tunnel to create a chamber in granite (Room 425 in **Fig. 11.6**), which was pressurized to ambient pore pressure of about 4 MPa. Stresses and displacements as well as microseismicity were monitored around the tunnel and the keys with a 16-channel microseismic system. In addition, AE measurements (up to 250 kHz) have been carried out utilizing 16 borehole sensors around one quadrant of a clay key to give highly detailed cracking information (AE 1 to AE16 in **Fig. 11.6**).

The AE events have been recorded during excavation of a 40 m long tunnel segment in direction of the maximum principal stress σ_1 (see insert at the bottom of the right-hand side in **Fig. 11.6**). The system monitored the AE activity in time periods where no excavation work took place.

Fig. 11.7 shows the location of approximately 15,350 AE events in four successive stages a to d within a time period of about 5 months. The **Fig. 11.7**a-d show a lateral view (at top of each figure), a plan view (below), and a cross-sectional view along the tunnel axis together with the contour of the tunnel and the key before and during excavation of the clay key. The events are marked by black dots.

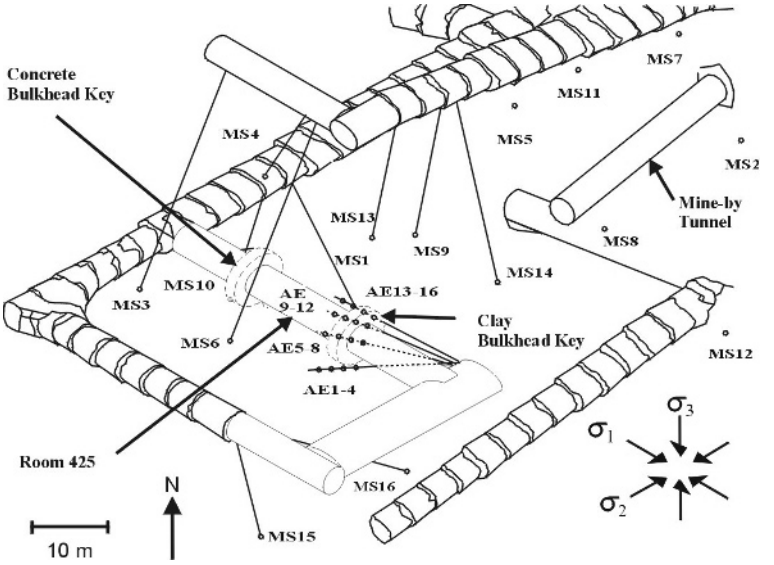

Fig. 11.6. Test site of the sealing experiment with locations of the AE network (AE1 to AE16) and MS network (MS1 to MS16). The orientations of the principal stresses are given in the insert at the bottom of the right-hand side (Collins and Young 2002).

All events are located in a 15 m long region in zones close to the tunnel floor. Only those parts are indicated by events which are orientated toward the sensor array. The opposite part of the floor is acoustically shaded by the tunnel itself. Before excavation of the clay key 1,119 AE events were located within a time period of 9 days (see **Fig. 11.7** a). The majority of the events were located in a time period of 3.5 months. In this time the clay key and the floor segment were completely excavated (see **Fig. 11.7** b and c). The locations cluster around the bottom of the key. Fig. 11.7d shows the events occurring in the time interval directly following the key excavation in the floor region and concentrated around the corners of the key. The gap in AE activity of about 1 m around the clay key in the tunnel floor correlates with low-stress regions as predicted from geomechanical modeling results. From the location of the AE events it can be concluded that the so-called excavation disturbed zone (EDZ) is limited to within 1 m around the clay key. In some regions it is less than 1 m wide (Collins and Young 2002).

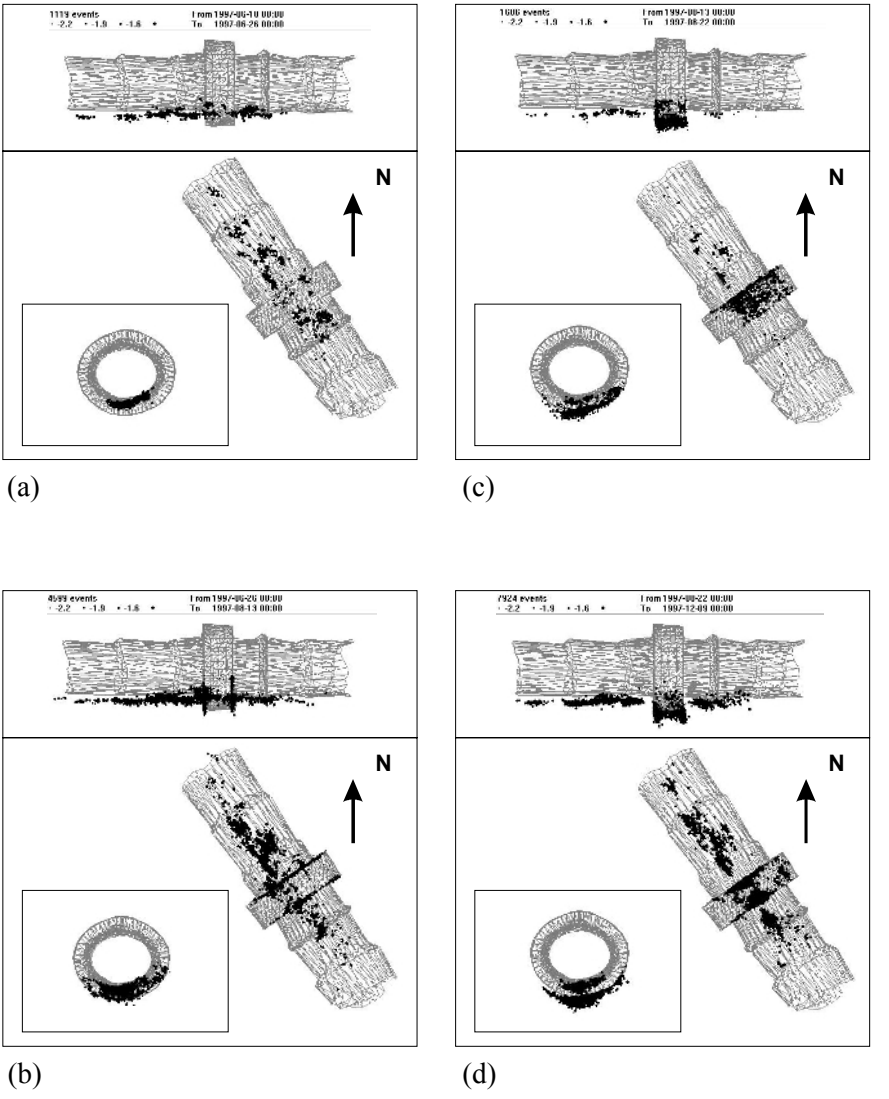

(a) (c)

(b) (d)

Fig. 11.7. Located AE events in four successive stages (a) to (d) in top view and lateral view parallel to the tunnel axis. **a):** before excavation of the clay key; **b)** to **d):** during excavation of the clay key (Collins and Young 2002).

11.4 AE Monitoring in Rock Salt

11.4.1 Measuring Techniques Used in Salt Mines

Like granite, rock salt is a favorable rock for underground disposal and storage of radioactive waste as it is capable of creep deformation without occurrence of fracture in a wide range of the conditions of state. Nevertheless, in presence of high deviatoric stress microcracks are generated. Microcracking touches the integrity of the rock so that permeability might increase which can be directly determined only by analysis of acoustic emission. The focus of this section will be on own work in this field. Therefore, in the following our measuring and evaluation technique is shortly described.

AE Sensors: The AE sensors used in salt mines detect AE signals in a comparatively broad frequency range from 1 to 100 kHz. The sensors are typical AE sensors which use a piezoelectric disk of PZT with broad resonance peak at 70 kHz. Usually, the measured frequencies are in the low frequency range below 30 kHz, only at small distance between the source and receiver below 20 m the high-frequency peak is more pronounced.

Source location: During long-term AE measurement in salt mines, a huge number of events (up to 350 located events per hour) can be detected and, therefore, fast data-acquisition systems are essential to process all data. In-situ location is a standard procedure during data acquisition (Eisenblätter et al. 1998). The locations of AE events are determined by inversion of the travel times of P-waves and S-waves, which are extracted from the signals. This is done in different steps. After pre-processing of the signals by filtering and smoothing operations, in a first step the P-wave onsets are automatically picked using high-quality signals only, i.e. signals with high signal-to-noise ratio.

From these P-wave onsets a first estimation of the source coordinates is made using an iterative least-squares procedure. If the residual error is larger than 0.8 m, the onsets with the largest residues are stepwise eliminated and a new solution is calculated until the residual error drops below the said limit. In order to be able to locate sources outside of the sensor network, we also consider the S-wave onsets. Therefore, we automatically pick the S-wave onsets in the time interval expected due to the result of the location using P-wave onsets only. In the second step of source location, we use the found S-wave onsets together with the remained P-wave onsets. P-wave and S-wave onsets with large residues are again eliminated until

the residual error falls below 0.8 m. Locations are considered valid only if at least ten onsets (P-wave or S-wave) have remained. An effect of such location procedure is that typical working noise with not clearly discernible onsets and, therefore, wrong arrival times are eliminated due to large travel time residuals.

In spite of the complex geometric situation with AE sensors in the vicinity of closely spaced excavations and resultant masking of direct wave propagation paths, we obtain a location accuracy of about one metre in distance up to 50 m around the sensor network, using the described procedure.

Fig. 11.8 shows the signals of a located event in salt rock. In this case, an array of eight AE sensors was used for source location. The onsets of the first signal peaks were automatically determined ("Tr"). In addition to the residual error, the agreement between calculated onsets of the P-wave ("L") and the S-wave ("T") with the observed onsets assesses the quality of location. In this example, the event is located within the sensor network in an undisturbed rock formation and, therefore, the location error is very small and amounts to about 20 cm.

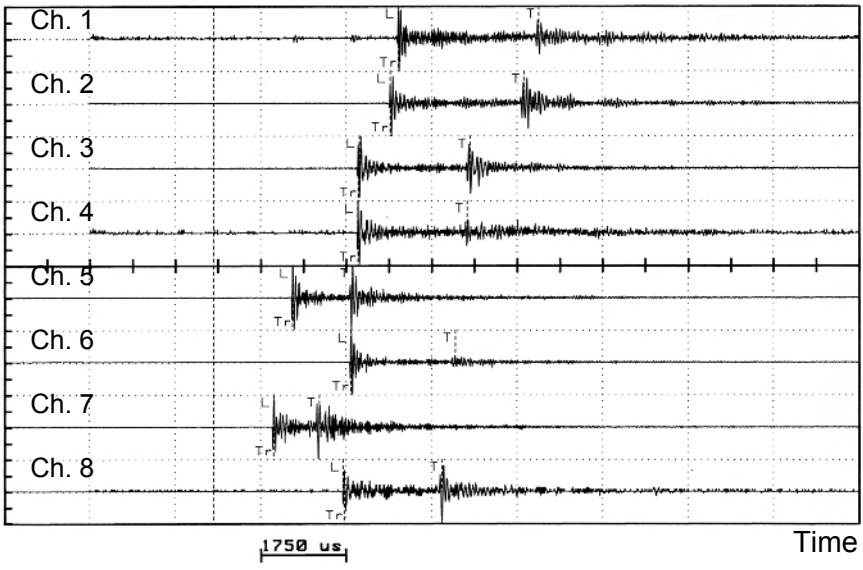

Fig. 11.8. Signals of a located AE event which was detected using 8 borehole sensors in rock salt (Eisenblätter et al. 1998).

AE magnitude and damping coefficient: To determine the magnitude of an AE event, source location is from upmost importance. The maximum

amplitudes A of all sensors in a network and the distances r of an AE source to the sensors are used to determine a measure of signal strength in an analogous way as with magnitude determination in seismology using a relation, which considers geometric wave attenuation as well as attenuation by damping:

$$A(r) \propto \frac{1}{r} \cdot \exp(-\alpha \cdot r) \tag{11.1}$$

where α means the damping coefficient. The amplitudes are specified in the logarithmic decibel (dB) scale. In a semi-logarithmic plot (**Fig. 11.9**) of the product $A \cdot r$ versus r of all sensors a linear relationship is obtained by a straight-line fit to the data. The value of the straight line at the reference distance of 50 m is determined and regarded as the magnitude of the AE event. The slope of the straight line corresponds to the damping coefficient. Generally, damping of high-frequency AE waves is caused by scattering and intrinsic absorption which will mainly occur at grain boundaries or microcracks, by small inclusions of other rock materials, gas, or water which are embedded in many rock formations, and by reflection, refraction, and mode conversion at boundaries between different rock materials.

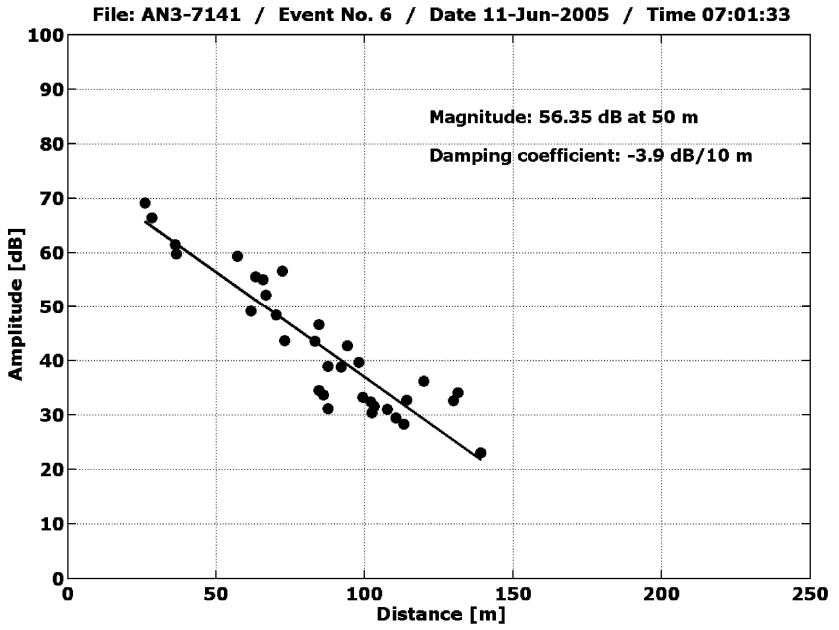

Fig. 11.9. Amplitudes of an AE event measured with 28 sensors corrected for geometric wave dispersion versus distance.

It can be seen from **Fig. 11.9** that travel paths of the signals range from 25 to 140 m. The slope of the line corresponds to a damping coefficient of 3.9 dB per 10 m which corresponds to an attenuation length of approximately 22 m. The attenuation length, in which the peak amplitude corrected for geometric wave dispersion, $A \cdot r/r_0$, is reduced to 37% ($1/e$), is a reciprocal measure of the damping coefficient. In **Fig. 11.9**, the value of this straight line corresponds to a magnitude of 56.35 dB at the reference distance r_0 = 50 m. It should be mentioned, that the damping coefficient and the magnitude are mean values which are determined at various travel paths from the source to the 28 sensors and in various directions.

AE energy: Another fundamental parameter for describing an AE event is the radiated seismic energy. The squared velocity signals of P- and S-waves are used to determine the seismic energy. The data of all sensors are plotted in the same manner as for magnitude determination. The value of the straight line extrapolated to 0 m corresponds to the seismic energy of an AE event. In such plots like **Fig. 11.9**, the deviation of data points from the straight line can be assumed as a measure of the sensor sensitivity in comparison to the mean sensitivity of all sensors. This assumption is true only if a large number of events from the whole monitored area are considered. In this case, source locations and source radiation patterns are not statistically important for the determination of sensor correction. Over long time periods, it is possible to observe a change of sensor sensitivity.

Event clustering: Besides event location, spatial and/or temporal clustering of events can be systematically investigated. Therefore, we developed a systematic search method for spatially and temporally clustered events which was applied on AE events in mines and laboratory measurements.

There are two parameters for this search, a time parameter *Par_t* and a distance parameter *Par_s*. The cluster search algorithm comprises two steps. In the first step, a search for so-called primary clusters starts at each event in chronological order. All the following events within a time interval of duration *Par_t* are examined whether their distance is below *Par_s*.

If at least two events are found which fulfill this condition, these events form together with the initial event a primary cluster of at least three events. This implies that a typical cluster of N events which is highly concentrated in time and space may form up to N-2 primary clusters. Therefore, in the second step all primary clusters with at least one common event are united to one cluster. Typical primary parameters were in the case of our measurements in mines time parameters *Par_t* between 10 minutes and one hour and distance parameters *Par_s* between 0.5 to 5 m. In the case of our measurements on rock specimens *Par_t* ranged between 30 seconds and 10 minutes and *Par_s* ranged between 5 to 50 mm.

In case of clustered events, the fractal dimension of the events is used to find linear, planar, or spatial clusters. The analysis of clusters aims at finding planar clusters, because planar clusters are the most hazardous structures compared with linear or spatial ones. A drop of the fractal dimension from 3 to 2 within a certain time period indicates a concentration and focusing of an initially diffuse spatial event distribution in a plane which forms the nucleus of a fracture.

The dimension of the cluster, the so-called fractal dimension D, can be estimated from the slope of a log-log plot of the correlation integral *C(R)* described by Hirata et al. [1987] as

$$C(R) = \frac{2}{N \cdot (N-1)} \cdot N_{r<R} \tag{11.2}$$

versus R. $N_{r<R}$ denotes the number of all pairs of events having a distance r smaller than R. N is the number of all events within the cluster. If the distribution has a fractal structure, *C(R)* is expressed by

$$C(R) \propto R^D. \tag{11.3}$$

Thus, if the AE events are distributed in a plane, the slope of 2 is expected. On the other hand, linear structures or spatial structures are represented by fractal dimensions of 1 or 3, respectively.

In order to find the mean orientation of a planar cluster the orientation is sought where the volume of a parallelepiped becomes minimal. The edge lengths of the parallelepiped are the mean deviations of the events from the centre of gravity in each coordinate axis. Two rotations around perpendicular axes are necessary to minimize this volume.

11.4.2 AE Monitoring in the Asse Salt Mine

In order to test various sealing designs as technical barriers in a repository in salt formations, a test site was build at the 945-m level in the Asse salt mine. Although the dam construction was stopped prematurely, this test site gave opportunity to monitor acoustic emission during drifting of two galleries.

Fig. 11.10 displays a map of the test site. Galleries and cross-drifts at the 945-m level are drawn in solid lines, the corresponding ones at the 878-m level are given in hatched lines. The grid lines represent a 20-m spacing. The 29 borehole sensors of the network are marked by black dots. The covered area has a linear dimension of approximately 100 m x 160 m.

The AE measurement began with only eight AE sensors (Numbers SE20 to SE27 of **Fig. 11.10**) located in the southern part of the test site. At this time no mining activity was going on at the test site. Thus the starting situation could be monitored in a time period of approximately 4 months.

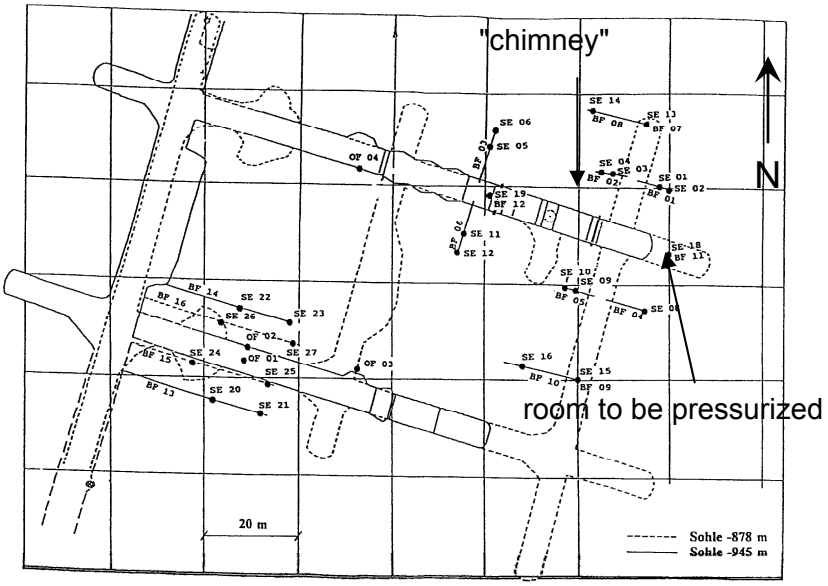

Fig. 11.10. Test site in a salt mine with the network of AE borehole sensors (black dots; Eisenblätter et al. 1998).

The AE locations in that time are shown in **Fig. 11.11** in a top view (x-y-plane) where the plan of galleries at the 945-m level is overlaid to the map of AE events. All events are located in the excavation disturbed zone (EDZ) close to walls of galleries. Only those walls are indicated by events which are orientated toward the sensor array.

After four months, special mining activities began. Within three months, two parallel drifts of 50 m and 90 m length, respectively, were excavated in the northern and southern region of the test site. During the experiment (duration 14 months), a total of 280,000 events were recorded, about 250,000 of these events in the time period of 11 months during and after excavation of the drifts.

During the drifting of new galleries the AE activity remarkably increased. Due to the stress redistribution in the mining area, the AE activity at the older drifts was very much enhanced, too. Caused by the short distance of the sensors from the south gallery, the increase during excavation of the southern drift was even higher.

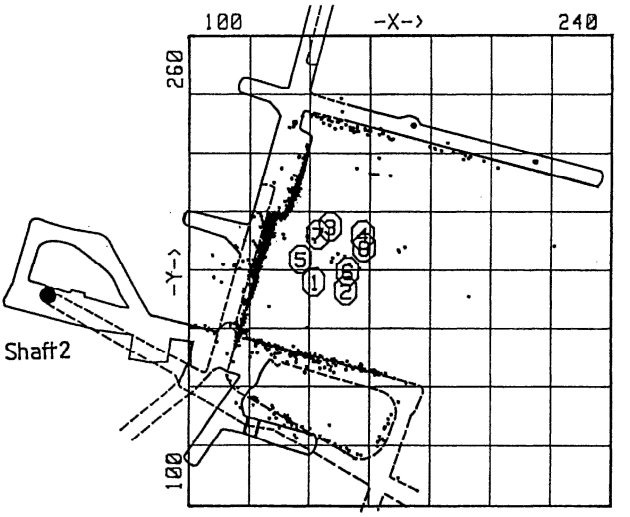

Fig. 11.11. Vertical view with gallery plan and AE sensor array (encircled numbers) and located AE events (small dots; Eisenblätter et al. 1998).

As mentioned above, the test dam in the northern drift itself was not finished when the project had to be stopped. At the end only a part of the overall design up to a chimney-like structure (see **Fig. 11.10**) was finished. The 10 m long room at the end of the gallery was originally planned to be pressurized (see **Fig. 11.10**). It was filled with gravel. In western direction, there follows a wall with sealings and a 7 m long block out of saline-concrete bricks was build. Then the chimney of about 8 m height and 2 m diameter follows which was planned to be filled with bitumina. shows the source location maps at the end of the monitoring period (at the left-hand side) and about one year later (right-hand side) in a top and a side view. Most galleries at both levels of -878 m and -945 m can be recognized. The circles mark the region of the finished part of the test dam. In the lateral views (bottom) the chimney is clearly indicated at the left. Some events occur in the roof region, whereas the right-hand figure shows almost no events in the gallery section filled with brick-work. In this area the sealing wall seems to stabilize the rock around the wall and microcrack formation has stopped.

In conclusion, nearly all events were found in zones close to walls and galleries. These excavation disturbed zones contain many small dilatant microcracks. The width of the zone is about 1 m, measured from the surface of the gallery. **Fig. 11.13** clearly demonstrates this fact in a projection parallel to a drift close to the sensor array. For a better orientation the measured profile of the drift is also shown.

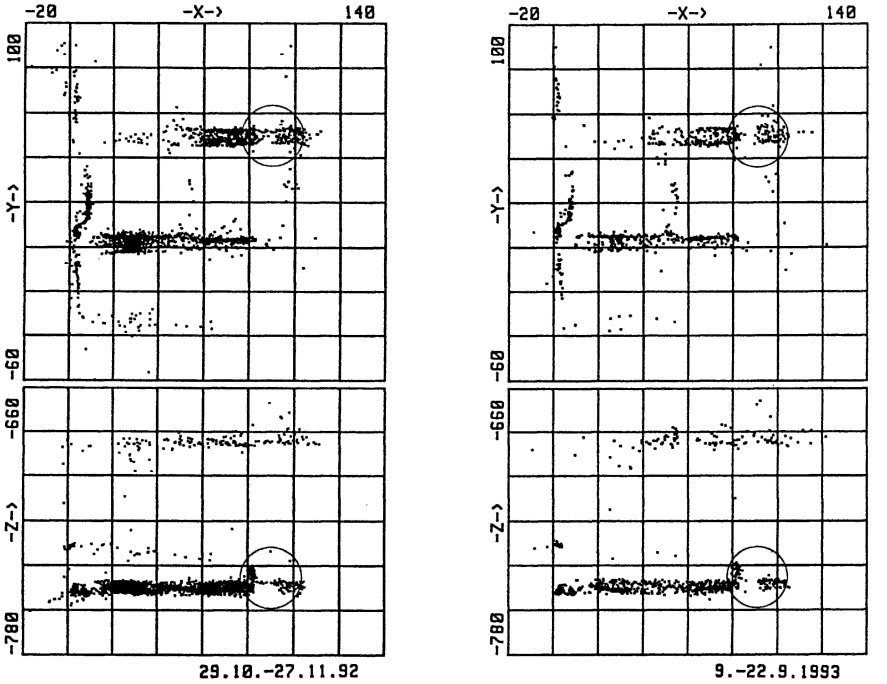

Fig. 11.12. Located events in a top view (top) and lateral view (bottom) for the time periods indicated at the bottom after stopping the experiment (left-hand side) and one year later (right-hand side; Eisenblätter et al. 1998).

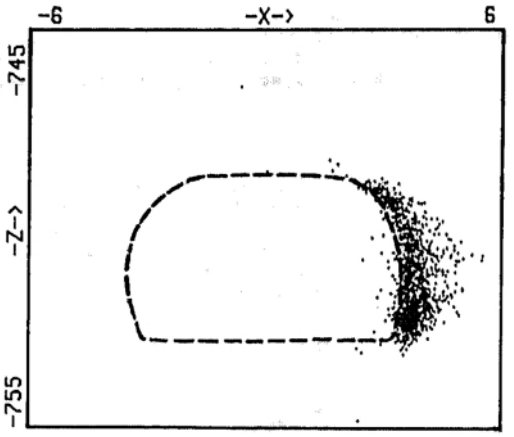

Fig. 11.13. Events in horizontal projection parallel to the gallery axis (Eisenblätter et al. 1998).

11.4.3 AE Monitoring in the Morsleben Repository

The following examples of field studies originate from two sections of the underground repository of Morsleben in a salt mine in northern Germany. Originally, each section was monitored by a network of 24 AE sensors since 1995 and 1997, respectively. Each network covers an area of 150 m x 100 m x 120 m. One of these two networks was recently enlarged to 48 channels and covers now a rock volume of about 250 m x 200 m x 120 m (Spies et al. 2004, 2005).

Central section: In the central section of the underground repository, the borehole sensors are distributed at three excavation levels and installed in 3 to 20 m deep boreholes. The average depth of the monitored volume is 400 m. Mining in these areas continued until the 1960s, but most of the rooms in the rock salt were mined more than 70 years ago.

The aim of the AE measurement is to investigate the micro- and macro-cracking processes which are important for the evaluation of the stability of cavities and the hydraulic integrity of the rock, which is of special interest in the case of an underground disposal of hazardous waste in salt rock.

Fig. 11.14 shows a cross-section through the central part perpendicular to the average direction of strike where cavities in rock salt were mined beneath thick anhydrite blocks. The actual geological situation and the arrangement of cavities is more complicated and strongly varying along strike. Stress redistribution causes high AE activity at the walls of the cavities (in the EDZ), particularly where cavities are close to one another, and at the boundary between rock salt and anhydrite.

But the temporal and spatial occurrence of the events is different. Apart from seasonal fluctuations that may be explained by variations in humidity, the AE activity along the walls of the cavities does not vary with time. Outside the cavities near the anhydrite border, the AE events occurred in clusters. In some cases, such clusters were repeatedly emitted in the same volume; in other cases, significant emission occurred only within a limited time period.

A very distinct cluster of approximately 800 events from the boundary of rock salt and anhydrite was observed within a time period of one day. These events form a planar ring structure with a diameter of approximately 10 m. **Fig. 11.15** (a) displays a plan view onto the plane of the cluster in a rotated coordinate system. A second cluster but with temporally dispersed activity occurred 20 m above the previous cluster (**Fig. 11.15** b). Both clusters are planar and show approximately the same orientation - which is in agreement with the general inclination and strike of the geological layers, see **Fig. 11.14**. By drilling of two boreholes into the center and the pe-

riphery of the first cluster it was confirmed that the cluster emerged at the boundary of rock salt and anhydrite. An open discontinuity was found some centimeters behind the boundary in a thin clay layer which belongs to the anhydrite formation (Spies et al. 2004). The investigated cluster indicates the intermittent growth of a roughly elliptical fracture plane. This is caused by the stresses resulting from the convergence of the mine cavities in ductile rock salt below a stiff anhydrite block. It is very likely that other observed clusters are located at boundaries of rock salt and anhydrite blocks as well. Nevertheless, up to now observed clusters were spatially isolated features and there was no evidence of significant expansion of the clusters.

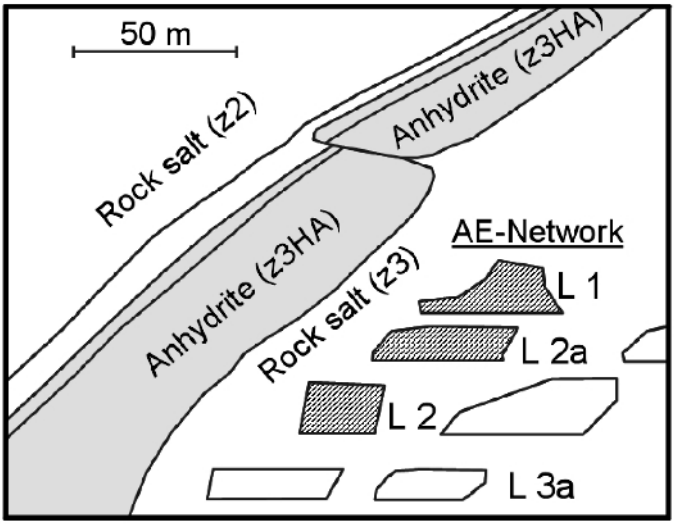

Fig. 11.14. Sketch of geology and geometry of rooms in the central mine segment where the AE network was installed (levels L1 to L3; Spies et al. 2005).

To maintain the integrity of the barrier to the top of the salt deposit and the stability of the rooms for a long time, it is planned to backfill selected rooms in the central part of the mine. The first cavity to be backfilled with salt concrete was Room 1an located at Level 3a (see **Fig. 11.16)** According to the sensor locations, the AE network is able to monitor the roof of the cavity but not the floor and the walls, because all sensors are located above the backfilled cavity. **Fig. 11.16** contains all located AE events in the year 2002 in a narrow spatial interval before starting backfilling of Room 1an. All AE events - about 6900 - in a distance of up to 5 m before and behind the cross-section were plotted. It can be stated that most of the activity

took place near the cavities, with especially high AE activity above the room at Level 2a (see **Fig. 11.16**).

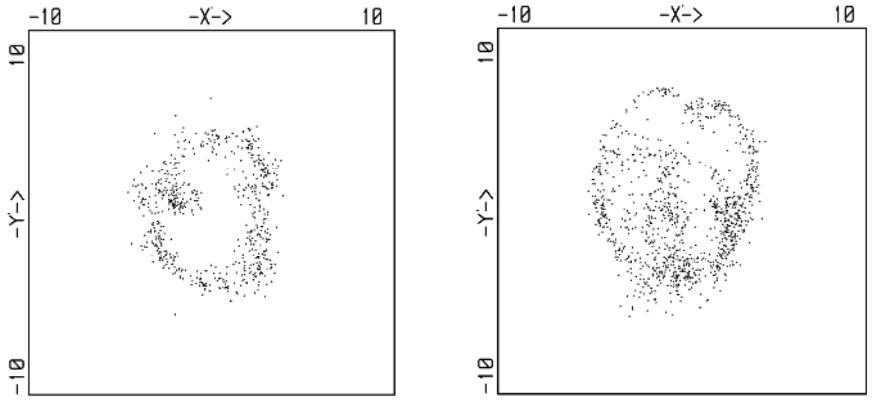

(a) (b)

Fig. 11.15. Plan view on the two clusters at the boundary of rock salt and anhydrite.

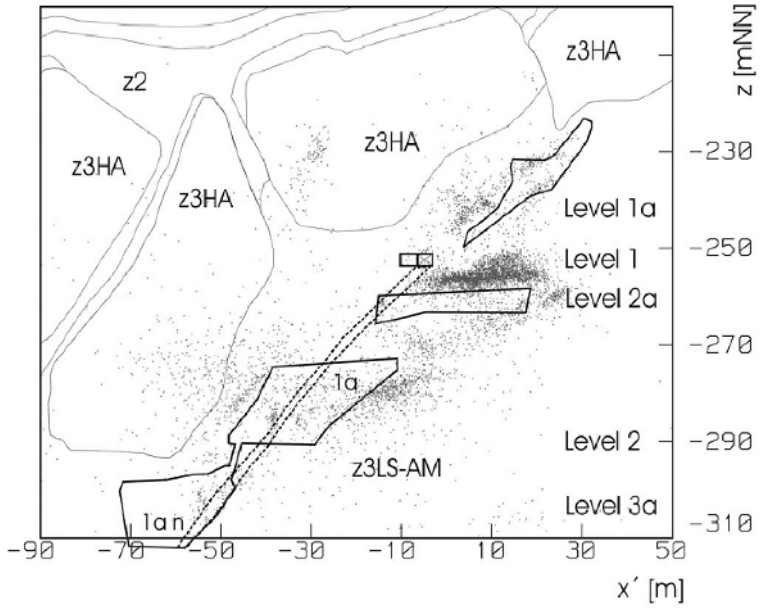

Fig. 11.16. Located AE events in a cross-section through the excavations before backfilling of Room 1an (Spies et al. 2005).

Fig. 11.17 shows the AE activity of a time interval of one week (about 6,200 events) two months after backfilling of Room 1an. Compared with the locations in **Fig. 11.16**, there was strong new AE activity in the roof of the backfilled room, whereas the activity above Level 2a nearly stopped.

Southern section: In the same underground repository, AE long-term monitoring has been carried out in the southern part. This mine section was excavated about 70 years ago in rock salt. **Fig. 11.18** shows a perspective view on this mine section where the long-term AE measurement is conducted. Nuclear waste is stored in the two lower Rooms 2 and 3. A drift is located at a level between the upper and lower rooms. The average depth level of the cavities is about 500 m. The AE sensors are indicated by the dark dots. This figure shows 41,521 located events (light dots) which were located in a time period of approximately 5 years; only the strongest events which were precisely located using at least 30 P- and S-wave arrival times are plotted.

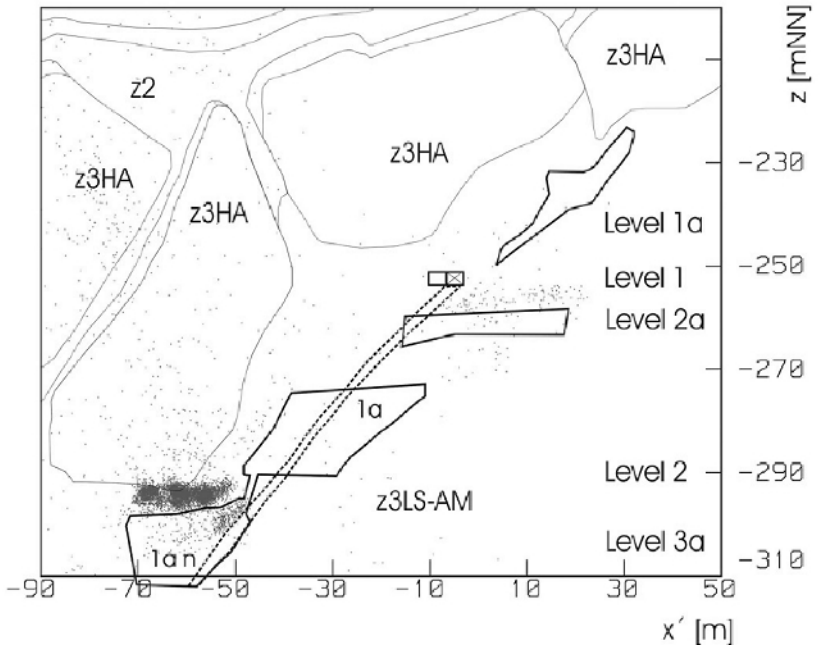

Fig. 11.17. Located AE events in a cross-section through the excavations after backfilling of Room 1an at Level 3a (Spies et al. 2005).

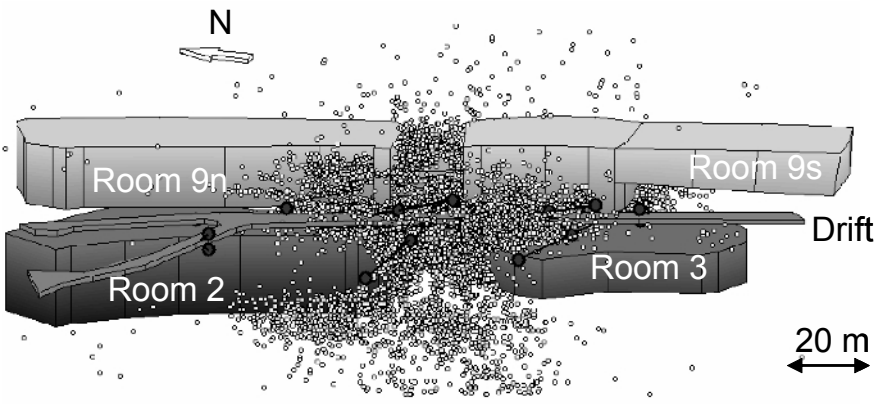

Fig. 11.18. Perspective view of cavities and the main drift at two levels (Rooms 9n and 9s and Disposal Rooms 2 and 3). The black dots indicate the AE sensors in boreholes, the light dots represent the locations of 41,521 AE events (Spies et al. 2004).

It can be seen, that most of the events accumulate in the pillar between Rooms 9n and 9s and in the areas between the upper Rooms 9n, 9s and the lower Rooms 2 and 3. The events in further distance from the galleries are caused by microfracturing at discrete anhydrite layers included in the rock salt formation. These AE events are caused by redistribution of stresses around the cavities which includes the nearby anhydrite layers, leading to stress concentrations.

Fig. 11.19 shows a plan view (horizontal projection) of the site. In this projection the contours of the rooms and the main drift are marked by continuous lines (Rooms 2 and 3) and dashed lines (Rooms 9s and 9n). 24 AE sensors are installed in boreholes of up to 30 m length which were drilled from the drift (gray area) because the rooms are not accessible anymore.

For a more detailed representation of all data including the smaller events, AE locations in the vertical profile S1 are given in **Fig. 11.20**. The location of profile S1 which is a cross-section through the cavities is indicated in the plan view of **Fig. 11.19**. Data from a time interval of one month - about 10,000 events - from a spatial interval of 20 m thickness were projected into the cross-section. The AE locations in **Fig. 11.20** show a dense accumulation of events between the corners of the higher and lower rooms. The reason for the high microcrack activity are "bandlike" structures of high shear stress leading to creep deformation of the rock salt accompanied by dilatancy (Spies et al. 2004).

Finite element calculations using a viscoplastic material law show good correlation between the calculated stresses and the located AE events

(Spies et al. 2004). Zones of high shear stresses and deformations between the excavations (shear bands) coincide well with the zones of dense accumulations of AE events. A detailed moment tensor analysis of the strongest events in the shear bands pointed out, that these events are due to shear mechanisms as well as tensile mechanisms (Manthei et al. 2001a).

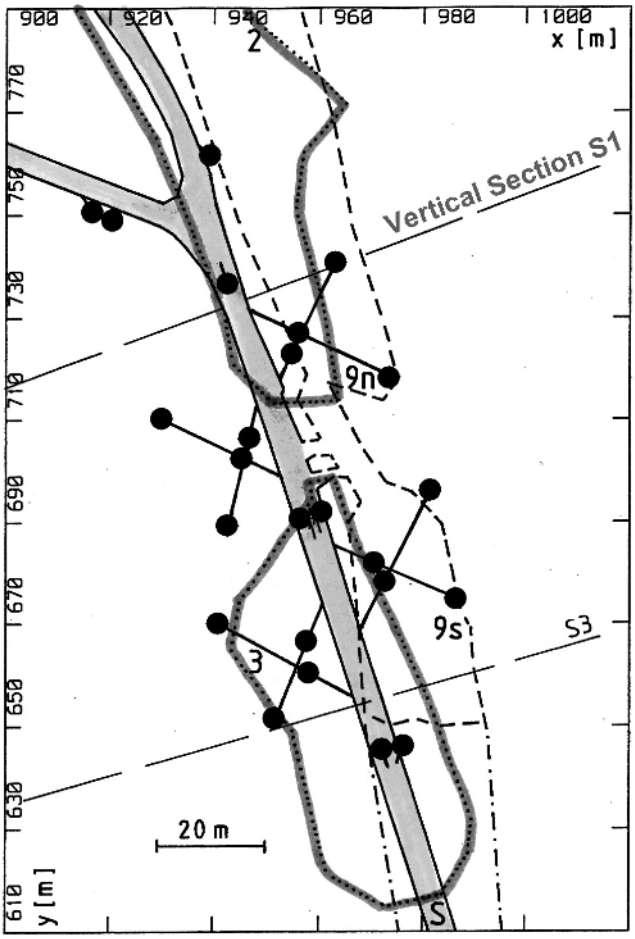

Fig. 11.19. Plan view of the two levels with Rooms 9n and 9s (bold continuous line) and Rooms 2 and 3 (dashed line) and the access drift (grey). The position of the borehole sensors are marked by black dots (Spies et al. 2004).

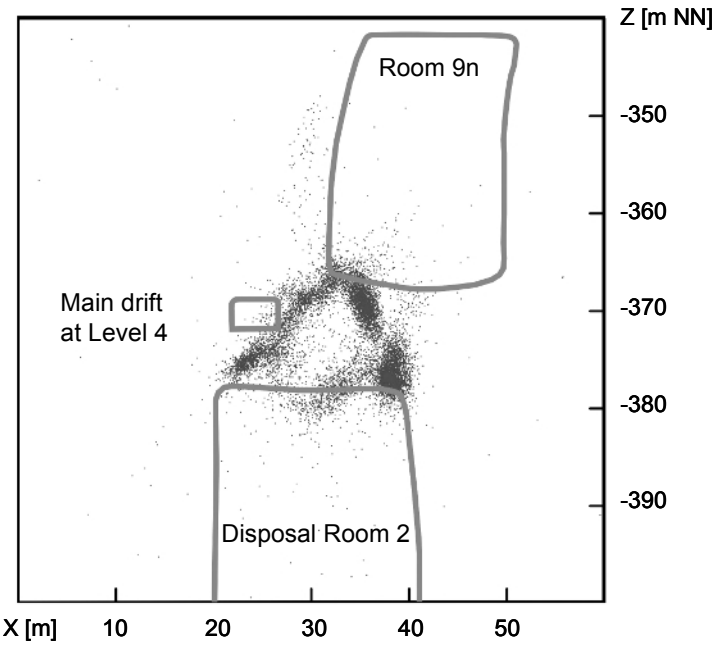

Fig. 11.20. Located AE events in vertical cross section S1 (see Fig. 11.19; Spies et al. 2004).

11.4.4 Attenuation Measurement in the Morsleben Repository

The located AE events between the four upper excavation levels in the central section (see **Fig. 11.14**) are shown in a top view in **Fig. 11.21**. The extension in vertical direction amounts to approximately 120 m. Only strong events (696,278 events) which were precisely located using at least 16 P- and S-wave arrival times are included in this figure. The locations of the AE borehole sensors are plotted as open circles. The events can be roughly separated into two Regions I and II (marked by ovals). The highest density of AE events was observed in Region I outside the AE network above the backfilled cavity (see Subsection 11.4.3 and **Fig. 11.17**). The events in Region II were preferably located along walls of open cavities which are to be backfilled in the future. Compared with Region I, most of the events of Region II occurred 50 m to 100 m higher than in Region I. The AE activity in this area is caused by the ongoing deformation (convergence) in the immediate vicinity of mine cavities and rock boundaries due to dilatancy under deviatoric stress conditions.

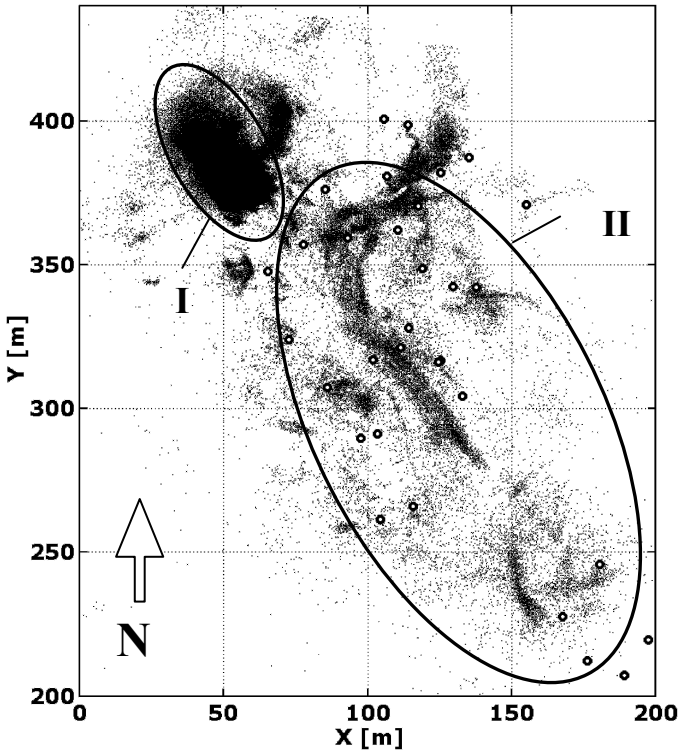

Fig. 11.21. Locations of AE events between November 15, 2004 and August 23, 2005 (696,278 events) in top view.

Fig. 11.22 displays the distribution of the mean attenuation length (see Subsection 11.4.1) of the events in a gray-scale density plot. The plot shows the attenuation length within horizontal cells of 5 m x 5 m; cells containing less than 10 events are displayed as white areas. Again, as in**Fig. 11.21**, Regions I and II are marked by ovals.

The lowest mean attenuation length of about 25 m occurred in Region II in a small zone between y = 250 m and y = 290 m (light grey cells). In this area microcracking still takes place at the contours of closely spaced cavities even a long time after excavation. On the other hand, the highest attenuation length of about 510 m was obtained in Region I above the backfilled cavity outside the sensor network (northwest direction). The highest and lowest attenuation lengths of 25 m and 510 m correspond to damping coefficients of 3.47 dB per 10 m and 0.17 dB per 10 m, respectively. Please remember (see Subsection 11.4.1) that the attenuation length is the reciprocal measure of the damping coefficient.

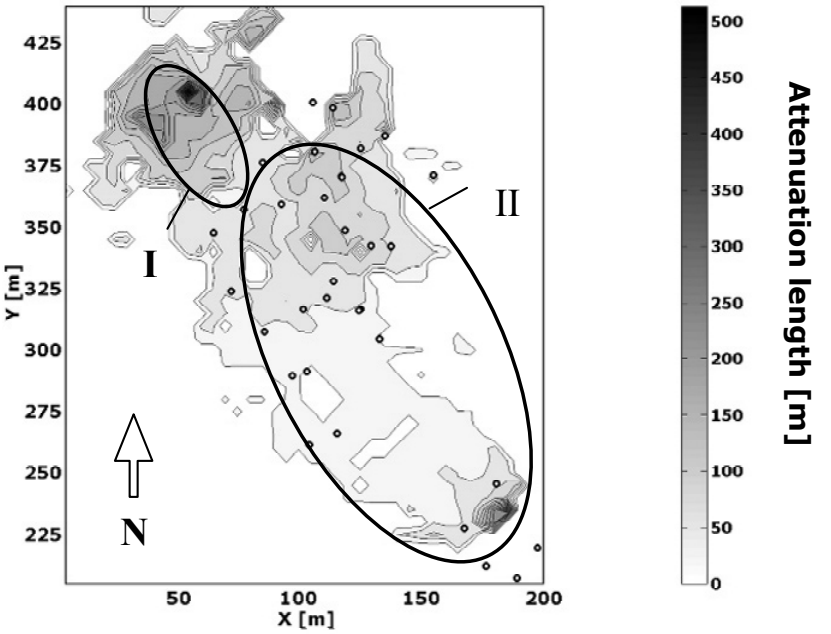

Fig. 11.22. Attenuation length obtained from AE events between November 15, 2004 and August 23, 2005 (696,278 events) in top view.

Scattering at microcracks occurs in regions of deviatoric stress, e.g. in the EDZ with thickness of a few metres at the contour of underground cavities. That may be the reason for the high damping values found in regions of closely spaced cavities like Region II. On the other hand, in Region I with the lowest attenuation, the AE signals mainly propagate through undisturbed rock salt to the AE sensors. It should be mentioned, that this kind of analysis does not consider the dependence of the radiation pattern from the orientation of the fracture plane of the source. However, this effect does not seem statistically important because of averaging over many events with different orientations of the fracture planes located in the whole monitored area.

11.4.5 Discussion

In salt rock, AE activity is detected around open cavities and at the boundaries between different rock types. Creep processes cause high AE activity due to high deviatoric stresses at the walls of the cavities in the excavation disturbed zone. This kind of AE activity is interpreted as ongoing

deformation (convergence) in the vicinity of the open cavities and it is always present until convergence has been stopped, e.g. by backfilling of the open cavities. Apart from seasonal fluctuations by the variation of humidity, the AE activity does not vary with time.

On the other hand, temporally and spatially clustered AE events were observed at the boundary between rock salt and anhydrite. These events are also caused by high deviatoric stresses resulting from the convergence of the ductile rock salt below the stiff anhydrite layer.

Because of its ductile behavior, rock salt is usually capable of performing creep deformation without occurrence of microcracking at stresses below the so-called dilatancy boundary. Above the dilatancy boundary microcracking occurs. Most of the microcracks occur on grain boundaries and form no continuous macroscopic fractures. Deviatoric stresses above the dilatancy boundary result in growth and opening of these microcracks which are mainly responsible for dilatancy and increase of permeability for fluids. Although these microcracks have small dimensions in the order of the grain size (millimeter range or centimeter range) of the rock salt, in the course of time in dilatant zones microcracks may join and form macroscopic fractures especially in pillars between open cavities and in locations of high stress due to edges of rooms which are superposed in different levels. In such highly stressed zones local instabilities may arise as spalling from the walls and roof falls. In this case the excavation disturbed zone migrates into the intact rock salt. The formation of new microcracks will be stopped not before the open cavities are closed by convergence or backfilling. Also around very old cavities active zones of microcracking exist. It should be mentioned that humidity very much accelerates creep in rock salt (Hunsche et al. 1994). This leads to higher AE activity in the disturbed zones around cavities in summer and autumn as compared to the other seasons.

11.5 AE Measurement During Hydraulic Fracturing Tests

The hydraulic fracturing method is able to measure the stress in rock directly. During a hydraulic fracturing test the hydraulic pressure in a sealed volume of a borehole is increased up to fracture initiation in the rock. For the determination of the in-situ stress state the dimension, shape and, orientation of the fractures are of upmost importance. The usually applied methods to determine the orientation of the fracture plane like overcoring, fissure forming with packer or visual inspection using a borehole camera are limited in borehole diameter and very expensive, in particular for hy-

draulic fracturing tests in greater borehole depths. All these methods need clearly discernible fissures at the borehole wall and assume that the direction of fracture propagation is not influenced by changes of the stress state close to the borehole. With other words, a change of the fracture direction due to stress redistribution in further distance from the borehole cannot be observed.

11.5.1 Hydraulic Fracturing Tests with AE Sensors in Separate Boreholes

The test site of the hydraulic fracturing tests was located in the salt mine Bernburg, Germany, at the 420-m level in the Leine rock salt. Eight piezoelectric AE borehole sensors were placed in four separate boreholes (10 m length, 100 mm diameter) around the central injection well.

Fig. 11.23 shows the test site in a perspective view. The western sidewall of a huge chamber of 120 m length, 25 m width, and 30 m height is approximately 20 m away from the access drift. The horizontal injection well (diameter 42 mm, length approximately 12 m) had been made from the side of the access drift, which cuts the barrier pillar. Due to the high degree of excavation the barrier pillar is under high compressional and differential stresses with maximal and minimal principal stresses of approximately 25 and 10 MPa, respectively. Six hydraulic fracturing tests and additional refracturing tests with an injected oil volume of 100 and 300 cm^3, respectively, and injection time intervals of 15 min have been carried out in the injection well, at depths of approximately 1.3, 2.0, 3.4, 5.8, 7.0, and 8.8 m. The AE events were located using P- and S-wave arrival times.

Fig. 11.24 shows an AE event recorded by eight channels during the hydraulic fracturing test in 5.8 m borehole depth. The signals are low-pass filtered with a corner frequency of 17 kHz which is below the resonance frequency of the sensor. The signals show clearly discernible P- and S-wave onsets which are very easy to pick automatically, and the onsets show similar wavelets. During six fracturing and refracturing tests, 735 AE events could be precisely localized with a residual error below 10 cm.

The orientations of the macroscopic fracture planes as indicated by AE measurement were compared with independent stress calculations. These FEM calculations based on long-term surface subsidence measurement and measurement of underground convergence. **Fig. 11.25** shows the result of these stress calculations in a vertical cross-section through the test site (upper figure).

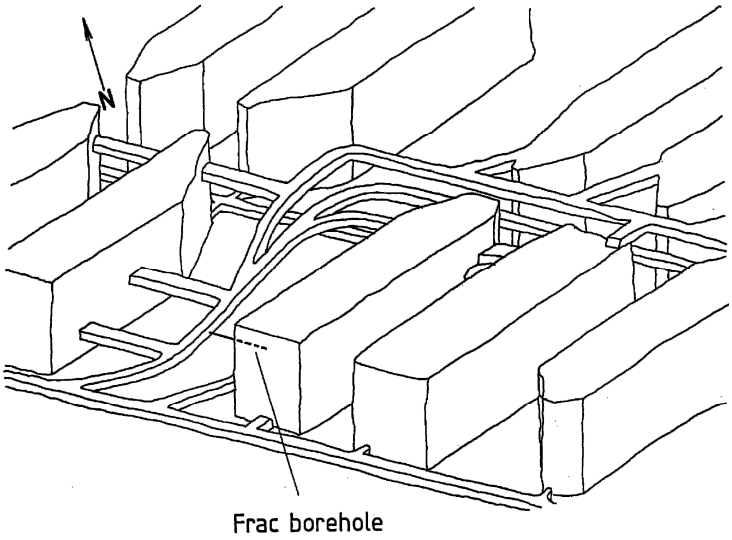

Fig. 11.23. Test site of hydraulic fracturing series at the 420-m level in the vicinity of huge chambers (Manthei et al. 2001b).

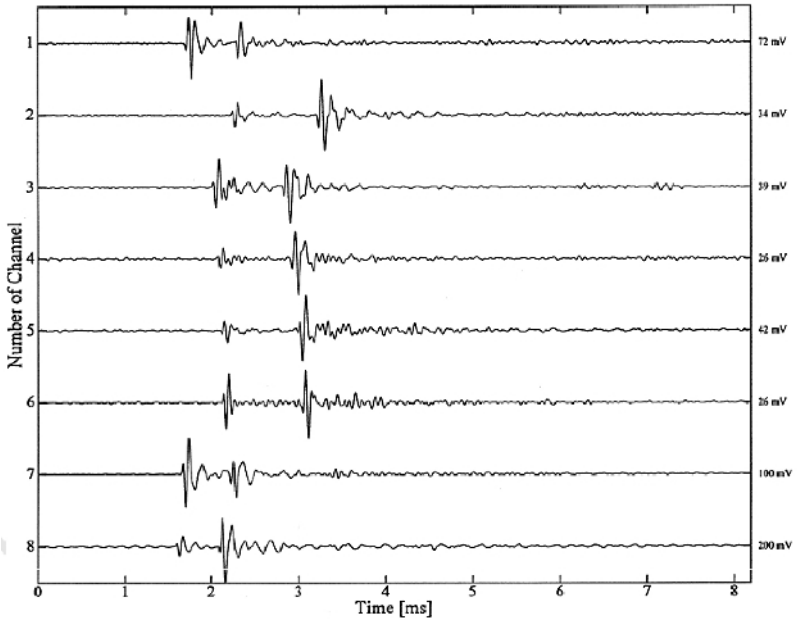

Fig. 11.24. Signals of an AE event from the hydraulic fracturing test in 5.8 m borehole depth. The traces of the eight channels are scaled to their maximum (Manthei et al. 2001b).

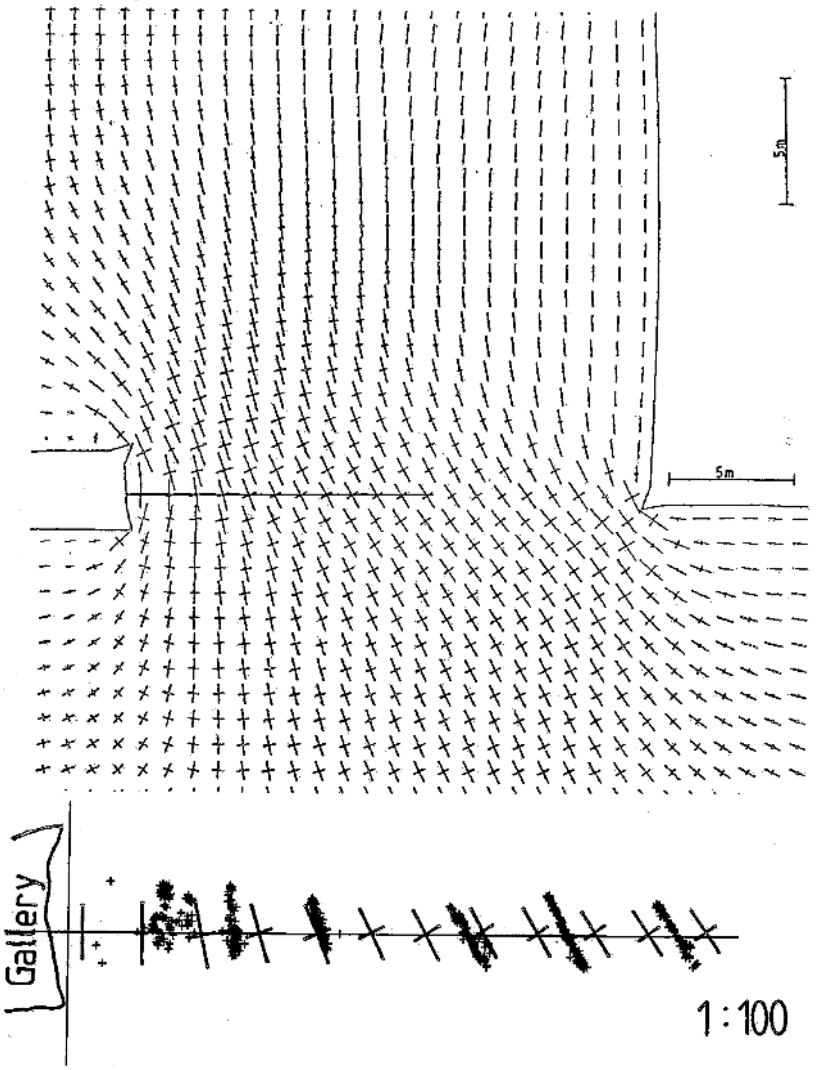

Fig. 11.25. Calculated stress field (top) around the test site together with the contours of the access drift (left-hand side) and the huge chamber (right-hand side). Enlarged view (bottom) of the stress field (crosses) along the injection well and the located AE events (Manthei et al. 2001b).

The horizontal line represents the injection well. A part of the contour line of the huge chamber can be seen at the right-hand side. At the left-hand side, the contour line of the access gallery is indicated. The crosses represent the orientations of the calculated principal stresses around the test site. It can be seen that in the vicinity of the free surfaces of the rooms

(wall, floor and roof) only the stress component parallel to the surface exists. In a larger distance from the surface the second stress component appears.

Fig. 11.25 shows at the bottom the orientation of the principal stresses along the injection well and the located events in the enlarged projection to the y-z plane (side view).

The orientation of the fracture planes as measured by acoustic emission agrees remarkably well with the orientation of the calculated principal stresses. It can be seen that the direction of the fracture planes appears to coincide with the maximum principal stress. Whereas in smaller borehole depths up to 2 m the macroscopic fracture planes are parallel to the gallery wall and perpendicular to the horizontal injection well, the fractures in greater depths are striking in y-direction at approximately 63°. This fact is observed for all fractures. These results confirm that fractures are oriented normal to the minimum principal stress (Manthei et al. 2001b).

11.5.2 Hydraulic Fracturing Tests with AE Sensors in the Same Borehole

In order to measure the crack orientation and extension, AE sensors are usually positioned in separate boreholes around a central borehole (see Subsection 11.5.1) where the fracturing tests take place. Recently, a new borehole tool was developed which is able to do the same job utilizing only one borehole. This borehole tool includes the hydraulic pressurization unit with the AE sensors. Due to the same distance between injection interval and sensor arrays the sensitivity of AE registration is always the same independent of the borehole depth. It is possible to trace back the realistic fracture propagation in distances up to 20 times of the borehole diameter. Other expensive inspection methods are not needed.

Since 1996, more than 100 fracturing tests have been performed on rock salt and anhydrite in horizontal as well as in vertical boreholes in different salt mines. In the following, after a short description of the experimental set-up one example will illustrate the capabilities of the new borehole tool.

The new borehole tool which was developed by IfG Leipzig and GMuG Ober-Mörlen in Germany (Manthei et al. 2003) is shown schematically in **Fig. 11.26**. It consists of two parts - the hydraulic pressurization unit in the middle and two AE sensor arrays at both ends. It is applicable to borehole diameters between 98 mm and 104 mm. The overall length of the borehole tool is about 2 m. Each sensor array includes four AE sensors in a cross-section perpendicular to the borehole axis. The distance between the AE arrays is approximately 1.5 m.

The sensors with integrated preamplifiers are placed in a common housing which is screwed to the pressurization unit. They are pressed pneumatically against the borehole wall. The preamplified signals are supplied to an 8-channel transient recorder card which is controlled by a portable personal computer. The transient recorder card (sampling rate 5 MHz, resolution 14 bit) is read each time a signal passes the trigger threshold. The borehole pressure and the pressure which is applied to the packer are measured using pressure cells. The signals of the pressure cells are digitized usually each second and stored on the hard disk of a notebook.

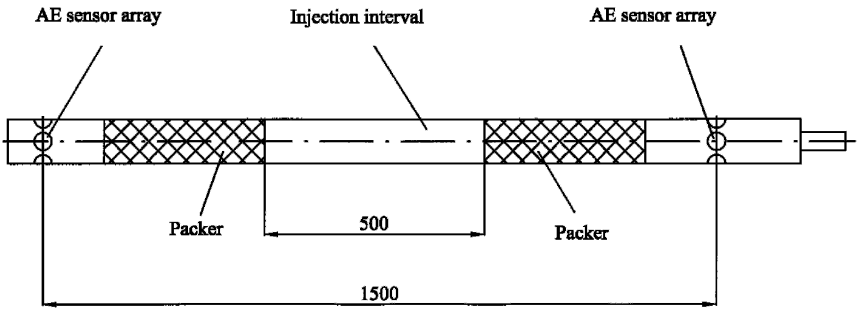

Fig. 11.26. Hydraulic fracturing tool (schematically; Manthei et al. 2003).

Fig. 11.27 gives an overview on all hydraulic fracturing tests in the salt mine Bernburg performed in a 15 m long horizontal borehole at depths of 2 m, 4 m, 7 m, and 10.4 m. The location of the sensor arrays and the injection interval is indicated by means of circles and rectangles, respectively. The y-axis is parallel to the injection well. Approximately 15,000 located events are shown in a top view (at the left-hand side) and in a lateral view (at the right-hand side). 11,216 of these events could be localized during the fracturing test in 2 m and 4 m borehole depths. On the contrary, in larger borehole depths fewer events (3,696) were located in spite of the fact that the same oil volume was injected. This observation may be explained by larger deviatoric stresses close to the contour of a gallery. The extension of the fractures is nearly independent of borehole depth.

In the following, the fracturing test in 4 m depth will be described in more detail. More than 5,100 AE events could be located during this test. After rotation of the coordinate system a nearly perfect plane fracture appears in the x'-y' plane in **Fig. 11.28**. The located events mark a clearly discernible fracture plane. The fracture initiated in the middle of the injection interval and propagated in radial direction transverse to the injection well. Most events are located at the crack tip (x'-z' plane). This is due to

the fact that during fast crack propagation at the beginning of each fracture phase AE events are emitted so frequently that they overlap each other and, therefore, cannot be located.

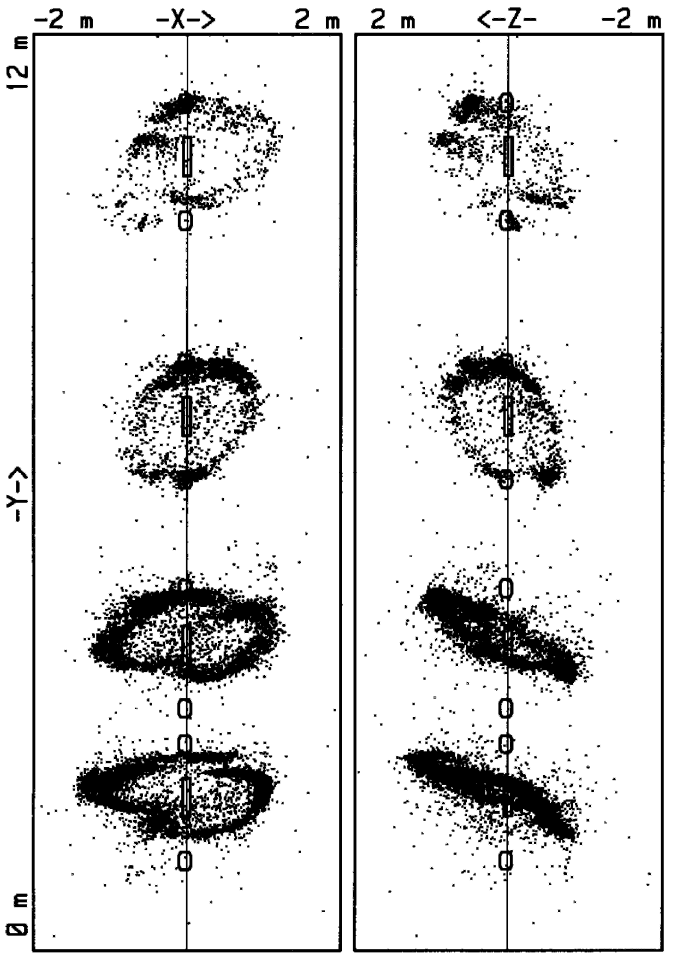

Fig. 11.27. Located AE events of a hydraulic fracturing series at the 500-m level of the salt mine Bernburg in projection to two coordinate planes. The location of the AE sensor arrays and the injection interval is indicated by means of circles and rectangles, respectively. The y axis is parallel to the injection well (Manthei et al. 2003).

Generally, the borehole tool is applicable in all rocks which show spontaneous and fast crack formation. Difficulties will occur in layered or multiply jointed rocks, because such rock types show a high attenuation and strong absorption of the elastic waves. The borehole tool was developed

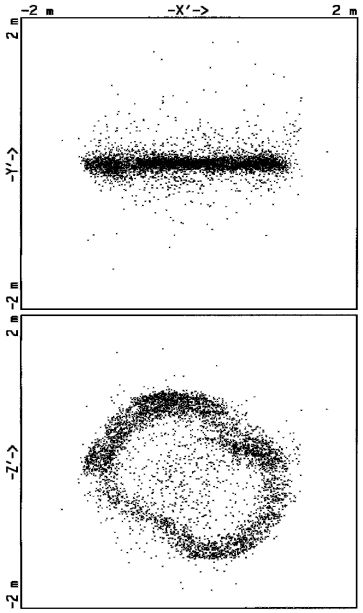

Fig. 11.28. Located AE events of a hydraulic fracturing test in 4 m borehole depth in projection to the rotated coordinate plane (Manthei et al. 2003).

and applied in underground waste disposal research projects where knowledge about the stress state in rock was needed to characterize strength, tightness, and deformation behaviour of the host rock which has to isolate hazardous radioactive or chemical wastes from the biosphere for a long time.

On the other hand, hydraulic fracturing measurements deliver valuable data like absolute magnitude and orientation of the minimum principal stress for the validation of structural models which are used to calculate the geomechanical evolution of the long-term stability of mines.

The borehole tool is also useful where stress measurement is needed to evaluate safety aspects in operating mines as well as to support the licensing procedure for sites of underground waste disposal. Further promising applications relate to tunnel excavation in rock and to the construction of geotechnical barriers like dams.

11.6 AE Measurements in Laboratory Studies on Rock Specimens

11.6.1 Overview on AE measurements on Rock Specimens

We start with an extensive literature overview on the applications of AE measurement on rock specimens in laboratory studies in the last 45 years as given in **Table 11.3**. This table is subdivided according to measurement and evaluation methods applied into three headings: Event counting and similar methods for measurement of AE activity like ring-down counting is the simplest applied method. This method is used to investigate the inelastic processes as for instance microcracking going on during deforma-

tion of rock. The so-called Kaiser effect is used to determine in-situ rock stress (Heading A).

To improve the understanding of the fracturing process by following up the spatial and temporal variation of hypocenters during microcrack formation, source location has to be used which necessitates four sensors at least (Heading B).

The most advanced methods applied to AE measurement in laboratory studies on rock specimens try to characterize the source mechanism of precisely located AE events analysing fault-plane solutions or calculating the moment tensors (Heading C).

Table 11.3. Overview on AE measurements on rock specimens

Reference	Rock type	Loading	Evaluation method
A: Event counting, inelastic deformation, statistical analysis, Kaiser effect			
Mogi [1962]	Mannari granite Inada granite Kitagisima granite Manazuru andesite Kitakanraku andesite Pumice	Bending	Event counting, statistic of AE
Goodman [1963]	Berea and Boise sandstone, quartz diorite	Uniaxial compression	Event counting, Kaiser effect
Brown and Singh [1966]	Bedford sandstone, Crab Orchard limestone, Chelmsford granite	Uniaxial tension loading,	Event counting, static fatigue
Scholz [1968b]	Westerly granite, Rutland quartzite, Calcite marble, Colorado rhyolite tuff, Pottsville sandstone, San Marcos gabbro	Uniaxial compression, Triaxial compression	Event counting, statistic of AE
Scholz [1968c, d]	Westerly granite, San Marcos gabbro	Uniaxial compression, Triaxial compression	Event counting, statistic of AE
Alheid and Rummel [1977]	Sandstone, Marble	Triaxial compression	Event counting, frictional sliding
Lockner and Byerlee [1977a]	Westerly granite, Weber sandstone	Triaxial compression	Source location, statistic of AE
Weeks et al. [1978]	Westerly granite	Triaxial compression	Source location, statistic of AE

Reference	Rock type	Loading	Evaluation method
A: Event counting, inelastic deformation, statistical analysis, Kaiser effect (continued)			
Kurita and Fujii [1979]	Granite	Uniaxial compression	Kaiser effect
Rong [1979]	Jinan gabbro, Changpin granite	Triaxial compression	Event counting, fracture strength
Sobolev et al. [1980]	Pyrophyllite	Uniaxial compression	Amplitude and frequency analysis
Ohnaka and Mogi [1982]	Shinkomatsu andsite, Mannari granite	Uniaxial compression	Event counting, statistic of AE
Shimada et al. [1982]	Mannari granite, Murotomisaki gabbro, Horoman dunite, Akaishi eclogite	Triaxial compression	Event counting, fracture strength
Lockner et al. [1982]	Graywacke Greenstone	Triaxial compression	Source location, statistic of AE
Holcomb and Costin [1986]	Westerly granite	Uniaxial compression	Kaiser effect
Hirata [1987]	Murata basalt	Triaxial compression	Event counting, statistic of AE
Hatton et al. [1990]	Loch Uisg microgranudiorite	Tensile loading	Event counting, statistic of AE
Glaser and Nelson [1992]	Dolostone Granite	Bending	Event counting, event classification
Cox and Meredith [1993]	Gosford sandstone	Uniaxial compression	Event counting, statistic of AE
Hashida and Takahashi [1993]	Iidate granite	Fracture toughness test	Event counting, fracture toughness
Hashida [1993]	Iidate granite	Fracture toughness test	Event counting, fracture toughness
Weiss [1997]	Granular ice	Uniaxial compression	Event counting, statistic of AE
Lavrov et al. [2001]	Rock salt, Clay	Uniaxial compression	Event counting, Kaiser effect
Lavrov et al. [2002]	Limestone	Uniaxial compression	Event counting, Kaiser effect

Reference	Rock type	Loading	Evaluation method
A: Event counting, inelastic deformation, statistical analysis, Kaiser effect (continued)			
Seto et al. [2002]	Inada granite, Shirahama sandstone	Uniaxial compression	Event counting, Kaiser effect
B: Event location, fracture process, hydraulic fracturing			
Scholz [1968a]	Westerly granite	Uniaxial compression	Event location, fracturing process
Lockner and Byerlee [1977b]	Westerly granite, Weber sandstone	Triaxial compression	Event location, rock failure mechanism
Lockner and Byerlee [1977c]	Weber sandstone	Confining pressure and differential stress	Event location, fluid-induced fracturing
Rothman [1977]	Crab Orchard sandstone	Uniaxial compression	Event location, rock failure mechanism
Sondergeld and Estey [1981]	Westerly granite	Uniaxial compression and cycling	Event location, event clustering
Majer and Doe [1986]	Rock salt	Triaxial compression	Event location, fluid-induced fracturing
Manthei and Eisenblätter [1989]	Rock salt	No confining pressure	Event location, fluid-induced fracturing
Masuda et al. [1990]	Inada granite	Triaxial compression	Event location, rock failure mechanism
Masuda et al. [1993]	Inada granite	Triaxial compression	Event location, fluid-induced fracturing
Zietlow and Labuz [1998]	Sioux quartzite, Berea sandstone, Charcoal granite, Rockville granite	Three-point bending	Source location, fracture zone
Pusch and Alkan [2002]	Rock salt	Triaxial compression	Source location, dilatancy
Alkan et al. [2003]	Rock salt	Triaxial compression	Source location, crack visualization
C: Event location, fault-plane solution, moment tensor analysis			
Sondergeld and Estey [1982]	Westerly granite	Uniaxial compression and cycling	Source location, fault-plane solution
Kuwahara et al. [1985]	Abukuma granite	Uniaxial and biaxial compression	Source location, fault-plane solution

Reference	Rock type	Loading	Evaluation method
C: Event location, fault-plane solution, moment tensor analysis (continued)			
Nishizawa et al. [1985]	Yugawara andesite	Uniaxial loading	Source location, fault-plane solution
Kusunose and Nishizawa [1986]	Andesite Granite	Uniaxial compression	Source location, fault-plane solution
Kranz et al. [1990]	Inada granite	Triaxial compression	Source location, fault-plane solution
Satoh et al. [1990]	Oshima granite	Triaxial compression	Source location, fault-plane solution
Shah and Labuz [1995]	Charcoal granite	Uniaxial loading	Source location, moment tensor analysis
Ishida et al. [1997]	Granite	Triaxial loading	Source location, fault-plane solution
Zang et al. [1998]	Aue granite	Uniaxial compression	Source location, focal mechanism, fracture zone
Zang et al. [2000]	Aue granite	Uniaxial compression	Source location, focal mechanism, fracture zone
Lei et al. [2000]	Hornblende schist	Triaxial compression	Source location, fault-plane solution, b-value
Sellers et al. [2003]	Quartzite	Uniaxial compression	Source location, moment tensor
Manthei [2005]	Rock salt	Triaxial compression	Source location, moment tensor

11.6.2 Event Counting, Kaiser Effect, b-Value, and Time Statistic

Event counting: The simplest one can easily perform is the counting of AE events utilizing only one AE sensor which is directly attached to the rock specimen. Generally, there is a good correlation between AE activity and deformation. So, AE is useful in analyzing fracture processes in rock. Some of the first laboratory AE measurements were carried out by Mogi [1962]. He found similarities between AE activity and earthquake occurrences. Many of the early laboratory studies on rock specimens were also aimed at studying these similarities. The article of David A. Lockner [1993] on the role of acoustic emission in the study of rock fracture gives

an excellent insight into common relations both in earthquake and AE studies. He writes: "*The impetus for this research has been to develop methods of predicting failure that could be applied to the problem of earthquake prediction. While this goal has not yet been achieved, significant advances in our understanding of brittle fracture have occurred along the way*" (Lockner 1993). In the context of earthquake prediction, parameters to be considered include time statistic, amplitude statistic, and source location.

Many early papers in the 1960s and 1970s have reported on the correlation between inelastic strain rate and AE activity, which was measured either by the AE event count or by the so-called ring down count, i.e. the number of times a burst signal crosses the detection threshold. Unconfined or confined loading tests of rock specimens were performed in order to find out how AE activity increases with deformation and whether a characteristic correlation exists between AE activity and inelastic strain. Such typical curves can be used for the indication of existing damage in the rock specimen by applying load well below specimen failure. On the basis of simple event counting, the relation of the AE activity and inelastic strain can be compared between specimens out of the same rock type from different provenance, between different kinds of rock type, and between rock types of different structure (e.g. heterogeneity, see Mogi 1962).

Kaiser effect: The Kaiser effect is a well-known phenomenon in AE studies. Kaiser [1953] discovered with repeated loading of tensile specimens that metals retain a memory of the previously applied stress. The Kaiser effect can be defined as the absence of acoustic emission at stress levels below the previously applied maximal stress. It can be used to provide useful information about irreversible processes in a particular rock. The Kaiser effect applies to deformation processes like plastic deformation and crack growth, whereas frictional motion between the flanks of existing cracks may generate repeated acoustic emission by stick slip processes during repeated loading of a specimen. This effect is to be seen also during repeated unloading of specimens containing cracks.

The Kaiser effect is often used to determine the so-called in-situ stress, i.e. the stress at the place in the rock mass the cores came from. Hardy [1989] reviewed theory and application of the Kaiser effect on rock specimens. At the 5th International Workshop on the Application of Geophysics in Rock Engineering in 2002, standards about terminology, apparatus, procedure, evaluation of results, and reporting in the application of the Kaiser effect for in-situ stress measurement were published by a working group for estimating the primary state of stress in a rock mass using the AE technique (N.N. 2002). For interested reader more insight in the application of

the Kaiser effect is given in several reviews and articles (e.g. Holcomb 1993). It should be noted that the Kaiser effect is not valid for all rock types (Lockner 1993). Some investigations show that AE starts well before reaching the maximal load level the specimen has experienced before.

b-value: In a statistical analysis of microcracking in rock, an important relationship is the frequency-magnitude distribution. In the simplest case of measurement with only one AE sensor, the magnitude is just the logarithmic peak amplitude. In case of a multi-channel measurement it makes sense to refer the AE event magnitude to a fixed distance from the AE source as shown in Subsection 11.4.1. The peak amplitude is usually given in the logarithmic decibel scale with reference to amplitude A_0 of 1 μV (Dunegan scale) before amplification. The reference distance r_0 has to be adapted to the specific application. Whereas in our measurements in mines we used a distance of 50 m as reference, in our laboratory measurements we used a reference distance of 100 mm.

Very often the number N of all events with peak amplitude above a level A, i.e. the cumulative event number, shows an exponential decay with increasing peak amplitude A.

$$N \propto \exp(-\beta \cdot A) \tag{11.4a}$$

Therefore, a double-logarithmic plot of log$N$ versus log$A$ shows a linear relationship of log$N$ versus log$A$:

$$\log N = a - b \cdot \log A \tag{11.4b}$$

a and b are constant. This relation is the same as the famous Gutenberg-Richter relation (Gutenberg and Richter 1954) for the frequency of earthquakes if log$A$ is replaced by the earthquake magnitude M (which is a logarithmic measure of the amplitude, too).

In the above Eq. 11.4 the constant a characterizes the mean activity level in the local region investigated. The constant b characterizes the relative frequency of low-amplitude events in comparison to high-amplitude events. A small b corresponds to a large portion of high-energy events, and vice versa: a large b corresponds to a large portion of low-energy events. In the case of earthquakes the a- and b-values are thought to be typical for the local region investigated.

In a distributive application Eq. 11.4 becomes:

$$\log n = m \cdot \log(A) \tag{11.5}$$

with $m = b + 1$, where n represents the number of events in the amplitude interval $[A, A + \mathrm{d}A]$.

It should be noted, that in AE measurement as well as in MS measurement the frequency-magnitude relation sometimes shows curvature, so that the classical Gutenberg-Richter *b*-value is not always adequate (Kijko et al. 1993). In this case the frequency-magnitude relation can be expressed by

$$\log N = a - b(M - M_{\min})^C \tag{11.6}$$

where M_{min} is the threshold of completeness and the parameter C controls the curvature. In a multichannel measurement, the threshold of completeness means the lowest magnitude an event should have to be localized by a sufficient number of channels. If the AE event is located outside the sensor network, the threshold of completeness increases with increasing mean distance between source and sensor. The higher this distance, the higher the threshold of completeness. If the event originates inside the sensor network, the level of completeness increases with increasing distance between sensors. For $C = 1$ the curvature of Eq. 11.6 disappears and the equation takes the same form as the classical relation of Gutenberg-Richter.

Time statistic: Up to now, the time statistic of AE events was investigated only very seldom. Nevertheless, one of the earliest writers in this field, Mogi [1962] already presented an extensive publication on the topic of time statistic of AE events observed on granite and pumice specimens loaded in bending experiments. He evaluated the time intervals τ between successive AE events at different stress levels. For the frequency $n(\tau)$ of these time intervals he found

$$n(\tau) \propto \exp(-\beta \cdot \tau) \tag{11.7}$$

where the constant β diminished with increasing stress level. From these results Mogi deduced that the events occurred independently and at random (Poisson process).

Mogi already knew examples for induced events from the aftershock series of earthquakes after a large main shock and from clusters of volcanic earthquakes. After the main shock at $t = 0$ the event rate of aftershocks has been found to decay with time according to an empirical relation

$$n(t) \propto t^{-p} \tag{11.8}$$

which is known as Omori's power law. Here p is constant, and $n(t)$ denotes the frequency of aftershocks occurring in a time interval $[t, t + \mathrm{d}t]$.

Scholz [1968d] showed that after the ultimate fracture of rock specimens of Westerly granite and San Marcos gabbro the AE rate obeyed

Omori's power law (Eq. 11.8). In this case an AE event was induced by a previous one (Polya process). Hirata [1987] analyzed AE signals that occurred while an unconfined basalt specimen was held at a constant high stress (at about 85% of ultimate stress). Individual bursts of events were treated as mainshock-aftershock sequences. He observed in most cases a transition from obeying an exponential decay law (Eq. 11.7) to Omori's power law (Eq. 11.8). Lockner [1993] re-evaluated some of Hirata's results.

Interestingly, both processes were also observed in metals (Erlenkämper 1980). **Fig. 11.29** and **Fig. 11.30** show sequences of AE signals in fracture mechanic experiments with annealed carbon steel and aluminium alloy, respectively.

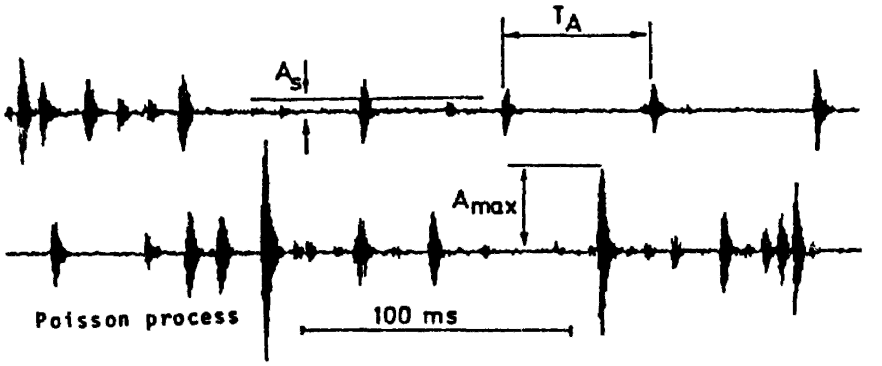

Fig. 11.29. Signals from fracture mechanical experiments on annealed C-steel (Erlenkämper 1980).

Whereas in annealed carbon steel the signals show a clear evidence for the existence of a Poisson process with independent events, the bursts of signals in aluminium alloy show distinct clusters of interdependent events.

As said before, such time statistic evaluations have been rarely carried out and, therefore, no more essential results can be quoted. It could be worth-while to investigate whether there exists a correlation between amplitude statistic and time statistic. A first attempt was made by Erlenkämper [1980] who found such a correlation in metals. Unfortunately, his work was not continued and applied to rock.

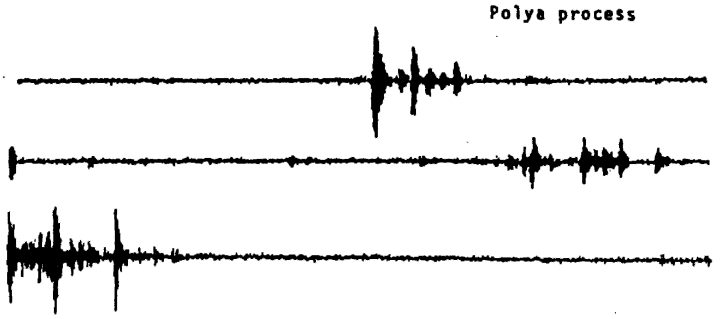

Fig. 11.30. Signals from fracture mechanical experiments on aluminium alloy. The time scale is the same as in **Fig. 11.29** (Erlenkämper 1980).

11.6.3 Clustering and advanced source location methods

As mentioned in Subsection 11.4.1, a cluster is a series of AE events which are spatially and temporally related. The more critical planar clusters are precursors of macroscopic crack formation. The formation of planar clusters is mostly associated with failure at pre-existing weakened zones or formation of new cracks in highly stressed zones due to stress redistribution.

A systematic search for clusters as described in Subsection 11.4.1 was applied on AE events, which were generated during a triaxial *extension* test of a cylindrical rock salt specimen (diameter 150 mm, length 300 mm) from the Asse salt mine, which was carried out in the laboratory of the Department for Waste Disposal Technology and Geomechanics at the Technical University of Clausthal, Germany. During the test the axial displacement and axial force, the radial pressure, and the volume change (dilatancy) of the specimen were measured and stored.

An array of 12 AE wide-band sensors was glued to the surface of the specimen. The AE measuring system included three four-channel transient recorder cards in a personal computer. These cards (sampling rate 10 MHz, resolution 14 bit, storage capacity 512 kByte per channel) were read each time when at least two channels were hit. The digitized signals were stored on the hard disk of the personal computer. Starting at an isotropic pressure of 5 MPa, an increasing confining load was applied in such a way that a constant axial strain rate of $8.33 \cdot 10^{-6}$ sec^{-1} was produced. The maximum and minimum principal stresses were in radial and axial direction, respectively. During the experiment (duration 5 hours) about 70,400 events were recorded. Approximately 50% and 25% of these events were locatable using at least 8 and 10 consistent P- and S-wave onsets, respectively.

Fig. 11.31 shows the 17,300 located events utilizing at least 10 onsets for source location projected onto the three coordinate planes (top view and two lateral views). The sensor positions are indicated by encircled numbers.

Because of the strong extension of the specimen and remaining source location errors, some sources are located out of the box, which represents the original shape of the rock specimen. The figure shows that the events are preferentially distributed in clouds over the whole specimen. Some accumulations of events can be observed.

The cluster analysis with primary parameters of 1 minute and 10 mm yields 297 primary clusters. Most of the primary clusters (280) comprise less than 10 events. At the end, the two biggest clusters with 142 (No. 1) and 81 events (No. 2) were plotted in **Fig. 11.32**. The sensor positions are marked by small crosses. Cluster No 1 and No 2 appeared within a time period of 5 and 2.5 minutes, respectively, after the test had been started.

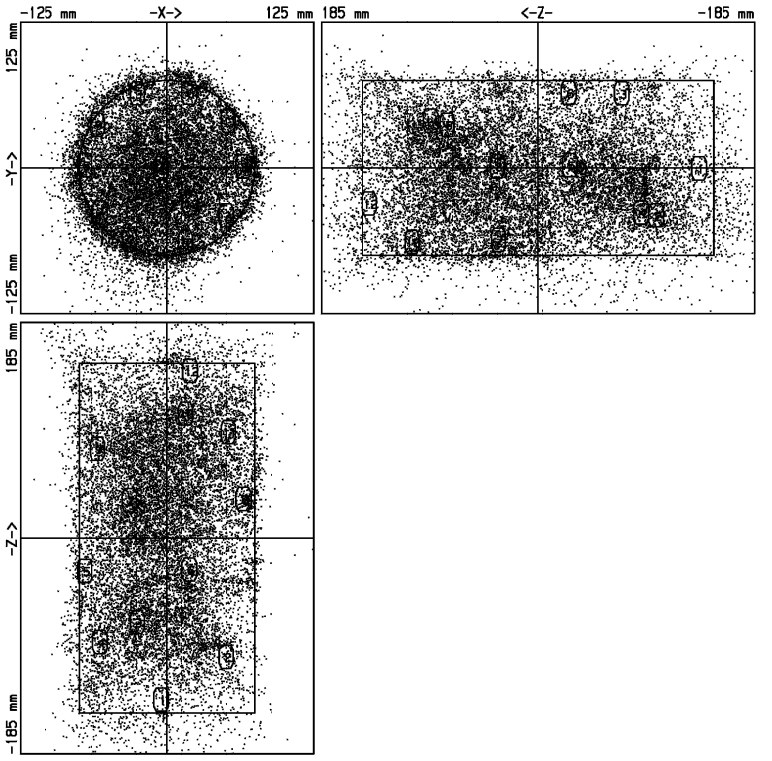

Fig. 11.31. Located events in top view and two lateral views. The circle and boxes mark the initial shape of the cylindrical specimen. The encircled numbers are indicating the position of the AE sensors.

Fig. 11.33 displays at the left-hand side the correlation integral (Eq. 11.2 in Subsection 11.4.1) versus the distance (bold line) of Cluster No. 1. In this diagram, the fractal dimensions *D* (Eq. 11.3) of 1, 2, and 3 are indicated by the thin straight lines (from left to right). The slope of 2 which proves true up to an interevent distance of about 2 cm represents a planar structure and is an evidence for critical AE activity. Indeed, the ultimate failure was a sudden tensile fracture of the specimen exactly at the position where cluster No. 1 occurred. Interestingly, in the time interval of approximately 4 hours between the occurrence of the cluster and the ultimate failure of the specimen no further AE events were emitted from the cluster region.

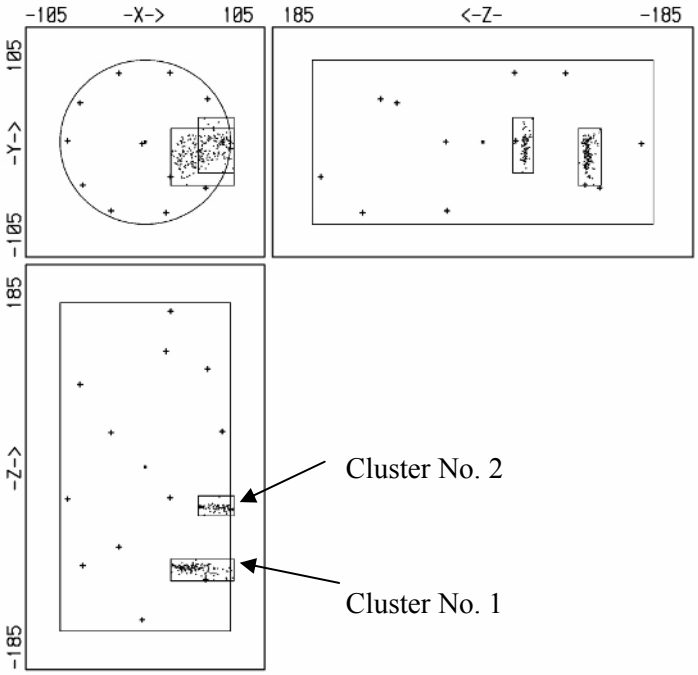

Fig. 11.32. Location of two big clusters with 142 (No. 1) and 81 events (No. 2) in the same manner as in **Fig. 11.31.**

At the right-hand side of **Fig. 11.33**, the orientations (small dots) of connecting lines between event pairs are plotted in an equal-area, lower hemisphere projection. Most orientations in **Fig. 11.33** are near the periphery of the hemisphere, thus indicating nearly horizontal inclination of the plane. The big filled dots indicate the orientation of the three coordinate axes. The normal vector of the plane is in the center of the hemisphere, i.e. nearly in z direction.

Systematic location errors could occur due to high deformation of the rock specimen. To minimize the travel-time residuals, systematic location errors associated with picking errors and the velocity variations due to microcracking were removed by the application of the joint-hypocenter determination (JHD) method (Frohlich 1979). Using the JHD method, "station corrections" can be determined that account for consistent inaccuracies of the wave velocity along the travel path especially near sensor positions. To delineate structures inside a clouded AE event distribution the collapsing method, which was first reported by Jones and Steward [1997], can be applied. This method describes how the location of an AE event can be moved within its error ellipsoid in order that the distribution of movements for every event of a cloud approximates that of normally distributed location uncertainties. This does not make the location uncertainties in the dataset smaller but it highlights structures already inherent within the unfocussed dataset.

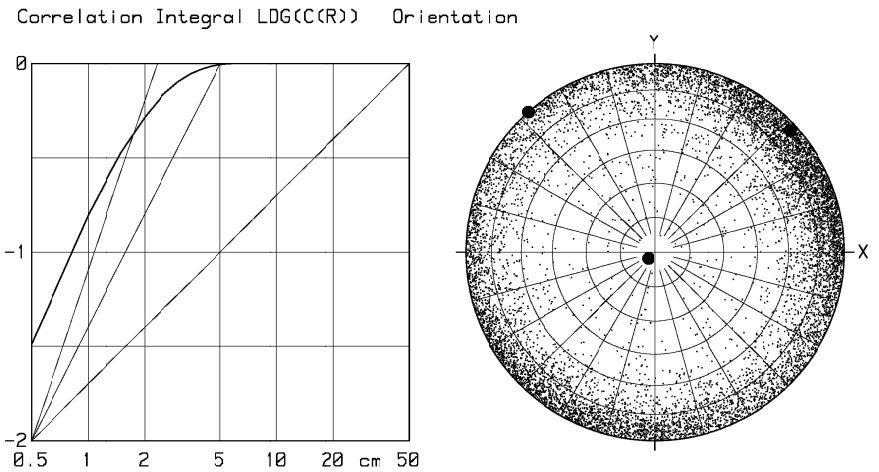

Fig. 11.33. Correlation integral and fractal dimension (left-hand side) of Cluster No. 1 and the orientations of connecting lines between event pairs (small dots) in an equal-area, lower hemisphere projection (right-hand side).

Nevertheless, the method can help to identify some structures in clouded source locations. The collapsing solution is not necessarily unique and depends on the collapsing algorithm. The existence of any structure found must be viewed with caution[1]. **Fig. 11.34** shows the result of the collapsing

[1] Personal conversation with Professor Niitsuma, Tohoku University, Sendai, Japan, 2003

method. Compared with **Fig. 11.31**, the events are more clustered. Some structures in the AE cloud have been revealed by this method.

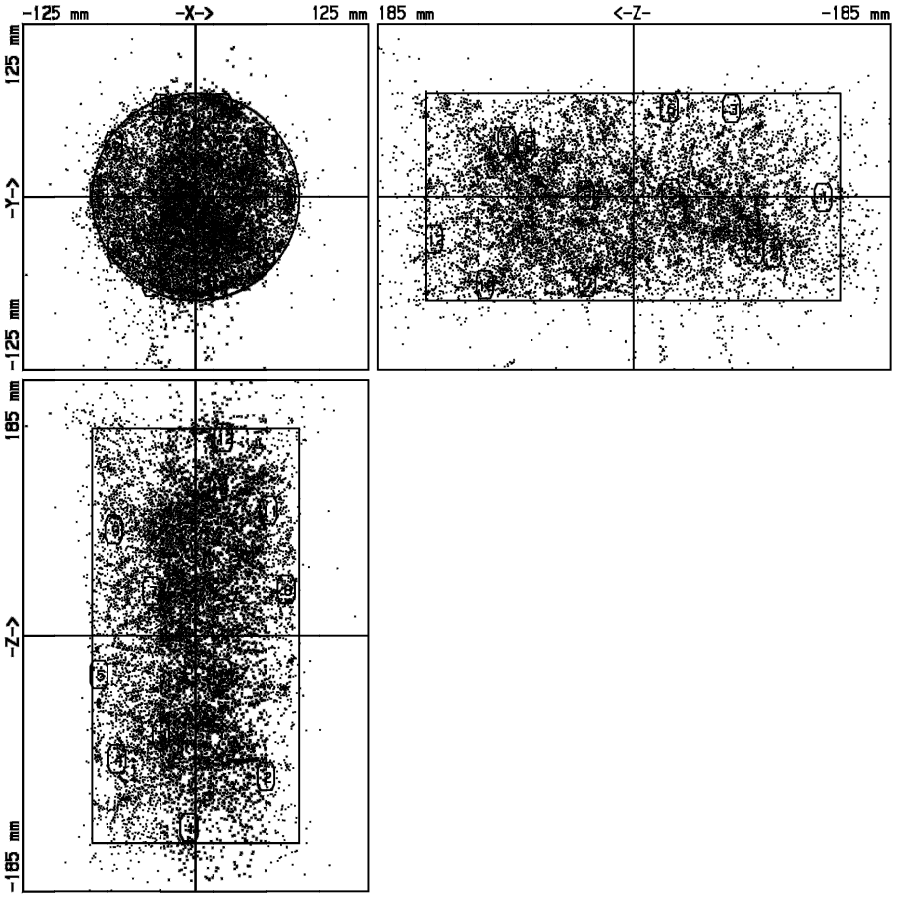

Fig. 11.34. Collapsed events after JHD location as seen in **Fig. 11.31**

11.6.4 Source Characteristics and Focal Mechanisms

The use of multichannel recording systems provides more quantitative analysis of source mechanisms utilizing the digitally stored AE signals. Two methods are in common use in source mechanism studies on rock specimens, fault-plane solution method and moment tensor analysis. In earthquake seismology, the classical method is the fault-plane solution

method. This method uses polarities and ray directions of the P-wave to constrain possible double-couple (DC) fault-plane solutions, but requires a very good sensor coverage of the focal sphere. The fault-plane solution method assumes pure shear slip along the fault plane which is realistic for tectonic earthquakes. Therefore, the fault-plane solution method is especially adapted to the situation of tectonic earthquakes within the earth where volume changes normally cannot occur.

On the contrary, in the case of laboratory investigations on rock specimens under uniaxial or triaxial load, volume changes in the source play an important role. Dilatancy can be explained as volume expansion caused by tensile opening. In contrast to the fault-plane solution method, the more complex moment tensor method is capable of describing sources with volumetric components like tensile cracks, deviatoric sources like shear cracks, or a mixture of both source types. The volumetric source components can be easily obtained using the isotropic part, or one-third of the moment tensor trace. With the moment tensor method, the source mechanisms are estimated in a least-squares inversion calculation from amplitudes of the first motion as well as from full waveforms of P and S waves. This method requires additional knowledge about the transfer function of the medium (the so-called Green's function) and sensor response.

Both methods have been applied in the field of AE in rocks. Some examples of the application of the fault-plane solution method are given by Sondergeld and Estey [1982], Kuwahara et al. [1985], Zang et al. [1998]. Because of an insufficient number of sensors these authors investigated only polarities of P-wave first motion to classify AE events recorded during uniaxial loading of rock specimens into shear and tensile types. A source with a uniform compressional polarity pattern was interpreted as a tensile type and one with compressional as well as dilatational first motions as a shear type. It was not possible to determine the source orientation or to quantify the volume change of the microcracks.

The moment tensor of each AE event can be evaluated if the displacements at a sufficiently large number of sensor positions are known. The displacement signal, which is emitted from the source, is distorted by the wave propagation in the specimen and by the sensor. Therefore, a well characterized material and sensor is crucial in evaluating the source mechanisms with the moment tensor method. For this reason, Manthei [2005] has emphasized rock and sensor characterization to be able to correct the measured signal amplitudes for wave attenuation, sensor directivity, and sensitivity.

A *compression* experiment on a cylindrical rock salt specimen of same dimensions and with the same measurement techniques as described in Subsection 11.6.3 was carried out in such a way that a constant axial strain

rate of $-8.33 \cdot 10^{-6}$ sec^{-1} was produced. In 4.5 hours the full waveforms of about 100.000 AE events could be stored.

Manthei [2005] demonstrates the application of the moment tensor method to analyse automatically this huge amount of AE events. The automatic procedure was separated into source location, data extraction, and stability checking of the inversion calculation. The effectiveness of automated evaluation procedures is listed in **Table 11.4**. This table presents the number of events evaluated with various automatic procedures.

The table shows, that 57% of the detected events were located using at least 8 consistent P- and S-wave arrival times. 30% of the detected events were more precisely located using at least 16 consistent arrivals. The source mechanism could be evaluated using the moment tensor method on about 15% of the detected events and stable moment tensor solutions were obtained on 12.5% of the detected events.

Table 11.4. Number of events obtained in automatic procedures such as registration of events up to moment tensor determination

Procedure	**Requirements**	**Number of events (%)**
Registration of events	at least 1 channel was hit	10^5 (100)
Source location	at least 8 consistent P- and S-wave arrival times	$5.7 \cdot 10^4$ (57)
Precise source location	at least 16 consistent P- and S-wave arrival times	$3 \cdot 10^4$ (30)
Moment tensor method	at least 10 clearly discernible P-wave first motions	$1.5 \cdot 10^4$ (15)
Stable moment tensor solutions	at least 10 clearly discernible P-wave first motions	$1.25 \cdot 10^4$ (12.5)

A decomposition of the moment tensor into two terms is defined as:

$$M = \frac{1}{3} \cdot \begin{pmatrix} tr(M) & 0 & 0 \\ 0 & tr(M) & 0 \\ 0 & 0 & tr(M) \end{pmatrix} + \begin{pmatrix} m_1^* & 0 & 0 \\ 0 & m_2^* & 0 \\ 0 & 0 & m_3^* \end{pmatrix} \tag{11.9}$$

where $tr(M) = m_1 + m_2 + m_3$ is the trace of the entire moment tensor with eigenvalues m_i and deviatoric eigenvalues $m_i^* = m_i - 1/3 \cdot tr(M)$. The first term describes the isotropic source component, which is important for quantifying the volume change in the source. The second term describes the deviatoric source components like the double couple (DC) or shear component.

The source mechanism can be classified through the parameter ε and the R value. Parameter ε is defined as $\varepsilon = m_2/max(|m_1|,|m_3|)$ where m_i are the eigenvalues of the moment tensor $(m_1 \geq m_2 \geq m_3)$. ε is zero for a shear mechanism, approximately 0.37 for a tensile mechanism with elastic parameters of rock salt, and ±1.0 for an explosion or implosion mechanism, respectively.

The R value as defined by Feignier and Young [1992] is the ratio of the isotropic component to the sum of the isotropic and deviatoric components:

$$R = \frac{tr(M)}{|tr(M)| + \sum_{i=1}^{3} |m_i^*|} \tag{11.10}$$

The ratio varies from –100% for pure implosion sources up to 100% for pure explosion sources. A pure shear failure mechanism is indicated by $R = 0$ and a pure tensile mechanism is indicated by a R value of approximately 67% for the elastic parameters of rock salt.

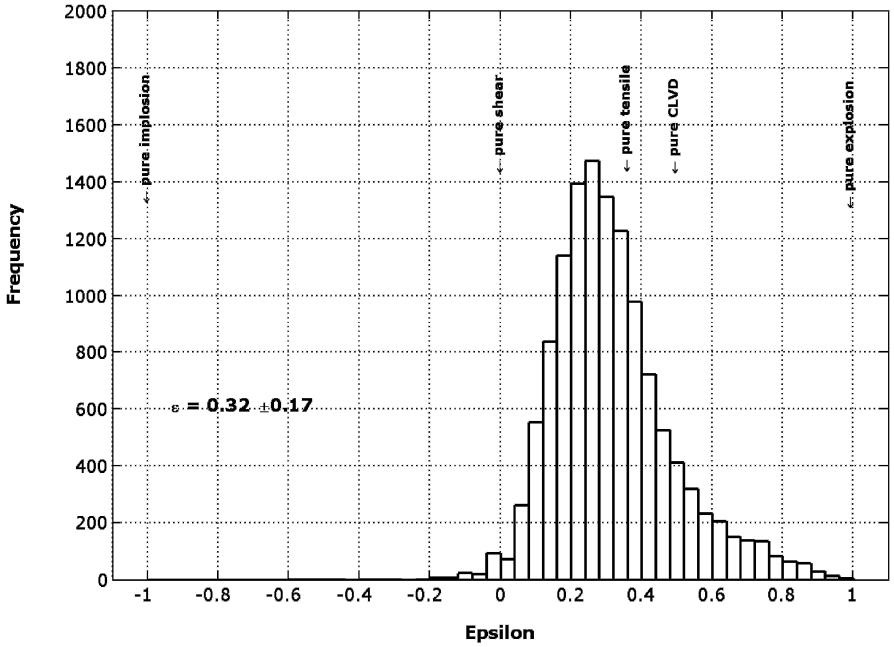

Fig. 11.35. Histogram of the ε values calculated by the eigenvalues of the moment tensor (Manthei 2005).

Manthei [2005] found that the observed AE events were predominantly of tensile type (fracture mechanical Mode I). Most of the events (approximately 90%) showed significant isotropic source components, which is in agreement with the applied deviatoric loading that leads to dilatation. The parameter ε and the R values (see **Figs. 11.35** and **11.36**) tend to values of pure tensile mechanisms (ε = 0.37 and R = 67%). He also found, that the tension axes normal to the planes of tensile cracks were predominantly orientated in the radial direction, that is in the direction of the minimum principal stress as expected for this crack type.

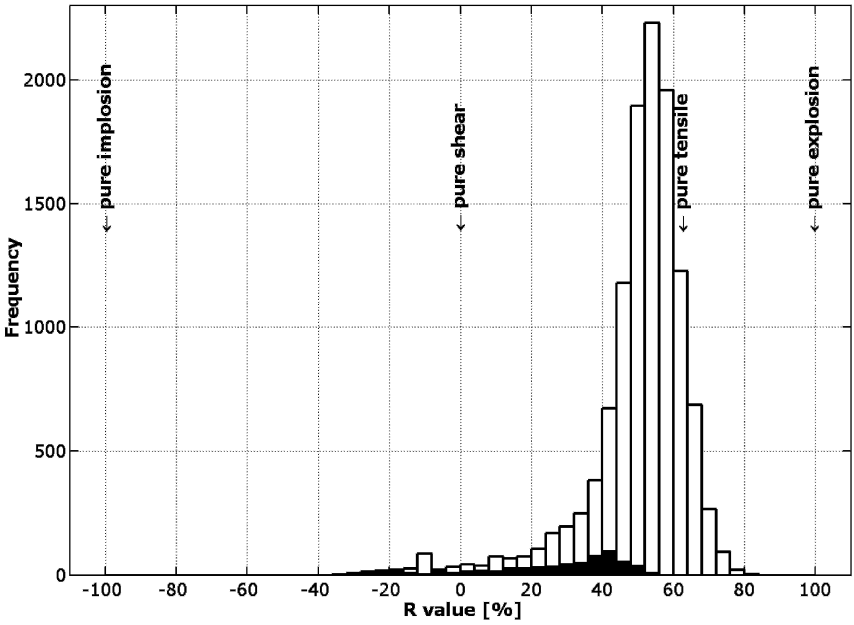

Fig. 11.36. Histogram of the R-value calculated from the moment tensor. Unfilled bars are indicating events with compressional first motions only and black bars are indicating events with at least one dilatational first motion (Manthei 2005).

These results correspond well with observations made by other authors during slow deviatoric loading of rock salt from the same provenance of the Asse mine. Alkan et al. [2003] performed two-dimensional model experiments on 10 mm thick rock salt slices to investigate which crack types occurred during dilatant loading. Under an optical microscope with a total magnification of 180 they observed intercrystalline cracks (Type 1) on grain boundaries. Most of these cracks occurred on grain boundaries which

were orientated in the direction of the maximum principal stress. Increasing the deviatoric stress resulted in growth and opening of these cracks. Contrary to this, transcrystalline cleavage cracks (Type 2) which formed during loading remained closed. Consequently, Type 1 cracking seems to be mainly responsible for dilatancy and an increase of permeability for fluids during deviatoric loading of rock salt.

Because of the limited accuracy of the AE source location, there was no direct proof that the cracking indicated by AE events occurs on grain boundaries. But combinations of all cited observations with our results lead us to the assumption that most AE events are caused by intercrystalline cracking with tensile opening of the cracks. This happens on grain boundaries parallel to the specimen axis.

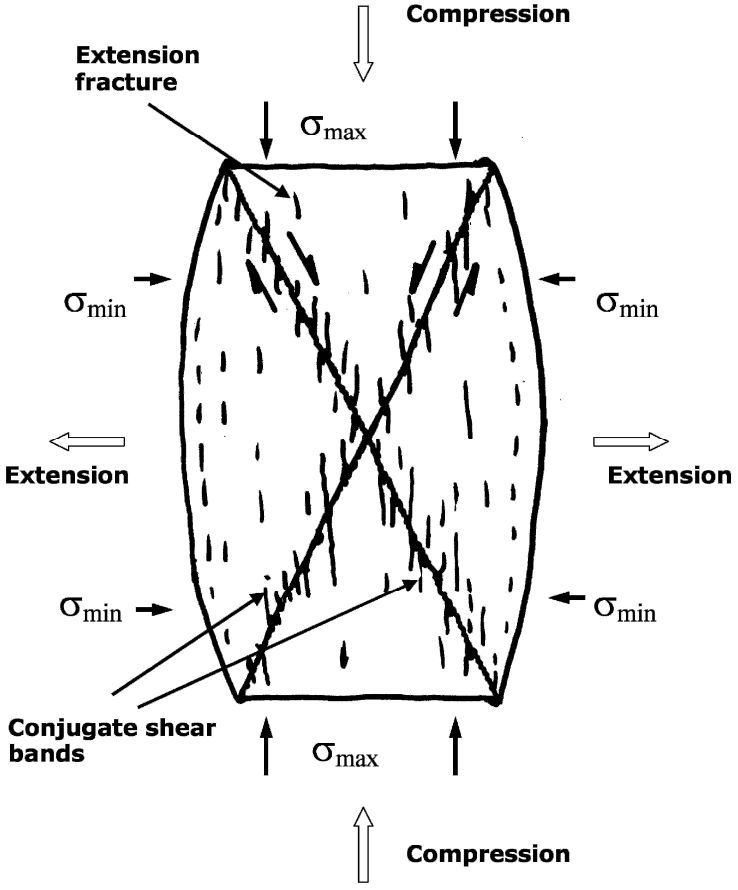

Fig. 11.37. Damage and fracture development during failure of the rock salt specimen (Herget 1988).

Stronger AE activity starts early in the loading immediately after passing the dilatancy boundary (DB). The first located AE sources in the specimen's interior indicate that the DB is reached. In later stages of the test, most microcracks keep the same orientation. This is in agreement with the visible damage development at different degrees of deformation which showed cracking parallel to the maximum principal stress direction. These so-called extension fractures are well-known from many rock specimen tests (Herget 1988). The extension fractures accumulate in zones of high shear stress, which form a cone of conjugate shear bands. In this highly damaged zone the ultimate shear fracture occurs (**Fig. 11.37**).

Zang et al. [1998] investigated the effect of stress anisotropy on brittle failure of granite under uniaxial compression. The experiment was performed on a Aue granite specimen (diameter 52 mm, length 100 mm) in a non-standard asymmetric compression test, in which 20% of the top surfaces of the core remain unloaded (compare with **Fig. 11.39**). The advantage of asymmetric compression compared to symmetric loading is to know in advance the nucleation and propagation path of the fracture.

Eight piezoelectric sensors, spring loaded to the specimen, were used for source location. The signals of the eight sensors were digitised with a sampling frequency of 5 MHz, 12 bit amplitude resolution, and a storage window of 512 samples. The signals of an additional wide-band sensor were evaluated online during test with respect to eight typical AE parameters like event number, arrival time, signal duration, time between two events, rise time, ring-down counts, maximal amplitude, and seismic energy.

In these experiments the AE rates of three sensors were used as feedback signal to control axial load for stabilization of the stress drop.

Fig. 11.38 shows the density of the located AE events in projection to the three coordinate planes (x-y-plane at top, z-y-plane in the middle, and x-z-plane at bottom) in this asymmetric compression test as schematically shown in **Fig. 11.39**. The crack growth is illustrated in four stages (a1 to a4) of approximately 130 located events each and the final stage a5 of stress accumulation after the pre-fracture (290 events). The y-z-plane represents a view onto the macroscopic fracture plane, which is growing from top left to about 10 mm above the bottom surface. The x-y-plane shows that the contour lines of high event density coincide with the locus of maximum shear stress from finite element calculations. After the complete shear fracture formation the AE activity shifted to the remaining part of the specimen.

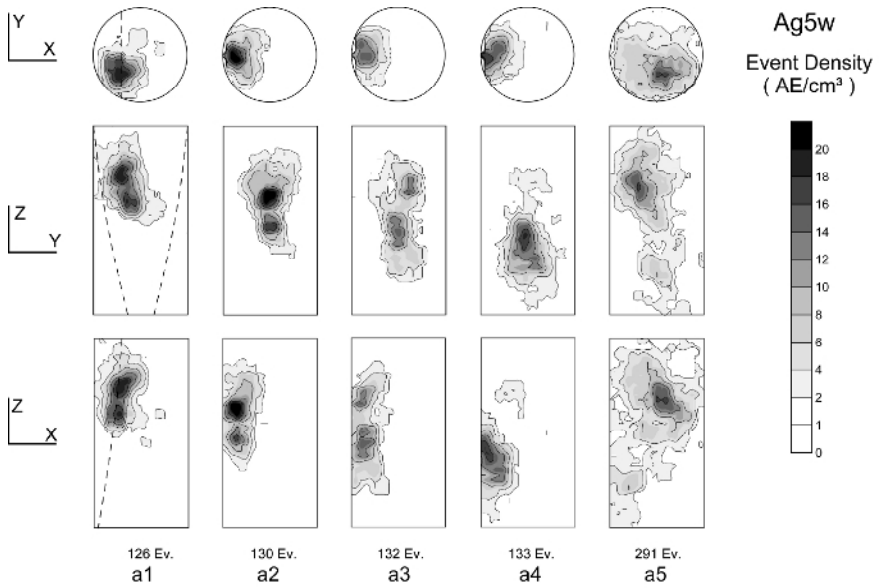

Fig. 11.38. Event density in projection in projection to the three coordinate planes in five successive stages of fracture growth. The fracture plane from core inspection is indicated by dashed lines (Zang et al. 1998).

The focal mechanisms of the located events were estimated from polarities of the automatically picked first motions. The polarity value *pol* of a single event is calculated by:

$$pol = \frac{1}{k}\sum_{i=1}^{k} sign(A_i), \tag{11.11}$$

where k is the number of channels. The polarity was used to separate Type S (shear) events ($-0.25 \le pol\ 0.25$) from Type T (tensile) events ($-1 \le pol < -0.25$) and Type C (compression) events ($0.25 \le pol < 1$).

If most of the sensors have compressional or dilatational first motions, the events were classified in Type T and Type C, respectively. Otherwise, the events were of Type S. According to this nomenclature, a source with a uniform compressional polarity pattern was interpreted as a tensile type, and one with compressional as well as dilatational first motions as a shear type. From all events emitted before and during fracturing of the specimen, 70% were of Type S, 20% of Type T and 10% of Type C. In **Fig. 11.39** single fault-plane solutions of the six strongest Type S events are plotted in projection on the x-z-plane. The polarities of the eight sensors are shown at the right-hand site of **Fig. 11.39** in an equal-area, lower hemisphere projec-

tion. The measured first motions polarities are fitted to theoretical radiation patterns of a pure DC mechanism. Black area and positive sign are indicating compressional first motion.

This figure shows that strong Type S events align along the expected fracture plane, but single nodal-plane orientations can be poorly constrained. Anyhow, the investigations on a set of 212 Type S events show predominantly dilatational first motions parallel to the z axis (vertical direction) and compressional first motions parallel to the x axis (horizontal direction). The average fault-plane solution of these events coincides with the orientation of the fracture plane.

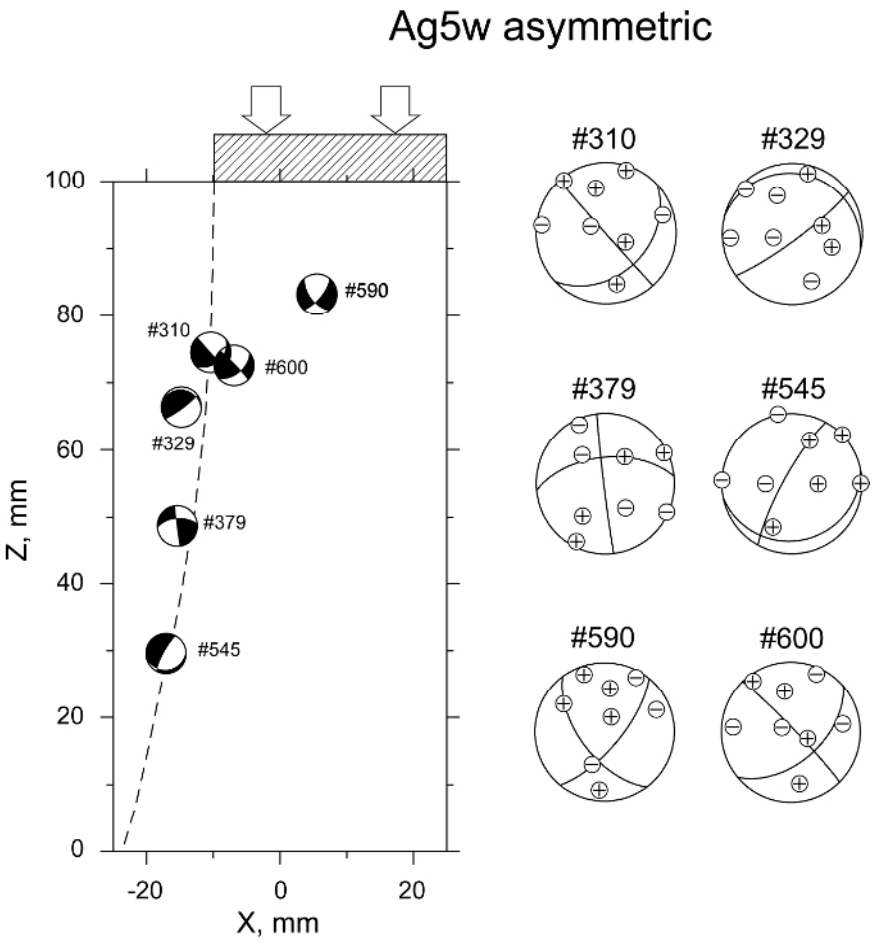

Fig. 11.39. Fault-plane solutions of the six largest Type S (shear) events (left-hand side) and its polarities (right-hand side). Black area (left) and positive sign (right) indicate compressional first motion (Zang et al. 1998).

11.6.5 Mechanical Properties, Deformation Behaviour, and Rock Stress

Well performed laboratory deformation tests were used to develop the constitutive equations which are prerequisites for the computer analysis of the coupled thermal, mechanical, and hydraulic processes in rock and for the prediction of the long-term behaviour of a rock formation especially for underground repositories or storage caverns (e.g. storage of gas and oil).

Pusch and Alkan [2002] investigated the gas permeation through cylindrical rock salt specimens under triaxial compression in relation to dilatancy development under deviatoric stress conditions. Similarly to previous studies, they observed a spontaneous increase in permeability by some orders of magnitude shortly after the DB (dilatancy boundary) was exceeded. The DB separates the elastic compression phase with volume decrease from the dilatant deformation phase with volume increase. They attributed this permeability increase to the percolation of gas along the extended grain boundaries of the rock salt. Simultaneous AE measurement demonstrated that the percolation begins simultaneously throughout the specimen.

Deformation tests are started at a certain isotropic stress state, the axial strain is increased with a constant strain rate (**Fig. 11.40**). The related evolution of volume, AE rate, ultrasonic wave velocities, and permeability is schematically shown.

All these measures are applicable to monitor the development of the properties of the rock during loading and deformation. The development of the dilatancy can be divided very roughly into three phases. Phase I characterizes a decrease of the volume attributed to elastic compression of the rock salt, a decrease of permeability and an increase of seismic velocity. The volume becomes nearly constant at the end of Phase I. It can be assumed that elastic compression processes and dilatancy processes balance at this point. Dilatant microcracking generates only weak AE activity.

The AE activity becomes stronger at the beginning of Phase II and increases with increasing strain. This stronger AE activity is indicating the development of an interconnected and transmissible network of microcracks. The DB separates the elastic compression phase with volume decrease from the dilatant deformation phase with volume increase. At a certain stage of deformation, the permeability rapidly increases due to the accumulation of cracks in the whole rock volume. This permeability increase is attributed to the percolation of fluid along extended grain boundaries. At the same time the seismic velocity is decreasing. Phase III characterizes a significant increase of the dilatancy and AE activity. The cracks

accumulate in zones of high shear stress, which form a cone of conjugate shear bands. In this highly damaged zone the ultimate shear fracture occurs at the end of Phase III (see **Fig. 11.37**).

To investigate the DB and its influence on the transport properties of rock salt used as radioactive waste repository in Germany, extensive experimental studies were performed in the laboratory of the Institute of Petroleum Engineering of the Clausthal Technical University. Triaxial stress dilatancy experiments were supported by AE measurements to define the DB as well as the effects of some process parameters on the definition of this critical stress conditions (Pusch and Alkan 2002).

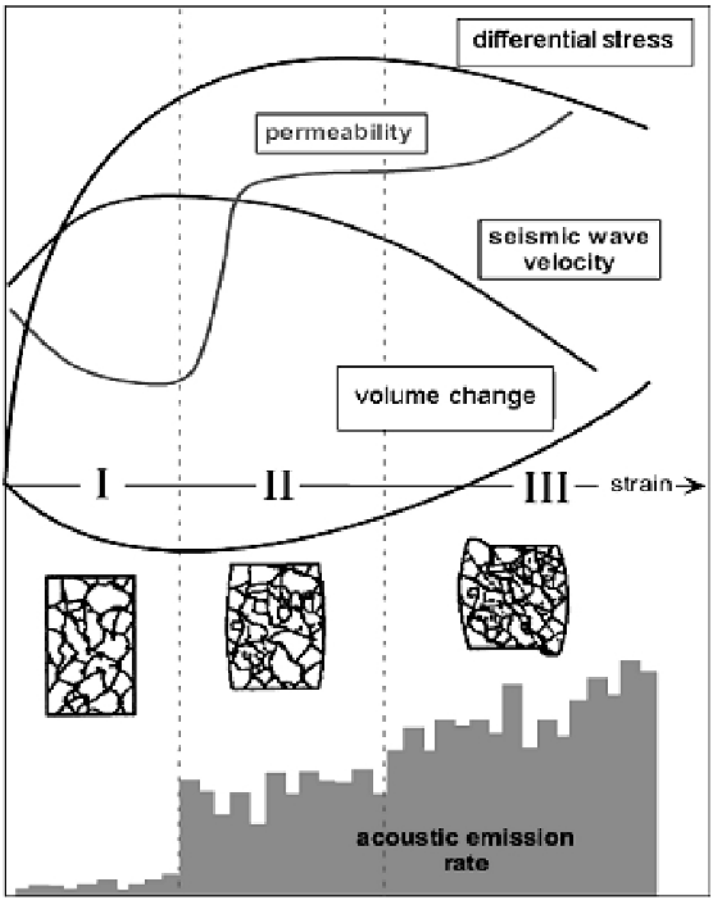

Fig. 11.40. Evolution of rock properties in a deformation test. Schematic illustrates volume change (porosity), AE rate, permeability, and seismic wave velocity (Popp et al. 2002).

The transition point where the number of AE events drastically increases can be graphically determined under the assumption that the number of events linearly increases as a function of the axial stress. **Fig. 11.41** exemplarily shows the number of events versus the axial stress which was measured during a triaxial compression test of a rock salt specimen (diameter 60 mm, length 300 mm) at a confining pressure of 6 MPa (Alkan and Pusch, 2002).

By volumetric measurements, i.e. by determination of the point of minimal volume, the DB was found at an axial stress of 35 MPa. The figure shows, that the slope of the straight line (dashed line in **Fig. 11.41**) changes after passing the DB. A flat slope before passing the DB is indicating weak AE activity. On the other hand, after passing the DB a much steeper slope is indicating high AE activity due to augmented energy release after passing the DB. It is assumed that the DB is the point where the slope changes (see **Fig. 11.41**). The intersection point of the straight lines gives the axial stress at the DB σ_{DB} of approximately 36 MPa, in fairly good agreement with the value by determination of volumetry.

The DB was determined at 10 cylindrical rock salt specimens with both methods. The results are presented in **Fig. 11.42**. In conclusion, the results of all experiments are within an acceptable deviation range. The continuous line in **Fig. 11.42** represents the calculated dilatancy boundary due to the constitutive equations as proposed by Pusch and Alkan [2002].

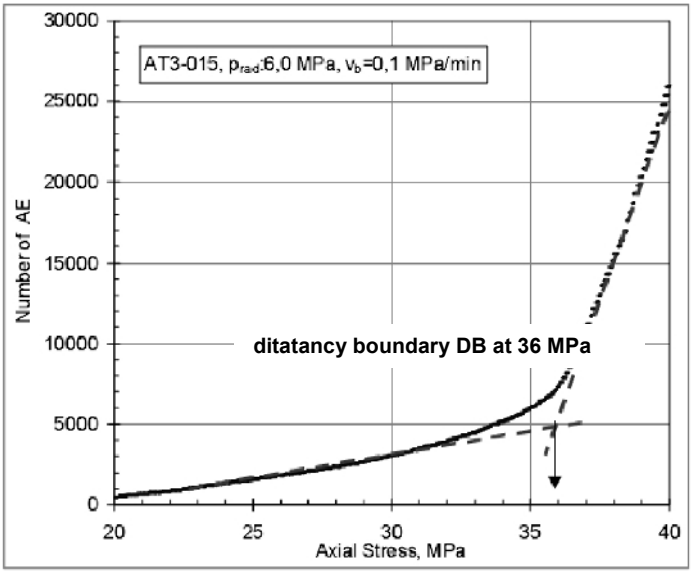

Fig. 11.41. Graphical determination of dilatancy boundary using AE activity

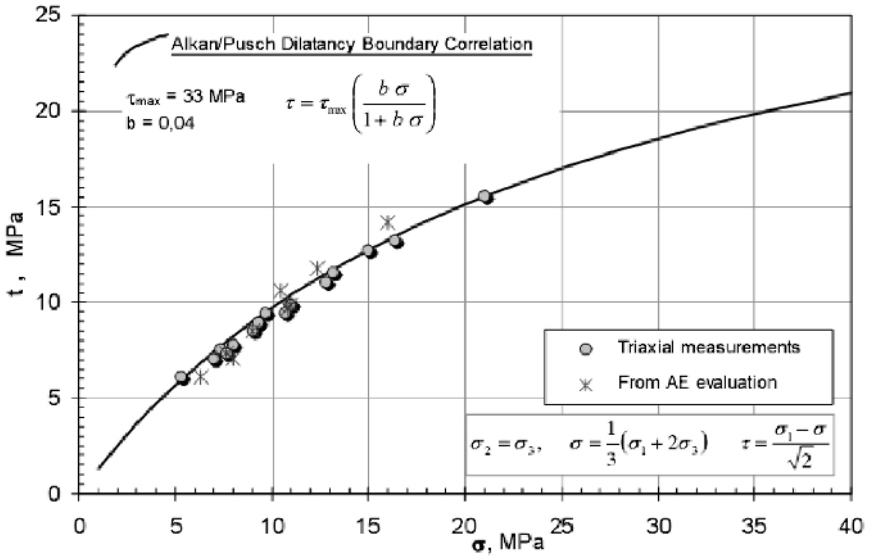

Fig. 11.42. Comparison of the dilatancy boundary measured using volumetric measurements and AE measurements. The continuous line shows the calculated dilatancy boundary using the obtained constitutive equations.

11.6.6 Discussion

The analysis of time and amplitude statistics of AE events measured in laboratory experiments on rock specimens seems to be a powerful means to discriminate between induced or stochastic events. Event location will give insight into the spatial distribution of microcracks. In case of clustered events, the fractal dimension of the events can be used to find planar clusters, which are the most critical structures forming the nucleus of eventual macroscopic fractures.

To investigate dilatation of rock the moment tensor method is an adequate method of describing sources with volumetric components such as tensile cracks. Tensile cracks are mainly responsible for dilatancy. Thus, it is possible to recognize zones of higher permeability for fluids which plays an important role for use of a rock formation as radioactive waste disposal.

Due to the higher sensitivity in laboratory experiments the number of detected AE events is much higher compared with measurements in mines. In order to process all detected events, it is essential to evaluate the AE events in various automatic procedures such as registration of events, location of events, determination of source mechanisms, and automatic stabil-

ity check of the moment tensor solutions. Besides the high sensitivity of AE event detection, laboratory measurements provide an opportunity of a very good sensor coverage of the focal sphere which is necessary for a precise source location and stable moment tensor solutions.

With respect to the practical application of these new tools in a radioactive waste disposal in rock, where zones of permeability for fluids are of upmost interest, it is to remark that a sufficient large number of sensors should be arranged in such a way that the focal sphere is well covered in all directions, which is essential for the use of only P-wave first motions for location. This is a question of accessibility for drilling wells for sensor installation. The sensors should be installed far enough from excavations and galleries so that the wave propagation will not be disturbed ("shaded") by excavated rooms and galleries.

Acknowledgement

The authors thank T. Spies, (Federal Institute for Geosciences and Natural Resources, Germany), A. Zang (GeoForschungsZentrum Potsdam, Germany), D.S. Collins (University of Toronto, Canada), R.P. Young (University of Liverpool, United Kingdom), T. Popp (Institute for Rock Mechanics, Germany), and H. Alkan (Gesellschaft für Anlagen- und Reaktorsicherheit, Germany) for providing the authors with original figures. The work on collapsing was carried out by H. Moryia (Tohoku University, Sendai, Japan) as a part of MURPHY/MTC International Collaborative Projects supported by NEDO (New Energy and Industrial Development Organization of Japan) and MESSC (Ministry of Education, Science, Sports and Culture of Japan).

References

Ahorner L, Sobisch HG (1988) Ein untertägiges Überwachungssystem im Kalibergwerk Hattorf zur Langzeiterfassung von seismischen Ereignissen im Werra-Kaligebiet (in German). Kali und Steinsalz 10(2):38-49

Albright JN, Pearson CF (1982) Acoustic Emission as a Tool for Hydraulic Fracturing Location: Experience at the Fenton Hill Hot Dry Rock Site. Soc Pet Eng J:5:23-530

Alheid HJ, Rummel F (1977) Acoustic Emission During Frictional Sliding Along Shear Planes in Rock. In: Hardy RH, Leigthon FW (eds) Proc 1st Conf on Acoustic Emission/Microseismic Activity in Geologic Structures and Materials, Trans Tech Publications, Clausthal-Zellerfeld, pp 149-154

Alkan H, Pusch G (2002) Definition of the Dilatancy Boundary Based on Hydro-Mechanical Experiments and Acoustic Detection, SMRI Fall Meeting, Bad Ischl, Austria, 7-9 October

Alkan H, Pusch G, Cinar Y (2003) Direct Visualization and Acoustic Detection of Microcrack Evolution in Rock Salt. SMRI Spring 2003 Meeting, Houston, Texas, USA, 27-30 April

Blake W, Leighton F (1970) Recent Developments and Applications of the Microseismic Method in Deep mines. In: Proc 11th Symp on Rock Mechanics, Berkeley 1969, AIME, New York, pp 429-433

Blake W (1972) Rock Bursts Mechanics. Quarterly of Colorado School of Mines, 67(1):64

Brace WF, Paulding BW, Scholz C (1966) Dilatancy in the fracture of crystalline rocks. J Geophys Res, 71:3939-3953

Brown JW, Singh MM (1966) An investigation of microseismic activity in rock under tension. Soc Min Eng, pp 255-265

Cai M, Kaiser PK, Martin CD (1998) A tensile model for the interpretation of microseismic events near underground openings. Pure Appl Geophys, 153:67-92

Cete A (1977) Seismic Source Location in the Ruhr District. In: Hardy RH, Leighton FW (eds) Proc 1st Conf on Acoustic Emission/Microseismic Activity in Geologic Structures and Materials, Trans Tech Publications, Clausthal-Zellerfeld, pp 231-241

Collins DS, Pettitt WS, Young RP (2002) High-resolution Mechanics of a Microearthquake Sequence. Pure Appl Geophys, 159:197-219

Cook NGW (1963) The seismic location of rockbursts. In: Fairhurst C (ed) Proc 5th Symp on Rock Mechanics, Pergamon Press New York, pp 493-516

Cox SJD, Meredith PG (1993) Microcrack Formation and Material Softening in Rock Measured by Monitoring Acoustic Emission. Int J Rock Mech Min Sci & Geomech 30:11-24

Eisenblätter J (1980) The origin of acoustic emission – Mechanisms and models. In: Acoustic Emission, Conference in Bad Nauheim, Deutsche Gesellschaft für Metallkunde e.V., pp 189-204

Eisenblätter J, Manthei G, Meister D (1998) Monitoring of Microcrack Formation around Galleries in Salt Rock. In: Hardy HR Jr (ed) (1998) Proc 6th Conf on Acoustic Emission/Microseismic Activity in Geologic Structures and Materials. Trans Tech Publications, Clausthal-Zellerfeld, pp 227-243

Erlenkämper S (1980) Time and Amplitude Statistics of Acoustic Emission Signals in Fracture Mechanic Experiments. In: Acoustic Emission, Conference in Bad Nauheim, Deutsche Gesellschaft für Metallkunde e.V., pp 165-188

Fairhurst C (ed) (1990) Proc 2nd Symp Rockbursts and Seismicity in Mines (RaSiM 2), Balkema, Rotterdam

Feignier B, Young RP (1992) Moment Tensor Inversion of Induced Microseismic Events: Evidence of Non-Shear Failure in the -4<M<-2 Moment Magnitude Range, Geophys Res Lett 19, 14:1503-1506

Frohlich C (1979) An Efficient Method for Joint Hypocenter Determination for Large Groups of Earthquakes. Computers and Geosciences, 5:387-389

Gibowicz SJ, Lasocki S (eds) (1997) Proc 4th Symp Rockbursts and Seismicity in Mines (RaSiM 4), Balkema, Rotterdam

Glaser SD, Nelson PP (1992) Acoustic Emission Produced by Discrete Fracture in Rock Part 2 – Kinematics of Crack Growth During Controlled Mode I and Mode II Loading of Rock. Int J Rock Mech Min Sci & Geomech 29:253-265

Goodman RE (1963) Subaudible noise during compression or rock. Geol Soc Amer Bull, 74:487-490

Gutenberg B, Richter CF (1954) Seismicity of the Earth, Princton Univ. Press

Hardy HR Jr, Leighton FW (eds.) (1977) Proc 1st Conf on Acoustic Emission/Microseismic Activity in Geologic Structures and Materials. Trans Tech Publications, Clausthal-Zellerfeld

Hardy HR Jr, Leighton FW (eds) (1980) Proc 2nd Conf on Acoustic Emission/Microseismic Activity in Geologic Structures and Materials. Trans Tech Publications, Clausthal-Zellerfeld

Hardy HR Jr (1982) Application of Acoustic Emission Techniques to Rock and Rock Structures: A state-of-the-Art Review. In: Drnevich VP, Gray RE (eds) Acoustic Emissions in Geotechnical Engineering Practice, ASTM STP 750, Philadelphia, pp 4-92

Hardy HR Jr, Leighton FW (eds) (1984) Proc 3rd Conf on Acoustic Emission/Microseismic Activity in Geologic Structures and Materials. Trans Tech Publications, Clausthal-Zellerfeld

Hardy HR Jr (ed.) (1989) Proc 4th Conf on Acoustic Emission/Microseismic Activity in Geologic Structures and Materials. Trans Tech Publications, Clausthal-Zellerfeld

Hardy HR Jr (1989) A Review of International Research Relative to the Geotechnical Field Application of Acoustic Emission/Microseismic Techniques. J Acoustic Emission 8(6):65-91

Hardy HR Jr (ed.) (1995) Proc 5th Conf on Acoustic Emission/Microseismic Activity in Geologic Structures and Materials. Trans Tech Publications, Clausthal-Zellerfeld

Hardy HR Jr (ed.) (1998) Proc 6th Conf on Acoustic Emission/Microseismic Activity in Geologic Structures and Materials. Trans Tech Publications, Clausthal-Zellerfeld

Hashida T, Takahashi H (1993) Significance of AE Crack Monitoring in Fracture Toughness Evaluation and Non-linear Rock Fracture Mechanics. Int J Rock Mech Min Sci & Geomech 30:47-60

Hashida T (1993) Fracture Toughness Testing of Core-based Specimens by Acoustic Emission. Int J Rock Mech Min Sci & Geomech 30:61-69

Hatton CG, Main IG, Meredith PG (1990) A comparison and structural measurements in scaling exponents during tensile subcritical crack growth. J Struc Geol, 15:1485-1495

Hente B, Quijano A, Dürr K (1989) Microseismic Observations in a Salt Mine with Reference to the Mine Survey Results. In: Hardy RH (ed) Proc 4th Conf on Acoustic Emission/Microseismic Activity in Geologic Structures and Materials. Trans Tech Publications, Clausthal-Zellerfeld, pp 171-179

Herget G (1988) Stresses in Rock. A. A. Balkema/Rotterdam/Brookfield

Hirata T (1987) Omori's Power Low Aftershock Sequences of Microfracturing in Rock Fracture Experiment. J Geophys Res 92:6215-6221

Holcomb DJ, Costin LS (1986) Detecting Damage Surfaces in Brittle Materials Using Acoustic Emission. J App Mech 108:536-544

Holcomb DJ (1993) General Theory of the Kaiser Effect. Int J Rock Mech Min Sci & Geomech 30:929-935

Hubbert MK, Willis DG (1957) Mechanics of Hydraulic Fracturing. Trans AIME 210:153-168

Hunsche U, Schulze O, Langer M (1994) Creep and failure behaviour of rock salt around underground cavities. In: Proc 16th World Mining Congress, Sofia, 5: pp 217-230

Ishida T, Chen Q, Mizuta Y (1997) Effects of fluid viscosity in hydraulic fracturing deduced from acoustic emission monitoring. In: Gibowicz SJ, Lasocki S (eds) Proc 4th Symp Rockbursts and Seismicity in Mines (RaSiM 4), Balkema, Rotterdam, pp 415-419

Jones RH, Stewart RC (1997) A method for determining significant structures in a cloud of earthquakes. J Geophys. Res 102:8245-8254

Kaiser J (1953) Untersuchungen über das Auftreten von Geräuschen beim Zugversuch (in German). Archiv für Eisenhüttenwesen 24:43-45

Kijko A, Funk CW, Brink AvZ (1993) Identification of anomalous patterns in time-dependent mine seismicity. In: Young RP (ed) (1993) Proc 3rd Symp Rockbursts and Seismicity in Mines (RaSiM 3), Balkema, Rotterdam, pp 205-210

Kranz RL, Satoh T, Nishizawa O, Kusunose K, Takahashi M, Masuda K, Hirata A (1990) Laboratory Study of Fluid Pressure Diffusion in Rock Using Acoustic Emissions. J Geophys Res 95:21593-21607

Kurita K, Fujii N (1979) Stress memory of crystalline rocks in acoustic emission. Geophys Res Lett 6:9-12

Kusunose K, Nihizawa O (1986) AE gap prior to local fracture of rock under uniaxial compression. J Phys Earth 34:S45-S56

Kuwahara Y, Yamamoto K, Kosuga M, Hirasawa T (1985) Focal Mechanisms of Acoustic Emission in Abukuma-Granite under Uniaxial and Biaxial Compressions. Tohoku Geophys J, 30:1-14

Lavrov AV, Filimonov YI, Shkuratnik VI (2001) Features of Acoustic Emission in Plastic Rocks. XI Session of the Russian Acoustical Society, pp 385-387

Lavrov AV, Wevers M, Vervoort A (2002) Acoustic Emission During Monotonic and Cyclic Deformation of a Brittle Snadstone. J Acoustic Emission 20:292-299

Lei X, Kusunose K, Rao MVMS, Nishizawa O, Satoh T (2000) Quasi-static fault growth and cracking in homogeneous brittle rock under triaxial compression using acoustic emission monitoring. J Geophys Res 105:6127-6139

Lockner DA, Byerlee JD (1977a) Acoustic Emission and Creep in Rock at High Confining Pressure and Differential Stress. Bull Seis Soc Amer 67:247-258

Lockner DA, Byerlee JD (1977b) Acoustic Emission and Fault Formation in Rocks. In: Hardy RH, Leigthon FW (eds) Proc 1st Conf on Acoustic Emis-

sion/Microseismic Activity in Geologic Structures and Materials, Trans Tech Publications, Clausthal-Zellerfeld, pp 99-107
Lockner DA, Byerlee JD (1977c) Hydrofracture in Weber Sandstone at high confining pressure and differential stress, J Geophys. Res 82:2018-2026
Lockner DA, Summers R, Moore D, Byerlee JD (1982) Laboratory Measurements of Reservoir Rock from Geysers Geothermal Filed, California. Int J Rock Mech Min Sci & Geomech 19:65-80
Lockner DA (1993) The Role of Acoustic Emission in the Study of Rock. Int J Rock Mech Min Sci & Geomech 30:883-899
Lord AE, Koerner RM (1983) Acoustic Emissions in Geological Materials. J Acoustic Emission 2:195-219
McGarr A, Bicknell J (1990) Estimation of the near-fault ground motion of mining-induced tremors from locally recorded seismograms in South Africa. In: Fairhurst C (ed) Proc 2nd Symp Rockbursts and Seismicity in Mines, pp 245-248
McGay NC, Wainwright EH (eds) (1984) Proc 1st Symp Rockbursts and Seismicity in Mines (RaSiM 1), South Africa Inst Min Metallurgy, South Africa
Majer EL, Doe TW (1986) Studying Hydrofractures by High Frequency Seismic Monitoring. Int J Rock Mech Min Sci & Geomech 23:185-199
Manthei G, Eisenblätter J (1989) Untersuchung der Rißbildung in Salzgestein mit Hilfe der Schallemissionsanalyse (in German). Materialwissenschaft und Werkstofftechnik 20:240-249
Manthei G, Eisenblätter J, Salzer K (1998) Acoustic Emission Studies on Thermally and Mechanically Induced Cracking in Salt Rock. In Hardy HR Jr (ed) (1998) Proc 6th Conf on Acoustic Emission/Microseismic Activity in Geologic Structures and Materials. Trans Tech Publications, Clausthal-Zellerfeld, pp 245-265
Manthei G, Eisenblätter J, Spies T (2000) Acoustic Emission in Rock Mechanics Studies, In: Kishi T, Ohtsu M, Yuyama S (eds) Acoustic Emission – Beyond the Millennium, Elsevier, pp 127-144
Manthei G, Eisenblätter J, Spies T, Eilers G (2001a) Source parameters of acoustic emission events in salt rock. J Acoustic Emission 19:100-108
Manthei G, Eisenblätter J, Dahm T (2001b) Moment Tensor Evaluation of Acoustic Emission Sources in Salt Rock. Construction and Building Materials 15:297-309
Manthei G, Eisenblätter J, Kamlot P (2003) Stress measurements in salt mines using a special hydraulic fracturing borehole tool. In: Natau O, Fecker E, Pimentel E (eds) Proc Int Symp on geotechnical measurements and modelling, Karlsruhe, Germany, pp 355-360
Manthei G (2005) Characterization of Acoustic Emission Sources in a Rock Salt Specimen under Triaxial Load. Bull Seis Soc Amer 95:1674-1700
Martin CD, Young RP (1993) The effect of excavation-induced seismicity on the strength of Lac du Bonnet granite. In: Young RP (ed) (1993) Proc 3rd Symp Rockbursts and Seismicity in Mines (RaSiM 3), Balkema, Rotterdam, pp 367-371

Masuda K, Nishizawa O, Kusunose K, Satoh T, Takahashi M, Kranz RL (1990) Positive Feedback Fracture Process Induced by Nonuniform High-Pressure Water Flow in Dilatant Granite. J Geophys Res 95:21583-21592

Masuda K, Nishizawa O, Kusunose K, Satoh T (1993) Laboratory Study of Effects of In Situ Stress State and Strength on Fluid-induced Seismicity. Int J Rock Mech Min Sci & Geomech 30:1-10

Miller AD, Julian BR, Foulger GR, (1998) Three-dimensional seismic structure and moment tensors of non-double-couple earthquakes at the Hemgill-Grensdalur volcanic complex, Iceland. Geophys J Int 133:309-325

Mogi K (1962) Study of the elastic shocks caused by the fracture of heterogeneous materials and its relation to earthquake phenomena. Bull Earthquake Res Inst 40:125-173

Mutke G, Stec K (1997) Seismicity in the upper Silesian Coal Basin, Poland: Strong regional seismic events. In: Gibowicz SJ, Lasocki S (eds) (1997) Proc 4th Symp Rockbursts and Seismicity in Mines (RaSiM 4), Balkema, Rotterdam, pp 213-217

Niitsuma H, Nagano K, Hisamatsu K (1993) Analysis of acoustic emission from hydraulically induced tensile fracture of rock. J Acoustic Emission 11:S1-S18

Nishizawa O, Onai K, Kusunose K (1985) Hypocenter Distribution and Focal Mechanism of AE Events During Two Stress Creep. In Yugawara Andesite. Pure Appl Geophys 122:36-52

N.N. (2002) Suggested method for in-situ stress measurement from a rock core using the Acoustic Emission technique. In: Proc. of 5th International Workshop on the Application of Geophysics in Rock Engineering, Toronto, Canada, pp 61-66

Obert L (1977) The Microseismic Method: Discovery and Early History. In: Hardy RH, Leigthon FW (eds) Proc 1st Conf on Acoustic Emission/Microseismic Activity in Geologic Structures and Materials, Trans Tech Publications, Clausthal-Zellerfeld, pp 11-12

Ohtsu M (1991) Simplified Moment Tensor Analysis and Unified Decomposition of Acoustic Emission Sources: Application to In Situ Hydrofracturing Test. J Geophys Res 96:6211-6221

Ohnaka M, Mogi K (1982) Frequency Characteristics of Acoustic Emission in Rocks Under Uniaxial Compression and Its Relation to the Fracturing Process to Failure. J Geophys Res 87:3873-3884

Phillips WS, Rutledge JT, House LS, Fehler MC (2002) Induced Microearthquake Patterns in Hydrocarbon and Geothermal Reservoirs: Six case Studies. Pure Appl Geophys 159:345-369

Popp T, Kern H, Schulze O (2002) Permeation and development of dilatancy in rock salt. In: Cristescu ND, Hardy HR Jr, Simionescu RO (eds), Basic and Applied Salt Mechanics. Proc. of the 5th Conf on the Mech Behavior of Salt, Bukarest 1999, Balkema, pp 95-124

Potvin Y, Hudyma M (eds) (2005) Proc 6th Symp Rockbursts and Seismicity in Mines (RaSiM 6), Australian Centre for Geomechanics, Australia

Pusch G, Alkan H, (2002) Gas Permeation Models Related to Dilatancy under Deviatoric Stress Conditions. SMRI Fall 2002 Meeting, Bad Ischl, Austria, Oct 7-9

Reid HF (1910) The mechanism of the earthquake. In: The California Earthquake of April 18, 1906: Report of the State Earthquake Investigation Commission, Carnegie Institute of Washington, Washington, DC, Vol 2, pp 16-28

Rong C (1979) Acoustic Emission on Rocks under Triaxial Compression with Various Stress Paths. Int J Rock Mech Min Sci & Geomech 16:401-405

Rothman RL (1977) Acoustic Emission in Rock Stressed to Failure. In: Hardy RH, Leigthon FW (eds) Proc 1st Conf on Acoustic Emission/Microseismic Activity in Geologic Structures and Materials, Trans Tech Publications, Clausthal-Zellerfeld, pp 109-133

Salmon MDG, Wiebols GA (1974) Digital Location of Seismic Events by an Underground Network of Seismometers Using Arrival Times of Compressional Waves. Rock Mechanics 6:141-166

Satoh T, Nishizawa O, Kusunose K (1990) Fault Development in Oshima Granite Under Triaxial Compression Inferred from Hypocenter Distribution and Focal Mechanism of Acoustic Emission. Tohoku Geophys J 33:241-250

Scholz, CH (1968a) Experimental Study of the Fracturing Process in Brittle Rock. J Geophys Res 73:1447-1454

Scholz CH (1968b) The frequency-magnitude relation of microfracturing in rock and its relation to earthquakes. Bull Seis Soc Amer 58:399-415

Scholz CH (1968c) Microfracturing and the Inelastic Deformation of Rock in Compression. J Geophys Res 73:1417-1432

Scholz CH (1968d) Microfractures, Aftershocks, and Seismicity. Bull Seis Soc Amer 58:1117-1130

Scott DF, Williams TJ, Friedel MJ (1997) Investigation of a rock-burst site. Sunshine Mine, Kellogg, Idaho. In: Gibowicz SJ, Lasocki S (eds) (1997) Proc 4th Symp Rockbursts and Seismicity in Mines (RaSiM 4), Balkema, Rotterdam, pp 311-315

Sellers EJ, Kataka MO, Linzer LM (2003) Source parameters of AE events and scaling with mining-induced seismicity. J Geophys Res 108:2418-2429

Seto M, Utagawa M, Katasuyama K (2002) Some fundamental studies on the AE method and its application to in-situ stress measurements in Japan. In: Proc 5th Int Workshop on the Application in Rock Engineering, Toronto, pp 67-71

Shah KR, Labuz JF (1995) Damage mechanisms in stressed rock from acoustic emission, J Geophys. Res 100:15527-15539

Shimada M, Cho A, Yukutaka H (1982) Fracture Strength of Dry Silicate Rocks at High Confining Pressures and Activity of Acoustic Emission. Tectonophysics 96:159-172

Sobolev GA, Spetzler HA, Koltsov A, Sondergeld CH (1980) Ultrasonic Radiation of a Crack in a Strained Rock Specimen. Izvestiya, Earth Physics 16:819-828

Sondergeld CH, Estey LH (1981) Acoustic Emission Study of Microfracturing During the Cyclic Loading of Westerly Granite. J Geophy Res 86:2915-2924

Sondergeld CH, Estey LH (1982) Source mechanics and microfracturing during uniaxial cycling of rock. Pure Appl Geophys 120:151-166

Spies T, Hesser J, Eisenblätter J, Eilers G (2004) Monitoring of the rockmass in the final repository Morsleben: Experiences with acoustic emission measurements and conclusions. In: Proc DisTec 2004, Berlin, pp 303-311

Spies T, Hesser J, Eisenblätter J, Eilers G (2005) Measurements of Acoustic Emission During Backfilling of Large Excavations. In: Potvin Y, Hudyma M (eds) (2005) Proc 6th Symp Rockbursts and Seismicity in Mines (RaSiM 6), Australian Centre for Geomechanics, Australia, pp 379-383

Strobach K (1983) Vom Urknall zur Erde (in German). Verlag J Neumann-Neudamm, Melsungen, Germany

Talebi S, Mottahed P, Pritchard CJ (1997) Monitoring seismicity in some mining camps of Ontario and Québec. In: Gibowicz SJ, Lasocki S (eds) (1997) Proc 4th Symp Rockbursts and Seismicity in Mines (RaSiM 4), Balkema, Rotterdam, pp 117-120

Trifu CI, Shumila V, Urbancic TI (1997) Space-time analysis of microseismicity and its potential for estimating seismic hazard in mines. In: Gibowicz SJ, Lasocki S (eds) (1997) Proc 4th Symp Rockbursts and Seismicity in Mines (RaSiM 4), Balkema, Rotterdam, pp 295-298

Van Aswegen G, Durrheim RJ, Ortlepp WD (eds) (2001) Proc 5th Symp Rockbursts and Seismicity in Mines (RaSiM 5), The South Africa Institute of Mining and Metallurgy, Symp Series 27

Weeks J, Lockner DA, Byerlee J (1978) Changes in b-Values During Movement on Cut Surfaces in Granite. Bull Seis Soc Amer 68:333-341

Weiss J (1997) The Role of Attenuation on Acoustic Emission Amplitude Distributions and b-Values. Bull Seis Soc Amer 87:1362-1367

Will M (1980) Seismoacoustic Activity and Mining Operations. In: Hardy RH, Leigthon FW (eds) Proc 2nd Conf on Acoustic Emission/Microseismic Activity in Geologic Structures and Materials, Trans Tech Publications, Clausthal-Zellerfeld, pp 191-209

Yaramanci U (1991) Hochfrequente Mikroseismizität im Steinsalz der Asse um den 945-m-Bereich (in German). GSF Report 32/91, Neuherberg

Young RP, Collins DS (2001) Seismic studies of rock fracture at the Underground Research Laboratory, Canada. Int J Rock Mech Min Sci & Geomech 38:787-799

Young RP (ed) (1993) Proc 3rd Symp Rockbursts and Seismicity in Mines (RaSiM 3), Balkema, Rotterdam

Young RP, Martin CD (1993) Potential Role of Acoustic Emission/Microseismicity Investigations in the Site Characterization and Performance Monitoring of Nuclear Waste Repositories. Int J Rock Mech Min Sci & Geomech 30:797-803

Zang A, Wagner FC, Stanchits S, Dresen G, Andresen R, Haidekker MA (1998) Source analysis of acoustic emission in Aue granite cores under symmetric and asymmetric compressive loads. Geophys J Int 135:1113-1130

Zang A, Wagner FC, Stanchits S, Janssen C, Dresen G (2000) Fracture process zone in granite. J Geophys Res 105:23651-23661

Zietlow WK, Labuz JF (1998) Measurement of the Intrinsic Process Zone in Rock Using Acoustic Emission. Int J Rock Mech Min Sci 35:291-299

12 Acoustic Emissions in Wood

Eric N. Landis

12.1 Introduction

Wood, like many heterogeneous materials, provides many interesting AE challenges. It is a biological material that has evolved to perform many functions. It is anisotropic, and it is heterogeneous over a very wide range of length scales. It is hydroscopic, and its mechanical properties are extremely sensitive to moisture content. From an AE standpoint it is an extremely dynamic material in that there are numerous microstructural phenomena that lead to AE activity, however, it is highly attenuative, particularly in a direction perpendicular to the grain.

In this chapter, after a brief overview of relevant wood structure issues, and an overview of the wide range of AE applications for wood and wood products, we focus on AE as a means to quantify damage and fracture due to mechanical loads.

12.2 Wood Structure

As with all materials, the structure of wood dictates the properties. This brief overview of wood structure is intended to provide a basis for interpretation of AE signals. Because of the wide range of relevant length scales, wood scientists traditionally separate wood structure into macrostructure and microstructure. It should be noted however, that the relevant length scales span a continuum from the molecular to the structural levels. A more complete reference on wood properties can be found in text of Bodig and Jayne [1993] or the U. S. Forest Service *Wood Handbook* [1999].

The macrostructure of solid wood is familiar for most people. The concentric ring structure in a log is formed by the uneven growth rate during the course of the year. Earlywood is characterized by large diameter cells

formed during the rapid growth period of spring and early summer, while latewood is characterized by small cells formed during late summer and autumn. The hollow cells are saturated in the green state, but are typically empty when the wood is used in structural applications. In fact, for in-service wood structures, variations in moisture content are due to variations in moisture in the cell wall (so-called bound water). Nearly all important mechanical properties are tied to the level of bound water. Fehler! Verweisquelle konnte nicht gefunden werden. **12.1** shows coordinate system used to describe what is generally characterized as a cylindrically orthotropic solid.

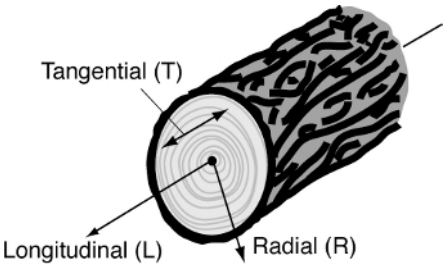

Fig. 12.1. Orientation directions for wood cross section.

Regarding wood microstructure, we typically focus our attention on the cell wall. Nature has developed an ingenious system to respond to the varying structural demands on the tree. As the tree grows, the cellulose arranges itself into microfibrils, which form the basis for the cell wall. In the section of the cell wall that provides the longitudinal strength and stiffness, the microfibrils have a helical orientation. This orientation is characterized by the microfibril angle, which is measured relative to the longitudinal axis of the cell. As one might visualize, small microfibril angles lead to relatively high strength and stiffness, while larger microfibril angles lead to lower strength and stiffness, but higher ductility.

The significance of the microfibril angle is that we find a systematic variation through the different parts of the tree. In so-called juvenile wood that is close to the center of the log, microfibril angle tends to be larger than the mature wood that appears in the outer layers of the log. The resulting variation in elastic properties can thus be significant even within a single tree.

12.3 Ultrasonic Properties

In addition to the anisotropy and heterogeneity described above, wood is a highly attenuative, dispersive material. A brief summary of relevant ultrasonic properties is presented here. A more complete coverage can be found in comprehensive treatments such as Bucur [1995].

Bulk primary wave velocities are typically in the range of 4000 to 6000 m/s in the longitudinal direction, but drop to 1000 to 2000 m/s in the radial or tangential direction. Because radial stiffness is higher than tangential stiffness, we generally see velocities in the radial direction about 50% higher than in the tangential direction. The spatial distribution of microfibril angles noted above provides an additional source of ultrasonic variability. At a very localized level, we have variations in properties between earlywood and latewood, while at a larger scale we have variations between juvenile wood and mature wood. At the lower end of the ultrasonic spectrum (50 – 200 kHz), the highly localized variations such as earlywood-latewood can be ignored.

An important practical consideration in AE applications to wood is the extremely high ultrasonic attenuation, which according to Beall [2002] is roughly an order of magnitude greater than even attenuative geologic materials such as concrete and rock. Since wood is dispersive, there is a frequency dependence on the attenuation, but typical values cited range from 30 dB/m in the longitudinal direction to 200 dB/m in the radial and tangential directions. Thus, in any conventional application of AE techniques to wood we either must mount the transducers relatively close to the source of activity, or we must restrict our interest to very high energy events.

12.4 Example Acoustic Emission Applications to Wood

Presented here is a brief summary of AE applications to wood. It should be noted that discussion here is restricted solid wood. There exists a broad array of literature covering AE applications to problems in wood-based composites such as particle board and oriented strand board. These studies are omitted here in the interest of brevity.

12.4.1 Mechanical Loading

An early example of AE monitoring in wood was conducted by DeBaise et al. [1966]. They presented cumulative AE event records for a variety of loading configurations of western white pine. The results they report illu-

strate fundamental AE properties subsequently observed by many others. Specifically, AE activity starts at very early stages of loading, between 5 and 20% of peak stress. For longitudinal tensile loading, AE events accumulate in a nonlinear manner to a point just preceding rupture, at which time event count jumps substantially, as illustrated in **Fig. 12.2**. Longitudinal compression loading resulted in a total event count several orders of magnitude smaller due to the very different failure mechanisms.

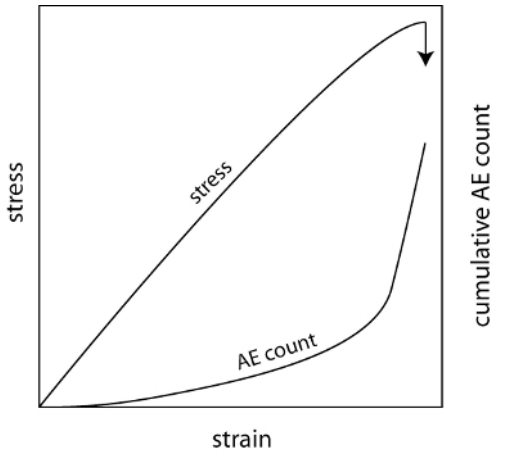

Fig. 12.2. Typical AE event distribution for wood under stress.

Ansell [1982a, 1982b] provided a link between AE properties and microstructural damage mechanisms. Specimens were examined using a scanning electron microscope to characterize damage mechanisms. Damage in earlywood and latewood sections was examined separately, and the following observations were. In latewood, AE counts accumulated rapidly at low strains, while the count increase was more gradual (but with periodic jumps) in earlywood. The conclusion was that this difference could be attributed to prestressing of the latewood, and that microfailure of the latewood leads to a redistribution of stresses. Step increases in AE events were attributed to both longitudinal and transverse rupture of the cell wall, while gradual event increases were attributed to slower shear processes in the cell wall as well as in between cells.

Examples of more recent studies relating AE activity to mechanical loading include that of Reiterer et al. [2000], who examined characteristics of emissions due to mode I fracture in the plane normal to the radial direction. A wedge-splitting configuration was used to achieve stable crack growth in both hardwoods and softwoods. Their observation was that the softwoods exhibited smoother crack growth as compared to the hard-

woods, which fractured in a sequence of abrupt jumps. The corresponding AE measurements showed a more steady distribution of event amplitude in the softwoods as compared to the hardwoods, which showed a series of bursts corresponding to the rapid crack growth. The authors attributed this to the formation of a process zone that distributes microcracking over a wider region in the softwoods.

In another example study, Aicher et al [2001] examined damage in softwood specimens loaded in tension in plane normal to the tangential direction. Their analysis included source locations, and they note that the source-receiver distance should not exceed 100 mm for proper analysis. They were able to relate the AE source locations to damage localization, although they note that the characteristic rapid increase in AE event rate was not accompanied by a visible change in specimen stiffness.

In an effort to track evolution of failure in glued joints, Gozdecki and Smardzewski [2005] combined finite element analysis of stress distributions with AE event counts. They observed characteristic regions of crack growth that produced AE bursts, and they showed an exponential relationship between AE counts and the tangential stresses that arise during loading of the bond line.

12.4.2 Moisture Effects and Other Studies

As the properties of wood are closely tied to moisture content, a number of studies have examined not only the effects of moisture on AE properties under mechanical loading, but also the AE activity resulting from wetting and drying.

Rice and Skaar [1990] examined AE rates from red oak in green (freshly cut) and partially dried conditions. No AE activity was seen in the green specimens until nonlinearities appeared in the load-deformation curve, immediately prior to rupture. Dried specimens, however, exhibited the classic AE activity previously discussed and illustrated in **Fig. 12.2**.

Quarles [1988] used pencil lead breaks on wood blocks of various species to study the effects that grain angle and moisture content might have on AE event rates. The conclusion was that there were significant differences between species, but only minor differences in the moisture content effects within species. Both Quarles [1990] and Sakui [1990] confirmed that AE signal attenuation was relatively constant up to fiber saturation point (the moisture content corresponding to saturated cell walls, but no water in the cell cavity). At moisture contents above fiber saturation point much more significant attenuation was observed.

Schniewind et al. [1996] used AE monitoring to examine issues of temperature and moisture content. Specifically they wanted to see if AE signals could be used as part of a control process for wood drying procedures. They separately examined mode I and mixed mode fracture, and found that mixed mode fracture induced significantly more AE activity.

Researchers have also applied AE techniques to examine effects of biological degradation in wood. Noguchi et al. [1986] and Imamura et al. [1991] both observed that in even slightly decayed specimens produced AE events at loads between 4 and 32% of maximum, while undamaged control specimens did not produce AE events until a load of 50% of maximum. Raczkowski et al. [1999] observed comparable results. Beall and Wilcox [1987] examined AE activity during radial compression of decayed and non-decayed white fir. They observed that as the mass loss from decay increased, the number of events at a given load level also increased. In an even more novel application, Noguchi et al. [1991] examined the use of AE monitoring to detect termite attack.

12.5 Application: AE Energy and Fracture

While there are many more interesting and relevant applications of AE monitoring to wood properties, we now choose to focus on a specific study to illustrate how AE techniques were evaluated in the context of fracture mechanics. The study is illustrative on both the value and difficulties of applying quantitative AE techniques to wood.

As detailed in Landis and Whittaker [2000], AE was used to monitor crack propagation in clear eastern hemlock due to mode I (tensile) fracture in a plane parallel to the tangential plane of the wood. The goal was to characterize AE energy release in absolute terms and relate that energy to measured fracture energy in the specimen. The hypothesis was that the detected AE energy should directly relate to the measured progressive fracture energy released during crack propagation. Presumably if we can remove the effects of material attenuation, then the AE energy should parallel fracture energy. Toward this end, we produced a series of clear-grained wood specimens of varying moisture contents. As fracture energy changes with changing moisture content (Bodig and Jayne 1993), we can produce a range of specimen properties for comparison.

The specimens were cut to a double cantilever configuration shown in **Fig. 12.3**, and conditioned to three different moisture contents. A series of eight AE sensors was mounted to the specimen at 2 cm intervals. AE data was collected by an eight-channel full waveform acquisition system (Digi-

tal Wave *Fracture Wave Detector*). The specimens were loaded in displacement control in a universal testing machine by gripping a rod that went through holes drilled through the side faces toward the end of each part of the double cantilever. In each test, load, end displacement (CMOD), and crack length were all recorded along with the AE waveforms. A total of 18 specimens were tested, and each test produced between 800 and 1200 AE events over the ten-minute length of the tests.

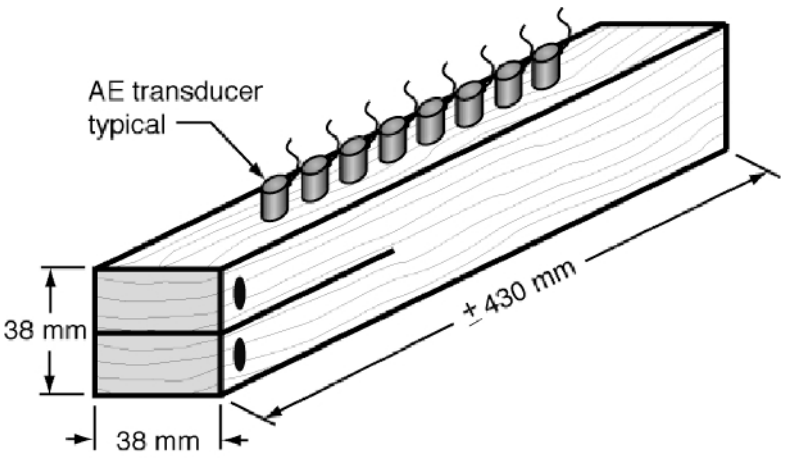

Fig. 12.3. Specimen geometry for AE/fracture experiments.

In our analysis of AE energy, we desired a measurement that carried the same units as the fracture energy (e.g. Joules). In conventional AE analysis, energy is assumed to be proportional to the time integral of the AE voltage waveform squared. However, the resulting units do not lend themselves to a direct energy accounting.

Following Achenbach [1973], one can show that the average power per unit area of an elastic wave of a single frequency component can be written as:

$$\hat{p} = \frac{1}{2}\rho c_L \omega^2 A^2$$

where ρ is the mass density, c_L is the longitudinal wave velocity, ω is the angular frequency and A is the amplitude. The units are energy per unit time per unit area. For broadbanded AE signals we must add up the contributions from all frequencies, which we can do by integrating our waveform in the frequency domain.

For each event, the analysis was done for the waveform recorded by the transducer closest to the crack tip. The closest transducer was assumed to have an incidence angle that is nearly normal, thus simplifying analysis. Measured voltage transients were converted to displacement transients by applying the manufacturer's calibration data and using frequency division:

$$U(n) = \frac{V(n)}{T(n)}$$

where *U(n)*, *V(n)*, and *T(n)* are frequency representations of the surface displacement transient, the transducer output, and the transducer transfer function, respectively. *n* varies from 0 to *N*, the number of sampled data points. For a discrete time increment, Δt, the corresponding frequency increment, is $1/N\Delta t$, and the corresponding angular frequency increment, $\Delta\omega$ is $2\pi N\Delta t$. Once the frequency representation of the surface displacements transient, *U(n)*, is determined, we can integrate over the entire frequency range:

$$\hat{p} = \sum_{n=0}^{N/2-1} \frac{c_L}{\rho} \left(\frac{2\pi n}{N\Delta t} \right)^2 U(n)^2$$

This equation represents the average power per unit area transmitted by the elastic wave. The resulting power can then be multiplied by the time length of the recorded AE waveform. That result is in turn multiplied by the area of the propagating wave front (assumed spherical) at a distance equal to the source-receiver distance. It should be noted that this analysis accounts for attenuation due to geometric spreading, however it does not account for material attenuation.

AE energy was calculated for each recorded event in each test. An example of the cumulative AE energy is shown in **Fig. 12.4**, along with the corresponding load. It is noted that the rate of AE energy jumps at a point corresponding to about 50% of peak load, and then eases off immediately after peak load. This jump in AE energy release occurs well before the onset of visible crack growth. However, following the conclusion of Reiterer et al. [2000], we could propose that this energy release is due to the initial formation of a fracture process zone.

For each specimen tested, strain energy release rate, G_I, and fracture energy, G_{IC} were calculated using traditional linear elastic fracture mechanics tools.

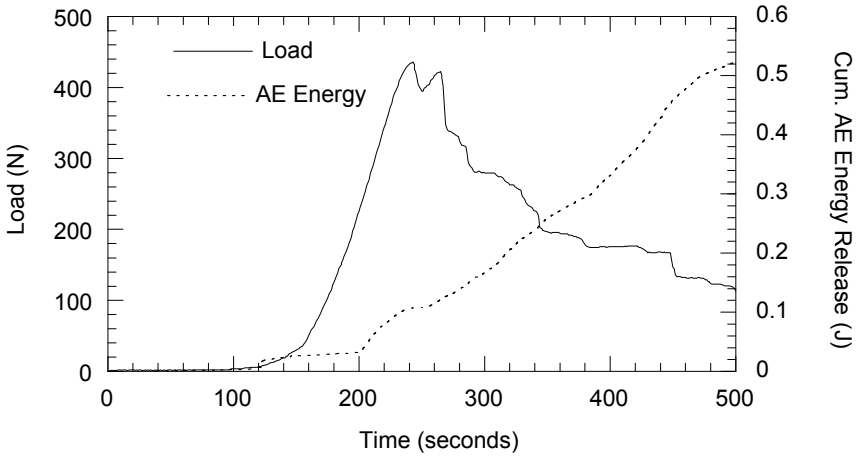

Fig. 12.4. Plots of load and AE energy release during test.

In order to compare the progressive energy dissipated by fracture to the progressive AE energy release, we calculated the cumulative work of fracture, *W(t)*, by integrating the product critical strain energy release rate and the crack area created over time:

$$W(t) = \int_0^t G_{IC} ba(\tau) d\tau$$

where *b* is the specimen (crack) width, and *a(t)* is the crack length at time *t*. A comparison of AE energy release and work of fracture is shown in **Fig. 12.5**. In the figure it can be seen that both AE energy and fracture energy increase in a roughly linear function with respect to time. A linear fit of both AE and fracture energy after 250 seconds produces slopes of 0.0095 J/s for fracture and 0.0014 J/s for AE. If we compare these slopes we could make the conclusion that for this particular specimen, fracture energy was being released at a rate almost seven times that of AE energy. This comparison was repeated for all specimens, and the resulting energy comparison is shown in **Fig. 12.6**. The fitted line shown has a slope of 0.16, indicating that on the average the rate of fracture energy released was over 6 times that detected by AE.

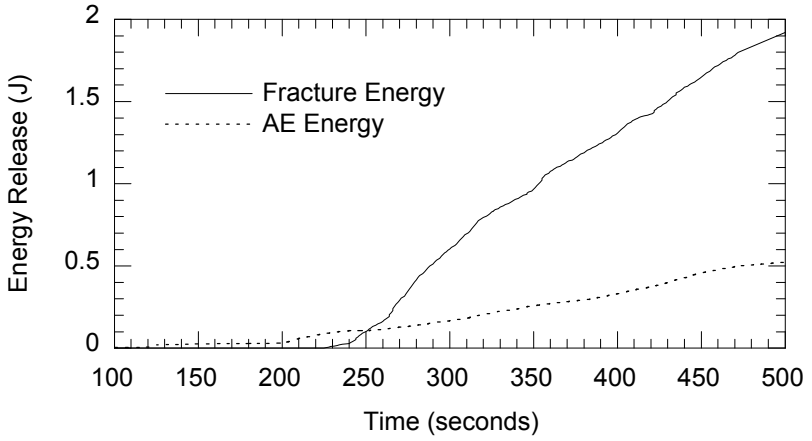

Fig. 12.5 Cumulative energy of fracture and acoustic emission.

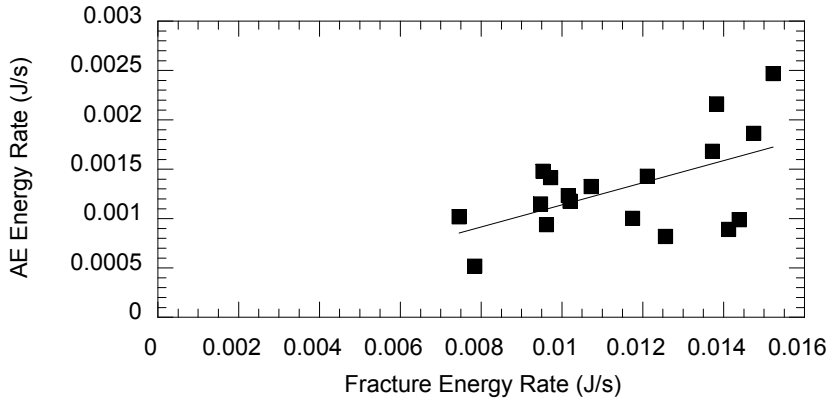

Fig. 12.6 Relationship between AE energy and fracture energy.

The work shows that while there is clearly a relationship between fracture energy and AE energy (supporting our original hypothesis), there is also a filtering process that takes place. AE monitoring alone is not sufficient to detect all measurable energy release. The results of this study quantitatively show the extent of the filtering processes. As noted, the analysis approach accounts for attenuation due to geometric spreading but not for material attenuation. If we use an attenuation rate of 200 dB/m, as previously cited for wave propagation in the radial and transverse directions, we should see attenuations of 4 to 5 dB. While this would account for some of

the differences, it is not enough to account for all the energy differences. Ultimately there are fracture and damage mechanisms such as crack bridging and creep that do not result in significant AE activity. That said, the results presented here could be very useful for nondestructive evaluation of arbitrary loading conditions that result in fracture.

12.6 Summary

In this chapter an array of acoustic emission applications to wood was presented. The intention was not to be comprehensive, but rather to present representative examples of active AE research efforts. It should be clear that there are many problems in which AE techniques can provide insight: damage and fracture, moisture effects and biological decay effects. The extreme variability of wood properties both between species and within a single tree presents a difficult challenge for interpretation of results. Nevertheless, AE will continue to complement the array of different experimental tools we use to advance our knowledge of this fascinating material.

References

Achenbach JD (1973) Wave Propagation in Elastic Solids. North-Holland, Amsterdam

Aicher S, Höfflin L, Dill-Langer G (2001) Damage Evolution and Acoustic Emissin of Wood at Tension Perpendicular to Fiber. Holz als Roh- und Werkstoff 59:104-116

Ansell MP (1982a) Acoustic Emission as a Technique for Monitoring Fracture Processes in Wood. Structural Uses of Wood in Adverse Environments. Meyer RW, Kellogg RM (eds) Van Nostrand R

Ansell MP (1982b) Acoustic Emission from Softwoods in Tension. Wood Science and Technology 16:35-58

Beall FC (2002) Overview of the use of Ultrasonic Technologies in Researc on Wood Properties. Wood Science and Technology 36:197-212

Beall FC, Wilcox WW (1987) Relationship of Acoustic Emission During Radial Compression to Mass Loss from Decay. Forest Products Journal 37(4):38-42.

Bodig J, Jayne BA (1993) Mechanics of Wood and Wood Composites. Krieger Publishing Company, Malabar, FL

Bucur V (1995) Acoustics of Wood. CRC Press, New York

DeBaise GR, Porter AW, Pentoney RE (1966) Morphology and Mechanics of Wood Fracture. Materials Res. Stds. 6(10):493-499

Gozdecki C, Smardzewski J (2005) Detection of Failurs of Adhesively Bonded Joints using the Acoustic Emission Method. Holzforschung 59:219-229

Imamura Y, Fujii Y, Noguchi M, Fujisawa K, Yukimune K (1991) Acoustic Emission During Bending Test of Decayed Wood. Mokuzai Gakkaishi 37(11):1084-1090

Landis EN, Whittaker DB (2000) Acoustic Emissions and the Fracture Energy of Wood. Condition Monitoring of Materials and Structures. Ansari F (ed) ASCE, Reston, VA, pp 21-29

Noguchi M, Nishimoto K, Imamura Y, Fujii Y, Okumura S, Miyauchi T (1986) Detection of Very Early Stages of Decay in Western Hemlock Wood Using AE. Forest Products Journal 36(4):35-36

Noguchi M, Fujii Y, Owada M, Imamura Y, Tokoro M, Tooya R (1991) AE Monitoring to Detect Termite Attack on Wood of Commercial Dimension and Posts. Forest Products Journal 41(9):32-36

Quarles SL (1988) The Effect of Physical and Structural Properties of Solid Wood on the Attenuation of Burst Type Emissions. Proc. 9th International Acoustic Emission Symposium, pp 642-649

Quarles SL (1990) The effects of Moisture Content and Ring Arrangement on the Propagation of Acoustic Signals in Wood. Journal of Acoustic Emission 9(3):189-195

Reiterer A, Stanzl-Tschegg SE, Tschegg EK (2000) Mode I Fracture and Acoustic Emission of Softwood and Hardwood. Wood Science and Technology 34(5):417-430

Raczkowski J, Lutomski K, Molinski W, Wos R (1999) Detection of Early Stages of Wood Decay by Acoustic Emission Technique. Wood Science and Technology 33:353-358

Rice RW, Skaar C (1990) Acoustic Emission Patterns from the Surface of Red Oak Wafers under Transverse Bending Stress. Wood Science and Technology 24:123-129

Sakui HA, Minamisawa A, Takagi K (1990) Effect of Moisture Content on Ultrasonic Velocity and Attenuation in Woods. Ultrasonics 28:382-385

Schniewind AP, Quarles SL, Lee SH (1996) Wood Fracture, Acoustic Emission, and the Drying Process. Part 1. Acoustic Emission Associated With Fracture. Wood Science and Technology 30:273-281

U.S. Forest Service (1999) "Wood Handbook - Wood as an Engineering Material." FPL-GTR-112, Madison, Wisconsin, USA

13 Superstructures

Mitsuhiro Shigeishi

13.1 Introduction

Development of highway networks has supported motorization, high economic growth and modernization all over the world. Thus, an enormous number of infrastructures, in particular, buildings and bridges have been constructed. However, many of them are currently known to have been aged and deteriorated after long-year service. In concrete structures, damages due to deteriorated or aged materials including corrosion of reinforcement and poor-workmanship responsible for initial cracking are often reported. Steel structures are deteriorated mostly by fatigue, resulting from increasing span length and overloading of traffic vehicles.

According to the standard specifications for concrete structures (JSCE 2001), the maintenance and management are explained in the following,

- step 1: Inspection,
- step 2: Evaluation of inspected results,
- step 3: Prediction by deterioration model, and
- step 4: Counter-measures for maintenance and management.

Thus, inspection procedures for the maintenance and management of structures are of fundamental importance prior to making a prediction model for deterioration and deciding counter-measures for repair and retrofit. The procedures could become diagnostic standards for evaluating the structural integrity.

There exist various methods for inspecting superstructures as bridges and buildings. So far, visual inspection is most extensively employed. Since defects, deterioration, and damage normally grow inside structure, a safety assessment cannot be based solely on the visual observation of cracks and signs of damages in structural elements. The technique should enable to provide definitive and quantitative evaluation in a short time. In

this respect, a variety of nondestructive evaluation (NDE) methods are being under investigation and in progress for practical use.

To inspect concrete and steel of superstructures, applications of AE techniques are in progress. The AE method is expected to become a very useful technique for evaluating the soundness or for detecting damages of the superstructure. This is because the measurement can be carried out without stopping traffic in a bridge or without evacuation of residents in a building. Here, successful results on the applications to buildings and bridges are stated. A promise for diagnosis and monitoring in the superstructures is discussed.

13.2 Building

For AE monitoring of existing concrete structures, it is essential to confirm that any AE signals responsible for the deterioration are not observed under service conditions. In the case that AE signals not of noises but due to deterioration process are detected, the monitoring and the analyses shall be conducted. The monitoring is performed continuously or routinely, and sometimes temporarily after the disasters. In this case, the selection and classification of AE signals which is closely associated with the deterioration are necessary.

In a historical masonry building, the efficiency of AE technique to monitor cracking is reported (Carpinteri & Lacidogna 2006). Comparing crack traces and AE activity, it is shown that AE measurement can be used to dynamically measure structures in service.

In an old reinforced concrete building, AE measurement was carried out in advance of rebuilding the house. A plan view of the two-story building is given in **Fig. 13.1**. Since the structure was old and not in service, the audible noises were readily observed due to the traffic load. At five locations circled in the figure, continuous monitoring was conducted for a week. To analyze AE data, two waveform parameters of the RA value and the averaged frequency stated in Chapter 4 were applied.

From the results of concrete specimens (Tsuji, Uchida et al. 2000), cracks are readily classified into tensile and shear cracks from two parameters as shown in **Fig. 13.2**. This classification is specified in the code (JCMS-III B5706 2003) and the parameters are determined as the moving average of more than 50 events. In the figure, R3, R6, and R15 represent the data detected with AE sensors of the resonance frequencies 30 kHz, 60 kHz, and 150 kHz, respectively. This implies that results are not dependent on characteristics of the sensors.

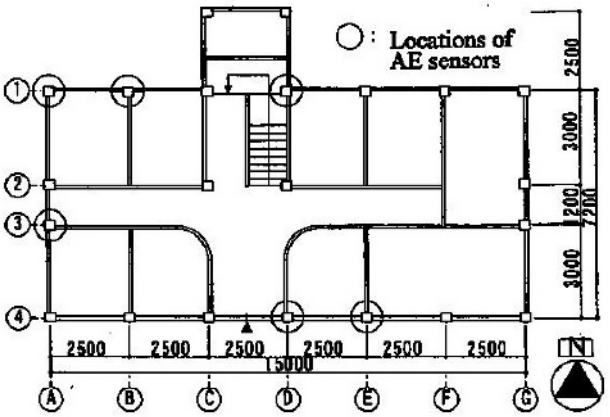

Fig. 13.1. Plan view of a reinforced concrete building.

Results of the classification are given in **Fig. 13.3**. Locations of the observation are labeled by the numbers from north to south and by the capital letter denoted from the left to the right as given in **Fig. 13.1**, and then the floor number is appended. As an example, 1A1 denotes the north-the left corner of the building at the fist floor. In the figure, AE waveforms are classified into a tensile type and a shear type based on the criterion in **Fig. 13.2**. High AE activities are observed at four locations 1B1, 1D1, 4E1 and 4D2. To investigate the conditions of concrete, core samples were take out after AE measurement from every location.

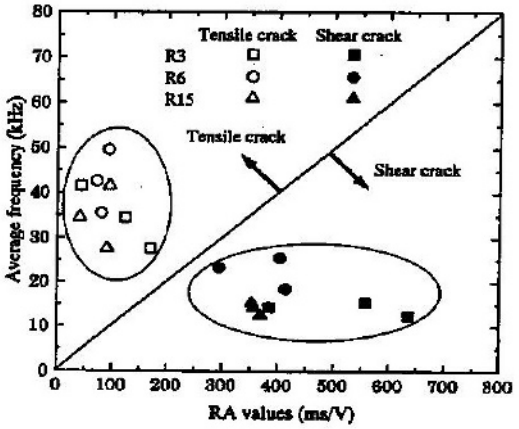

Fig. 13.2. Classification of crack types.

Then internal defects such as a cavity or a honeycomb were found at several locations, which are indicated by the letter "D". It is found that locations 1B1, 4E1 and 4D2 are indicated as defected, where AE waves of shear type are mostly observed. This implies that AE events were generated due to fretting of concrete at these defects. At one location 1D1, in contrast, tensile cracks are dominantly observed. Thus, it was concluded that tensile cracks were newly nucleated and extending at this location.

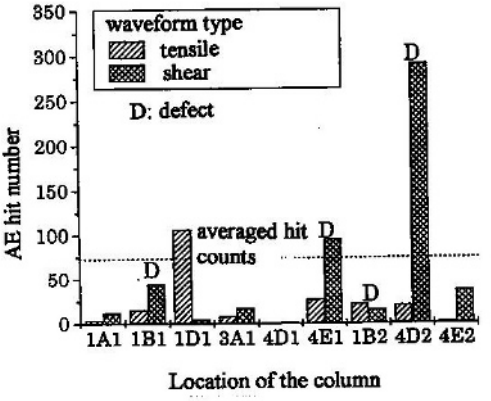

Fig. 13.3. AE events and locations.

13.3 Concrete Bridge

13.3.1 Reinforced Concrete Girder

In order to establish the procedure applicable to actual bridges of about 10 to 100 meter length, AE measurement was conducted in a bridge, of which girders were replaced (Shigeishi & Ohtsu 2004). A reinforced concrete (RC) girder bridge with a simple T shape is shown in **Fig. 13.4** that had served for about 45 years. All girders were dismounted for replacement, and one girder in the figure was tested. AE generating behavior under a repetitive bending load was measured, applying a large loading device. A sensor array and a loading condition are illustrated in **Fig. 13.5**. The purpose of this test was to investigate the Kaiser effect in a real-scale member.

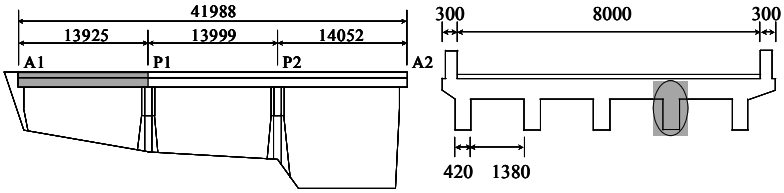

Fig. 13.4. A view of a road bridge in service.

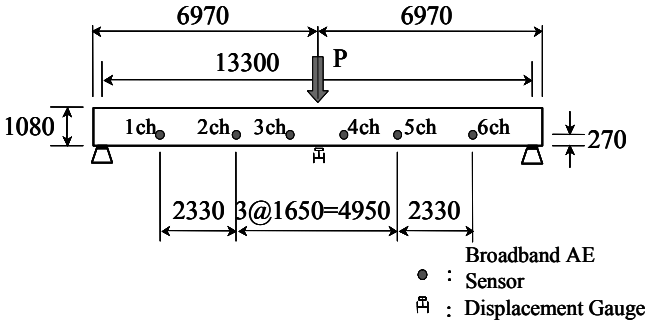

Fig. 13.5. Test set-up for the cyclic bending test in a dismantled girder.

Fig. 13.6. Loading device for a bending test of the girder.

In the loading test, the bending load was applied by using the steel frame shown in **Fig. 13.6**. A hydraulic jack was placed at the top center between two supports of the girder. The loading force was measured by a pressure gauge inserted between the jack and a loading bar along with a deflection gauge installed right below the loading section. Six broadband-type AE

sensors (UT1000, PAC) were attached on one side at the web of the girder as shown in **Fig. 13.5**. Output signals from AE sensors were amplified by 40 dB gain and the detection threshold was set to 38 dB referring to the sensor output.

As seen in **Fig. 13.7**, under a cyclic-incremental loading, the gradual increase of total number of AE hits was observed. From the both graphs, the Kaiser effect can be observed until the loading cycle of 150 kN, because a few AE hits are only observed and no increase in unloading cycles. Once the maximum repetitive load exceeded 200 kN, AE activity was observed even below the maximum previous load and tended to increase in unloading stages.

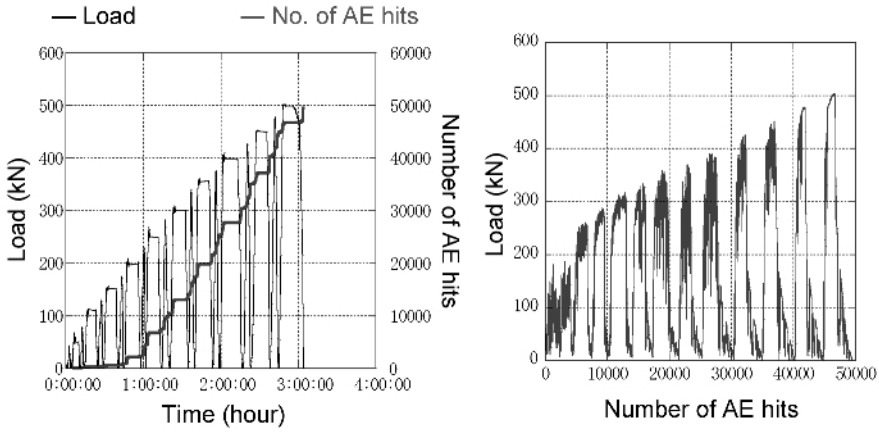

Fig. 13.7. AE generation behavior and loading cycles of the dismantled girder in a cyclic bending test.

Thus, it is demonstrated that the Kaiser effect is observed in a full-scale girder. For the comparison with AE results, residual deformations at the center of the girder are shown in **Fig. 13.8**.

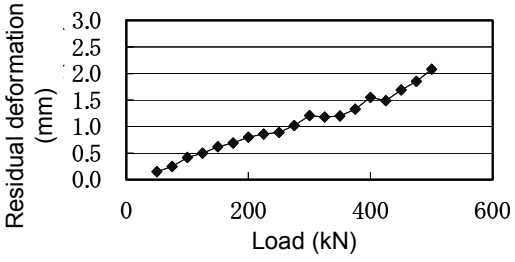

Fig. 13.8. Residual deformations at the center of the girder.

The deformations increase continuously with the increase in loading stages. Thus, no clear transition is observed at the load level of 200 kN, where the deformation exceeds 1.0 mm. Concerning the serviceability of the superstructure, deformations less than 2 mm are not critical, but AE observation suggests the beginning of deterioration over 200 kN cycles as the breakdown of the Kaiser effect.

In relation with the Kaiser effect, the recommended practice (NDIS2421 2000) provides a guideline to qualify the damage of reinforced concrete structures. Thus, a feasibility of the practice was studied. The Kaiser effect means the phenomenon that a material under load emits AE waves only after a primary load level is exceeded. During reloading, the material behaves elastically before the previous maximum load is reached. The Kaiser effect suggests that little or no AE events are recorded before the previous maximum stress level is achieved. However, the Kaiser effect comes to be vanished after the material once suffers from serious damages. In the definition of the Felicity effect, nucleation of the plastic zone in the material is suggested to be a cause for disappearance of the Kaiser effect. Based on these findings, two indices are newly proposed as the load ratio and the calm ratio, as stated in Chapter 4. A schematical illustration is given in **Fig. 13.9**.

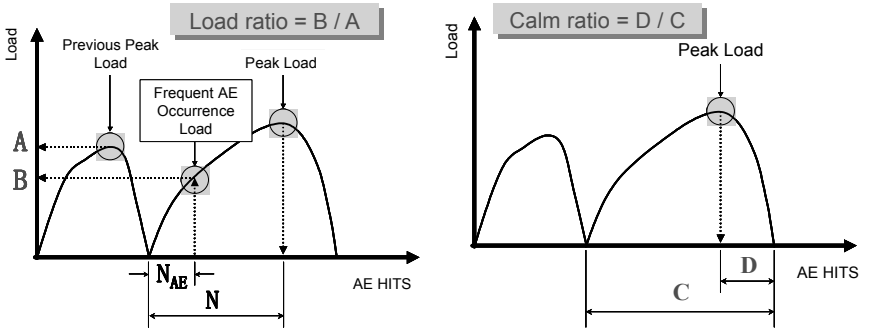

Fig. 13.9. Definitions of load ratio and calm ratio in a cyclic loading.

The load ratio and the calm ratio were estimated in the test of the dismantled girder. Results are shown in **Fig. 13.10**. It is clearly observed that with the increase in loading cycles, plotted points move from the sound zone to the serious damaged zone. The zones classified are not yet clearly described with threshold values, because these values are to be specified from experiments data of structural members. In the case of the present test, the loading cycle up to 200 kN is to be one threshold value. Thus the applicability of the recommended practice (NDIS 2421) is confirmed. Data

acquisition on reinforced concrete girders is promising to establish the criterion for the damage qualification.

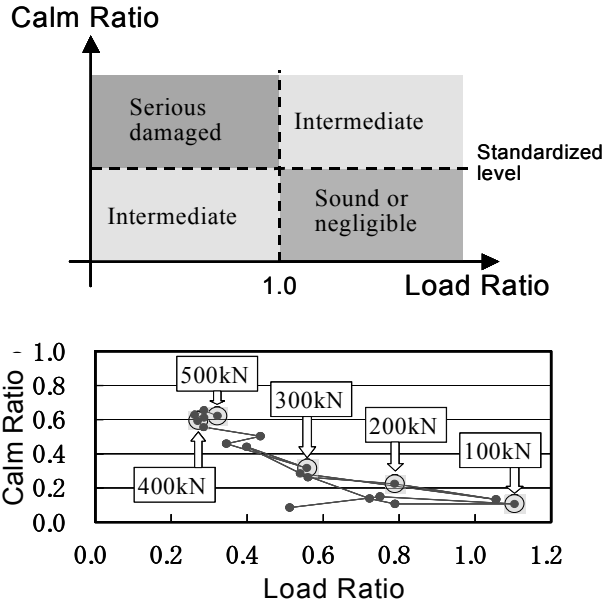

Fig. 13.10. Diagram of the load ratio and the calm ratio during the test.

13.3.2 Reinforced Concrete Slab

In the previous section, a full-scale girder was tested to qualify the damage. However, the main members of a superstructure seldom receive the extreme damage, except in accidents or after earthquakes. Results of the Inspection often report defects of local areas. At such parts subject to intensive repetitive stresses as floor slabs and bearings, serious damages are detected due to traffic loads in service.

Here, results of AE monitoring at a slab of a reinforced concrete bridge are given. The measurement was conducted in the bridge on a general highway in an urban area shown in **Fig. 13.11** (Shigeishi, Makizumi et al. 2003). In the measurement, AE parameters were recorded at the sensor output ratio of 42 dB as the threshold by using an AE signal waveform analyzer. 6-channel analog signal processing system was employed with six broadband AE sensors and 40 dB preamplifiers.

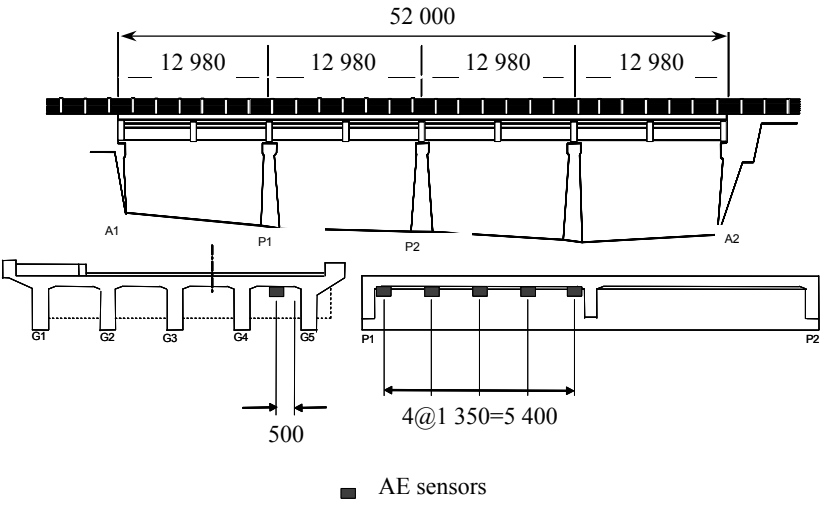

Fig. 13.11. AE monitoring on a slab of a road bridge.

Between piers P1 and P2 of the four-span bridge, AE sensors were arranged at the transverse beam as shown in **Fig. 13.11**. The sensors were arranged at interval of 1350 mm along the bridge axis at the center between the floor slab supports. The line selected for sensor arrangement corresponded to the line where the right-side wheels of vehicles run. In a test, heavy vehicles crossed the bridge under traffic control as shown in **Fig. 13.12**, and AE signals were recorded.

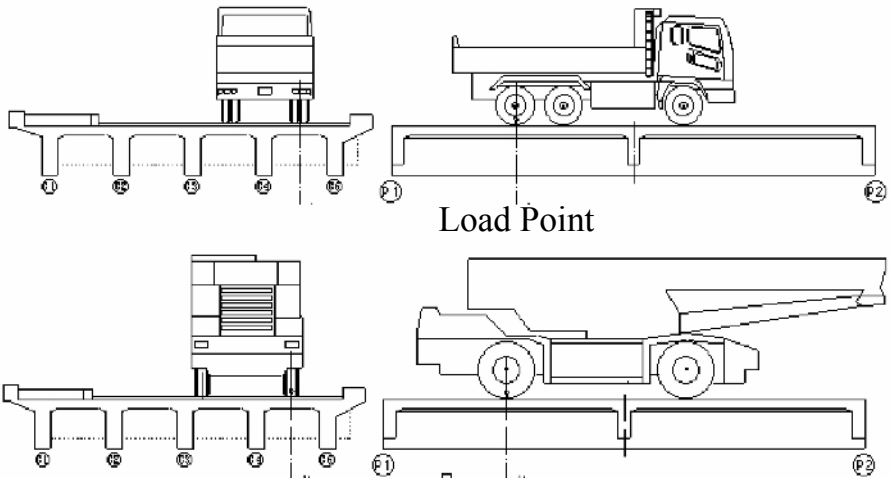

Fig. 13.12. AE measurement under heavy-vehicle loading.

When the vehicles moved at the normal speed of about 40 km/h, total AE energy detected by each channel is shown in **Fig. 13.13**. In the left figure, results of one-dimensional location are also given as cumulative AE events. It is observed that AE energy detected at channel 1 is remarkably large, probably because the sensor of channel 1 is close to the joint of pier P1 where wheels of vehicles could convey impact loads on the slab crossing over the joint. AE energy decreases as reaching to channel 5. This is because deformations at the central area are elastic enough as indicating the soundness state.

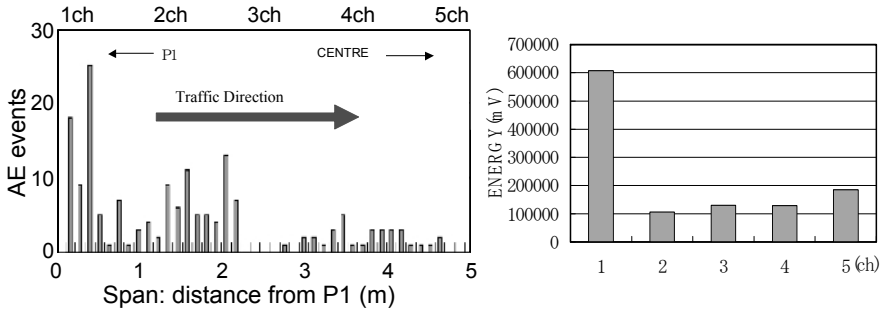

Fig. 13.13. Cumulative AE events and AE energy under traffic load (40 km/h).

In **Fig. 13.14**, total AE energy at each channel is compared with strain measured at reinforcing-steel rod under the slow-speed running (V=20 km/h) of a dump truck and a rafter crane. Both AE energy and the strain are highest at the position of channel 3. These are results obtained under slow-running traffic. Thus, AE activity and the strain at channel 1 are smaller than those of channel 3. Compared with AE activity in **Fig. 13.13** observed while the bridge is in service, distribution of AE energy is fairly different. This is because vehicles moved at low speeds and did not produce impact loads at the joints.

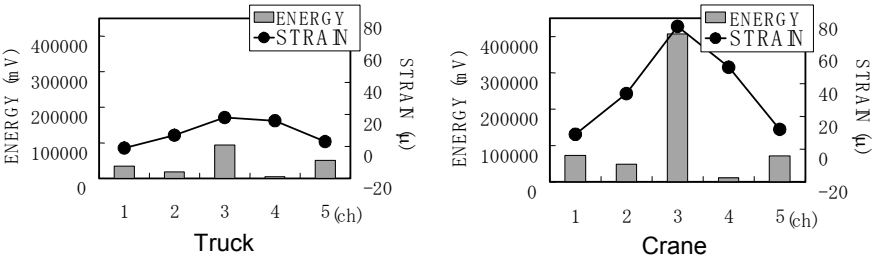

Fig. 13.14. AE energies and strains at rebar observed under slow heavy-load traffic (V=20 km/h).

In **Fig. 13.15**, total AE energy and strain at reinforcing rod by each channel are shown. These were observed under very slow loading (almost static condition :V=5 km/h). Concerning the strains at reinforcing rods, the values become larger at channel 1 and channel 5 than those of other locations. The energy also became greater at channel 1 and channel 5. Considering the observed distributions of AE energy, it is found that the impact load generates AE events near the joint, slow-moving load generates a low-frequency vibration associated with AE activity at channel 3, and AE activity due to quasi-static loading is similar to a bending-moment distribution under uniform load.

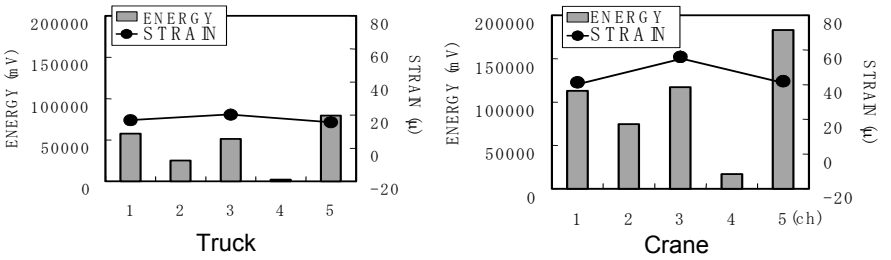

Fig. 13.15. AE energies and strains under quasi-static heavy loading (V=5 km/h).

From in-situ inspection of existing concrete bridges, it is clarified that the running speed of vehicles should be taken into consideration in the measurement. Otherwise, the damaged zone might not be correctly identified, because the impact loading could generate high AE activity at the joints. In other cases, vibration modes due to moving loads may affect AE activities at local areas.

13.4 Steel Bridge

Steel bridges are generally employed for longer spans than concrete bridges. With the recent trend for large bridges, the superstructures are not only made of steel frame, but also reduce their weights by adopting steel slabs. Currently, complicated floor framing composed of relatively small steel members has so many jointed or welded sections that initial defects are afraid to affect the durability, in particular, the fatigue deterioration Due to the increase in unpredictable of traffics and overloaded vehicles, severe damage in small steel members are highly concerned.

In a large bridge of steel box-girders shown in **Fig. 13.16**, cracks were visually found. Consequently, the activities of cracks were estimated by the AE method (Shigeishi 2004). The slab was covered with a waterproof

resin sheet and asphalt was directly layered above the sheet. During the measurement, the bridge was in service, carrying traffic.

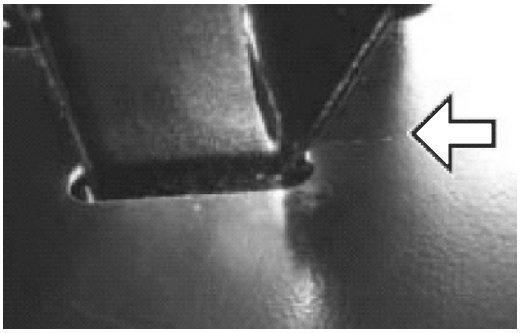

Fig. 13.16. Photo of a fatigue crack propagating from a weld line with a lateral beam through U-shaped rib stiffener.

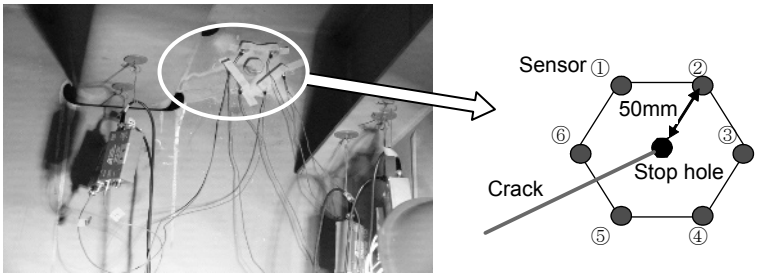

Fig. 13.17. AE measurement on lateral beam connecting with U-shaped rib plate.

In **Fig. 13.17**, sensor array is shown for AE measurement on a welded section of a steel-slab connecting with a lateral beam. By applying a ultrasonic test (UT), a crack was suspected at a location where the U-shaped rib plate was welded with the lateral beam. AE sensors were installed to locate sources around the stop-hole to arrest crack extension.

Six AE sensors of 150 kHz resonance-type (R15, PAC) were attached on the side of the lateral beam. As a result, AE sources were located around the hole as shown **Fig. 13.18**. High AE activity may indicate that a latent crack is propagating due to traffic load.

Then AE sources were also located by installing guard sensors as shown in **Fig. 13.19**. The guard sensors were employed to discriminate from sources originating from outside the area of interest. Because waves from outside the area can be detected at least one of the guard sensors (1, 2 or 3 shown in **Fig. 13.19**) before arriving at the sensor (4, 5 or 6) placed on the

area of interest, this technique is applicable to reject the noise from the outside. From the locations in **Fig. 13.20**, we can identify a probable crack-tip around AE cluster.

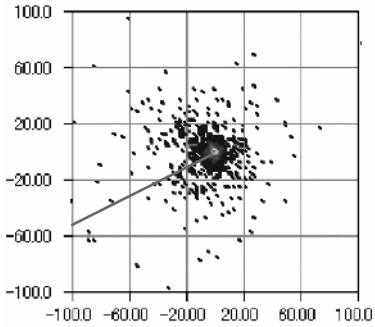

Fig. 13.18. AE sources located during the measurement.

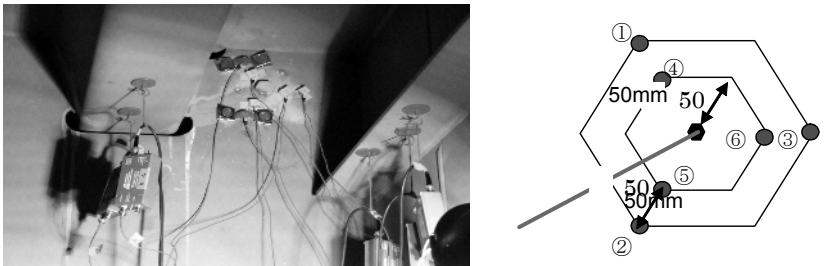

Fig. 13.19. AE measurement with guard sensor.

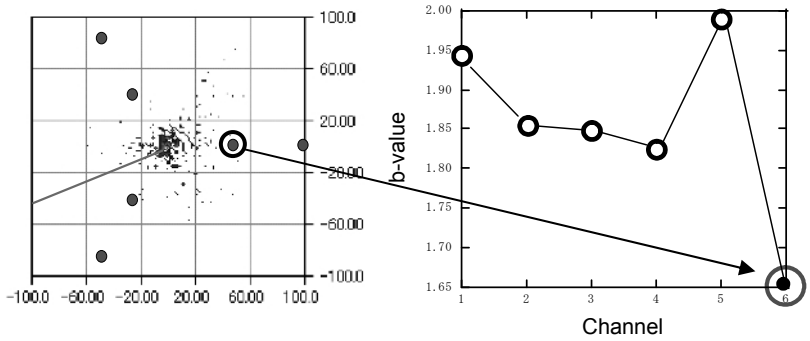

Fig. 13.20. AE sources located by guard sensors and b-values at 6 channels.

In **Fig. 13.20**, the b-values observed at 6 sensors are given. As can be seen from the graph, the b-value is remarkably small at AE sensor at channel 6 where the edge of AE cluster is identified in comparison with the b-values at the other AE sensors. This seems to suggest an orientation of probable crack propagation, because generation of large-scale AE events is identified from the b-value observed at channel 6.

13.5 Steel-Concrete Composite Slab

A steel-concrete composite slab is newly available in construction, of which concrete is placed in a steel mold that consists of steel side plates, top reinforcing bars and transverse ribs, and stud-planted bottom steel plates. Configuration of one type slab is shown **Fig. 13.21**. Compared with a reinforced concrete slab, this slab is expected to bear a large load- capacity and to have good endurance. Although these characteristics are favorable for bridge construction, visual inspection is very difficult in particular, for concrete and its interface with steel plate. As a result, effective inspection techniques for steel-concrete composite slabs are in demand and under development.

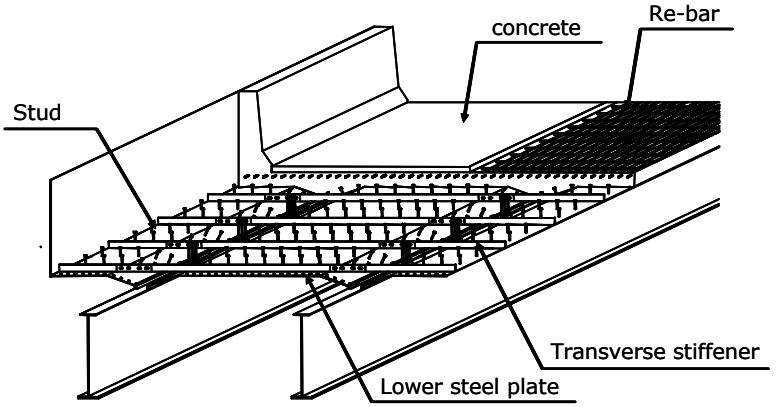

Fig. 13.21. Robinson-type of steel-concrete composite slab.

Applying the AE method, we performed cyclic tests of repetitive loading and fatigue loading (Itoh, Shigeishi et al. 2002). The case where delamination between concrete and steel plate occurs was investigated, which is regarded as one of the serious deterioration mechanisms in composite floor slabs. The fracture of studs and the fatigue damage of concrete were also examined from AE results.

A Robinson-type steel-concrete composite floor slab was of dimensions of 1540 mm x 159 mm x 1500 mm, which is shown in **Fig. 13.22**. To withstand deflections due to concrete casting, transverse ribs are arranged at the center and on both sides. The loading position was set at the top center of the specimen. A plate of dimensions 200 mm x 125 mm was installed as a loading plate. Load of 100 kN was first applied 2 million times at a frequency of 3 Hz, then 250 kN was applied 0.5 million times at 2 Hz, and finally 300 kN was applied 0.5 million times at 1 Hz.

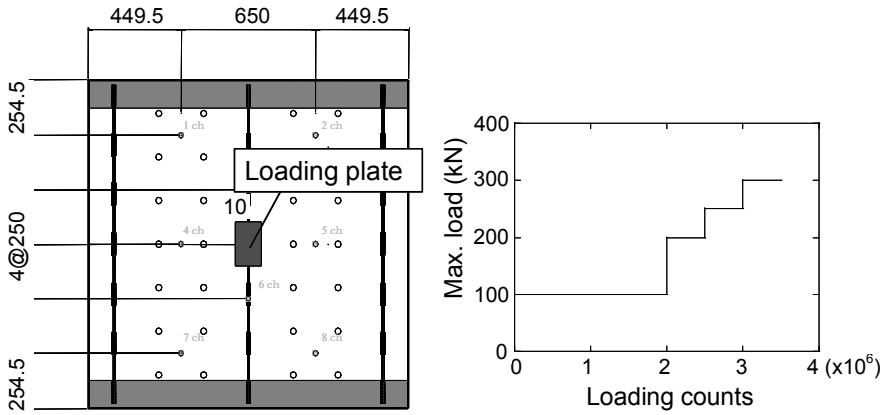

Fig. 13.22. Steel-concrete slab specimen and fatigue loading steps.

AE sensors were arranged on the bottom steel slab. Following every 10,000 times loading, we detected and recorded AE events generated during 300 times of loading. In **Fig. 13.23**, some of results after surface cracks were observed in concrete and at a final stage are shown. Before 2 million times of loading, AE events were actively observed when the deflections under the load position started increasing acceleratedly. After 2 million times of loading, AE events were observed at unloading cycles. As seen in the left graph, the calm ratios are equal to zero until cracks were nucleated. Approaching the final stage, the calm ratios become 1.0 as found in the right graph. Therefore, it suggests that the calm ratio is applicable to estimate the soundness of the steel-concrete composite slab in AE measurement, even though visual inspection is not available.

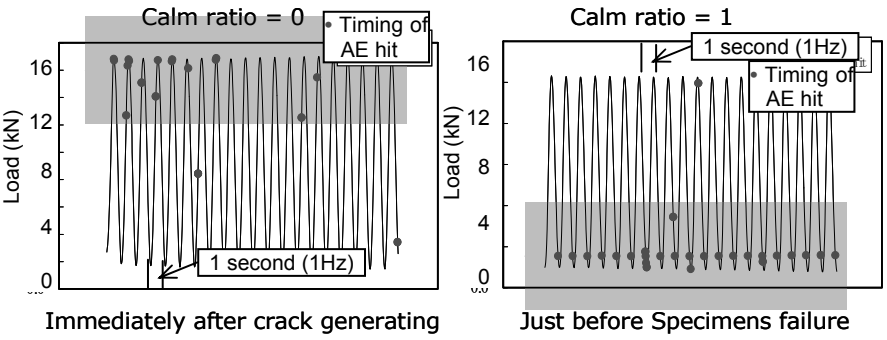

Fig. 13.23. AE generating behaviors and the calm ration during cyclic loading.

13.6 Concluding Remarks

AE measurement has been applied to the superstructures to evaluate the deterioration or the damage. In this case, in situ measurement under service or traffic loads is desirable. In these applications, the care for environmental noises is essential. This is because the measuring conditions at the site are varied one by one. It is quite important to conduct preliminary tests prior to actual tests on equipment setting and measuring conditions. Based on these well-cared preparations, valuable AE data are to be successfully obtained.

References

Carpinteri A, Lacidogna G (2006) Damage monitoring of an historical masonry building by the acoustic emission technique. Materials and Structures 39:161-167

Itoh T, Shigeishi M, Ohtsu M (2002) Acoustic emission in fatigue process of steel plate-concrete composite slab. Progress in Acoustic Emission 11:132-137

JSCE (2001) Standard specifications for concrete structures: maintenance. Japan Society of Civil Engineers, Tokyo

NDIS 2421 (2000) Recommended practice for in situ monitoring of concrete structures by acoustic emission. Japan Society for Non-Destructive Inspection, Tokyo

Shigeishi M, Makizumi T, Jo H, Ueda J (2003) AE monitoring of a reinforced concrete road bridge. Structural faults and repair 11 (CD-ROM): NDTB-SHIG

Shigeishi M, Ohtsu M (2004) Applicability of damage estimation based on acoustic emission activity under loading to practical reinforced concrete bridge. Bridge maintenance, safety, management and cost (CD-ROM):797-798

Shigeishi M (2004) A report of the development of acoustic emission application for inspection of bridge superstructure. A material of the technical committee on acoustic emission. Japan Society for Non-Destructive Testing 121:15-22

Tsuji N, Uchida M, Okamoto T, Ohtsu M (2000) Application of acoustic emission technique to evaluation of cracking in concrete structures. JSNDI, Progress in AE X:189-194

14 Substructures

Tomoki Shiotani

14.1 Introduction

A part of infrastructure, such as footing, pile and pier, is called a substructure, which mechanically supports structural members of the superstructure. When we investigate the damage of a structure, the superstructure is readily inspected because visual inspection is normally available. In contrast, the assessment of damages in the substructure is often not an easy task. For example, pile-foundations installed underground deeply into bearing strata can not be inspected visually. In this respect, AE measurement is expected to become a powerful technique for damage evaluation of the substructures.

14.2 Concrete Pile

Piles are made of wood, concrete, and metal and are generally pushed or driven into the ground in order to support the superstructures both statically and dynamically, such as buildings and bridges. Recently, prefabricated or cast-in concrete piles are employed for supporting the superstructures.

After the installation of piles into ground, it is normally difficult to evaluate the damage degree. So far, a pile integrity test (PIT) has been widely applied in foundation engineering (Middendorp & Reiding 1988). Following serious disasters due to great earthquakes in Kobe, Japan, the PIT was applied to estimate the soundness of existing piles. Results were not yet conclusive, because the procedure was originally developed for quality control of deep piles as the frequency range was lower than 1 kHz. The piles investigated in Kobe were not so deep as that the low frequency range was effective to the measurement. Consequently, an applicability of AE techniques was investigated in damaged concrete piles.

Concerning concrete piles, it is found that AE signals due to both crack initiation and crack growth could be observed (Shiotani, Shigeishi et al. 1999). It is suggestive that the secondary AE signals due to fretting at existing crack interfaces are observed in damaged concrete-piles. Paying a main attention to the secondary AE signals, the AE technique is going to be applied to diagnose the concrete-piles.

14.2.1 Basic Concept for AE Detection

A basic concept for AE monitoring has been proposed as illustrated in **Fig. 14.1** (Shiotani, Sakaino et al. 1997). When pile foundations are subjected to static or dynamic loading, AE activity could be generated due to fretting or friction in damaged areas. Then AE waves propagate through piles as well as ground. Installing AE sensors onto piles or within the wave-guide, the damage area generating AE signals can be located with a simple equation in Eq. 14.1 in the case of one-dimensional sensor array:

$$\mathrm{a} = \frac{l - v_p \delta \mathrm{t}}{2} \tag{14.1}$$

where l is a distance between AE sensors, v_p is the velocity of P wave in concrete piles (the case of pile-attached sensors) or that of waveguides (the case of waveguide-attached sensors). AE sources are located and thus the areas, where AE events are intensely generated, are identified as damaged. When we apply this technique, It is noted that:

- In the case that sensors can be installed in the piles in advance, not only the damaged area but also the progress of deterioration due to unexpected strong ground motions could be traced as AE activity.
- When the piles already damaged is investigated, external or internal load application is necessary to induce AE activity. In this concern, a short-term shakers or dynamic loading devices would be effectively employed.
- It is suggested, in principle, to conduct the long-term monitoring because of compensating temperature-induced stress variations or of monitoring the effects of aftershocks following the main shock in earthquakes.

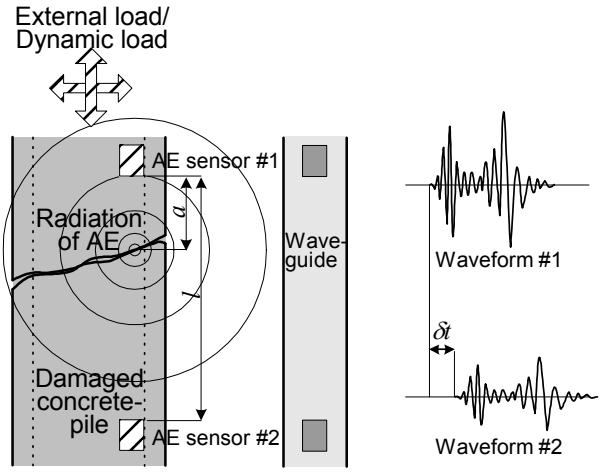

Fig. 14.1. Basic concept for detection of AE waves in a concrete-pile.

14.2.2 Application

AE monitoring was conducted at one site, where cast-in-place concrete piles were connected with a footing. Although the piles could bear heavy lateral-load, they were expected to be seriously damaged due to earthquakes. To induce AE events from the existing damages, a heavy-machinery was utilized. The load was first applied from one side of the footing. Subsequently, the heavy-machinery was placed on the footing to drive a dynamic load vertically to the piles. AE sensors were installed both in the borehole excavated in the pile and in the monitoring well excavated closely to the piles. AE waves detected were examined primarily with respect to their arrival times to determine one-dimensional locations, applying Eq. 14.1. Then estimated damages by AE measurement were compared with results of borehole camera observation, core samples drilled and wave velocities.

Test site and monitoring condition

In situ test was carried out in the reclamation land of Kishiwada City in Osaka Prefecture, Japan. Ground soil was composed of sandy gravel of 5 to 10 in SPT N-value underlying alternation of cohesive soil and sand. The land was reclaimed from the sea by 13 m in 1992. Pile foundation consisted of nine piles with connecting a footing of dimensions 9.0 m x 9.0 m

x 2.3 m. Inspection was conducted in pile No. 9 (P9) of 1.2 m diameter and 28.9 m length located at a corner of the footing as illustrated in **Fig. 14.2**. Induced AE waves due to shaking a heavily machinery were directly monitored by AE sensors placed on internal wall of a borehole P9 excavated in the pile. AE activity was also indirectly monitored by AE sensors set in a monitoring borehole B1 excavated. It is noted that the distance between the center of the pile and that of the well was 1.9 m.

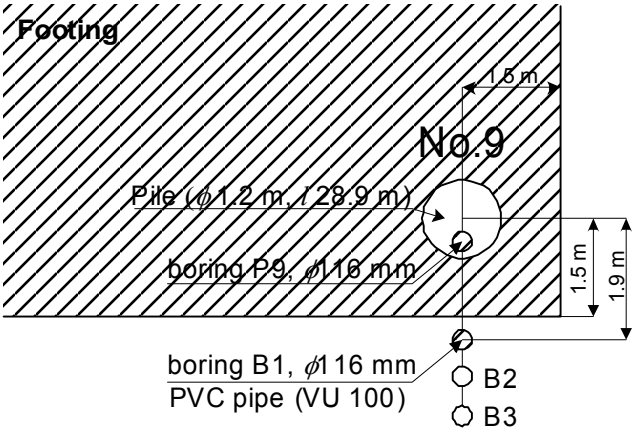

Fig. 14.2. Plan view of the pile foundation tested.

In **Fig. 14.3**, an array of AE sensors and zones of AE monitoring are illustrated. The depth of target was 11.5 m from the surface of the footing. In the case of direct AE monitoring, five AE sensors of 60 kHz resonance (R6, PAC) were arranged on a thin plate of 3 m long, where AE sensor was equally spaced by 50 cm. Thus, a set of AE sensors covered the area of 2 m square. The array was basically placed every 1.5 m deep with a 0.5 m overlap down to 11.0 m. In order to remove and set the sensor array at a design depth, a special device consisting of rubber balls with shifter levers was devised, which is shown in **Fig. 14.4**.

In the case of indirect AE monitoring, a polyvinyl-chloride (PVC) pipe was used to hold the sensors in the borehole. The arrangement of AE sensors was the same as that of direct monitoring, although the sensors were fixed in a rod of glass-fiber reinforced plastics. They were set at the design depths as to keep spaces between the sensors and the wall, and then the indirect AE monitoring was performed by replacing the spaces with water. Thus generated AE waves successively propagated through the sensors via ground, PVC pipes and water. It is noted that the wave-guide combining PVC pipes and water has as a twice sensitivity as that of conventional steel

wave-guide (Shiotani, Sakaino et al. 1997). Ten AE sensors of 60 kHz resonance (R6, PAC) were employed for detecting AE signals. The signals detected were amplified by 40 dB in a sensor-integrated preamplifier and AE hits over the 45-dB threshold were processed by a commercial AE system.

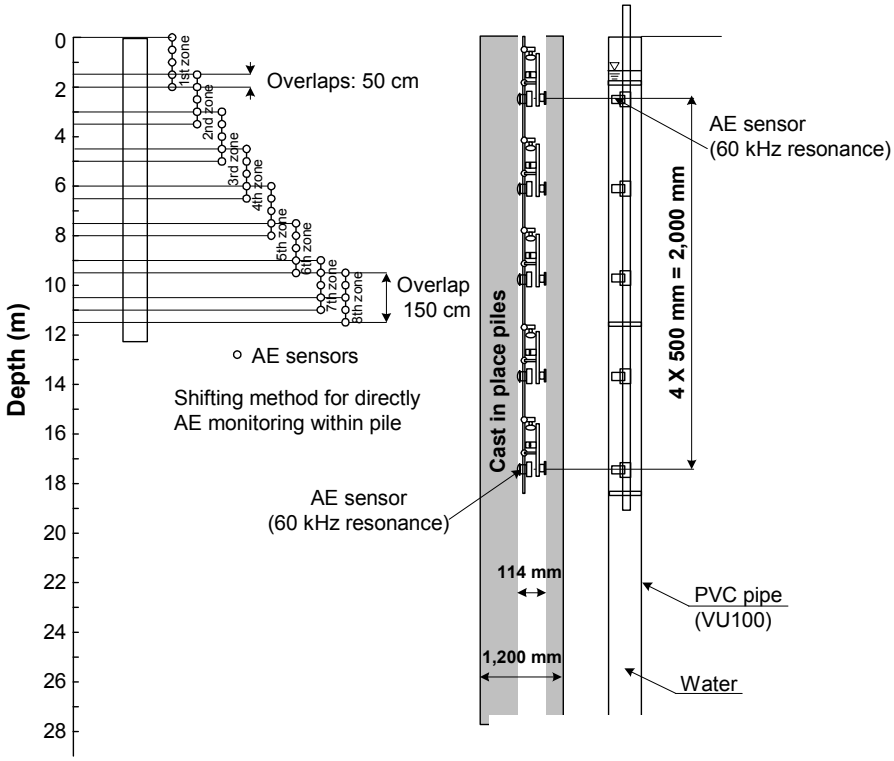

Fig. 14.3. AE sensor array and zones of AE monitoring (left: direct, right: indirect monitoring).

To induce AE activity from the existing cracks of the pile, a hydraulic excavator of 0.59 m^3 bucket capacity and 11.8 tons operating weight was used as a heavy-load shaker. The loading procedure by hydraulic excavator is illustrated in **Fig. 14.5**.

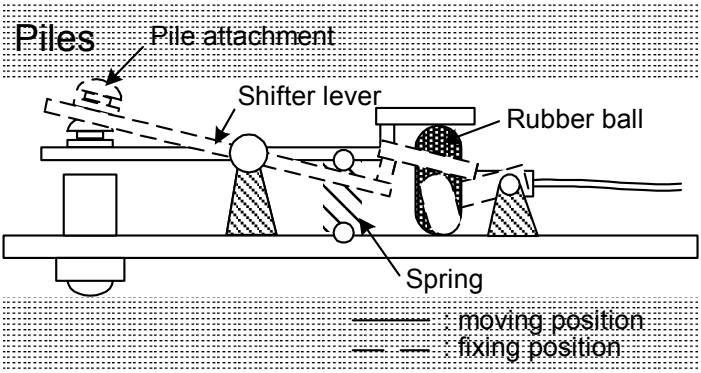

Fig. 14.4. Device to remove and set AE array in a borehole.

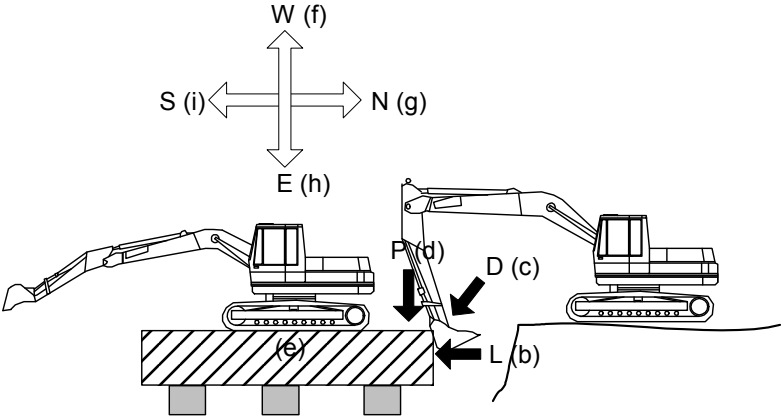

(a) BGN monitoring
(b) Lateral load
(c) Diagonal load
(d) Perpendicular load
(e) Placing machinery on footing
(f) Arm's expanding with up-and-down movements to the west
(g) ditto to the north
(h) ditto to the east
(i) ditto to the south
(j) removal from footing

Fig. 14.5. Loading procedure by a heavy-load hydraulic excavator.

Results

To observe the damage areas visually, a CCD camera was inserted into the pile. Accumulated numbers of cracks observed in every 0.5 m are summarized in **Fig. 14.6** (a). In **Fig. 14.6** (b), photos of core samples drilled are shown. It is estimated from **Fig. 14.6** (a) that the damage is particularly serious around the pile head. Cracks are further found at the depths ranging form 7.0 m to 8.0 m and from 8.5 m to 11.5 m. From **Fig. 14.6** (b), it is realized that locations of cracks in cores are really identical to those observed by the CCD camera.

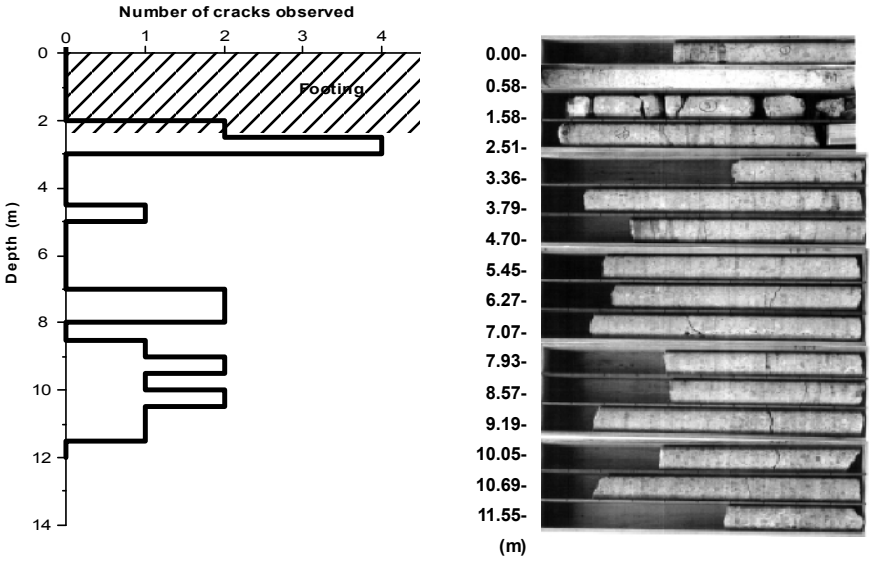

(a) Accumulated number of cracks with dept (b) Core samples

Fig. 14.6. Crack observation by the CCD Camera and core sample.

One-dimensional locations of AE sources during the test are shown in **Fig. 14.7**. AE sources are symbolized by circles where the magnitude of diameter reflects the number of AE counts. We focus on AE cluster at the shallow depth up to 2.0 m. It is found that a large number of AE sources of greater magnitude are started to be generated from the dynamic load at the period (g), followed by those of (h) and (i). Thus, AE activity associated with the damaged areas could be successfully induced by the heavily machinery. Additionally, AE events were dominantly found inside the footing up to 2 m depth. As found in **Fig. 14.6**, the damage of footing concrete is reasonably identified by core samples and the CCD camera observation.

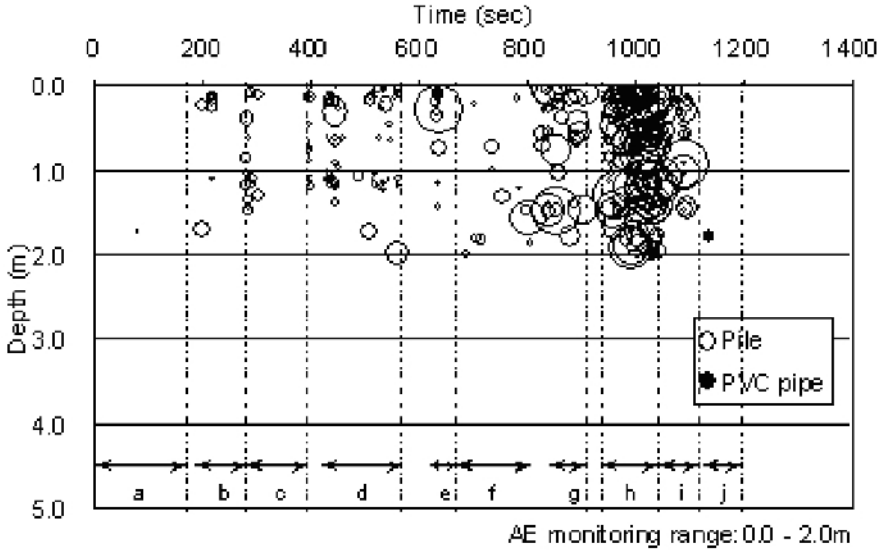

Fig. 14.7. Variations of 1-D source locations due to dynamic loading.

Fig. 14.8 shows some AE parameters analyzed at every 5 cm depth. From **Fig. 14.8** (a) and (b), it is observed that AE activities are intensively observed at the depths between 1.0 m and 1.5m, and around 2.0 m. At the depths from 3.0 m to 3.5 m, and around 5.0 m, a few AE events are observed. Locations of the damaged areas are most clearly identified by the average counts in **Fig. 14.8** (c). Large numbers of AE events are particularly generated at the depths 3.0-4.0 m, and 4.0-5.0 as well as in the footing. Almost the same AE activity as the direct monitoring is observed along the depth in the indirect AE monitoring as shown in **Fig. 14.8** (d).

The measurement of wave velocities was performed by using AE sensors placed in the pile. Elastic waves were artificially generated by hammering the surface of footing with a steel hammer. In **Fig. 14.9**, distribution of wave velocities in the pile is shown, compared with the graph in **Fig. 14.8** (c). Locations of lower wave-velocities denoted by arrows are in remarkable agreement with the damaged locations evaluated from high AE activities. Through these series of experiments, it is demonstrated that the AE technique is effective to evaluate the damage of concrete-piles.

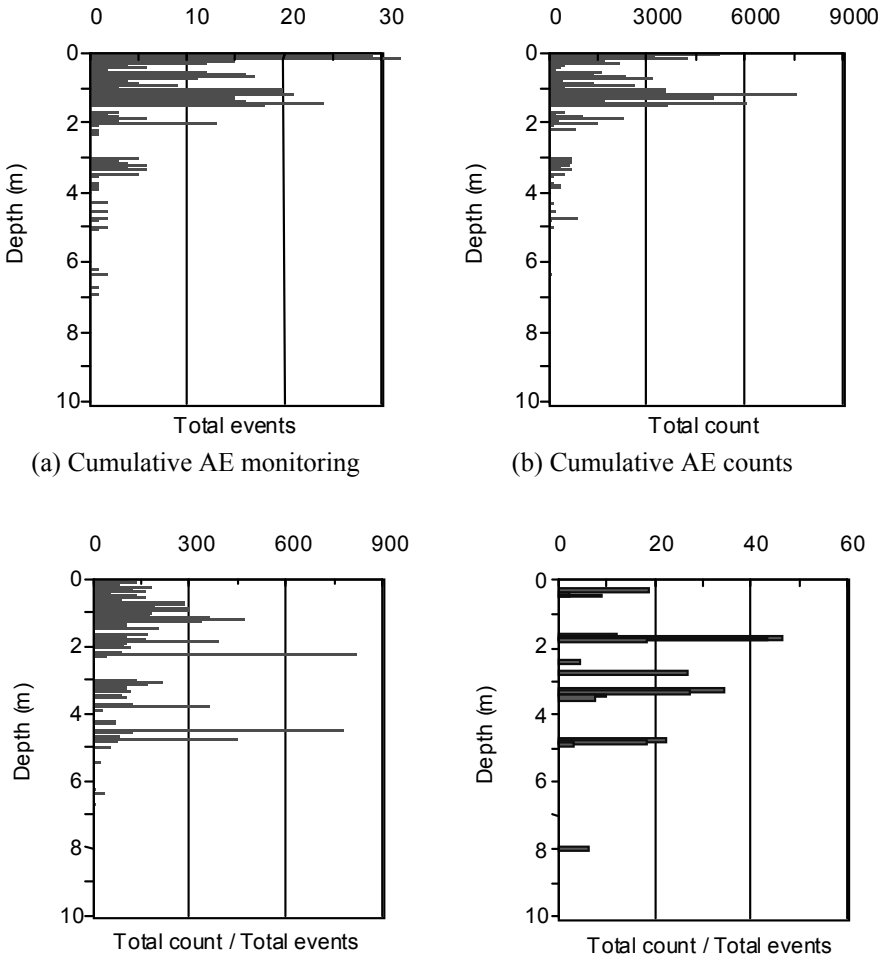

Fig. 14.8. AE parameters analyzed at every 5 cm depth. Results of direct monitoring are shown in graphs **(a)**, **(b)** and **(c)**. Graph **(d)** shows that of indirect monitoring.

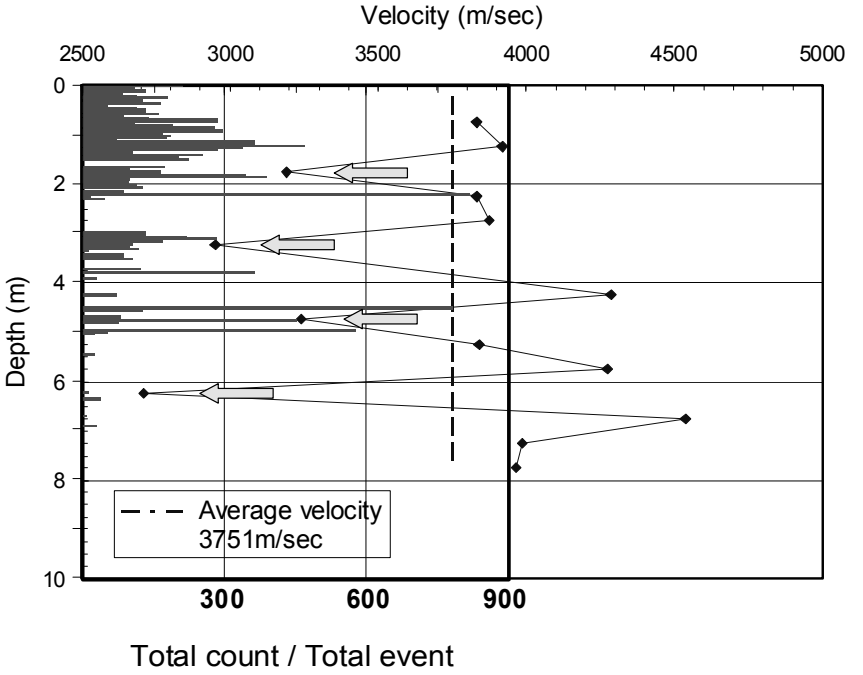

Fig. 14.9. Distribution of wave velocities along the depth with AE activity.

14.3 Railway Substructure

Railway structures have been constructed worldwide as fundamental infrastructure. In Japan, many of railway structures are more than 50 years old. Aging and deteriorations due to weathering, corrosion, earthquakes, and so forth have been seriously recognized. Accordingly, the maintenance of these structures has been in great demand. AE techniques definitely contribute to the assessment of railway structures, because the secondary AE activity can be driven by passing loads due to trains. In the case of monitoring train- or transportation-induced AE activity, one important issue is elimination of mechanically-impacted noises by the passage of trains. It is summarized here how the mechanical noises due to passage of trains were eliminated and quantitative evaluation of structural integrity was conducted.

14.3.1 Signals due to Train Passage

In the case of AE monitoring under active transportation loads, it is effective to detect the secondary AE activity due to mechanical impacts of dynamic loads. In general AE monitoring system are designed to detect higher frequency signals e.g. more than 10 kHz. In the case that a significantly large impact is driven, induced signals might initially have only lower frequency components of AE signals. Thus characteristics of these signals were studied in an actually damaged pier during the passage of rapid trains.

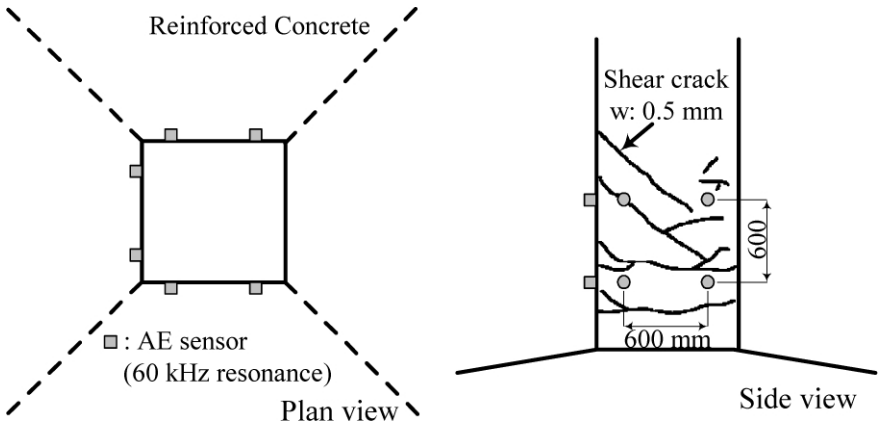

Fig. 14.10. Observed cracks along with an array of AE sensors.

Monitoring condition

A reinforced concrete pier for railway bridges had been damaged due to the strong ground motions of earthquakes. Not only bending cracks (up to 0.7 mm wide) but also shear cracks (up to 0.5 mm wide) were visually identified. In **Fig. 14.10**, observed cracks and the arrangement of AE sensors are illustrated. 12 AE sensors of 60 kHz resonance (R6, PAC) were densely arranged in the damaged area. On each of three sides, four sensors were placed with a 60 cm-square array. AE signals were amplified by 40 dB at preamplifiers and those exceeding 40 dB threshold were processed via AE monitoring system. Both AE parameters and waveforms were recorded in the system. In order to study relations between AE activity and the structural behaviors, three π-shaped displacement-meters (accuracy of ± 2 mm) were set below the lowest crack on three sides.

AE activity

AE activity during one train passage is shown in **Fig. 14.11**. Accumulated number of AE hits and AE events are plotted in the figure. It is noted that all AE signals detected are denoted as 'AE hits'. In only the case that AE sources were located within the pier by the source location, AE signals are defined as 'AE events'. According to deformations measured with the π displacement-meter, the pier started to be compressed and kept deformed for six seconds due to the train passage. Both AE hits and AE events were simultaneously observed, although they slightly followed the onset of deformations. Comparing the counts between AE hits and AE events, total number shows remarkably different values as 575 in AE hits and 21 in AE events. Even taking into account the propagation-attenuation of the signals, the difference would be still significant. It was suspected that undesirable signals (noises) were contained in AE hits, directly induced by the train passage.

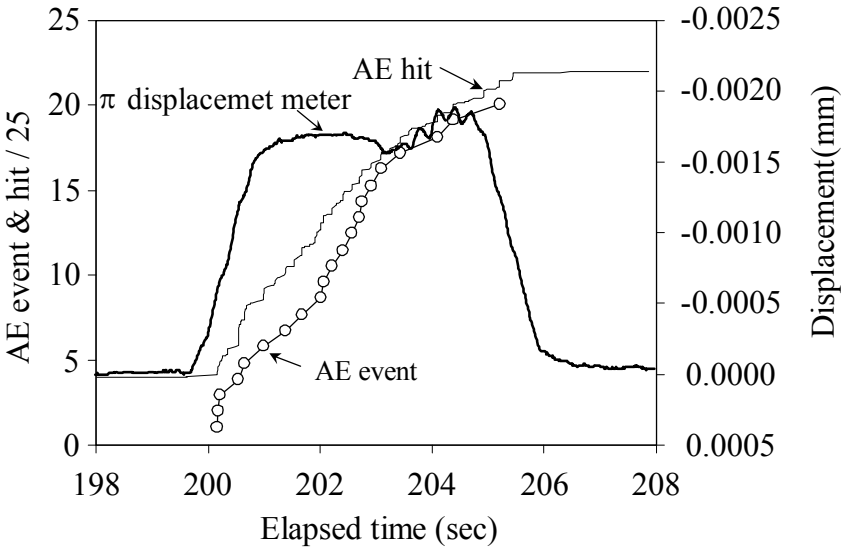

Fig. 14.11. AE activity and deformation with passing a train.

Acceleration monitoring under train passage

In order to know accelerations due to the train passage, accelerometers were placed in the gravity (vertical or axial) direction on the concrete pier. The frequency response of the accelerometer (750WI, TEAC) was from 3

Hz to 10 kHz. The acceleration signals were recorded in a signal recorder (GX-1, TEAC) with 500 Hz sampling frequency. In **Fig. 14.12**, a typical waveform of the acceleration and its frequency spectrum via FFT are shown. It is found that principal frequency components are distributed from 50 to 100 Hz. Since the lower-band frequency of AE system employed was 10 kHz, it was concluded that the frequency components of the acceleration due to the train passage are even lower than the frequency range of the AE system.

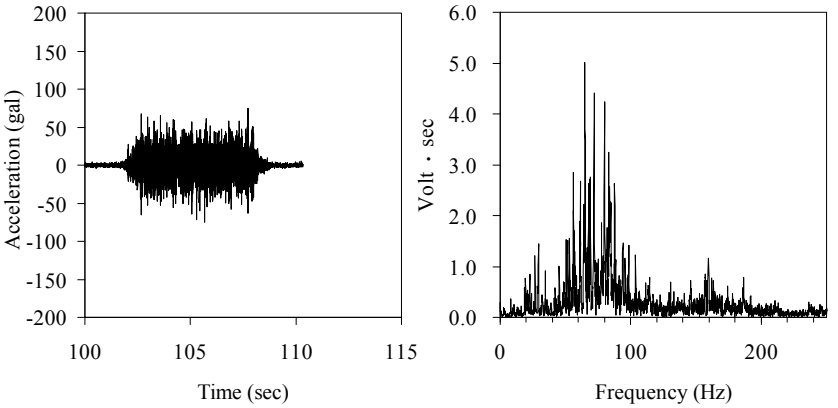

Fig. 14.12. A typical waveform of acceleration due to train passage.

AE monitoring of lower-frequency signals in a laboratory

In order to examine the response of the AE system for low-frequency AE phenomena, three forces of different frequencies: 30 Hz of 300 N, 40 Hz of 160 N and 50 Hz of 100 N were excited by a reaction-type shaker (Model F4/Z820WA, Wilcoxon Research, Inc.). The shaker was employed, because the driving frequencies were reproducible ranging from 10 Hz to 7.5 kHz. A brick wall was used as a propagation medium with a height of 1530 mm, a width of 1530 mm and a thickness of 430 mm. A brick (JIS type 2) was of dimensions 100 mm x 60 mm x 200 mm. The shaker was firmly stud-mounted on one side, and AE sensor of 60 kHz resonance (R6, PAC) was set on the other side of the brick wall with wax. With 430 mm propagation distance, AE signals were detected and recorded in the AE system with the same recording condition at the site mentioned above. The frequency response of the AE monitoring system ranged from 10 kHz to 10 MHz. It is noted that the experiment was preliminarily conducted by using higher frequency over 50 Hz. But the generated force

was not strong enough as to be detected. Thus, the frequencies lower than 50 Hz were driven in the experiments.

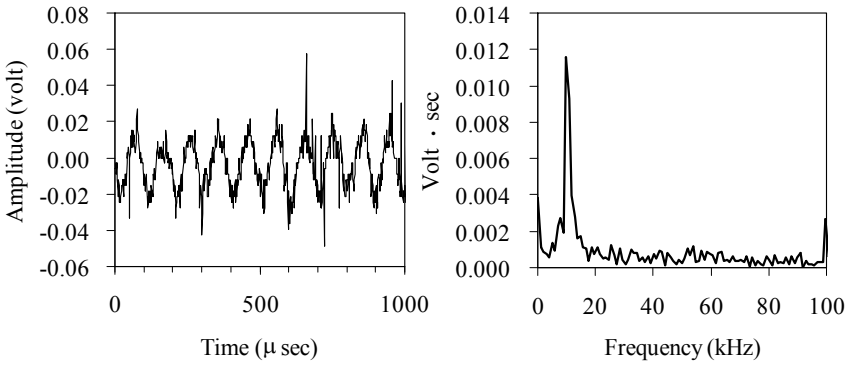

Fig. 14.13. A typical waveform and its frequency spectrum via FFT obtained by commercial AE system.

From result, it was found that frequency peaks were ranging from 7.8 kHz to 9.8 kHz even with excited by different frequencies from 30 Hz to 50 Hz. In **Fig. 14.13**, a typical waveform and its frequency spectrum via FFT in the case of 50 Hz drive are shown. A peak frequency is observed at 9.8 kHz. Obviously the peak frequency detected by the AE system is not identical to that of the excited force, but is considerably higher. This leads to the fact that train-induced dynamic impact readily generates AE activity, even though they might have lower frequency components as input signals. Therefore extraction of the secondary AE activity from all AE signals detected is necessary to evaluate the structural integrity of railway structures.

From these findings, two methods were considered to discriminate the noises and the secondary AE activity. One was the use of high-pass filter around 10 kHz, and the other was the spatial filter by means of source location algorithm. The former could be effective in only the case that structures have so many cracks that not only AE signals but also other higher frequency components attenuate during propagation. In the following, source location algorithm was found to be effective to elicit the secondary AE activity (Shiotani, Nakanishi et al. 2004).

14.3.2 Damage Evaluation

As given in Chapter 4, combination of the calm ratio and the RTRI ratio is known to be effective to estimate the structural damage in railway struc-

tures. In a cyclic fatigue test of a railway pier, the applicability of these indices was investigated in existing railway piers.

Experimental condition

To characterize AE activity during damage evolution, a railway pier of reinforced concrete (5.87 m high) , which was demolished after the test to construct underground structures for subways, was subjected to incremental cyclic-load test (Shiotani, Kobayashi et al. 2005). The cyclic load was controlled by the lateral displacement from the north direction with such a step-wise increment as 1, 2, 4, 8, 16, 32, 64, and 128 mm, applying two hydraulic jacks (maximum capacity of 392 kN). The tested pier and the sensor array are shown in **Fig. 14.14**. 16 AE sensors (60 kHz resonance; R6, PAC) covered the whole area of the pier, and 12 AE sensors (R6, PAC) placed locally onto the area in which stress concentration was expected. The former signals was processed and recorded with one AE system and the latter was analyzed by another. For other measurements, four strain-gauges were placed onto the four sides of the pier, and displacements on two sides of the north and the east side were measured via a laser displacement-meter. To measure internal stresses, a set of strain-gauges were attached to rebars located in four corners at three different heights of 400 mm, 1800 mm and 3200 mm from the ground. In addition to three-dimensional source location, one-dimensional source location was conducted to examine the feasibility.

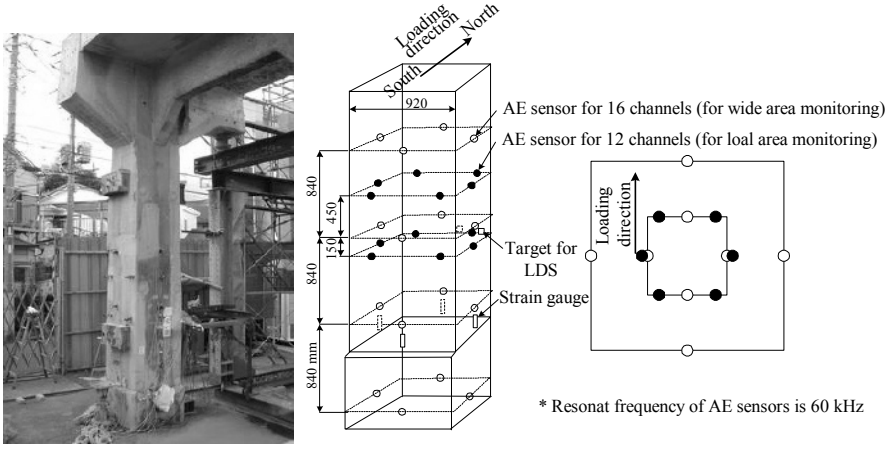

Fig. 14.14. Photo of measured railway pier of reinforced concrete (left) and sensor array (right).

General behavior

Relations between applied loads and the lateral displacements are shown in **Fig 14.15**. The onset of loading, the peak load and the termination of a loading cycle are denoted vertically by solid line, broken line and solid line, respectively. Up to 15000 sec elapsed, the load follows the responses of the lateral displacement. Then, the load decreases whereas the displacement is kept constant. This implies that fracture occurs either in the pier or the supporting ground. In **Fig. 14.16**, strains measured in rebars at height of 400 mm are shown. The strains of gauges 1 and 2 were installed in the south and those 3 and 4 were in the north. Since the displacement was given from the north, strains of gauges 3 and 4 show negative values implying compression and strains of gauges 1 and 2 reveal positive of tension. In strains of the gauge 2, a sudden increase is found at 16350 sec. elapsed.

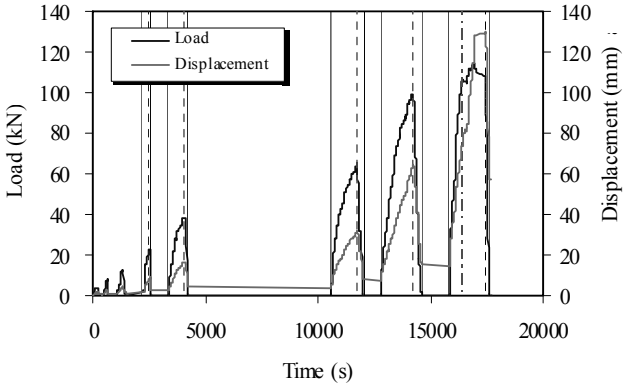

Fig. 14.15. Applied load and lateral displacement.

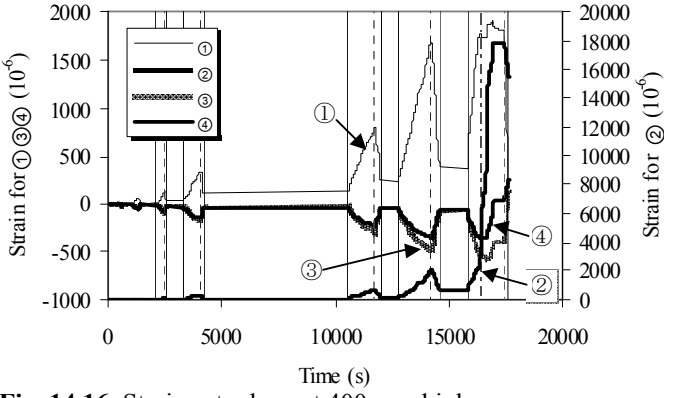

Fig. 14.16. Strains at rebars at 400 mm high.

According to a result of the strength test of rebar, the yield point was observed at 1500-1600 μ and the tensile strength was 2200-2300 μ. The strain at 16350 sec showed 2274 μ. It implies that this rebar had yielded and reached the tensile strength.

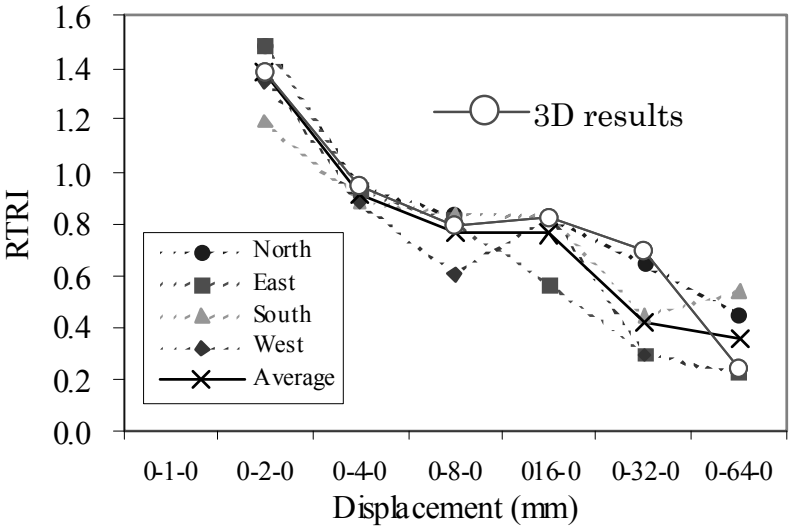

Fig. 14.17. Results of RTRI obtained from 1-D and 3-D analyses of AE locations.

AE activity

Results of RTRI on each surface obtained from one-dimensional (1-D) locations of AE sources as well as three-dimensional (3-D) locations are shown in **Fig. 14.17**. It is noted that since the RTRI obtained in each step denotes the damage condition in the previous stage. The figure shows the damage up to 64 mm displacement. At the first stage, the values quickly decrease due to displacement from 2 mm to 4 mm. But the values are still larger than 1.0 as the intact state. Meaningful decrease of the RTRI values are observed following 32 mm displacement. Since the values decrease lower than 0.8, it is considered that the pier was damaged seriously.

Comparing results obtained from AE events identified by 3-D locations with 1-D locations, the variations of RTRI values are similar as a function of given displacements. This leads to a finding that 1-D sources can provide the same useful information of damage as those of 3-D.

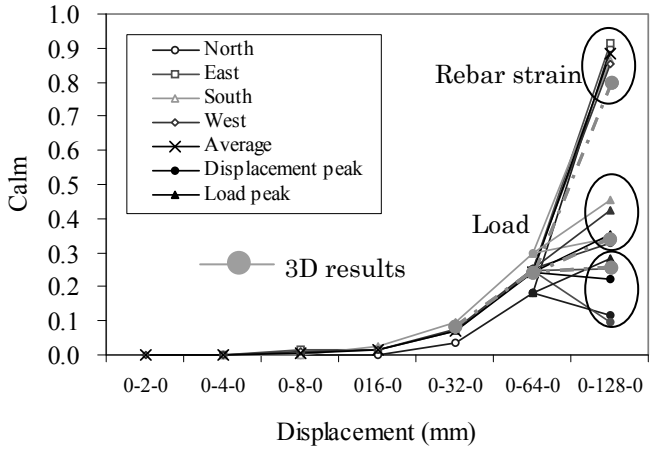

Fig. 14.18. Calm ratio obtained from 1-D and 3-D locations of AE events.

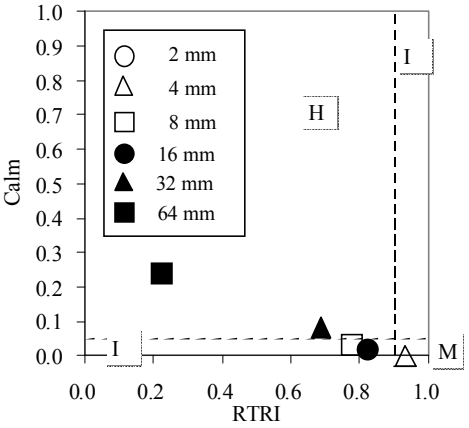

Fig. 14.19. Relations between the calm ratio and RTRI values.

Concerning the calm ratio, **Fig. 14.18** shows the variations of the calm ratios which vary in a similar manner to those in **Fig. 14.17**. In the case of the calm ratios, the damage was evaluated up to 128 mm displacement. It is noted in the figure that the calm ratios were calculated on the basis of three different behaviors of lateral displacement, applied load and rebar strain. From the figure, the calm ratios drastically increase after 32 mm lateral displacement. This trend agreed well with that of the RTRI values. At 128 mm displacement, considerable increase in the calm ratio is found in rebar but a slight increase is found for load and kept constant for displacement. Summarizing these results, it is found that the calm ratio based on the rebar-strain overestimates the damage. Therefore the calm ratio

based on either the load or the displacement is reasonable for estimation of the actual damage.

In **Fig. 14.19**, relations between the calm ratios and the RTRI values are plotted. In the graph, the criterion to qualify the damage (Ohtsu, Uchida et al., 2002) is given by broken lines. The zones denoted by H, I and M show the damage level as heavily damage (H), intermediate damage (I) and minor damage (M), respectively. Since the RTRI values up to 128 mm displacement could not be obtained, the two values calculated up to 64 mm lateral displacement are shown. From the criteria, the minor damage is qualified up to 4 mm displacement, the intermediate damages are evaluated between 8 mm and 16 mm displacements, and over 32 mm displacement heavily damage is assigned in the pier.

Application

In situ AE monitoring was performed in a pier (height x length x width = 5.5 m x 12.3 m x 2.6 m) of a railway bridge. The pier was made of plain concrete, and more than 70 years had passed since construction. During the service, the pier was deteriorated due to unexpected settlement, resulting macroscopic shear cracks. When the pier was tested, cracks observed were roughly repaired and traces were found along the crack. According to the document, a temporarily repair was conducted more than 10 years ago.

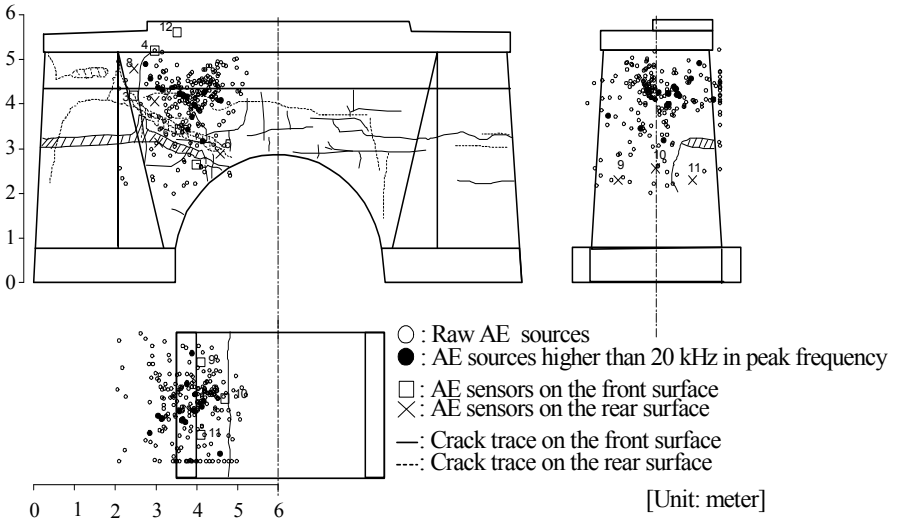

Fig. 14.20. AE sensor array and 3-D source locations of AE events in a concrete pier.

The site was located a suburb of Tokyo, and about 420 times of the train passages were repeated over the bridge in a day. Crack motions were measured by π-shaped displacement-meters. AE sensors arranged along one through-thickness shear crack are shown in **Fig. 14.20**. In the figure, results of AE source locations are also shown. 12 AE sensors with built-in preamplifier (R6I, PAC) were firmly fixed onto the pier surface with springs. AE monitoring condition was the same as the cyclic test mentioned above except for the threshold of 35 dB.

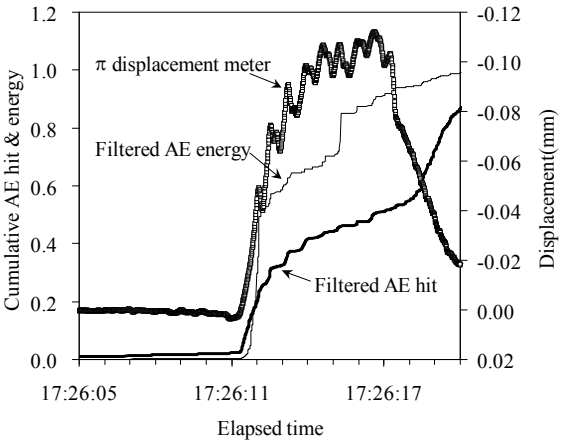

Fig. 14.21. AE activity with elapsed time along with deformations by π-shaped displacement-meter. Accumulated numbers of AE hits and AE energy are divided by 1029 and 20680, respectively.

AE activity with respect to elapsed time is drawn in **Fig. 14.21** along with deformations measured by the π-shaped displacement-meter. Filtered AE energy and hits with 20 kHz high-pass filter are shown. In the figure, sudden increases in AE energy and hits are observed with a slight delay following the increase in deformations.

Based on the detected AE activity and deformations by the π-displacement meter, the damage degree is qualified using the RTRI value and the calm ratio. Results are shown in **Fig. 14.22**. AE events from raw data are denoted with open circles (hit) and open triangles (energy), whereas those of high-pass filtering over 20 kHz are indicated by solid circles (hit) and solid triangles (energy). To simplify discussion, results on filtered AE activity are taken into consideration. AE activity is slightly varied, depending on parameters, but clearly shows that the calm ratios are large and the RTRI values are small. This suggested that the pier was heavily damaged.

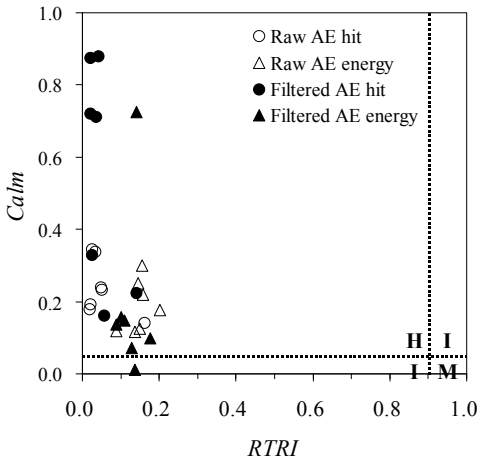

Fig. 14.22. Damage quantification with the calm ratio and the RTRI values. Dotted lines show the criteria for damage qualification. Labels H, I and M show heavy damage (H), intermediate damage (I) and minor damage (M), respectively.

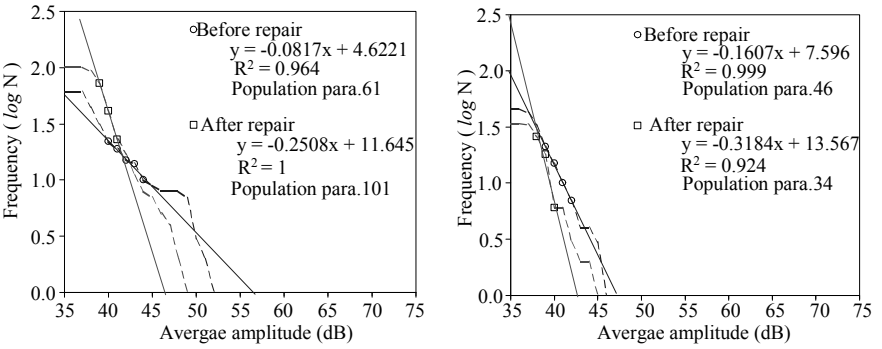

Fig. 14.23. Amplitude distributions in piers P3 (left) and P4 (right) on the basis of average peak amplitudes of all AE hits.

When obtaining the two indices of the calm ratio and the RTRI value, deformations should be incorporated with AE activity as loading process and unloading process when a train passes. However, there exists a difficult case to define these structural behaviors (Shiotani, Nakanishi et al. 2004). In this case, it is found that AE amplitude distributions, namely the b-value can give useful information of structural integrity. In **Fig. 14.23**, the amplitude distributions in two damaged piers of P3 and P4 are shown. In this case, AE monitoring was conducted along with the repair work by

epoxy injection. In the two piers, larger b-values (gradients of the curves) were obtained after repair work than before. It demonstrates that existing cracks responsible for AE generation become small after repair work. It is reported that the degree of damage can be classified with the Ib-value (Shiotani, Nakanishi et al. 2005), applying the following criterion;

- Serious damage: I*b*-values vary around 0.0 to 0.1,
- Intermediate damage: I*b*-values are between 0.1 and 0.2, and
- Intact or minor damage: I*b*-values are larger than 0.2.

14.3.3 Brick Arch

The damage evaluation for railway concrete structures can be applied to the brick structures (Shinomiya, Nakanishi et al. 2002). A photo of a continuous arch-bridge made of brick is shown in **Fig. 14.24**. At one span, a running crack was found as illustrated in **Fig. 14.25**. Six AE sensors of 60 kHz resonance (R6, PAC) were attached along the crack.

Fig. 14.24. Photo of a continuous arch bridge.

3-D locations of AE sources were obtained under train passage. This is because source characteristics of the secondary AE activity is investigated in relation with existing cracks. In a brick structure, high noises due to fretting between brick surfaces were expected. Thus, filtering was taken into account. Results of AE locations are shown in **Fig. 14.26**.

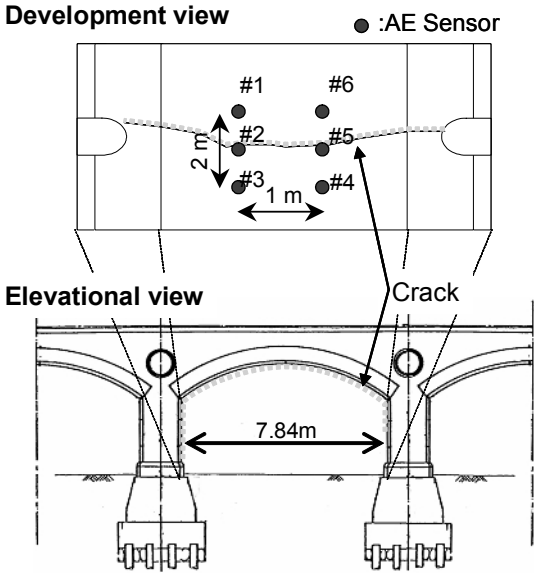

Fig. 14.25. An arch portion with a running crack and AE sensor array.

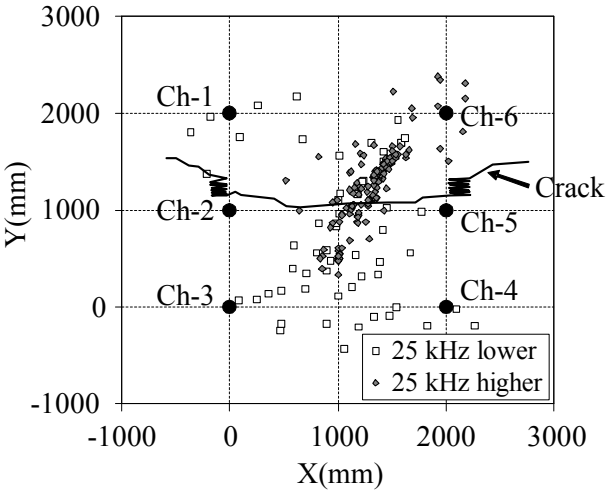

Fig. 14.26. Located AE sources with filtered effects.

It is found that AE events with 25 kHz high-pass filter are located close to the running crack. This suggests that AE sources are associated with the existing crack. In contrast, AE events with 25 kHz low-pass filter distribute widely, suggesting AE events due to fretting between bricks. Thus,

the secondary AE activity at the pre-existing crack is successfully detected in a brick structure.

14.4 Concluding Remarks

Applications to the substructures are extensively discussed. Results are really promising for actual monitoring and in situ observation. It is expected that a large amount of piers and foundations are already aged and damaged. Because the damages of these structures are not visually detected or readily identified by other techniques, AE technique could successfully contribute to monitor or inspect substructures.

References

Middendorp P, Reiding FJ (1988) Determination of discontinuities in piles by TNO integrity testing and signal matching techniques. Proc of the 3rd International Conference of the Application of Stress-Wave Theory to Piles, pp 33-43

Ohtsu M, Uchida M, Okamoto T, Yuyama S (2002) Damage assessment of reinforced concrete beams quantified by acoustic emission. ACI Structural Journal 99(4):411-417

Shinomiya T, Nakanishi Y, Morishima H, Shiotani T (2002) Damage diagnosis technique for brick structures using acoustic emission. Proceedings of 25th European Conference on Acoustic Emission Testing (EWGAE 2000), Czech Society of Non-destructive Testing, pp II/141-II/148

Shiotani T, Sakaino N, Ohtsu M, Shigeishi M (1997) Damage diagnosis of concrete-piles after earthquakes by acoustic emission. Proceedings of Fourth Far East Conference on Nondestructive Testing, KSNT, pp 579-588

Shiotani T, Shigeishi M, Ohtsu M (1999) Acoustic emission characteristics of concrete-piles. Elsevier Science, Construction and Buildings Materials 13:73-85

Shiotani T, Nakanishi Y, Iwaki K, Luo X, Haya H (2004) Evaluation of reinforcement in damaged railway concrete piers by means of acoustic emission. JSNDI, Progress in Acoustic Emission XII, pp 419-426

Shiotani T, Nakanishi Y, Luo X, Haya H, Inaba T (2004) Damage evaluation for railway structures by means of acoustic emission. Key Engineering Materials 270-273 Trans Tech Publications Ltd, Switzerland, pp 1622-1630

Shiotani T, Kobayashi K, Luo X, Haya H (2005) Damage quantification of railway concrete structures on the basis of AE monitoring. The Third US-Japan Symposium on Advancing Applications and Capabilities in NDE, ASNT, pp 328-334

Shiotani T, Nakanishi Y, Iwaki K, Luo X, Haya H (2006) Evaluation of reinforcement in damaged railway concrete piers by means of acoustic emission. AEWG, Journal of Acoustic Emission 23:260-271

Yuyama S, Okamoto T, Shigeishi M, Ohtsu M (1994) Quantitative evaluation and visualization of cracking process in reinforced concrete by a moment tensor analysis of acoustic emission. ASNT, Materials Evaluation 53:751-756

15 Wireless Sensing and Acoustic Emission Array Techniques

Christian U. Grosse

15.1 Wired and Wireless AE Equipment

So far, acoustic emission recording devices and data processing techniques have been described that are based on a wired transfer of data from the sensors to the pre-amplifier and to the AE recording unit. These systems are relatively expensive, vulnerable and time consuming to install. For this reason are applications for a long term monitoring of civil engineering structures rare and limited to eminent structures or objects with already known problems. However, there is a demand for routine applications of AE techniques after several disastrous events concerning buildings and bridges recently (see below). Moreover, developments in the construction design as well as demands from traffic and for a longer life time of structures call for a redesign of AE techniques that has to go hand in hand with a change of AE setup and data processing techniques also.

15.2 Necessity for a Continuous AE Sensing of Structures

Continuous structural health monitoring should provide data from a structure to better understand its structural performance and to predict its durability and remaining life time. In particular, the understanding of the structural performance becomes important at bridges that are more and more confronted with higher axle loads and higher train speeds as well as an increase of overall traffic due to the enlargement of the European Union. In this context a European Research Project was approved in the Sixth Framework Program called “Sustainable Bridges - Assessment for Future Traffic Demands and Longer Lives” [2007] where, among others, the Institute of Construction Materials of the University of Stuttgart is involved.

Another goal for an efficient monitoring approach to structures is safety. In Europe, many structures originate from the late 40ies or 50ies of the last century replacing structures destroyed during the Second World War. Many concrete bridges are designed for a typical lifetime of 60 to 80 years, what is reached or will be reached soon. Same is true for public buildings that were build using a variety of materials and material compositions. The sudden collapse of a training hall in Bad Reichenhall (Germany) in early January 2006 with the loss of 15 lives and the collapse of a new trade building in Katowice (Poland) several weeks later – more than 60 lost their lives – demonstrated these problems drastically. The collapse of a large highway bridge in 2007 in Minneapolis (USA) crossing the Mississippi River triggered also a discussion about the applicability and necessity for structural health monitoring including AET.

Finally, not only existing buildings are subjected to monitoring but also the construction process itself. Previously the contractor simply implemented a given design, but the current trend is for clients to commission certain performance requirements to be met with performance-based design. The emphasis of the industry is becoming the delivery of certain structural behavior states rather than simply building to a client's plan. The contracting process becomes the determination of the performance criteria, and delivery becomes a long-term fulfillment of these criteria. This can only take place if the performance states can be measured, and the measurement utilizes in a decision making process. The tools needed for both the evaluation of the delivery after construction and during operation are changing accordingly. The process is increasingly dependant on densely spaced sensor data, valid models to turn the data into physical behavior and decision making tools to determine whether the performance requirements are being met. Regarding proper sensing techniques there are new aspects of measuring structural performance and convert sensor data into useful information needed by stakeholders.

15.3 Basics of Monitoring Performance-based Structures

In a performance-based approach to build structures, all decisions, choices, and tradeoffs start with the required behavior-in-use rather than prescribed solutions for how to meet the stated needs. The supplier responds with an offering that includes the estimated performance of that offering. A validation method, through measurement, calculation, or testing, is necessary to evaluate the performance (over time) and to compare alternative solutions (Szigeti & Davis, 2005). The design/build team must warrantee and main-

tain structural performance to the level stated in the contract, for the extended duration of the contract. How that performance is established, verified and validated, is one of the areas that need further research. This requires measurement, hence sensors. This scenario opens a new perspective for overall optimal life-cycle management. A client may wish to measure the output values of ready made constructions; a contractor – on the other hand – may demonstrate the compliance to the required performance. The facility manager starts utilizing the performance data to optimize operation-phased maintenance and economy. Proactive interventions can be made when performance indicators start to deviate (e.g. Yanev 2003). Alarms can be generated based on deviations in the performance data, and repair plans augmented with actual real time data. The obvious needs for sensor generated data describe the reason for many efforts recently made to establish an entire new category of performance and condition monitoring services.

15.4 Sensors, MEMS and Motes

Traditionally the term sensor has been synonymous with transducer. However, a "sensor" will here be defined as comprising the traditional transduction elements along with substantial signal processing and computational ability (e.g. Glaser et al. 2005). These sensors can also be combined into comprehensive miniature sensing platforms incorporating transduction, signal processing, computational power, and wireless communication-platforms that are called Motes (e.g. Krüger et al. 2005; Grosse & Reinhardt 2007) (**Fig.15.1**, left).

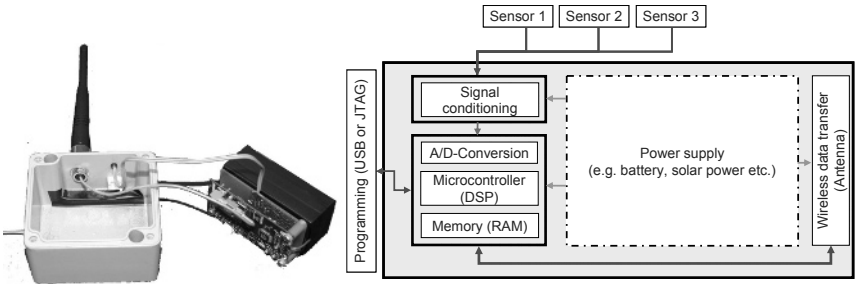

Fig. 15.1. Principle of a mote. Left: Mote including sensor and data processing board, radio transmission unit and antenna, container. Right: Concept of the sensor and data processing board.

Such a node is a complete, small measurement and communication system that has to be powered and cost optimized. It is composed of one or more sensors, a data acquisition and processing unit, a wireless transceiver and a battery power supply (**Fig. 15.1**, right). The acquisition and processing unit usually is equipped with a low power microcontroller offering an integrated analogue to digital converter (A/D) and sufficient data memory (RAM) to store the measurements. This unit also incorporates signal conditioning circuitry interfacing the sensors to the A/D.

Almost all types of sensors can be attached to such a sensor node as long as the power consumption is in relation to the purpose of the sensing system. Low-power sensors are first choice and that is the reason why micro-sensors called MEMS (micro electro-mechanical systems) are very attractive to be combined with such a system. MEMS are small integrated devices combining electrical and mechanical components that could be produced for about 50 € each. Because the process elements and internal linkage movements are now small, these MEMS-based transducers consume very little power. The low cost, low power and small size of MEMS-based transducers have revolutionized the way we can measure. This includes also the combination of sensor data and the formation of networks of sensors as well as combination with low power video techniques (VSLI cameras).

15.5 Sensor Networks and Protocols

Wireless sensor networks consist of many nodes (motes) having one or several different sensors on board. After the recording and a preliminary analysis of the data in the mote, the data has to be transmitted using, for example, a radio transmission system to a base station or supervisor for further data processing or proper generation of alarm messages. For the transmission of data using sensor nodes in a network of motes several topologies exist including the star and the multi-hop topology (Culler et al. 2003).

The main advantage of multi-hop techniques are the transmission power efficiency, because only a fraction of energy is necessary to transmit data compared to other techniques; the data are transmitted just to the next nodes and not necessarily to the sink. This reduces also the danger of interference since a node communicates only with a few others. However, this requires sophisticated network protocols including ad hoc configuration capabilities as well as self-configuration, calibration and encryption. As a

next step we have implemented a clustered multi-hop technology. Motes in a cluster (marked with a dashed circle in **Fig. 15.2**) share the data of all sensors attached to these motes. A pre-processing of the data is done in the cluster prior to transmission via the other clusters in the multi-hop network to the data sink (symbolized by the laptop in **Fig. 15.2**). This is the main advantage compared to telemetric systems where all data are transmitted. Intelligent data processing in the motes or clusters enables pattern recognition algorithms which can additionally reduce the power consumption. Only meaningful data are transmitted to the sink. The data sink is further extracting information out of the data using knowledge-based algorithms sending afterwards the information to the responsible person (construction engineer, owner) using automated email messages or short message systems of mobile phones.

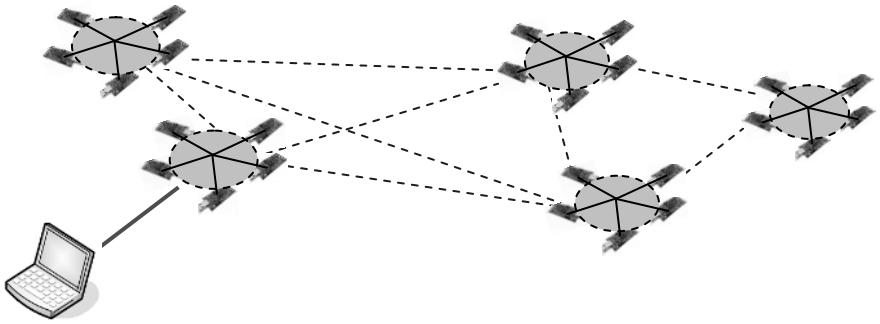

Fig. 15.2. Scheme of a multi-hop sensor network using clustered sensor nodes.

A sensing system based on wireless motes has several more advantages. Such a system is easy and cost efficient to be applied to structures. It can be used on one structure for a while and when or if the stakeholder decides to have enough data collected at this particular structural part the system can easily be deployed somewhere else. Additionally, a variety of sensors can be used to get information about the status of the structure. It is obviously very helpful not to base a structural health analysis on one physical quantity alone or on one sensor. The reliability of a monitoring system is fairly enhanced combining the information obtained at different sensor nodes. Further on, comparison of time series obtained by recording different physical quantities results in a drastic improvement of reliability and lowers the detection threshold of deterioration. Establishment of a correlation between data and structural performance is difficult and should be based on the data interpretation expertise of the user, implying a natural application of Bayesian statistics. Embedding some local processing capabilities within the sensor networks is desirable. For example, the tempera-

ture data gathered from numerous sensors could be fed into one or more other sensors on the network for processing. A weighted average could then be calculated and transmitted to the user, significantly reducing the amount of data flying around the network.

Finally, two other advantages of wireless sensor networks have to be stressed. Scalability can be an issue if the stakeholder wants to extend the monitoring area or need more data. Existing WSN techniques enables for self-organization of such networks so that sensor nodes can added or removed at any time without time consuming user guided reorganization of the WSN. Additionally, the implemented pre-processing algorithms might need an update from time to time to adjust to the user requirements or for a more efficient data reduction. Most of the developed sensor nodes have the capability to be reprogrammable, i.e. that the user can change the algorithms implemented in each sensor with the press of a button.

However, MEMS sensors are not available for all kind of applications regarding structural health monitoring in civil engineering. Therefore, sensor nodes are developed to enable *motes* to communicate with conventional sensors as well, i.e. in addition to MEMS. These sensing techniques are called hybrid sensor nodes. Although these sensors are low-power sensors, they will partly be replaced by MEMS as soon as they are available.

15.6 Hardware Developments

Separate boards for signal conditioning of strain and piezoelectric data (like acoustic emissions) have been developed by the University of Stuttgart in cooperation with EMPA (Eidgenössische Materialprüfanstalt, Switzerland). Implementation and development of the electric components, layout as well as manufacturing of prototypes is in progress. The boards are developed for a rough environment what included the implementation in sealed containers following the IP64/65 standards of water protection. As an energy source a high capacity 18 Ah battery was chosen at this stage of the project keeping in mind that it should be replaced by other techniques (solar power, energy harvesting techniques) depending on the application. In addition to the strain and piezoelectric data the ambient temperature and humidity can be measured by MEMS sensors implemented in the motes. A signal conditioning board for strain gage measurements was developed (**Fig. 15.3**) with the option of two parallel strain measurements at the same time. The board enables a full front-end for resistive sensors with temperature compensation, calibration and linearization (**Fig. 15.4**, right).

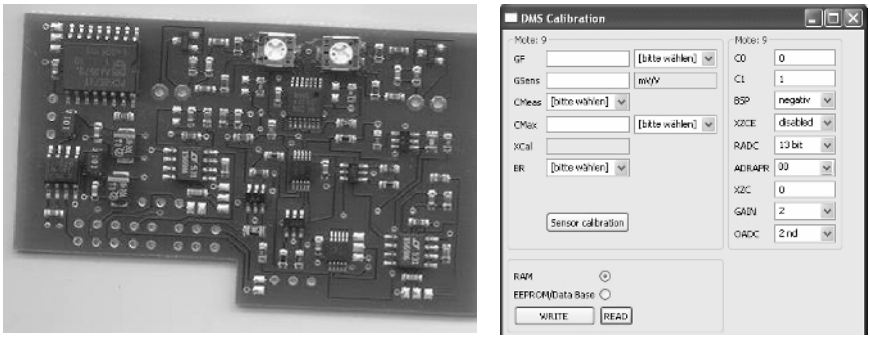

Fig. 15.3. Signal conditioning board for strain and developed graphical user interface.

Also a signal conditioning board for piezoelectric sensors was developed consisting of two channels per board with the opportunity to implement two boards in one sensor node. Each of the 4 channels can be filtered (high pass) and amplified individually. Antialiasing filters can be applied and a triggered recording of events is possible. Several modi to reduce the energy consumption are implemented as well. The A/D conversion is done using the TI microcontroller MSP430 from the mote. Comfortable user interfaces (GUI) were developed to control the devices. For first tests only one channel was used for acoustic emission (AE) monitoring (**Fig. 15.4**, left).

Fig. 15.4. "Concerto Bridge" in Brunswick equipped with wireless AE sensors (left) and with wireless strain sensors (right).

15.7 Monitoring Bridges Using Wireless Sensing Techniques

As a first test the equipment was installed for wireless measurements of strain and acoustic emissions during load at a large test facility (**Fig. 15.3**) of the *Technical University of Brunswick* in Northern Germany, and at a smaller structure of the University of Stuttgart. Since not all data of the large test are yet analyzed the test procedure of the small scale test as well as the implemented techniques will be described in the following.

The most common passive monitoring system involves acoustic monitoring, most commonly called acoustic emission (AE) (Grosse, Wanner et al. 2006). Acoustic emissions are elastic waves generated in conjunction with energy release during crack propagation and internal deformations in materials. Micro-structural changes or displacements occur very rapidly and can be produced by a wide variety of material responses to stress changes, from small scale changes within a crystal lattice structure to growth of macro-cracks. As stress waves propagate through a medium, the waveform shape is formed by the characteristics of the source, and affected by properties of the host material, and eventually the geometry of the host medium.

The primary tasks of an implemented AE system in WSN consists of signal detection, denoising, localization and other data analysis and signal characterization techniques as described in the following. This document does not give details of the data interpretation, because this will follow in another paper describing field tests. However, the interpretation will presumably be limited to an indication of a "zone of interest" further investigated by methods developed in and interpretation techniques based on results of ongoing work. It is expected that the correlation of the recorded AE data with the data obtained by each sensor (temperature, humidity, strain, etc.) will lead to further understanding of structural behavior. For example a cross-check of AE activity with increasing strain or with a sudden or abnormal increase of the ambient or inner structure temperature can give further insight into structural state. Such sensor data correlations will also decrease the amount of data transmitted after implementing intelligent data processing and correlation algorithms.

15.8 Signal Detection

The discrimination between noise and signals (from structure deterioration) is essential for failure monitoring. The environment (e.g. railway

bridges) is assumed to be very noisy. A noise analysis must be conducted using conventional hardware and sensors (broadband sensors) to characterize the frequency bands of noise at different bridges. This could be done during field tests at concrete, masonry and steel bridges separately. Algorithms to discriminate between signal and noise have to be developed and to be implemented into the motes. They could be based either on Fourier transforms or cross-correlations calculating the Magnitude Squared Coherence for example (Grosse, Glaser et al. 2006; Grosse & Reinhardt 2007) that was also described in Chap. 5. It is assumed that the AE signal form is governed by travel path effects which overpower signals from the fracture process, enabling for discrimination techniques. Denoising techniques and a waveform analysis can also help to detect signals and discriminate them.

15.8.1 Localization

There are diverse techniques for AE localization using very different algorithms. Most of the existing solutions are described in Chap. 6.2. Using AE techniques at civil engineering structures for monitoring rough and robust techniques are necessary like the "first hit" technique or planary techniques calculating 2D source coordinates. Traditional 3D-localization techniques are not implemented in wireless sensor networks because of processing time and power consumption from inter-array communications. In many cases, the signal-to-noise ratio is not good enough to apply 3D-localization. Other options are methods based on array techniques. Since sensor arrays are successfully used in seismology, array data analysis techniques were implemented in the described SHM motes. These techniques are now under test, requiring only data communication between motes in a cluster.

Fig. 15.5. Overview of setup for wireless AE measurements at the Stuttgart "ramp" (**left**) and wireless AE array setup (**right**).

15.8.2 Acoustic Emission Array Techniques

Acoustic emission experiments at a reinforced concrete bridge in Stuttgart-Vaihingen, Germany, have been set up to test and implement wireless acoustic emission techniques and in particular AE array techniques including localization, filtering (using wavelet techniques among others), beamforming, *f-k*-analysis, *VESPA*-processes.

A non-regular array consisting of eight wireless AE sensors was set up using the piezo-board described above (**Fig. 15.5**). Several routines were developed to record and establish robust data processing of acoustic emission data in the nodes. The recording and pre-processing in the motes was tested with a self-written GUI (**Fig. 15.6**). Artificial AE sources ("Hsu-Nielsen source" that is a procedure according to ASTM to break pencil leads) were used to test the soft- and hardware. These signals were recorded in up to ten meter distance from the central point of the array. Beamforming algorithms for AE signal detection were implemented similar to techniques used recently for data transmission in WLAN networks (IEEE 802.11n standard). Some features of these algorithms are described in the following section.

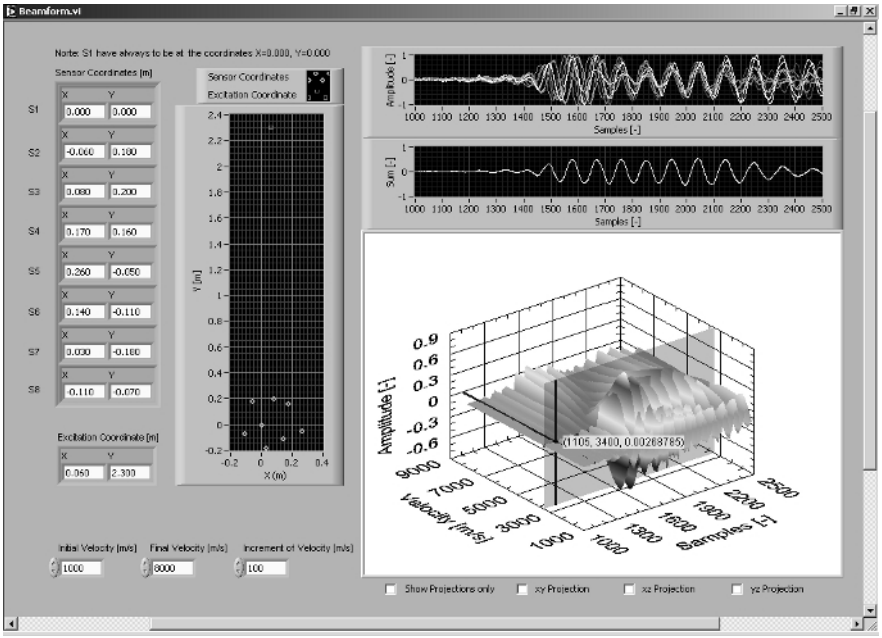

Fig. 15.6. Automatic recording and localization (left part of the figure) with red dots (green dots are the 8 sensors of the array) as well as the result of the beamforming for a certain triple point in the VESPAgram (see below).

15.8.3 Beamforming

A further step to apply acoustic emission analysis in a WSN is the implementation of beamforming techniques. Beamforming can be used to improve the signal-to-noise ratio of direct compression waves from known sources. It can furtheron be used do detect certain coherent signal phases if two or more are crossing the array and have to be discriminated. Finally it is useful for a rough localization of events. The principles of array techniques have been first developed for applications in electrical engineering e.g. for antenna or microphone arrays. In seismology, similar techniques were developed for the nuclear test ban treaty to monitor unusual seismic activity possibly originating from underground nuclear explosions.

The signal-to-noise ratio of a signal can be improved by stacking the coherent signals from each sensor after correcting for the different arrival or delay times. Therefore, the most important point during array beamforming is to find the best delay times for shifting the individual signals. A detailed description of the slowness can be found in the literature (Shearer 1999) while first ideas about application of these techniques are described in Grosse, Glaser et al. [2006] and in Grosse & Reinhardt [2007].

In the case that each channel (single-sensor recording) of an event is properly shifted in time for a certain back azimuth and slowness, all signals with the matching back azimuth and slowness will sum constructively. If more than one array is used a two-dimensional localization of the source of the incident wave is possible by calculating the point of intersection of at least two back azimuth lines in the plane of the sensor array. Beamforming techniques can also be applied to discriminate for a certain wave phase (Grosse et al. 2007). This is useful to detect wave modes hidden by reflected waves or in the coda of a preliminary wave or simply to discriminate between compressional and surface waves. For phase detection a 3D iteration problem has to be solved, iterating signal time, slowness, and amplitude.

Visual analysis can be done by generating a graph in the slowness-time domain, as shown in **Fig. 15.7** (upper graph). This example shows that phases with lower slowness of about $2*10^{-4}$ s/m arrives first at the array sensors than phases with a slowness of about $4*10^{-4}$ s/m. The first wave front with smaller amplitude is representing the compressional waves generated by the source traveling with a velocity above 4000 m/s. This phase is difficult to be detected in the time domain recordings at each sensor (eight traces in the lower part of **Fig. 15.7**). The slower wavefront following a few microseconds later with much larger amplitudes and a velocity around 2400 m/s is indicating the arrival of surface waves generated by the same source. Both wave types clearly are discriminated by using a novel

developed weighted VESPA (VElocity SPectral Analysis) technique (McLaskey et al. 2008). **Fig. 15.8** (lower graph) shows the result of such a VESPA process for one acoustic emission plotted in parallel with the beamforming array output (upper graph). In the lower graph the slowness values (right axis) are transformed into wave velocity values (left axis) for a better understanding. The P-wave arrives first at a velocity of about 4000 m/s while a stronger surface wave arrives at a later time and at a velocity of approximately 1800-2300 m/s. Reflections arrive after the direct P- and R-wave arrivals, but the beam power corresponding to these reflections is not as great as that corresponding to the direct wave phase arrivals because the variance scaled beam power formulation penalizes reflections because they are typically not as well correlated as those from the direct wave arrivals. Generally speaking, it is easy to determine the optimum slowness (wave velocity) for the delay and sum method for each phase (wave) out of such a graph.

15.9 Outlook

Condition control of building structures is a fundamental aspect in structural assessment business. In doing so NDT techniques are in principle applicable. Often the interpretation of condition control data is highly based on the level of experience of the engineers. To supplement the current inspection practice with a wireless sensor network system based on MEMS and hybrid sensors is currently under development. The network is equipped with motes and will be available for a very low budget. Since prototypes are already available, the system is now undergoing an optimization process regarding power consumption, data acquisition and data aggregation, signal analysis and data reduction.

Acoustic emission techniques can play a significant role for the monitoring of civil engineering structures since they are able to reveal hidden defects leading to structural failures long before a collapse occurs. However, most of the existing AE data analysis techniques seems not be appropriate for the requirements of a wireless network including distinct necessities for power consumption. The authors suggested with this paper approaches using array techniques. First tests showed promising results for both, reliable AE data analysis as well as power saving processes. Further developments based on this approach will show the efficiency of these techniques.

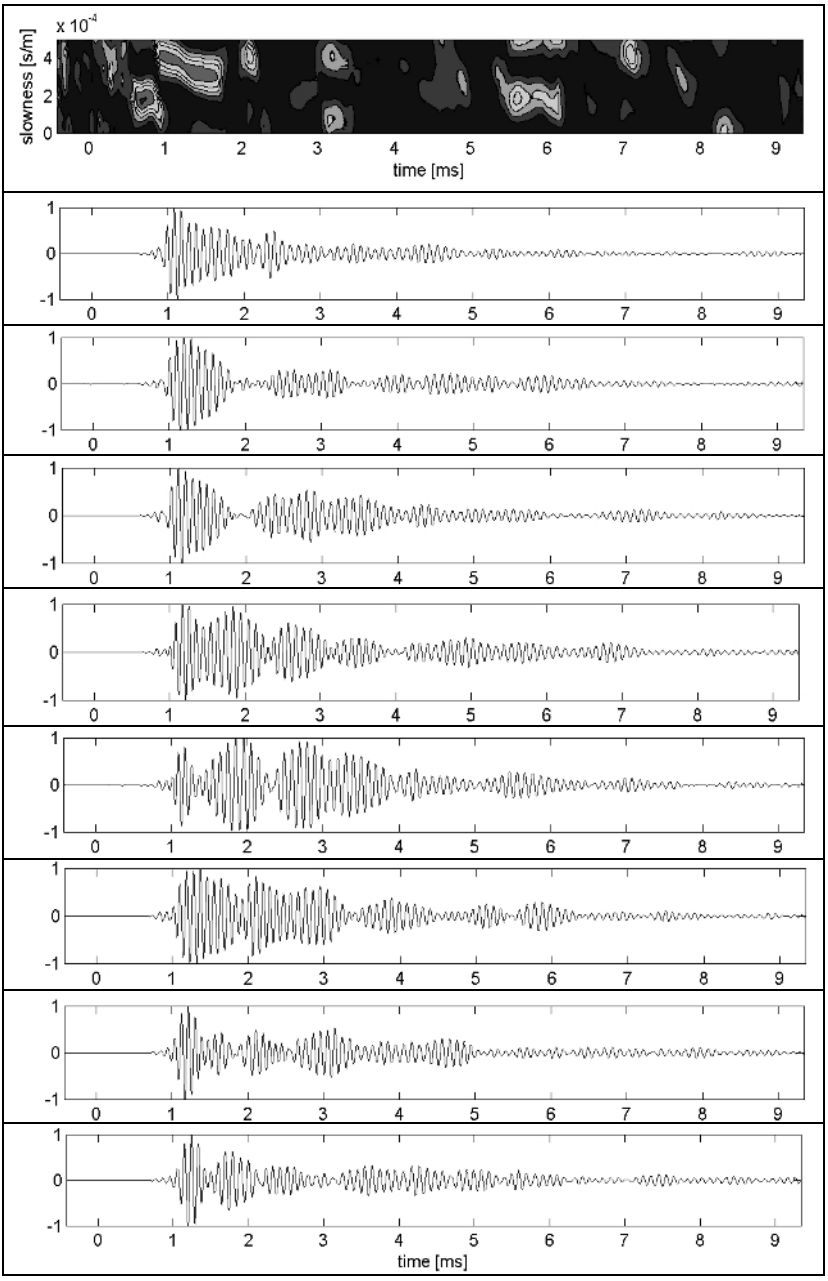

Fig. 15.7. Example of the detection of different wave types (compressional and surface waves) in the AE recordings of an eight channel sensor array using a weighted SN-VESPA process (diagram above the channels). By courtesy of Mr. P. Chatzichrisafis (Grosse et al. 2007).

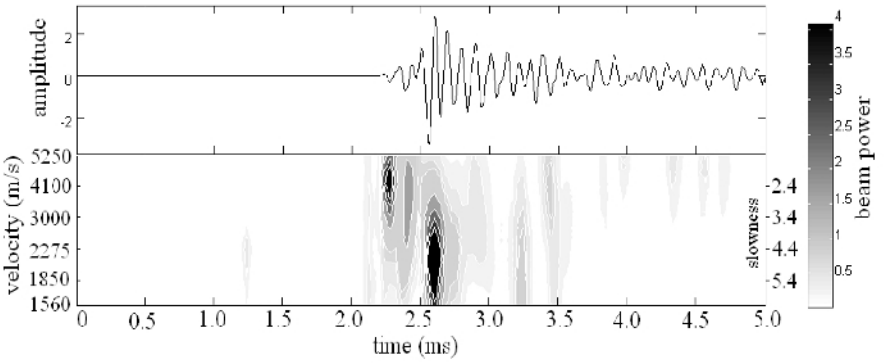

Fig. 15.8. Array output (top) and vespagram (bottom) for an AE event located 1.5 m from the sensor array (McLaskey et al. 2008).

References

Culler D, Woo A, Tong T (2003) Taming the Underlying Challenges of Reliable Multihop Routing in Sensor Networks. In: Proceedings of the First International Conference on Embedded Networked Sensor Systems

Glaser SD, Shoureshi R, Pescovitz D (2005) Future Sensing Systems. Smart Structures & Systems 1(1), pp 103 - 120

Grosse CU, Glaser SD, Krüger M (2006) Condition monitoring of concrete structures using wireless sensor networks and MEMS. Proc. SPIE 6174, Smart Structures and Materials 2006: Sensors and Smart Structures Technologies for Civil, Mechanical, and Aerospace Systems (eds Masayoshi Tomizuka, Chung-Bang Yun, Victor Giurgiutiu), pp 407-418

Grosse CU, Wanner A, Kurz JH, Linzer L (2006) Acoustic Emission. Chapter 1.1.2 in: Damage in Composite Materials - Simulation and Non-Destructive Evaluation (Busse et al. eds), Norderstedt: ISD-Verlag, pp 37-60

Grosse CU, Reinhardt HW (2007) A new concept for bridge monitoring using a wireless sensor network. Concrete Platform 2007, Belfast (in print) 13 p

Grosse CU, Krüger M, Chatzichrisafis P (2007) Acoustic emission techniques using wireless sensor networks. Proc. International Conference "Sustainable Bridges – Assessment for Future Traffic Demands and Longer Lives" (Bien et al. eds), Wrocław, Poland, Dolnoslaskie Wydawnictwo Edukacyjne publ., ISBN 978-83-7125-161-0, pp 191-200

Krüger M, Grosse CU, Marrón PJ (2005) Wireless structural health monitoring using MEMS. Key Engineering Mat. 293-294:625-634

McLaskey G, Grosse CU, Bachmaier S, Glaser SD, Krüger M (2008) Acoustic emission beamforming for enhanced damage detection. In: Sensors and Smart Structures Technologies for Civil, Mechanical, and Aerospace Systems 2008. Proceedings of SPIE 6932 (SPIE, Bellingham, WA 2008), paper 6932-119 (in print)

Shearer P (1999) Introduction to Seismology, Cambridge University Press, Cambridge, UK

Sustainable Bridges (2007) Sustainable Bridges – Assessment for Future Traffic Demands and Longer Lives, Integrated Project in the Sixth Framework Programme on Research, Technological Development and Demonstration of the European Union, FP6-PLT-001653, http://www.sustainablebridges.net

Szigeti F, Davis G (2005) Performance Based Building: Conceptual Framework. Final report. Performance Based Building Thematic Network, report "EUR 21990", EU 6th framework programme, ISBN 90-6363-051-4, 47 p.

Yanev B (2003) Structural Health Monitoring as a Bridge Management Tool. Structural Health Monitoring and Intelligent Infrastructure, pp 87-95

16 Opportunities, Limitations, Accuracy and Skill

Thomas Vogel, Barbara Schechinger

16.1 Introduction

This chapter tries to summarize experiences with acoustic emission (AE) of our own and of related projects from an application point of view. Only what worked under harsh practical conditions is stated. That is why many statements may be more cautious and less enthusiastic than they would be with an optimistic perspective of a basic researcher or a system developer. Nevertheless the authors believe that testing methods based on acoustic emission analysis (AE analysis) have a great potential for both condition assessment and monitoring of structures not only in the laboratory but also on site.

16.2 Opportunities and Limitations

16.2.1 General Characteristics of the AE Method

Different from other non-destructive testing methods AE analysis does not deal with a steady state but with a procedure that basically changes the condition of the structure. Therefore AE signals are unique; they cannot be reproduced and recordings cannot be repeated.

Condition survey can be achieved indirectly only by monitoring the change of a condition and by drawing conclusions hereof afterwards.

However, the weakness of the method for steady states is its strength for changing conditions and ongoing deterioration processes, because these can be monitored directly.

16.2.2 Properties of Wave Propagation

The propagation of elastic waves in a civil engineering structure depends on its geometry and shape as well as on the occurring construction elements. Each material has different properties of wave propagation (velocity, attenuation). Elements like reinforcement bars or prestressing tendons may lead to anisotropy and guided waves.

Energy is reflected by boundaries like conjunctions between materials, joints and open cracks or by the free surfaces. Their shape can be irregular and causes perturbations of the wave fronts. Aggregates and reinforcement bars have also a strong scattering effect on waves. The complexity of the recorded waveforms allows only the analysis of distinct parts of the signal, generally the interpretation of the first arrival of a wave.

Principally the composition of a structure is well known but too complex to be taken into account in detail for estimating all superposing phases. This is not necessary either; simplified models are used for source functions and wave propagation in the quantitative analysis. For concrete a homogeneous model is often an acceptable assumption.

The main limitation in applications of AE techniques in composite materials like concrete is the very high attenuation due to scattering of the waves that reduces the reach considerably. The reach achieved in practice depends also on the source energy and the sensitivity of the used sensors.

Table 16.1 gives an overview on practically achieved reaches in different application cases.

Obviously the practical reach depends also on the intended procedure of the signals. Pure counting of events will work for larger distances than localizing of the source or even more refined methods like the moment tensor inversion.

16.2.3 Distribution of Sensors

Besides the reach discussed in section 16.2.2 the sensor distribution has a great influence for quantitative AE methods like source localization.

The sensor distribution should be optimized for the expected source regions aiming at a good azimuthal coverage.

This may not be possible for structures where access to concrete surfaces is limited like bridges in operation (accessible from below only and not from the pavement), retaining walls, foundations, piles etc. In those cases accuracy in quantitative analysis results will decrease unless sensors are combined to an array.

Fig. 16.1 shows an example of a bridge subject to detection of wire breaks on the full length (Fricker and Vogel 2006). The sensors are placed at the edges of the hollow-core slab resulting in a transverse spacing of 6.50 m. The spacing in longitudinal direction reaches 8.30 m at the most.

Table 16.1. Reach of acoustic emission waves in different application cases

Material test specimen test site	Source Sensor type	Wave-type	Frequency	Reach [m]	Reference
Reinforced concrete, aggregates 0/16 mm uncracked beam laboratory	Pencil breaks various	Rayleigh-waves P-waves	< 50 kHz > 50 kHz -	1…> 2 < 1 0.3…0.6	(Köppel and Vogel 2000)
Prestressed concrete, aggregates 0/32 mm cracked beam open air test facility ETH Zurich	Concrete cracking Fuji KSB 250	P-waves	-	next crack	(Köppel and Vogel 2000)
Prestressed concrete, aggregates 0/32 mm Moesa bridge Roveredo CH	Wire breaks Pure Technologies Ltd.	Various	1–20 kHz	> 20	(Fricker and Vogel 2006)

16.2.4 Noise Sources

In the laboratory servo-controlled actuators and pumping stations have proven to disturb acoustic emission recording because they raise the noise level and eventually shield AE-events occurring simultaneously (**Fig. 16.3**).

On site the same effects may occur by other acoustic sources like traffic activities especially combined with uneven expansion joints, working activities (chipping hammer etc.) or operating machinery of any kind.

According to specific signal characteristics the recording system can be trained to distinguish signals in demand from deterioration by signals not in demand from noise sources (**Fig. 16.2**).

Unwanted signals are discarded in order not to charge the data storage and transmission facilities unnecessarily.

Filtering is less effective when expected data and noise are in the same frequency range or show similar wave characteristics.

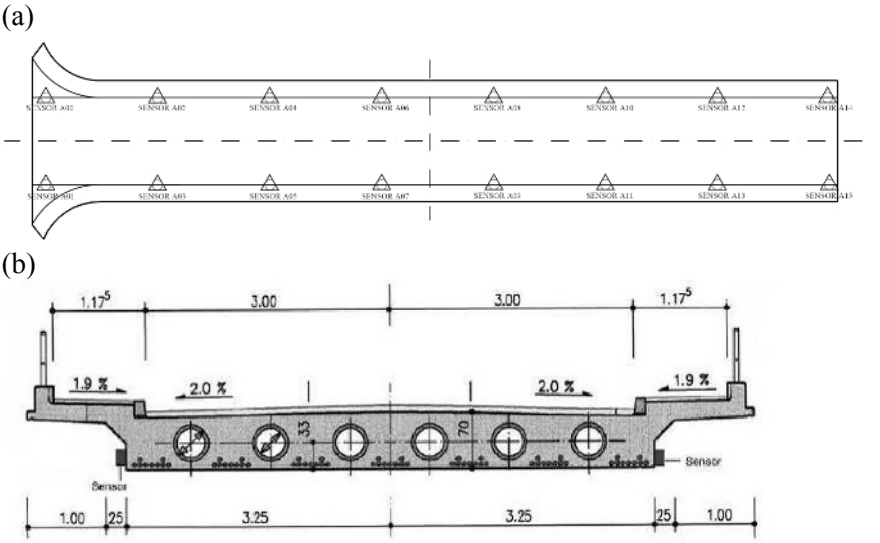

Fig. 16.1. Monitored bridge with sensor positions, from Fricker and Vogel [2006]; **(a)** plan, **(b)** cross section.

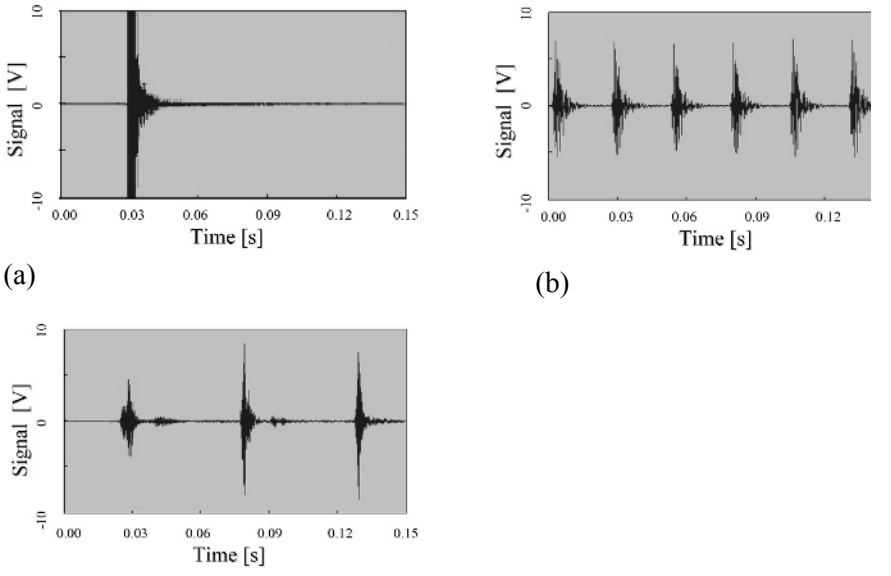

Fig. 16.2. Recorded signals from a prestressed concrete bridge due to different causes, from Fricker and Vogel [2006].
a) wire break, **b)** drilling **c)** chipping

16.2.5 Site Conditions

Sensor positions are chosen depending on the method to be applied, the area of the structure to be covered, the reach of the sensors, the expected sources and specific local conditions (cf. chapter 16.2.3). To keep the advantages of a non-destructive method, sensors are positioned not in the interior but on accessible surfaces of the structure. Unless wireless equipment is used, the wiring plays a dominant role in the concept of sensor positions, **Fig. 16.3** (a).

Normally sensors are either directly fixed onto the surface of the structure by hot glue or holders are glued which allow for clamping the sensors **Fig. 16.4** (a). Moisture, water and extreme temperatures may impede these operations.

Depending on the length of the measuring period and the use of the structure further conditions have to be taken into account, i.e. accessibility to personal in use, traffic, floods, storms, vandalism, etc.

Acquisition units need a dry and lockable room and electric power connection, preferably with the local power supply network, **Fig. 16.3** (b). For short term measurements simpler provisions may be adequate and mobile power sources may be an alternative but need provisions for a stable voltage, Fig. 16.4 (b). Access to the internet is a precondition for remote long-term monitoring.

(a)

(b)

Fig. 16.3. AE equipment for the detection of wire breaks, from (Fricker and Vogel 2006).
(a) Sensor and cabling in a conduit installed for that purpose.
(b) Acquisition unit in a rented room close to the monitored bridge.

(a) (b)

Fig. 16.4. AE equipment used in laboratory conditions and for a full-scale failure test outside of the laboratory, from Köppel and Vogel [2000].
(a) Sensors and wiring for a pull-out test in the laboratory.
(b) Acquisition unit protected against sun and rain by an umbrella.

16.2.6 Costs

Costs depend on three major factors: the amount of necessary equipment to cover the whole interesting area, the need for skilled personnel to interpret the produced data and – for monitoring purposes – the time the operation is expected to run.

As long as all sensors are individually connected with the acquisition unit, costs of the equipment depend merely on the number of applied sensors and the distances to be wired. The better the crucial zones of a structure can be identified the fewer sensors are necessary. Bus systems and wireless sensors may reduce the costs of wiring but the energy supply of wireless equipment has to be provided.

The more interpretation of the results can be automated the fewer costs incur for manually interpreting by engineers or natural scientists. Noise and valuable data can already be separated on site (cf. chapter 16.2.4). The interpretation of crucial findings will always remain a task for humans. A clear concept of information flow, threshold values and standard procedures for frequent situations can guarantee that only those persons are involved and produce costs that either can substantially contribute to decision processes or have to decide themselves.

For long-term applications the terms of contract for the equipment (buying or hiring) become important. Since some components of the measuring system are subject to further technical innovation, they are not reusable after the first application and have to be amortized over some few years. Buying may be more favorable than hiring and allows reducing the annual

costs once the equipment is amortized. On the other hand hiring may better allow benefiting from technical progress.

16.3 Accuracy

16.3.1 General

For interpreting the results the uncertainties of the applied AE method have to be known. They are influenced by measurement errors like picking uncertainties, an inadequate sensor distribution, too less sensors or systematic model errors. Artificial sources with known parameters can be used for testing the accuracy of an AE method.

Generally accuracy is higher under laboratory conditions than on site where more disturbances are faced. Laboratory tests are more controlled and have less noise. In laboratory tests greater accuracy can also be expected due to the smaller dimensions of the test specimens and smaller distances between AE sources and sensors. To record signals over long distances on site the used sensors should have a higher sensitivity and may be resonant in a lower frequency range. Accuracy is always related to the wavelength of the recorded signals. For localization e.g. the accuracy that can be achieved is in the range of the wave-length.

Analysis methods are expected to detect AE that are related to critical behavior of the structure with a high reliability. That means that close to all relevant signals should be recorded and measuring parameters, threshold values and the distance between sensors and sources have to be chosen appropriately.

Quantifying accuracy of AE analysis has to be linked with specific AE procedures. Some of these are treated subsequently.

16.3.2 Picking

Picking, i.e. determining the accurate onset time (arrival time of a certain phase of the wave front) at each sensor is a crucial procedure for many subsequent algorithms.

Picking accuracy depends on quality and frequency content of the signal. A high noise level and poorly covered frequency ranges can cause that onsets are not caught properly.

Picking may be executed manually by visually judging the waveform and identifying the arrival of a wave. This is a quite time consuming procedure and not applicable for a great number of signals.

There is a need to have reliable automatic tools for picking. Automatic pickers use more or less refined threshold criteria like fixed or floating thresholds using for instance the ratio of short time average (STA) and long time average (LTA) of the amplitude or energy based methods. Some methods are also used in geophysics; others were especially developed for AE analysis. More details are given in chapter 6 and in Schechinger and Vogel [2006].

In many cases a simple criterion is used to decide which signals should be stored for further analysis. By working off-line more refined criteria can be used. The results of subsequent procedures can give an indication on the quality of the picking.

16.3.3 Localization

The accuracy of localized events with known source position, i.e. artificial sources on a surface like pencil lead breaks, can be plotted as an error vector $\boldsymbol{r_s}$ connecting the calculated with the known position, **Fig. 16.5** (a). By converting the absolute values of the error vectors r_s into a density function an image of localization accuracy can be generated that allows for better interpretation, **Fig. 16.5** (b).

The main reasons for errors are imprecise onset times and the inhomogeneities of the material.

Wrong onset times (i.e. inaccurate picking) have a larger influence for sources outside the area or space formed by the sensor positions (cf chapter 6.3.5, **Fig. 16.6**). A variation of the assumed wave propagation velocity c_p changes the components of the error vector unevenly, **Fig. 16.6** (a), and obstacles on the wave propagation path like reinforcement bars lead to larger error vectors, **Fig. 16.6** (b).

In practical applications the real position of the source is not known. Nevertheless, the accuracy of localization can be estimated, when a signal is recorded by more than four sensors, by calculating the error of the source coordinates. These can be described as error ellipses in plane and as error ellipsoids in space, respectively (cf. chapter 6.3.5, **Fig. 6.14**). The accuracy of localization results can be used for judging the plausibility of mechanical processes (cf. chapter 6.4, **Fig. 6.17**).

Accuracy of localization reached in different real scale situations are shown in **Table 16.2**. It is quantified either by the absolute value of the localization error in cases where the source coordinates are known or by r_m

designating the mean radius of the error ellipse in cases where a statistical analysis could be executed.

In laboratory situations values within a few millimeter should be achieved, e.g. to follow cracking by localizing AE sources. In site applications, however, where larger structures are tested, accuracy in the centimeter- or decimeter range is sufficient.

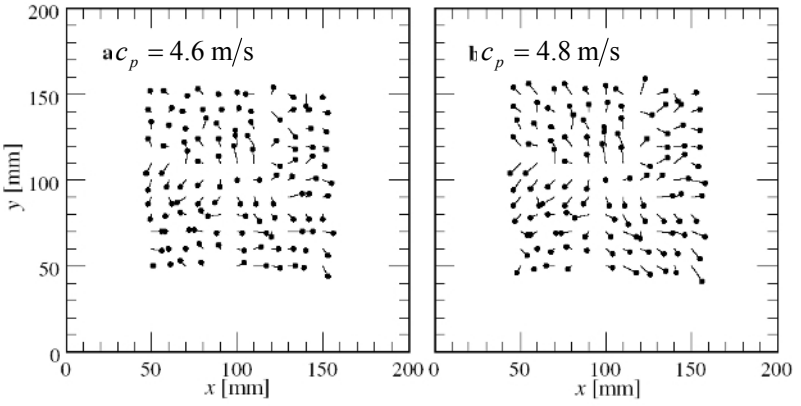

(a)

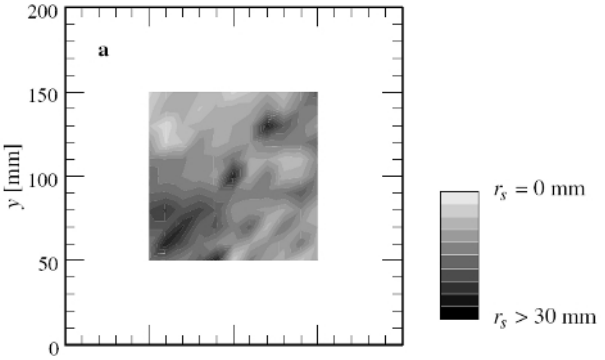

(b)

Fig. 16.5. Accuracy of localization with known source position, from Köppel and Vogel [2000].
(a) Error vectors rs for pencil breaks on the surface of a concrete cube with two different assumptions for the wave propagation velocity cp,
(b) Related density function for error values rs.

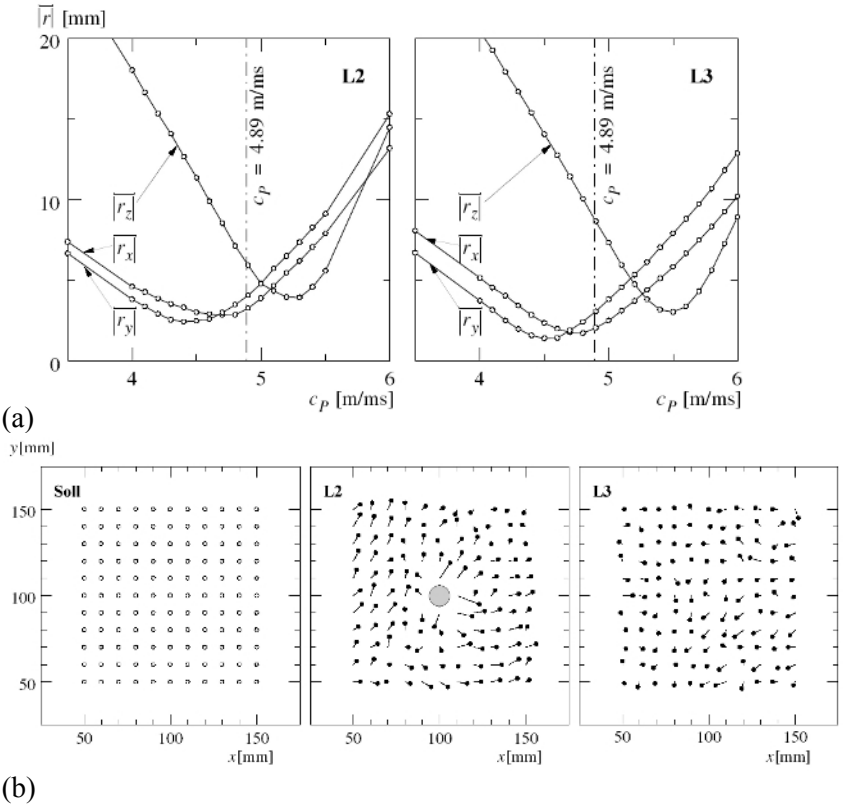

Fig. 16.6. Accuracy of localization with known source position, from Köppel [2002].
(a) Influence of a variation of the assumed wave propagation velocity on the three source coordinates for two different specimens L2 and L3.
(b) Influence of an embedded reinforcement bar (specimen L2) compared to plain concrete (specimen L3) on the error vectors.

16.3.4 Waveform Analysis

Waveforms are influenced by the characteristics of sensors and amplifiers. These must be known in order to be taken into account. Otherwise always the same measuring system has to be used and results are not comparable.

Since the propagation path plays a dominant role for the wave forms, it is difficult to extract source parameters. Condition changes in the material like cracking, changes of pore water content, degradation etc. may influ-

ence the recorded wave forms even if the source characteristics have not changed.

Table 16.2. Accuracy of the source localization in different application cases

Material test specimen test site	Source Sensor type	Procedure	Number of events (signals)	Accuracy	Reference
Prestressed concrete, aggregates 0/32 mm cracked beam open air test facility ETH Zurich	Concrete cracking Fuji KSB 250	signals recorded anywhere	1237000		Köppel and Vogel [2000]
		events recorded at 8 sensors	1'850 (100%)		
		automatically localized	159 (8.6%)	r_m < 15 mm	
		localized after manual picking	506 (27.4%)	r_m < 15 mm	
Unbonded tendons in concrete, aggregates 0/32 mm Huntington Railway Viaduct, UK	Wire breaks Pure Technologies Ltd.	Open tests	8 3 1 1	< 0.2 m < 0.5 m < 2.0 m not recorded	Tozer and Elliott [2000]
		Blind tests	6 4	< 0.2 m < 0.5 m	
Poorly grouted tendons in concrete, aggregates 0/32 mm Ponte Moesa, CH	Wire breaks Pure Technologies Ltd.	Blind tests	2	longitudinal 16-20 cm, transversal 26-66 cm	Fricker and Vogel [2006]

16.4 Skills

16.4.1 Planning of Tests

An indispensable precondition of the application of AE testing is a concept what incidents should be detected by the method and where they could appear. That requires a deeper understanding of

- the concept, the detailing and the performance of the structure
- the building materials concerned and their possible aging
- the possible failure mechanisms
- the required and the assumed safety level
- possible processes leading to detectable AE events.

The characteristics of wave propagation depending on energy level, frequency content and conditions along a possible wave propagation path form the basis to choose the appropriate method and adequate equipment.

Experience is necessary to estimate achievable reach and accuracy to design a suitable test set-up and to establish an optimal sensor arrangement.

16.4.2 Execution of Tests

Since AE occur due to irreversible processes tests cannot be repeated. That is why elaborateness is necessary in all stages of work. Placing sensors, wiring and tuning must be executed properly, because a malfunctioning or wrongly tuned sensor may not be detected before the tests have started.

Prior to measurements sensors and amplifiers are calibrated with artificial sources on the surface, measurement parameters like threshold values are set and set-ups are tested. All these procedures need experience that hardly can be formalized.

Data operation and storing ask for a systematic procedure, too. The large amount of data generated during a test can only be handled afterwards when properly named and sorted.

Spatial sense helps for recording the positions of the sensors and all localizing procedures.

16.4.3 Additional Required Skills on Site

Since most structures rise considerably above ground and the placement of sensors requires close access to almost all surfaces, scaffolds and lifts are used. They allow for safe operations, but do not prevent view to depth. That is why involved persons should not suffer from vertigo (**Fig. 16.7**).

In special cases it is more convenient to work with mountain climbing than with traditional construction site equipment requiring an according education and training of the involved staff (**Fig. 16.8**).

16.4.4 Analysis of Data

For recording, analysis and visualization of AE events powerful and flexible commercial software is available.

Fig. 16.7. Scaffold to access the soffit of a river bridge.

For more sophisticated analysis further tools can be developed which requires programming skills: In cases where existing procedures i.e. from geophysics are applied, these usually neither have a compatible data structure nor a suitable data range (km instead of mm, Hz instead of kHz). That means that output files from one procedure have to be converted into input files of the next one and data ranges should tried to be adjusted.

When the amount of data increases, these operations should be automatized by stack procedures. All these operations require related skills. If everything is automatized, however, a black box situation is created and nobody understands anymore what has really been done.

Since in research many procedures remain hand-operated an appropriate diligence and persistency is essential.

Like for all non-destructive testing methods there is a need to depict results in graphic form. Images have a large potential to discover both repetitions and abnormalities that would not be recognized in a pure numerical analysis. Imaging techniques need according special skills.

Fig. 16.8. Inspector climbing a structure using a double lanyard system, from (Federal Highway Administration 2005).

References

Federal Highway Administration (2005) Guidelines for the Installation, Inspection, Maintenance and Repair of Structural Supports for Highway Signs, Luminaries, and Traffic Signals. U.S. Dept. of Transp. http://www.fhwa.dot.gov/bridge/signinspection.cfm

Fricker S, Vogel T (2006) Site Installation and Testing of a Continuous Acoustic Monitoring. J Construction & Building Materials 21:501-510

Köppel S (2002) Acoustic emission analysis for the evaluation of concrete structures (in German). IBK report No 272, Institute of Structural Engineering ETH Zurich, vdf Zurich, p 174

Köppel S, Vogel T (2000) Acoustic emission analysis applied at tests with structural concrete (in German). IBK report No 259, Institute of Structural Engineering ETH Zurich, Birkhäuser Basel, p 164

Schechinger B, Vogel T (2006) Acoustic emission for monitoring a reinforced concrete beam subject to four-point-bending. J Construction & Building Materials 21:483-490

Tozser O, Elliott P (2000) Continuous Acoustic Monitoring of Prestressed Structures. In: Proceedings, 2000 Annual Conference Canadian Society of Civil Engineers – 3rd Structural Specialty Conference, London, Ontario.

Synonyms and often used Abbreviations

A/D	Analogue to digital converter
AE	Acoustic emission
AE analysis	Acoustic emission analysis or acoustic emission techniques
AIC	Akaike information criterion
ASTM	American Society for Testing and Materials
CEN	European Committee for Standardization
CLVD	Compensated linear vector dipole
CMOD	Crack-month opening displacement
DAS	Data acquisition system
DB	Dilatancy boundary
DC	Double-Couple
DFT	Discrete Fourier transformation
EDZ	Excavation disturbed zone
FDM	Finite difference method
FEM	Finite element method
FFT	Fast Fourier transformation
GUI	Graphical user interface
ISO	Isotropic component
JHD	Joint hypocenter determination
LMA	Long term average
MEMS	Micro electro mechanical systems
MS	Microseimic
MSC	Magnitude squared coherence
MTI	Moment tensor inversion
NDE	Non-destructive evaluation
NDT	Non-destructive testing
PDF	Propability density function
PMMA	Polymethylmethacrylat
PVDF	Polyvinylidene fluoride
P-Wave	Compressional wave
PZT	Lead zirconate titanate
RADAR	Radio Detection and Ranging
RC	Reinforced concrete
RMS	Root mean square
RMTI	Relative moment tensor inversion
S-Wave	Shear wave
S	Source function
SiGMA	Simplified Green's functions for moment tensor analysis
SEM	Scanning electron microscope
SM	Seismic moment
SRM	Standard reference material
STA	Short term average
TF	Transfer function
TR	Transient recorder
Tr	Trace (of a tensor)
URL	Underground research laboratory
UT	Ultrasonic test or ultrasonic testing
VESPA	Velocity spectral analysis
VRML	Virtual reality modeling language
WSN	Wireless sensor network

Index

1

1-dimensional (1-D) localization 103
1-dimensional localization 102, 123

2

2- or 3-dimensional localization 123
2-D localization 108
2-dimensional localization 103

3

3-D localization 105, 116
3-D velocity model 136

A

A/D(analog to digital) conversion 36
absolute calibration 30
accessibility 378
Accuracy 380
acoustic coupling 197
acoustic impedance 31
advantages of AE 5
AEWG 15
aggregate-restraint 208
Amplitude 40
amplitude distribution 209, 352
  b value 210
Amplitude Distribution 46
anisotropy 375
Anti-aliasing filter 37
apparent velocity 110
array localization
  array aperture 109
  sensor array 109
  Sensor array 111
Array localization 108
arrival time 105, 119, 122
arrival-time difference 37, 198
attenuation 36, 375
  Q value 36
automatic 97
automatic onset detection 96
automatic onset determination 101
automatic picker 98
automatic picking 97
automatized 386
average frequency 45, 199, 217
Average frequency 42

B

back-azimuth 109, 111, 114, 116
band-pass filter 200
beam forming 111
  beam packing 112
  beampacking 114, 115
  energy of the beam 112
  f-k analysis 113, 114, 115
  frequency wavenumber analysis 112
bending load 317, 318
bending test 181, 318
bending-mode failure 211
bending-moment 324
bottom steel 327
bottom steel slab 328
breeding water 204
brick 344
Brick 353
bridge construction 327
Burgers vector 153
buried pulse 147, 170
burst signal 4
b-value 46, 352

C

calibrated 385
calibration coefficient 175
calm ratio 44, 213, 320, 321, 328, 349, 351, 352
capacitive sensor 20
capacitive transducer 29
capillary break 30, 150

cast-in-place concrete pile 334
circle method 104
CMOD 214
composite floor slab 327
concrete bridge 324
concrete pier 342
concrete pile 332
concrete structure 314
conical transducer 27
consistency 204
constitutive behavior 5
contact time 30
Continuous emission 4
corrosion 214, 225
Costs 379
count 37, 198
Count/ring-down count 40
Counts to Peak 40
couplant 31
couple force 161
  double couple 161
crack 125, 127
crack kinematics 160
crack kinetics 157, 159
crack volume 154
creep strain 209
Curie point 34
cyclic bending test 319

D

damage evolution 186
damage mechanics 221
  damage evolution 221
  damage parameter 221
damage parameter 186
damage tensor 158
dB (decibels) 35
dead time 39
debonding 155
delta function 21, 145
diagonal crack 212, 225
differential evolution algorithm 132
dip plane 180
dipole force 160
dislocation 153
double-couple model 163
double-difference method 132, 133
duration 37, 198
Duration 41

E

earthquake 7
ed concrete building
  concrete 316, 317
  shear 316, 317
  tensile 317
eigenstrain 158
eigenvalue analyses
  eigenvalues 180
eigenvalue analysis 177
eigenvalues analyses
  eigenvalues 177
elastic wave 17, 19
  dispersive wave 142
  guided wave 17
  Lamb wave 17
  Love wave 17
  P wave 17, 148
  Rayleigh wave 17
  S wave 17, 148
  sonic wave 17
  SP wave 148
  ultrasonic wave 17
electro-magnetic noise 35
empirical Green's function 158
energy 37, 198
Energy 41
energy released 6
energy-moment 198
epicenter 104, 105
error ellipsoid 118, 123, 135
event 37, 198
event-counting 213
EWGAE 15

F

face-to-face 31
Far-field seismology 7
fatigue crack 325
fatigue damage 327
fatigue deterioration 324
fatigue loading 327, 328
Felicity ratio 43
Filtering 376
flat frequency response 9
floor slab 321, 322
Fourier transform 21, 156
four-point-bending test 127
fracture energy 307

fracture process zone 224
free vibration 23
Frequency 42
Frequency centroid 42
frequency spectrum 37, 198
friction process 6

G

gain 16
Gauss's integral theorem 143
generalized theory 146
geophysics 386
girder bridge 317
grid search 106, 135
  localization procedure for wood 106
guided waves 375

H

half-cell potential 216
  C.S.E 216
high-pass filter 345, 351, 354
hit 37, 198
Hit 40
hit-lockout time 39
Hooke's Law 5
hybrid method 133
hydro-fracturing 180
hyperbola 119
hyperbola method 104
hypocenter 105, 106
hypocentre 116

I

IAES 15
improved *b*-value 46
infrastructure 314
  bridge 314
  building 314
inhomogeneities 381
inhomogenities 125
Initial frequency 42
in-plane motion 192
inverse Fourier transform 156
inverse problem 95
iterative localization 122, 123, 124, 125
  accuracy 123
  density functions 124
  iterative linearized localization 118
  Reliability 123

J

joint hypocentre determination 132
Joint hypocentre determination 131
JSNDI 15

K

Kaiser effect 13, 213, 317, 319, 320
Kaiser Effect 43
kinematics 166
kinetics 166

L

L_1 norm 106
L_2 norm 106
Lamb wave 142
Lamb's problem 146, 147
Lamb's solution 29, 31, 170
laser vibrometer 30
leakage test 187
linearization 116
load ratio 44, 213, 320, 321
localization 6, 100, 375
  localization accuracy 120, 129, 131
  Localization accuracy 119
  localization algorithms 105
  nonlinear localization 134, 135
localization error 118, 122, 123
  spatial error 121
Localization errors 118
long-term monitoring 378
low-pass filter 354

M

main amplifier 200
Martensite transformation 11
martensite transformations 12
masonry building 315
  structure 315
maximum amplitude 198
mercury intrusion method 219
Micro-Electro-Mechanical Systems 9
micro-seismic activity 12
microseismicity 7

micro-seismology 8
Mindlin's solutions 22
mixture proportion 203
moment tensor inversion 169
monitoring 104

N

near-field seismology 7
NIST 27
nonlinear methods 132
non-slump concrete 205

O

One-dimensional location 338
onset 95, 98, 100, 101
onset time 380
optical fiber sensor 34
origin time 95
out-of-plane motion 182
over-reinforced 212

P

P wave 172
Parameter 39, 40
parameter-based AET 9
passage 350
peak amplitude 37
Peak frequency 42
pencil-lead break 30, 150, 158
penny-shaped tensile crack 155
picker 100
pickers 97
picking 97
Picking 380
pier 350
piezoelectric effect 19
pile 332
Pile 332
planar localization 103
point source 95, 116
pore distribution 219
post analysis 186, 192
pre-amplifier 200
probabilistic inversion 134
propagation 383
pull-push model 166

R

RA value 42, 45, 199, 217
RADAR 6
Railway 341
railway bridge 350
railway pier 346
rainfall 215
rate process 218
Rayleigh wave 150
receiver 96
reciprocity method 29
reflection coefficient 174
reinforced concrete (RC) 317
  bridge 317
reinforced concrete bridge 321
reinforced concrete building 315, 316
  concrete 315
  shear 315
  tensile 315, 316
reinforced concrete girder 320
reinforced concrete slab 327
reinforced concrete structure 320
reinforcing-steel rod 323
Relative localization 131
relocalization 133
reproducible 6
residuals 105, 106, 116, 117, 122, 123
resonance 22, 23
  Nominal resonance 23
Resonant transducer 9
Reverberation frequency 42
rise time 37, 198
Rise time 41
RMS (root mean square) voltage 37, 198
road bridge 318, 322
Robinson-type steel-concrete composite floor slab 328
rock-bursts 11
Roller-compacted concrete 204
RTRI 348, 349, 350, 351, 352
RTRI ratio 44, 345

S

S wave 172
sampling rate 40
scanning 3
scattering 375
secondary AE activity 341, 355

seismic wave 7
seismogram 7
seismology 7
self-restraint 208
SEM 218
sensitivity 375
sensor array 115
sensor distribution 375
sensor output ratio 321
shear-mode failure 212
signal characteristic 4
signal envelope 41
signal-to-noise 16
signal-to-noise ratio 6
Site conditions 377
Skills 384
slowness 110, 111, 112, 114
Snell's law 172
source 96, 108
  source coordinates 107
source coordinates 118, 134
source localization 122, 123, 127
  earthquake source localization 95
  source coordinates 95
source time 105
source-time function 154
SP wave 172
spatial filter 200, 345
split 154
standard source 197, 201
steel box-girder 324
Steel bridge 324
steel frame 318
steel member 324
steel mold 327
steel plate 327
steel side plate 327
steel slab 324
steel structure
  concrete 314
  fatigue 314
  structure 314
  traffic 314
Steel structure 314
steel-concrete composite 327
steel-concrete composite slab 327, 328
steel-slab 325
strain energy release rate 309
Substructure 332
superstructure 320, 321, 324, 329
superstructures
  bridge 315
  building 315
  concrete 315
  steel 315
  traffic 315
surface crack 225
surface pulse 147

T

tension-softening 224
the secondary AE activity 342, 345
three-point-bending test 126
threshold 39, 40
threshold level 198, 200, 213
tin-cry 11
traffic control 322
traffic load 44, 321, 323, 325, 329
Train 342
train passage 342, 343
training 385
transfer function 22
travel time 105, 116, 135
two-dimensional (2-D) problem 182
  in-plane motion 182
  out-of-plane motion 182

U

ultrasound 6
under-reinforced 212

V

VC test 204
VC value 204
VRML 189, 192, 225

W

water leakage 192
wave propagation 375
Waveforms 383
waveguide 29
weight matrix 117
wire breaks 375
wood 302
  structure 302
  ultrasonic properties 303

X

X-Ray 6

Z

zone location method 102